Advances in
INORGANIC CHEMISTRY

EDITED BY

Rudi van Eldik

University of Erlangen-Nürnberg
Erlangen
Germany

Jeremy Harvey

University of Bristol
Bristol
United Kingdom

VOLUME 62: Theoretical and Computational Inorganic Chemistry

ELSEVIER

Amsterdam • Boston • Heidelberg • London • New York • Oxford
Paris • San Diego • San Francisco • Singapore • Sydney • Tokyo
Academic Press is an imprint of Elsevier

ACADEMIC
PRESS

Academic Press is an imprint of Elsevier
32 Jamestown Road, London NW1 7BY, UK
Radarweg 29, PO Box 211, 1000 AE Amsterdam, The Netherlands
30 Corporate Drive, Suite 400, Burlington, MA 01803, USA
525 B Street, Suite 1900, San Diego, CA 92101-4495, USA

First edition 2010

Library of Congress Cataloging-in-Publication Data
A catalog record for this book is available from the Library of Congress

British Library Cataloguing in Publication Data
A catalogue record for this book is available from the British Library

ISBN: 978-0-12-380874-5
ISSN: 0898-8838

Printed and bound in USA

10 11 12 13 14 10 9 8 7 6 5 4 3 2 1

LIST OF CONTRIBUTORS

William Ames
Institut für Physikalische und Theoretische Chemie, Universität Bonn, Bonn, Germany

Marc Brüssel
Wilhelm-Ostwald Institut für Physikalische und Theoretische Chemie, Universität Leipzig, Leipzig, Germany

Gemma Christian
Institut für Physikalische und Theoretische Chemie, Universität Bonn, Bonn, Germany

Aleix Comas-Vives
Departament de Química, Universitat Autònoma de Barcelona, Bellaterra, Catalonia, Spain

Robert J. Deeth
Department of Chemistry, Inorganic Computational Chemistry Group, University of Warwick, Coventry, United Kingdom

E. Hey-Hawkins
Institut für Anorganische Chemie, Universität Leipzig, Leipzig, Germany

Thomas S. Hofer
Theoretical Chemistry Division, Institute of General, Inorganic and Theoretical Chemistry, University of Innsbruck, Innsbruck, Austria

Vidar R. Jensen
Department of Chemistry, University of Bergen, Bergen, Norway

Mario Kampa
Institut für Physikalische und Theoretische Chemie, Universität Bonn, Bonn, Germany

Barbara Kirchner
Wilhelm-Ostwald Institut für Physikalische und Theoretische Chemie, Universität Leipzig, Leipzig, Germany

Dimitrios G. Liakos
Institut für Physikalische und Theoretische Chemie, Universität Bonn, Bonn, Germany

Agustí Lledós
Departament de Química, Universitat Autònoma de Barcelona, Bellaterra, Catalonia, Spain

Aurora Martinez
Department of Biomedicine, University of Bergen, Bergen, Norway

Russell G. Mckinlay
Department of Chemistry, School of Engineering and Physical Sciences, Heriot-Watt University, Edinburgh, Scotland

Frank Neese
Institut für Physikalische und Theoretische Chemie, Universität Bonn, Bonn, Germany

Elaine Olsson
Department of Chemistry, University of Bergen, Bergen, Norway

Dimitrios A. Pantazis
Institut für Physikalische und Theoretische Chemie, Universität Bonn, Bonn, Germany

Martin J. Paterson
Department of Chemistry, School of Engineering and Physical Sciences, Heriot-Watt University, Edinburgh, Scotland

Maren Podewitz
Laboratorium für Physikalische Chemie, ETH Zurich, Zurich, Switzerland

Andreas B. Pribil
Theoretical Chemistry Division, Institute of General, Inorganic and Theoretical Chemistry, University of Innsbruck, Innsbruck, Austria

Bernhard R. Randolf
Theoretical Chemistry Division, Institute of General, Inorganic and Theoretical Chemistry, University of Innsbruck, Innsbruck, Austria

Markus Reiher
Laboratorium für Physikalische Chemie, ETH Zurich, Zurich, Switzerland

Bernd M. Rode
Theoretical Chemistry Division, Institute of General, Inorganic and Theoretical Chemistry, University of Innsbruck, Innsbruck, Austria

Michael Roemelt
Institut für Physikalische und Theoretische Chemie, Universität Bonn, Bonn, Germany

James R. Rustad
Department of Geology, University of California, Davis, CA, USA

Michael Seth
Department of Chemistry, University of Calgary, Calgary, AB, Canada

Tatyana E. Shubina
Computer-Chemie-Centrum and Interdisciplinary Center for Molecular Materials, Friedrich-Alexander-Universität Erlangen-Nürnberg, Erlangen, Germany

Panida Surawatanawong
Institut für Physikalische und Theoretische Chemie, Universität Bonn, Bonn, Germany

Knut Teigen
Department of Biomedicine, University of Bergen, Bergen, Norway

Gregori Ujaque
Departament de Química, Universitat Autònoma de Barcelona, Bellaterra, Catalonia, Spain

Shengfa Ye
Institut für Physikalische und Theoretische Chemie, Universität Bonn, Bonn, Germany

Stefan Zahn
Wilhelm-Ostwald Institut für Physikalische und Theoretische Chemie, Universität Leipzig, Leipzig, Germany

Tom Ziegler
Department of Chemistry, University of Calgary, Calgary, AB, Canada

Justyna M. Żurek
Department of Chemistry, School of Engineering and Physical Sciences, Heriot-Watt University, Edinburgh, Scotland

PREFACE

Volume 62 of Advances in Inorganic Chemistry is a thematic issue dedicated to Theoretical and Computational Inorganic and Bioinorganic Chemistry. Theory has always played an important role in inorganic chemistry, and with developments in computer power, computation now routinely provides valuable insight to the field in many different ways. This volume includes contributions highlighting the role of computation in a broad spectrum of inorganic chemistry, though inevitably many important subfields have been neglected. We hope it will prove interesting and inspiring to both computational and experimental researchers in the field.

Chapter 1, by Robert J. Deeth, reviews recent developments in the use of molecular mechanics force fields for transition metal compounds, covering both the theory of including crystal field-like orbital stabilization terms within molecular mechanics and applications to molecular dynamics simulations of metalloproteins. Chapter 2, by Michael Seth and Tom Ziegler, is one of several reviews that focus on methods to calculate spectroscopic observables for inorganic compounds. The particular topic is magnetic circular dichroism prediction with time-dependent density functional theory approaches, with applications ranging from an isolated permanganate ion to enzyme active sites. Chapters 3 and 4 describe studies of chemical behavior based on molecular dynamics studies in which the energy surface is computed "on the fly" with density functional theory or ab initio methods. Chapter 3, by Marc Brüssel, Stefan Zahn, E. Hey-Hawkins, and Barbara Kirchner, describes density functional theory-based studies and applications to nitrogen activation, while Chapter 4, by Bernd M. Rode, Thomas S. Hofer, Andreas B. Pribil, and Bernhard R. Randolf, focuses on the Hartree–Fock and other ab initio methods, with applications to the structure and dynamics of hydrated ions. Chapter 5, by Maren Podewitz and Markus Reiher, describes the theory involved in understanding electronic spin in molecular systems and especially clusters, going all the way back to the relativistic origin of the spin quantum number. Some technical discussion of broken-symmetry approaches to spin states of metal-containing clusters and a discussion of local spin concepts follows, as well as some applications. Chapter 6, by Àleix Comas-Vives, Gregori Ujaque, and Agustí Lledós, is an overview of catalytic hydrogenation mechanisms, largely based on density functional theory studies of potential energy surfaces. Mechanisms involving coordination of the

substrate to the metal and without such coordination are considered and compared. Chapter 7, by Tatyana E. Shubina, concerns the electronic structure and reactivity of metalloporphyrin species with divalent metal ions. The binding of small ligands to porphyrins is considered, as is the formation of the metalloporphyrins through metallation. Chapter 8, by Frank Neese, William Ames, Gemma Christian, Mario Kampa, Dimitrios G Liakos, Dimitrios A. Pantazis, Michael Roemelt, Panida Surawatanawong, and Shengfa Ye, is an overview of a large number of topics related to computational chemistry of open-shell transition metal compounds. The key topics described are reactivity, including the role of electronic structure, and in particular spin state, in iron-containing enzymes with iron- oxo active species; electron paramagnetic resonance, including the theory of how to compute spectroscopic observables; electronic structure and spectroscopy of metal–radical complexes; and magnetic properties of polymetallic clusters. Chapter 9, by Russell J. Mckinlay, Justyna M. Żurek, and Martin J. Paterson, is mainly about photochemistry of metal complexes, but includes also a general review of the theory of vibronic coupling in inorganic systems. Basic theory, electronic structure of metal carbonyl excited states, and quantum wave packet dynamics studies of dissociation and radiationless transitions are all discussed. Chapter 10, by James Rustad, is an example of how computational inorganic chemistry now has an impact well outside the traditional heart of the discipline—the title announces "A New Geology" based on computational insight. The review introduces the force-field methods that form the basis for much of the work in the area, and then discusses applications to proton transfer and to interfacial reactions on oxide materials. The final contribution, Chapter 11 by Elaine Olsson, Knut Teigen, Aurora Martinez, and Vidar R. Jensen, highlights another field in which computational inorganic chemistry now makes major contributions: bioinorganic chemistry. Some applications from this field are touched upon in some of the other chapters, of course, but Chapter 11 focuses purely on the biochemistry and reactivity of aromatic amino acid hydroxylase enzymes.

We trust the readers in the inorganic and bioinorganic chemistry communities will find this volume informative and useful.

Rudi van Eldik
University of Erlangen-Nürnberg
Germany

Jeremy Harvey
University of Bristol
United Kingdom

June 2010

MOLECULAR MECHANICS FOR TRANSITION METAL CENTERS: FROM COORDINATION COMPLEXES TO METALLOPROTEINS

ROBERT J. DEETH

Inorganic Computational Chemistry Group, Department of Chemistry, University of Warwick, Coventry CV4 7AL, United Kingdom

I. Introduction

Transition metal (TM) systems present a fundamental dilemma for computational chemists. On the one hand, TM centers are often associated with relatively complicated electronic structures which appear to demand some form of quantum mechanical (QM) approach (*1*). On the other hand, **all** forms of QM are relatively compute intensive and are impractical for conformational searching, virtual high-throughput screening, or dynamics simulations

THEORETICAL AND COMPUTATIONAL INORGANIC CHEMISTRY
VOLUME 62 ISSN 0898-8838 / DOI: 10.1016/S0898-8838(10)62001-6

since all these approaches may require many hundreds of thousands of individual calculations. Consequently, TM computational chemists tend to restrict themselves to smaller "model" systems with limited conformational freedom. This is particularly marked in bioinorganic chemistry where the calculation focuses on the "important" active site region but the bulk of the protein is not treated explicitly (*2,3*).

In contrast, those interested in purely "organic" systems have long enjoyed the advantages of "cheap," classical molecular mechanics (MM) and molecular dynamics (MD) to study the entire molecular system including the surrounding solvent. However, conventional MM is not well suited to TM systems since it does not provide a general way of accounting for the important effects arising from the d electrons (*4,5*). In response, hybrid QM/MM methods have appeared (*6*). The metal center and its immediate environment is handled by a "high level" QM method, typically based on Density Functional Theory (DFT), with the rest of the system treated by MM. As the many technical difficulties of QM/MM have progressively been solved—most importantly how to couple the quantum region to the classical region—QM/MM has grown in popularity. However, the inclusion of any QM, even on a relatively small piece of the whole system, soon exacts a huge cost in execution time. Just a few minutes per calculation soon equates to years of CPU time. The only options are either to use thousands of computers or to develop a method which is as accurate as QM, but many orders of magnitude more efficient. We have taken the second path by augmenting MM with additional terms designed to provide a physically meaningful description of metal–ligand bonding and thus be able to emulate the behavior of more sophisticated, but expensive, QM methods. However, in order to put our model into perspective, we must first appreciate the nature of "conventional" MM and its shortcomings when applied to TM systems.

II. Conventional Molecular Mechanics

Molecular mechanics in its simplest form expresses the total potential energy, E_{tot}, as a sum of terms describing bond stretching, E_{str}, angle bending, E_{bend}, torsional twisting, E_{tor}, and nonbonding interactions, E_{nb} (1). The latter can include both van der Waals (vdW) interactions and, by assigning to each atom a partial atomic charge, electrostatics.

$$E_{tot} = \sum E_{\mathrm{str}} + \sum E_{\mathrm{bend}} + \sum E_{\mathrm{tor}} + \sum E_{\mathrm{nb}} \qquad (1)$$

Each term in (1) is represented by a simple mathematical expression as exemplified in (2), where the k are appropriate force constants, θ are bond angles, τ are torsion angles, n is the torsional periodicity parameter, ϕ is the torsion offset, ρ are partial atomic charge, ε is the dielectric constant, A and B are Lennard-Jones vdW parameters, and the summations run over bonded atom pairs (ij), angle triples (ijk) and torsional quadruples ($ijkl$). The nonbonded terms are summed over the distances, d_{ij}, between unique atom pairs excluding bonded pairs and the atoms at either end of an angle triple. For the atoms at the ends of a torsion quadruple, the nonbonded term may be omitted or scaled.

$$\begin{aligned} E_{\text{tot}} = & \sum_{i,j} k_{ij}(r_{ij}-r_{0,ij})^2 + \sum_{i,j,k} k_{ijk}(\theta_{ijk}-\theta_{0,ijk})^2 \\ & + \sum_{i,j,k,l} \Big(k_{ijkl}[1+\cos(n_{ijkl}\tau-\phi_{ijkl})] \\ & + \left[\sum_{i<j} \frac{\rho_i \rho_j}{\varepsilon d_{ij}} \sum_{i<j} \left(\frac{A_{ij}}{d_{ij}^{12}} - \frac{B_{ij}}{d_{ij}^{6}} \right) \right] \end{aligned} \tag{2}$$

These potential energy terms and their attendant empirical parameters define the force field (FF). More complicated FFs which use different and/or more complex functional forms are also possible. For example, the simple harmonic oscillator expression for bond stretching can be replaced by a Morse function, E_{Morse} (3), or additional FF terms may be added such as the stretch-bend cross terms, E_{stb}, (4) used in the Merck molecular force field (MMFF) (*7–10*) which may be useful for better describing vibrations and conformational energies.

$$E_{Morse} = D\left\{1-e^{a(r-r_0)}\right\}^2 - D \tag{3}$$

$$E_{stb} = \sum_{i,j,k} \left\{ k_{ijk}(r_{ij}-r_{0,ij}) + k_{kji}(r_{jk}-r_{0,jk}) \right\} \theta_{0,ijk} \tag{4}$$

MM is a very successful model but it is clear from expressions such as (2) that the FF may comprise a very large number of parameters and since the quality of the FF will depend crucially on these parameters, developing a truly "universal" FF is an enormous (perhaps impossible) challenge (*11*). Consequently, FFs tend to be applicable to a specific class of molecular system such as small organic molecules (e.g., MMFF (*7–10*)), or large biomolecules like proteins and DNA (e.g., AMBER (*12*) or CHARMM (*13*)) for which the expressions in (2) are suited.

Fortunately, these specific classes encompass an enormous amount of organic chemistry and biology plus the FFs are continually being revised to increase their applicability.

The computational efficiency of a FF approach also enables simulations of dynamical behavior—molecular dynamics (MD). In MD, the classical equations of motion for a system of N atoms are solved to generate a search in phase space, or *trajectory*, under specified thermodynamic conditions (e.g., constant temperature or constant pressure). The trajectory provides configurational and momentum information for each atom from which thermodynamic properties such as the free energy, or time-dependent properties such as diffusion coefficients, can be calculated.

MD introduces a time dependence but to avoid numerical instability, the time step δt needs to be quite small (~1 fs) which places strong limitations on the total simulation time. Nevertheless, compared to QM-based schemes such as Carr-Parinello MD, classical MD is currently the only really viable method for computing the dynamical behavior of large systems like biomolecules for any appreciable length of time.

Consequently, MM and MD have become extremely powerful and useful computational tools for studying a wide variety of chemical and biological problems. However, a significant proportion of real systems also rely on TM centers for their structure and/or function. The presence of TM coordination soon exposes fundamental shortcomings in simple FF equations like (2).

III. Shortcomings of MM for TM Systems: Angular Potentials

The angular geometry at the metal center cannot easily be accommodated by a FF expression like (2) since each angle-bend triad has a single reference value. This is not a problem for carbon chemistry since the three common geometries—tetrahedral, trigonal planar, and linear—are each associated with a single valence angle—109.5°, 120°, and 180° respectively but, for common coordination symmetries like octahedral and trigonal bipyramidal, there are multiple reference angles for the same A-M-A set (Fig. 1).

This "unique labeling problem" (*14*) originally required the definition of "multiple equilibrium positions and redundant atom labelling schemes…" resulting in a "tedious over-definition of the molecular topology" (*14*).

More elegant solutions have been proposed such as the SHAPES FF (*14*) or analytical expressions for the angular

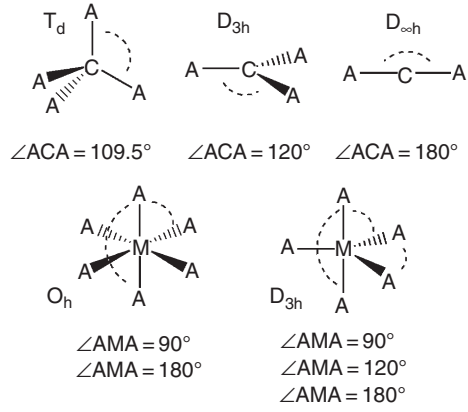

FIG. 1. Valence angles at central atom for various regular geometries.

potential around metal centers based on the angular overlap model (AOM) (*15*), but perhaps the simplest and most general scheme is to use the Gillespie–Nyholm or valence shell electron pair repulsion (VSEPR) idea that the groups around a central atom will arrange themselves so as to maximize their separation or, equivalently, to minimize their mutual repulsions. Kepert put this essentially "points on a sphere" (POS) approach onto a more quantitative footing by minimizing the ligand–ligand repulsion assuming an inverse dependence on the ligand–ligand distance, with powers ranging from 4 to 8, and successfully rationalized the structures of some 5000 main group compounds (*16*). Within MM, a POS or ligand–ligand repulsion scheme removes the angle-bend term at the metal and thus reference θ_0 values are not required. This approach has been adopted by Hambley and Comba in their MOMEC program (*17*) and we have followed suit (*18*).

IV. Effects from d Electrons

The d electrons of classical Werner-type coordination complexes have a significant impact on structure and reactivity. For example, the experimental hydration enthalpies of the divalent aqua ions (black diamonds, Fig. 2) deviate substantially from any monotonic variation on crossing the series from left to right (*19*).

The "double-hump" behavior depicted in Fig. 2 is usually rationalized in terms of the ligand field stabilization energy (LFSE). The LFSE is a function of the d configuration and the magnitude

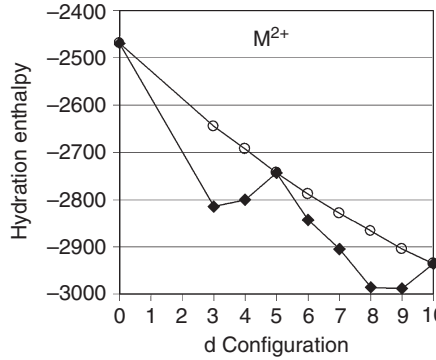

FIG. 2. Variation of experimental hydration enthalpies (solid diamonds) from d^0 Ca^{2+} through to d^{10} Zn^{2+}. The open circles represent the values once d electron stabilization energy effects are removed (after Johnson and Nelson (*19*)).

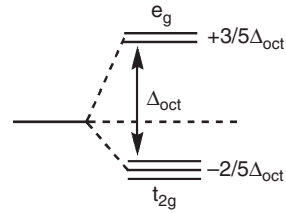

FIG. 3. Octahedral d-orbital splitting diagram from which the one-electron contribution to the LFSE can be computed.

of the ligand field splitting, Δ_{oct} (Fig. 3), which can be independently derived from spectroscopic data by fitting the d–d absorption bands of these nominally octahedral species (*20*). If the experimental hydration enthalpies are "corrected" using the spectroscopic Δ_{oct} values, a remarkably smooth line is obtained (open circles in Fig. 2).

Any computational treatment of TM systems must account for the LFSE. QM methods achieve this implicitly but d-electron effects must be explicitly added to MM (*4*). Some effects can be modeled within conventional MM. For example, low-spin d^8 complexes are planar by virtue of the LFSE (*21,22*), but a planar structure can also be enforced using a "normal" out-of-plane term (*22*). However, the simplest *general* model for describing d-orbital energies is ligand field theory (LFT) (*23*) which was itself derived from the earlier electrostatic crystal field theory (CFT) (*24*) approach.

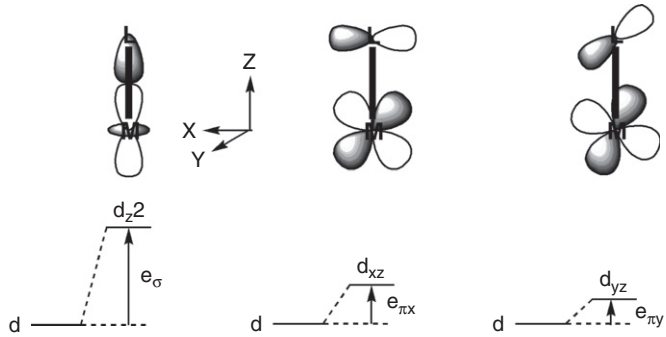

FIG. 4. Definition of AOM e parameters in terms of local M–L bonding. The σ interaction is always destabilizing ($e_\sigma > 0$) while π bonding in the two mutually perpendicular directions to the M–L vector (the local z axis) is shown for a π donor ($e_\pi > 0$).

Although the properties which can be computed are limited, LFT has provided for over half a century a reasonably useful, semi-quantitative picture of metal–ligand bonding in Werner-type coordination complexes (*3,25–27*). In the present context, the advantage of LFT is its computational efficiency. Therefore, we added LFT to MM to give the ligand field molecular mechanics (LFMM) method (*28*).

Since MM is intrinsically bond centered, the most convenient way to express the LFSE is based on the angular overlap model of Schaeffer and Jorgensen (*29*). The total ligand field potential, V_{LF}, is assumed to be the sum of contributions from the M-L bonds each modeled by AOM parameters describing separate σ and π interactions as illustrated in Fig. 4.

This construction provides a more physically realistic description of the M-L bond which ultimately enables LFMM to mimic far more expensive quantum chemical methods. The AOM is superior to CFT since it retains all the appropriate symmetry behavior but allows us to focus on individual ligands. The d-orbital energies are thus, in general, a function of all the ligands although in high-symmetry cases such as O_h, there may be a convenient separation into σ and π interactions.

For example, in AOM terms, the octahedral splitting Δ_{oct} is given by (5) and illustrated in Fig. 5 for the particular case of a π-donor ligand for which e_π is positive.

$$\Delta_{\mathrm{oct}} = 3e_\sigma - 4e_\pi \tag{5}$$

LFMM does have a small computational overhead. A 5 × 5 matrix describing the ligand field potential, V_{LF}, must be constructed

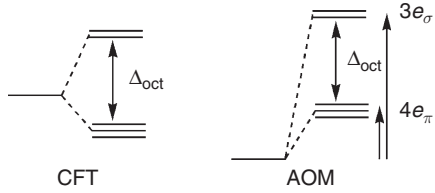

FIG. 5. Comparison of CFT barycenter (left) versus AOM barycenter (right).

and diagonalized to extract the d-orbital energies and hence the LFSE (*30*). The matrix elements depend on angular factors, F, which are functions of the coordinates of the N ligands, and the AOM radial e_k parameters, where $k = \sigma, \pi x$ and πy (**6**).

$$< d_i|V_{LF}|d_j >= \sum_{l}^{N} \sum_{k}^{symm} F_{ik}^{l} F_{kj}^{l} e_k^l \qquad (6)$$

In addition, LFMM also requires additional parameters over conventional MM. Inevitably, therefore, there is a trade off between relatively expensive QM calculations which can be started immediately versus very much faster LFMM calculations which may require an initial period for parameter development and optimization.

V. Ligand Field Molecular Mechanics

Ligand field molecular mechanics (LFMM) merges conventional MM for the "organic" parts of a TM complex with an AOM treatment of the LFSE for the metal center (*4*). The LFSE only accounts for the effects of the d electrons and is infinitely negative at zero M-L distances so the FF must include "normal" terms for M–L stretching (a Morse function is used) and L–M–L angle bending (a ligand–ligand POS term is used). The LFSE contribution is thus fully integrated into the MM calculations and the electronic effects feed directly into determining the structure and energy. The LFMM method is therefore distinct from Comba's MM/AOM method (*31*) which uses a "pure" MM approach to generate the structure followed by a subsequent AOM calculation to compute various ligand field properties such as d-d spectra and EPR g-values.

The following are the main features of the LFMM model(*18*):

1. A general functional form for the distance dependence of the AOM parameters (7);

$$e_\lambda = a_0 + a_1 r + a_2 r^{-2} + a_3 r^{-3} + a_4 r^{-4} + a_5 r^{-5} + a_6 r^{-6} \qquad (7)$$

2. A purely repulsive ligand–ligand term, A_{LL}/r^n to help determine the angular geometry;
3. Separate M-L σ and π bonding including asymmetric π interactions (i.e., $e_{\pi x} \neq e_{\pi y}$);
4. An explicit AOM d-s mixing term, e_{ds}, to treat the configuration interaction between the valence metal s orbital and the d functions (in D_{4h} $[CuCl_4]^{2-}$, e.g., the Cu 4s mixes with $3d_z2$ depressing the latter by about 6000 cm^{-1} (*32*));
5. An energy term using the same form as equation 7 to account for the spin-pairing energy for low-spin electronic configurations (*33*);
6. Analytical energy gradients;
7. Implementation into a fully functional molecular modeling package (*18*), the molecular operating environment (MOE) (*34*).

Each molecule is divided into two regions as illustrated in Fig. 6 for a $[M(ethylenediamine)_2]^{n+}$ complex. The coordination region contains the metal and its immediately bonded donor atoms (e.g., the MN_4 unit) and the ligand region comprises everything except

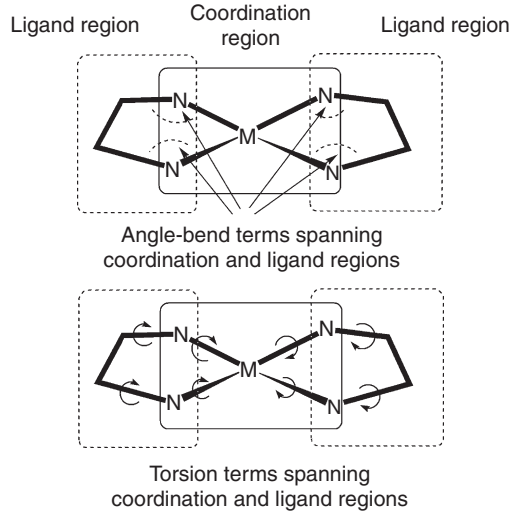

FIG. 6. Schematic representation of division into coordination and ligand regions and FF terms which span the two.

the metal atom (e.g., the ethylenediamine ligands). The LFMM routines independently compute all energy terms in the coordination region and the MOE FF file treats all the interactions in the ligand region plus M–N–C angle, N–M–N–C torsion and M–N–C–C torsion terms which span both.

The construction in Fig. 6 may at first sight seem like that used in QM/MM approaches. However, the metal is the only "QM" atom plus there are no "link" atoms. The LFMM thus provides a uniform, seamless theoretical treatment of the entire molecule.

VI. LFMM Parameterization

The more sophisticated treatment of M-L bonding in LFMM increases the number of parameters compared to "standard" MM with up to five AOM parameters required. Many of these parameters are strongly correlated with other "conventional" FF terms. For example, e_σ, the ligand–ligand repulsion term, A_{LL}, and the Morse function parameters will all have a strong influence on the M-L bond distance. Consequently, and to simplify parameter optimization, our general strategy is to fix as many of the AOM variables as possible by recourse to experimental and/or computed data before optimizing the remaining FF terms, in particular, the Morse function parameters α and r_0.

AOM parameter values for a variety of M–L combinations have already been determined from conventional ligand field analysis. For example, e_σ values for Cu^{II}-N amines have been reported for a series of complexes spanning a wide range of bond lengths (*32*) and e_σ for a Cu–N distance of 2.0 Å is around 6000 cm^{-1}. Alternatively, we can use DFT calculations to estimate d-orbital energies which are then subject to a separate AOM analysis to derive the required parameter values. Note that a special "spherical configuration" construction is used to better simulate the ligand field (*21,35*). That is, the molecular orbitals of mainly d-orbital parentage are identified and then a subsequent single point DFT calculation is carried out where the populations of these five orbitals are set to $n/5$ where n is the formal number of d electrons.

Once parameter values have been determined for particular bond distances, we need to choose a distance dependence. For hard donors like N and O, an inverse sixth power is normally chosen while for softer donors, $1/r^5$ or $1/r^4$ is used. However, the particular power dependence is not critical given the subsequent optimization of Morse and ligand–ligand repulsion terms. It also turns out that a distant-dependent AOM term delivers values which work reasonably well for any metal. For example, even

though e_σ for $[Co^{III}(NH_3)_6]^{3+}$ at about 7200 cm^{-1} is much larger than in Cu(II) complexes, the Co–N distance is shorter such that essentially the same LFMM parameter suffices in each case.

The particular values and power dependence for the d-s mixing term are also not too critical although a certain threshold must be achieved. Tetragonally elongated Jahn–Teller distortions of d^9 CuN_6 species (*36*) and the trigonal geometry of the oxidized copper center in Type 1 metalloproteins (*37*) can be achieved with an inverse sixth order power dependence and an associated a_6 parameter of at least 300,000 kcal mol^{-1} $Å^6$. However, since e_{ds} also depends on symmetry—e.g., it makes no contribution for octahedral complexes—there are many systems where d-s mixing has a minimal effect.

Finally, the "spin-pairing" energy term is only applied to low-spin states and is usually obtained from DFT calculations on a simple model homoleptic system such as the metal hexaammine. That is, values for the other AOM parameters are determined for the high-spin complex as outlined above and then the Morse function parameters and ligand–ligand parameters are optimized using a weighted penalty function method similar to Norrby's (*38*). Keeping everything else fixed, the spin-pairing term is then separately optimized against the DFT structure and relative spin-state energy of the low-spin species.

Once suitable AOM parameters have been determined, they are fixed and a subsequent optimization of Morse and/or ligand–ligand repulsion parameters is carried out for a more diverse set of training complexes. The latter can be experimental X-ray structures from the Cambridge Structural Database or DFT-optimized structures or a combination of the two. This procedure has two advantages. First, experimental structures inherently treat all effects like dispersion forces and quantum mechanical exchange and correlation which can be hard for quantum chemistry to reproduce. Secondly, notwithstanding the first point, theoretical methods like DFT can be used to access structures and energy states which cannot be realized experimentally. This significantly enhances the utility of the LFMM parameters.

In the following sections, this versatility is illustrated using selected applications of LFMM.

VII. Simple Metal, Simple Ligand: Ga(III) Hydroxamates

Many bacteria secrete compounds called siderophores specifically to sequester iron either from the environment or from other organisms. Siderophores show extremely high affinities

for Fe^{3+} with binding constants for bacterial species of the order of log $\beta > 30$ (*39*).

Streptomyces coelicolor produces a tris-hydroxamato tetrapeptide coelichelin with four stereocenters in the peptide chain. The putative peptides were identified via genome mining (*40*) although their stereochemistries were ambiguous. Since only tiny quantities of coelichelin could be isolated, single crystals were not available and so the structure could not be confirmed by X-ray diffraction. Consequently, a series of NMR experiments were undertaken. Complexing the molecule facilitates the structure elucidation but the natural choice of Fe^{3+} is strongly paramagnetic, hence the diamagnetic Ga^{3+} complex is used instead since the Fe^{3+} and Ga^{3+} have similar ionic radii (*41*) and thus their complexes have similar structures.

While not technically a transition metal, for the purposes of LFMM modeling, Ga^{3+} and high-spin Fe^{3+} are essentially comparable since both have formally zero LFSEs. LFMM parameters were developed on the basis of limited X-ray structural data augmented by density functional theory calculations (*40*). In addition to being optically active, asymmetrical $M(A\text{-}B)_3$ tris-chelates have *fac* and *mer* geometrical isomers. Using [Ga(N-methylhydroxamate)$_3$] as a model, DFT established that the *fac* and *mer* forms are virtually equi-energetic. To further enhance the LFMM FF, the energy required to twist the *fac* form from its approximately octahedral configuration to an eclipsed trigonal geometry was estimated (~12 kcal mol^{-1}, Fig. 7) and these data were used to refine the M–L Morse and ligand–ligand repulsion parameters. This is another example of how specific DFT calculations can be used to significantly enhance the quality of the derived FF.

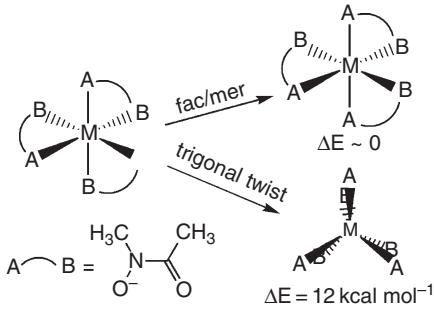

FIG. 7. Schematic showing DFT-calculated energy changes for structural variations of a model Ga-trishydroxamate complex which are then used to develop FF parameters.

Thirteen measurements were obtained from the NMR experiments—five H-H distances and eight H-C-C-H torsions—which were compared to those predicted by computing all possible isomers of [Ga(coelichelin)]. Note that the calculations were not constrained apart from fixing the chirality at each stereocenter. This contrasts with the typical use of NMR constraints which are usually explicitly included to restrain the geometry. In our case, only one combination of chiral centers gave uniform, simultaneous agreement with all the experimental data (Fig. 8).

VIII. Simple Metal, Complex Ligand: Mn(II) Carboxylates

Carboxylates bind readily to transition metal cations (*42*). They are common in coordination chemistry and play a significant role at the active sites of many metalloproteins (*43*).

Carboxylates exhibit diverse coordination modes (Fig. 9) from monodentate, where the ligand is part of a chelate ring (Fig. 9, top left), through symmetrical or asymmetrical bidentate, to bridging via syn and/or anti linkages.

Modeling this diversity computationally is a challenge for FF methods, especially for the bidentate modes, since the method should automatically determine the preferred mode as well as "flip"—i.e., smoothly switch from short-long asymmetric bidentate through symmetric to long-short asymmetric bidentate.

Both oxygens of the carboxylate need to be connected to a metal center. A computational description of the desired flipping motion can then be obtained using an Mn–O–C angle potential function with multiple minima, an approach similar in spirit to that proposed by Allured *et al.* (*14*) for dealing with multiple L–M–L angles in, for example, planar Rh(I) complexes. Even though the angle-bending term in MMFF only requires a cubic expansion (*44*), MOE also includes a quartic term (8) which, with a negative value for k_2 and a positive value for k_4, gives two minima corresponding to the two M–O-–C angles for asymmetric bidentate coordination (Fig. 10).

$$\mathrm{E}_\theta = k_2(\theta-\theta_0)^2 + k_3(\theta-\theta_0)^3 + k_4(\theta-\theta_0)^4 \qquad (8)$$

On balance, the FF derived from a reasonably large and diverse training set gives accurate structures (Fig. 11). Any significant discrepancies suggest "interesting" behavior due to environmental effects. In such cases, explicit solvation improves the computed results (*45*).

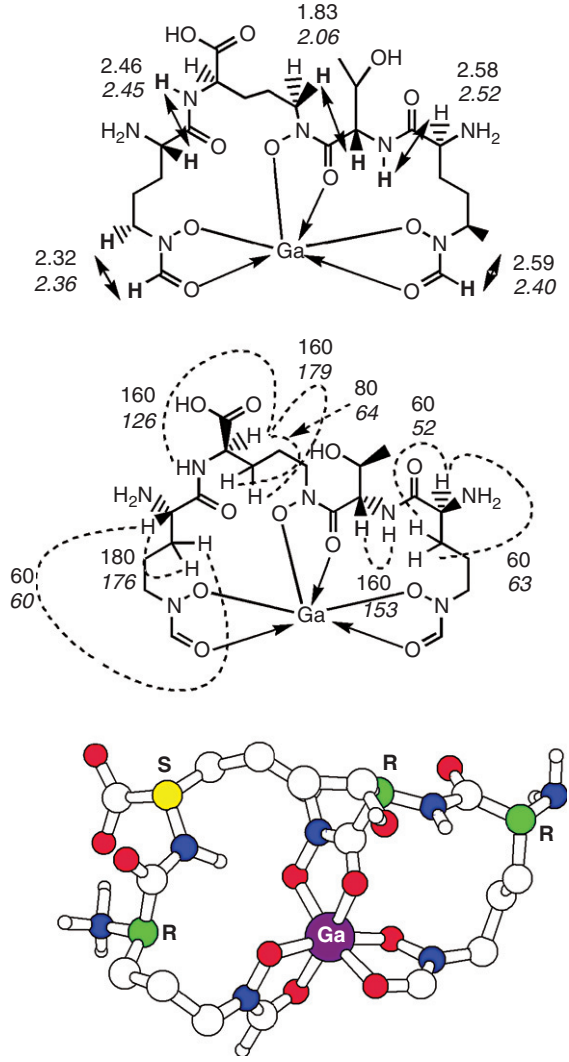

FIG. 8. Comparison of NMR-derived and computed structural data for [Ga(coelichelin)]. Top: ROESY-derived H–H distances (normal text) and LFMM distances (italic). Middle: HMBC-derived H–X–Y–H torsion angles (normal text) and LFMM torsions (italic). Bottom: The LFMM calculated structure which best reproduced the NMR constraints. Non-polar hydrogens omitted for clarity and chiral centers are labeled R or S as appropriate. (Distances in Å and angles in degrees.)

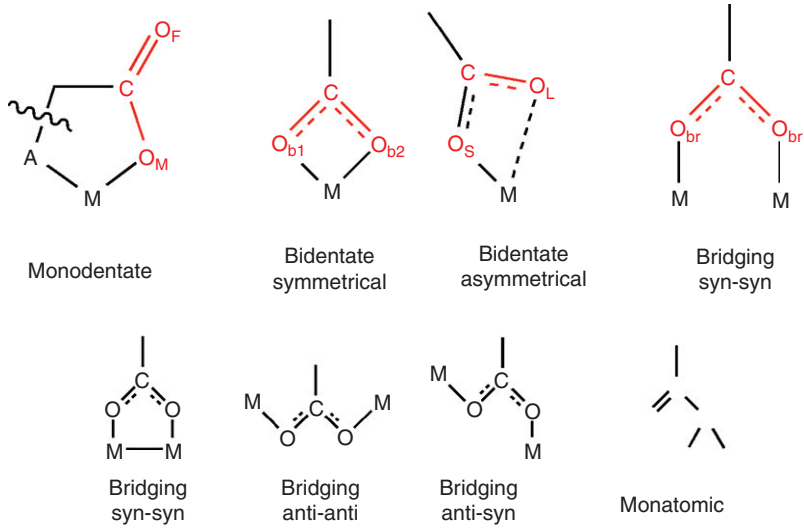

FIG. 9. Potential carboxylate binding modes. The modes shown on the top row are considered explicitly in developing LFMM parameters although anti-anti and anti-syn bridging modes are within the scope of the parameterization.

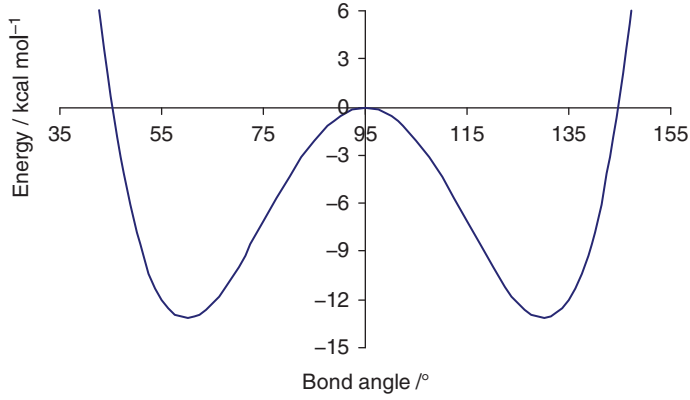

FIG. 10. Sketch of angle-bending potential of the form $E_\theta = k_2(\theta - \theta_0)^2 + k_4(\theta - \theta_0)^4$ with $k_2 = -70$ kcal mol^{-1} radian^{-2} and $k_4 = 93$ kcal mol^{-1} radian^{-4}.

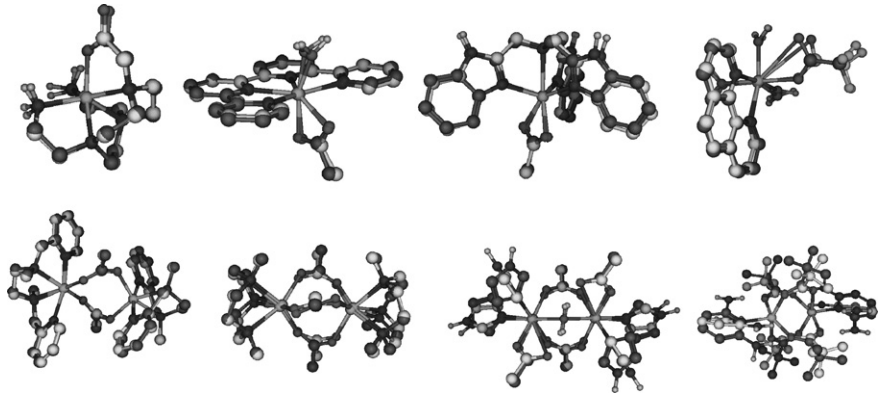

FIG. 11. Overlay of X-ray (yellow carbons) and MM calculated (blue carbons) structures for selected mono- and dinuclear complexes.

IX. Difficult Metals: Jahn–Teller Effects in Cu(II) and the *trans* Influence in Pt(II)

The Jahn–Teller effect has fascinated chemists for decades (*46*). Perhaps the best studied inorganic system is the d^9 Cu(II) center (*47–50*). Nominally octahedral $Cu^{II}L_6$ systems generally display tetragonally elongated structures which can be simply rationalized in terms of the d-electron stabilization energy. Under the influence of a tetragonal distortion, the ^2E_g state of the parent octahedral system splits into two states, $^2A_{1g}$ corresponding to a $d_{z^2}{}^1 d_{x^2-y^2}{}^2$ or $\{d_{z^2}\}^1$ configuration and $^2B_{2g}$ corresponding to a $d_{z^2}{}^2 d_{x^2-y^2}{}^1$ or $\{d_{x^2-y^2}\}^1$ configuration, with the latter having the lower energy for an elongation. The lowering of the electronic energy, ΔE_{JT}, drives the distortion (Fig. 12). Hence, the qualitative nature of the Jahn–Teller distortions in Cu(II) complexes is fairly well understood.

A quantitative treatment of the Jahn–Teller effect is more challenging (*46*). A major issue is that many theoretical models explicitly or implicitly assume the Born–Oppenheimer approximation which, for octahedral Cu(II) systems in the vibronic coupling regime, cannot be correct (*46,51*). Hitchman and co-workers solved the vibronic Hamiltonian in order to model the temperature dependence of the molecular structure and the attendant spectroscopic properties, notably EPR spectra (*52*). Others, including us, take a more simplistic approach (*53,54*) but, in either case, a similar Mexican hat potential energy description of the principal features of the Jahn–Teller effect in homoleptic Cu(II) complexes emerges (Fig. 13).

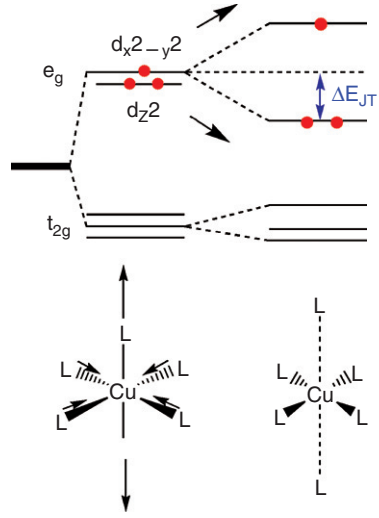

FIG. 12. Schematic energy level diagram illustrating the Jahn–Teller stabilization energy accompanying a tetragonal elongation of an octahedral Cu(II) complex.

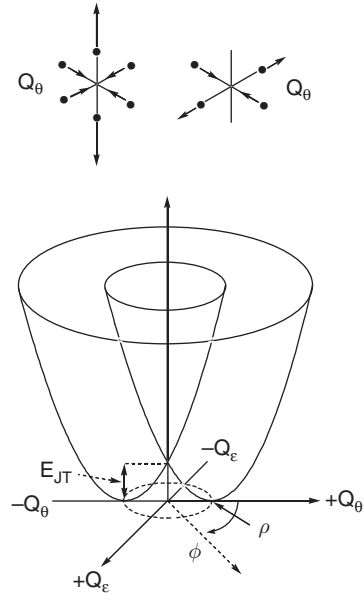

FIG. 13. Top: Schematic representation of the two components of the Jahn–Teller-active vibrational mode for the E⊗e Jahn–Teller coupling problem for octahedral d^9 Cu(II) complexes. Bottom: Resulting first-order "Mexican hat" potential energy surface for showing the Jahn–Teller radius, ρ, and the first-order Jahn–Teller stabilization energy, E_{JT}.

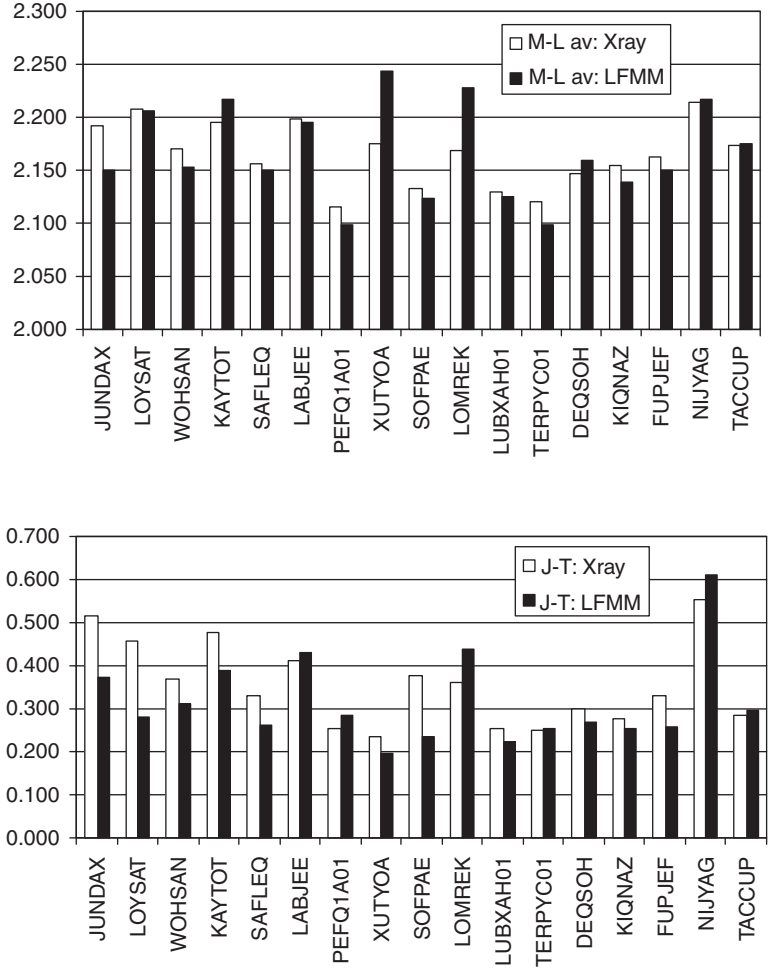

FIG. 14. Observed (white bars) and calculated (black bars) structural data for CuN_6 complexes (CSD refcodes shown on the x axis). Top: averaged Cu–N distance; Bottom: averaged axial distance minus averaged equatorial distance.

Following two earlier, more general studies of copper(II) coordination complexes (*4,55*), a comprehensive LFMM study of the Jahn–Teller effect in $Cu^{II}N_6$ systems was undertaken (*36*) based on a selection of structures from the Cambridge Structural Database (CSD) (*56,57*). AOM parameters had previously been derived based on ligand field analyses of d-d spectral data (*32*). Agreement between theory and experiment is good (Fig. 14).

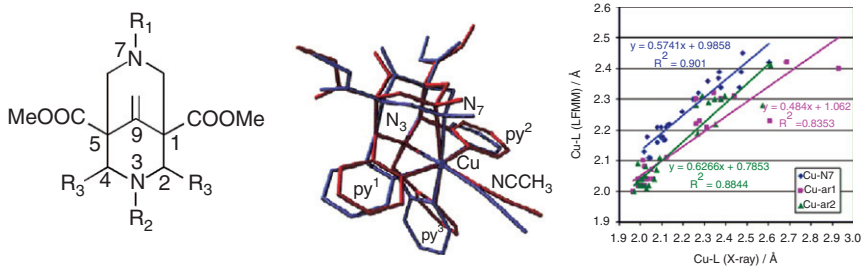

FIG. 15. Left: general representation of a bispidine ligand. Center: example overlay of LFMM (red) and X-ray (blue) structure. Right: comparison of LFMM and X-ray Cu–L bond lengths (Å). ar1 and ar2 correspond to the R_3 substituents.

Even though it was based solely on tetragonally elongated structures, the LFMM FF also describes the tetragonally compressed structure corresponding to the transition state between successive elongated minima. For $[Cu(tach)_2]^{2+}$ (CSD refcode TACCUP), the barrier estimated experimentally using variable temperature EPR is ~300 cm^{-1} while LFMM gives 270 cm^{-1} (*36*).

A recent study of 23 Cu(II)-bispidines complexes with 19 different ligands (*58*) is further proof that LFMM provides an excellent description of the whole of the Mexican hat PE surface. Depending on the ligand, all three elongation axes can be located. In each case, theory and experiment agree (Fig. 15).

The *trans* influence is another common electronic effect observed in coordination complexes. It is perhaps best known in planar d^8 species such as Pt(II) complexes and we have developed an LFMM treatment for a range of ligands (*21*). Since we use homoleptic complexes as the basis for parameterization and not all species are available experimentally, this study was based exclusively on DFT.

The *trans* influence manifests as a variation in a given Pt-L distance which depends on the nature of the ligand opposite. Strong σ donors like hydride and phosphines exert big changes while weaker donors like chloride and water cause smaller changes. The LFMM FF captures the *trans* influence quite well (Figs. 16 and 17). LFMM calculations give a decreasing *trans* influence series: $H^- > PH_3 > SH_2 > Br^- > Cl^-$, Pyridine, $NH_3 > H_2O$. This compares well with the DFT calculated series: $H^- > PH_3 > SH_2$, Br^-, Pyridine, NH_3, Cl^-, $> H_2O$. Both the DFT and LFMM data are in agreement with the order reported in the literature.

Further, for PtA_2B_2 species, LFMM and DFT predictions for which of the *cis* or *trans* forms is more stable in solution also agree in virtually all cases (Fig. 18) (*21*).

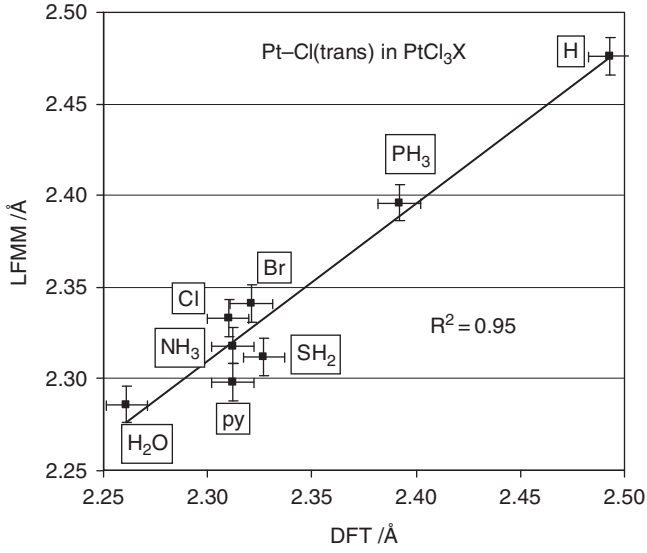

FIG. 16. Correlation between computed *trans* Pt–Cl distances (Å) in [$PtCl_3X$] complexes. Error bars are 0.01 Å.

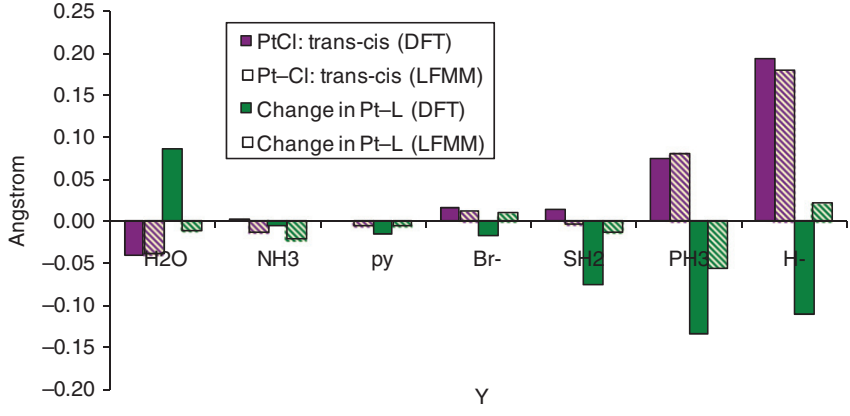

FIG. 17. Difference in *cis* and *trans* Pt–Cl bond lengths in [$Pt^{II}Cl_3Y$] (in purple) and change in Pt–Y bond length in [$Pt^{II}Cl_3Y$] compared to the homoleptic species [$Pt^{II}Y_4$] (green).

X. Spin States

Many TM ions can support multiple spin states. Usually, a change in spin is accompanied by significant geometrical changes. For example, high-spin d^8 six-coordinate Nickel(II) amine

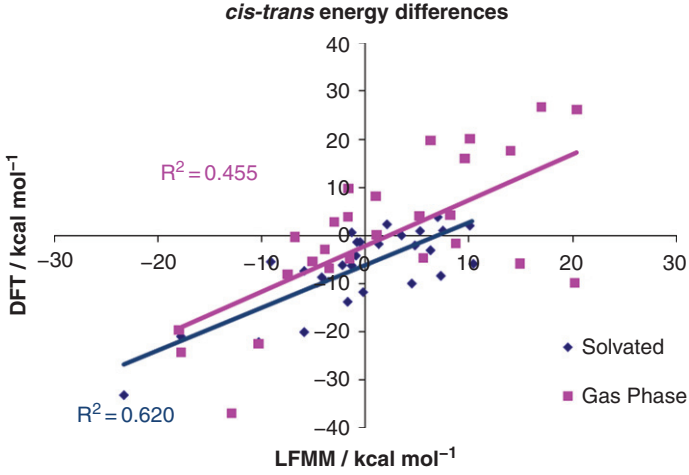

FIG. 18. Comparison of the computed energy differences between *cis* and *trans* PtA_2B_2 species in the gas phase (pink square) or in solution (blue diamonds).

complexes have Ni-N bond lengths around 2.1 Å while low-spin Ni(II)-amines are square planar with Ni-N distances around 1.9 Å. An early application of LFMM (*4*) demonstrated that a single set of Ni-N parameters could be found which reproduced the structures of both high- and low-spin species. However, the structure-based FF did not include a treatment for d-d interelectron repulsion and so could not directly address the issue of which spin state is lowest.

A slightly more sophisticated LFMM treatment was developed for the $[CoF_n(CN)_{6-n}]^{3-}$ series (*59*). $[CoF_6]^{3-}$ is high-spin $^5T_{2g}$ while $[Co(CN)_6]^{3-}$ is low-spin $^1A_{1g}$. In contrast to Ni(II), however, both spin states are essentially octahedral although $^5T_{2g}$ is formally Jahn–Teller active. Since the intervening mixed-ligand species are not known experimentally, the "reference" data were computed using DFT. This included computing the structures and relative energies for each complex in both spin states. Once again, we see the utility of DFT which provides experimentally inaccessible data which can be used to construct a better LFMM FF.

The LFMM parameterization was based only on the homoleptic systems but was able to reproduce DFT for all the mixed-ligand systems. The spin state changes from high to low already for $[CoF_5(CN)]^{3-}$. However, the interelectron repulsion was an additive correction and could not play a role in determining the structures.

Subsequently, LFMM was extended with an explicit "spin-pairing" energy (*18*). This is an empirical term with the same functional form as the AOM parameters (Eq. 7) and is significantly easier to implement than to express the ligand field stabilization energy as a function of the many-electron Russell-Saunders terms (*60*). Preliminary indications (*61*) for Fe(II) species suggest the approach is satisfactory and we expect to be able to use LFMM to study phenomena like spin crossover.

XI. Metalloproteins and Molecular Dynamics: Copper Proteins

Having demonstrated that LFMM works well for relatively small coordination complexes, the next challenge was to extend the treatment to larger biomolecules like metalloproteins. For such large, conformationally flexible species, the options available to the inorganic computer modeler are restricted, particularly if one wishes to include effects from the protein backbone. Clearly, a completely quantum approach is prohibitive while conventional MM suffers from the same limitations as for smaller systems with respect to the immediate environment around the metal. A popular strategy, then, is to combine QM and MM into a hybrid QM/MM scheme where the active site is treated with a relatively high-level QM approach while the rest of the protein is handled via conventional MM (*6*). Notwithstanding the complexities of linking the quantum and classical regions where, typically, several C–H bonds in the quantum region correspond to C–C bonds in the "real" system, we are still left with the conformational search issue. Even if only a small part of the entire system is treated quantum mechanically, that will be enough to preclude the large numbers of calculations required, say, for MD.

In contrast, LFMM/LFMD is much faster and provides a uniform treatment over the whole molecule (i.e., there are no link atoms). Moreover, proteins behave like giant ligands. They may be exquisitely complex and varied but, at the end of the day, the intrinsic bonding interaction between, say, Cu(II) and the N_δ of imidazole is essentially the same whether the imidazole is a free ligand or happens to be part of a histidine which is, in turn, connected to a peptide backbone. Hence, if an LFMM FF can be constructed for small coordination complexes containing biologically relevant donors, then it should work for whole proteins.

This proposition is amply verified by Type I (T1) copper proteins (*37,62*). T1 centers are involved in electron transfer with perhaps the most famous example being plastocyanin (Pc), a crucial part of photosynthesis, and the first T1 protein to be

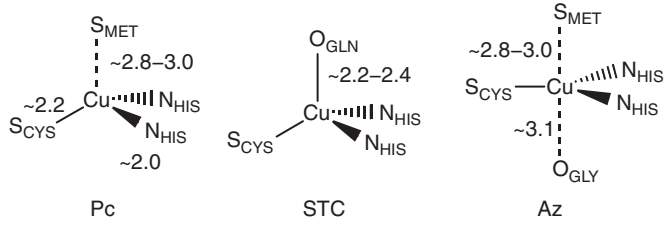

FIG. 19. Schematic representation of oxidized Type I copper centers.

characterized by single crystal X-ray crystallography (Fig. 19). T1 centers possess some unusual structural and spectroscopic properties compared to "typical" Cu coordination complexes (*63*). The active sites are distorted four or five coordinate and they all contain a short, strong Cu-S interaction to a cysteine residue and two Cu-N(histidine) bonds. For Pc, the fourth donor is a thioether sulfur from methionine while for stellacyanin (STC), it is an oxygen from a glutathione residue. Azurin (Az) is pentacoordinate with both a methionine S donor and an oxygen, although the latter is a peptide carbonyl O from a glycine residue.

The LFMM FF for the oxidized Cu(II) centers was designed around suitable homoleptic species, viz., $[Cu(imidazole)_4]^{2+}$, $[Cu(SCH_3)_4]^{2-}$, $[Cu(S(CH_3)_2)_4]^{2+}$, and $[Cu(O{=}CH_2)_4]^{2+}$ (*37*). These complexes represent models for Cu-histidine, Cu-cysteine, Cu-methionine, and Cu-glutamine O/peptide O respectively. Only the first of these species is known experimentally. However, it is amply documented that DFT gives excellent structures for metal complexes (*64,65*) so we can access the remaining species computationally (Fig. 20).

This FF was then applied to a model of the Pc active site (Fig. 20, bottom) which had previously been the subject of extensive DFT studies (*66*). The latter concluded that the "unusual" structural features reported on the basis of the X-ray structure—an approximately trigonal CuN_2S(cysteine) coordination with a short Cu-S(cysteine) bond and a very long Cu-S(methionine) apical interaction—were reproduced in the gas-phase optimization of the model $[Cu(imidazole)_2(SCH_3)(S(CH_3)_2)]^+$ complex. Apparently, contrary to the prevailing wisdom (*67,68*), the protein does not exert a significant strain on the metal coordination. Rather, the geometry is dominated by the Cu-S(cysteine) bond. Hence, the protein is not "entatic" (*67*). Instead, evolution has generated a ligand set which is difficult for man to realize synthetically but which is perfectly suited to its purpose. However, from a coordination chemistry perspective, the structure and bonding in T1 centers are not special.

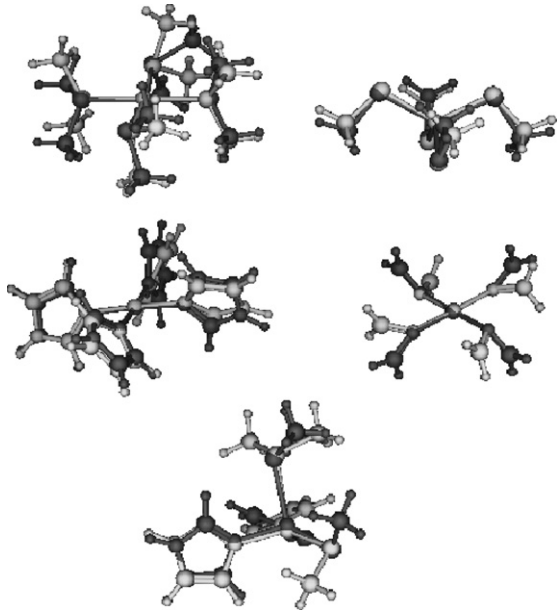

FIG. 20. Overlay of DFT-optimized (blue) and LFMM-optimized (yellow) model structures, clockwise from top left: $[Cu(DMS)_4]^{2+}$, $[Cu(SCH_3)_4]^{2-}$, $[Cu(O{=}CH_2)_4]^{2+}$, $[Cu(imid)_2(SCH_3)(DMS)]^{+}$, and $[Cu(imid)_4]^{2+}$. NB: blue structure for $[Cu(imid)_4]^{2+}$ taken from CSD (refcode GADGOH).

Nevertheless, the T1 structure reflects important electronic effects from the ligands and the d^9 configuration. Since LFMM is designed to capture these effects explicitly, it gives the same result as DFT. That is, the overall structure is trigonal with short Cu-SCH_3 and very long Cu-$S(CH_3)_2$ bonds. Once again, we have used selected DFT calculations to help build a better LFMM FF. As shown in Fig. 21, the FF clearly carries over very well to the complete proteins. Geometrical data for the same three proteins are given in Table I.

Many metalloproteins contain more than one metal center. Tyrosinase, for example, has a dinuclear Type 3 (T3) copper active site which, in its oxidized form, comprises two Cu(II) centers each held by three histidine groups with a μ-η^2:η^2 peroxido bridging ligand (Fig. 22).

Before constructing a LFMM FF, we first established that, for the purposes of structural calculation, the two Cu centers can be treated independently (*69*). Cu-N parameters were already available so we focussed on Cu-O interactions using [μ-O_2{Cu

TABLE I

COMPARISON OF PDB AND LFMM Cu–L BOND LENGTHS FOR PROTEINS SHOWN IN FIGURE. 21

1AAC	*PDB*	*LFMM*	*1JER*	*PDB*	*LFMM*	*1DYZ*	*PDB*	*LFMM*
HIS53	1.954	2.029	HIS46	1.960	2.045	GLY45	2.720	2.666
CYS92	2.108	2.148	CYS89	2.178	2.176	HIS46	2.040	2.014
HIS95	2.033	2.023	HIS94	2.043	2.028	CYS112	2.135	2.184
MET98	2.904	2.859	GLN99	2.209	2.253	HIS117	1.988	2.062
						MET121	3.260	2.924

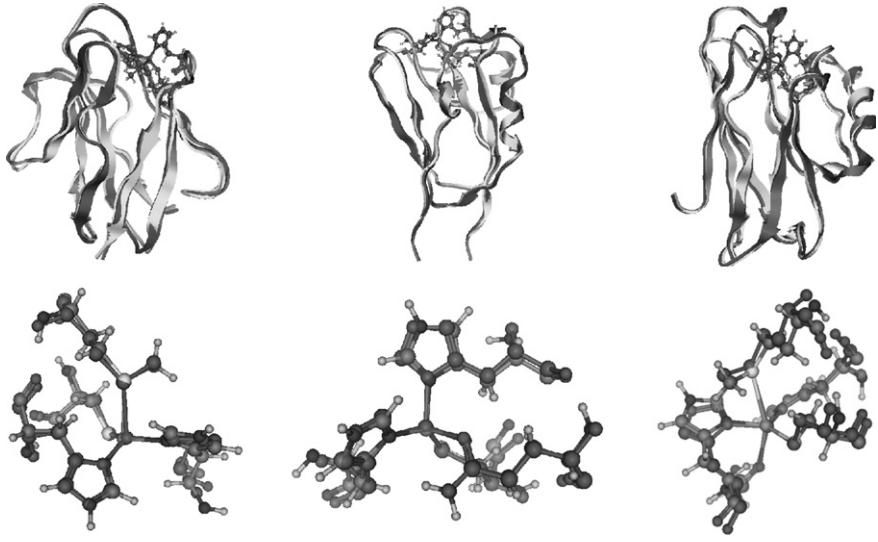

FIG. 21. Rmsd overlays of experimental (blue) and computed (yellow or CPK) backbone carbons (top) and active sites (bottom) for Amicyanin (left), Stellacyanin (middle), and Azurin (right) (PDB codes 1AAC, 1JER, 1DYZ).

$(NH_3)_3\}_2]^{2+}$ as a simple computational model and four other biomimetic species which had already been structurally characterized (Fig. 23).

The $[Cu_2O_2]^{2+}$ moiety in these systems is planar and an interesting feature of the LFMM analysis (*69*) is that this feature could be enforced via asymmetric Cu-O π interactions. By computing how the d-orbital energies varied as a function of the folding angle, α (Fig. 24), values for the in-plane and out-of-plane AOM π-bonding parameters were determined.

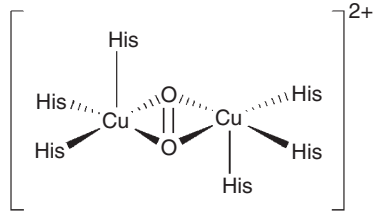

FIG. 22. Schematic representation of the oxidized T3 active site in Tyrosinase

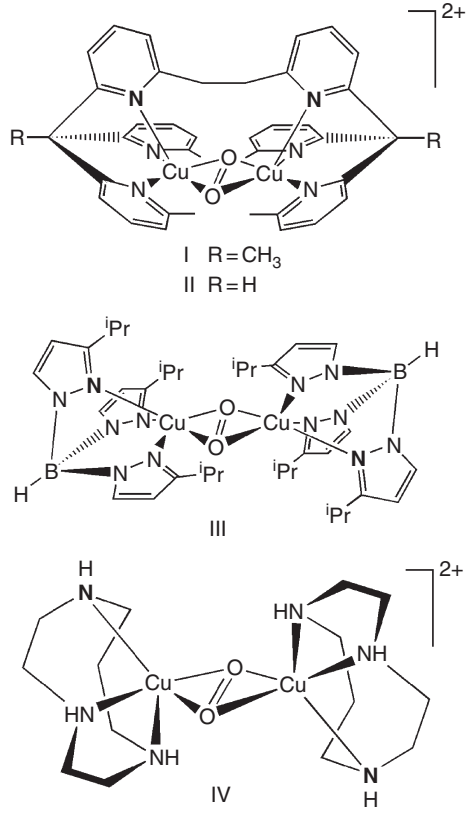

FIG. 23. Small molecule analogs of the T3 center.

The resulting FF gave good agreement with both X-ray crystallographic and DFT results (Fig. 25) which encouraged us to apply it to a long timescale (16 ns) LFMD simulation of the full tyrosinase protein (*70*). Clearly, no QM-based scheme is able to access such a relatively long simulation time.

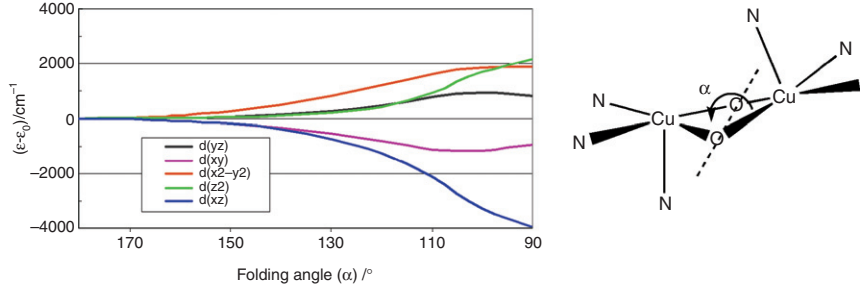

FIG. 24. Definition of the folding angle, α, and the relative change in d-orbital energies as a function of α.

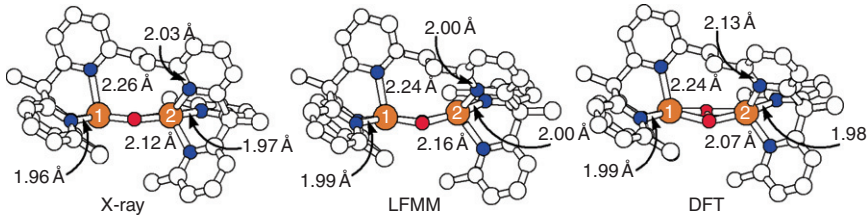

FIG. 25. Comparison of experimental and computed structures for I (see Figure. 23).

Soluble tyrosinase (sTr) itself crystallizes with a "caddie protein," ORF378 (the green ribbon in Fig. 26), which was removed in the LFMD simulations. As also shown in Fig. 26, this does not have a significant effect on the protein backbone. However, the absence of ORF378 in the simulations leads to some significant local variations in the active site structure.

In particular, the MD simulations give, on average, a planar $[Cu_2O_2]^{2+}$ moiety while the crystal structure shows a pronounced "butterfly" fold around the O-O bond, presumably due to the interaction with the ORF378 tyrosine residue near the active site (Fig. 27).

One of the questions surrounding the mechanism of tyrosinase concerns the initial site of attack. As a control, LFMD simulations of a model for the sTy active site, Meim6 (Fig. 28), give identical behavior for each Cu center consistent with its symmetry. In contrast, the LFMD simulations clearly distinguish the two copper sites in the sTy enzyme which must result from the protein environment (Fig. 29).

On the basis of the simulations, we proposed (*70*) a slightly modified mechanism for tyrosine hydroxylation (Fig. 30).

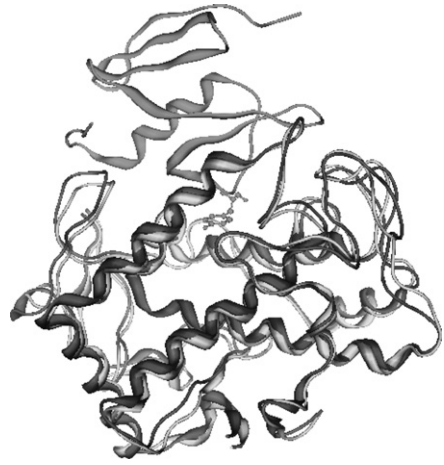

FIG. 26. Overlay of LFMD-averaged backbone structure of sTy (yellow) with the X-ray structure of sTy (blue) and the caddie protein, ORF378 (green). Tyr_{98} from the caddie protein is shown explicitly.

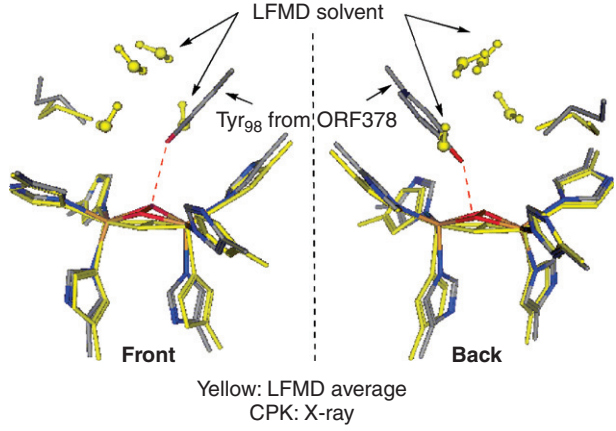

FIG. 27. Active site detail from X-ray structure (CPK coloring) and averaged LFMD structure (yellow) highlighting the putative hydrogen bond (red dashed line) responsible for the "butterfly" distortion of the $[Cu_2O_2]^{2+}$ unit in the X-ray which is not seen in the averaged LFMD geometry and the occupation by solvent of the space vacated by the caddie protein in the LFMD simulation.

XII. Bond Energies and Reaction Mechanisms: Water Exchange

Aqua complexes are fundamental in coordination chemistry and have been extensively studied (*71,72*). Our interest in $[M(OH_2)_n]^{m+}$ species was two-fold. First, given the wealth of

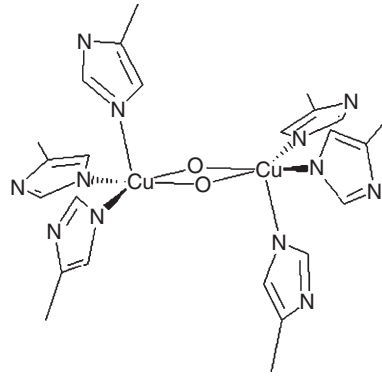

FIG. 28. Model compound, Meim6, for copper T3 active site.

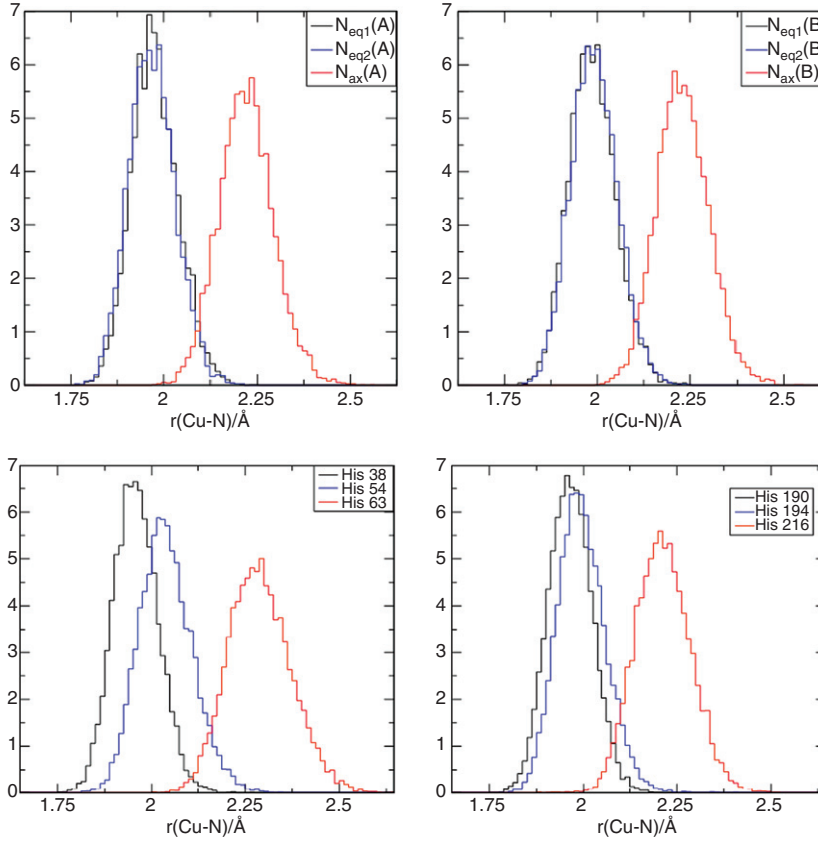

FIG. 29. Histograms of the Cu–N bond lengths from LFMD simulations. Top: results for the final 4 ns of a 12 ns simulation of the model active site, Meim6 (see Fig. 28). Bottom: results for the final 4 ns of a 16 ns simulation for sTy.

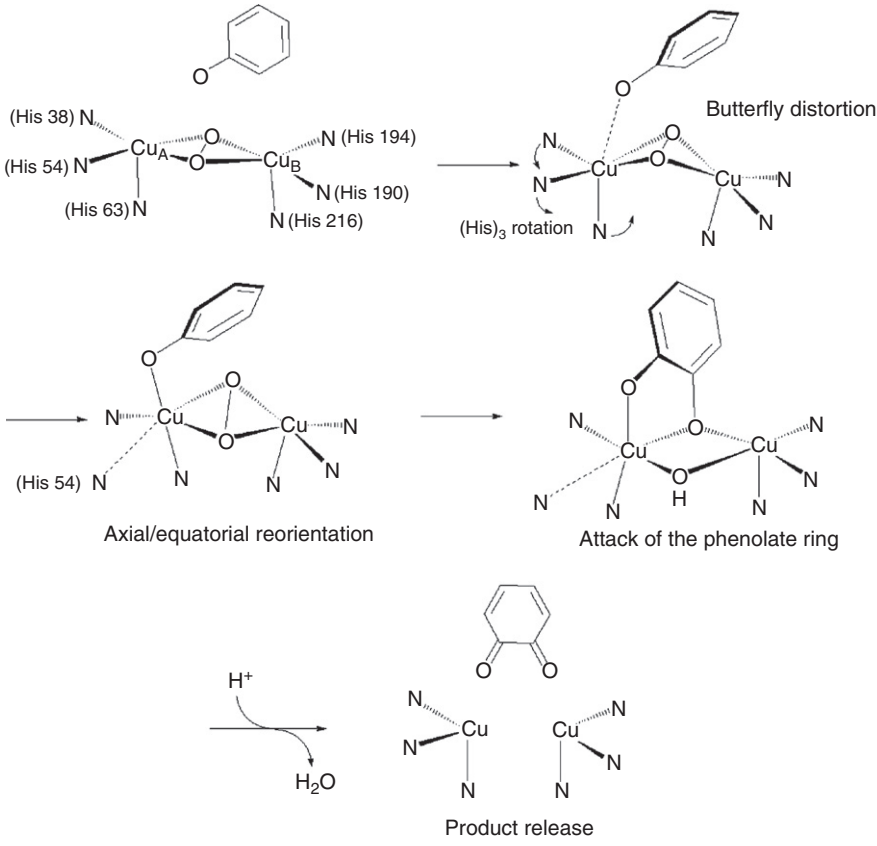

FIG. 30. Modified mechanism for monophenolic hydroxylation by sTy based on LFMD simulations.

experimental data, could we develop an LFMM FF which could reproduce the absolute energetics of M-OH_2 bonding as shown in Fig. 2? Secondly, would such a FF apply to modeling the water exchange process?

Using available experimental data such as Δ_{oct}, X-ray structures, and solvation enthalpies, augmented by DFT calculations of symmetric stretching frequencies and the relative σ/π ratio in the M-O bond, the first goal was straightforward (*73*).

At first sight, the second goal appeared more challenging. Traditionally, MM has been supposed unsuitable for modeling reaction mechanisms where bonds are made and broken. The change of connectivity between reactant(s) and product(s) generates different reference states, the reaction energies cannot usually be directly compared and the FF is not able to locate a reasonable

transition state (TS). However, since MM is empirical, it is possible to design FFs for modeling reaction pathways although additional parameterization work is required (*74*).

Several schemes are now available for modeling TSs within a MM framework. SEAM searching (*74,75*), where the minimum energy point along the "seam" connecting the reactant and product PE surfaces is located, is appealing since it is conceptually straightforward, can be easily implemented in existing codes, and provides a fairly good estimate of the true TS. Exchange reactions have the added advantage that the net reaction energy is zero. In addition, Basolo and Pearson had long ago reported an approximate correlation between the change in crystal field stabilization energy and the reaction rate (*76*). Their model estimated this crystal field activation energy (CFAE) based on fairly crude symmetry approximations with a square pyramidal (SQP) or trigonal bipyramidal (TBP) geometry serving for a dissociative TS, while a pentagonal bipyramidal (PBP) or octahedral wedge (OW) structure was used for an associative TS (Table II).

These data provide some qualitative guides to the kinetic behavior of octahedral species. If the change in the d-electron stabilization energy (i.e., the CFAE) is negative for a particular mechanism, the reaction is favored and the complex should be relatively labile—i.e., the substitution process should occur easily. Conversely, if the CFAE is positive, the reaction is disfavored and the complex should be relatively kinetically inert.

A quick inspection of Table II soon reveals that octahedral d^1 and d^2 complexes should be labile (negative CFAE for associative pathways) while d^3 species should be inert. High-spin d^6 and d^7 species should be labile while high-spin d^8 complexes should be relatively inert. In the case where there is no stabilization energy contribution, the reactivity is expected to follow that of

TABLE II

CRYSTAL FIELD ACTIVATION ENERGIES (IN D_Q UNITS) FOR ASSOCIATIVE (OW AND PBP) AND DISSOCIATIVE (SQP AND TBP) SUBSTITUTION REACTIONS OF HIGH-SPIN OCTAHEDRAL COMPLEXES

Number of d electrons	SQP	OW	PBP	TBP
0, 5, 10	0.0	0.0	0.0	0.0
1, 6	–0.57	–2.08	–1.28	1.28
2, 7	–1.14	–0.68	–2.56	2.56
3, 8	2.00	1.81	4.26	5.74
4, 9	–3.14	–2.80	3.19	6.81

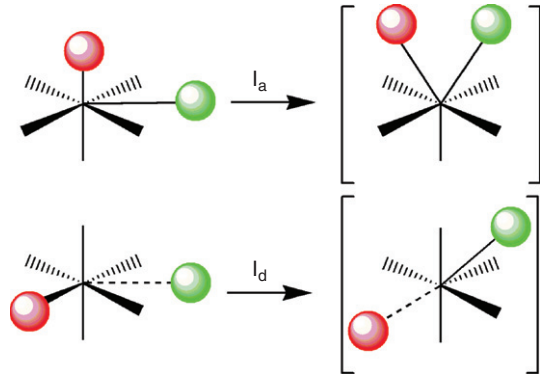

FIG. 31. Schematic of model transition states pathways.

main group ionic species which are labile. These qualitative predictions are born out by experiment.

LFMM is a completely general ligand field treatment plus no symmetry constraints are applied. Thus, we can expect that the LFMM FF should provide an even better correlation with experiment than Basolo and Pearson's CFT approach.

Approximate TS structures were located based on the pathways shown in Fig. 31 using the SEAM search algorithm. However, for associative interchange, this leads to an inconsistency in that in order to have different connectivities in reactant and product states, there are only six explicit M-O bonds while the TS should have seven. Consequently, the seventh ligand is explicitly connected and the structure reoptimized using a simple Newton–Raphson procedure. For vanadium, the SEAM structure is sufficiently good for this procedure to locate a true first-order saddle point (Fig. 32, left) (*73*).

The LFMM reaction barriers correlate very well with experiment and even predict a mechanistic changeover from associative interchange for Mn(II) to dissociative interchange for Fe(II) and Co(II) in agreement with the change in signs of the volumes of activation (Fig. 33).

The correlation between the lowest computed barriers (irrespective of mechanism) and the logarithm of the experimental rate constants, k, is shown in Fig. 34. Given that the LFMM parameterization is based solely on ground state properties and that not all possible pathways have been considered, the agreement is remarkable and suggests that LFMM should provide a good basis for more exact treatments of reaction pathways and their attendant TSs.

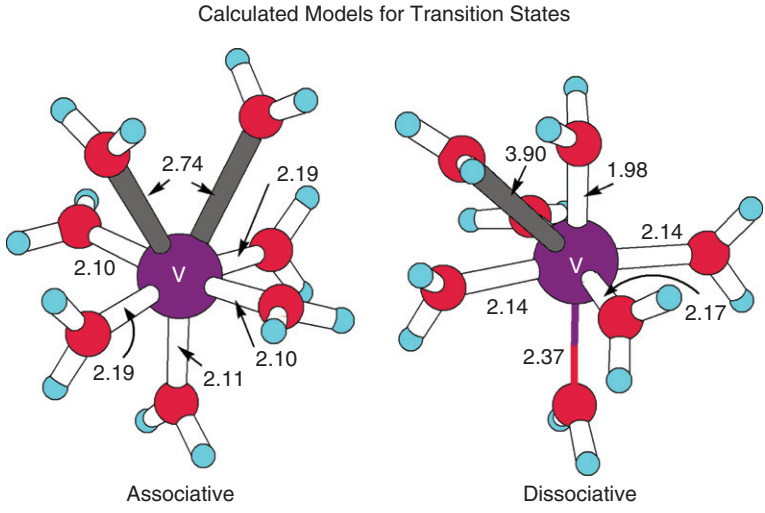

FIG. 32. LFMM model TSs for water exchange at $[V(OH_2)_6]^{2+}$.

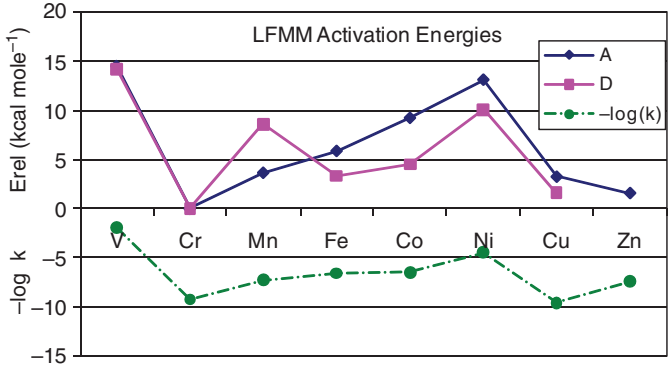

FIG. 33. Calculated activation energies relative to Cr(II) (top portion) compared to –log k, (bottom portion) where k are the experimental exchange-rate constants. No suitable D pathway could be located for Zn which is therefore omitted from the graph.

XIII. Effects of M-L π Bonding

The final application of LFMM concerns a subtle yet unexpectedly significant Jahn–Teller effect. The classic examples of Jahn–Teller distortions are associated with $d^9$and high-spin d^4 systems with orbitally degenerate ground states of E symmetry

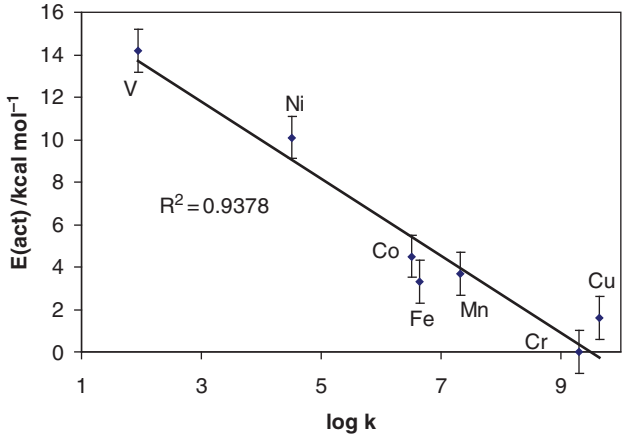

FIG. 34. Correlation between experimental log k values and calculated activation energies with the latter showing an estimated uncertainty of ±1 kcal mol^{-1}.

and a pronounced "σ-type" tetragonal elongation which is easy to spot. In principle, octahedral d^1, d^2, d^6, and d^7 are also formally Jahn–Teller active (with T ground states), but here the asymmetric d-orbital occupation is in the π-type t_{2g} orbitals and since π-interactions are smaller than σ, the observation of apparently "octahedral" complexes like $[Fe(OH_2)_6]^{2+}$ has been taken as evidence that π-type Jahn–Teller effects are relatively unimportant. Certainly, applications of ligand field theory to species like $[Fe(OH_2)_6]^{2+}$ and $[Co(OH_2)_6]^{2+}$ have assumed effective octahedral symmetry.

The Jahn–Teller coupling for an orbitally triplet state is complicated. In $[Fe(OH_2)_6]^{2+}$, for example, in addition to the e_g vibration which is also active for E ground states (Fig. 35), there are a number of triply degenerate vibrational modes. The result is that while the only mechanism for raising the degeneracy in a d^9 E⊗e system is a vibration which alters the M-L bond lengths (*53*), the "π-type" Jahn–Teller systems can distort in other ways. In particular, if the ligand is capable of asymmetric π bonding, it is possible to remove the orbital degeneracy by rotation around the M-L bond (*77*). Hence, relative to the relevant orbitally degenerate starting point (T_h symmetry for $[M(OH_2)_6]^{2+}$ complexes, Fig. 36, left) the "distorted" geometry can retain six identical M-O distances (Fig. 36, right) and thus "masquerade" as an apparently "octahedral" system.

These subtle changes in ligand orientation may nevertheless lead to significant lowering of the energy. For $[Fe(OH_2)_6]^{2+}$, the

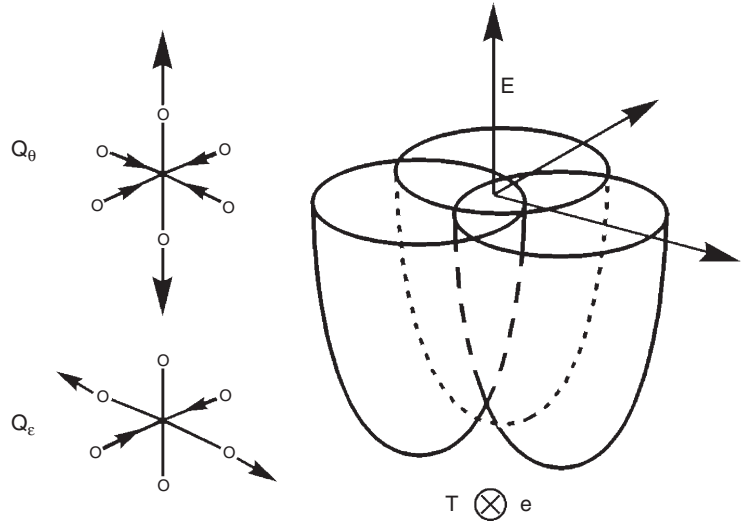

FIG. 35. Schematic representation of the first-order potential energy surface for T⊗e vibronic coupling. The two components of the ε_g vibrational mode are shown on the left.

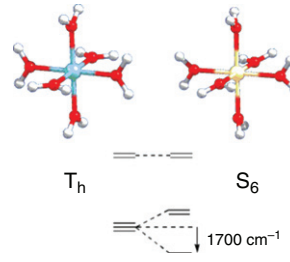

FIG. 36. Ligand field stabilization energy change for d^6 $[Fe(OH_2)_6]^{2+}$ associated with a geometrical "distortion" from T_h to S_6 symmetry assuming $e_{\pi\perp} = 1400\ cm^{-1}$.

energetic stabilization of 1700 cm^{-1} (~5 kcal mol^{-1}) is about 60% of that calculated for $[Cu(OH_2)_6]^{2+}$ while for model systems with strongly asymmetric π-bonding ligands like the imidazolate anion, a substantial torque is exerted around the M-L bond which effectively "locks" the ligand orientation to align with the appropriate d function (77). Such "ligand field torques" could have a significant and hitherto unrecognized effect on bioinorganic systems where TMs bound to histidines are common.

XIV. Conclusions

The main driver behind developing LFMM is computational efficiency. Although DFT has undoubtedly revolutionized the theoretical treatment of TM systems, there are many instances where all QM methods, even DFT, are simply not viable. Comprehensive conformational searching, molecular dynamics, and virtual screening represent hundreds of thousands of individual calculations and QM methods are too expensive. We are forced to turn to classical models but, for TM centers, this presents a whole new set of challenges. However, since we cannot easily make QM orders of magnitude faster, our only option is to make MM "smarter" and thus able to cope with the extra demands of coordination complexes.

Our solution is to add an explicit treatment of the ligand field stabilization energy (LFSE) to an otherwise more-or-less conventional MM treatment. The LFSE calculation is based on the Angular Overlap Model (*29*) which has separate parameters for describing M-L σ and π interactions. Thus, the physical basis for metal–ligand bonding in LFMM is on a par with QM methods which facilitates LFMM giving results comparable to DFT but up to four orders of magnitude faster.

The "price" we pay is an increase in the number of parameters. However, given the extensive amounts of "ligand field" data in the literature augmented with selected DFT results, reasonable values for the AOM parameters can be set at the beginning and fewer LFMM parameters need to be explicitly optimized. Nevertheless, finding suitable parameters "by hand" is laborious and we are currently developing a range of automatic optimization tools which include sophisticated machine-learning algorithms.

For those systems we have studied so far, many "classical" ligand field features are successfully captured by LFMM: e.g., the "double hump" variation of structural and thermodynamic properties due to the LFSE (*73*), σ- (*36,58,78*) and π-type (*77*) Jahn–Teller effects, the *trans* influence (*21*), and spin state effects (*18,33,59*). LFMM is equally at home with small molecules and large proteins and potential future coordination chemistry applications are enormous.

As for further extension of the LFMM methodology, we are currently exploring organometallic systems in particular those containing cyclic π-bonded ligands like η^5-cyclopenadiene and η^6-benzene. Preliminary results for half-sandwich Ru-arene compounds, which are potential anticancer drugs under investigation by Professor Peter Sadler of this department, are encouraging and will be reported in due course.

Summary

Computer modeling of transition metal (TM) systems is difficult. Most workers therefore resort to quantum methods like density functional theory (DFT). However, all quantum methods are relatively slow and compute-intensive procedures like high-throughput screening, conformational searching, and molecular dynamics are largely impractical due to the sheer number of individual computations involved. In contrast, classical molecular mechanics (MM) is fast enough to cope with these large numbers of calculations in a reasonable time on a relatively modest computer. Unfortunately, MM is not well suited to TM systems since it misses important d-electron effects which are implicit in DFT. Thus, since we cannot make DFT faster, we must make MM smarter. Combining ligand field theory with MM—ligand field molecular mechanics (LFMM)—provides a much more sophisticated description of metal–ligand bonding. Diverse applications spanning coordination and bioinorganic chemistry demonstrate that LFMM provides DFT accuracy at MM prices and is thus a very powerful, general tool for modeling TM systems.

References

1. Ziegler, T.; Autschbach, J. *Chem. Rev.* **2005**, *105*, 2695–2722.
2. Kirchner, B.; Wennmohs, F.; Ye, S. F.; Neese, F. *Curr. Opin. Chem. Biol.* **2007**, *11*, 134–141.
3. Siegbahn, P. E. M.; Blomberg, M. R. A. *Chem. Rev.* **2000**, *100*, 421–437.
4. Burton, V. J.; Deeth, R. J.; Kemp, C. M.; Gilbert, P. J. *J. Am. Chem. Soc.* **1995**, *117*, 8407–8415.
5. Deeth, R. J.; Anastasi, A.; Diedrich, C.; Randell, K. *Coord. Chem. Rev.* **2009**, *253*, 795–816.
6. Lin, H.; Truhlar, D. G. *Theor. Chem. Acc.* **2007**, *117*, 185–199.
7. Halgren, T. A. *J. Comput. Chem.* **1996**, *17*, 490–519.
8. Halgren, T. A. *J. Comput. Chem.* **1996**, *17*, 520–552.
9. Halgren, T. A. *J. Comput. Chem.* **1996**, *17*, 553–586.
10. Halgren, T. A.; Nachbar, R. B. *J. Comput. Chem.* **1996**, *17*, 587–615.
11. Rappe, A. K.; Casewit, C. J.; Colwell, K. S.; Goddard, W. A.; Skiff, W. M. *J. Am. Chem. Soc.* **1992**, *114*, 10024–10035.
12. Pearlman, D. A.; Case, D. A.; Caldwell, J. W.; Ross, W. S.; Cheatham, T. E.; Debolt, S.; Ferguson, D.; Seibel, G.; Kollman, P. *Comput. Phys. Commun.* **1995**, *91*, 1–41.
13. Brooks, B. R.; Bruccoleri, R. E.; Olafson, B. D.; States, D. J.; Swaminathan, S.; Karplus, M. *J. Comput. Chem.* **1983**, *4*, 187–217.
14. Allured, V. S.; Kelly, C. M.; Landis, C. R. *J. Am. Chem. Soc.* **1991**, *113*, 1–12.
15. Carlsson, A. E.; Zapata, S. *Biophys. J.* **2001**, *81*, 1–10.
16. Kepert, D. L. "*Inorganic Stereochemistry*"; Springer-Verlag: Berlin/Heidelberg/New York, **1982**.

17. Comba, P.; Hambley, T. W. "*Molecular Modeling of Inorganic Compounds*"; VCH: Weinheim, **1995**.
18. Deeth, R. J.; Fey, N.; Williams-Hubbard, B. J. *J. Comput. Chem.* **2005**, *26*, 123–130.
19. Johnson, D. A.; Nelson, P. G. *Inorg. Chem.* **1995**, *34*, 5666–5671.
20. Figgis, B. N.; Hitchman, M. A. "*Ligand Field Theory and Its Applications*"; John Wiley and Sons Ltd.: New York, **2000**.
21. Anastasi, A.; Deeth, R. J. *J. Chem. Theory Comput.* **2009**, *5*, 2339–2352.
22. Cundari, T. R.; Fu, W.; Moody, E. W.; Slavin, L. L.; Snyder, L. A.; Sommerer, S. O.; Klinckman, T. R. *J. Phys. Chem.* **1996**, *100*, 18057–18064.
23. Ballhausen, C. J. "*Introduction to Ligand Field Theory*"; McGraw-Hill: New York, **1962**.
24. Bethe, H. A. *Ann. Phys.* **1929**, *3*, 133.
25. Gerloch, M.; Woolley, R. G. *Prog. Inorg. Chem.* **1983**, *31*, 371–446.
26. Gerloch, M.; Woolley, R. G. *J. Chem. Soc. Dalton Trans.* **1981**, 1714–1717.
27. Bridgeman, A. J.; Gerloch, M. *Prog. Inorg. Chem.* **1997**, *45*, 179–281.
28. Deeth, R. J. *Coord. Chem. Rev.* **2001**, *212*, 11–34.
29. Schaeffer, C. E.; Jorgensen, C. K. *Mol. Phys.* **1965**, *9*, 401.
30. Deeth, R. J.; Foulis, D. L. *Phys. Chem. Chem. Phys.* **2002**, *4*, 4292–4297.
31. Comba, P.; Hambley, T. W.; Hitchman, M. A.; Stratemeier, H. *Inorg. Chem.* **1995**, *34*, 3903–3911.
32. Deeth, R. J.; Gerloch, M. *Inorg. Chem.* **1984**, *23*, 3846–3853.
33. Deeth, R. J.; Anastasi, A. E.; Wilcockson, M. J. *J. Am. Chem. Soc.* **2010**, *132*, 6876–6877.
34. MOE; "*Chemical Computing Group*"**2007**(Ed.); Montreal: Montreal, 2007
35. Deeth, R. J. *Faraday Discuss.* **2003**, *124*, 379–391.
36. Deeth, R. J.; Hearnshaw, L. J. A. *Dalton Trans.* **2006**, 1092–1100.
37. Deeth, R. J. *Inorg. Chem.* **2007**, *46*, 4492–4503.
38. Norrby, P. O.; Brandt, P. *Coord. Chem. Rev.* **2001**, *212*, 79–109.
39. Dhungana, S.; Harrington, J. M.; Gebhardt, P.; Moellmann, U.; Crumbliss, A. L. *Inorg. Chem.* **2007**, *46*, 8362–8371.
40. Lautru, S.; Deeth, R. J.; Bailey, L. M.; Challis, G. L. *Nat. Chem. Biol.* **2005**, *1*, 265–269.
41. Cotton, F. A.; Wilkinson, G. "*Advanced Inorganic Chemistry*"; 5th edn. John Wiley and Sons: New York, **1988**.
42. Mehrotra, R. C.; Bohra, R. "*Metal Carboxylates*"; Academic Press: New York, **1983**.
43. Frausto da Silva, J. J. R.; Williams, R. J. P. "*The Biological Chemistry of the Elements: The Inorganic Chemistry of Life*"; Clarendon Press: Oxford, UK, **1991**.
44. Halgren, T. A. *J. Comput. Chem.* **1999**, *20*, 720–729.
45. Deeth, R. J. *Inorg. Chem.* **2008**, *47*, 6711–6725.
46. Bersuker, I. B. *Chem. Rev.* **2001**, *101*, 1067–1114.
47. Simmons, C. J. *New J. Chem.* **1993**, *17*, 77–95.
48. Hathaway, B. J. *Struct. Bonding* **1984**, *57*, 55–118.
49. Hathaway, B. J. *Coord. Chem. Rev.* **1981**, *35*, 211–252.
50. Hitchman, M. A. *Comments Inorg. Chem.* **1994**, *15*, 197.
51. Bersuker, I. B. *J. Comput. Chem.* **1997**, *18*, 260–267.
52. Riley, M. J.; Hitchman, M. A.; Mohammed, A. W. *J. Chem. Phys.* **1987**, *87*, 3766–3778.
53. Deeth, R. J.; Hitchman, M. A. *Inorg. Chem.* **1986**, *25*, 1225–1233.
54. Comba, P.; Zimmer, M. *Inorg. Chem.* **1994**, *33*, 5368–5369.

55. Burton, V. J.; Deeth, R. J. *J. Chem. Soc. Chem. Commun.* **1995**, 573–574.
56. Allen, F. H. *Acta Crystallogr.* **2002**, *B58*, 380–388.
57. Fletcher, D. A.; McMeeking, R. F.; Parkin, D. *J. Chem. Inf. Comput. Sci.* **1996**, *36*, 746–749.
58. Bentz, A.; Comba, P.; Deeth, R. J.; Kerscher, M.; Seibold, B.; Wadepohl, H. *Inorg. Chem.* **2008**, *47*, 9518–9527.
59. Deeth, R. J.; Foulis, D. L.; Williams-Hubbard, B. J. *Dalton Trans.* **2003**, 3949–3955.
60. Darhovskii, M. B.; Razumov, M. G.; Pletnev, I. V.; Tchougreeff, A. L. *Int. J. Quantum Chem.* **2002**, *88*, 588–605.
61. Deeth', R.J.Unpublished work.
62. Deeth, R. J. *Chem. Commun.* **2006**, 2551–2553.
63. Solomon, E. I.; Szilagyi, R. K.; George, S. D.; Basumallick, L. *Chem. Rev.* **2004**, *104*, 419–458.
64. Hocking, R. K.; Deeth, R. J.; Hambley, T. W. *Inorg. Chem.* **2007**, *46*, 8238–8244.
65. Bray, M. R.; Deeth, R. J.; Paget, V. J.; Sheen, P. D. *Int. J. Quantum Chem.* **1997**, *61*, 85–91.
66. Ryde, U.; Olsson, M. H. M.; Pierloot, K.; Roos, B. O. *J. Mol. Biol.* **1996**, *261*, 586–596.
67. Vallee, B. L.; Williams, R. J. P. *Proc. Natl. Acad. Sci. U.S.A.* **1968**, *59*, 498–505.
68. Malmstrom, B. G. *Eur. J. Biochem.* **1994**, *223*, 711–718.
69. Diedrich, C.; Deeth, R. J. *Inorg. Chem.* **2008**, *47*, 2494–2506.
70. Deeth, R. J.; Diedrich, C. *J. Biol. Inorg. Chem.* **2010**, *15*, 117.
71. Richens, D. T. *Chem. Rev.* **2005**, *105*, 1961–2002.
72. Richens, D. T. *"The Chemistry of Aqua Ions"*; John Wiley & Sons: New York, **1997**.
73. Deeth, R. J.; Randell, K. *Inorg. Chem.* **2008**, *47*, 7377–7388.
74. Jensen, F.; Norrby, P. O. *Theor. Chem. Acc.* **2003**, *109*, 1–7.
75. Jensen, F. *J. Comput. Chem.* **1994**, *15*, 1199–1216.
76. Basolo, F.; Pearson, R. G. *"Mechanisms of Inorganic Reactions"*; John Wiley & Sons Inc: New York, **1967**.
77. Deeth, R. J.; Anastasi, A.; Randell, K. *Dalton Trans.* **2009**, 6007–6012.
78. Deeth, R. J.; Hearnshaw, L. J. A. *Dalton Trans.* **2005**, 3638–3645.

CALCULATION OF MAGNETIC CIRCULAR DICHROISM SPECTRA WITH TIME-DEPENDENT DENSITY FUNCTIONAL THEORY

MICHAEL SETH and TOM ZIEGLER

Department of Chemistry, University of Calgary, 2500 University Dr NW, Calgary, AB T2N 1N4, Canada

I. Introduction

In 1846 Michael Faraday reported the first observation of magnetic optical activity (*1–2*). Upon shining plane-polarized light through lead borate glass in the presence of a magnetic field, he found that the plane of polarization of the light was rotated when no such rotation existed in the absence of the magnetic field. This phenomenon is now called magnetic optical rotation (MOR) or the Faraday effect. A few years later it was shown by Verdet that the angle of rotation was proportional to the strength of the applied magnetic field (*3*). The constant of proportionality has become known as the Verdet constant.

In experiments considering normal optical rotation as a function of the energy of the incident light in an absorbing region of

THEORETICAL AND COMPUTATIONAL INORGANIC CHEMISTRY
VOLUME 62 ISSN 0898-8838 / DOI: 10.1016/S0898-8838(10)62002-8

the spectrum, not only is the light's plane of polarization rotated but the polarization is also lost to some extent as ellipticity is introduced. Both the optical rotation and induced ellipticity can be explained in terms of circularly polarized light. The former occurs because the transmitting medium has differing refractive indices for left and right circularly polarized light, while the latter is due to differing absorption coefficients of left and right circularly polarized light. The ellipticity was thus called circular dichroism (CD).

It might be imagined that a similar relationship would hold for MOR and this indeed proved to be the case. A few experiments involving the magnetic circular dichroism (MCD) of cobalt were carried out in the 1930s (*4–6*) and some of the basic physical ideas behind MCD were described (*7*) but otherwise, little interest was shown in MCD.

This changed in the 1960s. The technology of spectroscopy and magnets had improved significantly and research groups were beginning to measure MCD spectra (*8,9*). At the same time, a comprehensive presentation of the theory of MCD was produced by Stephens and Buckingham (*9,10*). In this work it was shown that the MCD intensity of a transition to state J as a function of ω could be written as

$$\frac{\Delta A}{\omega} = clB\chi \sum_J \left(A_J \left(-\frac{\partial f(\omega-\omega_J)}{\partial \omega} \right) + \left(B_J + \frac{C_J}{kT} \right) f(\omega-\omega_J) \right) \qquad (1)$$

where c, l, B, and T are the experimental parameters representing the concentration, path length, magnetic field amplitude, and temperature, respectively, k is Boltzmann's constant, and χ is a collection of constants. The term f is a band-shape function. As far as possible, equations in this review will be written in atomic units and we therefore write the energies of the incident light and the transition to state J as ω and ω_J rather than $\hbar\omega$ and $\hbar\omega_J$ in Eq. (1) and elsewhere. Equation (1) is written in its modern form with the MCD defined in terms of ΔA, the difference in absorption of left and right circularly polarized light, rather than the induced ellipticity θ or the molar ellipticity $[\theta]_M$ that were used in the initial derivation and many early applications.

Equation (1) suggests that the MCD intensity is made up of three contributions, one with the shape of the derivative of an absorption band and a further two with form of an absorption band, one of which is temperature dependent. These three contributions to a spectrum are called A, B, and C terms and each has an associated parameter, A_J, B_J, and C_J. The parameters are signed quantities and MCD intensity can be positive or negative. From

the formulation of Stephens and Buckingham each of the parameters can be interpreted in terms of the properties of the ground and excited states of the transition that produced the MCD intensity (*9*). Each of these parameters will be considered in more detail when the theory of MCD is described in Section II.A. It should be noted that more than one definition of each of A_J, B_J, and C_J has been used in the literature. All through this review we use the definitions recommended in the book by Piepho and Schatz (*11*).

With the advances in experimental techniques and theory, MCD spectroscopy became a viable analytical technique and found application in many areas of chemistry (*11–17*). The distinct spectral forms of *A, B,* and *C* terms and the fact that MCD intensity can be positive or negative make an MCD measurement a useful complement to an absorption spectrum. MCD has been found to be rather more useful than MOR as the latter type of spectrum is generally more difficult to interpret (*12*).

It was quickly recognized that a nonrelativistic formulation of MCD led to predictions that were qualitatively wrong for some paramagnetic metal halides (*18–20*). The introduction of spin–orbit coupling created addition contributions to the *C* term parameters and produced predictions in qualitative agreement with experiment. It was not until some time later that general formulations of the new terms caused by spin–orbit coupling appeared (*21–23*). The spin–orbit-induced *C* terms have played an important role in modern applications of MCD spectroscopy as they have proven to be extremely useful in the study of metalloenzymes (*15,24–26*).

Theoretical analysis has always been an important part of MCD spectroscopy. The parameters A_J, B_J, and C_J can be extracted from an experimental spectrum by a fit to a suitable set of functions or through the method of moments (*27–28*). The interpretation of these parameters is generally not a trivial task. For smaller, symmetrical molecules group theory has been used to good effect to extract information from an MCD spectrum (*11*). In recent years, quantum chemical calculation has proven a very useful aid in the interpretation of the often-complicated spectra of larger, nonsymmetric molecules.

The direct calculation of the MCD spectra of small to medium-sized molecules in a routine way through quantum mechanics obviously would be an extremely useful tool to help in the understanding of an experimental spectrum. Significant work in this area has taken place in the last few years. In this review we describe our contribution to the topic.

In Stephens' and Buckingham's seminal work the theories of MOR and MCD were developed together as real and imaginary

components of a complex MOR (*9*). In this approach the most important term for MCD is

$$\frac{\Delta A}{\omega} \propto \mathrm{Im}\left[i\alpha^{(1)}(\omega)\right]B \tag{2}$$

where $\alpha^{(1)}(\omega)$ is the first-order correction to the frequency-dependent polarizability due to a magnetic field and i is the square root of –1. Given the close relationship between MCD and MOR implicit in this derivation we call this formulation "MCD from the imaginary part of the Verdet constant" or Im[*V*].

In later work, Stephens rederived Eq. (1) starting from the difference of absorption coefficients of left and right circularly polarized light and applying the theory of radiation absorption in the presence of a magnetic field (*29*). In this approach the leading contribution to MCD is

$$\frac{\Delta A}{\omega} \propto \left[\sum_J |\langle A|M|J\rangle|^2 f(\omega-\omega_J)\right]^{(1)} B \tag{3}$$

where M is the electric dipole moment operator, A is the ground state, J is an excited state, and $<A|M|J>$ is thus the transition moment. The superscript (1) again indicates the first-order correction due to the presence of a magnetic field. In most modern applications, MCD is usually defined following this second formulation.

These two differing approaches to deriving equations for MCD intensity have each inspired methodologies for calculating MCD spectra from first principles. The first quantum chemical calculations of an MCD spectrum utilized the transition moment approach and obtained the parameters of interest by direct calculation of the wave functions of the ground and excited states involved. In the early 1990s Jensen and coworkers calculated A_J and B_J parameters of acetylene using wave functions obtained from state-averaged complete active space self-consistent field (CASSCF) followed by configuration interaction (CI) calculations (*30–31*). About 10 years later, Honda and coworkers evaluated B_J and, where appropriate, A_J parameters of CH_3I, ethene, ortho and parabenzoquinone, and Cl_2, Br_2, and I_2 using single-excitation CI (CIS) and including relativistic effects (*32–33*). At about the same time Sterzel and coworkers simulated the spectra of two naphthalenetetracarboxy diimides using wave functions from CASSCF calculations (*34*). Bolvin has calculated the spin–orbit induced C terms of the Creutz-Taube ion with wave functions derived from a CASSCF calculation including dynamic correlation second order (CASPT2) and spin–orbit coupling (*35*). The most complete

treatment of MCD spectroscopy based on explicit calculation of wave functions is that implemented by Ganyushin and Neese (*36*). In this approach CASSCF or multireference CI wave functions are perturbed by an operator that includes the magnetic field, spin–orbit coupling, and spin–spin coupling to enable the inclusion of all contributions to the MCD intensity as well as the influence of zero-field splitting (ZFS) of the ground state. Thus far, this approach has been applied to the diatomic molecules CH, NH, and OH, the octahedral complex $[Fe(CN)_6]^{3-}$, and a series of tetrahedral Co(II) complexes (*36,37*). The final examples of this type of MCD calculation represent a slightly different approach to the problem. Shillady and Tindle have calculated the MCD spectra of indole and melatonin at the CIS level with a small basis set for the purpose of comparison with semi-empirical complete neglect of differential overlap spectroscopic (CNDO/S) parameterization CIS calculations (*38*). Shillady and Tindle present some example CIS MCD calculations in their textbook (*39*). At this point we should mention the contributions of Michl who has made extensive use of semi-empirical methods as part of his detailed analysis of the MCD of aromatic molecules (*14*).

Rather than directly calculate excited state wave functions to obtain information about electronic transitions, quantum mechanics presents the alternative approach of considering the response of the ground state to incident light. When the frequency of the light corresponds to a transition energy of the system the response can be used to obtain transition dipole moments. With the addition of a magnetic field as a second perturbation MCD can be calculated. The first application that utilized response theory is that by Coriani and coworkers in 1999 (*40*). In this study frequency-dependent quadratic response functions were used in combination with CASSCF and Hartree–Fock (HF) references to evaluate the *B* term parameters of ethene and *p*-benzoquinone. Their methodology was extended to include coupled-cluster calculations by Kjærgaard and coworkers and applied to the *B* terms of a series of azobenzenes and phosphabenzene (*41*). A further extension to include solvent effects and density functional theory (DFT) was provided by Solheim *et al.* and used to calculate the *B* term parameters of several benzoquinones (*42*). An alternative Lagrangian and gauge-including atomic orbital (GIAO)-based formulation was presented recently by Kjærgaard *et al.* and applied to the evaluation of the *B* term parameters of pyrimidine, phosphabenzene, and pyridine with HF and DFT reference calculations (*43*).

The calculations described in the previous paragraph focus on the response of a system when the frequency of the incoming light

matches a resonance of that molecule. An alternative response-based approach has been proposed by Solheim and coworkers that is more in the spirit of the imaginary part of the Verdet constant formulation (Eq. 2) of MCD (*44*). This method makes use of nonlinear complex polarization propagators (*45*) that include a lifetime parameter to avoid the divergence in the response when a resonance is approached to calculate the influence of a magnetic field on the frequency-dependent polarizability. Solheim and coworkers applied their methodology to the calculation of the spectra of p-benzoquinone; tetrachloro-p-benzoquinone; cyclopropane; and Mg, Ni, and Zn porphyrin in combination with hybrid DFT (*44,46*).

In our own work we have considered both the transition moment (*47–50*) and imaginary Verdet (*51*) formulations as starting points for MCD implementations. We chose to work within the framework of time-dependent density functional theory (TDDFT) (*52,53*). TDDFT can be used to calculate excitation energies and transition moments (*54*) and has become perhaps the most widely used method within computational chemistry for calculating properties associated with excited states. For our purposes, it provides the best combination of reasonable accuracy, computational cost, widespread acceptance, and ease of use. This combination of factors means that an MCD implementation within TDDFT would be able to handle problems of interest to us, that is medium-sized molecules including 50 or more atoms, and at the same time be of use to a range of others in the computational community who might be interested in calculating MCD spectra from scratch. TDDFT is a form of response theory and our approach therefore has much in common with the other response-based methods mentioned in the previous paragraphs.

This review summarizes our efforts up to this time. In the next section an overview of our formulation will be presented. We will start with a summary of the theory of MCD. We will then provide a short summary of TDDFT theory to establish our starting point. Bringing together MCD and TDDFT theory allows us to formulate our approach for calculating MCD spectra. To finish the theoretical section we provide some notes on the steps of a calculation and interpretation of the results.

In the second half of the review some applications of our implementation are presented. We start with test calculations on smaller molecules that provide an opportunity to demonstrate what is required in the calculation of each type of contribution to MCD intensity. In the final sections some of our most recent applications that consider larger systems and more current problems are reviewed.

The theoretical section is necessarily rather terse. For more details concerning MCD (*9,11–13,17,21,55*), TDDFT (*52–54*), and our approach to the calculation of MCD spectra (*47–51*) consult the publications cited here.

Most of the methodologies discussed in Section II.C have been implemented into the Amsterdam Density Functional program package and are available from the 2009 release onward (*56–58*).

II. Theory

A. MCD Spectroscopy

In this section we will develop expressions for MCD parameters in terms of transition dipole moments. These expressions will follow conventional treatments for the most part but with an emphasis on quantities and notation that work well with TDDFT.

In an MCD experiment the difference in absorption intensity of left and right circularly polarized light in the presence of a static magnetic field directed along the direction of light propagation is measured as a function of the energy of the incident light.

$$\Delta A(\omega) = A_- - A_+ = (\varepsilon_- - \varepsilon_+)cl = \Delta\varepsilon(\omega)cl \tag{4}$$

where the concentration c is typically in mol m^{-3}, the path length l in cm, and $\Delta\varepsilon$ is the difference in absorption coefficients.

If the substance under investigation is chiral, $\Delta\varepsilon$ will be nonzero even in the absence of a magnetic field because of electronic CD. MCD can be considered as an additive contribution to ΔA or $\Delta\varepsilon$ that is due to the presence of a magnetic field. CD arises from a different mechanism than MCD and will not be considered further here.

If we make the dipole approximation the following expression is obtained for the difference of absorption coefficients of left and right circularly polarized light:

$$\Delta\varepsilon(\omega) = \chi\omega \sum_{aJj\gamma} \frac{N_a}{3N} \left(\langle Aa|M_\gamma^-|Jj\rangle^2 - \langle Aa|M_\gamma^+|Jj\rangle^2 \right) f(\omega - \omega_J) \tag{5}$$

where the ground state A may be degenerate with components labeled by a and the excited state J with possible degenerate components labeled by j. N_a is the population of component a of the ground state and N is the total population. It will be assumed that none of the excited states are populated. The $M_\gamma^\pm$ are the

electric dipole moment operators corresponding to left and right circularly polarized light along the directions $\gamma = x,y,z$. f is a normalized band-shape function. χ is a collection of constants

$$\chi = \frac{5N_0\pi^3\alpha^2\log_e}{5hcn} \tag{6}$$

where N_0 is Avogadro's number, α is the magnetic permeability of the medium, h is Planck's constant, c is the speed of light, and n is the refractive index of the medium. The ratio α^2/n describes the attenuation of the applied magnetic field as it moves through the substance under investigation. We assume in all cases that $\alpha^2/n=1$, a good approximation in nonmagnetic matrices (*17*).

The presence of a magnetic field along direction γ adds the following term to the Hamiltonian describing the system of interest:

$$H^{(1)\gamma} = \mu_\gamma B \tag{7}$$

where B is the amplitude of the applied magnetic field and μ_γ is the magnetic dipole moment operator.

$$\mu_\gamma = -\mu_B(L_\gamma + 2S_\gamma) \tag{8}$$

μ_B is the Bohr magneton and L_γ and S_γ are the operators corresponding to the projection of the orbital and spin angular momentum along direction γ. Any state for which L_γ has a nonzero expectation value we will describe as "orbitally degenerate," while states for which S_γ has a nonzero expectation value will have the usual label of "spin degenerate."

The electric dipole moment operator is independent of spin and, in the absence of spin–orbit coupling, the spin part of the magnetic moment operator will have no influence on MCD. We shall therefore neglect the spin part of Eq. (8) until we come to spin–orbit-induced MCD in Section II.A.4.

All of the equations that will be presented describe MCD that is averaged over all possible orientations. All operators are defined in a molecule-fixed axis system and the light and magnetic field will be felt equally from all directions. This is reflected in Eq. (5) through the summation over directions γ and the factor of 1/3.

We prefer to work with purely real or imaginary operators rather than the complex operators $M_\gamma^{\pm}$. These operators can be converted into a more convenient form with the identity:

$$\sum_\gamma \left(|\langle Aa|M_\gamma^-|Jj\rangle|^2 - |\langle Aa|M_\gamma^+|Jj\rangle|^2 \right) = i\sum_{\alpha\beta\gamma} \varepsilon_{\alpha\beta\gamma}\langle Aa|M^\alpha|Jj\rangle\langle Jj|M^\beta|Aa\rangle \tag{9}$$

where α and β run over *x,y,z* and $\varepsilon_{\alpha\beta\gamma}$ is the three-dimensional Levi-Civita symbol and is defined to be 1 if $\alpha\beta\gamma$ is a cyclic permutation of *xyz*, –1 if it is some other permutation, and 0 otherwise.

If states *A* and *J* are nondegenerate it is simple to show that the MCD as defined in Eq. (5) is zero in the absence of a magnetic field. If *A* and/or *J* is degenerate then the MCD of the transition between individual components may be nonzero but the total MCD of the transition summed over all degenerate components will be zero.

From Eq. (5) the transition dipoles, the band-shape function, and the population of the ground state components can depend on the applied magnetic field. MCD is caused by the influence of the magnetic field on these three quantities. The three perturbations each correspond to one of the terms in Eq. (1). The perturbation of the transition dipole creates a *B* term, the perturbation of the band-shape function leads to an *A* term, and the perturbation of the ground state populations provides a *C* term.

For the purposes of the following analysis, magnetic field-free quantities will be superscripted with (0), while first derivatives with respect to the magnetic field applied in the direction γ will have a superscript $(1)\gamma$.

If we expand Eq. (5) in a power series in the magnetic field *B* about $B=0$ the zeroth order term will be zero and the three terms that are linear in *B* will be sufficient to describe many MCD spectra. We will therefore consider the first derivative of Eq. (5) with respect to *B*. An important exception where terms of higher order in the magnetic field are often needed will be described in Section II.A.5.

A.1. B terms

The MCD due to the first derivative of the transition dipole moments is

$$\Delta\varepsilon_B = \omega B \chi \mu_B \sum_J B_J f\left(\omega - \omega_J^{(0)}\right) \tag{10}$$

$$B_J = -\sum_{aj\alpha\beta\gamma} \varepsilon_{\alpha\beta\gamma} \frac{2i}{3|A|} \langle Aa|M^\alpha|Jj\rangle^{(1)\gamma} \langle Jj|M^\beta|Aa\rangle^{(0)} \tag{11}$$

where Eq. (5) has been modified using Eq. (9). B_J is the *B* term parameter. We follow the usual convention of MCD and include μ_B with the constants rather than the MCD parameter (*11*). The perturbation therefore corresponds to the angular momentum operator L_γ rather than the magnetic dipole moment operator. The factor of $1/|A|$, the degeneracy of the ground state, has replaced the term

dependent on the population of the ground state components, $N_a^{(0)}/N$. For the time being, it is assumed that the ground state is not orbitally degenerate though it can be spin degenerate.

Equation (11) will be nonzero for all transitions that are dipole allowed. The MCD spectrum of all molecules will therefore include contributions from B terms.

A.2. A terms

The second contribution to the MCD that will be considered is the A term. A terms arise because of the change in the band-shape function f due to the applied magnetic field. In this context, the rigid-shift approximation (*11*) is usually applied. By making the rigid-shift approximation it is assumed that the center of the band-shape function moves as ω_J changes but that the shape of f otherwise does not change. If this is the case then

$$\Delta\varepsilon_A = \omega B \chi \mu_B \sum_J A_J \frac{\partial f\left(\omega - \omega_{Jj}^{(0)}\right)}{\partial \omega} \tag{12}$$

$$A_J = \sum_{\alpha\beta\gamma aj} \varepsilon_{\alpha\beta\gamma} \frac{i}{3|A|} \omega_{Jj}^{(1)\gamma} \langle Aa|M^\alpha|Jj\rangle^{(0)} \langle Jj|M^\beta|Aa\rangle^{(0)} \tag{13}$$

where we have used the following relation that follows from the rigid-shift approximation:

$$\frac{\partial f\left(\omega - \omega_{Jj}^{(0)}\right)}{\partial B} = \frac{1}{3} \sum_\gamma \omega_{Jj}^{(1)\gamma} \frac{\partial f\left(\omega - \omega_{Jj}^{(0)}\right)}{\partial \omega} \tag{14}$$

We follow the usual convention that a positive A term (and positive A_J) corresponds to a derivative feature with negative MCD below $\omega_J^{(0)}$ and positive MCD above $\omega_J^{(0)}$(*11*). Equations (13) and (14) are valid provided that $\omega_{Jj}^{(1)\gamma} B$ is significantly smaller than the absorption bandwidth.

Since our perturbation is magnetic, the energy of a state will be changed to first order only if that state is degenerate. As has already been noted, spin degeneracy makes no contribution to MCD intensity in the absence of spin–orbit coupling. Therefore, the A_J parameter of a given transition will be zero unless the point group of the molecule under investigation includes a degenerate irreducible representation and either the ground or excited state of the transition is orbitally degenerate.

For the moment we assume that the ground state is not orbitally degenerate. Thus, for $\omega_{Jj}^{(1)\gamma}$ to be nonzero we require an

excited state that is degenerate and a representation of the degenerate state that diagonalizes the angular momentum operator. Such a representation is complex. A formulation in terms of a real representation can be achieved by making use of the principle of spectroscopic stability (*11*)

$$\sum_{j} \langle n|O_1|\bar{j}\rangle\langle\bar{j}|O_2|l\rangle = \sum_{j'} \langle n|O_1|j'\rangle\langle j'|O_2|l\rangle \tag{15}$$

where O is an arbitrary operator, n and l are arbitrary functions, and $\bar{j}$ and j' represent two sets of orthonormal basis functions related by a unitary transformation.

The expression of this principle that is useful in the current context is

$$\sum_{j} \langle Jj|O_1|Jj\rangle\langle\overline{A}|O_2|Jj\rangle\langle Jj|O_3|\overline{A}\rangle = \sum_{jj'} \langle Jj'|O_1|Jj'\rangle\langle A|O_2|Jj\rangle\langle Jj'|O_3|A\rangle \tag{16}$$

where a line over a state indicates the complex representation and the states without a line are in an arbitrary representation. Using Eq. (16), Eq. (13) is transformed into

$$A_J = \sum_{\alpha\beta\gamma a j j'} \varepsilon_{\alpha\beta\gamma} \frac{i}{3|A|} \omega_{Jjj'}^{(1)\gamma} \langle Aa|M^{\alpha}|Jj\rangle^{(0)} \langle Jj'|M^{\beta}|Aa\rangle^{(0)} \tag{17}$$

where a real representation of the degenerate excited state J is chosen. The factor $\omega_{Jjj'}{}^{(1)\gamma}$ is no longer the straightforward derivative of the excitation energy. It will be defined more exactly in Section II.C.2.

A.3. C terms

The final part of Eq. (5) that can depend on the applied magnetic field is the populations of the components of the ground state N_a.

$$N_a(B)/N = \frac{1}{3}\sum_{\gamma} \exp\left(-E_{Aa}^{(1)\gamma}B/kT\right) / \sum_{\gamma a} \exp\left(-E_{Aa}^{(1)\gamma}B/kT\right) \tag{18}$$

for a given temperature T. $E_{Aa}{}^{(1)\gamma}$ is the derivative of the energy of a component of the ground state with respect to a magnetic field along direction γ. Spin degeneracy is again neglected for the time being. A ground state that is orbitally degenerate is therefore required for $E_{Aa}{}^{(1)\gamma}$ to be nonzero.

Since $E_{Aa}{}^{(1)\gamma}$ is a ground state property it can be calculated directly from the ground state orbitals.

$$E_{Aa}^{(1)\gamma} = -\mu_B \langle Aa^{(0)}|L_\gamma|Aa^{(0)}\rangle = -\mu_B \sum_i \int \phi_i^{(0)} l_\gamma \phi_i^{(0)} \tag{19}$$

where l_γ is the one-electron operator for angular momentum about the γ axis and the index i runs over occupied orbitals.

If $kT >> E_{Aa}{}^{(1)\gamma} B$ then

$$\frac{N_a}{N} \approx \frac{1}{|A|} + \frac{1}{3|A|} \sum_\gamma E_{Aa}^{(1)\gamma} B/kT \tag{20}$$

and

$$\Delta\varepsilon_C = \omega B \chi \mu_B \sum_J (C_J/kT) f\left(\omega - \omega_J^{(0)}\right) \tag{21}$$

where

$$C_J = -\frac{2i}{3|A|} \sum_{\alpha\beta\gamma aa'j} \varepsilon_{\alpha\beta\gamma} \langle Aa^{(0)}|L_\gamma|Aa'^{(0)}\rangle \langle Aa|M^\alpha|Jj\rangle^{(0)} \langle Jj|M^\beta|Aa'\rangle^{(0)} \tag{22}$$

The principle of spectroscopic stability has again been applied to obtain Eq. (22) in terms of a real representation of the ground state.

It is clear from Eqs. (21 and 22) that the MCD due to C terms will be temperature dependent with increasing intensity as the temperature is lowered. This form of MCD will occur only if the ground state of the molecule under investigation is orbitally degenerate.

A.4. C terms from spin–orbit coupling

It was noted earlier that, in the absence of spin–orbit coupling, the spin part of the magnetic moment operator makes no contribution to MCD and spin degeneracy also plays no role in MCD spectroscopy. It was also noted that neglecting spin–orbit coupling led to qualitative errors in the predicted MCD spectra of some spin-degenerate systems. In this section we will present equations for the additional contributions to MCD that occur once spin–orbit coupling is included.

At this stage we will take the spin–orbit operator to have the general form

$$H^{\mathrm{SO}} = \sum_\gamma H_\gamma^{\mathrm{SO},r} S_\gamma \tag{23}$$

where S_γ is the projection of the spin angular momentum operator along axis γ and $H_\gamma{}^{\mathrm{SO},r}$ operates on the spatial part of the wave

function and has the same symmetry properties as the angular momentum operator L_γ.

If we consider the effects of spin–orbit coupling, we see that in many ways it is analogous to the influence exerted by a magnetic field. Similarly to before, three terms in Eq. (5) depend on spin–orbit coupling, the excitation energy ω_J (and thus f), the transition dipoles, and the populations of the components of the ground state.

We will consider molecules where the ground state may be spin degenerate but not orbitally degenerate. The first-order spin–orbit correction to the energy of a state is zero unless that state is orbitally and spin degenerate. Therefore, the influence of spin–orbit coupling on the population of the ground state components is not considered here and we are left with two terms that can be perturbed by spin–orbit coupling.

If a molecule has a spin-degenerate ground state the splitting of the ground state components (labeled AM) due to the presence of a magnetic field is

$$E_{AM}^{(1)\gamma} = -2\mu_B M \tag{24}$$

where M is the projection of the spin angular momentum along axis γ. Here the g-tensor is approximated by 2.0 and $E^{(1)\gamma}$ is therefore the same for all directions γ. At this level of approximation the axis of spin quantization is defined by the direction of the applied magnetic field.

We consider first the MCD caused by the spin–orbit splitting of the excited state. If an excited state has both spin and orbital degeneracy then it will be split to first order in the spin–orbit coupling. We denote that splitting by

$$\omega_{Jj}^{(1)'} = \sum_{\gamma} \omega_{Jj}^{(1)'\gamma'} \tag{25}$$

where γ' indicates a directional component of the spin–orbit operator. For the time being γ' is independent of the direction of the magnetic field γ. A quantity perturbed by spin–orbit coupling is distinguished by a quantity perturbed by a magnetic field by the use of the superscript (1)'.

Equations (24) and (25) can be used to define a further contribution to Eq. (21) that is first order in the magnetic field and first order in the spin–orbit interaction. These contributions to the MCD intensity are also temperature dependent and are also called C terms.

$$\Delta\varepsilon_C^{\mathrm{SO},1} = \omega B \chi \mu_B \sum_J \left(C_J^{\mathrm{SO},1}/kT \right) \frac{\partial f\left(\omega - \omega_J^{(0)}\right)}{\partial \omega} \tag{26}$$

where

$$C_J^{\mathrm{SO},1} = \frac{2}{3|A|} \sum_{\alpha\beta\gamma\gamma' jM} \varepsilon_{\alpha\beta\gamma} M \omega_{Jj}^{(1)'\gamma'} \langle AM|M^\alpha|Jj\rangle^{(0)} \langle Jj|M^\beta|AM\rangle^{(0)} \quad (27)$$

Here the components of excited state J are expressed in a representation that diagonalizes the spin–orbit operator. In general, this will be a complex representation. The principle of spectroscopic stability can again be used to express the components of J in a representation that we denote jM. This representation is made up of space and spin parts where the spin part diagonalizes the spin operator.

$$C_J^{\mathrm{SO},1} = \frac{2i}{3|A|} \sum_{\alpha\beta\gamma\gamma' jj' MM'M''} \varepsilon_{\alpha\beta\gamma} M \omega_{Jjj'M'M''}^{(1)'\gamma'} \langle AM|M^\alpha|JjM'\rangle^{(0)} \langle Jj'M''|M^\beta|AM\rangle^{(0)} \quad (28)$$

Equation (28) can be simplified if we recognize that since the electric dipole operators are independent of spin any term will be zero unless $M=M'=M''$. Furthermore, as noted earlier, the axis of spin quantization is the direction of the applied magnetic field and terms will also be zero unless $\gamma=\gamma'$. Therefore,

$$\sum_{\gamma\gamma' MM'M''} \omega_{Jjj'M'M''}^{(1)'\gamma'} = \sum_{\gamma M} M \omega_{Jjj'}^{(1)'\gamma} \quad (29)$$

The term $\omega_{Jjj'}^{(1)'\gamma}$ is the part of the first-order contribution to the excited state spin–orbit splitting that comes from the spatial part of the spin–orbit operator and the factor of M comes from integration over spin. If we require that $M=M'=M''$ and use Eq. (29) in Eq. (28) then we arrive at an expression that is very similar to the equation for A_J

$$C_J^{\mathrm{SO},1} = \frac{2i}{3|A|} \sum_{\alpha\beta\gamma jj' M} \varepsilon_{\alpha\beta\gamma} M^2 \omega_{Jjj'}^{(1)'\gamma} \langle AM|M^\alpha|JjM\rangle^{(0)} \langle Jj'M|M^\beta|AM\rangle^{(0)} \quad (30)$$

Equation (26) is valid provided the spin–orbit coupling element $\omega_{Jjj'}^{(1)'\gamma}$ is smaller than the bandwidth of the transition under consideration.

From Eq. (30) we see that the MCD from the spin–orbit splitting of a spatially degenerate excited state will have the same form as that from the splitting of the excited state by a magnetic field (an A term) but its intensity will be temperature dependent and will also depend on the size of the spin–orbit splitting of the excited state.

The second contribution to the temperature-dependent MCD from spin–orbit coupling involves the perturbation of the transition dipoles to give

$$\Delta\varepsilon_C^{\mathrm{SO},2} = \omega B\chi\mu_B \sum_J \left(C_J^{\mathrm{SO},2}/kT\right) f\left(\omega - \omega_J^{(0)}\right) \tag{31}$$

where

$$C_J^{\mathrm{SO},2} = \frac{2i}{3|A|} \sum_{\alpha\beta\gamma M} \varepsilon_{\alpha\beta\gamma} M^2 \langle AM|M^\alpha|JM\rangle^{(1)'\gamma} \langle JM|M^\beta|AM\rangle^{(0)} \tag{32}$$

where it has been assumed that the excited state is not orbitally degenerate in order to simplify the equations somewhat. The fact that the electric dipole operators are independent of spin has again been used simplify Eq. (32) in much the same way that Eq. (30) was simplified. Here again the spin part of the spin–orbit operator has been reduced to a factor of M and the transition dipole is perturbed only by the spatial part of the spin–orbit coupling.

Equation 32 has a very similar form to the expression for B_J (Eq. 11).

If the contributions from Eqs. (26) and (31) are added to Eq. (1) we can define an alternative equation for MCD intensity

$$\frac{\Delta A}{\omega} = clB\chi \sum_J \left(\left(A_J + \frac{C_J^{\mathrm{SO},1}}{kT} \right) \frac{\partial f(\omega - \omega_J)}{\partial \omega} + \left(B_J + \frac{C_J + C_J^{\mathrm{SO},2}}{kT} \right) f(\omega - \omega_J) \right) \tag{33}$$

where the Bohr magneton has been merged into χ.

Since the angular momentum operator and the spatial part of a spin–orbit operator have the same symmetry, from a computational point of view the process of calculation of $C_J^{\mathrm{SO},1}$ or $C_J^{\mathrm{SO},2}$ is almost identical to that of obtaining A_J or B_J, respectively.

In order to differentiate between them, C terms that are caused by orbital degeneracy of the ground state will be called "classical" C terms while C terms that are caused by spin–orbit coupling will be called "spin–orbit induced" C terms.

A.5. Approximations

Several approximations were made in the derivations described in the previous sections. The purpose of these approximations was to simplify individual equations and to allow the simple form of Eq. (33) to be possible. The approximations will not

always be reasonable. In this section we shall discuss when some of these approximations should be abandoned and the consequences of requiring a more exact treatment.

Given that the intensity of C terms increases as the temperature is lowered, experimental studies of paramagnetic molecules are often performed at very low temperatures to increase the observed signal. Under these conditions the assumption that $kT >> E_{A\alpha}{}^{(1)\gamma}B$ will not be reasonable. The nonlinear behavior of the MCD as a function of magnetic field and temperature that is observed at low T can also provide further insight into the properties of the molecule under investigation (*21*). If $kT >> E^{(1)\gamma}{}_{A\alpha}B$ is not true then the term $E^{(1)\gamma}{}_{A\alpha}\mu_B B/|A|kT$ from Eqs. (18)–(22) must be replaced by $\exp(-E^{(1)\gamma}{}_{A\alpha}\mu_B B/kT)/Q$ or the term $2M\mu_B B/|A|kT$ from Eqs. (24)–(32) must be replaced by $\exp(-2M\mu_B B/kT)/Q$ where Q is the partition function. This replacement allows the MCD of paramagnetic molecules at low temperature to be described and introduces no particular computational difficulties. It does, however, make it impossible to define C term parameters or simple equations like Eqs. (1 and 33).

The second approximation that can be relaxed is the assumption that the energies of the components of the ground state are given by the simple form presented by Eqs. (19 and 24). These assumptions imply that $g = 2\mathrm{I}$ and that no other terms are required to describe the energy. The simple form of the g-tensor implies that the splitting in the components of the ground state caused by the magnetic field is isotropic. If the true g-tensor is used the populations of the components of the ground state become dependent on the orientation of the molecule. As a consequence, the axis of spin quantization in general will not be coincident with the direction of the magnetic field. This makes the expressions obtained from integration over spin a little more complicated. Furthermore, orientational averaging can no longer be performed analytically and numerical integration is required (*21*).

A further term that can contribute to $E^{(1)\gamma}{}_{A\alpha}$ is the ZFS (*59,60*). As implied by its name, ZFS splits the components of a state in the absence of a magnetic field. For states that are only spin degenerate, ZFS occurs when the spin $S>1/2$. Like the g-tensor, ZFS causes the axis of spin quantization to deviate from the direction of the magnetic field. The consequences with respect to spin integration and orientational averaging are similar to those caused by the use of a non-isotropic g-tensor. ZFS is made up of two terms, one second-order in spin–orbit coupling and the other from spin–spin coupling (*59*). The calculation of ZFS within DFT has been the subject of several recent publications (*61–65*).

The additional requirements introduced by the non-isotropic g-tensor or ZFS complicate the MCD formalism somewhat but do not introduce significant additional computational cost nor do they prevent the definition of a C term parameter consistent with Eq. (33) (provided that $kT >> E^{(1)\gamma}{}_{A\alpha}B$).

The third approximation is the assumption that the absorption bandwidth is greater than the spin–orbit splitting of a spatially degenerate excited state. If the spin–orbit splitting is large enough that the components can be resolved then the components of the excited state must be treated individually. As a consequence, the MCD of the transition cannot be described by a single derivative band shape and the principle of spectroscopic stability cannot be applied. It is possible that the spin–orbit splitting of an excited state leads to resolved bands, particularly if very heavy elements are involved. It is much less likely that the Zeeman splitting of an excited state will be greater than the bandwidth. For magnetic fields of a few Tesla, magnetic interactions are of the order of a few wavenumbers.

A.6. MCD from the imaginary part of the Verdet constant

In the previous sections the MCD equations were developed starting from the transition moment definition of MCD. As described in the introduction, MCD has also been defined through the complex optical rotation Φ

$$\Phi = \phi + i\theta \tag{34}$$

where ϕ is the observable optical rotation and θ is the ellipticity induced in plane-polarized light.

If the electric and magnetic dipole moments in the presence of frequency-dependent electric and static magnetic fields are expanded in a series, the leading terms give the following expression for Φ (*9*)

$$\Phi(\omega) = -i\omega\chi' \sum_{\alpha\beta} \left(-\beta^{(0)}_{\alpha\beta}(\omega) + \sum_{\gamma} \varepsilon_{\alpha\beta\gamma} \alpha^{(1)\gamma}_{\alpha\beta}(\omega) B \right) \tag{35}$$

The imaginary and real parts of the frequency-dependent response of the electric dipole moment to a magnetic field (β) are responsible for optical rotation and CD, respectively, while the imaginary and real parts of the first-order correction to the frequency-dependent electric polarizability $\alpha^{(1)}$ are responsible for the MOR and MCD, respectively.

An alternative approach to the calculation of MCD is suggested by its definition in terms of the complex rotation. Rather than

making use of the transition moments and excitation energies of the system of interest to provide expressions for the components of the MCD intensity, it can be obtained through direct calculation of the perturbed frequency-dependent polarizability $\alpha^{(1)}$. Since the real part of Φ due to $\alpha^{(1)}$ is described by the Verdet constant we describe this alternative way of calculating MCD as being from the imaginary Verdet constant (Im[*V*]).

The transition-based and Im[*V*]-based approaches are complementary in that in the first formulation, the MCD equations are defined at excitation energies and then the observed band shapes are added in an ad hoc manner through the band-shape function *f,* while the frequency-dependent polarizability is defined for all energies of incident light except the excitation energies where it is divergent. These divergences can be avoided through the use of an additional bandwidth parameter (Section II.C.3).

B. Time-Dependent Density Functional Theory

In the previous section several equations were described that can be used to calculate MCD spectra. If the spectra are to be calculated using the transition-based approach described in Sections II.A.1–II.A.4, a number of quantities must be evaluated. These include the perturbed and unperturbed excitation energies, the perturbed and unperturbed transition moments between the ground and excited states, and/or the magnetic moment of the ground state. If an MCD spectrum is to be calculated with the imaginary Verdet approach described in Section II.A.6, then the first-order correction to the frequency-dependent polarizability due to a magnetic field is required.

Quantum mechanics offers a variety of ways to calculate these quantities as should be clear from the variety of methods used to calculate MCD spectra that are mentioned in Section I. In this section we will briefly describe TDDFT, the theory upon which our approach is based, focusing upon the aspects that are relevant for MCD.

DFT is a ground state theory. In order to calculate MCD spectra it is obviously necessary to know something about excited states. TDDFT allows DFT calculations to provide the necessary information about excited states.

B.1. Basics of TDDFT

In this section the convention that occupied orbitals are indexed by the letters *i,j,k,*…, virtual orbitals are indexed by

a,b,c,…, and orbitals with arbitrary occupation are indexed by *p, q,r,…* will be followed. The orbital spin is denoted by a Greek index σ, *τ, υ,….* If an equation is written in terms of an atomic orbital (AO) basis then the AOs are indexed by the Greek letters *μ, ν, λ,….*

In its most basic form, TDDFT is analogous to DFT except that the density obtained is time-dependent (or frequency dependent after a Fourier transformation).

$$\rho(r,t) = \sum_i \phi_i^*(r,t)\phi_i(r,t) \tag{36}$$

ρ(r,ω) is often described as a perturbation series starting with the static density perturbed by a time-dependent potential

$$\rho(r,\omega) = \rho(r,0) + \rho^{(1)}(r,\omega)\ldots \tag{37}$$

For chemical applications of the type we are interested in, theories based on the first-order correction to the density from a first-order correction to the potential $V^{(1)}(\omega)$ (linear-response TDDFT) are typically used. The interested reader is referred to the reviews for the details of how $\rho^{(1)}$ is calculated (*52,54*).

If the frequency-dependent perturbation is an electric field then $\rho^{(1)}$ can be used to calculate the frequency-dependent polarizability that must be perturbed to evaluate the imaginary Verdet constant.

$$\alpha_{\alpha\beta}(\omega) = -\int M^{\alpha}\rho^{(1)\beta}(\omega) = -\sum_{ai\sigma} m_{ai\sigma}^{\alpha} D_{ai\sigma}^{(1)\beta}(\omega) \tag{38}$$

where $m_{ai}{}^{\alpha}$ is an integral of the one-electron electric dipole moment operator corresponding to direction α over orbitals a and i

$$m_{ai\sigma}^{\alpha} = \langle \phi_{a\sigma} | m^{\alpha} | \phi_{i\sigma} \rangle \tag{39}$$

and $D_{ai\sigma}{}^{(1)\beta}(\omega)$ is an element of the density matrix perturbed to first order by a frequency-dependent electric field directed along axis β.

The frequency-dependent polarizability, and therefore $\rho^{(1)}$ diverges when ω is equal to an excitation energy. Casida (*54*) made use of this property to derive a TDDFT equation for the excitation energy to an excited state J that is essentially the DFT form of the random phase approximation (RPA) equation:

$$\omega_J \begin{pmatrix} \mathbf{I} & 0 \\ 0 & \mathbf{I} \end{pmatrix} \begin{pmatrix} X \\ Y \end{pmatrix}_J = \begin{pmatrix} \mathbf{A} & \mathbf{B} \\ \mathbf{B}^* & \mathbf{A}^* \end{pmatrix} \begin{pmatrix} X \\ Y \end{pmatrix}_J \tag{40}$$

where

$$\mathbf{A}_{ai\sigma,bj\tau} = \delta_{\sigma\tau}\delta_{ab}\delta_{ij}\left(\varepsilon_{b\tau}-\varepsilon_{j\tau}\right) + \boldsymbol{K}_{ai\sigma,bj\tau} \tag{41}$$

$$\mathbf{B}_{ai\sigma,bj\tau} = \boldsymbol{K}_{ai\sigma,jb\tau} \tag{42}$$

$$\boldsymbol{K}_{ai\sigma,bj\tau} = (ai\sigma|bj\tau) + \left(ai\sigma|f^{xc}_{\sigma\tau}|bj\tau\right) - \delta_{\sigma\tau}c_{\mathrm{X}}(ab\sigma|ij\tau) \tag{43}$$

$$(pq\sigma|rs\tau) = \int dr_1 \int dr_2 \phi^*_{p\sigma}(r_1)\phi_{q\sigma}(r_1)\frac{1}{|r_1-r_2|}\phi_{r\tau}(r_2)\phi^*_{s\tau}(r_2) \tag{44}$$

$$\left(pq\sigma|f^{xc}_{\sigma\tau}|rs\tau\right) = \int dr_1 \int dr_2 \phi^*_{p\sigma}(r_1)\phi_{q\sigma}(r_1)f^{xc}_{\sigma\tau}(r_1,r_2)\phi_{r\tau}(r_2)\phi^*_{s\tau}(r_2) \tag{45}$$

where ε_p is the energy of orbital p and f_{xc} is the exchange-correlation kernel. The factor c_{X} is the fraction of exact exchange included in the functional.

Equation (40) is a generalized eigenvalue equation. The eigenvalue ω_J is interpreted as the excitation energy from the ground state to the Jth excited state. The vectors $\boldsymbol{X}_J$ and $\boldsymbol{Y}_J$ are the first-order correction to the density matrix at an excitation and describe the transition density between the ground state and the excited state J.

In general, all orbitals obtained in a nonrelativistic DFT calculation can be chosen to be real. If this is the case then Eq. (40) can be converted into a pair of lower dimensional problems

$$\omega^2_J(X+Y)_J = (\mathbf{A}-\mathbf{B})(\mathbf{A}+\mathbf{B})(X+Y)_J \tag{46}$$

$$\omega^2_J\left(X^\dagger-Y\right)_J = \left(X-Y^\dagger\right)(\mathbf{A}-\mathbf{B})(\mathbf{A}+\mathbf{B}) \tag{47}$$

If the functional applied does not include any exact exchange then ($\mathbf{A}$–$\mathbf{B}$) will be a diagonal matrix that only depends on the orbital eigenvalues. The working equation then becomes a single standard eigenvalue equation:

$$\omega^2_J F_J = \Omega F_J \tag{48}$$

where

$$\begin{aligned} \Omega &= \mathrm{S}^{-1/2}(\mathbf{A}+\mathbf{B})\mathrm{S}^{-1/2} \\ \mathrm{S} &= (\mathbf{A}-\mathbf{B})^{-1} \\ F_J &= \sqrt{\omega}\mathrm{S}^{1/2}(X+Y)_J = \frac{\mathrm{S}^{-1/2}}{\sqrt{\omega}}(X-Y)_J \end{aligned} \tag{49}$$

The transition dipole between ground state A and excited state J is

$$\langle A|M^{\alpha}|J\rangle = \sum_{ai\sigma} \left(m^{\alpha}_{ai\sigma} X_{J,ai\sigma} + m^{\alpha *}_{ai\sigma} Y_{J,ai\sigma}\right) \tag{50}$$

where m is the electric dipole moment integral over molecular orbitals as before.

The TDDFT equations quoted in this section describe a system in the absence of a magnetic field. Equations (40)–(50) therefore provide a method for calculating the unperturbed excitation energy $\omega^{(0)}$ and the unperturbed transition moments $\langle A|M^{\alpha}|J\rangle^{(0)}$.

It remains to show how the perturbed quantities may be calculated within the TDDFT framework. This is the subject of the next section.

C. MCD WITH TDDFT

The perturbed quantities we are interested in are $\omega^{(1)}$ and $\langle A|M^{\alpha}|J\rangle^{(1)}$ where the perturbation is imaginary

$$H^{(1)^*} = -H^{(1)} \tag{51}$$

Differentiating Eq. (50) with respect to an imaginary perturbation gives

$$\langle A|M^{\alpha}|J\rangle^{(1)} = \sum_{ai\sigma} \left(m^{\alpha(1)}_{ai\sigma} (X_{ai\sigma} - Y_{ai\sigma})^{(0)}_{J} + m^{\alpha(0)}_{ai\sigma} (X_{ai\sigma} + Y_{ai\sigma})^{(1)}_{J}\right) \tag{52}$$

We therefore need to evaluate two perturbed quantities in order to obtain $\langle A|M^{\alpha}|J\rangle^{(1)}$, the perturbed integrals $m_{ai\sigma}{}^{\alpha(1)}$ and the perturbed transition density $(\boldsymbol{X}+\boldsymbol{Y})_{J}{}^{(1)}$.

C.1. Magnetically perturbed integrals

The term $m_{ai\sigma}{}^{\alpha(1)}$ is the first-order correction to the integral of the electric dipole moment operator in the α direction over orbitals a and i. The perturbed integral will depend on the change of the orbitals in the presence of a magnetic field or spin–orbit coupling.

$$m^{\alpha(1)}_{pq\sigma} = \left\langle \phi^{(1)}_{p\sigma} \middle| m^{\alpha} \middle| \phi^{(0)}_{q\sigma} \right\rangle + \left\langle \phi^{(0)}_{p\sigma} \middle| m^{\alpha} \middle| \phi^{(1)}_{q\sigma} \right\rangle \tag{53}$$

If our orbitals are described by a set of atom-centered basis functions then

$$\phi_{p\sigma}^{(1)} = \sum_{q\tau} U_{p\sigma q\tau}^{(1)} \phi_{p\tau}^{(0)} + \sum_{v} C_{vq\sigma}^{(0)} \chi_v^{(1)} \tag{54}$$

where χ_v is a basis function, $C_{vq\sigma}^{(0)}$ an MO coefficient, and $U_{p\sigma q\tau}^{(1)}$ is the derivative of an MO coefficient in the MO basis. Since the unperturbed orbitals are chosen to be real $\phi_{p\sigma}^{(1)}$ can be chosen to be purely imaginary. Equation (54) allows for orbitals of differing spin ($\sigma \neq \tau$) to mix together in the case where the perturbation is spin–orbit coupling. However, as was noted earlier, transitions between states with different spin projection M do not contribute to the MCD to first order in the perturbation. We shall therefore only include orbital perturbations that conserve M and include just one spin index σ.

The $U^{(1)}$ coefficients corresponding to occupied–virtual orbital pairs can be obtained from the magnetic form of the coupled-perturbed Kohn–Sham (CPKS) equations

$$\left(\mathbf{A}^{(0)} - \mathbf{B}^{(0)}\right) U^{(1)} = b^{(1)} \tag{55}$$

where $\boldsymbol{U}^{(1)}$ is a vector made up of the virtual–occupied coefficients and the vector $\boldsymbol{b}^{(1)}$ is the $\boldsymbol{U}^{(1)}$-independent portion of the Fock matrix differentiated with respect to the perturbation. The vector $\boldsymbol{b}^{(1)}$ is also indexed by virtual–occupied pairs of orbitals. For a field-independent basis ($\chi^{(1)}$=0) ${b_{ai\sigma}}^{(1)}$ is simply the corresponding element of the perturbation Hamiltonian ${H_{ai\sigma}}^{(1)}$.

If the calculation of interest involves a functional that does not include exact exchange, the KS potential will be independent of the perturbation to first order except through the term $H^{(1)}$ and, as noted earlier, ($\mathbf{A}^{(0)}$–$\mathbf{B}^{(0)}$) will have a very simple form. Any $\boldsymbol{U}^{(1)}$ coefficient will then be trivial to calculate through

$$U_{pq\sigma}^{(1)} = \frac{H_{pq\sigma}^{(1)}}{\varepsilon_{q\sigma}^{(0)} - \varepsilon_{p\sigma}^{(0)}} \tag{56}$$

If the functional used does include exact exchange then ($\mathbf{A}^{(0)}$–$\mathbf{B}^{(0)}$) will not be diagonal and the solution of Eq. (55) will require rather more effort. In this case the occupied–occupied and virtual–virtual blocks of $U^{(1)}$ can be obtained from the occupied–virtual block

$$U_{pq\sigma}^{(1)} = \frac{1}{\varepsilon_{q\sigma}^{(0)} - \varepsilon_{p\sigma}^{(0)}} \left(\sum_{ai\sigma} \left(K_{pq\sigma,ai\sigma}^{(0)} - K_{pq\sigma,ia\sigma}^{(0)} \right) U_{ai\sigma}^{(1)} + H_{pq\sigma}^{(1)} \right) \tag{57}$$

If the perturbation is spin–orbit coupling then a field-independent basis set is used in the calculation of interest ($\chi_\nu^{(1)}$=0) and the $U^{(1)}$ coefficients are all that is needed to calculate the perturbed integrals. If the perturbation is a magnetic field then a field-independent basis set can be used. However, it is often desirable to utilize a field-dependent basis set such as GIAOs (*66–69*) that reduces the origin dependence of the results obtained. With such a basis set the evaluation of perturbed integrals is somewhat more involved as the $\chi_\nu^{(1)}$ terms are no longer zero.

C.2. Magnetically perturbed TDDFT

The remaining perturbed terms needed are $\omega^{(1)}$ and $(\boldsymbol{X}+\boldsymbol{Y})_J^{(1)}$. We have described a methodology for obtaining these terms based on the differentiation of Eq. (40) with respect to a static magnetic perturbation (*47*). This approach, magnetically perturbed TDDFT, has a lot in common with the equations derived by Ortiz, van Caille and Amos and Furche and Ahrichs (*70–73*) that consider the RPA equation or the RPA-like form of TDDFT in the presence of a real perturbation.

Differentiating Eq. (40) with respect to a magnetic perturbation, making use of the identities $\mathbf{A}^{(1)*}=-\mathbf{A}^{(1)}$ and $\mathbf{B}^{(1)*}=-\mathbf{B}^{(1)}$ and reducing the dimension of the resulting equation gives

$$\begin{aligned}\left[\left(\mathbf{A}^{(0)}-\mathbf{B}^{(0)}\right)\left(\mathbf{A}^{(0)}+\mathbf{B}^{(0)}\right)-\omega_J^{(0)2}\mathbf{I}\right](\mathrm{X}+\mathrm{Y})_J^{(1)} \\ = \omega_J^{(1)}\left[\omega_J^{(0)}(\mathrm{X}+\mathrm{Y})_J^{(0)}-\left(\mathbf{A}^{(0)}-\mathbf{B}^{(0)}\right)(\mathrm{X}-\mathrm{Y})_J^{(0)}\right] \\ -\left(\mathbf{A}^{(0)}-\mathbf{B}^{(0)}\right)\left(\mathbf{A}^{(1)}-\mathbf{B}^{(1)}\right)(\mathrm{X}-\mathrm{Y})_J^{(0)} \\ -\omega_J^{(0)}\left(\mathbf{A}^{(1)}+\mathbf{B}^{(1)}\right)(\mathrm{X}+\mathrm{Y})_J^{(0)}\end{aligned} \tag{58}$$

and

$$\omega_J^{(1)}=\frac{1}{2}\left[(\mathrm{X}+\mathrm{Y})_J^{(0)}\left(\mathbf{A}^{(1)}-\mathbf{B}^{(1)}\right)(\mathrm{X}-\mathrm{Y})_J^{(0)}+(\mathrm{X}-\mathrm{Y})_J^{(0)}\left(\mathbf{A}^{(1)}+\mathbf{B}^{(1)}\right)(\mathrm{X}+\mathrm{Y})_J^{(0)}\right] \tag{59}$$

Only the equation for $(\boldsymbol{X}+\boldsymbol{Y})^{(1)}$ is considered as $(\boldsymbol{X}-\boldsymbol{Y})^{(1)}$ is not needed to calculate MCD.

These equations can again be further simplified if the functional utilized does not include exact exchange

$$\left[\Omega^{(0)}-\omega_J^{(0)2}\mathbf{I}\right]\boldsymbol{F}_J^{(1)}=\left[2\omega_J^{(0)}\omega_J^{(1)}\mathbf{I}-\omega_J^{(0)}\Omega^{(1)}\right]\boldsymbol{F}_J^{(0)} \tag{60}$$

$$\omega_J^{(1)} = \frac{1}{2} F_J^{(0)\dagger} \Omega^{(1)} F_J^{(0)} \tag{61}$$

$$\Omega^{(1)} = \mathbf{S}^{-1/2}\left(\mathbf{A}^{(1)} - \mathbf{B}^{(1)}\right)\mathbf{S}^{1/2} + \mathbf{S}^{1/2}\left(\mathbf{A}^{(1)} + \mathbf{B}^{(1)}\right)\mathbf{S}^{-1/2} \tag{62}$$

$$F_J^{(1)} = \sqrt{\omega_J^{(0)}}\mathbf{S}^{1/2}(X+Y)_J^{(1)} \tag{63}$$

Given expressions for $\mathbf{A}^{(1)}$ and $\mathbf{B}^{(1)}$, Eqs. (58)–(63) provide the means to evaluate the required perturbed excitation energies and transition densities. The derivation of $\mathbf{A}^{(1)}$ and $\mathbf{B}^{(1)}$ is fairly involved and it will only be very briefly outlined here. For further details see (*47*).

The $\mathbf{A}^{(0)}$ and $\mathbf{B}^{(0)}$ matrices as defined in Eqs. (41 and 42) depend on the orbital energies and several two-electron integrals collected into the K elements defined in Eq. (43). The orbitals are chosen to be real. In this basis the derivatives of orbital energies with respect to a magnetic perturbation are zero. Therefore, only the derivatives of the K elements are needed to evaluate $\mathbf{A}^{(1)}$ and $\mathbf{B}^{(1)}$.

Much like the derivatives of integrals over the electric dipole operator, finding derivatives of the elements of the K elements requires the orbital derivatives. We assume that the functional and thus the kernel f_{xc} do not change in the presence of a magnetic field. This is a reasonable assumption for functionals that do not depend on the current density. If the basis set is not dependent on the perturbation the resulting expressions for $\mathbf{A}^{(1)}$ and $\mathbf{B}^{(1)}$ are

$$\begin{aligned}
\mathrm{A}^{(1)}_{ai\sigma,bj\tau} &= \delta_{ab}\delta_{\sigma\tau}\left(\varepsilon^{(0)}_{i\sigma} - \varepsilon^{(0)}_{j\sigma}\right)U^{(1)}_{ij\sigma} - \delta_{ij}\delta_{\sigma\tau}\left(\varepsilon^{(0)}_{a\sigma} - \varepsilon^{(0)}_{b\sigma}\right)U^{(1)}_{ab\sigma} \\
&\quad + \sum_k \left(U^{(1)}_{ak\sigma}K^{(0)}_{ki\sigma,bj\tau} + U^{(1)}_{bk\tau}K^{(0)}_{ai\sigma,kj\tau}\right) + \sum_c \left(U^{(1)}_{ci\sigma}K^{(0)}_{ac\sigma,bj\tau} + U^{(1)}_{cj\tau}K^{(0)}_{ai\sigma,bc\tau}\right) \\
\mathrm{B}^{(1)}_{ai\sigma,bj\tau} &= \sum_k \left(-U^{(1)}_{ak\sigma}K^{(0)}_{ki\sigma,jb\tau} - U^{(1)}_{bk\tau}K^{(0)}_{ai\sigma,jk\tau}\right) + \sum_c \left(U^{(1)}_{ci\sigma}K^{(0)}_{ac\sigma,jb\tau} + U^{(1)}_{cj\tau}K^{(0)}_{ai\sigma,cb\tau}\right)
\end{aligned} \tag{64}$$

Equation (64) suggests useful approximate forms of $\mathbf{A}^{(1)}$ and $\mathbf{B}^{(1)}$. If we consider the simple $U^{(1)}$ coefficients obtained in a nonhybrid calculation (Eq. 56) the terms dependent on the orbital energies in the first two terms of $\mathbf{A}^{(1)}$ cancel to leave the perturbation integral ${H_{pq}}^{(1)}$. All of the other terms in Eq. (64) would be expected to be small as they depend on a perturbation Hamiltonian integral divided by a relatively large orbital energy difference multiplied by a K element that is often small. A potentially useful approximation would be to neglect all of the terms including a

K element in Eq. (64). This approximate form will be much easier to calculate as $\mathbf{B}^{(1)}$ will be zero and $\mathbf{A}^{(1)}$ will have far fewer terms.

While we are discussing the evaluation of $\omega^{(1)}$, a final point should be addressed. In Section II.A the idea of spectroscopic stability was mentioned in several places. The use of spectroscopic stability introduced terms of the form $\omega_{Jjj'}^{(1)}$ that were related to the derivative of the excitation energy. If the perturbation is imaginary the derivatives of the excitation energies as given by Eqs. (59 and 61) require degenerate transition densities in a complex representation. According to the principle of spectroscopic stability the real representation can be used leading to

$$\omega_{Jjj'}^{(1)} = \frac{1}{2}\left[\left(\mathrm{X}+\mathrm{Y}\right)_{Jj}^{(0)\dagger}\left(\mathbf{A}^{(1)}-\mathbf{B}^{(1)}\right)\left(\mathrm{X}-\mathrm{Y}\right)_{Jj'}^{(0)} + \left(\mathrm{X}-\mathrm{Y}\right)_{Jj}^{(0)\dagger}\left(\mathbf{A}^{(1)}+\mathbf{B}^{(1)}\right)\left(\mathrm{X}+\mathrm{Y}\right)_{Jj'}^{(0)}\right] \tag{65}$$

or

$$\omega_{Jjj'}^{(1)} = \frac{1}{2} F_{Jj}^{(0)\dagger}\Omega^{(1)}F_{Jj'}^{(0)} \tag{66}$$

In this section we have described the calculation of $\omega^{(1)}$ and $\langle A|M|J\rangle^{(1)}$ with TDDFT perturbed by a magnetic field. These quantities, in combination with $\omega^{(0)}$ and $\langle A|M|J\rangle^{(0)}$ obtained from an unperturbed TDDFT calculation, can be used with Eqs. (11, 17, 30, or 32) as appropriate to evaluate, respectively, B_J, A_J, $C_J^{\mathrm{SO},1}$, or $C_J^{\mathrm{SO},2}$ and thus an MCD spectrum using Eq. (33). We have explicitly avoided orbitally degenerate ground states and therefore cannot yet calculate classical C terms. This problem will be discussed in Section II.C.4 but before doing so, we will describe the calculation of MCD intensity from the imaginary part of the Verdet constant where the MCD intensity itself is calculated rather than parameters associated with the various MCD terms.

C.3. A and B terms from the imaginary part of the Verdet constant

The second approach to calculating MCD starts from its definition in terms of the real part of first-order correction to the frequency-dependent polarizability in the presence of a magnetic field (Section II.A.6). This definition can be used to consider all types of MCD linear in the magnetic field (*9*). Our current implementation is restricted to systems with a closed-shell ground state. We shall therefore only consider the calculation of A and B terms by this method.

The frequency-dependent polarizability is given by Eq. (38). Differentiation of this equation with respect to a static magnetic field provides the quantity needed to calculate MCD (or MOR).

$$\frac{\partial \alpha_{\alpha\beta}(\omega)}{\partial B_\gamma} = \alpha_{\alpha\beta}^{(1)\gamma}(\omega) = -\sum_{\mu\nu} \left(m_{\mu\nu}^{\alpha(01)\gamma} D_{\mu\nu}^{(10)\beta}(\omega) + m_{\mu\nu}^{\alpha} D_{\mu\nu}^{(11)\beta\gamma}(\omega) \right) \quad (67)$$

where the superscripts (10), (01), and (11), respectively, indicate perturbation by a frequency-dependent electric field, a static magnetic field, and both fields. Equation (67) has the electric dipole integrals and density matrix in a basis of AOs. The first term includes the derivatives of electric dipole moment integrals over AOs with respect to a magnetic field. This term is zero unless a field-dependent basis set is used.

The second term of Eq. (67) includes the density matrix perturbed by an electric field in the beta direction and a magnetic field in the gamma direction. It would be preferable to avoid calculating such a second-order quantity. The derivation of an expression for $D^{(11)\beta\gamma}(\omega)$ in terms of first-order quantities was achieved in our lab *(74)*. In this derivation the influences of the electric and magnetic fields are treated on a similar footing through the U coefficients obtained from solution of the appropriate perturbed KS equations. For the electric perturbation these equations are coupled and frequency-dependent, while the U coefficients corresponding to the magnetic field were assumed to come from the uncoupled form of Eq. (55) (nonhybrid functionals). Although the derived equation is more attractive than Eq. (67) from a computational point of view, it is rather cumbersome, particularly when GIAOs are used. The interested reader is referred to Ref. (*74*) for its full definition.

Solution of Eq. (67) as it stands will not yield an MCD spectrum. The frequency-dependent polarizability diverges at frequencies corresponding to excitations, the frequencies where MCD intensity is greatest. As presented in Ref. (*74*) the perturbed polarizability will be purely imaginary and only the MOR (the real Verdet constant) will be obtained (*75*). This difficulty can be surmounted by the introduction of a damping factor into the excitations or, equivalently, a complex component to the frequency ω (*51*). The divergences in $\alpha_{\alpha\beta}{}^{(1)\gamma}(\omega)$ will then be moved off the real number line. Once a damping factor is introduced the perturbed polarizability will have both real and imaginary components allowing the MCD intensity to be calculated from the real part. The value of the damping factor is not a number derived from theory but is chosen so that the spectrum obtained has bandwidths close to those observed experimentally. A similar

technique has also been used to calculate the frequency-dependent polarizability near an excitation (*76,77*), optical rotation (*45,78*), and CD spectra (*79*).

C.4. The C term: spatially degenerate ground states and TRICKS-TDDFT

From Eq. (22) it might seem that the C term parameter of an excitation from an orbitally degenerate ground state would be the most straightforward MCD parameter to calculate. Only the magnetic moment of the ground state and the unperturbed transition dipoles are required. No quantities derived from TDDFT and then perturbed by a magnetic field are needed. In fact, calculation of C_J provides a different challenge because of the requirement that the ground state is orbitally degenerate.

Describing an orbitally degenerate state requires multiple Slater determinants. Although it is possible to construct KS theories that allow for densities corresponding to more than one determinant (*80*), the functionals used in most applications are expected to be reliable only in combination with a single determinantal approach (*81*). Degenerate states with orbital degeneracy have been described by a single determinant by utilizing orbitals with fractional occupations. Formulations of TDDFT exist that are able to handle partially occupied orbitals (*82*). It is not clear if TDDFT with fractional orbitals can correctly describe the excitations of a orbitally degenerate state however. Several groups have considered approaches to DFT that are in some sense multideterminental (see, for instance, Ref. *83–87*). These approaches do not yet appear to be mature enough to enable the routine calculation of the spectra of molecules with orbitally degenerate ground states.

We have proposed an alternative method that avoids the problem of the orbitally degenerate ground state (*88,89*). In a KS-DFT calculation the lowest energy state of a given symmetry can be described (*90*). Thus, states other than the ground state can be investigated provided the orbital and/or spin symmetry of these states is different from that of the ground state and no other state of the same symmetry is lower in energy. Furthermore, the results of each of these different calculations can be used as a starting point for a TDDFT calculation.

If the most obvious reference state is problematic, as is the case if the ground state has orbital degeneracy, an alternative choice of reference can be useful provided a TDDFT calculation starting from the alternative reference can access all of the states of interest (including the problematic ground state). Given a reference density

and set of orbitals, the transition densities obtained from a TDDFT calculation are made up of a combination of all possible single electron excitations from the reference occupied orbitals. Thus, a TDDFT calculation should be able to describe any transition that is considered as a one-electron transition with respect to the reference. A choice of reference that differs from both the troublesome ground state and the excited state of interest by a single electron excitation will lead to a TDDFT calculation that can provide significant insight into the transition that we are really interested in. Similar ideas have been used earlier in the context of coupled cluster and single reference CI calculations (*91–93*) as well as spin-degenerate TDDFT calculations (*94*).

In the context of orbitally degenerate ground states the alternative reference was termed a transformed reference via an intermediate configuration (TRIC) and the overall method was called TRIC-KS TDDFT or TRICKS-TDDFT (*88*).

TRICKS-TDDFT is best understood through an example. Consider a tetrahedral molecule that has a doublet ground state with a single electron in an orbital with symmetry e. The overall symmetry of the ground state is therefore ^2E. An orbital diagram for the molecule is pictured in Fig. 1a. Suppose that we are interested in a transition from the ground state to an excited $^2T_2$ state, a transition that might be observed in the spectrum of a tetrahedral d^1 transition metal complex. This second state would have the same electron configuration as the ground state except that the unpaired electron formally in the e orbital is now in a t_2 orbital (Fig. 1b). It is likely that the lowest energy $^2A_1$ state will have the same electron configuration as the other two states just mentioned except that the unpaired electron is now in a a_1 orbital (Fig. 1c). The ^2E and T_2 are related to the $^2A_1$ state by a transition that should be well described by one-electron excitations. The $^2A_1$ state can be used as the reference for a TDDFT calculation in a straightforward manner. This TDDFT calculation will provide the energies of the $^2A_1 \rightarrow {}^2E$ and $^2A_1 \rightarrow T_2$ transitions. The difference of these two energies will be the excitation energy

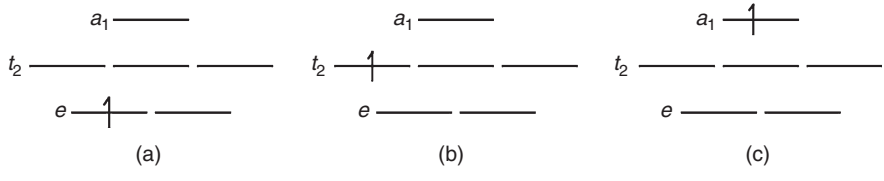

FIG. 1. Orbital diagrams of a tetrahedral molecule. (a) ^2E ground state. (b) $^2T_2$ excited state. (c) $^2A_1$ nondegenerate excited state.

of interest that of the $^2E \rightarrow T_2$ transition. Not all transitions of a molecule with orbitally degenerate ground state can be investigated through a TRIC. Quite a range of transitions can be described by TRICKS-TDDFT however (*88*). This approach can be particularly useful in combination with spin-flip TDDFT.

As described so far, TRICKS-TDDFT can give access to excitation energies that would otherwise be unavailable. In order to calculate C term parameters using Eq. (22) the magnetic moment of the ground state components and the transition dipoles between the ground and excited states of interest are also needed.

The ground state magnetic moment can be obtained from a DFT calculation of the ground state with fractionally occupied orbitals. Such a calculation will provide orbitals with the correct symmetry that can be used with Eq. (19).

In order to obtain transition dipoles we make use of an idea proposed by Casida (*54*) where the excited state wave function Ψ_J is approximated by

$$\Psi_J \approx \sum_{ai} X_{ai}^J a_a^\dagger a_i \Psi_{TRIC} \tag{68}$$

where X^J is the transition density from the TRIC to state J, $a^\dagger$ and a are creation and annihilation operators and Ψ_{TRIC} is the TRIC Slater determinant. With Ψ_J and Ψ_A obtained from Eq. (68) the transition dipole between states A and J is

$$\langle \mathbf{A}|M^\alpha|J\rangle^{(0)} = \sum_{aib,a\neq b} X_{ai}^J X_{bi}^{\mathbf{A}} m_{ab}^\alpha - \sum_{aij,i\neq j} X_{ai}^J X_{aj}^{\mathbf{A}} m_{ij}^\alpha + \sum_{ai} X_{ai}^J X_{ai}^{\mathbf{A}} \left(m_{aa}^\alpha + \sum_{j\neq i} m_{jj}^\alpha \right) \tag{69}$$

So far, TRICKS-TDDFT has only been used to evaluate excitation energies, absorption intensities, and classical C-term parameters. With this procedure it should be possible to calculate other properties related to electronic transitions including the remaining types of MCD parameter.

C.5. An MCD calculation

The calculation of MCD parameters using perturbed excitation energies and transition moments is achieved through the following steps:

1. Solve reference state KS equations to obtain φ_p and ε_p.
2. Evaluate required integrals over the electric and magnetic dipole moment and spin–orbit coupling operators as well as GIAO contributions, if needed.

3. Perform TDDFT calculation to obtain $\omega_J^{(0)}$ and $(\boldsymbol{X}+\boldsymbol{Y})_J^{(0)}$ or $\boldsymbol{F}_J^{(0)}$.
4. Solve magnetic CPKS equations to obtain U-coefficients (Eqs. 55 and 57).
5. Evaluate $m_{pq}^{\alpha\ (1)\gamma}$ (Eq. 53).
6. Evaluate $\omega_{Jjj'}^{(1)\gamma}$ if nonzero (Eq. 59 or 61).
7. Solve Eq. (58) or (60), respectively, to obtain $(\mathbf{X}+\mathbf{Y})_J^{(1)}$ or $\mathbf{F}_J^{(1)}$.
8. If the system of interest has a spin-degenerate ground state, calculate the g-tensor and/or ZFS if required, determine the energy of the components of the ground state in the presence of the applied magnetic field, and evaluate the necessary temperature-dependent factors.

Steps 4–7 need to be carried out twice if both B and $C^{\mathrm{SO},2}$ term parameters are to be calculated.

Once MCD parameters are obtained a spectrum can be simulated with a suitable choice of the band-shape function f. We have used Gaussian and Lorentzian functions for this purpose. In either case, a width parameter must be chosen. This parameter is generally chosen such that the widths of the peaks in the simulated spectrum are similar to those in the observed spectrum.

Step 7 is likely to be the most computationally demanding step of an MCD calculation based on transition moments. Step 5 will take very little computer time as will step 4 if a functional that does not include exact exchange is used and step 8 will be quick if the influences of the g-tensor and ZFS are neglected or not needed. Steps 2 and 5 will take more time and steps 1, 4 (with a hybrid functional the magnetic CPKS equations must be solved), and 8 (if the g-tensor or ZFS is calculated) may take a significant amount of computer time. Step 3 will consume a large proportion of the computational time of an MCD calculation and may be the most expensive step under some circumstances.

Step 7 is worth considering in further detail. Equations (58) and (60) have the form $(\mathbf{M}-\omega\mathbf{I})X=b$ where ω is an eigenvalue of matrix $\mathbf{M}$, vector X is the unknown perturbed transition density, and b is a known vector. Thus, step 6 involves the solution of a large system of equations corresponding to a nonpositive definite singular matrix $(\mathbf{M}-\omega\mathbf{I})$ that, in the case of Eq. (58), is also asymmetric. There is a significant body of literature in the field of numerical mathematics devoted to solving problems of this type (*95–97*). After trying a few different approaches we settled upon a preconditioned biconjugate gradient method (*95*).

The vectors corresponding to the zero eiegenvalues of the matrix (**M**–ω**I**) are the eigenfunctions of the matrix **M** corresponding to eigenvalue ω. These eigenfunctions will be available from the TDDFT calculation and can be projected out of the trial solution of the system of equations to improve convergence.

The calculation of MCD intensity from the imaginary Verdet constant includes fewer steps, in part because the current implementation is limited to closed-shell molecules. The process followed is as follows:

1. Solve reference state KS equations to obtain φ_p and ε_p.
2. Evaluate required integrals over the electric and magnetic dipole moment operators as well as GIAO contributions, if needed.
3. Solve magnetic CPKS equations to obtain U-coefficients due to the applied magnetic field.
4. For a given frequency ω and choice of lifetime parameter, solve frequency-dependent complex CPKS equations to obtain U-coefficients due to the applied electric field.
5. Evaluate the remaining Fock and density matrix terms needed to build the perturbed polarizability.

Steps 2 and 5 require relatively little computer time. As for the transition-based approach, step 3 can require significant computational effort if a hybrid functional is used and otherwise requires negligible effort. Step 4 is the most expensive step and will need to be repeated for enough values of ω to sufficiently cover the range of energies of interest.

C.6. Interpretation and analysis

The usefulness of MCD spectroscopy comes from the insight that it provides into the electronic structure of the ground and excited states of a molecule and into the nature of the transitions between these states. Much of this analysis comes from interpretation of the observed MCD intensity and measured MCD parameters in terms of the equations presented in Section II.A. In this section we will provide a few brief details about information that can be extracted from MCD parameters and some possible theoretical analysis techniques.

A parameter that has proven useful in the interpretation of experimental MCD spectra is the dipole strength. The dipole strength of a transition to state J, D_J, can be derived from an absorption spectrum. D_J is defined as

$$D_J = \frac{1}{3|A|} \sum_{\alpha a j} |\langle Aa|M^{\alpha}|Jj\rangle|^2 \tag{70}$$

The dipole strength is a measure of the intensity of the transition to state J in the absorption spectrum and is closely related to the oscillator strength. The MCD intensity and thus MCD parameters produced by a particular transition are proportional to the absorption intensity of that transition.

The dependence on absorption intensity can be removed by considering the MCD parameters divided by D_J. The quantities A_J/D_J, B_J/D_J and the other possible ratios are independent of the absorption intensity and only depend on the size of the interaction with the magnetic field. A_J/D_J is therefore a measure of the difference between the magnetic dipole moment of state J and the ground state. C_J/D_J can provide the magnetic dipole moment of the ground state. B_J/D_J and $C_J^{\mathrm{SO},2}/D_J$ depend on how strongly the ground and excited states of the transition are perturbed by the magnetic field and spin–orbit coupling, respectively. $C_J^{\mathrm{SO},1}/D_J$ is directly related to the spin–orbit coupling constant of the excited state.

A further advantage of these ratios is that they are largely matrix-independent. Measured MCD parameters can depend on the environment through the term α^2/n that is included in the collection of constants χ. D_J generally has the same environmental dependence as the MCD parameters and it is to be expected that the ratios would be much less sensitive to environmental effects.

The dipole strength parameter is straightforward to obtain in a TDDFT calculation.

We have expressed the parameters B_J and $C_J^{\mathrm{SO},2}$ in terms of perturbed transition dipoles (Eqs. 11 and 32) as this form provides the best starting point for an formulation in terms of TDDFT. In standard formulations of MCD the perturbed transition dipole $\langle A|M^\alpha|J\rangle^{(1)}$ is generally divided into contributions from the perturbation of the ground and excited states

$$\langle A|M^\alpha|J\rangle^{(1)} = \langle A^{(1)}|M^\alpha|J^{(0)}\rangle + \langle A^{(0)}|M^\alpha|J^{(1)}\rangle \qquad (71)$$

and $\langle A^{(1)}|$ and $|J^{(1)}\rangle$ are then expanded in the set of unperturbed states using standard perturbation theory. This sum over states (SOS) type approach enables a given B term or spin–orbit induced C term to be interpreted in terms of the interactions of the field-free states of a molecule (*11,17,21*).

Similar information can be obtained from a TDDFT calculation of the MCD B_J or $C_J^{\mathrm{SO},2}$. In order to do so, rather than solving Eqs. (58) or (60) directly, the perturbed transition density can be expanded in the basis of eigenvectors of the appropriate matrix. For example, to solve Eq. (60) the eigenvectors of $\Omega^{(0)}$are used

$$F_J^{(1)} = \sum_{K \neq J} \frac{\omega_J^{(0)} F_K^{(0)\dagger} \Omega^{(1)} F_J^{(0)}}{\omega_J^{(0)2} - \omega_K^{(0)2}} F_K^{(0)} \tag{72}$$

Although this constitutes a sum over transition densities, we will refer to this method of finding the perturbed transition density as a SOS method. The solution of Eq. (58) or (60) by conventional linear system solvers will be referred to as a "Direct" calculation.

Calculation of the MCD intensity of a closed-shell molecule through the imaginary Verdet constant produces a result as a function of ω but no further breakdown of the intensity. There are advantages to this approach but it does mean that individual *B* and *A* term parameters are not calculated. An MCD spectrum calculated from Im[*V*] can yield *A* and *B* term parameters by fitting the spectrum with suitable band-shape functions in much the same way the parameters can be extracted from an experimental spectrum.

In the first derivation of MCD equations by Stephens and Buckingham the perturbed polarizability was expanded in a SOS fashion yielding *A, B,* and *C* term parameters (*9*). We have performed a similar analysis but with an expansion in terms of transition densities (*51*). In this analysis it was shown that $\alpha_{\alpha\beta}{}^{(1)\gamma}$ can be divided into contributions indexed by two occupied orbitals, by two virtual orbitals, or by one occupied and one virtual orbitals (*51*). Of these contributions the "occ–occ" and "vir–vir" are expected to be larger than the "occ–vir" terms. By eliminating the occ–vir terms a simpler equation for $\alpha_{\alpha\beta}{}^{(1)\gamma}$ is obtained that follows the spirit of the approximation to Eq. (64) mentioned in Section II.C.2. It was also shown that this approximate equation can be converted into the form of SOS-type equations that include *B* term parameters (*51*).

From Eq. (72) we see that the contribution to the MCD intensity from the perturbation to the transition density can be identified with the MCD due to the mixing of the excited state *J* with other excited states. The remainder of the MCD intensity from *B* terms and spin–orbit-induced C terms is due to the perturbation of the integrals over the electric dipole moment operator (Eq. 52). The perturbed integrals thus include the contribution to the MCD from the mixing of excited states with the ground state. The perturbed integrals are written in terms of unperturbed orbitals (Eqs. 53 and 54) rather than unperturbed states or transition densities as this form is much easier to compute. With some further effort the contribution to the MCD from the perturbed integrals can also be analyzed in terms of transitions.

III. Applications

A. Small Molecules

We have validated our theoretical approach by simulating MCD spectra of a large range of species. In this section we will survey the results of some of these studies. The emphasis will be on metal complexes with a few examples from organic chemistry.

The first system to be discussed is ethene. Ethene is a closed-shell molecule with a point group that only includes nondegenerate irreducible representations. Its MCD spectrum therefore can only include *B* terms. Despite this restriction, the ethene MCD spectrum is a useful testing ground and many of the insights obtained can be usefully applied to other MCD calculations.

Following the section on ethene, the studies of a series of small transition metal complexes will be described. Each set of molecules will have MCD spectra that feature different types of contribution allowing the particular requirements of each type of calculation to be covered in turn.

All of the calculations described here use local functionals that do not include exact exchange. The best choice of functional for calculating MCD spectra is still an open question. In our experience, the MCD parameters produced with different local functionals do not vary much (*83*). The exception to this rule is functionals that are asymptotically correct. Asymptotically correct functionals tend to give excitation energies that differ from those produced by standard local functionals, particularly for Rydberg and charge-transfer transitions. The MCD parameters produced by asymptotically correct functionals tend to follow a similar pattern when compared with results of other local functionals. A few studies have considered hybrid functionals (*42,43*). This work found that hybrid functionals were superior in some applications. More work in this area is needed.

Unless otherwise noted, MCD parameters were calculated through the transition-based approach and any perturbed transition densities were obtained by direct solution of the systems of equations using the full forms of the $\mathbf{A}^{(1)}$ and $\mathbf{B}^{(1)}$ matrices.

A.1. Ethene

The MCD spectrum of ethene has been studied theoretically a number of times and has become a standard test case for MCD implementations (*32,33,40,48,51,98*). Its greatest virtues as a test case are that it has few atoms and electrons and fairly high symmetry. It is therefore possible to calculate the MCD spectrum

of ethene with very large basis sets and using computational approaches that would not be feasible for larger molecules. This will allow us to get some idea of the errors that might be introduced when calculating the spectrum of a larger system where a more limited range of computational parameters are feasible.

On the down side, the absorption spectrum of ethene is not straightforward to calculate. Two major transitions can be found in the range of energies that is covered by the MCD spectrum (*99,100*). The first transition is assigned as $\pi \rightarrow \pi^*$ or $1^1A_{1g} \rightarrow 1^1B_{1u}$ under D_{2h} symmetry. The second transition is a Rydberg ($\pi \rightarrow 3s$) excitation that is assigned as $1^1A_{1g} \rightarrow 1^1B_{3u}$. To describe such a transition using TDDFT requires a basis set that includes diffuse functions and an asymptotically correct functional. The excited state potential energy surface corresponding to the $\pi \rightarrow \pi^*$ transition has a saddle point at the ground state geometry and as a result the absorption spectrum shows significant vibronic effects (*101–104*). These two issues mean that even predicting the first two excitation energies of ethene is difficult. Accurately simulating the MCD spectrum of ethene will be even more difficult. The purpose of this section therefore will not be to explain how to reproduce the experimental MCD spectrum of ethene with high accuracy. That remains an area warranting further study.

The B term parameters of the lowest two allowed transitions of ethene calculated with different methods and different choices of computational parameters (*48,51,98,105*) are summarized in Table I. Included in the table are results obtained with four different basis sets. In combination with these basis sets the MCD parameters were obtained in the transition-based approach through solution of Eq. (60) by direct numerical solution (labeled "Direct" in Table I) and by expansion in a set of transition densities according to Eq. (72) (labeled "SOS"). In some cases approximate forms of the $\mathbf{A}^{(1)}$ and $\mathbf{B}^{(1)}$ matrices were used (labeled "Approx," see Eq. (64) and the discussion following it). MCD parameters derived from a fit to a spectrum obtained by calculation of the imaginary part of the Verdet constant are labeled as Im[V]. The parameters obtained from a fit to the spectrum obtained from the approximate form of Im[V] (see Section II.C.3) are labeled Im[V]-Approx, while parameters obtained from a SOS expansion based on Im[V]-Approx are denoted by Im[V]-SOS. The asymptotically correct SAOP functional (*106,107*) is used in all cases.

Also listed in Table I are some timing information for the QZ3P-1D basis set. Absolute times are not really very meaningful as they depend on the computer hardware being used. The values quoted are scaled so that the Direct calculation has a value of

TABLE I

B-Term Parameters of the $1^1A_{1g}\rightarrow1^1B_{3u}$ and $1^1A_{1g}\rightarrow1^1B_{1u}$ Transitions of Ethene. also Included is the Calculation Time Relative to a Direct Calculation[a]

Method	Basis set[b]								
	DZP		TZ2P		QZ3P-1D			QZ3P-3D	
	1^1B_{3u}	1^1B_{1u}	1^1B_{3u}	1^1B_{1u}	1^1B_{3u}	1^1B_{1u}	Time[c]	1^1B_{3u}	1^1B_{1u}
ω_J[a]	8.15	8.12	7.51	7.85	7.36	7.67		7.30	7.66
SOS(10)[d]	265.69	–266.16	–22.31	26.01	–15.90	18.21	0.73		
SOS(20)[d]	263.27	–265.05	–24.38	25.69	–15.85	11.26	1.18		
SOS(50)[d]	263.35	–268.21	–24.83	25.06	–16.63	3.28	2.58		
SOS(100)[d]	263.47	–269.18	–24.41	21.97	–16.88	4.22	4.98		
SOS(250)[d]	263.45	–269.61	–24.43	21.48	–16.86	3.46	11.28		
SOS(336)[d]	263.45	–269.61							
SOS(500)[d]			–24.43	21.48	–16.88	3.37	24.27		
SOS(704)[d]			–24.42	21.48					
SOS(1000)[d]					–16.87	3.37	12.04		
SOS(1096)[d]					–16.87	3.37			
SOS(20)Approx[d,e]								–11.00	–2.46
SOS(50)Approx[d,e]								–10.93	–4.34
SOS(150)Approx[d,e]								–12.55	–6.49
SOS(250)Approx[d,e]					–17.09	4.91	10.50	–12.77	–6.14

Direct [f]	263.45	–269.61	–24.42	21.48	–16.87	3.37	1.00		
Direct Approx[e,f]	265.53	–267.56			–17.09	4.92	0.94		
Im[V][g]	264.81	–267.97						–12.87	–3.69
Im[V]-Approx[h]	264.87	–266.70						–13.01	–2.16
Im[V]-SOS(250)[i]	264.59	–266.62						–12.90	–1.83

[a] All MCD parameters in atomic units. Excitation energy ω_J in eV.
[b] DZP is double-ζ plus polarization, TZ2P is triple-ζ plus two polarization, QZ3P-1D is quadruple-ζ plus three polarization, and one diffuse and QZ3P-3D is quadruple-ζ plus three polarization and three diffuse functions.
[c] Time to calculate MCD parameters relative to Direct calculation. Includes any unperturbed TDDFT calculation (*105*).
[d] Sum over states formalism (Eq. 72). The value in brackets indicates the number of transition densities included in the summation. 336, 704, and 1096 densities are the maximum possible for the DZP, TZ2P, and QZ3P-1D basis sets, respectively (*98,48,105*).
[e] Approximate form of the $\mathbf{A}^{(1)}$ and $\mathbf{B}^{(1)}$ matrices applied (Eq. 64).
[f] Parameters from direct solution of Eq. 60 (*48,105*).
[g] Parameters from a fit of the MCD intensity derived from the imaginary part of the Verdet constant (*51*).
[h] Parameters from a fit of the MCD intensity derived from an approximate form of the imaginary part of the Verdet constant (*51*).
[i] Sum over states expansion of the approximate form of the imaginary part of the Verdet constant. 250 transition densities included in the summation (*51*).

1.00. Therefore, a timing value less than 1.00 is faster than a Direct calculation and values greater than 1.00 are slower. The timing data includes the time required to perform the TDDFT calculation that is also required to produce the unperturbed transition densities and excitation energies as well as the time required to calculate the MCD parameters.

A number of conclusions can be drawn from the results in Table I. The transition moment-based and Im[V] approaches with the same basis set and similar approximations give similar results. The calculations that utilize the approximate form of the $\mathbf{A}^{(1)}$ and $\mathbf{B}^{(1)}$ matrices often give good results but not always. In particular, the B term parameter of the $1^1A_{1g}\rightarrow 1^1B_{1u}$ transition with the basis sets including diffuse functions has a large relative error when calculated with the approximate approaches compared to the exact methods. The SOS methods are all converged to the direct result by the time 250 transitions is reached. However, the 250 transition SOS calculation is more than 10 times more costly than the Direct calculation. The most obvious conclusion from Table I is that the quality of the ground state orbitals, unperturbed transition moments, and energies are very important. The choice of basis set clearly has a strong influence.

The timing results strongly point to the Direct method over the SOS approach with the possible exception of cases where only semi-quantitative results are needed and only a very small number of transitions is included. The timings of the Im[V] method are not listed in Table I but we believe that in order to produce B term parameters of similar quality as the direct values listed here between one and two orders of magnitude more computer time would be required further suggesting a preference for the Direct method.

The SOS and Im[V] schemes are likely to be useful at times however. In the DZP calculations the two excitations are nearly degenerate (Table I). From Eq. (72) we see that when two transitions are nearly degenerate they would be expected to be mixed strongly by a magnetic field leading to a large perturbation to the transition density and a large B term parameter. The majority of the B term parameter would be due to the mixing of the two nearly degenerate transitions and provided they are both included in the sum then a SOS calculation including a limited number of states should be able to produce results of low relative error. The same argument can be made for the spin–orbit-induced C terms of spin-degenerate molecule. In the case of the DZP ethene calculations the error in the SOS calculation with 10 transitions is only about 1% compared to the direct result.

Near-degenerate states lead to oppositely signed *B* terms that occur at nearly the same energy leading to a overall spectral feature that looks like an *A* term and is called a pseudo-*A* term (*11*). In many cases it may be that a quick SOS calculation may be sufficient to describe a pseudo-*A* term. We have had some success in describing the MCD spectra of furan, pyrrole, and related compounds through this approach (*98*).

The Im[*V*] scheme for the calculation of MCD spectra can also be the preferred approach under some circumstances because of the differing scaling properties of the three ways to evaluate MCD spectra. The amount of computer time required by the Direct method scales approximately linearly with the number of *B* term parameters needed. The SOS approach scales linearly with the number of transitions needed in the summation. On the other hand, the Im[*V*] method scales linearly with the range of energies of interest and is independent of the number of transitions present in that energy range. Thus, if the goal is to calculate the MCD intensity in a region with a high density of states, the Im[*V*] method may be the most efficient choice.

It is interesting to see what kind of MCD spectrum will be predicted by the parameters of Table I. Five simulated spectra are plotted in Fig. 2. These spectra are derived from the *B*-term parameters from Direct calculations with the DZP, TZ2P, and QZ3P-1D basis sets and the SOS(250) Approx and Im[*V*] calculations with the QZ3P-3D basis set. The simulated spectra were obtained from the MCD parameters following Eq. (1) or (33)

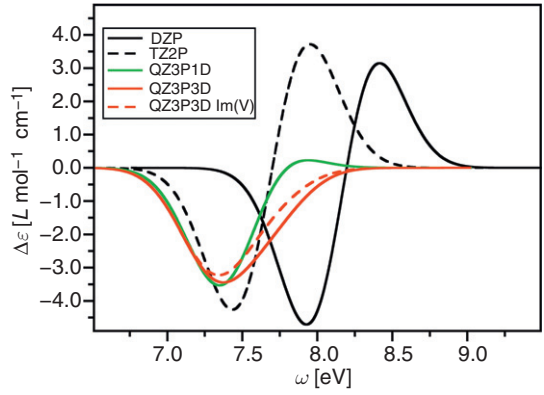

FIG. 2. Simulated MCD spectrum of ethene using the electronic transition-based method with the Direct method of equation solution and different basis sets *48,105*). Also included is the simulated spectrum resulting from the Im[*V*] approach with a large basis set (*51*).

divided by the concentration and path length to give $\Delta\varepsilon$. Where needed, the band-shape functions were chosen to be normalized Gaussian functions. From Fig. 2 several things become apparent. First, despite the large difference in B term parameters between the calculations, the magnitude of the MCD intensity produced by those parameters is similar. All five spectra have minima in the range –4.0 to –5.0 L mol^{-1} cm. This is most apparent in the DZP and TZ2P spectra where the parameters differ by an order of magnitude but the simulated spectra look very similar, if shifted in energy. The increase in MCD parameters when going from TZ2P to DZP is countered by greater overlap of oppositely signed bands as the difference in energy of two near-degenerate bands becomes smaller. The spectra obtained with basis sets that include diffuse functions are obviously different from the DZP and TZ2P spectra but show many similarities to each other again despite the differences in MCD parameters.

These results illustrate the problem facing an experimentalist wishing to extract MCD parameters from a spectrum where bands overlap: No unique set of parameters exists for a given overlapping spectrum. Those wishing to simulate spectra face similar challenges in that the spectrum obtained may change significantly or very little as the parameters used to simulate that spectrum change.

The DZP and TZ2P results have been analyzed in more detail (*48*). The proportion of the MCD intensity due to perturbation of the ground state is small in both cases. As expected, the largest part of the B term parameters come from the $1^1A_{1g}\rightarrow 1^1B_{1u}$ and $1^1A_{1g}\rightarrow 1^1B_{3u}$ transitions mixing with each other.

It has been noted that, unless a suitable perturbation-dependent basis set is used, calculated A, B, and classical C term parameters will depend on the choice of origin of the molecular coordinate system. The Im[V] approach was developed from the beginning with this issue in mind and an origin-invariant version was implemented that makes use of GIAOs (*51,74*). Test calculations found that the gauge dependence of MCD (and MOR) calculated with a DZP quality basis set is weak, particularly below 10 eV, which is generally our area of interest (*51,78*). Kjærgaard and coworkers observed similar behavior (*43*). Given these results, it was decided to implement the calculation of A and B terms and classical C term parameters from the transition-based approach without the added complication of GIAOs. When calculating MCD with a method that is not gauge-invariant, gauge errors should be small provided that the coordinate origin is placed near to the center of mass of the molecule and the basis set chosen is not too small. A basis set of double-ζ plus polarization quality seems to be large enough for this purpose.

Finally, some comparison between the calculated and experimental MCD spectra of ethene can be made. The experimental MCD spectrum of ethene shows significant vibrational fine structure (*100*). Three series of bands have been identified. The lowest energy series produces weak negative MCD intensity and is assigned to the $1^1A_{1g} \rightarrow 1^1B_{1u}$ ($\pi \rightarrow \pi^*$) transition. At higher energy is a second series of bands with intense negative MCD intensity assigned to the $1^1A_{1g} \rightarrow 1^1B_{3u}$ ($\pi \rightarrow 3s$) Rydberg transition. A third series of peaks with positive MCD intensity are found in the same region as the Rydberg excitation. The MCD spectra calculated with the largest basis set reproduces some of these features. The order of the two major transitions is reversed but the sign and relative intensity of the MCD due to each excitation is predicted correctly. Initial speculation suggests that the third series of peaks may arise from transitions that are dipole forbidden under D_{2h} symmetry (*100*). The TDDFT calculations do find some transitions in the required region but without the inclusion of vibronic effects it is not possible to determine whether any of these transitions is responsible for the observed MCD intensity.

A.2. Transition metal d^0 oxy- and thioanions

The calculations of ethene MCD parameters described in the previous section provided a number of insights into the best way to calculate MCD spectra but were lacking in some areas. In particular, ethene only gives rise to *B* terms. We shall now turn to a series of highly symmetric tetrahedral d^0 metal complexes, including the permanganate and dichromate ions, where *A* as well as *B* terms are involved.

As tetrahedral closed-shell molecules, all dipole-allowed transitions of these complexes will be to an excited state with $^1T_2$ symmetry.

The lowest transition energies of permanganate and dichromate will be ligand to metal charge transfer (LMCT) in nature. From symmetry arguments, it can be shown that the transition described by the $t_1 \rightarrow e$ one-electron transition of a tetrahedral d^0 complex will have an A_J/D_J ratio of –0.5 (*108,109*).

The experimental spectra of MnO_4^- and CrO_4^{2-} each include two bands with the characteristic shape of an *A* term (*28,108*). In both cases the *A* term lower in energy was found to have an A_J/D_J ratio of close to –0.5 providing strong evidence for the assignment of the lowest excitation in each case as $t_1 \rightarrow e$. Following the success of this early study, the MCD spectra of other d^0 tetrahedral oxy- and thioanions were recorded (*110–117*). These spectra were also dominated by *A* terms. In all cases the A_J/D_J ratio of the first *A* term

was close to –0.5. The MCD spectra did not provide definitive evidence for the assignments of other peaks in the spectra of these species other than to confirm that the most intense peaks were indeed caused by excitations to states with T_2 symmetry. The observed A terms were not always completely symmetrical indicating that some bands included significant contributions from B terms or in fact involved more than one A term.

The MCD spectra of 10 oxy- and thioanions were simulated (*49*). The calculation of the term $\omega_J^{(1)}$ needed to evaluate the parameter A_J (Eqs. 59 or 61) requires only a single matrix-vector multiply followed by a dot-product. Thus, the calculation of the A_J parameters requires much less computer time than the evaluation of the B_J parameters.

The simulated MCD spectra produced from the calculated parameters were generally in good agreement with the experimental spectra. The experimental and theoretical spectra of two typical examples, MnO_4^- and MoS_4^{2-}, are compared in Fig. 3. The TDDFT calculations found that the first excitation of all of the molecules was described as an almost pure $t_1 \rightarrow e$ one-electron excitation and the corresponding calculated A_J/D_J ratios were close to –0.5. Many of the species were predicted to have two more bands within the experimental region. One of these two bands was often relatively weak and was therefore not observed experimentally. The TDDFT calculations found that the composition of these higher excitations generally included significant contributions from more than one one-electron excitation, perhaps explaining why experimental attempts to provide a definitive assignment in terms of a single excitation were unsuccessful.

Contributions from B terms to the spectra were calculated to be small for most transitions in agreement with the observed spectra that are made up primarily of derivative-shaped bands. An

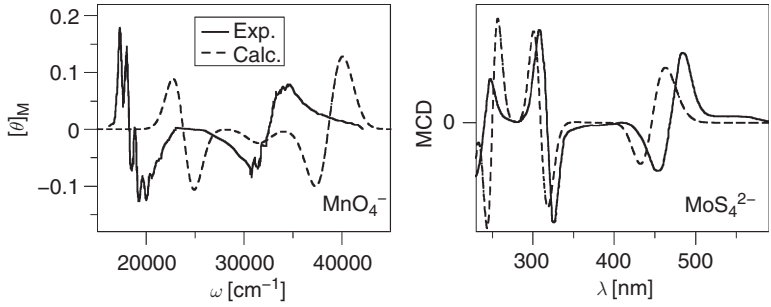

FIG. 3. Simulated (*49*) and experimental (*108,110*) MCD spectra of MnO_4^- and MoS_4^{2-}.

analysis of the B_J parameters in terms of Eq. (52) revealed that in general, the small values of B_J arose because the contribution due to perturbation of the ground state nearly canceled that due to perturbation of the excited state. In some cases the B terms did make a significant contribution, most notably in the spectrum of VS_4^{3-}. In contrast, asymmetry in the major derivative-shaped peaks of OsO_4 and MoO_4^{2-}, an observation that could be attributed to the presence of significant B terms, was found to be due to overlapping A terms of opposite sign (*49*).

A.3. Octahedral d^5 iron complexes

An early example of the application of classical C terms can be found in the assignment of the spectrum of $[Fe(CN)_6]^{3-}$ (*108,109,118*). Cyanide is a strong field ligand and $[Fe(CN)_6]^{3-}$ should thus have a low-spin d^5 electron configuration with T_{2g} symmetry. Its MCD spectrum would therefore be expected to show *A, B,* and temperature-dependent C terms. Since its ground state is orbitally degenerate then it should be possible to interpret its MCD spectrum in terms of classical C terms. This proved to be the case.

The absorption spectrum of $[Fe(CN)_6]^{3-}$ includes three major bands. From a consideration of the MO diagram of $[Fe(CN)_6]^{3-}$ these bands all correspond to LMCT excitations. Two of the transitions are expected to be to states with T_{1u} symmetry and one to a state with T_{2u} symmetry (*119–121*). The exact assignments of the three bands could not be extracted from the absorption spectrum. It was shown that in an MCD spectrum the C term for a $T_{2g} \rightarrow T_{1u}$ transition will be positive, while a $T_{2g} \rightarrow T_{2u}$ C term will be negative (*108*). An MCD spectrum therefore should be able to provide a definitive assignment of the spectrum of $[Fe(CN)_6]^{3-}$.

The MCD spectrum of $[Fe(CN)_6]^{3-}$ was duly measured and the three bands in the spectrum were found to correspond to states assigned as T_{1u}, T_{2u}, T_{1u} in order of increasing energy (*108*). A few other low-spin octahedral d^5 complexes were investigated with MCD and similar results were obtained (*122–125*).

A third set of related compounds that also was studied with MCD are the C_{4v} complexes $[Fe(CN)_5L]^{3-}$ where L is NH_3, H_2O, PH_3, SCN^-, or N_3^- (*126*). These complexes are expected to have a ground state with exact or approximate ^2E symmetry. The experimental MCD spectra of some of the C_{4v} complexes studied could be interpreted in a similar way to those of the octahedral complexes but the spectra of the complexes where L is SCN^- or N_3^- were somewhat different. The observed MCD of the first band of the SCN^- complex is weak and temperature-independent. If the

observed MCD is assumed to be due to C terms only this leads to the rather unsatisfying result of C_J/D_J ratios that varied with temperature and were much too small in comparison with the other complexes. The behavior of the second band in the MCD spectrum of the SCN^- complex is more typical of a C term but shows positive MCD rather than negative as is the case for the other complexes. The N_3^- complex is different from all of the other complexes in that it shows very little MCD intensity at all in the region of the first transition (*126*).

As noted in Section II.C.4, the calculation of C term parameters for molecules with orbitally degenerate ground states requires a rather different approach to the process applied for the other types of parameter. The iron complexes described in the last few paragraphs provided a useful opportunity to test this methodology. The calculated MCD spectra for $[Fe(CN)_6]^{3-}$ and the two related complexes where a CN^- ligand is substituted by SCN^- and N_3^- will be discussed here (*89,127*).

The first task in an MCD calculation of a molecule with an orbitally degenerate ground state is to evaluate the magnetic moment of the ground state and as a result the C_J/D_J ratio (Eq. 22). Orbitals for the ground state of the complexes of interest were obtained from calculations where electrons were spread evenly between the degenerate orbitals (2/3 of a β electron in each t_{2g} orbital component in the case of $[Fe(CN)_6]^{3-}$ and ½ a β electron in each e orbital component for the molecules with overall C_{4v} symmetry). The magnetic moment of the ground state components was obtained from the sum of the occupied orbital magnetic moment integrals. The C_J/D_J ratios of the $[Fe(CN)_6]^{3-}$ and other O_h molecules calculated in this way were in reasonable agreement with the experimental values. In contrast, the calculated ratios of the C_{4v} molecules were similar in size to those of the O_h complexes and much larger than the experimental values (*127*).

The second term in Eq. 22 required to evaluate the MCD intensity due to C terms of orbitally degenerate molecules is the transition dipole moments between the ground state and the excited states of interest. This was achieved through TRICKS-TDDFT calculations (Section II.C.4). The TRIC used to study $[Fe(CN)_6]^{3-}$ was formed by exciting a β electron from the highest occupied a_{1g} orbital to fill the hole in the t_{2g} orbital and give an overall $^2A_{1g}$ state. In the case of the C_{4v} complexes, the hole in the e orbital could be filled with an electron from any one of an a_1, a_2, b_1, or b_2 orbital. The choice of the TRIC from any of the four options made little difference to the final results (*89*).

The calculated MCD spectrum of $[Fe(CN)_6]^{3-}$ and the absorption and MCD spectra of $[Fe(CN)_5SCN]^{3-}$ are plotted in Fig. 4.

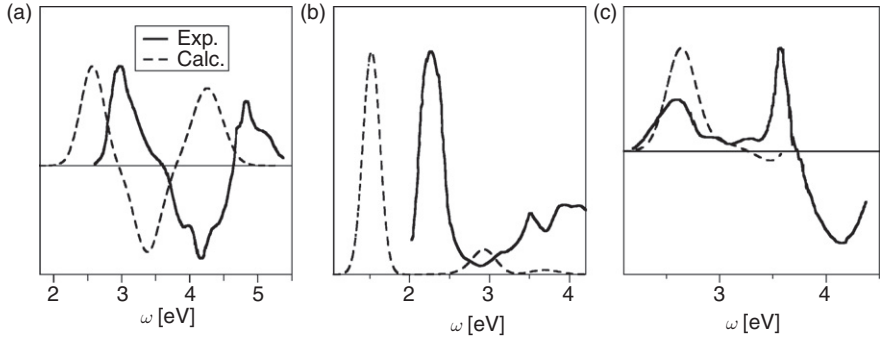

FIG. 4. (a) Simulated (*89*) and experimental (*108*) MCD spectra of $[Fe(CN)_6]^{3-}$. (b) Simulated (*89*) and experimental (*126*) absorption spectra of $[Fe(CN)_5SCN]^{3-}$. (c) Simulated (*89*) and experimental (*126*) MCD spectra of $[Fe(CN)_5SCN]^{3-}$.

The TRICKS-TDDFT intensities of $[Fe(CN)_6]^{3-}$ are consistent with the experimental spectrum and the excitation energies are somewhat overestimated leading to a simulated MCD spectrum correct in form but blue shifted.

The calculated excitation energies of the C_{4v} molecules explain the inconsistencies in their MCD spectra. The spectra of these complexes were initially interpreted in terms of a perturbed O_h symmetry (*126*). The calculations showed that while the higher energy T states are split very little in the C_{4v} symmetry complexes, the 1^2T_{2g} state and, in particular, the 1^2T_{1u} state are split significantly in the C_{4v} environment (*89*). The first band in the absorption spectrum thus corresponds to a $^2E \rightarrow {}^2E$ excitation but the other part of the transition to the "$^2T_{1u}$" state, a $^2E \rightarrow {}^2A_1$ transition is found in the second band. The $^2E \rightarrow {}^2E$ transition is more intense and results in a spectrum with a prominent first band (Fig. 4b).

Under C_{4v} symmetry, the C term of a $^2E \rightarrow {}^2E$ excitation will be exactly zero (*11*). Thus, the MCD intensity of the lowest energy bands of the SCN^- and N_3^- is weak and largely temperature-independent because it includes no contribution from a classical C term. The $^2E \rightarrow {}^2A_1$ transition from the 1^2T_{1u} state can be found in the second band of the absorption and MCD spectra. This transition contributes an intense positive C term. The negative MCD at higher energies is due to a $^2E \rightarrow {}^2B_2$ transition.

The comparison between the simulated and experimental MCD spectra of $[Fe(CN)_5SCN]^{3-}$ in Fig. 4c is a little deceptive. The simulated spectrum only includes contributions from classical C terms and is red shifted relative to experiment by about

1 eV (*89*). Thus, the positive peak in the simulated spectrum corresponds to the second positive peak in the experimental spectrum. As has already been noted, the first experimental peak is largely temperature independent and is likely to be mostly due to B terms.

As far as computational cost is concerned, the evaluation of the ground state magnetic moment is trivial and the TRICKS-TDDFT part is simply a normal TDDFT calculation of excitation energies but with an unusual choice of reference state orbital occupations. Preliminary results indicate that the accuracy of TRICKS-TDDFT excitation energies is similar or perhaps a little inferior to that of standard TDDFT calculations (*88*).

A.4. $VO(H_2O)_5^{2+}$

The MCD spectrum of $VO(H_2O)_5^{2+}$ provides a useful test case for our approach to calculating spin–orbit coupling induced C terms of a molecule with no orbitally degenerate states (*50*). The MCD spectrum of $VO(H_2O)_5^{2+}$ was recorded in order to gain insight into the assignment and the influence of spin–orbit coupling on its absorption spectrum (*128*). $VO(H_2O)_5^{2+}$ has symmetry close to C_{4v} but the highest symmetry it can show exactly is C_{2v}. Under this symmetry, its ground state has $^2B_2$ symmetry. The only mechanism through which $VO(H_2O)_5^{2+}$ can show temperature-dependent MCD intensity is by the mixing of states with spin–orbit coupling. Any temperature-independent MCD will be due to B terms.

The MCD spectrum of $VO(H_2O)_5^{2+}$ was measured at room temperature and at 4.2 K (*128*). The most interesting part of the spectrum is the first band, shown in Fig. 5. At room temperature the band is weak and has the shape of a negative A term. The feature must be a pseudo-A term caused by two nearly degenerate states. The approximate C_{4v} symmetry of this molecule suggests that the near degeneracy is caused by an E state that is split to a small extent by the perturbation to C_{2v} symmetry. Upon lowering the temperature to 4.2 K, a pseudo-A term is again obtained for the first band. However, the intensity of the MCD is increased by more than an order of magnitude and the pseudo-A term is now positive. These results strongly suggest that the MCD at room temperature is due to B terms, while at 4.2 K the band is dominated by spin–orbit coupling induced C terms.

Calculations were able to reproduce most of the important features of the experimental MCD spectra (*50*). The excitation energies are significantly overestimated but the first two excited states are nearly degenerate with $^2A_1$ and $^2A_2$ symmetry and would become an E state under C_{4v} symmetry. The calculated

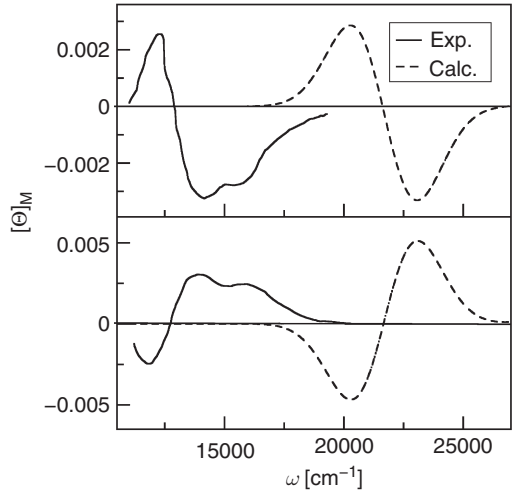

FIG. 5. Simulated (*50*) and experimental (*128*) MCD spectra of $[VO(H_2O)_5]^{2+}$. Top: 300K. Bottom: 4.2K.

B_J and C_J parameters of these two states produce simulated spectra that are dominated by the B terms at 300 K and then by the C terms at 4.2 K (Fig. 5).

As described in Sections II.A.1 and II.A.4, the numerical procedures required to calculate B term parameters and C terms induced by the perturbation of the transition moment by spin–orbit coupling are nearly identical. Almost all of the comments concerning the calculation of B terms made in Section III.A.1 apply equally well to the spin–orbit-induced C terms. The major difference between the two types of calculation is that the spin–orbit interaction is often significantly larger than the influence of a magnetic field.

B. PORPHYRINS

Porphyrin complexes and the many important biological or commercial compounds that are based upon the porphyrin structure show distinct intense electronic spectra that vary in form depending on the exact structure of the ligand and the identity of the central metal ion. Simple porphyrin complexes have D_{4h} symmetry as do many porphyrin derivatives. A large number of lower symmetry related molecules can be approximated successfully as D_{4h}. Porphyrin complexes can be closed-shell or open-shell depending on the identity of the central metal. MCD spectroscopy, a technique that it sensitive to the space and spin symmetry of the ground

and excited states, has proven to be a useful tool in the quest to understand the electronic structure of porphyrin compounds (*16,24,129–134*).

Given the importance of porphyrin compounds, it was decided that it would be interesting to calculate the MCD spectra of some representative porphyrin complexes.

This section is divided into two parts. In the first part, detailed calculations of some closed-shell porphyrins (*135,136*) will be described. Our investigations of a pair of open-shell complexes (*50,127*) will be discussed briefly in the second part.

B.1. Closed-shell complexes

In this section we will consider several complexes. The particular systems that were investigated are composed of a central metal ion M (M=Zn^{2+}, Mg^{2+}, or Ni^{2+}) with porphyrin (P), tetraphenylporphyrin (TPP), tetraazoporphyrin (TAP), or phthalocyanine (Pc) as the ligand. The absorption and MCD spectra of the porphyrin and TPP complexes are sufficiently similar to each other that they can be discussed together. The review of the TAP and Pc results will be presented later.

The experimental studies of the MCD spectra of porphyrin and TPP complexes (*134,137,138*) have generally focused on the first two major bands. The first band, the Q band, appears near 2 eV and is has low intensity in the absorption spectrum. The second band, the *B* or Soret band, starts at around 3 eV and has greater intensity in the absorption spectrum. Both bands exhibit some fine structure that may indicate that more than one excitation contributes to each band.

Porphyrin absorption spectra are typically interpreted in terms of the model due to Gouterman (*16,139–141*) where the Q and B bands are described in terms of four orbitals. In this model, the two occupied orbitals are ligand π-bonding in nature with overall symmetries a_{1u} and a_{2u} and the two virtual orbitals are ligand π^* and make up the two components of an e_g orbital under D_{4h} symmetry. In the porphyrin and TPP complexes the a_{1u} and a_{2u} orbitals are nearly degenerate. The Gouterman model predicts that the Q band transition is formed by a mixture of the $a_{1u} \rightarrow e_g$ and $a_{2u} \rightarrow e_g$ one-electron excitations with the same sign. This combination gives low intensity. The B band transition is made up of the same excitations but with opposite sign. The band is predicted to have high intensity.

Computational studies have largely confirmed the Gouterman assignment of the Q band but there has been less agreement as to the assignment of the B band (*132,142–146*). The Ni complexes are predicted to follow the Gouterman model with the majority of

the intensity of the B band being due to a transition that is a mixture of the $a_{1u} \rightarrow e_g$ and $a_{2u} \rightarrow e_g$ one-electron excitations (*146*). Some studies predict similar behavior for the Mg and Zn complexes (*143,145*), while others find that more than one transition provides significant intensity in the B band region and that these transitions do not follow the Gouterman model but are rather a mixture of the $a_{1u} \rightarrow e_g$ and $a_{2u} \rightarrow e_g$ excitations and also the $b_{2u} \rightarrow e_g$ excitation (*144,146*).

Given these results, it is likely that the observed fine structure of the Q band is due to vibrational effects, while in the B band it may be due to the presence of other transitions. Our calculations are similar to those of references (*144*) and (*146*). We find that other transitions not included in the Gouterman model contribute to the intensity of the absorption spectrum B band (*135*).

All of the transitions that make significant contributions to the absorption spectra of the complexes under consideration here have E_u overall symmetry. Since all of the molecules have a closed-shell electronic configuration, their MCD spectra would be expected to have contributions from A and B terms.

The observed spectra consist of a positive A term at the location of each band (*134,137,138*). The Q band MCD is weaker and, like the absorption spectrum, more than one band is observed in this region. The MCD in the B band region is more intense.

A Gouterman-type four-orbital analysis can be applied to the calculation of the A_J/D_J ratios of the Q and B bands of the complexes provided the integrals $< a_{1u} | l_z | e_g >$ and $< a_{2u} | l_z | e_g >$ are known (*135,147*). This simple analysis is in agreement with experiment and predicts that the A terms of both the Q and B bands will be positive with the A_J/D_J ratio larger for the Q band than the B band (*135*).

The A and B term parameters of all complexes described in this section were calculated using the approximate form of the $\mathbf{A}^{(1)}$ and $\mathbf{B}^{(1)}$ matrices (Section II.C.2). The B term parameters were calculated using a SOS approach including the lowest 50 transitions. Test calculations found that the difference between the results obtained with the approximate and full forms of the $\mathbf{A}^{(1)}$ and $\mathbf{B}^{(1)}$ matrices were small (*105*).

The results of these calculations follow a similar pattern to the earlier studies of the absorption spectra (*146*). In the case of the Q bands, the more sophisticated MCD calculation utilizing TDDFT is only a refinement of the four-orbital model. A single A term is predicted with small overall MCD intensity but significant A_J/D_J ratio. This provides further evidence that the more complicated series of bands observed in the Q band of the absorption and MCD spectra is due to vibronic effects. In the cases of NiTPP and

ZnTPP, a positive B term is predicted to make a noticeable contribution to the overall MCD intensity resulting in an asymmetric A term. This seems to be in agreement with the experimental spectra of these two complexes where the positive lobe of the A terms of the respective Q bands is larger (*134,137*).

The qualitative details of the simple model are also reproduced in the B band region of Ni porphyrin and NiTPP. The MCD is due to the A term of the $2E_u$ transition. While the A_J parameter of the B band is larger than that of the Q band, the B band A_J/D_J ratio is smaller. A third transition assigned as $b_{2u} \rightarrow e_g$ ($3E_u$) placed approximately 0.2 eV above $2E_u$ is found to contribute in a very small way to the MCD intensity.

The situation for the B band is rather different for the Zn and Mg complexes. As has already been noted, the $b_{2u} \rightarrow e_g$ excitation as well as the Gouterman excitations contributes to the two-intense transitions in this band. A second $a_{2u} \rightarrow e_g$ excitation also is found to make a significant contribution to the transition densities. Furthermore, the $2E_u$ and $3E_u$ transitions are predicted to be nearly degenerate. If the Gouterman-like model for predicting A_J/D_J ratios is extended to include the b_{2u} orbital and the additional a_{2u} orbital, then either a positive or a negative A term can be predicted to be observed depending on the exact composition of the transitions (*135*). The A term from the TDDFT calculations is found to be large and negative, not at all like the experimental spectrum. The predicted spectrum of Zn porphyrin based on only the A term contribution is shown in Fig. 6a.

Since the $2E_u$ and $3E_u$ states are nearly degenerate, they can be strongly mixed by the magnetic field leading to significant B terms for these two transitions. As was found for some of the ethene calculations (Section III.A.1), when two transitions are nearly degenerate their B terms are often approximately equal in magnitude and opposite in sign leading to the appearance of a pseudo-A term. This is again observed in our calculations of the MCD spectra of the complexes of Zn and Mg with porphyrin and TPP (Fig. 6b). The pseudo-A term has the appearance of a positive A term and the total MCD from both A and B terms (Fig. 6c) also has the appearance of a positive A term in agreement with experiment. These results thus suggest that in some cases, the B-band MCD of porphyrin and TPP complexes is due to the interaction of two states rather than a single state.

As was the case for the absorption spectrum, different calculations of the B band MCD of ZnP and MgP have produced different interpretations of the observed spectral features. Solheim *et al.* have recently calculated the MCD spectra of ZnP, MgP, and NiP using their complex polarization propagator method and a hybrid

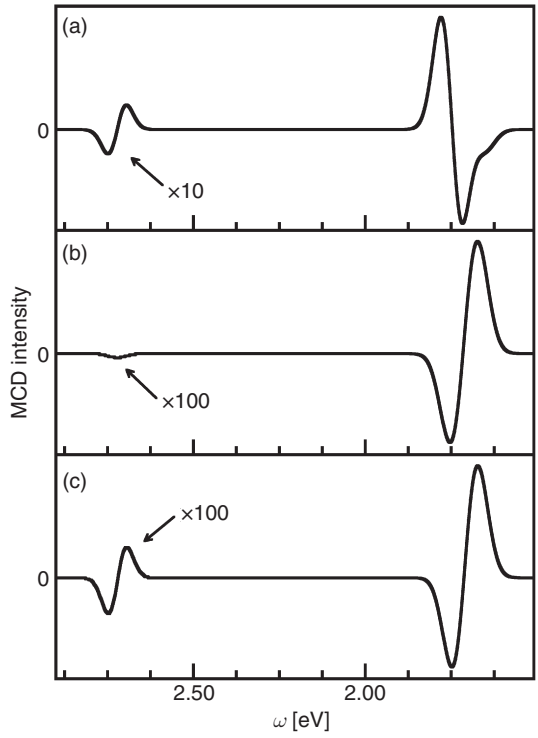

FIG. 6. Simulated MCD spectra of zinc porphyrin (*135*). (a) Including A terms only. (b) Including B terms only. (c) Including both A and B terms.

functional (*46*). The observed spectra were also well reproduced in this work but in all cases it was found that the MCD of the B band was due only to the transition to the $2E_u$ state as the $3E_u$ state was found to be rather further away in energy.

The complex polarization propagator approach is very similar to the method of calculating MCD through the imaginary part of the Verdet constant. We would expect that, given the same reference orbitals, the method employed by Solheim *et al.* (*44*) would give results at least qualitatively similar to those obtained by us. The differences between the two calculations probably occur because of the different functional choices in much the same way that the assignments of the absorption spectra differ between calculations with hybrid (*145*) and nonhybrid (*146*) functionals. These results serve to emphasize that the success of an MCD calculation relies upon the quality of the underlying ground state orbitals and the TDDFT calculation. A rather unusual aspect in this case is the fact that while the two calculations predict different MCD parameters, the two simulated spectra are very similar.

The near degeneracy of the occupied a_{1u} and a_{2u} orbitals strongly influences the absorption and MCD spectra of the porphyrin and TPP complexes discussed in the previous paragraphs. In TAP and Pc complexes this degeneracy is lifted due to the presence of four more nitrogen atoms in the conjugated ring. The resulting absorption spectrum has Q and B bands that are more similar in intensity though the Q band usually has a rather smaller bandwidth. In terms of the MCD spectrum, the Q band shows a strong positive *A* term and the B band has significantly less intensity (*148–150*). The observed B band MCD indicates the presence of a positive *A* term but the bands are not symmetric and also include some fine structure suggesting contributions from *B* terms or other more than one transition. Some further small bands next to the large *A* term of the Q-band were again observed. These bands are also likely to be vibronic in origin.

Much like the porphyrin and TPP complexes, the observed MCD of the Q band of the TAP and Pc complexes is relatively straightforward to reproduce. TDDFT calculations find that this transition is dominated by the $a_{1u} \rightarrow e_g$ one-electron excitation (136,151–153) and the calculated A_J parameters are large and positive.

The B band again proves more challenging. The experimental B band in the MCD spectrum of ZnTAP has the form of a positive *A* term with a larger negative lobe (*148*). Calculations find that this MCD comes from the transition to the $4E_u$ state. The calculated MCD intensity reproduces well what is observed with the combination of a positive *A* term and a large negative *B* term. The transitions to the $2E_u$ and $3E_u$ states are predicted to provide little in the way of MCD intensity.

The MCD B band of MgPc and ZnPc is much weaker than the corresponding Q bands and have a more complicated form (*149,150*). The calculations find six E_u states in the energy range covered by the B band of these two molecules and that 3–4 of these states contribute noticeably to the MCD (*136*). Near degeneracies again lead to significant contributions from *B* terms. The simulated and experimental B bands do have some similarities but are significantly different. A reduction of the influence of the *B* terms on this band improves the agreement between theory and experiment suggesting that the calculated *B* term parameters of the B band may be too large (*136*).

B.2. Open-shell complexes

Two open-shell Pc complexes have been investigated in our group. The systems of interest were MnPc, a molecule believed to have a ^4E_g ground state (*154*), and CuPc, a molecule with a $^2B_{1g}$

ground state (*155*). The former molecule would be expected to show temperature-dependent MCD intensity due to classical C terms, while the latter molecule would be expected to show temperature-dependent MCD only if spin–orbit coupling is considered. These two molecules were chosen just as test cases and were considered in rather less detail than the closed-shell systems (*50,127*).

The calculations found the ground state of MnPc to be ^4E_g with a $e_g{}^3a_{1g}{}^1b_{1g}{}^1$ set of partially occupied orbitals. Only the C_J/D_J ratios of the transitions of MnPc were evaluated using angular momentum integrals from orbitals obtained in a calculation where the single e_g β electron was split between the two components of the degenerate orbital. Once saturation effects were included (the experimental spectrum was recorded at 5 K) the agreement between the calculated and experimental C_J/D_J ratios was found to be very good (*127*).

Just the Q band of CuPc was investigated but contributions from all possible MCD terms were included in the analysis. Similarly to the closed-shell Pc complexes, the Q band is due to the $a_{1u}\rightarrow e_g$ one-electron excitation. In the closed-shell systems, this excitation can lead to a singlet or a triplet state with the spin-allowed singlet transition being much more intense. In CuPc the unpaired electron on Cu couples with the singlet and triplet to give two doublets and a quartet (*156*). Though both doublets are fully allowed by symmetry the "singdoublet" is expected to be more intense. Calculations confirm this prediction (*50*). The excited state has ^2E_u symmetry and therefore can show contributions to its MCD from A terms, B terms, and both types of spin–orbit induced C term.

Experimentally, a band with the form of a positive A term is observed. The intensity of this feature is found to only be very weakly temperature dependent (*155*). This behavior is reproduced by the calculations (*50*). The MCD intensity is mostly due to a positive A term caused by the splitting of the excited state degeneracy by the magnetic field. The spin–orbit splitting of the excited state is calculated to be very small at 0.5 cm^{-1} (compared to the experimental value of 1.5 cm^{-1}) leading to a small $C_J^{SO,1}$ parameter that only makes a small contribution to the total MCD intensity. The calculated B terms and C terms from mixing of states mediated by spin–orbit coupling contribute a barely noticeable amount of positive MCD intensity.

C. Metallonzymes

In recent years, some of the most impressive applications of MCD spectroscopy have come in the area of metalloenzymes

(*15,24–26*). MCD can be particularly useful in the study of enzymes containing open-shell metal ions because of its sensitivity to the electronic structure at the active site.

As was described in Section II.A.4, the temperature-dependent component of an MCD spectrum of a molecule with a spin-degenerate ground state is caused by spin–orbit coupling. The spin–orbit operator has one-electron and two-electron parts with the one-electron part dominating (*157*). The exact form of the one-electron operator depends on the form of the relativistic Hamiltonian used but any reasonable operator scales approximately as Z_N/r_{iN}^3, where Z_N is the charge on nucleus N and r_{iN} is the distance between electron i and nucleus N. Thus, spin–orbit coupling is caused by the presence of a nuclear charge, increases as the size of that charge increases and the influence of a nucleus decays rapidly as an electron moves away from a nucleus. In the context of metalloenzymes, this means that spin–orbit coupling will be strongest at the metal site and the strongest temperature-dependent MCD intensity will come from transitions that are most strongly influenced by the metal atom.

C.1. Blue copper proteins

Blue copper proteins are a family of metalloproteins that have been found to play an important role in a number of electron-transfer reactions in nature. Solomon and coworkers have studied a range of blue copper enzymes in detail to produce a thorough description of how molecular and electronic structure interact to provide the function of these enzymes (*26,158*).

We have studied the blue copper proteins plastocyanin, azurin, cucumber basic protein (CBP) and nitrite reductase (NiR) (*159,160*). We shall focus on these four in the remainder of this section.

Blue copper proteins in their oxidized form contain a Cu^{2+} ion in the active site. The copper atom has a rather unusual tetrahedral/trigonal pyramidal coordination formed by two histidine residues, a cysteine and a methionine residue. One of the models of plastocyanin used in our computational studies (*160*) is pictured in Fig. 7. Among the four proteins, the active sites differ in the distance of the sulfur atoms from the Cu center and the distortion from an approximately trigonal pyramidal to a more tetrahedral structure in the order azurin, plastocyanin, CBP and NiR. This unusual geometrical arrangement of the active site leads to it having a number of novel electronic properties (*26*).

The significant experimental effort put into characterizing the blue copper proteins has made them attractive targets for computation (*161–163*). These computational studies have provided

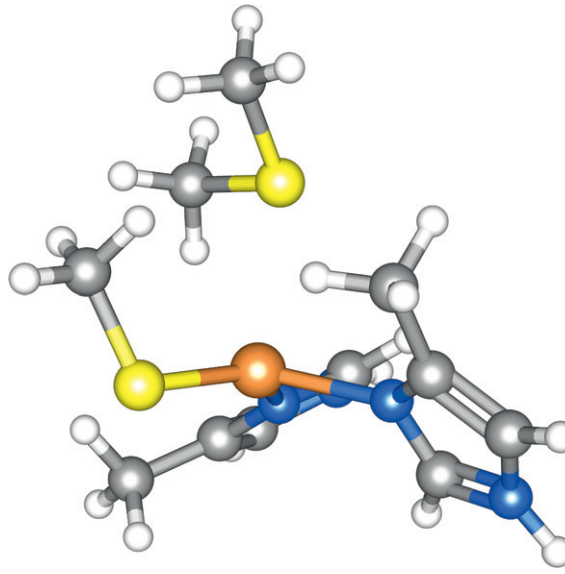

FIG. 7. Model of the active site of plastocyanin.

significant insight into their electronic structure. Some theoretical results, particularly in the areas of assignment of the absorption spectrum, energy order and composition of the ground state orbitals and EPR parameters have not been in complete agreement with experiment. Given that MCD spectroscopy has been an important tool in the study of blue copper proteins, these systems are also an interesting target for MCD calculations.

The absorption spectra of blue copper proteins typically include one major peak and two other peaks of varying size in the range 10,000–30,000 cm^{-1} (*164–166*). MCD spectroscopy has proved useful in assigning these peaks. The electronic excitations of the active site can be classed as either $d \rightarrow d$ or LMCT transitions. The $d \rightarrow d$ transitions will involve excited states where the electron hole remains on the Cu atom while the LMCT transitions will move the hole to the ligands, in particular the sulfur atoms of the Met and Cys groups. Thus the $d \rightarrow d$ transitions would be expected to be more strongly influenced by spin–orbit coupling and this should be reflected in the relative size of the C_J/D_J ratios of the bands in their MCD spectra.

The C_J/D_J ratios are generally obtained by fitting the observed MCD and absorption spectra to a series of Gaussian band-shape functions under the assumption that all of the MCD intensity is due to temperature-dependent MCD (*164–166*). Following the fit, eight transitions were identified in the spectrum of each protein.

Except for NiR, these eight transitions can be placed into two groups of four on the basis of their C_J/D_J ratio. The lower energy four transitions were assigned as $d \rightarrow d$ on the basis of a larger C_J/D_J ratio (~0.1) and the higher energy four transitions were assigned as LMCT on the basis of a smaller C_J/D_J ratio (~0.01). NiR has five transitions with C_J/D_J ratios of approximately 0.1 and the first four of these are assigned as $d \rightarrow d$ (*165*).

The simulated and experimental MCD spectra of plastocyanin, azurin, CBP and NiR are given in Fig. 8. The calculations approximate the active sites with 39-atom models (*160*). A larger 52-atom model of plastocyanin produced similar results to the equivalent 39-atom calculation (*159*). The calculations find more than a dozen transitions in the energy range of interest for each system but of these transitions, less than ten have significant MCD intensity, a value that is more in line with the eight transitions observed experimentally. The simulated spectra include all of the important peaks observed experimentally though their relative intensity is not always reproduced with high accuracy. Nevertheless, the qualitative similarity between the experimental and calculated spectra does suggest that calculations of this type will be able to provide useful assistance to the sometimes-difficult task of interpreting metalloenzyme MCD spectra.

A number of useful insights can be derived from the calculated results. As would be expected, at the experimental temperature of

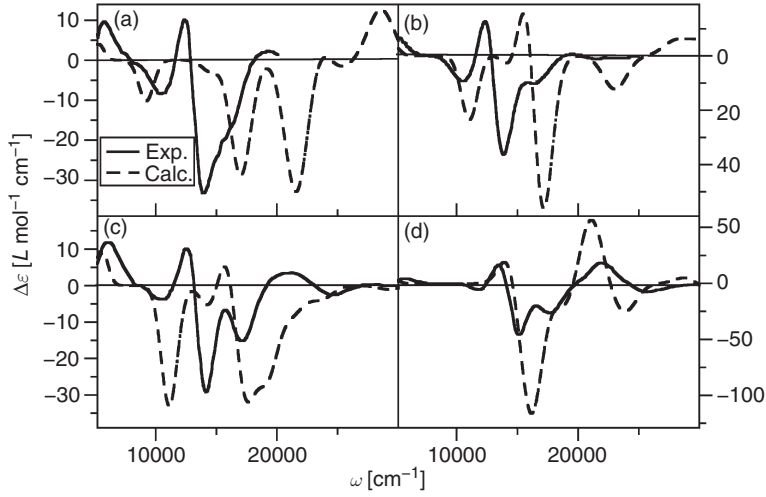

FIG. 8. Simulated (*160*) and experimental (*165,166*) MCD spectra of (a) azurin, (b) plastocyanin, (c) cucumber basic protein, and (d) nitrite reductase.

4.5 K the contribution to the MCD intensity from B terms is negligible. The pseudo-A term that is the dominant feature in all of the experimental spectra is due to two nearly degenerate transitions. The transitions of course interact strongly with each other once spin–orbit coupling is considered. The calculated MCD parameters of the near-degenerate transitions cannot be explained in terms of their interaction with each other alone and other excited state are found to make important contributions. For most of the other transitions, the MCD intensity is found to have significant contributions from the perturbation of both the ground and excited states of the transition.

The calculated absorption spectra of these four enzyme models are also qualitatively similar to the measured spectra. In general, C_J/D_J ratios of the lower energy transitions are predicted to be larger than those of the higher energy transitions similarly to what was found in the experimental studies. The difference between the C_J/D_J ratios of the lower and higher energy transitions is smaller in the calculations than the experimental relationship. This is consistent with the finding that DFT calculations tend to produce orbitals that include too much mixing between the metal and ligand orbitals (*158*). In the experimental studies it was found that from plastocyanin to CBP to NiR the division between the *d-d* and LMCT transitions becomes less clear-cut. That is, while the C_J/D_J ratios of the lower energy transitions are still larger than those of the higher energy peaks, the difference decreases. This trend is reproduced by the calculations (*160*).

The expression for the contribution to the spin–orbit induced MCD intensity from perturbation of the ground state is somewhat reminiscent of an expression for the Δg quantity of EPR spectroscopy. The similarity lies in the paramagnetic term, Δg^p. This term is composed of integrals of a spin–orbit operator over molecular orbitals similar to the expression for the perturbation of the ground state in the presence of spin–orbit coupling (Eqs. 52–56). The paramagnetic contribution to Δg dominates for blue copper proteins and it was suspected that the MCD parameters and Δg^p may have some sort of relationship. It was found that many of the terms that make large contributions to Δg^p do play a role in the MCD intensity but no simple relationship was found (*160*).

C.2. Molybdoproteins

In this section, calculations of the MCD spectra of the Mo-containing proteins, sulfite oxidase (*167*), and dimethyl sulfoxide (DMSO) reductase, (*168*) will be discussed. These two

species have several properties in common in the context of MCD spectroscopy. The Mo active site in both systems catalyzes a redox reaction where it is believed that Mo is present in the IV, V, and VI oxidation states at some point during the catalytic cycle (*169*). The Mo(VI) forms of the active sites are fairly well characterized. A crystal structure is available for both sulfite oxidase (*170*) and DMSO reductase (*171*). No crystal structures have been obtained for the reduced forms and their geometrical and electronic structure is less well understood. Many spectroscopic techniques that could be applied to these systems are hindered by the presence of other chromophores. The sensitivity of MCD to the immediate neighborhood of the Mo atom makes it a useful technique for the study of the paramagnetic Mo(V) systems.

The sulfite oxidase enzyme performs the oxidation of sulfite to sulfate by oxygen transfer from a molybdenum atom. The enzyme also includes a heme ring that produces significant MCD intensity. The study of the Mo active site of sulfite oxidase by MCD spectroscopy is thus not immune to the influence of other chromophores. A form of the enzyme can be produced that contains paramagnetic Mo(V) and diamagnetic Fe(II) (*172*). This allows the Mo site MCD to be deconvoluted from the heme MCD to some extent as the latter is temperature independent. The MCD due to the Mo site could not be determined with any confidence in the regions where the heme MCD intensity was greatest, leading to a partial spectrum (Fig. 9b) (*172*). The positive peak at 22,250 cm^{-1} has been assigned as LMCT from the cysteine sulfur. More tentatively, the intense positive MCD at 26,000 cm^{-1} and the partial positive peak at

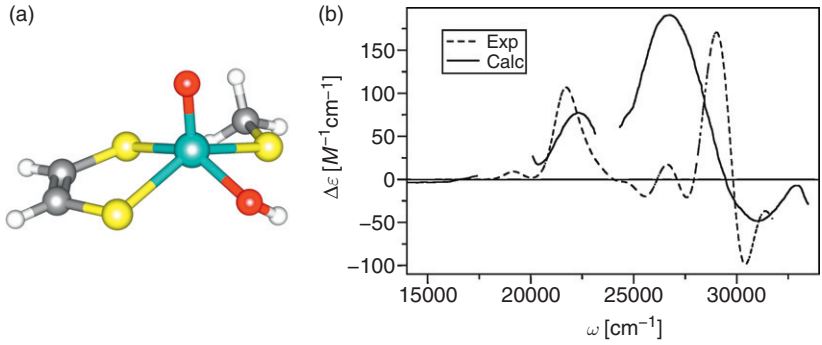

FIG. 9. (a) Model of sulfite oxidase Mo active site. (b) Simulated (*167*) and experimental (*172*) MCD spectra of sulfite oxidase.

lower energy were assigned as LMCT from the 1,2-dithiolate sulfur atoms (*172*).

The MCD spectrum of a possible model of the Mo(V) active site was calculated (Fig. 9a). The calculated spectrum reproduces many of the features of the experimental spectrum lending confidence to the choice of model of the active site and the assignments that come from the calculation. The experimental spectrum contains fewer peaks than that obtained from calculation, perhaps due to an underestimation of the bandwidth or an overestimation of the excitation energy of the transition that produces intense positive MCD just below 30,000 cm^{-1}.

The theoretical assignments of the first two peaks are the same as those suggested by Helton *et al.* (*172*). A number of transitions were found to contribute to the higher energy part of the spectrum between 24,000 and 30,000 cm^{-1}. The negative MCD at the high end of the spectrum is assigned to another LMCT transition from the cysteine sulfur.

Of the nine transitions that make significant contributions to the MCD spectrum, it was found that for seven transitions the perturbation of the excited state provided the major part of the MCD intensity while in two cases it was found that perturbation of the ground state was dominant.

The reduction of DMSO catalyzed by molybdenum is an important step in the process of anaerobic respiration carried out by a number of bacteria (*169*). Much like sulfite oxidase, early MCD studies of DMSO reductase were complicated by the presence of heme iron (*173*). The discovery of two enzymes that do not include an iron center led to the measurement of MCD spectra of *Rhodobacter sphaeroides* DMSO reductase that could be assigned exclusively in terms of transitions of the Mo site (Fig. 10b) (*174*). The six major peaks are assigned as LMCT transitions from the three highest energy occupied orbitals to the two lowest unoccupied orbitals (*174*).

The calculated MCD spectrum of a model system (Fig. 10a) has the same form as the experimental spectrum but is red-shifted by about 2000 cm^{-1} (Fig. 10b). A total of sixteen transitions are found over the range of interest. The assignment of the spectrum from the TDDFT calculation suggests that the spectra are indeed dominated by LMCT transitions though all four possible $d \rightarrow d$ transitions do contribute. Twelve transitions assigned as LMCT include assignments from four different ligand orbitals to three different Mo *d* orbitals are found to be present. Much like sulfite oxidase, the MCD intensity from most of the transitions is dominated by the contribution from perturbation of the excited state by spin–orbit coupling. For two transitions, perturbation of the ground state is the most important contribution.

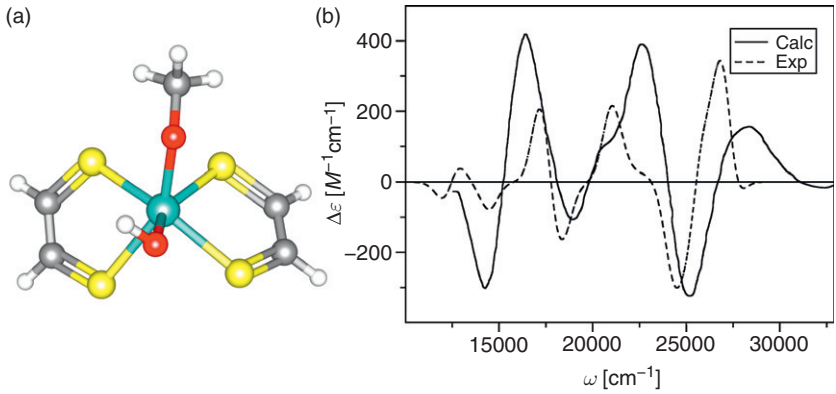

FIG. 10. (a) Model of DMSO reductase Mo active site. (b) Simulated (*168*) and experimental (*174*) MCD spectra of DMSO reductase.

IV. Concluding Remarks

In a recently published textbook MCD was described as a "challenge for theoreticians" (*39*). The simulation of an MCD spectrum, requiring the consideration of electronic transitions, a magnetic field, possibly spin–orbit coupling and perhaps small effects like ZFS, does present a number of challenges. From the work of several research groups (*33,35,36,40–44*) and our contributions described in this review, it appears that theoreticians are well on the way to meeting the challenge of MCD.

All molecules will show an MCD spectrum. The spectrum of many types of molecule can now be simulated, often through more than one theoretical approach. Several areas need further study however. It would be useful if all types of MCD spectrum could be calculated at a range of levels of theory so that a scientist interested in predicting a spectrum would be able to choose an approach that suitably fits their needs. More benchmark calculations are needed to improve our understanding of the limitations of the present methods. These calculations would be aided by the availability of more high-quality spectra of small molecules that would be suitable test cases. While the MCD spectra of many molecules can now be calculated, one area that probably still cannot be studied with confidence is paramagnetic molecules that include very heavy elements. In this case spin–orbit effects will be very large and perturbational treatments like those applied thus far are unlikely to provide accurate results.

The field of the calculation of MCD spectra from first principles has matured rapidly. It is now possible for any researcher to

obtain quantum chemical programs that can simulate MCD spectra. Further refinements over the next few years should mean that the calculation of MCD will soon be as routine as evaluation of many other popular types of spectrum.

List of Symbols

MCD and TDDFT each has their own extensive system of notation. We have tried to make the symbols used distinct through choice of font and context. As an additional aid we have included a list of the symbols and abbreviations used in this review along with their meaning:

Symbols	Description
A	Absorption intensity
ΔA	Difference in absorption intensity of left and right circularly polarized light (Eq. 4)
A term	MCD spectral feature with derivative band shape (Section II.A.2).
A_J	Intensity parameter of an A term associated with the transition to state J.
$\|A\alpha>$	The ground state. If the ground state is degenerate an arbitrary component is labeled α.
$\|A\|$	Degeneracy of the ground state.
$\mathbf{A}$	Diagonal block of the orbital Hessian matrix used in TDDFT (Eqs. 38–43).
B	Amplitude of applied magnetic field.
B term	MCD spectral feature with absorption band shape (Section II.A.1)
B band	Second major band in porphyrin absorption spectrum.
B_J	Intensity parameter of a B term associated with the transition to state J.
$\mathbf{B}$	Off-diagonal block of the orbital Hessian matrix used in TDDFT (Eqs. 38–43).
C term	Temperature-dependent MCD spectral feature (Sections II.A.3 and II.A.4
C_J	Intensity parameter of a C term caused by orbital degeneracy in the ground state and associated with the transition to state J (Section II.A.3). The corresponding band in and MCD spectrum has an absorption band shape.
$C_J^{SO,1}$	Intensity parameter of a C term caused by spin–orbit splitting in the ground or excited state. J denotes the excited state of the transition. The accompanying spectral feature has a derivative band shape (Section II.A.4).
$C_J^{SO,2}$	Intensity parameter of a C term caused by spin–orbit mixing of the states of a paramagnetic molecule. J denotes the excited state of the transition. The accompanying spectral feature has an absorption band shape. (Section II.A.4).

c	Concentration or the speed of light.
CASPT2	CASSCF plus dynamic correlation correction to the energy to second order.
CASSCF	Complete active space self-consistent field.
CBP	Cucumber basic protein.
CD	Circular dichroism.
CI	Configuration interaction.
CIS	CI including single electron excitations.
CNDO/S	Complete neglect of differential overlap/spectroscopic parameterization.
CPKS	Coupled-perturbed Kohn-Sham.
D_J	Dipole strength parameter of transition to state J. Associated with the absorption intensity (Section II.C.6).
D_{ai}	Element of the density matrix
DFT	Density functional theory
DMSO	Dimethyl sulfoxide.
E	Energy.
$\boldsymbol{F}$	Transition density vector from a TDDFT calculation with a nonhybrid functional.
f	Band-shape function.
f_{xc}	Exchange-correlation kernel.
g	Electron paramagnetic resonance g-tensor.
$\Delta g, \Delta g^{\mathrm{p}}, \Delta g^{\mathrm{d}}$	Deviation of g from free electron value (g_{e}), paramagnetic and diamagnetic components.
GIAO	Gauge-including atomic orbital.
H^{SO}, $H^{\mathrm{SO},r}$	Spin–orbit operator and the part of the spin–orbit operator that acts on the spatial part of the wave function.
Im[V]	Imaginary part of the Verdet constant.
i	Square root of –1.
$\|Jj\rangle$	Excited state J with general degenerate component j.
k	Boltzmann constant.
L_γ	Total angular momentum operator corresponding to direction γ.
l	Path length.
l_γ	One-electron angular momentum operator corresponding to direction γ.
LMCT	Ligand-metal charge transfer.
M	Quantum number corresponding to the projection of the spin angular momentum along the axis of quantization.
M^α	Total dipole moment operator of direction α.
M^+, M^-	Total electric dipole moment operator corresponding to left (-) and right (+) circularly polarized light.
m^α_{pq}	One-electron electric dipole moment integral over orbitals p and q.
MCD	Magnetic circular dichroism.
MOR	Magnetic optical rotation.
N	Total population of all states.
N_a	Population of the component a of the ground state.
n	Refractive index.
NiR	Nitrite reductase.
Pc	Phthalocyanine
Q	Partition function.
Q band	First major band in porphyrin absorption spectrum.
r_{ij}	Distance between bodies i and j.

$\mathbf{S}$	$(\mathbf{A}^{(0)}–\mathbf{B}^{(0)})^{-1}$ in a calculation involving a nonhybrid functional (Eq. 49).
S_γ	Operator corresponding to the projection of spin angular momentum about the axis γ.
SOS	Sum over states.
T	Temperature.
TAP	Tetraazoporphyrin.
TDDFT	Time-dependent density functional theory
TPP	Tetraphenylporphyrin.
TRIC	Transformed reference via an intermediate configuration.
TRICKS	TRIC Kohn–Sham
$\boldsymbol{U}^{(1)}$	Coefficients describing the first-order change of molecular orbital coefficients in the presence of a perturbation.
U coefficient	Element of the $\boldsymbol{U}^{(1)}$ matrix.
V	Verdet constant.
$(\boldsymbol{X+Y})_J$, $\boldsymbol{X_J}$	Transition density between the ground state and state J.
Z_N	Nuclear charge of nucleus N.
ZFS	Zero-field splitting.
α, β, γ	Cartesian direction, x, y, or z.
$\alpha_{\alpha\beta}(\omega)$	Component of the frequency-dependent polarizability tensor corresponding to directions α and β
ε	Absorption coefficient.
$\Delta\varepsilon$	Difference in absorption coefficients of left and right circularly polarized light.
ε_p	Energy of orbital p.
$\varepsilon_{\alpha\beta\gamma}$	Three-dimensional Levi-Civita symbol $\varepsilon_{\alpha\beta\gamma}$=1 if $\alpha\beta\gamma$ is a cyclic permutation of xyz, –1 if it is some other permutation and 0 otherwise.
θ	Induced ellipticity.
$[\theta]_M$	Molar ellipticity = θ/clB
μ_B	Bohr magneton.
μ_γ	Operator of total magnetic dipole moment corresponding to direction γ.
Φ	Complex optical rotation.
φ	Optical rotation
ϕ_p	Molecular orbital.
χ	A collection of physical constants.
χ_ν	Atomic orbital basis function.
ψ	Wave function.
ω	Frequency of incident light.
ω_J	Frequency of transition from ground state to state J.
(0),(1),(01), (10),(11)	Superscript indicating order of perturbation. Multiple indices indicate multiple perturbations.

Acknowledgments

We would like to thank Elizabeth Hernandez-Marin, Mykhaylo Krykunov, and Hristina Zhekova for helpful discussions. We are grateful to the National Sciences and Engineering Research Council

of Canada (NSERC) for funding and the government of Canada for a Canada research chair in theoretical inorganic chemistry.

References

1. Faraday, M. *Phil. Mag.* **1846**, 28, 294.
2. Faraday, M. *Phil. Trans. Roy. Soc.* **1846**, 1.
3. Verdet, E. M. *Ann. Chim. Phys.* **1854**, 41, 370.
4. Schérer, M. *Compt. Rend.* **1932**, 195, 950.
5. Schérer, M. *Compt. Rend.* **1933**, 196, 1724.
6. Verhaeghe, J.; van Eyck, M. *Compt. Rend.* **1939**, 208, 993.
7. Carroll, T. *Phys. Rev.* **1937**, 52, 822.
8. Schooley, D. A.; Bunnenberg, E.; Djerassi, C. *Proc. Natl. Acad. Sci. USA* **1965**, 3, 579.
9. Buckingham, A. D.; Stephens, P. J. *Annu. Rev. Phys. Chem.* **1966**, 17, 399.
10. Stephens, P. J. Theoretical studies of Magneto-optical phenomena, PhD Thesis, Oxford University, Oxford, **1964**.
11. Piepho, S. B.; Schatz, P. N. *"Group Theory in Spectroscopy With Applications to Magnetic Circular Dichroism"*; Wiley: New York, NY, **1983**.
12. Stephens, P. J. *Annu. Rev. Phys. Chem.* **1974**, 25, 201.
13. Thulstrup, E. W. *"Aspects of Linear and Magnetic Circular Dichroism of Planar Organic Molecules"*; Springer: Berlin, **1980**; No. 14 In Lecture Notes in Chemistry.
14. Michl, J. *Tetrahedron* **1984**, 40, 3845.
15. Kirk, M. L.; Peariso, K. *Curr. Opin. Chem. Biol.* **2003**, 7, 220.
16. Mack, J.; Stillman, M. J.; Kobayashi, N. *Coord. Chem. Rev.* **2007**, 251, 429.
17. Mason, W. R. *"A Practical Guide to Magnetic Circular Dichroism Spectroscopy"*; Wiley: Hoboken, NJ, **2007**.
18. Denning, R. G. *J. Chem. Phys.* **1966**, 45, 1307.
19. Bird, B. D.; Briat, B.; Day, P.; Rivol, J. C. *Symp. Faraday Soc.* **1969**, 3, 70.
20. Denning, R. G.; Spencer, J. A. *Symp. Faraday Soc.* **1969**, 3, 84.
21. Neese, F.; Solomon, E. I. *Inorg. Chem.* **1999**, 38, 1847.
22. Oganesyan, V. S.; George, S. J.; Cheesman, M. R.; Thomson, A. J. *J. Chem. Phys.* **1999**, 110, 762.
23. Oganesyan, V. S.; Thomson, A. J. *J. Chem. Phys.* **2000**, 113, 5003.
24. Cheeseman, M. R.; Greenwood, C.; Thomson, A. J. In: *"Advances in Inorganic Chemistry"*; vol. 36; Ed. Sykes, A. G.; Academic Press: San Diego, CA, **1991**, pp. 201–255.
25. Solomon, E. L.; Pavel, E. G.; Loeb, K. E.; Campochiaro, C. *Coord. Chem. Rev.* **1995**, 144, 369.
26. Solomon, E. I. *Inorg. Chem.* **2006**, 45, 8012.
27. Stephens, P. J. *Chem. Phys. Lett.* **1968**, 2, 241.
28. Stephens, P. J.; Mowery, R. L.; Schatz, P. N. *J. Chem. Phys.* **1971**, 55, 224.
29. Stephens, P. J. *J. Chem. Phys.* **1970**, 52, 3489.
30. Jensen, J. O.; Adams, G. F.; Chabalowski, C. *Chem. Phys. Lett.* **1990**, 172, 379.
31. Jensen, J. O.; Adams, G. F.; Chabalowski, C. *J. Chem. Phys.* **1991**, 94, 1332.
32. Honda, Y.; Hada, M.; Ehara, M.; Nakatsuji, H.; Downing, J.; Michl, J. *Chem. Phys. Lett.* **2002**, 355, 219.
33. Honda, Y.; Hada, M.; Ehara, M.; Nakatsuji, H.; Michl, J. *J. Chem. Phys.* **2005**, 123, 164113.

34. Sterzel, M.; Anrejak, M.; Pawlikowski, M. T.; Gawroński, J. *Chem. Phys.* **2004**, 300, 93.
35. Bolvin, H. *Inorg. Chem.* **2007**, 46, 417.
36. Ganyushin, D.; Neese, F. *J. Chem. Phys.* **2008**, 128, 114117.
37. Sundararajan, M.; Ganyushin, D.; Ye, S.; Neese, F. *Dalton Trans.* **2009**, 6021.
38. Shillady, D. D.; Castevens, C. M.; Trindle, C.; Sulik, J.; Klonowski, P. *Biophys. Chem.* **2003**, 105, 471.
39. Trindle, C.; Shillady, D. *"Electronic Structure Modelling. Connections Between Theory and Software"*; CRC Press: Boca Raton, FL, **2008**.
40. Coriani, S.; Jørgensen, P.; Rizzo, A.; Ruud, K.; Olsen, J. *Chem. Phys. Lett.* **1999**, 300, 61.
41. Kjærgaard, T.; Jansík, B.; Jørgensen, P.; Coriani, S.; Michl, J. *J. Phys. Chem. A* **2007**, 111, 11278.
42. Solheim, H.; Frediani, L.; Ruud, K.; Coriani, S. *Theor. Chem. Acc.* **2007**, 119, 231.
43. Kjærgaard, T.; Jørgensen, P.; Thorvaldsen, A. J.; Sańek, P.; Coriani, S. *J. Chem. Theory Comp.* **2009**, 5, 1997.
44. Solheim, H.; Ruud, K.; Coriani, S.; Norman, P. *J. Chem. Phys.* **2008**, 128, 094193.
45. Norman, P.; Ruud, K.; Helgakar, T. *J. Chem. Phys.* **2004**, 120, 5027.
46. Solheim, H.; Ruud, K.; Coriani, S.; Norman, P. *J. Phys. Chem. A* **2008**, 112, 9615.
47. Seth, M.; Ziegler, T. *J. Chem. Phys.* **2007**, 127, 134108.
48. Seth, M.; Krykunov, M.; Ziegler, T.; Autschbach, J.; Banerjee, A. *J. Chem. Phys.* **2008**, 128, 144105.
49. Seth, M.; Krykunov, M.; Ziegler, T.; Autschbach, J. *J. Chem. Phys.* **2008**, 128, 234102.
50. Seth, M.; Ziegler, T.; Autschbach, J. *J. Chem. Phys.* **2008**, 129, 104105.
51. Krykunov, M.; Seth, M.; Ziegler, T.; Autschbach, J. *J. Chem. Phys.* **2007**, 127, 244102.
52. Gross, E. K. U.; Dobson, J. F.; Petersilka, M. In: *"Topics in Current Chemistry"*; vol. 181; Ed Nalewajski, R. F.; Springer: Berlin, **1996**, pp. 81–172.
53. Marques, M. A. L.; Ullrich, C. A.; Nogueira, F.; Rubio, A.; Burke, K.; Gross, E. K. U., Eds: *"Time-dependent Density Functional Theory"*; Springer: Berlin, **2006**, Vol. 706 of Lecture Notes in Physics.
54. Casida, M. E. In: *"Recent Advances in Density Functional Theory"*; vol. 1; Ed. Chang, D. P.; World Scientific: Singapore, **1995**, pp. 155–192.
55. Stephens, P. J. *Adv. Chem. Phys.* **1976**, 35, 197.
56. te Velde, G.; Bickelhaupt, F. M.; Baerends, E. J.; Fonseca Guerra, C.; van Gisbergen, S. J. A.; Snijders, J. G.; Ziegler, T. *J. Comput. Chem.* **2001**, 22, 931.
57. Fonseca Guerra, C.; Snijders, J. G.; te Velde, G.; Baerends, E. J. *Theor. Chim. Acta* **1998**, 99, 391.
58. Baerends, E. J.; Autschbach, J.; Bashford, D.; Bérces, A.; Bickelhaupt, F. M.; Bo, C.; Boerrigter, P. M.; Cavallo, L.; Chong, D. P.; Deng, L.; Dickson, R. M.; Ellis, D. E.; Fan, L.; Fischer, T. H.; Fonseca Guerra, C.; Ghysels, A.; Giammona, A.; van Gisbergen, S. J. A.; Götz, A. W.; Groeneveld, J. A.; Gritsenko, O. V.; Grüning, M.; Harris, F. E.; van der Hoek, P.; Jacob, C. R.; Jacobsen, H.; Jensen, L.; van Kessel, G.; Koostra, F.; Krykunov, M.; van Lenthe, E.; McCormack, D. A.; Michalak, A.; Mitoraj, M.; Neugebauer, J.; Nicu, V. P.; Noodleman, L.; Osinga, V. P.; Patchkovskii, S.; Philipsen, P. H. T.; Post, D.; Pye, C. C.; Ravenek, W.; Rodriguez, J. I.;

Ros, P.; Schipper, P. R. T.; Schreckenbach, G.; Seth, M.; Snijders, J. G.; Sóla, M.; Swart, M.; Swerhone, D.; te Velde, G.; Vernooijs, P.; Versluis, L.; Visscher, L.; Visser, O.; Wang, F.; Wesolowski, T. A.; van Wezenbeek, E.; Wiesenekker, G.; Wolff, S. K.; Woo, T. K.; Yakovlev, A. L.; Ziegler, T. ADF2009.01, SCM, Theoretical Chemistry, Vrije Universiteit, Amsterdam, The Netherlands, 2009, http://www.scm.com.
59. *"Methods of Molecular Quantum Mechanics"*, 2nd edn., Ed. McWeeny, R.; Academic Press: San Diego, CA, **1992**.
60. Boča, R. *Coord. Chem. Rev.* **2004**, 248, 757.
61. Pederson, M. R.; Khanna, S. N. *Phys. Rev. B* **1999**, 60, 9566.
62. Aquino, F.; Rodriguez, J. H. *J. Chem. Phys.* **2005**, 123, 204902.
63. Neese, F. *J. Am. Chem. Soc.* **2006**, 128, 10213.
64. Neese, F. *J. Chem. Phys.* **2007**, 1237, 164112.
65. van Wüllen, C. *J. Phys. Chem. A* **2009**, 113, 11535.
66. London, F. *J. Phys. Radium* **1937**, 8, 397.
67. Hameka, H. F. *Mol. Phys.* **1958**, 1, 203.
68. Ditchfield, R. *Mol. Phys.* **1974**, 27, 789.
69. Wolinski, K.; Hilton, K. J. F.; Pulay, P. *J. Am. Chem. Soc.* **1990**, 112, 8251.
70. Ortiz, J. V. *J. Chem. Phys.* **1994**, 101, 6743.
71. Van Caillie, C.; Amos, R. D. *Chem. Phys. Lett.* **1999**, 308, 249.
72. Van Caillie, C.; Amos, R. D. *Chem. Phys. Lett.* **2000**, 317, 159.
73. Furche, F.; Ahlrichs, R. *J. Chem. Phys.* **2002**, 117, 7433.
74. Banerjee, A.; Autschbach, J.; Ziegler, T. *Int. J. Quantum Chem.* **2005**, 101, 572.
75. Krykunov, M.; Banerjee, A.; Ziegler, T.; Autschbach, J. *J. Chem. Phys.* **2005**, 122, 074105.
76. Blase, X.; Ordejón, P. *Phys. Rev. B* **2004**, 085111.
77. Jensen, L.; Autschbach, J.; Schatz, G. C. *J. Chem. Phys.* **2005**, 224115.
78. Krykunov, M.; Autschbach, J. *J. Chem. Phys.* **2006**, 125, 034102.
79. Krykunov, M.; Kundrat, M. D.; Autschbach, J. *J. Chem. Phys.* **2006**, 125, 194110.
80. Levy, M.; Perdew, J. P. In: *"Density Functional Methods in Physics"*; Eds. Dreizler, R. M.; da Providencia, J.; Plenum: New York, NY, **1985**, pp. 11–30.
81. Perdew, J. P.; Ruzinsky, A.; Constantin, L. A.; Sun, J.; Csonka, G. I. *J. Chem. Theory Comp.* **2009**, 5, 902.
82. Guan, J.; Casida, M. E.; Salahub, D. R. *J. Mol. Struct. (THEOCHEM)* **2000**, 527, 229.
83. Ulrich, C. A.; Kohn, W. *Phys. Rev. Lett.* **2001**, 87, 093001.
84. Khait, Y. G.; Hoffmann, M. R. *J. Chem. Phys.* **2004**, 120, 5005.
85. Gräfenstein, J.; Cremer, D. *Mol. Phys.* **2005**, 103, 279.
86. Gräfenstein, J.; Cremer, D. *Theor. Chem. Acc.* **2009**, 123, 171.
87. Yamananka, S.; Nakata, K.; Takada, T.; Kusakebe, K.; Ugaide, G. M.; Yamaguchi, K. *Catal. Lett.* **2006**, 35, 242.
88. Seth, M.; Ziegler, T. *J. Chem. Phys.* **2005**, 123, 144105.
89. Seth, M.; Ziegler, T. *J. Chem. Phys.* **2006**, 124, 144105.
90. Gunnarsson, O.; Lundqvist, B. I. *Phys. Rev. B* **1974**, 13, 4274.
91. Krylov, A. I. *Chem. Phys. Lett.* **2001**, 338, 375.
92. Krylov, A. I. *Chem. Phys. Lett.* **2001**, 350, 522.
93. Slipchenko, L. V.; Krylov, A. I. *J. Chem. Phys.* **2002**, 117, 4694.
94. Wang, F.; Ziegler, T. *J. Chem. Phys.* **2005**, 122, 074109.
95. Press, W. H.; Teukolsky, S. A.; Vetterling, W. T.; Flannery, B. P. *"Numerical Recipes in Fortran 90"*; Cambridge University Press: Cambridge, MA, **1996**.

96. Saad, Y. *"Iterative Methods for Sparse Linear Systems"*; Available online http://www-users.cs.umn.edu/~saad/books.html, **2000**.
97. *"Numerical Mathematics"*, 2nd edn., Eds. Quarteroni, A.; Sacco, R.; Saleri, F.; Springer: Berlin, **2007**, Vol. 37 of Texts in Applied Mathematics.
98. Seth, M.; Ziegler, T.; Autschbach, J. *J. Chem. Theory Comp.* **2007**, 3, 434.
99. Merer, A. J.; Mulliken, R. S. *Chem. Rev.* **1969**, 69, 639.
100. Brith-Lindner, M.; Allen, S. D. *Chem. Phys. Lett.* **1977**, 47, 32.
101. Petrongolo, C.; Buenker, R. J.; Peyerimhoff, S. D. *J. Chem. Phys.* **1982**, 76, 3655.
102. Baeck, K. K.; Martinez, T. J. *Chem. Phys. Lett.* **2003**, 375, 299.
103. Barbatti, M.; Paier, J.; Lischka, H. *J. Chem. Phys.* **2004**, 121, 11614.
104. Hazra, A.; Chang, H. H.; Nooijen, M. *J. Chem. Phys.* **2004**, 121, 2125.
105. Seth, M. unpublished results.
106. Gritsenko, O. V.; Schipper, P. R. T.; Baerends, E. J. *Chem. Phys. Lett.* **1999**, 302, 199.
107. Schipper, P. R. T.; Gritsenko, O. V.; van Gisbergen, S. J. A.; Baerends, E. J. *J. Chem. Phys.* **2000**, 112, 1344.
108. Schatz, P. N.; McCaffery, A. J.; Suëtaka, W.; Henning, G. N.; Ritchie, A. B.; Stephens, P. J. *J. Chem. Phys.* **1966**, 45, 722.
109. Ballhausen, C. J. *"Molecular Electronic Structure of Transition Metal Complexes"*; McGraw-Hill: New York, NY, **1979**.
110. Petit, R. H.; Briat, B.; Müller, A.; Diemann, E. *Mol. Phys.* **1974**, 27, 1373.
111. Collingwood, J. C.; Day, P.; Denning, R. G.; Robbins, D. J.; Disipio, L.; Oleari, L. *Chem. Phys. Lett.* **1972**, 13, 567.
112. Petit, R. H.; Briat, B.; Müller, A.; Diemann, E. *Chem. Phys. Lett.* **1973**, 27, 540.
113. Quested, P.; Robbins, D. J.; Day, P.; Denning, R. G. *Chem. Phys. Lett.* **1973**, 22, 158.
114. Bowman, A. H.; Evans, R. S.; Schreiner, A. F. *Chem. Phys. Lett.* **1974**, 29, 140.
115. Barton, T. J.; Grinter, R.; Thosmson, A. J. *Chem. Phys. Lett.* **1976**, 40, 399.
116. Grinter, R.; Zimmerman, R. L.; Dunn, T. M. *J. Mol. Spectrosc.* **1984**, 107, 12.
117. Cox, P. A.; Robbins, D. J.; Day, P. *Mol. Phys.* **1975**, 30, 405.
118. Upton, A. H. P.; Williamson, B. E. *J. Phys. Chem.* **1994**, 98, 71.
119. Naiman, C. S. *J. Chem. Phys.* **1961**, 35, 323.
120. Basu, G.; Bedford, R. L. *J. Chem. Phys.* **1962**, 37, 1933.
121. Naiman, C. S. *J. Chem. Phys.* **1963**, 39, 900.
122. Henning, G. H.; McCaffery, A. J.; Schatz, P. N.; Stephens, P. J. *J. Chem. Phys.* **1968**, 48, 5656.
123. McCaffery, A. J.; Schatz, P. N.; Lester, T. E. *J. Chem. Phys.* **1969**, 50, 379.
124. Piepho, S. B.; Lester, T. E.; McCaffery, A. J.; Dickinson, J. R.; Schatz, P. N. *Mol. Phys.* **1970**, 19, 781.
125. McCaffery, A. J.; Rowe, M. D.; Rice, D. A. *J. Chem. Soc. Dalton Trans.* **1973**, 1605.
126. Gale, R.; McCaffery, A. J. *J. Chem. Soc. Dalton Trans.* **1973**, 1344.
127. Seth, M.; Autschbach, J.; Ziegler, T. *J. Chem. Phys.* **2005**, 122, 094112.
128. Robbins, D. J.; Stillman, M. J.; Thomson, A. J. *J. Chem. Soc. Dalton* **1974**, 813.
129. Sutherland, J. C. In: *"Porphyrins"*; vol. 3; Ed. Dolphin, D.; Academic Press: New York, NY, **1978**, pp. 225–248.

130. Holmqvist, B. In: *"Porphyrins"*; vol. 3; Ed. Dolphin, D.; Academic Press: New York, NY, **1978**, pp. 249–270.
131. Stillman, M. J.; Nyokong, T. In: *"Phthalocyanines Properties and Applications"*; Eds. Leznoff, C. C.; Lever, A. B. P.; VCH Publishers Inc: New York, NY, **1989**, pp. 133–137.
132. Stillman, M. J. In: *"Phthalocyanines Properties and Applications"*; vol. 3; Eds. Leznoff, C. C.; Lever, A. B. P.; VCH Publishers Inc: New York, NY, **1993**,, pp. 227–296.
133. Mack, J.; Stillman, M. J. *Coord. Chem. Rev.* **2001**, 219–221, 993.
134. Goldbeck, R. A. *Acc. Chem. Res.* **1988**, 21, 95.
135. Peralta, G. A.; Seth, M.; Ziegler, T. *Inorg. Chem.* **2007**, 46, 9111.
136. Peralta, G. A.; Seth, M.; Zhekova, H.; Ziegler, T. *Inorg. Chem.* **2008**, 47, 4185.
137. Keegan, J. D.; Bunnenberg, E.; Djerassi, C. *Spectrochim. Acta, Part A* **1984**, 40, 287.
138. Choi, S.; Phillips, J. A.; Ware, W.Jr.; Wittschieben, C.; Medforth, C. J.; Smith, K. M. *Inorg. Chem.* **1994**, 33, 3873.
139. Gouterman, M. *J. Chem. Phys.* **1959**, 30, 1139.
140. Gouterman, M. *J. Mol. Spectrosc.* **1961**, 6, 138.
141. Gouterman, M.; Wagnière, G.; Snyder, L. C. *J. Mol. Spectrosc.* **1963**, 11, 108.
142. Baraldi, I.; Carnevali, A.; Ponterini, G.; Vanossi, D. *J. Mol. Struct. (THEOCHEM)* **1995**, 333, 121.
143. Rubio, M.; Roos, B. O.; Serrano-Andrés, L.; Merchán, M. *J. Chem. Phys.* **1999**, 110, 7202.
144. Sundholm, D. *Chem. Phys. Lett.* **2000**, 317, 392.
145. Nguyen, K. A.; Pachter, R. *J. Chem. Phys.* **2001**, 114, 10757.
146. Baerends, E. J.; Riccardi, G.; Rosa, A.; van Gisbergen, S. J. A. *Coord. Chem. Rev.* **2002**, 230, 5.
147. VanCott, T. C.; Rose, J. L.; Misener, G. C.; Williamson, B. E.; Schrimpf, A. E.; Boyle, M. E.; Schatz, P. N. *J. Phys. Chem.* **1989**, 93, 2999.
148. Miwa, H.; Ishii, K.; Kobayashi, N. *Chem. Eur. J.* **2004**, 10, 4422.
149. Nyokong, T.; Gasnya, Z.; Stillman, M. J. *Inorg. Chem.* **1987**, 26, 1087.
150. Ough, E.; Nyokong, T.; Creber, K. A. M.; Stillman, M. J. *Inorg. Chem.* **1988**, 27, 2724.
151. Rosa, A.; Ricciardi, G.; Baerends, E. J.; van Gisbergen, S. J. A. *J. Phys. Chem. A* **2001**, 105, 3311.
152. Ricciardi, G.; Rosa, A.; Baerends, E. J. *J. Phys. Chem. A* **2001**, 5242.
153. Nemykin, V. N.; Hadt, R. G.; Belosludov, R. V.; Mizuseki, H.; Kawazoe, Y. *J. Phys. Chem. A* **2007**, 111, 12901.
154. Williamson, B. E.; VanCott, T. C.; Boyle, M. E.; Misener, G. C.; Stillman, M. J.; Schatz, P. N. *J. Am. Chem. Soc.* **1992**, 114, 2412.
155. Dunford, C. L.; Williamson, B. E. *J. Phys. Chem. A* **1997**, 101, 2050.
156. Henriksson, A.; Roos, B.; Sundbom, M. *Theor. Chim. Acta* **1972**, 27, 303.
157. Heß, B. A.; Marian, C. M.; Peyerimhoff, S. D. In: *"Modern Electronic Structure Theory, Part 1"*; Ed. Yarkony, D. R.; World Scientific: Singapore, **1996**, Vol. 2 of Advanced Series in Physical Chemistry, pp. 152–278.
158. Solomon, E. I.; Szilagyi, R. K.; George, S. D.; Basumalik, L. *Chem. Rev.* **2004**, 104, 419.
159. Seth, M.; Ziegler, T. *Inorg. Chem.* **2009**, 48, 1793.
160. Zhekova, H.; Seth, M.; Ziegler, T. *J. Phys. Chem*. A. **2010**, 114, 6308.
161. Penfield, K. W.; Gewirth, A. A.; Solomon, E. I. *J. Am. Chem. Soc.* **1985**, 4519.

162. Sinnecker, S.; Neese, F. *J. Comput. Chem.* **2006**, 27, 1463.
163. Remenyi, C.; Reviakine, R.; Kaupp, M. *J. Phys. Chem. B* **2007**, 111, 8290.
164. Gewirth, A. A.; Solomon, E. I. *J. Am. Chem. Soc.* **1988**, 110, 3811.
165. LaCroix, L. B.; Shadle, S. E.; Wang, Y.; Averill, B. A.; Hedman, B.; Hodgson, K. O.; Solomon, E. I. *J. Am. Chem. Soc.* **1996**, 118, 7755.
166. LaCroix, L. B.; Randall, D. W.; Nersissian, A. M.; Hoitink, C. W. G.; Canters, G. W.; Valentine, J. S.; Solomon, E. I. *J. Am. Chem. Soc.* **1998**, 120, 9621.
167. Hernandez-Marin, E.; Seth, M.; Ziegler, T. *Inorg. Chem.* **2009**, 48, 2880.
168. Hernandez-Marin, E.; Seth, M.; Ziegler, T. *Inorg. Chem.* **2010**, 49, 1566.
169. Hille, R. *Chem. Rev.* **1996**, 96, 2757.
170. Kisker, C.; Schindelin, H.; Pachero, A.; Wehbi, W.; Garret, R.; Rajagopalan, K.; Enermark, J.; Rees, D. *Cell* **1997**, 91, 973.
171. Li, H.; Temple, C.; Rajagopalan, K.; Schindelin, H. *J. Am. Chem. Soc.* **2000**, 122, 7673.
172. Helton, M. E.; Pacheco, A.; McMaster, J.; Enemark, J. H.; Kirk, M. L. *J. Inorg. Biochem.* **2000**, 80, 227.
173. Benson, N.; Farrar, J. A.; McEwan, A. G.; Thomson, A. J. *FEBS* **1992**, 307, 169.
174. Finnegan, M. G.; Hilton, J.; Rajagopalan, K. V.; Johnson, M. K. *Inorg. Chem.* **1993**, 32, 2616.

THEORETICAL INVESTIGATION OF SOLVENT EFFECTS AND COMPLEX SYSTEMS

Toward the calculations of bioinorganic systems from *ab initio* molecular dynamics simulations and static quantum chemistry

MARC BRÜSSEL[a], STEFAN ZAHN[a], E. HEY-HAWKINS[b] and BARBARA KIRCHNER[a]

[a]Wilhelm-Ostwald Institut für Physikalische und Theoretische Chemie, Universität Leipzig, Linnéstr. 2 D-04103 Leipzig, Germany
[b]Institut für Anorganische Chemie, Universität Leipzig, Johannisallee. 29 D-04103 Leipzig, Germany

I. Introduction

In recent years the fast increasing computing power has allowed a much more reliable insight into bioinorganic systems by computational approaches. Mostly, static quantum chemistry

THEORETICAL AND COMPUTATIONAL INORGANIC CHEMISTRY
VOLUME 62 ISSN 0898-8838 / DOI: 10.1016/S0898-8838(10)62003-X

calculations in combination with the Kohn–Sham (KS) density functional theory (*1,2*) (DFT) are found in literature. This approach has proven as a powerful and feasible tool for systems containing transition metals (*3–14*). Nonetheless, it is commonly known that DFT, with computational cost much lower than that of conventional correlated methods, can suffer strongly from the self-interaction problem (*15,16*). However, there are several correction schemes, which deal with this problem (*17–22*). Furthermore, DFT fails for the right description of dispersion forces (*23–27*) which surely become more important with increasing system size. Within the last years several approaches were proposed and successfully employed to consider these weak interactions within DFT (*28–51*). Alternatively, more accurate methods were commonly applied in the context of such systems (*7,9,10,14,52*). Although many successful calculations were carried out with the above-mentioned approaches, i.e., the important electronic structure of bioinorganic systems is very well described by static quantum chemistry approaches, with increasing system size further problems occur: First, it becomes much more difficult to consider all important degrees of freedom (conformations) and second all possible reaction pathways are difficult to grasp with increasing system size.

One solution to such problems is provided by *ab initio* molecular dynamics (AIMD) simulations (*11,53–57*). These are still very expensive, but they include dynamical aspects and they are thus one of the most powerful tools to investigate bioinorganic systems if many conformations and unexpected events play a role. A necessary prerequisite will always be that inexpensive electronic structure methods such as DFT can be applied to the bioinorganic system of interest.

Due to the dynamical components many advantages emerge:

1. Different conformations will be easily obtained.
2. Mechanistic studies can be conducted via a dynamical route.
3. Solvent effects beyond continuum approximation can be studied.
4. Spontaneous events can be discovered.

Within our review we would like to highlight some selected research protocols for possible AIMD studies of bioinorganic systems, see Section II. In Section II.A we give a very brief introduction to the method as well as some references to useful reviews of the methodology. Next we introduce the research protocols (Section II.B) and after this we show the outcome of such protocols at two selected examples, see Section II.C. Additionally, we shortly introduce at selected examples solvation

in static quantum chemistry as well as the shared electron number (SEN) approach, a tool to analyze molecular interactions, see Section III.

II. AIMD Simulations

Since the work of Dirac (*58*) and the work of Ehrenfest (*59*) the theoretical foundations for AIMD were laid, because with Dirac a theory of time-dependent self-consistent field equations for the nuclear and electronic motion was provided and because with Ehrenfest the classical-quantum mechanical (time-dependent electronic structure) equations were given (*57*). However, it was the seminal article of Roberto Car and Michele Parrinello in 1985 (*53*) acting as a catalyst for AIMD simulations which is reflected in the exponential growth of its quotations (*57*). The aim of the article was clear: To derive a new method in order to "(i) compute ground-state electronic properties of large and/or disordered systems at the level of state-of-the-art electronic structure calculations and (ii) perform AIMD simulations where the only assumptions are the validity of classical mechanics to describe ionic motion and the Born - Oppenheimer (BO) approximation to separate nuclear and electronic coordinates" (*53*). For this purpose Car and Parrinello had to apply a beautiful trick which we describe below, because at this time just solving the electronic structure problem on the fly with the so-called Born–Oppenheimer molecular dynamics (BOMD) was infeasible due to the expensive repeated matrix diagonalization growing with the size of the problem. Car and Parrinello expressed this computational bottleneck in the description that "the theoretical prediction of equilibrium geometries, when these are not known from experiment, still remains an unsolved problem in most cases" (*53*).

As we assume that some of the interested readers are not familiar with the method we want to provide in the following Section II.A a very brief overview of the AIMD methodology mainly in the representation of Car–Parrinello molecular dynamics (CPMD) simulations but also with passing mention of the BOMD simulations (time-independent electronic structure). This will be followed by some recent methodological aspects of importance to bioinorganic systems carried out mainly in our group, see Section II.B. In this section we will also point to the literature covering other important aspects such as, for, example hybrid approaches. After this we will give in Section II.C two case studies of how AIMD can be successfully applied to bioinorganic systems.

A. Short Overview of Method

In the introduction we explained that AIMD adds a dynamical (time) component to the otherwise static consideration of bioinorganic systems. In order to achieve this, the theory is formulated in the framework of classical mechanics. As we want the bioinorganic system to carry out motions, we need equations that describe this motion. These equations of motion can be derived in the Hamilton or the Lagrange formalism by setting up, for example, the Lagrangian $\mathcal{L}$ being a function of the kinetic energy (K) and the potential energy (potential, U):

$$\mathcal{L}(\mathbf{R}^N,\mathbf{p}^N) = \underbrace{K(\mathbf{P}^N)}_{\text{kin. energy}} - \underbrace{U(\mathbf{R}^N)}_{\text{potential}} = \sum_{I=1}^{N} \frac{1}{2} M_I \dot{\mathbf{R}}_I^2 - U(\mathbf{R}_I) \qquad (1)$$

with $\mathbf{R}_I$ being the position of the nucleus I with the mass M_I and $\mathbf{p}_\mathrm{I}$ being the momentum related to the velocity $\dot{\mathbf{R}}_I = \mathbf{p}_I/M_I$. The equations of motion can be obtained from the following relation:

$$\frac{d}{dt}\frac{\partial \mathcal{L}}{\partial \dot{\mathbf{R}}_I} = \frac{\partial \mathcal{L}}{\partial \mathbf{R}_I} \qquad (2)$$

This means that all moving nuclei (atoms) are treated as classical particles which is a serious approximation, but which was found to work very well (*60,61*). Applying the Euler–Lagrange equation (Eq. 2) to the Lagrangian $\mathcal{L}$ (Eq. 1) leads to the same equations as the well-known Newton's second law (Eq. 3). Or in other words, in classical mechanics the derivative of the Lagrangian is taken with respect to the nuclear positions.

$$\sum_{I=1}^{N} M_I \ddot{\mathbf{R}}_I = \sum_{I=1}^{N} \frac{\partial \mathcal{L}}{\partial \mathbf{R}_I} = -\sum_{I=1}^{N} \frac{\partial \mathrm{U}}{\partial \mathbf{R}_I} = \sum_{I=1}^{N} \mathbf{F}_I \,. \qquad (3)$$

Using Eq. (3), we obtain the acceleration ($\ddot{\mathbf{R}}_I$) of the particle with the mass M_I, from the force $\mathbf{F}_I$ acting on this particle.

Practically, we carry out the following steps with the aid of computers:

1. Guess start positions $\mathbf{R}_I$(t=0) and start velocities $\dot{\mathbf{R}}_I(t=0)$ of each atom.
2. Calculate new positions and velocities from the force $\mathbf{F}_I$ and thereby move atoms.

The important question concerning all methods is, where does the force come from?

Traditional molecular dynamics simulations uses pre-defined potentials usually in the pairwise additivity approximation (U^{MD} (R_{IJ})). This means that a pair potential, i.e., a potential between each set of two atoms I and J, is parametrized. It also means that the adiabatic and especially the BO approximations have to be valid, i.e., a separation of nuclear and electronic variables is possible and the coupling terms (non-diagonal and diagonal) can be neglected (*62,63*). Therefore, points on the ground state BO potential are calculated and in a second step these are fitted to an analytical expression. Thus, the problem of the high dimensionality of the global potential energy surface (PES) is reduced drastically. From the potentials the forces are obtained by taking the derivatives:

$$\mathbf{F}_I = -\frac{\partial U(\mathbf{R}_I)}{\partial \mathbf{R}_I} = -\sum_{i \neq j}^{N} \frac{\partial U^{\mathrm{MD}}(|\mathbf{R}_I - \mathbf{R}_J|)}{\partial \mathbf{R}_I} \tag{4}$$

On the contrary in AIMD we just obtain the force from an electronic structure calculation on the fly. We will come back to this point, but first we want to see how to propagate the atoms.

The time evolution of the system can be followed for as long as desired, so far as computational resources permit. Usually this is done by implementing integration algorithms of the following form (velocity Verlet) into a MD program:

$$\mathbf{R}_I(t + \Delta t) = \mathbf{R}_I(t) + \dot{\mathbf{R}}_I(t)\Delta t + \frac{\mathbf{F}_I(t)}{2M_I}\Delta t^2 + \mathcal{O}(\Delta t^3) \tag{5}$$

$$\dot{\mathbf{R}}_I(t + \Delta t) = \dot{\mathbf{R}}_I(t) + \frac{\mathbf{F}_I(t + \Delta t) + \mathbf{F}_I(t)}{2M_I}\Delta t + \mathcal{O}(\Delta t^3) \tag{6}$$

Is is immediately apparent how the new positions $\mathbf{R}_I(t + \Delta t)$ can be calculated from the previous positions $\mathbf{R}_I(t)$, the previous velocities $\dot{\mathbf{R}}_I(t)$, and the "old" forces $\mathbf{F}_I(t)$. Similarly the new velocities can be obtained from knowledge of previous velocities and forces $\mathbf{F}_I(t)$ and from the new forces which are available as soon as the new positions (which are those one time step further) from Eq. (5) are calculated. We want to give only a qualitative derivation of Eqs. (5) and (6) for more interested readers we refer to the original literature (*60*). We introduce a small time step Δt and carry out a numerical step-by-step integration of the

equations of motion. Carrying out Taylor expansion series leads to Eqs. (7–8). $\mathbf{B}_I$(t) is the cubic Taylor coefficient. Replacing the acceleration $\ddot{\mathbf{R}}_I(t)$ in Eq. (7) with the force $\mathbf{F}_I$(t) we obtain Eq. (5).

$$\mathbf{R}_I(t+\Delta t) = \mathbf{R}_I(t) + \dot{\mathbf{R}}_I(t)\Delta t + \frac{1}{2}\ddot{\mathbf{R}}_I(t)\Delta t^2 + \frac{1}{6}\mathbf{B}_I(t)\Delta t^3 + \mathcal{O}(\Delta t^4) \tag{7}$$

$$\dot{\mathbf{R}}_I(t+\Delta t) = \dot{\mathbf{R}}_I(t) + \ddot{\mathbf{R}}_I(t)\Delta t + \frac{1}{2}\mathbf{B}_I(t)\Delta t^2 + \mathcal{O}(\Delta t^3) \tag{8}$$

We now want to estimate $\mathbf{B}_I$(t) by known quantities. To achieve this we carry out another Taylor expansion and rearrange the resulting equation to obtain an expression for $\mathbf{B}_I(t)$ (Eq. 9).

$$\ddot{\mathbf{R}}_I(t+\Delta t) = \ddot{\mathbf{R}}_I(t) + \mathbf{B}_I(t)\Delta t + \mathcal{O}(\Delta t^2)$$

$$\frac{1}{2}\mathbf{B}_I(t)\Delta t^2 = \frac{\Delta t}{2}(\ddot{\mathbf{R}}_I(t+\Delta t) - \mathbf{R}_I(t)) + \mathcal{O}(\Delta t^3) \tag{9}$$

Now we are able to substitute $\mathbf{B}_I$(t) in Eq. 8 from Eq. 9. After replacing the acceleration $\ddot{\mathbf{R}}_I(t)$ with the force $\mathbf{F}_I(t)$ we finally obtain Eq. 6. There are several others algorithms to integrate the equations of motion (e.g., leapfrog, Verlet). The consequences of different equation of motion integration schemes with regard to AIMD are discussed in the excellent review of Remler and Madden (*54*).

Within this integrator framework it is possible to carry out traditional molecular dynamics simulations. Next to the structure of the bioinorganic system and the surrounding solvent, many thermodynamic and transport properties can be calculated from a trajectory, see Ref (*64*) for explanations. Another methodology that is often applied if, for example, the particle is a molecule and for some reasons the intra-molecular potential is unknown or infeasible to calculate, are constraints that fix the molecule in its equilibrium position. Further application of constraint technology to which we will come back below is the enforcement of a reaction by changing, for example, the distance of two molecules along the course of the simulations. Of course this enforced-reaction approach needs a description of the PES that incorporates this particular reaction, e.g., AIMD. Turning back to the technique of constraints one needs to add in principle only constraint forces $\mathbf{G}_I$ to the forces $\mathbf{F}_I$ with which the nuclei (or atoms or molecules) are propagated (moved).

$$M_I\ddot{\mathbf{R}}_I = \mathbf{F}_I + \mathbf{G}_I \tag{10}$$

In practice the equation of motion is solved first without considering the constraint force and in the next step the constraint forces are obtained by correcting the positions such that the molecule conserves its minimum structure, i.e., such that the constraints are fulfilled. For small molecules direct inversion is possible, for large molecules iterative procedures are applied (*60*). This means that each constraint is corrected after the other until a certain convergence is reached. This algorithm is called Shake (*65*). Another important aspect of simulations concerns periodic boundary conditions. A virtual replication of the central box at each of its planes is carried out in order to avoid surface effects. A detailed description can be found in the excellent textbooks of Allen and Tildesley (*60*) and Frenkel and Smit (*61*).

Turning back to how the forces can be obtained, the first thought that comes to one's mind is that instead of using a pre-parametrized potential the electronic structure can be calculated on the fly according to the BO approximation as mentioned in the introduction to Section II. In such calculations the electronic structure part consists in solving a time-independent quantum problem.

$$U(\mathbf{R}_I) = \min_{\{\phi_i\}} E^{\mathrm{el}}[\{\phi_i\}; \mathbf{R}_I] \tag{11}$$

This Eq. (11) solves the Schrödinger equation with an optimized set of orbitals $\{\phi_i\}$ at current nuclear position $\mathbf{R}_I$ in order to provide the forces for calculating the next step. Schematically, this reads:

1. Carry out a molecular dynamics step.
2. Stop.
3. Solve the electronic structure problem at the current positions.
4. Use the obtained force in order to proceed with 1.

Many available codes use this kind of approach in order to carry out AIMD simulations. In fact some codes are not even implemented with the Car – Parrinello methods (e.g., cp2k). About the advantages and disadvantages of BOMD over CPMD the interested reader is referred to the seminal book of Marx and Hutter (*57*).

Now we want to introduce briefly the basic concepts of the CPMD approach. The basic idea of CPMD simulations can be expressed by (*57*):

A two-component quantum-classical problem is mapped onto a two-component purely classical problem with employing the constraints that quantum mechanics has to be fulfilled at all times.

This will lead to two separate energy scales at the expense of losing the physical time information of the quantum subsystem dynamics. The according Lagrangian (Eq. 1) reads:

$$\mathcal{L} = \underbrace{\sum_{I=1}^{N} \frac{1}{2} M_I \dot{\mathbf{R}}_I^2 + \sum_i \mu \langle \dot{\phi}_i | \dot{\phi}_i \rangle}_{\text{kin. energy}} - \underbrace{\varepsilon^{el}[\{\phi_i\}; \mathbf{R}_I]}_{\text{potential}} \tag{12}$$

The second term of Eq. (*12*) describes the fictitious kinetic energy of the electrons. The term contains an arbitrary parameter (fictitious mass parameter) μ with appropriate units of energy times a squared time.

An excellent discussion of how this parameter has to be chosen can also be found in Ref. (*57*). A critical point of view about the fictitious mass parameter and about arguments used for the justification of the CPMD approach is given in Ref. (*66*). The dot in this Lagrangian indicates the time derivative, thus it is apparent that the coefficients of the wavefunctions can be propagated in the same way like a nuclear position variable. The potential is now a functional of the electronic energy E^{el} plus the constraints which are enforced in order to satisfy quantum mechanics, i.e., the wavefunction which is altered, because it has now the meaning of a dynamical variable, has to stay orthonormal, see second term of Eq. (13): The additional constraint is introduced by the standard Lagrange multipliers approach, where the Λ_{ij} are the Lagrange multipliers and δ_{ij} is the well-known Kronecker delta (Eq. 13).

$$\varepsilon^{\text{el}}[\{\phi_i\}; \mathbf{R}_I] = E^{\text{el}} + \sum_{ij} \Lambda_{ij} (\langle \phi_i | \phi_j \rangle - \delta_{ij}) \tag{13}$$

As the electronic energy is a function of the nuclear position as well as function of the wavefunctions ϕ_i, its derivative is once taken not only with respect to the nuclear position but also with respect to the wavefunction. The Euler – Lagrange equations then read:

$$\frac{d}{dt} \frac{\partial \mathcal{L}}{\partial \dot{\mathbf{R}}_I} = \frac{\partial \mathcal{L}}{\partial \mathbf{R}_I} \quad \text{and} \quad \frac{d}{dt} \frac{\partial \mathcal{L}}{\partial \langle \dot{\phi}_i |} = \frac{\partial \mathcal{L}}{\partial \langle \phi_i |} \tag{14}$$

It leads us again to the equations of motion, in this case to the Car–Parrinello equations of motion, given below. The reader may wonder why only the deviation Eq. (*12*) with respect to the complex conjugated function is taken. The equation, which is obtained by variation of $|\phi_j\rangle$ is the adjoint to

Eq. (16). It contains the same information as Eq. (16), because Λ_{ij} is self-adjoint.

$$M_I \ddot{\mathbf{R}}_I = -\frac{\partial E^{\mathrm{el}}}{\partial \mathbf{R}_I} + \sum_{ij} \Lambda_{ij} \frac{\partial}{\partial \mathbf{R}_I} \langle \phi_i | \phi_j \rangle \tag{15}$$

$$\mu |\ddot{\phi}_i\rangle = -\frac{\delta E^{\mathrm{el}}}{\delta \langle \phi_i |} + \sum_j \Lambda_{ij} |\phi_j\rangle \tag{16}$$

The forces on the nuclei are given by

$$\mathbf{F}(\mathbf{R}_I) = -\frac{\partial E^{\mathrm{el}}}{\partial \mathbf{R}_I} + \sum_{ij} \Lambda_{ij} \frac{\partial}{\partial \mathbf{R}_I} \langle \phi_i | \phi_j \rangle \tag{17}$$

and the forces on the electrons are given by

$$\mathbf{f}_i = \mathbf{f}(\phi_i) = -\frac{\delta E^{\mathrm{el}}}{\delta \langle \phi_i |} + \sum_j \Lambda_{ij} |\phi_{ij}\rangle \tag{18}$$

This means for the implementation:

1. Optimize wavefunction once for the given start position.
2. Calculate the forces on electrons and nuclei.
3. Calculate new positions for nuclei and new coefficients for wavefunction.
4. Use constraint algorithm to enforce orthogonality constraint.

The according algorithm is given by the scheme below. The resemblance to Eq. (5) is immediately apparent. Because we follow the line of Ref. (*57*). these equations are valid for the special case of KS-DFT in the plane wave basis set representation as electronic structure method. This leads to the simplification that the second term in the first line of Eq. (15) vanishes, because the orthonormality constraint depends now only on the orbitals but not on the nuclear positions. Furthermore, the wavefunction (now KS orbitals in the plane wave representation) is replaced by the expansion coefficients $\mathbf{c}_i$ of the plane waves. The possibility of different integrators for equations of motion was alluded above, the following scheme for the expansion coefficients is also based on the velocity Verlet algorithm as can be recognized. The constraint is enforced by the Rattle algorithm; therefore, the new "positions" of the coefficients *without applying constraints* $\tilde{\mathbf{c}}_i(t + \Delta t)$ read:

$$\tilde{\mathbf{c}}_i(t + \Delta t) = \mathbf{c}_i(t) + \dot{\mathbf{c}}_i(t)\Delta t + \frac{\mathbf{f}_i(t)}{2\mu} \Delta t^2 \tag{19}$$

Next we correct the constraints which are expressed in the second term of the following Eq. (20):

$$\mathbf{c}_i(t+\Delta t) = \tilde{\mathbf{c}}_i(t+\Delta t) + \sum_j \frac{\Lambda^{\mathbf{c}}_{ij}}{2\mu}\Delta t^2\, \mathbf{c}_j(t) \tag{20}$$

$\Lambda^{\mathbf{c}}_{ij}$ are the constraints dependent now only on the electronic part. For their determination we again refer to the Ref. (*57*). Of course the nuclei are also propagated, we obtain their positions according to the first line of Eq. (5). From these new "positions," i.e., new nuclear positions and new coefficients, we can get the forces on the nuclei $\mathbf{F}_i(t+\Delta t)$ and the ones on the coefficients $\mathbf{f}_i(t+\Delta t)$. Again we start with deriving the "velocities" of the coefficients as:

$$\dot{\mathbf{c}}'_i(t+\Delta t) = \dot{\mathbf{c}}_i(t) + \frac{\mathbf{f}_i(t)}{2\mu}\Delta t + \frac{\mathbf{f}_i(t+\Delta t)}{2\mu}\Delta t \tag{21}$$

and correct them afterward by determining the constraints:

$$\dot{\mathbf{c}}_i(t+\Delta t) = \dot{\mathbf{c}}'_i(t+\Delta t) + \sum_j \frac{\Lambda^{\dot{\mathbf{c}}}_{ij}}{2\mu}\Delta t\, \mathbf{c}_j(t+\Delta t) \tag{22}$$

This is subsumed in a few words the basic ingredients of AIMD and especially the ones of CPMD. The difference to classical simulations can now be understood in terms of the forces that are available as electronic structure calculations of the global PES and not as a pre-parametrized dimensionally reduced pair potential for which the transferability is questionable. According to the well-known "no free lunch" theorem the computational bottleneck interferes elsewhere, namely the length of trajectories from AIMD are so short and the system size is still so small that often important properties such as, for example, transport properties are out of the range of these kind of simulations. However, keeping in mind Dirac's famous 1929 statement: "The underlying physical laws necessary for the mathematical theory of a large part of physics and the whole of chemistry are thus completely known, and the difficulty is only that the exact application of these laws leads to equations much too complicated to handle" and the fact that the developments of computers contributed largely in order to tackle "these complicated equations" and adding the enthusiastic statement made in the 1970s by Enrico Clementi: "We can calculate everything," we see that CPMD and AIMD in general are a large step toward a real theoretical prediction. Therefore, this kind of techniques or methods are one step further into the direction of the so-called "virtual laboratory" (*57*).

B. Interesting Methodological Aspects

So far we learned from Section II.A what AIMD constitutes. In the following we will discuss the question: What can be done with the aid of AIMD? Some of the many answers to this simple question are as follows:

1. Analyze wavefunction.
2. Determine possible mechanisms.
   (a) Insert a reactive species into the simulation box.
   (b) Start simulations from high-energy state or from the transition state.
   (c) Increase the constraint stepwise in order to determine possible mechanisms.
   (d) Do a free energy calculation.
3. Study solvent effects.
4. Explicitly treat relativistic effects.

B.1. Analyze wavefunction

The most striking feature of AIMD and the novelty over traditional molecular dynamics simulations is the fact that the electronic structure is available all the time. Therefore, the analysis of the wavefunction in the course of the simulation or along the trajectory is one of the major subjects that can contribute to the understanding on the molecular and on the electronic level. The importance of analyzing the wavefunction in bioinorganic systems has been shown in many applications, see also Section III.B. In order to analyze the wavefunction in a chemically more intuitive way, it is useful to localize it. In the framework of AIMD this is, for example, done by calculating the maximally localized Wannier functions (MLWF) and the corresponding expectation values of the position operator for a MLWF basis the so-called maximally localized Wannier centers (MLWCs), see Fig. 1 (*67–72*). With the help of the MLWC it is possible to compute molecular dipole moments (*72–82*). Furthermore, it is possible with the MLWC to obtain molecular properties, e.g., IR spectra (*75,76,82–85*).

An analysis of the Wannier functions in CPMD simulations of one dimethyl sulfoxide (DMSO) molecule dissolved in water was carried out by us in 2004 in order to gain more insight into the unusual properties of the DMSO–water mixture (*72*). In this special case, we have utilized MLWCs to calculate molecular dipole moments of the DMSO molecule in gas phase and aqueous solution. Comparing those two a large increase of the local dipole

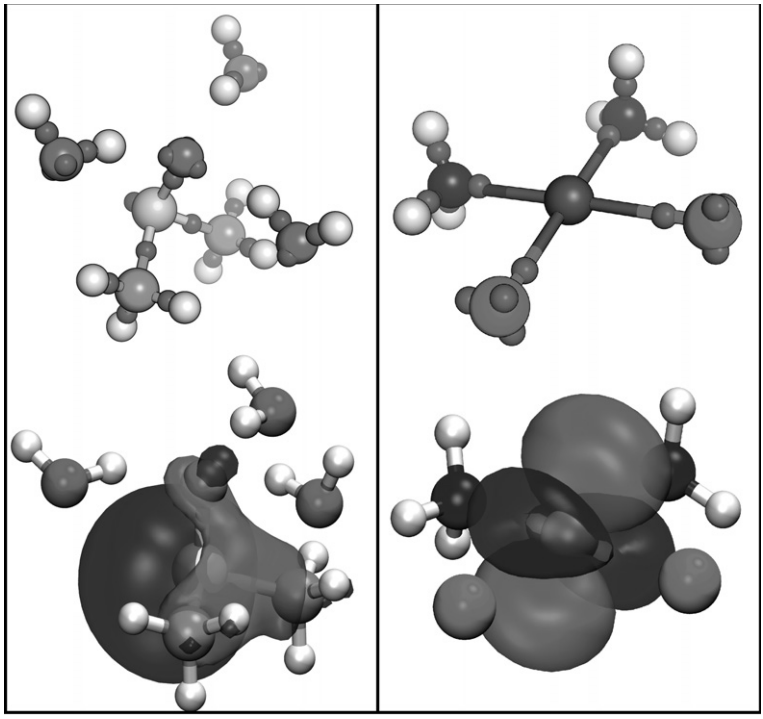

FIG. 1. We show on the left-hand side the MLWCs (above) in pink and the HOMO-Wannier orbital (below) together with a ball-and-stick model of a 1-DMSO-3-H_2O water cluster. On the right the same is depicted for the $[PdCl_2(NH_3)]_2$ complex.

moment from 3.97 D (isolated molecule) (4.08 D for isolated molecule employing temperature) to 7.39 D (DMSO in 63 solved water molecules) was found, see Table I. This large solvent effect could then be explained on the basis of strong hydrogen bonding at the DMSO oxygen atom but also weak interactions at the methyl groups. The dipole moment decomposition into local contributions

TABLE I

PARTIAL DIPOLE MOMENTS AS OBTAINED FROM MLWCS. μ^{gas}: DIPOLE MOMENT OF THE GAS PHASE DMSO μ^{gas}; μ^{aq}: DIPOLE MOMENT OF DMSO IN AQUEOUS SOLUTION μ^{aq}. ALL VALUES IN DEBYE

	Tot	S–O	Me	S
μ^{gas}	4.08	7.91	1.87	5.21
μ^{aq}	7.39	9.74	1.22	5.11

from the S–O bond and the methyl groups gave insight into the electrostatic response of DMSO in aqueous solution.

One center has been attributed to the central sulfur atom because it is impossible to assign it either to the S–O bond or the methyl groups, as can be seen in Table I and Fig. 1. As expected, the main contribution to the total dipole moment of DMSO stems from the S–O bond dipole, see third row of Table I. The methyl groups contribute only in a small way. Whereas the S–O bond dipole increases, the methyl group dipole moments decrease upon solvation which is in accordance with the observed red-shift and blue-shift from many IR experiments. The increase of the DMSO dipole moment upon solvation is about 81%. This increase can only partly be explained by the 23% increase of the S–O bond dipole. A much larger share is due to the reduction of about 35% of the methyl group.

We want to introduce briefly another concept to localize electrons. The so-called ELF (*86,87*) (electron localization functions) is sometimes used in CPMD simulations to visualize electron pairs (*88–91*). The ELF is neither an observable nor an orbital. It is just a value without any dimension depending only on the electron density. Because it is more understandable we explain the ELF approach with the original definition from Becke and Edgecombe (*92*) which was given for Hartree – Fock orbitals. The ELF approach was extended to DFT by Savin *et al.* (*93*). However, the expressions obtained are formally identical. The same-spin pair probability density (SSPP) is the probability to find a second like-spin electron near the reference electron (*92*), i.e., we can indicate high probabilities of electron (lone) pairs with this concept. The SSPP of the real system will be considered in relation to the same probability density of the uniform electron gas. A high value of the ELF indicates a low probability of finding a spin-like electron near the reference electron compared to the SSPP of the uniform electron gas. An important fact is that localization in this approach means only high values of the ELF, but not a physical localization of electrons. Nevertheless, there are some critical points considering the theory of the ELF: The analytical expression for the ELF was not derived from physical considerations. Producing “dealable” values was the main criterion for the choice of the analytical expression. Also the comparison with uniform electron gas is arbitrary.

B.2. Determine possible mechanisms

One very appealing advantage of AIMD consists in new routes that can be applied to investigate reaction mechanisms. Since

bioinorganic systems usually bear a complicated electronic structure, this possibility was not feasible for those systems before AIMD. Once again, the AIMD simulations technique is especially suitable for the purpose of determining reaction mechanisms in such systems as it is able to adjust spontaneously to different molecular binding scenarios while at the same time it also describes the time evolution of the system by molecular dynamics simulations. Four protocols are described in more detail in the following: (i) inserting a reactive species into a chemical medium in order to observe a spontaneous event, (ii) starting at a local maximum or mechanistically well-defined high-energy nonstationary structure in order to provide a starting point for relaxations into a valley or starting at a structure below a barrier, which is so small ($\Delta G^{\ddagger}<kT$) that the reaction actually does occur, (iii) employing growing/changing constraints in the course of the simulation, or (iv) using constraints along a possibly good reaction coordinate and forcing the reaction to occur in order to carry out a thermodynamic integration. The latter technique allows to calculate a free energy ΔG and $\Delta G^{\ddagger}$ (size of barrier) if the transition state is located by integrating the constraint force, i.e., thermodynamic integration (*61*). At each constraint value the sampling introduces a considerable arbitrariness. Therefore, large sampling times may be anticipated.

i) Insert reactive species into your simulation box

The simulations are always carried out in the same fashion. The reactive species (e.g., an ion or a radical) is added, into a box of pre-equilibrated solvent molecules. Sometimes solvent molecules have to be removed in order to provide free space for the reactive species. Afterward the so prepared system is studied with the help of AIMD simulations. This approach was successfully used to gain insight into the transport of protons and accordingly hydroxyl anions in water (*94–99*). An overview about this topic is given in Refs. (*100,101*). We present here a work, which concerns itself with a diffusion process, similar to that of a proton in water. CPMD simulations were performed with a box containing 31 molecules $AlCl_3$ as solvent and additional an 1,3-methylethyl-imidazolium chloride ion pair (*90*). Two different starting conditions led to two trajectories from which we collected structural data. For both simulations, we found large anions within the equilibrium phase: In both trajectories at longer simulation time, the anion size converged to four monomer units, i.e., to the $Al_4Cl_{13}^-$ species. The cluster size fluctuations indicated that a kind of Grotthus diffusion must play a role in such an acidic mixture. A possible mechanism of such a reaction changing the

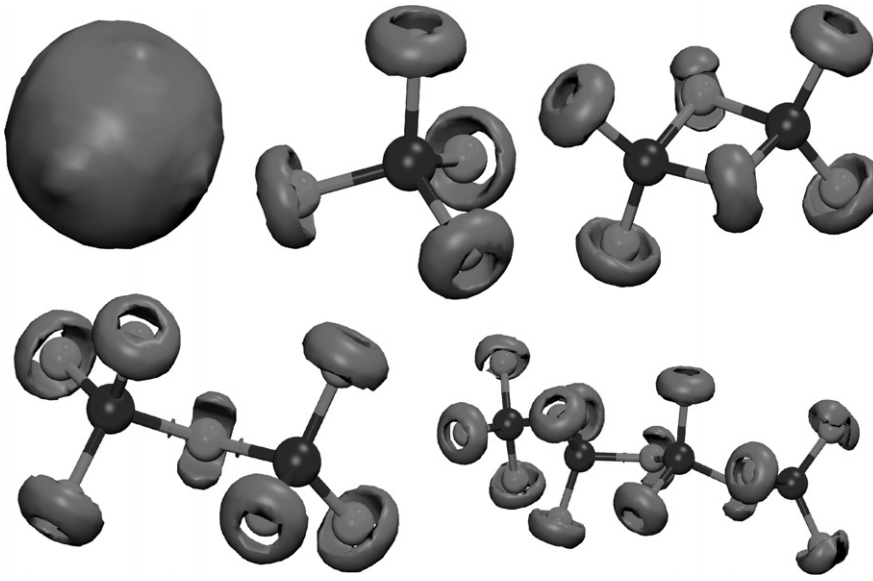

FIG. 2. We show the electron localization function (ELF) of (from left to right and from above to below) the Cl^-, the $AlCl_4^-$, the Al_2Cl_6, the $Al_2Cl_7^-$, and the $Al_4Cl_{13}^-$ species. The purple colored space indicates high values of ELF or electron pairs. Therefore, electron deficiency can be recognized from the half open spheres.

anionic species was observed to be given by many steps of chlorine rattling, bond breaking, and bond forming. It was possible to determine with the aid of the (*86,87*) ELF a probable rationale for the formation of larger anions: Large anionic species are formed simply to account for the "lack of electrons" present in the acidic melt, see Fig. 2 (*90*). The electron deficiency per unit is smaller in larger clusters, it is so to speak solvated and thus leveled out.

ii) Increase the constraint stepwise in order to determine possible mechanisms or iii) start simulations from a high-energy state

This particular protocol is described in detail in the case study Section II.C. Therefore, we shall mention here only briefly that it is possible to change the constraint in each step along one trajectory in order to explore possible reaction mechanisms. If the simulations are started close to a transition state to run down a hill, we should in principle also be able to start from many slightly different situations in order to obtain a statistically averaged thus unbiased situation and thus an average passage time for the down-hill process. However, following only a single

trajectory down-hill yields a time for this process; its order of magnitude might be considered as a first hint and a possible reaction mechanism.

iv) Do a free energy calculation

The technique of thermodynamic integration is excellently described in the book of Smit and Frenkel (*61*) and in the book of Pohorille and Chipot (*102*). In order to sample the energy landscape of the reaction properly one stepwise increasing the constraint simulation is not sufficient enough. Thermodynamic integration and other techniques need the generation of several trajectories at fixed constraint along the reaction coordinate in order to allow for the right statistical description. Very sophisticated alternatives to thermodynamic integration like potential energy leveling (*103*), transition path sampling (*104–107*), metadynamics (*108–110*), applying the Jarzynski equality (*111*), the Crook fluctuation relation (*112*), or the Evans–Searles fluctuation relation (*113*) were alternatively developed.

For one example we applied thermodynamic integration in order to test the influence of the basis set on the reaction of a hypothetical proton transfer in a water dimer (*114*). Thus, we carried out molecular dynamics simulations enforcing the self-dissociation reaction of the water dimer. Not surprisingly, we found strongly varying results of the calculated forces for a chosen cutoff along the reaction coordinates. The basis set superposition errors of the dimer interaction energy were analyzed along the free-energy surface, i.e., along the trajectories. Based on this analysis a qualitative and quantitative estimate depending on the particular point of the free-energy surface could be provided. Namely, at the intermolecular O···H distance close to the equilibrium geometry the errors were smaller than at shorter O···H distances. However, the distribution at the equilibrium distance was more unsymmetrical than the distribution at short distances. It was wider, and the standard deviation was larger than at shorter distances at which the basis set superposition error was larger.

B.3. Study solvent effects

Nearly all chemical reactions take place in solution. Further it is well-known that the solvent can have strong influence on reactions. Due to the influence of the solvent a question arises: How many molecules are needed to reproduce the effects of the solvent on the reaction? (*115*) Different molecular dynamics approaches for solvent effects have been reported in literature. There are a

great number of AIMD simulations dealing with that question (*116–121*). Further classical molecular dynamics were performed to understand the solvation from a statistical viewpoint (*122*). There are also efforts, in order to combine data from classical molecular dynamics approaches with the advantages of DFT methods (*123*). Path-integral molecular dynamics were used to describe the quantum effects of the nuclei, which can be important in the case of a hydrogen transfer (*124,125*). Worth mentioning are also some other approaches to describe large systems, i.e., central molecule(s) and surrounding solvent shell, e.g., the hybrid quantum-mechanical/molecular mechanical (QM/MM) method (*126*). Here is an important region treated explicitly with the QM method, while the outer solvation shell is described with MM models. There are several examples in literature where this combined approach is used to investigate complex systems and much work with regard to AIMD was carried out in the R öthlisberger group and in the Carloni group (*127–143*). We do not continue to deal with it, because there are already some very good reviews about this topic (*12,144–147*).

For the description of a solution of alanine in water two models were compared and combined with one another (*79*), namely the continuum model approach and the cluster ansatz approach (*148,149*). In the cluster approach snapshots along a trajectory are harvested and subsequent quantum chemical analysis is carried out. In order to learn more about the structure and the effects of the solvent shell, the molecular dipole moments were computed. To harvest a trajectory and for comparison AIMD (here CPMD) simulations were carried out (*79*). The calculations contained one alanine molecule dissolved in 60 water molecules. The average dipole moments for alanine and water were derived by means of maximally localized Wannier functions (MLWF) (*67–72*). For the water molecules different solvent shells were selected according to the three radial pair distributions between water and the functional groups. An overview about the findings is given in Tables II and III.

TABLE II

SUMMARY OF THE AVERAGE DIPOLE MOMENTS μ. $ISO_{NEUTRAL}$: GAS PHASE; ISO_{ION}: ZWITTERION IN THE GAS PHASE; SOLV: SOLVATED ALANINE (AVERAGE FROM THE TRAJECTORY)

Molecule	Alanine			Water
	($iso_{neutral}$)	(iso_{ion})	(solv)	
μ [D]	5.7	9.3	15.9	3.3

TABLE III

AVERAGE DIPOLE MOMENTS μ IN DIFFERENT SOLVATION SHELLS

Functional group	All			$-CH_3$		$-NH_3^+$			$-COO^-$		
Solvation shell	1	2	3	1	2	1	2	3	1	2	3
μ[D]	3.29	3.32	3.25	3.27	3.36	3.28	3.30	3.27	3.35	3.31	3.25

For the water molecules an average dipole moment of 3.3 D was found. This is a 10% larger value than previously found for bulk water (*72*). An important result is the high average dipole moment of the solvated alanine (15.9 D). The dipole of the ionic isolated alanine (9.3 D) is about 55% of an alanine molecule solvated by 60 water molecules. It is obvious that the large increase of the dipole moment must have substantial influence on the properties of alanine in the aqueous phase. Also the results from average dipole moments of water molecules belonging to different solvent shells are remarkable. In particular, the average dipole moment in proximity of alanine's $-COO^-$ group decayed continuously with increasing distance, while, surprisingly close to the $-CH_3$ and $-NH_3^+$ group, the dipole moment first grew before its value dropped. These calculated values give an idea of the structure of the solvation shell of alanine. Recent discussions of the over all structure of water around a biologically important solute are found in Ref (*150,151*).

In a cluster ansatz approach (*148,149*), snapshots of alanine surrounded by different water molecule shells were considered. One of the important questions is: How many water molecules have to be included in a cluster calculation to converge the average dipole moment of alanine? Another question arises, if one wants to test the efficiency of the common solvation models implemented in static calculations. The dipole moments from the cluster approaches utilizing both maximally localized Wannier functions (MLWF) as well as Weinhold's natural population analysis (NPA) served to approximate the dipole moments of the total trajectory. A set of 50 snapshots was used for all calculations to ensure statistical accuracy. In order to receive a good description for the solvation of alanine, different numbers of solvent shells for the functional groups were tested. Namely **set0** only the isolated alanine; **set1** consists of the first shell around $-NH_3^+$ and $-COO^-$ group; **set2** first and second shell for the $-NH_3^+$ and $-COO^-$ group; **set3** first shell for the $-NH_3^+$, $-COO^-$, and $-CH_3$ group; and **set4** unites **set3** and **set2**. For all sets different types

TABLE IV

AVERAGE DIPOLE MOMENTS OF ALANINE [D]

Method	set0	set1	set2	set3	set4
PW/MLWC	10.99	14.10	15.08	14.59	15.56
GBS/NPA	12.13	12.86	13.14	13.15	13.45
GBS^{COSMO}/NPA	14.39	13.67	13.45	13.62	13.51

of calculations were accomplished. In particular, a plane wave approach without periodic boundary conditions (reference for the continuum model approach due the same level of theory), static calculations using a Gaussian-type basis set (GBS) and static calculations using GBS and a conductor-like screening model (COSMO). An overview of the results is given in Table IV. With these results one is able to estimate how many water molecules have to be included in a cluster calculation in order to compare to the 15.9 D obtained by the AIMD. Sufficient convergence is found for two solvent shells around the $-NH_3^+$ and $-COO^-$ group and one solvent shell around the $-CH_3$ group. Further it was possible to compare the static calculations of the dipole moment obtained with NPA to the plane waves/MLWC approach. Dipole moments of alanine provided by NPA are overestimated for **set0** and underestimated for all other sets. However, they are still as large as 84–89% of the reference value (PW/MLWC) and show the correct trend when further adding solvent molecules. It is important to note that the COSMO model on its own does not reproduce the solvent effects quantitatively correctly. It is necessary to include at least one explicit solvent shell around the polar groups in order to obtain satisfying results.

B.4. Explicit treatment of relativistic effects

Bioinorganic systems often contain heavy elements that need to be treated with an explicit relativistic method. It is now possible to carry out an explicit relativistic electronic structure calculation on the fly (*152*). The scalar-relativistic Douglas – Kroll – Hess method was implemented by us recently in the BOMD simulation framework (*152*). To use the relativistic densities in a non-relativistic gradient calculations turned out to be a valid approximation of relativistic gradients. An excellent agreement between optimized structures and geometries obtained from numerical gradients was observed with an error smaller than 0.02 pm.

Hydrogen halide dimers [(HX_2), with X = F, Cl, Br, I] served as small test systems for BOMD simulations. The relativistic effects manifested in the larger amplitude of motion than in the non-relativistic simulation, in the smaller frequency of motion, and in larger distances for the relativistic picture. Several schemes to treat the relativistic effect locally were introduced. The errors of these localization schemes were found to be small for geometries which are similar to the equilibrium structure. They become larger for smaller distances, introducing a slight bias toward closed packed configurations. However, these schemes allow the treatment of only particular atoms or molecules relativistically, while the rest can be described with lower computational methods. Please note that the main bottleneck lies in the size of the basis set which is needed for the relativistic calculation not in the relativistic treatment itself.

C. Case Studies on Nitrogen Fixations

The biological and technical (Haber – Bosch) nitrogen fixation are important processes. In both cases inert dinitrogen is converted to more reactive ammonia. Ammonia is a very important building block both in biological systems and in industry. Hence increased efforts were made to synthesize a well-defined catalyst which is able to reduce dinitrogen under mild conditions (*153,154*). Since the structure of the enzyme nitrogenase is known and the FeMo cofactor seems to be the active center of the enzyme, the information was used to synthesize different model complexes. Both for theoretical and for experimental investigations the model complexes are important, because they represent smaller and simpler systems. Further it should be possible with the model complexes to elucidate important steps in the mechanism of the dinitrogen reduction.We review two examples of CPMD simulations with different model complexes, namely the initial dinitrogen reduction step in Sellmann-type complexes (*155*) and the ammonia–dinitrogen exchange in Schrock-type complexes (*156*) (Fig. 3). Unfortunately it was not possible in the experiment to reduce nitrogen with **1N2** and **2N2** instead various side reactions were observed. Despite this fact simulations were accomplished, in order to find out whether the suggested mechanism (Fig. 3) is at least conceivable or impossible. Especially for the second step in the proposed mechanism the CPMD simulations were carried out. Each simulation takes place on the neutral PES of complex **1N2** and accordingly **2N2** after they were protonated and reduced. Three points on the

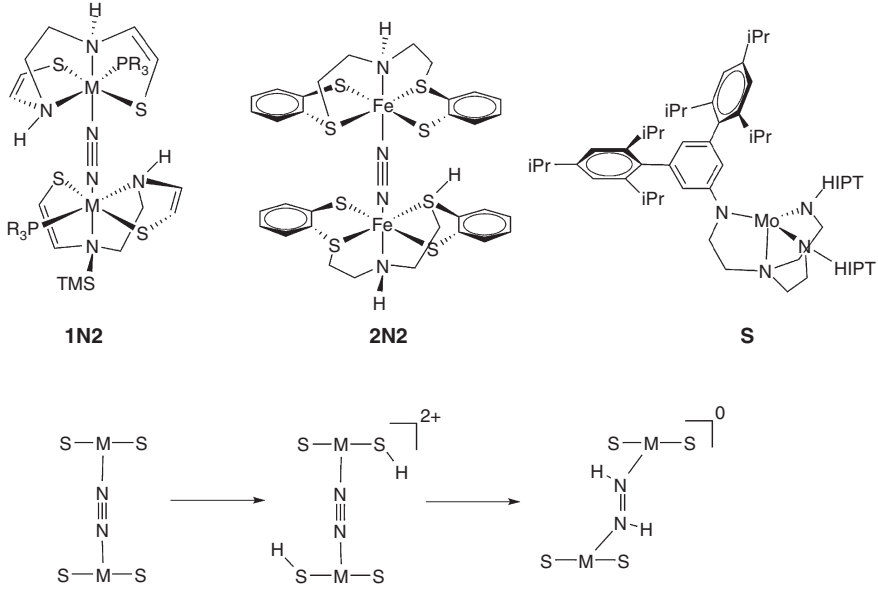

FIG. 3. Model complexes for nitrogen fixation (top); postulated mechanism for the reduction of dinitrogen with Sellmann-type complexes (bottom).

surface are important (Fig. 4): **C** represents the stable diazene complex, **B1** the neutral diprotonated complex, and **B2** the bended structure, obtained during the course of the reaction from **B1** to **C**. Starting points of the simulations were the high-energy structures **B1** and **B2**. An overview about the results is

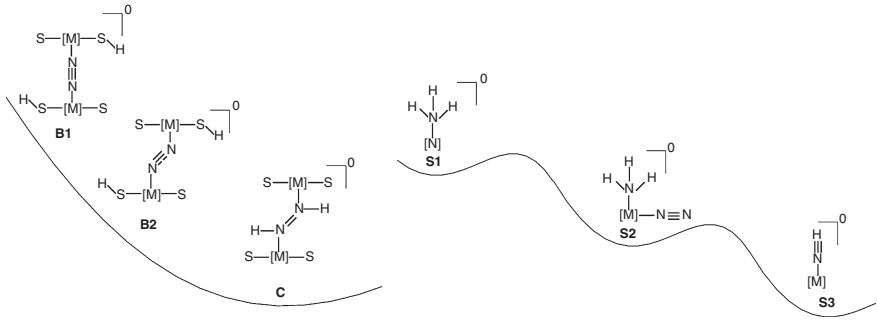

FIG. 4. Schematic drawing of the potential energy surfaces for the CPMD simulations. PES of Sellmann-type complexes (left); PES of Schrock-type complex (right).

TABLE V

SUMMARY OF THE CPMD SIMULATION RESULTS FOR THE SELLMANN-TYPE COMPLEXES.

Complex	Starting point	Constraints	T [K]	Final point
2N2	B1	no	320	Ligand dissociation
2N2	B1	HMN_2 angles	100	C
2N2	B1	no	100	C
1N2	B2	no	50	C

given in Table V. With the aid of the simulation results a three-step mechanism for the hydrogen atom transfer onto dinitrogen upon reduction seems probable. In the first step an increase of the N-H distance arises. Afterward the MNN angles are bent. The bending is important because it activates the complex for the final hydrogen transfer. The last step contains the vibration of the NH bond, which is controlled by the Metal-sulfur-hydrogen (MSH) angle and simultaneous vibration of the Metal-nitrogen-nitrogen (MNN) angles with opposite phase. By the simulations one can answer a few questions. The most important fact is that reduction with Sellmann-type complexes is possible in principle. In addition, it could be shown that the ligand must be changed to suppress side reactions observed in the simulations. The observed side reactions could also explain why Sellmann-type complexes are not able to reduce nitrogen at the moment. In the second case simulations were carried out for the Schrock-type complex **S** to get a detailed mechanistic understanding of the ammonia–dinitrogen ligand exchange (*156*). Each simulation takes place on the neutral PSE of complex **S**, ammonia, and dinitrogen. Three points on the surface are important (Fig. 4): **S1** represents **S** coordinated by an ammonia, **S2** a stable six-coordinate intermediate, where dinitrogen and ammonia are coordinated at the molybdenum, and **S3** represents **S** coordinated by dinitrogen alone. For steric reasons two different possibilities exist for dinitrogen to approach **S1** and accordingly for ammonia to leave **S2** (path a and path b). An overview of the results is given

TABLE VI

SUMMARY OF THE CPMD SIMULATION RESULTS FOR THE SCHROCK-TYPE COMPLEXES.

Starting point	Path	Constraints	T [K]	Final point
S1	b	Mo-N_2 distance	320	S2
S1	a	Mo-N_2 distance	320	S2
S2	b	Mo-NH_3 distance	320	S3
S2	a	NH_3-Mo-N(HIPT) angle	320	S3

in Table. VI. The approach of the dinitrogen and the leaving of the ammonia are calculated with "relaxed constraints," for a more detailed description of the methodology, we refer to the original publication (*156*). Different ways for the ligand exchange could be identified by CPMD simulations. An important result is a route via the six-coordinate intermediate. This leads to the conclusion that the ligand exchange proceeds over an addition-elimination mechanism involving a six-coordinate intermediate.

III. Static Quantum Chemical Calculations

A. Solvation in Static Quantum Chemistry

An efficient alternative compared to the expensive AIMD is static quantum chemistry calculations. These calculations may employ post-Hartree – Fock approaches which sometimes even outnumber the accuracy of the experiment. However, these approaches are limited to very small systems in vacuo, rarely found in chemistry. Therefore, less reliable approaches like the KS-DFT approach are commonly used (*3–14*). Static quantum chemistry calculations employing post-Hartree – Fock methods as well as KS-DFT have one major drawback, they lack the description of a dynamic solvation shell. Model non-polar solvation by vacuo seems reasonable but the situation changes dramatically if one wants to investigate charged particles in a polar solvent. One solution is continuum solvation models (*157–159*) like the polarizable continuum model (160) or the COSMO (*161*). Another possibility is the microsolvation for which solvent molecules are added to the investigated system. Microsolvation can be used to study reactions of solvent molecules with solutes, e.g., proton transfer, or strong directional impacts of the solvent. Within the following section we are going to present scopes and limits of modeling solvation in static quantum chemistry at a selected example, a mechanistic study of an inhibited alcoholysis of P - Cl bonds.

Commonly P – Cl bonds enter rapid reactions with O – or N – nucleophiles. However, this could not be found for *ortho*-carborane (*12*) derivatives where the carbon atoms carry P – Cl moieties, see Fig. 5. Even in the presence of methanol and triethylamine as a base, low yields and rates were observed (162). The carborane group can be excluded as cause of the observation because the alcoholysis was found for *meta*-carboranes or monosubstituted *ortho*-carboranes. Therefore, a mechanistic study was carried out to reveal the agent of the unexpected experimental observation.

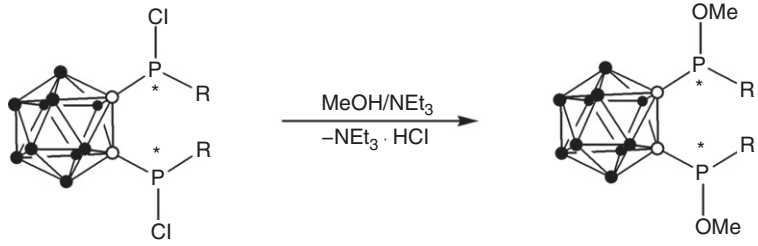

FIG. 5. Illustration of the inhibited methanolysis of P – Cl bounds observed for *ortho*-carborane (*12*) derivatives.

In general, a reaction can be suppressed by thermodynamics or kinetics. Thermodynamics can be obtained much easier than kinetics from static quantum chemistry calculations. For thermodynamics one must only determine the free reaction enthalpy while the whole reaction path with all transition states must be investigated for kinetics. In our selected example, an endergonic reaction was found for the disubstituted *ortho*-carborane (*12*) derivatives without considering solvation (*163*). This was also the case for the monosubstituted *ortho*-carborane (*12*). Only if solvation was considered both reactions became exergonic with a comparable value. Therefore, thermodynamics could be excluded if solvation is considered. The further investigation focused upon kinetics by determining the activation barrier of the S_{N2}-like pathway, see Fig. 6. A transition state was only found if an additional methanol molecule was considered in terms of microsolvation (*162,163*). The obtained activation barrier for the disubstituted *ortho*-carborane (*12*) was 10 kJ/mol higher than for the monosubstituted *ortho*-carborane (*12*) pointing toward a kinetic inhibited alcoholysis of P – Cl in disubstituted *ortho*-carboranes, but the activation barrier was below 80

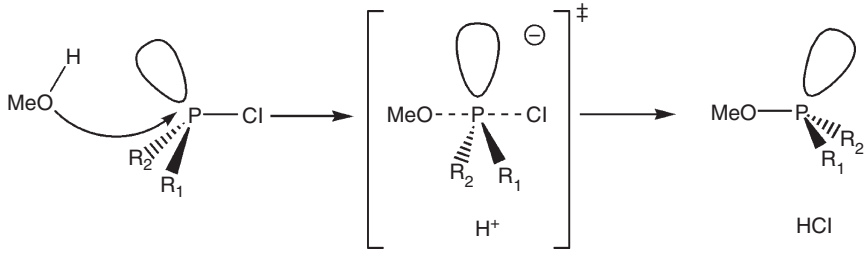

FIG. 6. Sketch detailing the transition state of alcoholysis for P – Cl bonds.

kJ/mol for both compounds. Therefore, only a comparison of the reactive and inhibited compound allowed the conclusion of a kinetically inhibited alcoholysis because errors in the employed approach as well as modeling of the solvation lead to significant deviations from the experimental value. Microsolvation as well as continuum solvation models are a good choice to provide an informative basis for trends of experimental observations.

B. Hydrogen Bond Detection by the SEN Approach

Static quantum chemistry approaches are dominantly employed with KS-DFT in bioinorganic chemistry (*3–4*). This proceeding shows a good performance ratio to obtain energies and structures of the potential surface. However, the user of computational chemistry may be interested in more than a single structure or an energy value. Approaches capable of extracting further information from the wavefunction would be helpful. Numerous tools to analyze the electronic structure were reported in the literature (*92,164–170*). They can be employed for a better understanding on a selected interaction or reaction and are mostly available in AIMD as well as static quantum chemistry. Here, we will shortly introduce one orbital analysis approach, the SEN analysis (*167*), which has been proven as a suitable tool for hydrogen bond detection.

The SEN approach was firstly employed by Reiher *et al.* for hydrogen bonds (*171*). Originally, Ehrhardt and Ahlrichs proposed the SEN approach as the simplest possible relationship between the two-center SEN σ and the covalent bond energy providing a quantitative measure for the strength of a covalent bond (*167,172*). Later, Reiher *et al.* used a simple linear relationship between the two-center SEN σ and the hydrogen bond strength E_{HB}, $E_{HB} = a\sigma$ (*171*). They fitted the parameter a to different hydrogen-bond energies, which were obtained through static calculations of some selected systems. Unfortunately, no general parameter a could be determined because a depends on the basis set as well as the selected functional. However, the observed standard deviation for a according to Student's t distribution was less than 3.5 kJ/mol. The results were further improved if the parameter a was separately adjusted to different reference sets. The sets were obtained by dividing the initial reference set into subsets of different atoms according to their type and hydrogen bond donor/acceptor functionality (173), see Fig. 7 for illustration of hydrogen bond donor and acceptor atom.

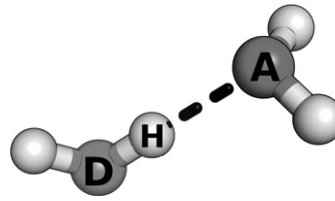

FIG. 7. Illustration of hydrogen bond donor (D) and acceptor (A) atom.

Especially, the subdivision in different hydrogen bond acceptor atom sets improves the performance of the SEN approach while a subdivision depending on the hydrogen bond donor atom showed only a minor improvement compared to the general fit of Reiher *et al.* Thus, the SEN approach has proven as a tool to investigate hydrogen bonds of, e.g., transition metal compounds (*171,174–177*), peptides (*178*), enzymes (*179*), DNA and RNA (*173*), molecular switches (*180*), ionic liquids (*181,182*), and rotaxanes (183). However, the SEN approach is not solely restricted to hydrogen bond detection. This approach can also be applied to determine the covalent interaction between metal atoms (*184*) or phosphorus atoms (*162,185*). Therefore, it is suitable for different kind of interactions.

IV. Conclusion

In this chapter we briefly introduced the method of AIMD simulations for application toward bioinorganic systems. We showed at several examples the potential of this method for complex systems. The major advantage of this method as compared to a classical molecular dynamics simulations consists of the possibility to calculate the electronic structure on the fly. This allows several aspects to become within the reach for bioinorganic systems such as (i) analyzing the wavefunction on the fly (along a reaction), (ii) determining possible reaction mechanisms with very sophisticated constraint dynamics and/or free-energy determination schemes, (iii) studying explicitly solvent effects and using advanced electronic structure techniques such as the explicit relativistic Douglas – Kroll – Hess method. We showed at two bioinorganic examples for nitrogen fixation how AIMD can aid in understanding such systems. Thus, there is much open potential to investigate these systems in situations in which solvent effects or electronic structure effects play a major role. Additionally, we

shortly introduce at selected examples synthesized by the group of one present author (Hey – Hawkins) some useful tools of static quantum chemical strategies which allow to analyze the bonds and electronic structure of bioinorganic systems. These or similar systems will be future subjects for the study with AIMD.

Acknowledgment

We are grateful to the Graduate School of Excellence Build-MoNa (funded by the Deutsche Forschungsgemeinschaft) for financial support. This work was supported by the DFG and the ESF, in particular by the projects KI-768/4-1 and KI-768/4-2 from the ERA-chemistry, KI-768/5-1,KI-768/6-1, and KI-768/5-2 of the SPP-IL program. Computer time from the RZ Leipzig, the HLRS Stuttgart, the DEISA computer center, and NIC J ülich are gratefully acknowledged.

References

1. Hohenberg, P.; Kohn, W. *Phys. Rev. B* **1964**, *136*, 864–871.
2. Kohn, W.; Sham, L. J. *Phys. Rev. A* **1965**, *140*, 1133–1138.
3. Chermette, H. *Coord. Chem. Rev.* **1998**, *178-180*, 699–721.
4. Cundari, T. R. *Chem. Rev.* **2000**, *100*, 807–818.
5. Frenking, G.; Fröhlich, N. *Chem. Rev.* **2000**, *100*, 717–774.
6. Dedieu, A. *Chem. Rev.* **2000**, *100*, 543–600.
7. Siegbahn, P. E.M.; Blomberg, M. R.A. *Chem. Rev.* **2000**, *100*, 421–438.
8. Shaik, S.; Kumar, D.; de Visser, S. P.; Altun, A.; Thiel, W. *Chem. Rev.* **2005**, *105*, 2279–2328.
9. Ziegler, T.; Autschbach, J. *Chem. Rev.* **2005**, *105*, 2695–2722.
10. Kirchner, B.; Wennmohs, F.; Ye, S.; Neese, F. *Curr. Opin. Chem. Biol.* **2007**, *11*, 134–141.
11. Thar, J.; Reckien, W.; Kirchner, B. *Top. Curr. Chem.* **2007**, *268*, 133–171.
12. Senn, H. M.; Thiel, W. *Top. Curr. Chem.* **2007**, *268*, 173–290.
13. Herrmann, C.; Reiher, M. *Top. Curr. Chem.* **2007**, *268*, 85–132.
14. Reiher, M. *CHIMIA* **2009**, *63*, 140–145.
15. Cohen, A. J.; Mori-Sanchez, P.; Yang, W. *Science* **2008**, *321*, 792–794.
16. Zhang, Y.; Yang, W. *J. Chem. Phys.* **1998**, *109*, 2604–2608.
17. Perdew, J. P.; Zunger, A. *Phys. Rev. B* **1981**, *23*, 5048–5079.
18. Polo, V.; Kraka, E.; Cremer, D. *Mol. Phys.* **2002**, *100*, 1771–1790.
19. Tavernelli, I. *J. Phys. Chem.* **2007**, *111*, 13528–13536.
20. Oberhofer, H.; Blumberger, J. *J. Chem. Phys.* **2009**, *131*, 064101.
21. VandeVondele, J.; Sprik, M. *Phys. Chem. Chem. Phys.* **2005**, *7*, 1363–1367.
22. Sit, P. H.L.; Cococcioni, M.; Marzari, N. *Phys. Rev. Let.* **2006**, *97*, 028303.
23. Kristyán, S.; Pulay, P. *Chem. Phys. Lett.* **1994**, *229*, 175–180.
24. Pérez-Jordá, J. M.; Becke, A. D. *Chem. Phys. Lett.* **1995**, *233*, 134–137.
25. Meijer, E. J.; Sprik, M. *J. Chem. Phys.* **1996**, *105*, 8684–8689.
26. Cybulski, S. M.; Seversen, C. E. *J. Chem. Phys.* **2005**, *122*, 14117.
27. Jensen, F. *Introduction to Computational Chemistry*; Chichestered. ; John Wiley & Sons, **2007**.

28. Lundqvist, B. I.; Andersson, Y.; Shao, H.; Chan, S.; Langreth, D. C. *Int. J. Quantum Chem.* **1995**, *56*, 247–255.
29. Andersson, Y.; Langreth, D. C.; Lundqvist, B. I. *Phys. Rev. Lett.* **1996**, *76*, 102–105.
30. Kohn, W.; Meir, Y.; Makarov, D. E. *Phys. Rev. Lett.* **1998**, *80*, 4153–4156.
31. Elstner, M.; Porezag, D.; Jungnickel, G.; Elsner, J.; Haugk, M.; Frauenheim, T.; Suhai, S.; Seifert, G. *Phys. Rev. B* **1998**, *58*, 7260–7268.
32. Kamiya, M.; Tsuneda, T.; Hirao, K. *J. Chem. Phys.* **2002**, *117*, 6010–6015.
33. Šindelka, M.; Špirko, V.; Jungwirth, P. *J. Chem. Phys.* **2002**, *117*, 5113–5123.
34. Seifert, G.; Köhler, T.; Tenne, R. *J. Phys. Chem. B* **2002**, *106*, 2497–2501.
35. Wu, Q.; Yang, W. *J. Chem. Phys.* **2002**, *116*, 515–524.
36. Dion, M.; Rydberg, H.; Schröder, E.; Langreth, D. C.; Lundqvist, B. I. *Phys. Rev. Lett.* **2004**, *92*, 246401.
37. von Lilienfeld, O. A.; Tavernelli, I.; Rothlisberger, U.; Sebastiani, D. *Phys. Rev. Lett.* **2004**, *93*, 153004.
38. Zimmerli, U.; Parrinello, M.; Koumoutsakos, P. *J. Chem. Phys.* **2004**, *120*, 2693–2699.
39. Dobson, J. F.; Wang, J.; Dinte, B. P.; McLennan, K.; Le, H. M. *Intl. J. Quantum Chem.* **2005**, *101*, 579–598.
40. Ángyán, J. G.; Gerber, I. C.; Savin, A.; Toulouse, J. *Phys. Rev. A* **2005**, *72*, 012510.
41. Johnson, E. R.; Becke, A. D. *J. Chem. Phys.* **2006**, *124*, 174104.
42. Grimme, S. *J. Comput. Chem.* **2006**, *27*, 1787–1799.
43. Grimme, S. *J. Chem. Phys.* **2006**, *124*, 034108.
44. Jurečka, P.; Černý;, J.; Hobza, P.; Salahub, D. R. *J. Comput. Chem.* **2007**, *28*, 555–569.
45. Grimme, S.; Antony, J.; Schwabe, T.; Mück-Lichtenfeld, C. *Org. Biomol. Chem.* **2007**, *5*, 741–758.
46. Silvestrelli, P. L. *Phys. Rev. Lett.* **2008**, *100*, 053002.
47. Zahn, S.; Kirchner, B. *J. Phys. Chem. A* **2008**, *112*, 8430–8435.
48. Lin, I.-C.; Rothlisberger, U. *Phys. Chem. Chem. Phys.* **2008**, *10*, 2730–2734.
49. Sato, T.; Nakai, H. *J. Chem. Phys.* **2009**, *131*, 224104.
50. Kong, J.; Gan, Z.; Proynov, E.; Freindorf, M.; Furlani, T. R. *Phys. Rev. A* **2009**, *79*, 042510.
51. Foster, M. E.; Sohlberg, K. *Phys. Chem. Chem. Phys.* **2010**, *12*, 307–322.
52. Ghosh, A.; Taylor, P. R. *Curr. Opin. Chem. Biol.* **2003**, *7*, 113–124.
53. Car, R.; Parrinello, M. *Phys. Rev. Lett.* **1985**, *55*, 2471–2474.
54. Remler, D. K.; Madden, P. A. *Mol. Phys.* **1990**, *70*, 921–966.
55. Payne, M. C.; Teter, M. P.; Allan, D. C.; Arias, T. A.; Joannopoulos, J. D. *Rev. Mod. Phys.* **1992**, *64*, 1045–1097.
56. Kirchner, B. *Phys. Rep.* **2007**, *440*, 1–111.
57. Marx, D.; Hutter, J. "*Ab Initio Molecular Dynamics: Basic Theory and Advanced Methods*"; Cambridge University Press: Cambridge, **2009**.
58. Dirac, P. A.M. *Proc. Camb. Philos. Soc.* **1930**, *26*, 376–385.
59. Ehrenfest, P. *Z. Phys. A* **1927**, *45*, 455–457.
60. Allen, M. P.; Tildesley, D. J. "*Computer Simulation of Liquids*"; Clarendon Press: Oxford, **1987**.
61. Frenkel, D.; Smit, B. "*Understanding Molecular Simulation: From Algorithms to Applications*"; Academic Press: New York, NY, **2002**.
62. Szabo, A.; Ostlund, N. S. "*Modern Quantum Chemistry: Introdsuction to Advanced Electronic Structure Theory*"; Dover Publications: Mineola, NY, **1996**.
63. McQuarrie, D. A.; Simon, J. D. "*Physical Chemistry: A Molecular Approach*"; University Science Books: Sausalito, CA, **1997**.

64. Huber, H.; Dyson, A. J.; Kirchner, B. *Chem. Soc. Rev.* **1999**, *28*, 121–133.
65. Ryckaert, J.-P.; Ciccotti, G.; Berendsen, H. J.C. *J. Comput. Phys.* **1977**, *23*, 327–341.
66. Tangney, P. *J. Chem. Phys.* **2006**, *124*, 044111.
67. Wannier, G. H. *Phys. Rev.* **1937**, *52*, 191–197.
68. Kohn, W. *Phys. Rev. B* **1973**, *7*, 4388–4398.
69. Marzari, N.; Vanderbilt, D. *Phys. Rev. B* **1997**, *56*, 12847–12865.
70. Silvestrelli, P. L. *Phys. Rev. B* **1999**, *59*, 9703–9706.
71. Berghold, G.; Mundy, C. J.; Romero, A. H.; Hutter, J.; Parrinello, M. *Phys. Rev. B* **2000**, *61*, 10040–10048.
72. Kirchner, B.; Hutter, J. *J. Chem. Phys.* **2004**, *121*, 5133–5142.
73. Silvestrelli, P. L.; Parrinello, M. *Phys. Rev. Lett.* **1999**, *82*, 3308–3311.
74. Souza, I.; Martin, R. M.; Marzari, N.; Zhao, X.; Vanderbilt, D. *Phys. Rev. B* **2000**, *62*, 15505–15520.
75. Gaigeot, M.-P.; Sprik, M. *J. Phys. Chem. B* **2003**, *107*, 10344–10358.
76. Iftimie, R.; Tuckerman, M. E. *J. Chem. Phys.* **2005**, *122*, 214508.
77. Masia, M.; Forbert, H.; Marx, D. *J. Phys. Chem. A* **2007**, *111*, 12181–12191.
78. Todorova, T.; Hünenberger, P. H.; Hutter, J. *J. Chem. Theory Comput.* **2008**, *4*, 779–789.
79. Thar, J.; Zahn, S.; Kirchner, B. *J. Phys. Chem. B* **2008**, *112*, 1456–1464.
80. Spickermann, C.; Thar, J.; Lehmann, S. B.C.; Zahn, S.; Hunger, J.; Buchner, R.; Hunt, P. A.; Welton, T.; Kirchner, B. *J. Chem. Phys.* **2008**, *129*, 104505.
81. Scipioni, R.; Schmidt, D. A.; Boero, M. *J. Chem. Phys.* **2009**, *130*, 024502.
82. Donadio, D.; Cicero, G.; Schwegler, E.; Sharma, M.; Galli, G. *J. Phys. Chem. B* **2009**, *113*, 4170–4175.
83. Bernasconi, M.; Silvestrelli, P. L.; Parrinello, M. *Phys. Rev. Lett.* **1998**, *81*, 1235–1238.
84. Sharma, M.; Donadio, D.; Schwegler, E.; Galli, G. *Nano Lett.* **2008**, *8*, 2959–2962.
85. Chen, W.; Sharma, M.; Resta, R.; Galli, G.; Car, R. *Phys. Rev. B* **2008**, *77*, 245114.
86. Silvi, B.; Savin, A. *Nature* **1994**, *371*, 683–686.
87. Savin, A.; Nesper, R.; Wengert, S.; Fässler, T. F. *Angew. Chem. Int. Ed.* **1997**, *36*, 1808–1832.
88. Kirchner, B.; Stubbs, J.; Marx, D. *Phys. Rev. Lett.* **2002**, *89*, 215901.
89. Gourlaouen, C.; Gérard, H.; Parisel, O. *Chem. Eur. J.* **2006**, *12*, 5024–5032.
90. Kirchner, B.; Seitsonen, A. P. *Inorg. Chem.* **2007**, *46*, 2751–2754.
91. Durlak, P.; Latajka, Z.; Berski, S. *J. Chem. Phys.* **2009**, *131*, 024308.
92. Becke, A. D.; Edgecombe, K. E. *J. Chem. Phys.* **1990**, *92*, 5397–5403.
93. Savin, A.; Jepsen, O.; Flad, J.; Andersen, O. K.; Preuss, H.; von Schnering, H. G. *Angew. Chem. Int. Ed.* **1992**, *31*, 187–188.
94. Tuckerman, M.; Laasonen, K.; Sprik, M.; Parrinello, M. *J. Chem. Phys.* **1995**, *150*, 150–161.
95. Tuckerman, M. E.; Marx, D.; Klein, M. L.; Parrinello, M. *Science* **1997**, *275*, 817–820.
96. Marx, D.; Tuckerman, M. E.; Hutter, J.; Parrinello, M. *Nature* **1999**, *397*, 601–604.
97. Geissler, P. L.; Dellago, C.; Chandler, D.; Hutter, J.; Parrinello, M. *Science* **2001**, *291*, 2121–2124.
98. Tuckerman, M. E.; Marx, D.; Parrinello, M. *Nature* **2002**, *417*, 925–929.
99. Tuckerman, M. E.; Chandra, A.; Marx, D. *Acc. Chem. Res.* **2006**, *39*, 151–158.

100. Marx, D. *ChemPhysChem* **2006**, *7*, 1848–1870.
101. Kirchner, B. *ChemPhysChem* **2007**, *8*, 41–43.
102. Chipot, C.; Poharille, A.; (Eds.) "*Free Energy Calculations: Theory And Applications In Chemistry And Biology (Springer Series In Chemical Physics)*"; Springer GmbH & Co. KG: Berlin, **2007**.
103. van Gunsteren, W. F. *Mol. Phys.* **1980**, *40*, 1015–1019.
104. Dellago, C.; Bolhuis, P. G.; Csajka, F. S.; Chandler, D. *J. Chem. Phys.* **1998**, *108*, 1964–1977.
105. Bolhuis, P. G.; Chandler, D.; Dellago, C.; Geissler, P. L. *Annu. Rev. Phys. Chem.* **2002**, *53*, 291–318.
106. Dellago, C.; Bolhuis, P. G.; Geissler, P. L. *Adv. Chem. Phys.* **2002**, *123*, 1–78.
107. Geissler, P. L.; Dellago, C. *J. Phys. Chem. B* **2004**, *108*, 6667–6672.
108. Iannuzzi, M.; Laio, A.; Parrinello, M. *Phys. Rev. Lett.* **2003**, *90*, 238302.
109. Ensing, B.; Vivo, M. D.; Liu, Z.; Moore, P.; Klein, M. L. *Acc. Chem. Res.* **2006**, *39*, 73–81.
110. Laio, A.; Parrinello, M. *Proc. Natl. Acad. Sci.* **2002**, *99*, 12562–12566.
111. Jarzynski, C. *Phys. Rev. Lett.* **1997**, *78*, 2690–2693.
112. Crooks, G. E. *J. Stat. Phys.* **1998**, *90*, 1481–1487.
113. Evans, D. J.; Searles, D. J. *Adv. Phys.* **2002**, *51*, 1529–1585.
114. Thar, J.; Hovorka, R.; Kirchner, B. *J. Chem. Theory Comput.* **2007**, *3*, 1510–1517.
115. Bessac, F.; Maseras, F. *J. Comput. Chem.* **2007**, *29*, 892–899.
116. Blumberger, J. *J. Am. Chem. Soc.* **2008**, *130*, 16065–16068.
117. Petit, L.; Vuilleumier, R.; Maldivi, P.; Adamo, C. *J. Comput. Chem.* **2008**, *4*, 1040–1048.
118. Bernasconi, L.; Baerends, E. J.; Sprik, M. *J. Phys. Chem. B* **2006**, *110*, 11444–11453.
119. Bernasconi, L.; Blumberger, J.; Sprik, M.; Vuilleumier, R. *J. Chem. Phys.* **2004**, *121*, 11885–11899.
120. Coudert, F.-X.; Vuilleumier, R.; Boutin, A. *ChemPhysChem* **2006**, *7*, 2464–2467.
121. Petit, L.; Vuilleumier, R.; Maldivi, P.; Adamo, C. *J. Phys. Chem. B* **2008**, *112*, 10603–10607.
122. Takayanagi, T.; Yoshikawa, T.; Kakizaki, A.; Shiga, M.; Tachikawa, M. *J. Mol. Struct. (THEOCHEM)* **2008**, *869*, 29–36.
123. Sulpizi, M.; Raugei, S.; VandeVondele, J.; Carloni, P.; Sprik, M. *J. Phys. Chem. B* **2007**, *111*, 3969–3976.
124. Yoshikawa, T.; Motegi, H.; Kakizaki, A.; Takayanagi, T.; Shiga, M.; Tachikawa, M. *Chem. Phys.* **2009**, *365*, 60–68.
125. Hayes, R. L.; Paddison, S. J.; Tuckerman, M. E. *J. Phys. Chem. B* **2009**, *113*, 16574–16589.
126. Gordon, M. S.; Freitag, M. A.; Bandyopadhyay, P.; Jensen, J. H.; Kairys, V.; Stevens, W. J. *J. Phys. Chem. A* **2001**, *105*, 293–307.
127. Spiegel, K.; Rothlisberger, U.; Carloni, P. *J. Phys. Chem. B* **2006**, *110*, 3647–3660.
128. Vidossich, P.; Carloni, P. *J. Phys. Chem. B* **2006**, *110*, 1437–1442.
129. Boero, M.; Ikeda, T.; Ito, E.; Terakura, K. *J. Am. Chem. Soc.* **2006**, *128*, 16798–16807.
130. Magistrato, A.; Ruggerone, P.; Spiegel, K.; Carloni, P.; Reedijk, J. *J. Phys. Chem. B* **2006**, *110*, 3604–3613.
131. Vargiu, A. V.; Ruggerone, P.; Magistrato, A.; Carloni, P. *J. Phys. Chem. B* **2006**, *110*, 24687–24695.

132. Biarnés, X.; Nieto, J.; Planas, A.; Rovira, C. *J. Biol. Chem.* **2006**, *281*, 1432–1441.
133. Magistrato, A.; Togni, A.; Rothlisberger, U. *Organometallics* **2006**, *25*, 1151–1157.
134. Raugei, S.; Carloni, P. *J. Phys. Chem. B* **2006**, *110*, 3747–3758.
135. Bucher, D.; Guidoni, L.; Rothlisberger, U. *Biophys. J.* **2007**, *93*, 2315–2324.
136. Leenders, E. J.M.; Guidoni, L.; Röthlisberger, U.; Vreede, J.; Bolhuis, P. G.; Meijer, E. J. *J. Phys. Chem. B* **2007**, *111*, 3765–3773.
137. Gossens, C.; Tavernelli, I.; Rothlisberger, U. *J. Am. Chem. Soc.* **2008**, *130*, 10921–10928.
138. Masson, F.; Laino, T.; Tavernelli, I.; Rothlisberger, U.; Hutter, J. *J. Am. Chem. Soc.* **2008**, *130*, 3443–3450.
139. Murugan, N. A.; Ågren, H. *J. Phys. Chem. A* **2009**, *113*, 2572–2577.
140. Masson, F.; Laino, T.; Rothlisberger, U.; Hutter, J. *ChemPhysChem* **2009**, *10*, 400–410.
141. Moret, M.-E.; Tavernelli, I.; Rothlisberger, U. *J. Phys. Chem. B* **2009**, *113*, 7737–7744.
142. Colombo, M.; *et al. CHIMIA* ***2002****, 56*, 13–19.
143. Spiegel, K.; Magistrato, A. *Org. Biomol. Chem.* **2006**, *4*, 2507–2517.
144. Thiel, W. *J. Mol. Struct. (THEOCHEM)* **1997**, *398*, 1–6.
145. Lin, H.; Truhlar, D. G. *Theor. Chem. Acc.* **2007**, *117*, 185–199.
146. Friesner, R. A.; Guallar, V. *Annu. Rev. Phys. Chem.* **2005**, *56*, 389–427.
147. Lin, H.; Truhlar, D. G. *Theor. Chem. Acc.* **2007**, *117*, 185–199.
148. Hermansson, K.; Knuts, S.; Lindgren, J. *J. Chem. Phys.* **1991**, *95*, 7486–7496.
149. Eggenberger, R.; Gerber, S.; Huber, H.; Searles, D.; Welker, M. *J. Chem. Phys.* **1992**, *97*, 5898–5904.
150. Troitzsch, R. Z.; Tulip, P. R.; Crain, J.; Martyna, G. J. *J. Biophys* **2008**, *95*, 5014–5020.
151. Tulip, P. R.; Bates, S. P. *J. Chem. Phys.* **2009**, *131*, 015103.
152. Thar, J.; Kirchner, B. *J. Chem. Phys.* **2009**, *130*, 124103.
153. Fryzuk, M. D.; Johnson, S. A. *Coord. Chem. Rev.* **2000**, *200*, 379–409.
154. Schrock, R. R. *Angew. Chem. Int. Ed.* **2008**, *47*, 5512–5522.
155. Kirchner, B.; Reiher, M.; Hille, A.; Hutter, J.; Hess, B. A. *Chem. Eur. J.* **2005**, *11*, 574–583.
156. Schenk, S.; Kirchner, B.; Reiher, M. *Chem. Eur. J.* **2009**, *15*, 5073–5082.
157. Cramer, C. J.; Truhlar, D. G. *Chem. Rev.* **1999**, *99*, 2161–2200.
158. Orozco, M.; Luque, F. J. *Chem. Rev.* **2000**, *100*, 4187–4226.
159. Tomasi, J.; Mennucci, B.; Cammi, R. *Chem. Rev.* **2005**, *105*, 2999–3093.
160. Miertš, S.; Scrocco, E.; Tomasi, J. *Chem. Phys.* **1981**, *55*, 117–129.
161. Klamt, A.; Schüürmann, G. *J. Chem. Soc., Perkin Trans. 2*(5) **1993**, 799–805.
162. Stadlbauer, S.; Frank, R.; Maulana, I.; Lönnecke, P.; Kirchner, B.; Hey-Hawkins, E. *Inorg. Chem.* **2009**, *48*, 6072–6082.
163. Frank, R.; Master's Thesis, University of Leipzig, Leipzif, **2008**.
164. Löwdin, P.-O. *Phys. Rev.* **1955**, *97*, 1474–1489.
165. Davidson, E. R. *J. Chem. Phys.* **1967**, *46*, 3320–3324.
166. Bader, R. F.W. *Acc. Chem. Res.* **1985**, *18*, 9–15.
167. Ehrhardt, C.; Ahlrichs, R. *Theor. Chim. Acta* **1985**, *68*, 231–245.
168. Reed, A. E.; Curtiss, L. A.; Weinhold, F. *Chem. Rev.* **1988**, *88*, 899–926.
169. Pipek, J.; Mezey, P. G. *J. Chem. Phys.* **1989**, *90*, 4916–4926.
170. Herrmann, C.; Reiher, M.; Hess, B. A. *J. Chem. Phys.* **2005**, *122*, 034102.
171. Reiher, M.; Sellmann, D.; Hess, B. A. *Theor. Chem. Acc.* **2001**, *106*, 379–392.

172. Heinzmann, R.; Ahlrichs, R. *Theor. Chim. Acta.* **1976**, *42*, 33–45.
173. Thar, J.; Kirchner, B. *J. Phys. Chem. A* **2006**, *110*, 4229–4237.
174. Reiher, M.; Salomon, O.; Sellmann, D.; Hess, B. A. *Chem. Eur. J.* **2001**, *7*, 5195–5202.
175. Schneider, S.; Schmitt, M. O.; Brehm, G.; Reiher, M.; Matousek, P.; Towrie, M. *Photochem. Photobiol. Sci.* **2003**, *2*, 1107–1117.
176. Reiher, M.; Brehm, G.; Schneider, S. *J. Phys. Chem. A* **2004**, *108*, 734–742.
177. Schenk, S.; Le Guennic, B.; Kirchner, B.; Reiher, M. *Inorg. Chem.* **2008**, *47*, 3634–3650.
178. Reiher, M.; Kirchner, B. *J. Phys. Chem. A* **2003**, *107*, 4141–4146.
179. Schmidt, M.; Zahn, S.; Carella, M.; Ohlenschläger, O.; Görlach, M.; Kothe, E.; Weston, J. *ChemBioChem* **2008**, *9*, 2135–2146.
180. Zahn, S.; Reckien, W.; Kirchner, B.; Staats, H.; Matthey, J.; Lützen, A. *Chem. Eur. J.* **2009**, *15*, 2572–2580.
181. Kossmann, S.; Thar, J.; Kirchner, B.; Hunt, P. A.; Welton, T. *J. Chem. Phys.* **2006**, *124*, 174506.
182. Nockemann, P.; Thijs, B.; Driesen, K.; Janssen, C. R.; Van Hecke, K.; Van Meervelt, L.; Kossmann, S.; Kirchner, B.; Binnemans, K. *J. Phys. Chem. B* **2007**, *111*, 5254–5263.
183. Kirchner, B.; Spickermann, C.; Reckien, W.; Schalley, C. A. *J. Am. Chem. Soc.* **2010**, *132*, 484–494.
184. Gómez-Ruiz, S.; Zahn, S.; Kirchner, B.; Böhlmann, W.; Hey-Hawkins, E. *Chem. Eur. J.* **2008**, *14*, 8980–8985.
185. Bauer, S.; Tschirschwitz, S.; Lönnecke, P.; Frank, R.; Kirchner, B.; Clarke, M. L.; Hey-Hawkins, E. *Eur. J. Inorg. Chem.* **2009**, *2009*, 2776–2788.

SIMULATIONS OF LIQUIDS AND SOLUTIONS BASED ON QUANTUM MECHANICAL FORCES

THOMAS S. HOFER, BERND M. RODE*, ANDREAS B. PRIBIL and BERNHARD R. RANDOLF

Theoretical Chemistry Division, Institute of General, Inorganic and Theoretical Chemistry, University of Innsbruck, Innrain 52a, A-6020 Innsbruck, Austria

I. Introduction

There is no doubt that liquid systems represent the majority of chemical work and that all biochemical processes require solvent water for their functionality. At the same time it is clear that the liquid state with a density like a solid but a mobility comparable to the gas phase is the most difficult one for theory. Although classical model systems based on electrostatic and van der Waals forces can provide some insight into the physicochemical behavior of liquids and solutions, specific properties of species formed in a pure liquid or by a solute with the solvent require a more sophisticated approach, which is often attempted by quantum mechanical (QM) calculations of model systems. Such model calculations supply information, however, for an isolated system in the gas

THEORETICAL AND COMPUTATIONAL INORGANIC CHEMISTRY
VOLUME 62 ISSN 0898-8838 / DOI: 10.1016/S0898-8838(10)62004-1

phase, usually only with a few solvent molecules, and for a temperature of 0 K. In such calculations, the influence of a solvent can be considered by simple electrostatic models such as the "polarized continuum model (PCM)" (*1,2*), which are helpful but cannot reflect all the details of solute–solvent interactions at molecular level.

The need to reliably describe liquid systems for practical purposes as condensed matter with high mobility at a given finite temperature initiated attempts, therefore, to make use of statistical mechanical procedures in combination with molecular models taking into account structure and reactivity of all species present in a liquid and a solution, respectively. The two approaches to such a description, namely Monte Carlo (MC) simulations and molecular dynamics (MD), are still the basis for all common theoretical methods to deal with liquid systems. While MC simulations can provide mainly structural and thermodynamical data, MD simulations give also access to time-dependent processes, such as reaction dynamics and vibrational spectra, thus supplying — connected with a higher computational effort — much more insight into the properties of liquids and solutions.

There is another important reason, however, why simulations, in particular MD, have become such an important tool for the investigation of liquid systems, and these are the limitations of experimental methods for the analysis of such systems. Diffraction methods for the determination of structural properties can only deliver an average picture, collected over a relatively long time. The simultaneous presence of several molecular species in a liquid or even more in a solution makes it very difficult to develop satisfactory models to be fitted to the experimental data for the elucidation of "true" structures, and the more components are present in a solution the more ambiguous becomes the interpretation. Other spectroscopic techniques such as nuclear magnetic resonance and IR/Raman can help to resolve some of these problems, but they are also limited due to their timescale, and whenever the dynamics of the liquid system studied occur on the picosecond or subpicosecond scale, only very few and not universally applicable experimental techniques (in particular femtosecond laser pulse spectroscopy (*3–5*)) are available for conclusive interpretation of species formation and structural data. Simulations offer the possibility to analyze in detail all pair correlations of atoms in the system and hence provide a very detailed picture of all species formed in a liquid system and the corresponding structures through radial distribution functions (RDF), angular distribution functions (ADF), and coordination number distributions (CNDs). Thus a good basis for models to

be employed for the fitting of diffraction data is obtained. MD simulations deliver additional information about dynamical processes through mean residence times (MRTs) or lifetime of structures with weak bonds, e.g., hydrogen bonds, thus leading to a very detailed characterization of the liquid system at molecular level. The velocity autocorrelation function (VACF) of such a simulation can be easily converted to the power spectrum of the vibrational motions of the system by Fourier transformation, providing an immediate comparison with infrared and Raman frequencies obtained for it. In order to obtain accurate intensities of the vibrational motion the respective dipole derivatives have to be computed as well and hence only frequency information can be obtained from the power spectra.

It is obvious that this enormous potential of simulation methods to supply detailed information about composition, structure, and dynamics of a liquid system crucially depends on the validity and accuracy of the basic input into the simulation, i.e., the potentials describing all interactions between the components of the system. Any insufficiency of these potentials can have serious consequences for the correctness of the data obtained. Usually these potentials are either constructed from experimental data or—the most common approach—from QM calculated energy surfaces. The quality of such constructions depends not only on the amount and completeness of data points but also on their inherent accuracy, e.g., the level of the quantum chemical calculation method. A further problem of such potentials is the usual truncation of their construction to 2-body potentials, assuming pairwise additivity of interactions. Already in an early stage of simulations it was recognized that 3-body terms can be of essential importance for a correct description of liquids and in particular of solutions with strongly interacting components such as ions (*6,7*). In principle such higher interaction terms can be constructed from *n*-body energy surfaces, which, however, are already quite complicated for 3-body potentials and much more for higher terms. For molecules with low symmetry and different active sites, such a construction becomes almost impossible for reliable pair potentials and almost unfeasible for 3-body and higher potentials. One way to avoid this difficulty is the design of polarizable potentials which try to implicitly include higher terms by a built-in flexibility of the electrostatic interactions (*8*). For small molecules, e.g. for water itself, this approach has been quite successful, but it will not be very helpful for the aforementioned asymmetric larger molecules. Force field methods have thus an inherent limitation, which allows to treat large biomolecules with an accuracy sufficient for many purposes, but they will

not produce satisfactory and reliable results for pure liquids and solutions.

The straightforward solution for these problems would be the calculation of energies/forces "on the fly" at every simulation step by means of quantum mechanics. However, even for a very modest simulation box of a few hundred molecules, this approach is computationally not affordable. Two ways have been proposed, therefore, to solve this dilemma: the further reduction of the simulation box and the use of approximate QM calculation procedures, and the partition of the system into a QM and a classical part.

The first way has been followed in what has become known as Car–Parrinello molecular dynamics (CPMD) (*9*). A solute and 60–90 solvent molecules are considered to represent the system, and the QM calculations are performed with density functionals, usually of generalised gradient approximation type (GGA), such as the Becke-Lee-Young-Parr (BLYP) (*10*) or the Perdew-Burke-Enzerhofer (PBE) (*11,12*) functionals. It is clear that the semiempirical character of concurrent density functional theory (DFT) methods and the use of these simple functionals imply a number of error sources and do not really provide a method-inherent control procedure to test the reliability of results. Recently it has been shown that these functionals even do not enable a correct description of the solvent water itself, as at ambient temperature they will describe water not as liquid but as supercooled system (*13,14*). As will be outlined later, even the use of the much more accurate, but still semiempirical hybrid functional B3LYP (*15*) carries on some of the DFT-inherent problems.

The approach with the partitioning of the system into a QM and a classical molecular mechanical (MM) part, thus usually termed hybrid QM/MM procedure, provides a reasonable reduction of the computational effort by restricting the time-consuming QM calculation of forces to the most relevant part of the liquid system. The main error sources in this approach are a too small choice of the QM region, an inadequate level of theory for the QM calculation, the choice of suitable potentials for the MM part of the system, and smooth transitions of particles between QM and MM region. In conventional QM/MM procedures, the whole system is first evaluated at MM level and then corrected by the QM data. This means that classical potential functions (with all their problems and difficulty of construction) are needed for all components of the system. A recently developed methodology can reduce the need for such potentials to the solvent only, as will be outlined below.

As mentioned the size of the QM region and the level of theory employed for it are crucial for the reliability and accuracy of results. The minimal size selection of solute and first solvation

layer is a too strong restriction for many systems, in particular for strongly interacting ions. On the other hand, too simple QM procedures such as semiempirical molecular orbital (MO) methods or *ab initio* methods with single zeta basis sets also lead to wrong results. Many tests have finally shown that *ab initio* Hartree–Fock (HF) level with at least double zeta plus polarization basis sets is required to produce sufficiently accurate results. Correlated *ab initio* methods, even Møller-Plesset second order perturbation theory (MP/2), would lead to an unaffordable computational effort, but they can be used to estimate the accuracy of HF level by calculations of small solute–solvent clusters at different levels of theory. Unfortunately also DFT level does not appear a suitable solution. QM/MM simulations employing the B3LYP functional, which are almost equally time consuming as *ab initio* HF calculations, have shown that hydrogen bonds as well as solvation structures (*16,17*) are too rigid and thus give a wrong picture of structure and dynamics of solvents and solutions.

At this point some misleading nomenclature in publications of simulations has to be clarified. Frequently simulations based on DFT functionals are termed "*ab initio* MD" and "first principle" or "non-empirical." This is indeed not correct as all available density functionals are of a more or less semiempirical nature, as pointed out by their developers themselves, e.g., by Becke in his presentation of the B3LYP functional (*15*). The term "*ab initio*" should be reserved, therefore, for simulations where for the QM part a true *ab initio* procedure, i.e., HF or correlated methods like MP/2 or better, is employed. Only by this one is also enabled to perform a method-inherent control of accuracy and deficiencies by increasing the level of theory from a one-determinantal to a multi-determinantal method.

While the QM/MM approach has been successfully used for a large number of very different systems (*18–20*) it is still subject to significant improvements. One of these improvements is the recently developed quantum mechanical charge field (QMCF MD) methodology, which will be presented in more detail here, demonstrating its capabilities with a number of applications to quite different liquid systems, in particular to electrolyte solutions.

II. Methodology of the QMCF Approach

A. System Partitioning and Definition of Forces

The separation of the system into a QM region containing the chemically most challenging part of the system and a MM region (*21–25*) is retained in the QMCF framework (*26,27*). The forces in

the subregions are treated according to the applied QM level and the chosen potential model, respectively. While the execution of these individual computations is straightforward, the coupling between the QM and MM regions is considered the most challenging step.

For coupling purposes the QM particles are separated into two sets — those which are near the QM center and those located close to the QM/MM border. For QM atoms close to the center the intermolecular distances to MM particles are typically larger than the non-Coulombic cutoff distances and, therefore, these atoms only require a Coulombic term to account for the coupling between the QM and the MM particles. A correction term compensating for the Coulombic cutoff such as Ewald summation or a reaction field is typically applied. Atoms close to the interface region have small intermolecular distances and consequently, non-Coulombic interactions have to be included in addition to the Coulombic forces to achieve a proper coupling.

According to these considerations three subregions are defined as depicted in Fig. 1. The inner and outer parts of the QM region are termed the QM core and QM layer zone, respectively. As discussed solutes in the QM core do not require the application of non-Coulombic potentials—composite species with complex potential energy surfaces can be treated in a straightforward way, while complex potential functions are required in the case of classical and even conventional QM/MM simulation studies. Interactions at close solute-solvent distances are treated exclusively via quantum mechanics and account for polarization, charge transfer, as well as many-body effects. The solute-solvent

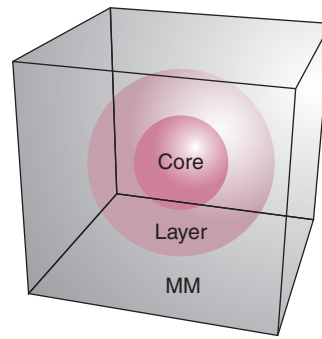

FIG. 1. Overview of the regions defined in a QMCF simulation: the chemically most relevant part is treated by QM while MM is applied in the remaining part. The QM region is further separated into the "QM core" and the "QM (solvation) layer."

interaction beyond the QM region is accounted for by Coulombic interactions only.

This approach requires that all atoms of the solute species remain close to the QM center—if a solute particle were located too close to the interface between QM and MM region, in addition to the Coulombic interactions, non-Coulombic potentials would be required and the advantages of the QMCF methodology lost. This also implies that only species for which non-Coulombic potentials are available are allowed in the "QM layer" region. Hence, this second QM zone is also referred to as "solvation layer" as it is exclusively composed of solvent particles. Besides solvent molecules this could also apply to other species such as counterions assuming that non-Coulombics are provided for these species as well.

The size assigned to the "core" and "layer" regions is an important consideration for such simulations. The size of the solute determines the minimum radius of the "core region," but it is often necessary to include the first hydration layer as well, for instance when hydrated ions are studied. The distance of all particles included in the "QM core" to the QM/MM interface should exceed the non-Coulombic cutoff distance of all involved interactions. In the case of water the minimum size of the "layer region" is 2.5–3.0 Å.

In the case of ionic species it proved advantageous to include at least two layers of hydration in the entire QM region. For composite solutes this condition leads to an enormous computational effort. However, as these species are in general less polarizing than ions, the size of the core zone can be chosen to include the solute and eventually a part of the first hydration layer only.

A further improvement realized in the QMCF framework is the assignment of QM-derived point charges to all QM atoms by population analysis in every step of the simulation. This treatment accounts for polarization, charge transfer, and many-body effects and their respective dependence on the geometry of the system. Comparative simulation studies confirmed that this treatment is advantageous over the assignment of fixed partial charges along the course of a simulation.

For instance, the effective charge of hydrated aluminum(III) ion was found to range in between +2.0 and +2.5 instead of the formal charge of +3.0, resulting from polarization and charge transfer effects between solvent and ion. Coupling artifacts near the QM/MM border have been observed in QM/MM simulations using a fixed charge scheme, as the formal charge leads to too strong intermolecular forces between the MM solute and the ionic species: a contraction of the MM region was observed leading to a "pressure" acting on the QM zone. The QM particles have to

adapt to this external force and deformation of the solute structure was observed. These artifacts have been significantly reduced by the application of subsequently evaluated QM charges, as all changes in the electron density are incorporated in the QM/MM coupling in the course of the simulation.

Following this rationale the forces in the respective regions have been defined as

$$F_J^{\text{core}} = F_J^{\text{QM}} + \sum_{I=1}^{M} \frac{q_J^{\text{QM}} \cdot q_I^{\text{MM}}}{r_{IJ}^2} \cdot \left[1 + 2 \cdot \frac{\varepsilon + 1}{2\varepsilon - 1} \cdot \left(\frac{r_{IJ}}{r_{\text{c}}} \right)^3 \right] \qquad (1)$$

F_J^{core} is the force acting on the "core" particle J, which is composed of the forces resulting from the QM treatment F_J^{QM} and the Coulombic interactions between particle J and all M MM atoms.

As discussed earlier the charges of the QM atoms are derived by means of a population analysis, whereas the charges of the respective solvent model are used for all MM particles. The reaction field (*28*) formalism was employed in this equation to account for the error resulting from the Coulombic cutoff given as r_c. ε is the dielectric constant of the medium beyond the Coulombic cutoff. Alternatively, an Ewald summation technique (*29*) could be applied as well.

The force acting on a "layer" particle J F_J^{layer} is obtained by adding non-Coulombic interactions F_{IJ}^{nC} between the target particle J and all MM atoms to the expression derived for "core" particles.

$$F_J^{\text{layer}} = F_J^{QM} + \sum_{I=1}^{M} \left\{ \frac{q_J^{\text{QM}} \cdot q_I^{\text{MM}}}{r_{IJ}^2} \cdot \left[1 + 2 \cdot \frac{\in + 1}{2 \in -1} \cdot \left(\frac{r_{IJ}}{r_{\text{c}}} \right) \right] + F_{IJ}^{nC} \right\} \qquad (2)$$

The force of an MM particle J consists of the intermolecular forces resulting from the remaining $(M-1)$ MM atoms plus the forces resulting from the QM/MM coupling.

In the majority of cases the force associated with the MM interactions is composed of a Coulombic term (typically a long-range correction is applied), non-Coulombic forces (Lennard-Jones 6-12 type potentials are the most commonly used formulation), and intramolecular force field contributions. The QM/MM coupling is composed of the Coulombic interactions with all core (N_1) and layer (N_2) atoms plus non-Coulombic forces with all atoms in the "layer" region (N_2). As the latter contributions correspond to the coupling terms in the "core" and "layer" regions, no violation of momentum conservation occurs.

$$F_J^{\mathrm{MM}} = \sum_{\substack{I=1 \\ I \neq J}}^{M} F_{IJ}^{\mathrm{MM}} + \sum_{I=1}^{N_1+N_2} \frac{q_I^{\mathrm{QM}} \cdot q_J^{\mathrm{MM}}}{r_{IJ}^2} \cdot \left[1 + 2 \cdot \frac{\varepsilon + 1}{2\varepsilon - 1} \cdot \left(\frac{r_{IJ}}{r_{\mathrm{c}}} \right)^3 \right] + \sum_{I=1}^{N_2} F_{IJ}^{\mathrm{nC}} \tag{3}$$

In this definition, the force contributions between "core" and MM particles are composed of Coulombic interactions only.

As the partial charges of the QM region are reevaluated in every step of the simulation and vary according to geometrical changes and the associated change of polarization, these force contributions can be considered as a fluctuating field of charges, which designates the name of this framework as "QMCF" in order to distinguish this methodology from alternative QM/MM approaches.

B. Particle Migration Between the QM and MM Region

When particles are exchanged between QM and MM region, a smoothing treatment is invoked to prevent discontinuities of forces. The solvent potential model describing the interaction of solute particles in the MM zone should account for molecular flexibility, as all molecular vibrations are accessible in the QM part. The use of rigid models is not advised, as molecules would freeze in unfavorable conformations whenever a QM to MM transition takes place.

Typically, a small region of 0.2 Å width is defined near the QM/MM interface. Forces of all particles located in this volume are evaluated twice: first according to the definition of the "layer" region (F^{layer}) and second assuming that the respective particle were already part of the MM region (F_J^{MM}). According to the molecular center of mass a smoothing factor $S(r)$ is computed, which is utilized to calculate the smoothing force F_J^{Smooth}.

$$F_J^{\mathrm{Smooth}} = S(r) \cdot (F_J^{\mathrm{layer}} - F_J^{\mathrm{MM}}) + F_J^{\mathrm{MM}} \tag{4}$$

For the smoothing function $S(r)$ a continuous function increasing from zero to one is chosen:

$$\begin{aligned} S(r) &= 1, && \text{for } r \leq r_1 \\ S(r) &= \frac{(r_0^2 - r^2)^2 (r_0^2 + 2r^2 - 3r_1^2)}{(r_0^2 - r_1^2)}, && \text{for } \quad r_1 < r \leq r_0 \\ S(r) &= 0, && \text{for } r > r_0 \end{aligned} \tag{5}$$

The radius r is the distance of the molecular centers of mass from the center of the QM region, r_0 and r_1 define the upper and lower boundaries of the smoothing zone. The typical width of the smoothing region is set to 0.2 Å, which was identified as optimal choice to avoid transition artifacts and ensure smooth transitions of all molecules. Although the forces of the exchanging particles are continuously changed, a small violation of momentum conservation is observed. Artificial diffusion effects were observed when long simulation trajectories (a few nanoseconds) are computed (*30*). The large computational effort of the QM computations limits the achievable time span of QMCF MD simulations, and hence the observed deviations are too small to have any noticeable effect. However, too large smoothing regions (e.g., a width of 0.5 Å) have been found to lead to a significant violation of momentum conservation (*30*).

Recently, advanced smoothing procedures have been developed (*30*–*32*), but the increase of the computational effort (up to N^2 energy and force computations, N being the number of molecules in the smoothing zone) makes these approaches too expensive for investigations utilizing hybrid QM/MM approaches. As long as the simulation time is substantially below the nanosecond scale, no noticeable improvement of the accuracy is achieved, although the increase in computation time is dramatic. Hybrid MM/MM approaches such as the combination of reactive and non-reactive force fields (*33*) appear to be a more appropriate target for such techniques.

C. Electrostatic Embedding in a Periodic Environment

Difficulties related to the Coulombic interaction between QM and MM particles are just one source of QM/MM transition artifacts — the QM treatment itself may lead to some errors close to the QM/MM interface region. Based on the assignment of molecules to the specific regions, the QM part is not "aware" of its vicinity. This leads to a typical expansion of the molecular orbitals and the electron density into the virtual vacuum environment (*27*,*34*). Such a description does not correspond to the system within the bulk of a liquid, as the shape of the electron density should be influenced by the surrounding charge distribution. The electric field of these surrounding charges is inhomogeneous, and simplistic approaches such as implicit solvation models (*2*) (e.g., PCM) aimed at representing the influence of the surrounding solvent homogeneously are not expected to yield a reasonable description of all important solvation effects.

The electrostatic embedding technique (*21,35–37*) is a frequently used methodology to tackle this problem in QM/MM studies. Atomic point charges of all atoms in the MM region formulate a perturbation to the Hamiltonian of the QM region and are thus able to influence the shape of the molecular orbitals. Negative point charges lead to a repulsion, positive charges to an attraction of the electron density. This approach significantly improves the description of the QM region within a QM/MM method, but does not significantly increase the computational effort, as the point charges act on the less demanding one-electron contributions.

The improved description of hydrogen bonds crossing the QM/MM border is a typical example of the benefits of electrostatic embedding: the modified electron density resulting from the influence of the surrounding point charges leads to a variation of the QM-derived charges on the QM atoms which are utilized in the QM/MM coupling. A shift of charges for oxygen and hydrogen atoms is observed whenever a hydrogen bond is formed with an MM atom. While a significant improvement in the accuracy of the QM/MM coupling is achieved, only a modest increase of computational effort is observed.

The electrostatic embedding method is included in numerous quantum chemistry packages and although quantum chemical computations using this technique are straightforward, some difficulties in its application in the context of QM/MM approaches are encountered (*27,34*). The main problems are associated with the derivation of forces in a periodic environment which has to be employed to ensure that the system reflects the bulk of a liquid.

The *periodic boundary condition* assumes the system to periodically extend in all directions of space. Particles leaving the simulation box on one side reenter through the opposite side. Artifacts resulting from double counting must be avoided—interactions are computed with the closest image, i.e., either the original atom or a respective image particle situated in an adjacent box. This condition is referred to as the *minimum image convention* (cf. Fig. 2a) (*28*).

However, as quantum chemical methods treat all contributions of the *n*-body interaction simultaneously, a periodic treatment cannot be invoked when localized basis sets are utilized and a special treatment has to be employed to maintain periodicity (*27,34*). Ignoring the incompatibility of the periodic environment and the *n*-body treatment of quantum chemical methods would lead to severe artifacts, which should be avoided at all costs.

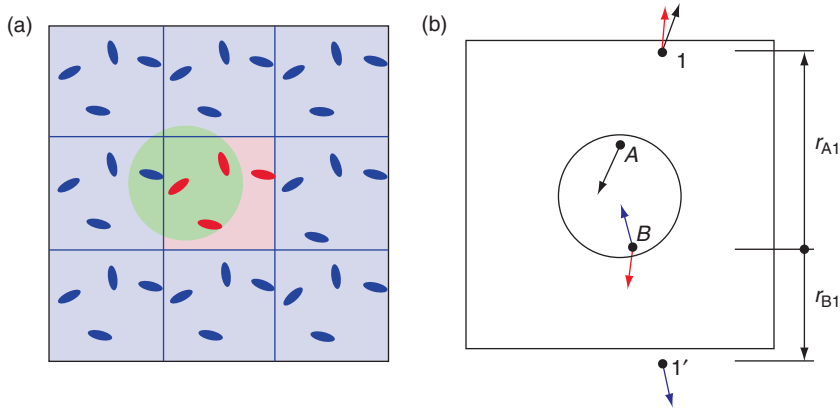

FIG. 2. (a) Periodic images surrounding the simulation box. Interactions are computed with respect to the nearest image which is indicated by the circle. (b) Violation of the *minimum image convention* resulting from the interaction of QM particle *B* with point charge 1.

Figure 2b demonstrates a situation arising in the course of a QM treatment with electrostatic embedding. While the interaction between QM atom *A* and point charge 1 is valid, the minimum image convention requires that QM atom *B* interacts with the periodic image 1′. Three errors are associated with this wrong treatment of the interaction: The distance between particle *B* and 1 is too large, the resulting force vector points into a wrong direction, and whenever particle 1 is imaged through the box a sudden change in the interparticle distance is observed leading to a discontinuity in energy and forces. These severe shortcomings result from the violation of the minimum image convention and, therefore, the electrostatic embedding scheme cannot be utilized in this form to derive forces in a periodic system.

An alternative procedure is to include the point charges in the energy calculation, but to discard the embedding during the force computation (*27*,*34*). This procedure leads to a modification of the molecular orbitals under the influence of the external field of charges, resulting in different forces between QM atoms and different QM partial charges. Afterward, the coupling between the QM and MM particles is carried out according to Coulomb's law as discussed earlier. All crucial requirements connected to the correct periodic treatment such as minimum image convention, associated Coulombic cutoffs, plus application of a long-range cutoff correction term can be realized using this framework.

This electrostatic embedding strategy has been successfully applied in a variety of QMCF MD simulations of hydrated systems (*38*–*43*). The embedding technique in connection with improvements of the QM/MM coupling leads to a significantly increased accuracy of the description of the systems compared to conventional QM/MM MD procedures. The QMCF framework is compatible with any affordable quantum chemical level and will enable the application of correlated *ab initio* methods (e.g., MP/2) in the near future.

D. Computational Effort and Accuracy Considerations

The required computational effort for a MD study is governed by various elements. Foremost the number of particles N is a crucial factor, as the number of interactions is proportional to N^2 or even higher (N^{3-4}), if quantum chemical methods are applied as it is the case in CPMD simulations. In the present CPMD simulations the number of water molecules employed ranges between 60 and 90, which are treated on GGA density functional level. In the context of QMCF simulation studies of hydrated systems a solute and up to 50 solvent molecules treated by *ab initio* quantum mechanics are surrounded by 500–1000 water MM molecules to ensure that a sufficient number of bulk molecules is included.

The total length of a simulation to observe all processes of interest is another important factor. The time step of a simulation is determined by the fastest moving particles, i.e., the hydrogen atoms. A vibrational cycle of the O–H water bond has a period of approximately 10 fs. To achieve approximately 50 steps per period, the time step of the simulation has to be set to 0.2 fs. In order to study solvation structures of ions in solution a minimum simulation time of 10 ps is required plus at least 2 ps for equilibration of the system, provided that the system is properly pre-equilibrated using classical simulations. In many cases the equilibration time required is even longer. Considering the time step of 0.2 fs the total number of simulation steps is at least 60,000. Labile solvate species showing ligand exchanges require even longer simulation times, typically ranging from 110,000 to 250,000 steps, corresponding to simulation times of 20–50 ps.

Another very important choice is the level of theory to perform the energy and force evaluation, which is strongly correlated with the computational effort. Force field methods based on parametrized potentials are less demanding — systems containing a few

thousand molecules can be executed within a few hours. In the case of hybrid QM/MM methods the chosen QM accuracy level, the basis sets assigned to the QM atoms, and the size of the QM region corresponding to the number of molecules included are crucial considerations.

These factors strongly influence the computational effort and the accuracy of results. The application of QM methods to an entire simulation cube containing several hundred molecules by *ab initio* methods is far beyond the capability of present computational equipment. CPMD simulation introduces a compromise between accuracy and computational effort by utilizing density functionals of the GGA type and reducing the system size to (and sometimes below) the necessary minimum.

CPMD simulations have been widely employed in a large number of theoretical studies, but significant error sources such as the fictive electron mass, usage of plane wave functions, and inherent methodical problems tied to the formulation of DFT (unphysical self-interaction, wrong kinetic energy, dependence on parametrizations) (*44*–*46*) require empirical corrections of the framework in order to obtain results in agreement with experiment. Recent studies of pure water at ambient condition predicted a supercooled structure (*13*) and a melting point in the order of 410–415 K (*14*). As structure and dynamics of the pure solvent are predicted in a wrong way, the same can be concluded whenever a solvated species is treated by this method.

The quality of hybrid QM/MM simulations strongly depends on the size of the high-level region and the employed QM methodology. Methods showing low accuracy enable larger QM regions and vice versa. In the majority of cases the QM zone should be chosen as large as possible. This restricts the theoretical level to a single determinantal treatment, i.e., either DFT or *ab initio* HF theory. Although they imply several methodical limitations as mentioned earlier, density functional methods have become increasingly popular within the last decades. A most significant finding associated with DFT is the requirement of a calibration source which is discussed in detail in recent literature (*44*).

The method of choice has to be carefully evaluated prior to a simulation study to assess whether a chosen functional is appropriate for a particular system. Ionic solvates are strongly dominated by Coulombic interactions and significant polarization effects are observed resulting from the presence of the charged solute. The unphysical self-interaction inherent to DFT is a striking disadvantage in these cases. Furthermore, the parametrization

of the functionals is in most cases focused on neutral molecules rather than charged atomic systems. Geometry optimization studies of ion-water clusters comparing DFT with correlated ab initio methods have confirmed these conclusions (*47–54*).

The HF level on the other hand suffers from missing a treatment of the correlation of the electrons. This methodical shortcoming is a significant error source for many applications, in particular when the molecular interactions are weak. However, the error becomes less important for systems with a strong interaction such as hydrated ions. Again, a comparative study of ion–water clusters treated at various QM accuracy levels has enabled the assessment of the performance of the HF method (*47–54*). For example, in the case of the strongly polarizing ion Al(III) (*47*) the average ion-water distance and the associated energies of the $[Al(H_2O)_n]^{3+}$ (n=1, 2, 3, 4, 6, 8) clusters confirmed that the HF method leads to a more accurate description, comparable to more demanding correlated ab initio methods (MP/4 SDQ, CCD, QCISD), than popular density functionals. Less polarizing systems show smaller, but still significant differences.

QM/MM MD simulations of pure water, whose intermolecular interactions have been described as moderate (*55*), have shown that DFT is not a suitable approach to describe the forces in this system. The liquid's description is too rigid (*16,17*), although the water–water interaction energies and the hydrogen bond distances are in agreement with experiment, whereas the HF method yields dynamical data in better agreement with experiments, but slightly weaker and longer hydrogen bonds.

Following this rationale it can be concluded that the *ab initio* HF level appears to be the most reliable compromise between accuracy and computational effort to study ions in aqueous solution at present. Despite the shortcomings attributed to a single determinantal treatment, the accurate treatment of many-body, polarization, and charge transfer effects in the vicinity of the solute species and the capability to study systems containing hundreds of solvent molecules are key features of QM/MM methods aimed at a reliable description of solution phenomena. However, ongoing hard- and software development will enable the application of more accurate QM techniques within the near future.

Further aspects governing computational effort and accuracy are related to the explicit treatment of relativistic effects, which are pronounced for atoms with high atomic numbers, as their core electrons reach velocities that make the influence of special relativity significant. Contraction of bond lengths and a shifting of orbital energies are observed compared to the non-relativistic treatment. An efficient way to include a major fraction of these

effects is the use of effective core potentials (ECPs), which are used to represent a predetermined number of core electrons. ECPs can be constructed in a way that includes relativistic effects. Furthermore, ECPs reduce the computational effort of a QM computation, as the total number of electrons in the system is decreased. An accurate relativistic treatment of all remaining electrons using relativistic QM approaches is still too demanding to be applied in QM/MM simulations with present computational facilities.

The number of basis functions (defined by the chosen basis sets) used to construct the molecular orbitals also strongly affects the effort/accuracy ratio. The use of minimal basis sets yielded wrong results (*56*), whereas reasonable agreement with experiment is obtained when double zeta plus polarization basis sets are applied. Correlated methods require larger basis sets to include as much electron correlation as possible. This implies that in addition to the increased computational demand of such methods, a further increase of the computational cost results due to the requirement of using larger basis sets.

A careful consideration and appropriate balancing of these factors has to be carried out, thereby taking the available computational facilities into account. In the case of QM/MM simulations the computing time spent for the evaluation of the classical potential functions, the integration of the equations of motion, thermostatization, are negligible compared to the QM computation. Parallel execution of quantum chemical software by distributing parts of the computation to several processors is a very common technique, but due to limitations in the parallelizability depending on the efficiency of the software and the architecture of the computational equipment the reduction of the computing time decreases with increasing number of processors.

A typical overall CPU time of 5 min per step at HF level with a minimum of 60,000 steps along the simulation leads to a total net computation time of 5000 h corresponding to 7 months. These dimensions of computation times demonstrates why the application of correlated *ab initio* methods is still not feasible. As a comparison of energies and geometries of ion-water clusters at different levels of theory has revealed that correlated QM methods lead only to marginal changes, the application of the HF level to describe the interaction of charged species in polar solvents appears to be a reasonable compromise between accuracy and computational effort. Systems showing weak interactions such as hydrophobic solutes in polar solvents or apolar systems require the inclusion of electron correlation to obtain a reliable description. In such cases DFT methods could prove as an alternative, as the majority of functionals are parametrized for this class of molecules.

III. Applications of the QMCF MD Methodology

In the following recent applications of the new *ab initio* simulation technique will be demonstrated, which would have posed serious difficulties to conventional QM/MM MD schemes, which need analytical solute–solvent interaction potentials and where some artifacts as outlined in the previous chapter would certainly cause errors in the results. These applications will be grouped to hydrated cations and anions, in another section also hydrated neutral molecules forming hydrogen bonds to the solvent water and hydrolysis processes will be discussed. In all cases structural and dynamical data of the solutions will be presented.

A number of tools have been employed for the analysis of simulation trajectories. Structural data can be extracted via RDFs, which can be independently obtained for any desirable atom–atom pair distribution, and from ADFs for any angle of relevance. CNDs supply a clear picture of different species being formed within the simulation time, which for QM simulations usually ranges between 10 and 50 ps. Therefore, different species observed means that for almost all experimental timescales these species are present simultaneously and that the experiment delivers a time-averaged picture of them. For the reactivity of solutes, however, the detailed species distribution is of great importance, in particular for understanding reaction mechanisms. It is possible to analyze RDF and ADF separately for all of the (differently coordinated) species, thus obtaining detailed structural information for each of them.

The dynamics of solute–solvent interactions can be extracted as well from the simulation data. Very important for this purpose are the MRTs, either of a ligand bound to a solute or of a solvent molecule in the immediate neighborhood of others. The most convenient tool to obtain MRT data is the "direct method" (*57*), in which all exchange events are directly counted and which also enables a comparison of attempted and successful exchange processes (where the latter are usually identified by a separation of the interacting particles for more than 0.5 ps), classified by the R_{ex} values, corresponding to the number of attempts needed to achieve one successful exchange. The VACF of the particles deliver a further important set of data from the simulation. Fourier transformation of the VACF produces the spectrum of all molecular vibrations, thus enabling an immediate comparison with IR/Raman spectra and the calculation of force constants for the determination of bond strengths between solute and solvent. In the examples discussed below, these methods have been employed, and the details of the analysis can be found for each

case in the references listed. The examples have been selected with particular focus on inorganic substances, especially metal ions and composite ions with particular relevance for aqueous solutions.

A. Hydrated Cations

The characteristic structural data such as ion–ligand distances and coordination numbers and dynamical data, in particular ligand MRTs, number of needed exchange attempts, and force constants for the ion–water stretching vibration are collected for all cations discussed in Tables I and II, respectively.

Single-atom cations, which for different reasons are non-trivial in their properties, will be the first focus of interest. The ions Pd(II) and Pt(II) in water have long been considered as 4-coordinated square planar hydrates, until recent diffraction data and classical simulations have shed some doubt on this opinion (*58*, *59*). The QMCF MD simulations have clearly shown that besides four strongly bound equatorial ligands in both cases two additional, more labile axial ligands are coordinated to the metal ion, and this distorted octahedral structure has been verified experimentally by recent extended Xray absorption fine structure (EXAFS) data (*40,60*). The elongated metal–water distance of the axial ligands facilitates a rapid exchange of these water molecules and makes almost every second exchange attempt successful.

A second highly interesting set of cations are the divalent group IV metal ions Ge(II), Sn(II), and Pb(II), which are characterized

TABLE I

Hydration Structure Parameters for Cations Determined By QMCF MD Simulations[a]

Cation	r_{M1}	r_{M2}	CND_{1sh}	CND_{2sh}	Ref.
Pd^{2+}	2.0/2.7	4.4	4/1–2 (5.9)	–(8.0)	(*40*)
Pt^{2+}	2.1/2.7	4.4	4/1–2 (5.8)	–(7.8)	(*60*)
Ge^{2+}	2.0/2.5	4.22	2–4/0–5 (3.3/2.5)	6–14 (9.4)	(*86,87*)
Sn^{2+}	2.4/3.0	4.9	6–11 (7.8)	15–27 (22)	(*88*)
Pb^{2+}	2.7	5.07	7–10 (8.1)	17–28 (25.3)	(*89*)
Be^{2+}	1.6	3.8	4	7–12(9)	(*62*)
Al^{3+}	1.9	4.9	6	14–20(12.8)	(*90*)
U^{4+}	2.5	4.8	9	17–21	(*91*)

[a] First and second peak maximum Ion-O RDF r_{M1}, r_{M2} in Å. CND and average value in brackets for the first CND_{1sh} (separated where different regions are formed) and second CND_{2sh} coordination sphere.

TABLE II

FIRST AND SECOND SHELL DYNAMICS OF HYDRATED CATIONS DETERMINED BY QMCF MD SIMULATIONS

Cation	$\tau^{0.5}$	R_{ex}	ν Ion-O	F_{Ion-O}	Ref.
Pd^{2+}	2.8	2.3	n.a.	n.a	(*40*)
Pt^{2+}	3.2	1.7	n.a.	n.a.	(*60*)
Ge^{2+}	5.8 (6.6/1.7)	7.7	362/138	101/14.7	(*86,87*)
Sn^{2+}	2.4 (2.5/1.2)	3.4	250/144	52/17.2	(*88*)
Pb^{2+}	5.53	2.7	196	33.6	(*89*)
Be^{2+}	3.9^a	14.2^a	653	144	(*62*)
Al^{3+}	17.7^a	21.1^a	560	194	(*90*)
U^{4+}	8.1^a	5.9^a	n.a.	n.a.	(*91*)
H_2O	1.3	6.6	—	—	QMCF H_2O

First and second shell[a] dynamics of solvent molecules: MRTs $\tau^{0.5}$ in ps. Ratio of attempted and successful exchanges R_{ex}, ion oxygen stretching frequencies in cm^{-1}, and their corresponding force constants in Nm^{-1}.

by the presence of a lone electron pair. While in the solid state the structural influence of this lone pair is well documented, its role for structure and dynamics in the liquid state has not been known so far. Conventional QM/MM simulations with one hydration shell in the QM region proved insufficient for an accurate evaluation of data, but the QMCF MD method was able to identify in much detail the lone-pair effects, which are strongly different for each of the three ions. In the case of Ge(II) and Sn(II) they lead to a hydration structure with two different hemispheres with ligands of different binding distance and strongly different exchange characteristics, thus forming several hydrate complexes within the picosecond scale. Also the calculated force constants for the metal–water stretching vibration clearly distinguish between ligands in both hemispheres. In the case of the heavier Pb(II) ion the first hydration shell is more homogeneous and shows a slower ligand exchange than Sn(II) which, however, still enables the simultaneous presence of several hydrate species. This phenomenon was only revealed after increasing the QM region to include also the full second hydration shell and applying the refined embedding scheme of the QMCF formalism—a one-shell QM treatment of hydrated Pb(II) had not shown any ligand exchanges within the simulation period [61]. The overall success rate of exchange processes increases with the size of the hydrate—the larger the ion, the less attempts are needed. The examples of this series of ions seem an excellent proof that only simulations taking into account all QM effects within two hydration layers could lead to a reasonable description of the ions' hydrate

complexes, especially because the construction of accurate ion–water potentials taking into account the presence of the lone pair appears an almost impossible task.

Highly charged and thus strongly polarizing cations are another challenge for simulations of their aqueous solution, as their hydrates are characterized by very pronounced charge transfer effects as well. The construction of interaction potentials based on *ab initio* calculated energy surfaces encounters special problems due to artificial charge allocations in the corresponding gas phase calculations and the strength of many-body effects. Thus for such systems the possibility to work without solute–solvent potentials and to consider all charge transfer effects in an *n*-body calculation in every step of the simulation as provided by the QMCF MD method is of great advantage. The examples illustrating this capability are the ions Be(II) with the smallest charge/radius relation, Al(III), and one of the few cations present in +4 form in water, U(IV). All of them show a stable first hydration shell with 4, 6, and 9 water ligands in the cases of Be(II), Al(III) and U(IV), respectively. Despite the strong polarization power of the ions, the second shell shows fast exchange processes and thus a considerably broad CND. Both Be(II) and Al(III) show a structural influence on the solvent even beyond the second shell. This influence is not visible as a distinct third shell in the RDF, but can be proven by the comparison of water triples beyond the second shell compared to the bulk water structure (*62*,*63*). The comparison of these strongly polarizing ions finally characterizes Al(III) as the strongest known polarizing ion in aqueous solution. This can be deduced from the dynamical data, in particular from the very long MRT value for the second hydration shell of Al(III) and the large force constant for the Al–O vibration. The small ions keep their second shell in an apparently quite stable structure, as many exchange attempts are needed for a successful ligand move. The heavier and larger U(IV) ion does not show this effect to a significant extent; the number of attempts needed is similar to that of pure water.

The study of composite cations encounters further problems for classical and conventional QM/MM simulations, as their lower symmetry makes the evaluation of interaction energy surfaces and analytical potential functions describing them difficult. In these cases the QMCF MD method provides an elegant solution as well, renouncing solute–solvent potential functions. This advantage could be well demonstrated in studies on the dimer of Hg(I) (*39*), the titanyl ion (*64*), and the uranyl ions of U(V) (*65*) and U(VI) (*66*). Whereas the Hg_2^{2+} ion still has a fairly regular hydration structure although with a quite peculiar shape, the

TABLE III

COMPOSITE CATIONS: MEAN LIGAND RESIDENCE TIMES $J_{0.5}$ IN PS DETERMINED BY QMCF MD SIMULATIONS (Hg_2^{2+}.1ST SHELL, OTHER IONS AT OXYGEN SITES)

Cation	$\tau_{0.5}^{1sh}$	$\tau_{0.5}^{O}$	Ref.
Hg_2^{2+}	3.0	—	(*39*)
TO^{2+}	n.a.	3.6	(*64*)
UO_2^{+}	n.a.	2.2	(*65*)
UO_2^{2+}	n.a.	2.5	(*66*)

TiO^{2+} ion shows a tightly bound hydration on the Ti side with five water ligands, and a very labile hydration on the O side, where exchange processes occur with the same speed as in the second hydration shell of the Ti side (Table III). Strong charge fluctuations between Ti and O atoms demonstrate the importance of the continuous charge evaluation in the QMCF MD simulation for the evaluation of Coulombic interaction energies. In the case of the Uranyl ions a regular planar hydration structure perpendicular to the O–U–O axis with four (U(V)) and five (U(VI)) stably bound ligands is observed (Table IV). Water ligands bound to the oxygen atoms of the ions are very flexible and thus responsible for a rapid ligand exchange. The simulation of these heavy ions has also proven that the chosen *ab initio* method for the QM region, connected with relativistically corrected ECPs, is suited for virtually all elements of the periodic system.

TABLE IV

HYDRATION STRUCTURE PARAMETERS FOR COMPOSITE CATIONS DETERMINED BY QMCF MD SIMULATIONS[a]

Cation	r_M	$r_M(O\cdots H)$	CND_{1sh}	CN_O	Ref.
Hg_2^{2+}	2.4	–	3.7	–	(*39*)
TiO^{2+}	2.1	–	5	0.7	(*64*)
UO_2^{+}	2.51	2.0	4	1.2	(*65*)
UO_2^{2+}	2.49	2.2	5	0.5	(*66*)

[a] First and second peak maximum ion-O RDF r_{M1}, r_{M2} in Å. CND and average value in brackets for the first CND_{1sh} coordination sphere.

For most of the systems discussed here as well as for the anions presented below, visualizations in the form of video clips have been produced and are freely available from the site www.molvision.com (*67*).

Another interesting subject in the application of QM simulations, in particular the QMCF MD method, was the study of metal–ion complexes with other ligands than water in aqueous solution. The complexes of Ni(II) (*68–70*), Cu(II) (*69–71*), and Zn (II) (*69,70,72,73*) with an increasing number of ammonia ligands serve as a model for complexes with *N*-coordinated ligands in general. The common feature observed besides specific structural rearrangements is an increase of the water ligand exchange rates by orders of magnitude as a function of the number of ligands binding via nitrogen to the metal ion. This can be seen from MRT values accessible through simulations of 10–20 ps for the remaining water ligands in the amine complexes, after one or more ammonia ligands are attached to the metal–ion. From these model simulations one can predict that such metal–ion complexes with larger *N*-binding ligands should enable faster first shell exchange processes for O-binding ligands.

B. Hydrated Anions and Neutral Molecules

Anions in water also form hydrate complexes, but of an entirely different chemical nature than cations. The central binding mechanism between the ions and the solvent is — besides weak electrostatic interactions — the formation of hydrogen bonds and thus the interplay between solute–solvent and solvent–solvent interactions via such bonds. Hydrogen bonding also means that the ion–solvent interactions are much weaker than typical cation–solvent binding energies. This weakness of interactions is also a challenge with respect to the QM calculation method employed and to the level of basis sets needed. Besides anions also neutral molecules dissolved in water can interact with the solvent via hydrogen bonds and some typical examples will be presented, therefore, in the same section as the anions. As examples for the anions the tetrahedral oxoanions ClO_4^-, SO_4^{2-}, and PO_4^{3-} have been chosen; HF and HCl represent typical acids and CO_2 and $HCONH_2$ neutral molecules with the possibility to form hydrogen bonds to the solvent. The structural and dynamical data resulting from QMCF MD simulations of these species in water are collected in Tables V–VIII, respectively.

At this point it has to be mentioned that *ab initio* calculations at the HF level are not ideal for the study of hydrogen-bonded

TABLE V

HYDRATION STRUCTURE PARAMETERS FOR COMPOSITE ANIONS DETERMINED BY QMCF MD SIMULATIONS[a]

Anion	r_M(O··· H)	r_M(H ··· O)	CND_H	CND_O	Ref.
PO_4^{3-}	1.75	–	–	2.8–4 (3.3)	(*41,92,93*)
SO_4^{2-}	1.97	–	–	2–3.5 (2.8)	(*42,43,92*)
ClO_4^-	2.17	–	–	1–4 (2.5)	(*41,92*)
HCO_3^-	1.9	1.6–2.6	0–1 (0.3)	0–4 (2.1)	(*94*)
$HAsO_4^{2-}$	1.7	1.3–2.8	1–2(1.1)	2–3(2.5)	(*95*)

[a] Peak maxima for hydrogen bonds ion-H r_{M1}, r_{M2} in Å. CND and average values in brackets for water–ion coordination.

TABLE VI

MRTS $\tau^{0.5}$ IN PS AND THE RATIO OF ATTEMPTED AND SUCCESSFUL EXCHANGE PROCESSES, R_{EX} (AVERAGE FOR ALL COORDINATION SITES). $\tau_O^{0.5}$, $\tau_{OH}^{0.5}$ DENOTE THE MRTS AT NON-PROTONATED AND THE PROTONATED OXYGEN SITES IN PS

Anion	$\tau^{0.5}$	R_{ex}^a	$\tau_O^{0.5}$	$\tau_{OH}^{0.5}$	Ref.
PO_4^{3-}	3.9	3.1	n.a.	n.a.	(*41,92,93*)
SO_4^{2-}	2.6	7.4	n.a.	n.a.	(*42,43,92*)
ClO_4^-	1.5	5.2	n.a.	n.a.	(*41,92*)
HCO_3^-	1.6	15.3	1.0	0.8	(*94*)
$HAsO_4^{2-}$	1.9	11.2	1.5	0.5	(*95*)

TABLE VII

HYDRATION STRUCTURE PARAMETERS FOR NEUTRAL MOLECULES DETERMINED BY QMCF MD SIMULATIONS[a]

Solute	r_{M1}	CND_1(av) H	Ref.
CO_2 (O)	2.1	0–2 (0.6)	(*79*)
HCON H_2(O)	2.0	0–4 (2.05)	(*96*)
HCON H_2(Hc)	2.2	0–3 (0.83)	(*96*)
HCON H_2(Ht)	2.1	0–2 (0.89)	(*96*)
HF (F)	2.0	3–9 (5.6)	(*97*)
HF (H)	1.62	1.0	(*97*)
HCl (Cl)	3.51	7–16 (12)	(*81*)
HCl (H)	1.84	1.0	(*81*)

[a] r_{M1} denotes the peak of RDF for acceptor–donor H bond distances and their coordination number and average in brackets CND_1 (av).

TABLE VIII

MRTs of Coordinated Water Molecules in Ps for Donor and Acceptor Sites

	$\tau^{0.5}$	Ref.
CO_2 (O)	2.0	(*79*)
$HCONH_2$ (O)	0.95	(*96*)
$HCONH_2$ (Hc)	1.0	(*96*)
$HCONH_2$ (Ht)	1.5	(*96*)
HF (F)	2.1	(*81*)
HF (H)	2.5	(*81*)
HCl (Cl)	2.1	(*97*)
HCl (H)	0.8	(*97*)

systems, as they usually deliver too long bond distances associated with a slightly too weak binding energy. However, comparisons with correlated *ab initio* methods haven proven that they still work considerably better than DFT methods, which predict much too rigid H bonds (*13,14,17,74*). As procedures like MP/2 and higher are still prohibitively computer time consuming, HF remains the only possible compromise at this time.

The data obtained by any simulation technique for pure water are important for a comparison of hydrogen bonding. A QMCF MD simulation of pure water predicts that each water molecule forms in average two stronger hydrogen bonds and one to three further hydrogen bonds, which are less stable due to an unfavorable geometrical arrangement of water molecules in the immediate neighborhood. This is in good agreement with several experimental studies (*4,75–78*) and the average lifetime of the water–water hydrogen bonds resulting as 0.5 ps agrees well with the value obtained by femtosecond laser pulse spectroscopy (*3–5*). The MRT of a water in the first coordination shell of another one resulted as 1.3 ps, which serves as a reference value for the stability of hydration of anions and neutral molecules.

The comparison of the tetrahedral oxoanions clearly shows the influence of negative charge: phosphate forms a large and more stable hydration shell than sulfate and perchlorate, but due to rapid exchanges, the coordination number still varies considerably. The reduced charge of the sulfate ion leads to a lower average coordination number and a shorter MRT of the ligands. This trend is continued in the case of the monovalent perchlorate, whose mean ligand residence time is so similar to water that it can almost be considered as structure breaking. This weak

hydrogen bonding causes an extremely large variation of the number of water molecules coordinated to this anion. The number of exchange attempts needed for a successful event does not follow the trend of the charges: the least number is needed in the case of phosphate and the largest number for sulfate. This is probably a consequence of two opposite trends, namely the number of incoming ligands in a suitable orientation to form an additional stable hydrogen bond and the average number of ligands available in the set of hydrate species.

Two more anions have been included in this comparison, as they particularly demonstrate the capability of the new simulation technique, namely hydrogen carbonate and hydrogen arsenate. These anions are characterized by a high asymmetry and the presence of different binding sites for hydrogen bonding, oxygen atoms, and an OH group. It is evident that the construction of a suitable potential function for the interaction with water would be a most difficult and tedious, if not unfeasible, task while their treatment by the QMCF method is straightforward.

Already the structural parameters obtained for hydrogen carbonate and hydrogen arsenate ions in Table V reveal quite some peculiarities resulting from composition and symmetry of these species. Despite the low charge the H bond distance from water to the oxygen atoms is relatively short, while the number of O-coordinating water molecules is lower than for the tetraoxoanions with the same charge. The OH hydrogen also coordinates water molecules within a wide variation of distances, 0.3 in average in the case of the monovalent HCO_3^- ion and 1.1 in that of the divalent $HAsO_3^{2-}$. The overall MRTs for the complete first hydration shell of these anions are similar to that of the perchlorate ion, indicating only a weak structure-forming ability (cf. Table VI). These values include also water molecules below and above the molecular plane of hydrogen carbonate and in the interstitial regions of hydrogen arsenate, and, therefore, an analysis of the ligand MRT for the different coordination sites was carried out. It leads to values below the pure water reference value for both sites in HCO_3^- and for the OH hydrogen of $HAsO_4^{2-}$, classifying all of these as clearly structure breaking. Even the value of 1.5 for the oxygen sites of hydrogen arsenate is the same as for perchlorate and hence not an indication for a significant kinetic stabilization. On the other hand the amount of exchange attempts needed to achieve a replacement of a water ligand is remarkably high in both cases, and it suggests that a lower symmetry of the solute can have a considerable influence on this parameter, partly compensating the lability of hydrogen bonding. The particular high

R_{ex} value of HCO_3^- is affirmative for this conclusion. Differences between coordination sites in less symmetric solutes will also be shown in the subsequent paragraph.

Not only anions, but also polar neutral molecules can be stabilized in aqueous environment by hydrogen bonding, and two examples have been chosen to demonstrate the capability of *ab initio* QMCF MD simulations for this class of compounds. One is carbon dioxide, which is of eminent importance for growth of plants and production of oxygen and which has become a specific issue in the climate debate; the other one formamide, which itself is a good solvent, but also an important model compound for peptide bonds with different coordination sites acting as hydrogen bond acceptor and donor, respectively. Due to the size of the solutes, the QM region (core plus layer) is considerably larger than in the case of simple ions, similar to that of the composite anions. Two more neutral molecules studied were the acids HF and HCl, because of their fundamental importance in inorganic chemistry and their differences in acid strength.

Some structural results of the QMCF MD simulations of the hydrated neutral molecules in an elementary box containing 1000 water molecules are collected in Table VII, and Table VIII summarizes dynamical data from these simulations. The data selected for this presentation are all focused on water coordination and hydrogen bonding.

CO_2 oxygens form up to 2 H bonds to solvent molecules, but in average only 0.6 per oxygen. These bonds are thermodynamically less stable than the water–water H bonds (*17,74*), thus explaining the volatility of the gas molecule in aqueous solution, but the MRT value for water coordinated to CO_2 is significantly higher than that of pure water, indicating a kinetic stabilization of the hydrate of carbon dioxide. The QMCF MD simulation (*79*) has also revealed a rather marginal role of CO_2 compared to water for the IR absorption spectrum of CO_2 in water aerosols or droplets, which should be considered in the discussion of the relative importance of both components as "greenhouse gases," in particular as Solomon and coworkers (*80*) have recently highlighted the importance of stratospheric water vapor for decadal rates of warming and the need for a closer examination of the representation of stratospheric water vapor changes in climate models.

In formamide, all sites except H–C form H bonds (cf. Fig. 3), but the number of them is quite flexible. Oxygen can coordinate the largest number of water ligands, the NH hydrogens show different properties, as the *cis* hydrogen competes with oxygen for water ligands, which leads to a slightly lower average

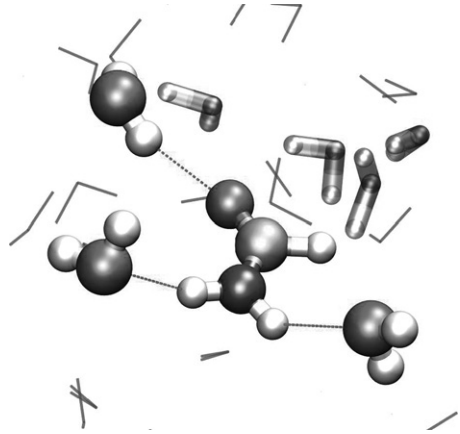

FIG. 3. Formamide coordination environment snapshot taken from a QMCF MD simulation.

coordination number and a slightly larger H–O distance. On the other hand, the ligands coordinated to the *trans* hydrogen have the longest MRT slightly higher than for pure water whereas the MRT values of O and H(*cis*) are below that of pure water, which means an increased mobility of water molecules in their neighborhood.

The two acids HF and HCl differ in many aspects. While both of them form only one H bond to a water molecule with their hydrogen atoms, the coordination of water molecules to the halogen atom is strongly different, both in the CND range and in the average number of ligands. Water molecules at these sites are stabilized in both cases (MRT value higher than pure water), but the different properties of the two acids are well reflected in the stability of H bonds between the acid hydrogen and water. In the case of HF this bond is clearly stabilized over water–water H bonds, while the coordination of water to H of hydrochloric acid is highly labile. This lability coincides with the observation of several proton transfer attempts from HCl to the H-coordinated water (*81*), and with a longer simulation time than 10 ps one could certainly observe the dissociation process to chloride and a hydronium ion. Such attempted proton transfer reactions were not observed for HF in water within the same simulation time, well reflecting the stronger acidity of HCl compared to HF. In the following section, other systems will be presented, where proton transfer reactions occur already on the subpicosecond timescale.

C. Hydrolysis Processes

The dynamics of solutions not only does include the formation and dissociation of species, but can lead to reactions forming new species by formation and cleavage of chemical bonds, thus leading to molecules and/or ions not present in the original elementary box. To describe such processes is evidently only possible if the components involved are fully described by quantum mechanics or if very specific "reactive potentials" are known (*82,83*). To create such potentials is not only a very difficult and delicate task, it also requires an *a priori* knowledge of all possible new species evolving during the reactions, whereas quantum mechanics covers all possible and thus also before unknown processes. The large QM region of QMCF MD simulations enables the description of such reactions in a quite straightforward and convenient way, as no potential functions except those for solvent–solvent interactions are needed and the movements of species are correctly described as long as they do not come close to the QM/MM border.

Hydrolysis is a very common process in solution chemistry, and it is observed for cations as well as for anions. For each case an example is presented here, As^{3+} for cation hydrolysis and AsO_4^{3-} for the anionic analog. In both cases the hydrolysis reaction leading to hydronium and hydroxyl ions, respectively, occurs on the subpicosecond range, which makes an experimental investigation of them almost unfeasible.

As^{3+} captures in two subsequent steps two OH^- groups from first shell water molecules, forming the $As(OH)_2^+$ cation and releasing two protons into the solution, which immediately combine with water molecules to form hydronium ions (*84*). Figure 4 depicts these processes by means of distance plots, and they are further illustrated by a video clip available at the site www.molvision.com.

AsO_4^{3-} captures one proton from an adjacent water ligand, and the hydroxyl ion formed interacts with other solvent molecules, forming water and releasing another ion, while the arsenate transforms to the apparently stable hydrogen arsenate discussed previously. The speed of the migrations of the proton and the hydroxyl ion in water confirms an early assumption that the high electric conductance of aqueous solutions is based on a rapid interconversion of hydronium and hydroxyl ions to water molecules generating new ions of the same type from the interacting solvent molecules (*85*). Figure 5 illustrates the hydrolysis reaction of the arsenate ion, and for this system a video clip is also available from the same site listed above.

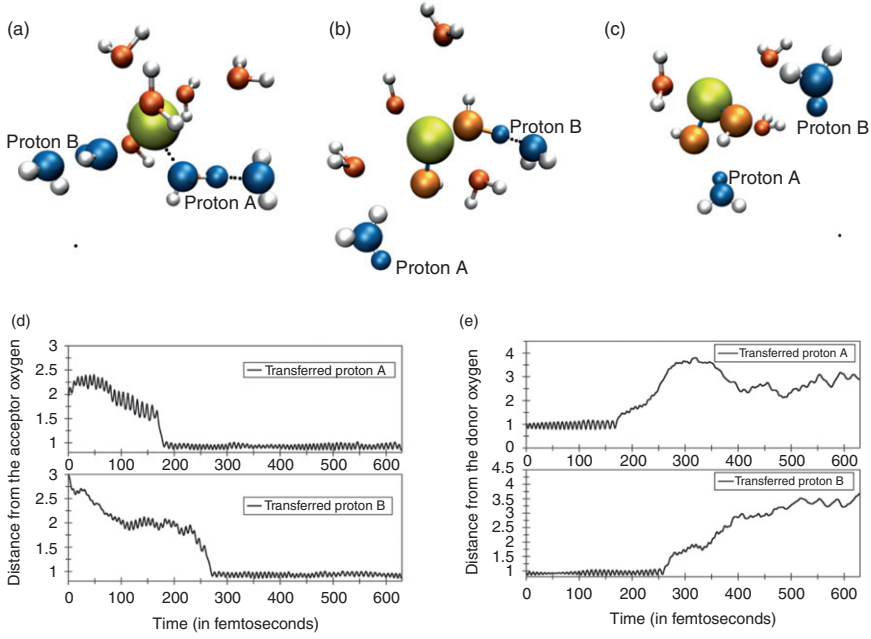

FIG. 4. (a) and (b) The hydrolysis event, depicting the transfer of the protons (marked as protons A and B) to the neighboring waters. (c) The resulting $As(OH)_2^+$ with the two nascent H_3O^+ ions. (d) and (e) The distance of the transferred protons A and B from the donor and acceptor oxygen atoms, respectively.

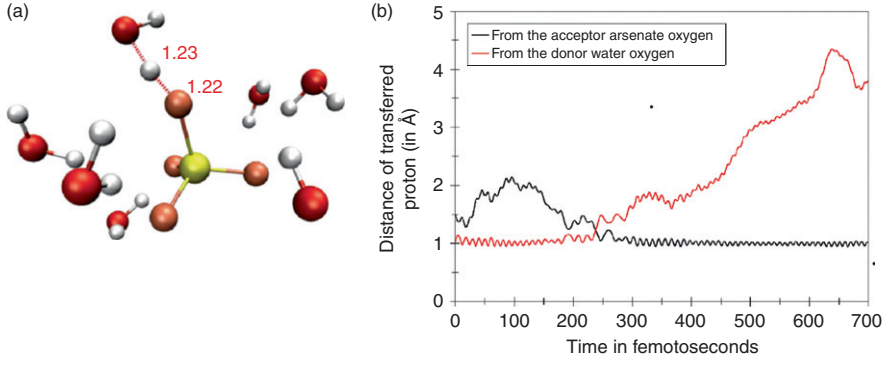

FIG. 5. (a) The intermediate of the proton transfer from the water to arsenate oxygen atom. (b) The plot of the distance of the transferred proton from the donor water oxygen and acceptor arsenate oxygen.

IV. Conclusions

The variety of examples presented here can be seen as good evidence that simulations have become a valuable, partly indispensiable tool for the study of chemicals in solution. The inclusion of *ab initio* QM procedures for the calculation of forces in every step of the simulation ensures the necessary accuracy of the simulation results to predict both structural and dynamical data, thus also providing a correct picture of the molecular and supermolecular species formed simultaneously in solution. The recently developed QMCF MD methodology has overcome several of the previous problems of MD simulations, mostly not only because of the possibility to renounce any kind of empirical or fitted solute–solvent potentials, but also because of an improved embedding scheme and the use of actual atom populations for the calculation of Coulombic forces. Besides its universality of application to various chemical compounds it also offers a straightforward way of further improvement and method-inherent quality control by the employment of correlated *ab initio* methods, although at a price which is not yet affordable with present computational facilities, but should become feasible within a few years.

The accuracy achieved through *ab initio* quantum mechanics and the capabilities of simulations to analyze structural elements and dynamical processes in every detail and separately from each other have not only made the simulations a valuable and sometimes indispensable basis for the interpretation of experimental studies of systems in solution, but also opened the access to hitherto unavailable data for solution processes, in particular those occurring on the picosecond and subpicosecond timescale. The possibility to visualize such ultrafast reaction dynamics appears another great advantage of simulations, as such visualizations let us keep in mind that chemistry is mostly determined by systems in continuous motion rather than by the static pictures we are used to from figures and textbooks. It can be stated, therefore, that modern simulation techniques have made computational chemistry not only a universal instrument of investigation, but in some aspects also a frontrunner in research. At least for solution chemistry this seems to be recognizable from the few examples presented here, as many of the data would not have been accessible with contemporary experimental methods.

Acknowledgment

Financial support for this work provided by the Austrian Science Fund (FWF) is gratefully acknowledged.

References

1. Rotzinger, F. P. *Chem. Rev.* **2005**, *105*, 2003.
2. Cramer, C. J.; Truhlar, D. G. *Chem. Rev.* **1999**, *99*, 2161.
3. Dantus, M.; Rosker, M. J.; Zewail, A. H. *J Chem. Phys.* **1987**, *87*, 2395–2397.
4. Fecko, C.; Eaves, J.; Loparo, J.; Makoff, A. T.; Geissler, P. *Science* **2003**, *301*, 1698–1702
5. Schreiber, E. "*Femtosecond Real-Time Spectroscopy of Small Molecules and Clusters(Environmental Intelligence Unit)*"; Springer: Berlin, **1998**.
6. Clementi, E.; Corongui, G. *Int. J. Quant. Chem., Symp*. **1983**, *10*, 31.
7. Detrich, J. H.; Clementi, E.; Corongui, G. *Chem. Phys. Lett.* **1984**, *112*, 426.
8. Yu, H.; van Gunsteren, W. F. *Comp. Phys. Commun.* **2005**, *172*, 69–85.
9. Car, R.; Parrinello, M. *Phys. Rev. Lett.* **1985**, *55*(22), 2471–2474.
10. Becke, A. D. *Phys. Rev. A.* **1988**, *38*(6), 3098–3100.
11. Perdew, J. P.; Burke, K.; Ernzerhof, M. *Phys. Rev. Lett.* **1996**, *77*, 3865.
12. Perdew, J. P.; Burke, K.; Ernzerhof, M. *Phys. Rev. Lett.* **1997**, *78*, 1396.
13. Schmidt, J.; VandeVondele, J.; Kuo, I.; Sebastiani, D.; Siepmann, J.; Hutter, J.; Mundy, C. J. *J. Phys. Chem. B* **2009**, *113*,11959–11964.
14. Yoo, S.; Zeng, X. C.; Xantheas, S. *J. Chem. Phys.* **2009**, *130*, 221102.
15. Becke, A. D. *J. Chem. Phys.* **1993**, *98*(7), 5648–5652.
16. Xenides, D.; Randolf, B. R.; Rode, B. M. *J. Chem. Phys.* **2005**, *122*, 4506.
17. Xenides, D.; Randolf, B. R.; Rode, B. M. *J. Mol. Liquids*, **2006**, *123*, 61.
18. Rode, B. M.; Schwenk, C. F.; Hofer, T. S.; Randolf, B. R. *Coord. Chem. Rev.* **2005**, *249*, 2993.
19. Rode, B. M.; Hofer, T. S. *Pure Appl. Chem.* **2006**, *78*, 525.
20. Hofer, T. S.; Pribil, A. B.; Randolf, B. R. *Pure Appl. Chem*. **2008**, *80*, 1195–1210.
21. Lin, H.; Truhlar, D. G. *Theor. Chim. Acta* **2007**, *117*, 185.
22. Warshel, A.; Levitt, M. *J. Mol. Biol.* **1976**, *103*, 227.
23. Field, M. J.; Bash, P. A.; Karplus, M. *J. Comp. Chem.* **1990**, *11*(6), 700–733.
24. Gao, J. *J. Am. Chem. Soc.* **1993**, *115*, 2930–2935.
25. Bakowies, D.; Thiel, W. *J. Phys. Chem.* **1996**, *100*(25), 10580–10594.
26. Rode, B. M.; Hofer, T. S.; Randolf, B. R.; Schwenk, C. F.; Xenides, D.; Vchirawongkwin, V. *Theor. Chim. Acta* **2006**, *115*, 77.
27. Hofer, T. S.; Randolf, B. R.; Rode, B. M. In: "*Challenges and Advances in Computational Chemistry and Physics*"; vol. 6; Ed. Canuto, S.; Molecular Dynamics Simulation Methods Including Quantum Effects. Springer: Heidelberg, **2008**.
28. Allen, M. P.; Tildesley, D. J. "*Computer Simulation of Liquids*"; Oxford Science Publications: Oxford, **1990**.
29. Hockney, R.; Eastwood, J. W. "*Computer Simulation using Particles*"; Taylor & Francis: New York, **1988**.
30. Heyden, A.; Lin, H.; Truhlar, D. G. *J. Phys. Chem. B* **2007**, *111*, 2231.
31. Kerdcharoen, T.; Morokuma, K. *Chem. Phys. Lett*. **2002**, *335*, 257.
32. Bulo, R. E.; Ensing, B.; Sikkema, J.; Visscher, L. *J. Chem. Theory Comput*. **2009**, *5*(9), 2212–2221.
33. Buehler, M. J.; van Duin, A. C. T.; Goddard III, W. A. *Phys. Rev. Lett*. **2006**, *96*, 095505.
34. Hofer, T. S.; Pribil, A. B.; Randolf, B. R.; Rode, B. M. *Adv. Quant. Chem*. **2010**, *59*, 213.
35. Laio, A.; VandeVondele, J.; Rothlisberger, U. *J. Chem. Phys*. **2002**, *116*, 6941.
36. Voloshina, E.; Gaston, N.; Paulus, B. *J. Chem. Phys*. **2007**, *126*, 134115.
37. Kästner, J.; Thiel, S.; Senn, H. M.; Sherwood, P.; Thiel, W. *J. Chem. Theory Comput* **2007**, *3*(3), 1064–1072.

38. Fatmi, M. Q.; Hofer, T. S.; Randolf, B. R.; Rode, B. M. *J. Comp. Chem*. **2007**, *28*, 1704.
39. Hofer, T. S.; Randolf, B. R.; Rode, B. M. *Chem. Phys*. **2008**, *349*, 210.
40. Hofer, T. S.; Randolf, B. R.; Shah, S. A. A.; Rode, B. M.; Persson, I. *Chem. Phys. Lett*. **2007**, *445*,193.
41. Hofer, T. S.; Randolf, B. R.; Rode, B. M. *Chem. Phys*. **2008**, *346*, 182.
42. Vchirawongkwin, V.; Persson, I.; Rode, B. M. *J. Phys. Chem. B* **2007**, *111*, 4150.
43. Vchirawongkwin, V.; Rode, B. M. *J. Phys. Chem*. **2007**, *10*, 1016.
44. Kutzelnigg, W. In: "*Trends and Perspectives in Modern Computational Science*"; Eds. Maroulis, G.; Simos, T.; International Science Publishers (VSP): Leiden, **2006**, p. 23.
45. Bartlett, R. J.; Schweigert, I. V.; Lotrich, V. F. *J. Mol. Struct. (Theochem.)* **2006**, *764*, 33.
46. Bartlett, R. J.; Lotrich, V. F.; Schweigert, I. V. *J Chem. Phys*. **2005**, *06*, 2205.
47. Hofer, T. S.; Randolf, B. R.; Rode, B. M. *Phys. Chem. Chem. Phys*. **2005**, *7*, 1382.
48. Hofer, T. S.; Randolf, B. R.; Rode, B. M. *J. Comp. Chem*. **2005**, *26*, 949.
49. Hofer, T. S.; Rode, B. M. *J. Chem. Phys*. **2004**, *121*, 6406.
50. ofer, T. S.; Rode, B. M.; Randolf, B. R. *Chem. Phys*. **2005**, *312*, 81.
51. Hofer, T. S.; Pribil, A. B.; Randolf, B. R.; Rode, B. M. *J. Am. Chem. Soc*. **2005**, *127*, 14231.
52. Schwenk, C. F.; Hofer, T. S.; Rode, B. M. *J. Phys. Chem. A* **2004**, *108*, 1509.
53. Hofer, T. S.; Scharnagl, H.; Randolf, B. R.; Rode, B. M. *Chem. Phys*. **2006**, *327*, 31.
54. Hofer, T. S.; Randolf, B. R.; Rode, B. M. *J. Phys. Chem. B* **2006**, *110*, 20409.
55. Stone, A. J. "*The Theory of Intermolecular Forces*"; Oxford University Press: Oxford, **1995**.
56. Kerdcharoen, T.; Liedl, K. R.; Rode, B. M. *Chem. Phys*. **1996**, *211*, 313–323.
57. Hofer, T. S.; Tran, H. T.; Schwenk, C. F.; Rode, B. M. *J. Comp. Chem*. **2004**, *25*, 211–21.
58. Martinez, J. M.; Torrico, F.; Pappalardo, R. R.; Marcos, E. S. *J. Phys. Chem. A* **2004**, *108*, 15851.
59. Torrico, F.; Pappalardo, R. R.; Marcos, E. S.; Martinez, J. M. *Theor. Chim. Acta* **2006**, *115*, 196–203.
60. Hofer, T. S.; Randolf, B. R.; Rode, B. M.; Persson, I. *J. Chem. Soc., Dalton Trans*. **2009**, 1512–1515
61. Hofer, T. S.; Scharnagl, H.; Randolf, B. R.; Rode, B. M. *Chem. Phys*. **2006**, *327*, 31–42.
62. Azam, S. S.; Hofer, T. S.; Bhattacharjee, A.; Lim, L. H. V.; Pribil, A. B.; Bernhard, R. B.; Rode, B. M. *J. Phys. Chem. B* **2009**.
63. Bhattacharjee, A.; Hofer, T. S.; Rode, B. M. *Phys. Chem. Chem. Phys*. **2008**, *10*, 6653–6657.
64. Fatmi, M. Q.; Hofer, T. S.; Randolf, B. R.; Rode, B. M. *J. Comp. Chem*. **2007**, *28*, 1704.
65. Frick, R. J.; Hofer, T. S.; Pribil, A. B.; Randolf, B. R.; Rode, B. M. *Phys. Chem. Chem. Phys*. **2010**, DOI: 10.1039/c003169k.
66. Frick, R. J.; Hofer, T. S.; Pribil, A. B.; Randolf, B. R.; Rode, B. M. *J. Phys. Chem. A* **2009**, *113*, 12496–12503.
67. Tran, H. T.; Rode, B. M. http://www.molvision.com, **2002**
68. Schwenk, C. F.; Hofer, T. S.; Randolf, B. R.; Rode, B. M. *Phys. Chem. Chem. Phys*. **2005**, *7*, 1669.

69. Rode, B. M.; Hofer, T. S. *Pure Appl. Chem*. **2006**, *78*, 525–539.
70. Hofer, T. S.; Pribil, A. B.; Randolf, B. R. *Pure Appl. Chem*. **2008**, *80*(6), 1195–1210.
71. Schwenk, C. F.; Rode, B. M. *Phys. Chem. Chem. Phys*. **2003**, *5*, 3418.
72. Fatmi, M. Q.; Hofer, T. S.; Randolf, B. R.; Rode, B. M. *Phys. Chem. Chem. Phys*. **2006**, *8*, 1675.
73. Fatmi, M. Q.; Hofer, T. S.; Randolf, B. R.; Rode, B. M. *J. Phys. Chem. B* **2007**, *111*, 151.
74. Xenides, D.; Randolf, B. R.; Rode, B. M. *J. Chem. Phys*. **2005**, *122*(17), 17450601–17450610.
75. Bakker, H.; Woutersen, S.; Nienhuys, H. *Chem. Phys*. **2000**, *258*, 233–245.
76. Head-Gordon, T.; Hura, G. *Chem. Rev*. **2002**, *102*, 2651–2670.
77. Myneni, S.; Luo, Y.; Nslund, L.; Cavalleri, M.; Ojamae, L.; Ogasawara, H.; Pelmenschikov, A.; Wernet, P.; Vterlein, P.; Heske, C.; Hussain, Z.; Pettersson, L.; Nilsson, A. *J. Phys.: Condens. Matter* **2002**, *14*, 213–219.
78. Lock, A.; Bakker, H. *J. Chem. Phys*. **2002**, *117*(4), 1708–1715.
79. Moin, S. T.; Pribil, A. B.; Lim, L. H. V.; Hofer, T. S.; Randolf, B. R.; Rode, B. M. *Int. J. Quant. Chem*. **2010**, DOI: 10.1002/qua.22640.
80. Solomon, S.; Rosenlof, K.; Lim, L. H. V.; Hofer, T. S.; Randolf, B. R.; Rode, B. M. *Int. J. Quant. Chem.* **2010**, *327*, 1219–1223.
81. Kritayakornupong, C.; Vchirawongkwin, V.; Hofer, T. S.; Rode, B. M. *J. Phys. Chem. B* **2009**, *112*(38), 12032–12037.
82. van Duin, A. C. T.; Dasgupta, S.; Goddard III, W. A. *J. Phys. Chem. A* **2001**, *105*, 9396.
83. Mahadevan, T. S.; Garofalini, S. H. *J. Phys. Chem. B* **2007**, *111*, 8919.
84. Bhattacharjee, A.; Hofer, T. S.; Pribil, A. B.; Randolf, B. R.; Rode, B. M. *Chem. Phys. Lett*. **2009**, *473*(1–3), 176–178.
85. Bhattacharjee, A.; Hofer, T. S.; Pribil, A. B.; Randolf, B. R.; Rode, B. M. *Chem. Phys. Lett*. **2010**, *12*(23), 6244–6246.
86. Azam, S. S.; Lim, L. H. V.; Hofer, T. S.; Randolf, B. R.; Rode, B. M. *J. Comp. Chem*. **2010**, *31*(2), 278–285.
87. Azam, S. S.; Hofer, T. S.; Randolf, B. R.; Rode, B. M. *Chem. Phys. Lett*. **2009**, *470*, 85–89.
88. Lim, L. H. V.; Hofer, T. S.; Pribil, A. B.; Rode, B. M. *J. Phys. Chem. B* **2009**, *113*, 4372–4378.
89. Bhattacharjee, A.; Hofer, T. S.; Pribil, A. B.; Randolf, B. R.; Lim, L. H. V.; Lichtenberger, A. F.; Rode, B. M. *J. Phys. Chem. B* **2009**, *113*, 13007–13013.
90. Hofer, T. S.; Randolf, B. R.; Rode, B. M. *J. Phys. Chem. B* **2008**, *112*(37), 11726–11733.
91. Frick, R. J.; Pribil, A. B.; Hofer, T. S.; Randolf, B. R.; Bhattacharjee, A.; Rode, B. M. *Inorg. Chem*. **2009**, *48*(9), 3993–4002.
92. Simos, T. E. (Ed.), "*Structure and Dynamics of Composite Anions in Aqueous Solution*"; American Institute of Physics (AIP): New York, **2007**.
93. Pribil, A. B.; Hofer, T. S.; Randolf, B. R.; Rode, B. M. *J. Comp. Chem*. **2008**, *29*(14), 2330–2334.
94. Vchirawongkwin, V.; Pribil, A. B.; Rode, B. M. *J. Comput. Chem*. **2010**, *31*(2), 249–257.
95. Bhattacharjee, A.; Pribil, A. B.; Lim, L. H. V.; Hofer, T. S.; Randolf, B. R.; Rode, B. M. *J. Phys. Chem. B* **2010**, *114*(11), 3921–3926.
96. Weiss, A. "*Hydrogen Bond Formation of Formamide and N-Methylformamide in aqueous solution, studied by Quantum Mechanical Charge Field Molecular Dynamics (QMCF-MD)*"; University of Innsbruck: Innsbruck, **2010**.
97. Kritayakornupong, C.; Vchirawongkwin, V.; Rode, B. M. *J. Comput. Chem*. **2010**, *31*(8), 1785–1792.

SPIN INTERACTIONS IN CLUSTER CHEMISTRY

MAREN PODEWITZ and MARKUS REIHER*

Laboratorium für Physikalische Chemie, ETH Zurich, Wolfgang-Pauli-Strasse 10, 8093 Zurich, Switzerland

I. Introduction

Inorganic clusters, especially when composed of open-shell transition-metal atoms, feature interesting molecular properties of technological importance. They may serve as molecular magnets, as reaction centers for complex chemical transformations, as quantum dots, or for the physical realization of quantum computer algorithms (*1–20,160*). While planning the synthesis of well-defined clusters is a challenge in itself, the theoretical design of clusters with given properties is one of the most interesting problems in contemporary theoretical chemistry.

THEORETICAL AND COMPUTATIONAL INORGANIC CHEMISTRY
VOLUME 62 ISSN 0898-8838 / DOI: 10.1016/S0898-8838(10)62005-3

The accurate quantum mechanical *first-principles* description of all interactions within a transition-metal cluster represented as a collection of electrons and atomic nuclei is a prerequisite for understanding and predicting such properties. The standard semi-classical theory of the quantum mechanics of electrons and atomic nuclei interacting via electromagnetic waves, i.e., described by Maxwell electrodynamics, turns out to be the theory sufficient to describe all such interactions (*21*). In semi-classical theory, the motion of the "elementary particles" of chemistry, i.e., of electrons and nuclei, is described quantum mechanically, while their electromagnetic interactions are described by classical electric and magnetic fields, $\boldsymbol{E}$ and $\boldsymbol{B}$, often represented in terms of the non-redundant four components of the 4-potential, namely the scalar potential ϕ and the vector potential $\boldsymbol{A}$.

The motion of elementary charged particles produces magnetic fields $\boldsymbol{B} = \nabla \times \boldsymbol{A} \equiv \mathrm{curl}\boldsymbol{A}$. Through the principle of minimal coupling these enter the interaction operators of the quantum mechanical Hamiltonian. It can then be shown, as we shall review, that the magnetic-field-dependent terms in the Hamiltonian contain all (electron) spin interactions within the molecule described by the Hamiltonian. The magnetic field generated by the nuclear spins is usually considered as a contribution to the external electromagnetic field as we shall see. A key to such spin interactions is necessarily a consistent relativistic formulation of quantum mechanics because all magnetic interactions vanish in the strict non-relativistic limit with infinite speed of light c.

In this review we shall first establish the theoretical foundations of the semi-classical theory that eventually lead to the formulation of the Breit–Pauli Hamiltonian. The latter is an approximation suited to make the connection to phenomenological model Hamiltonians like the Heisenberg Hamiltonian for the description of electronic spin–spin interactions. The complete derivations have been given in detail in Ref. (*21*), but turn out to be very involved and are thus scattered over many pages in Ref. (*21*). For this reason, we aim here at a summary that is as brief and concise as possible so that all relevant connections between different levels of approximation are evident. This allows us to connect present-day quantum chemical methods to phenomenological Hamiltonians and hence to establish and review the current status of these *first-principles* methods applied to transition-metal clusters.

A special focus will be on phenomenological Hamiltonians involving electronic spin interactions. For this it is necessary to define atomic surrogate spin operators—so-called local spin operators—that may be directly related to the effective spins in

the Heisenberg Hamiltonian or in the Spin Hamiltonian of magnetic resonance spectroscopies. Thorough insights into these concepts are mandatory to be able to model and predict chemical reactions catalyzed by transition-metal clusters and to understand decoherence effects in such clusters.

II. Theoretical Foundations

In quantum chemistry, the total energy E of a molecule can be calculated as an expectation value of its wave function Ψ and the energy operator—referred to as the Hamiltonian H,

$$E = \frac{\langle \Psi | H | \Psi \rangle}{\langle \Psi | \Psi \rangle} . \tag{1}$$

As the wave function Ψ is not known analytically for systems larger than a hydrogen-like atom, suitable approximate wave functions have to be found and the accuracy of Eq. (1) depends of course on the level of approximation. A survey of the various quantum chemical methods to generate approximated wave functions can be found in Refs. (*22,23*). Here, we shall only present the foundations of Hartree–Fock and density functional theory (DFT) needed in later sections.

The total wave function Ψ of a molecule comprising N electrons and M nuclei depends on $3N$ electronic coordinates $\{\boldsymbol{r}_i\}$ and all $3M$ nuclear coordinates $\{\boldsymbol{R}_I\}$. It can be approximated as a product of a nuclear wave function χ ($\{\boldsymbol{R}_I\}$) and an electronic wave function Ψ_{el} ($\{\boldsymbol{r}_i\}$),

$$\Psi(\{r_i\};\{\boldsymbol{R}_I\}) \approx \chi(\{\boldsymbol{R}_I\}) \cdot \Psi_{\text{el}}^{\{\boldsymbol{R}_I\}}(\{\boldsymbol{r}_i\}), \tag{2}$$

where the electronic wave function depends parametrically on the nuclear coordinates as indicated by the superscript to Ψ_{el}. In transition-metal cluster chemistry, we are often interested in the electronic part of the wave function only because it provides the electronic structure from which all molecular properties of the system can be calculated.

The most simple ansatz is to approximate this N-electron wave function by a product Ψ^{HP} of N one-electron functions ϕ_i ($\boldsymbol{r}$) (Hartree product of orbitals),

$$\Psi_{\text{el}}(\boldsymbol{r}_1,\boldsymbol{r}_2,\ldots,\boldsymbol{r}_N) \rightarrow \Psi^{\text{HP}} = \phi_1(\boldsymbol{r}_1)\phi_2(\boldsymbol{r}_2)\ldots\phi_N(\boldsymbol{r}_N), \tag{3}$$

where we omitted the superscript $\{\boldsymbol{R}_I\}$ for convenience.

Every fermionic wave function has to be antisymmetric when exchanging the coordinates of any two particles (Pauli principle) which is not fulfilled for a simple product ansatz as in Eq. (3). Therefore, we explicitly have to antisymmetrize the Hartree product Ψ^{HP} and obtain the Slater determinant:

$$\Psi_{\mathrm{el}} \approx \Psi^{\mathrm{SD}} = \hat{A}\,\Psi^{\mathrm{HP}}(\boldsymbol{r}_1,\boldsymbol{r}_2,\ldots,\boldsymbol{r}_N) = \hat{A}[\phi_1(\boldsymbol{r}_1)\phi_2(\boldsymbol{r}_2)\ldots\phi_N(\boldsymbol{r}_N)], \quad (4)$$

where $\hat{A}$ is the antisymmetrization operator,

$$\hat{A} = \frac{1}{\sqrt{N!}}\sum_{\nu=1}^{N!}(-1)^{\nu}P_{\nu} = \frac{1}{\sqrt{N!}}\left[1 - \sum_{ij}P_{ij} + \cdots\right], \quad (5)$$

and ν denotes all $N!$ permutations P_ν of coordinates. If the permutations are constructed from an even number of pair exchanges P_{ij}, ν is even—and odd otherwise.

In the most simple case of one pair of coordinates being interchanged the permutation operator P_{ij} acts as follows on a Hartree product:

$$P_{ij}[\phi_a(r_i)\phi_b(r_j)] = \phi_a(r_j)\phi_b(r_i). \quad (6)$$

Prior to choosing the wave-function approximation it is, however, necessary to set up the electronic Hamiltonian H that describes all interactions of elementary particles. Therefore, we start with the derivation of the full semi-classical many-electron Hamiltonian describing all interactions relevant for chemical problems and subsequently discuss approximations to this full-fledged quantum chemical Hamiltonian.

A. Relativistic Semi-Classical Many-Electron Hamiltonian

The many-particle Hamiltonian for a set of electrons and nuclei can be expressed as the sum of kinetic and pair-interaction operators,

$$H = T_{\mathrm{nuc}} + T_{\mathrm{el}} + V_{\mathrm{el-el}} + V_{\mathrm{el-nuc}} + V_{\mathrm{nuc-nuc}}. \quad (7)$$

which can be written as

$$\begin{aligned} H &= \sum_{I}^{M} h_{\mathrm{nuc}}(I) + \sum_{i}^{N} h^{D}(i) + \sum_{i>j}^{N} g(i,j) + V_{\mathrm{el-nuc}} + V_{\mathrm{nuc-nuc}} \\ &= H_{\mathrm{el}} + T_{\mathrm{nuc}}, \end{aligned} \quad (8)$$

where we have not absorbed the electron–nucleus interaction $V_{\mathrm{el-nuc}}$ in the one-electron operators $h^D(i)$. Under the assumption of

infinitely heavy nuclei Eq. (8) conveniently separates into an electronic Hamiltonian H_{el} and a vanishing nuclear part T_{nuc}. From now on we only consider the electronic Hamiltonian for a set of fixed nuclei.

For a quasi-relativistic framework as relevant to chemistry (*21*), we may neglect the magnetic retardation between the electrons and the nuclei and therefore employ standard Coulombic interaction operators for the electrostatic interaction. The interaction between the electrons and the nuclei is not specified explicitly but we only describe the interactions by some external 4-potential. For the sake of brevity this 4-potential shall comprise *all* external contributions. Explicit expressions for the interaction between electrons and nuclei will be introduced at a later stage. Furthermore, we can neglect the relativistic nature of the kinetic energy of the nuclei and employ the non-relativistic kinetic energy operator denoted as $h_{\mathrm{nuc}}(I)$,

$$h_{\mathrm{nuc}}(I) = \frac{\boldsymbol{p}_I^2}{2m_I} \,. \tag{10}$$

The second term in Eq. (8) denotes the sum of the relativistic one-electron Dirac Hamiltonians of moving electrons in some additional external electromagnetic field (ϕ_{ext}, $\boldsymbol{A}_{\mathrm{ext}}$),

$$h^{\mathrm{D}}(i) = c\boldsymbol{\alpha}_i \cdot \left(\boldsymbol{p}_i - \frac{q_{\mathrm{e}}}{c}\boldsymbol{A}_{\mathrm{ext}}\right) + (\beta_i - 1)m_{\mathrm{e}}c^2 + q_{\mathrm{e}}\phi_{\mathrm{ext}}. \tag{11}$$

$\boldsymbol{A}_{\mathrm{ext}}$ is the vector potential of the external field (yielding a magnetic field) and $c\boldsymbol{\alpha}_i$ the Dirac velocity operator. Here, $\boldsymbol{\alpha}_i$ is a vector of the three 4×4 Dirac matrices containing Pauli spin matrices $\boldsymbol{\sigma} = (\sigma_x, \sigma_y, \sigma_z)$, whereas β_i is the fourth 4×4 Dirac matrix. The charge of the electron is given by $q_{\mathrm{e}} = -e$, c is the speed of light, m_{e} the electron's rest mass, and $\boldsymbol{p}_i$ its momentum operator. As the one-electron Hamiltonian has a 4×4 structure the corresponding one-electron eigenfunction ψ must be of the same dimension. In the standard representation ψ is a vector of four functions called spinor. It is often split into an upper 2-spinor that is also referred to as the large component and indicated by the superscript L and a lower 2-spinor referred to as the small component marked by the superscript S,

$$\psi = \begin{pmatrix} \psi_1 \\ \psi_2 \\ \psi_3 \\ \psi_4 \end{pmatrix} = \begin{pmatrix} \psi^{\mathrm{L}} \\ \psi^{\mathrm{S}} \end{pmatrix}, \tag{12}$$

because of the 2×2 super-block structure of h^{D}. The one-electron Dirac equation in an external field may be written as

$$\mathrm{i}\hbar \frac{\partial}{\partial t}\psi = [c\boldsymbol{\alpha} \cdot \boldsymbol{\pi} + \beta m_{\mathrm{e}} c^2 + q_{\mathrm{e}}\phi_{\mathrm{ext}}]\psi, \tag{13}$$

when combining the momentum operator $\boldsymbol{p}$ and the external vector field in $\boldsymbol{\pi}$ (in Gaussian units used throughout),

$$\boldsymbol{p} \rightarrow \boldsymbol{\pi} = \boldsymbol{p} - \frac{q_e}{c}\boldsymbol{A}_{\mathrm{ext}}. \tag{14}$$

One may now write Eq. (13) in split notation,

$$\mathrm{i}\hbar \frac{\partial}{\partial t}\begin{pmatrix} \psi^{\mathrm{L}} \\ \psi^{\mathrm{S}} \end{pmatrix} = c\begin{pmatrix} (\boldsymbol{\sigma} \cdot \boldsymbol{\pi})\psi^{\mathrm{S}} \\ (\boldsymbol{\sigma} \cdot \boldsymbol{\pi})\psi^{\mathrm{L}} \end{pmatrix} + m_{\mathrm{e}}c^2\begin{pmatrix} \psi^{\mathrm{L}} \\ -\psi^{\mathrm{S}} \end{pmatrix} + V\begin{pmatrix} \psi^{\mathrm{L}} \\ \psi^{\mathrm{S}} \end{pmatrix}, \tag{15}$$

where we abbreviated $q_{\mathrm{e}}\phi_{\mathrm{ext}}$ by V.

The third term in Eq. (8) is the sum over all electron–electron repulsion operators abbreviated by $g(i, j)$, which is in the case of the relativistic many-electron Hamiltonian equal to

$$g(i,j) = V_{\mathrm{C}}(i,j) + \text{magnetic terms} + \text{retardation terms}, \tag{16}$$

with V_{C} being the instantaneous Coulomb interaction which is the correct electron–electron interaction in the case of $c \longrightarrow \infty$,

$$g(i,j) \overset{c\rightarrow\infty}{\rightarrow} V_{\mathrm{C}}(i,j) = \frac{q_{\mathrm{e}}^2}{|\boldsymbol{r}_i - \boldsymbol{r}_j|}. \tag{17}$$

As a next step we also need to specify the magnetic and retardation interactions experienced by an electron i and generated by all other electrons. In a first approximation retardation is neglected and we assume that electron i experiences the electromagnetic field immediately. For the scalar potential $\phi_{j,\mathrm{unret}}$, and the vector potential $\boldsymbol{A}_{j,\mathrm{unret}}$ created by electron j and felt by electron i the classical expression reads:

$$\phi_{\mathrm{j,unret}}(\boldsymbol{r}_i,\boldsymbol{r}_j) = \frac{q_j}{r_{ij}} \text{ and } \mathrm{A}_{\mathrm{j,unret}}(\boldsymbol{r}_i,\boldsymbol{r}_j) = \frac{\dot{\boldsymbol{r}}_j}{c}\frac{q_j}{r_{ij}}. \tag{18}$$

Here, q_j is the charge of electron j, r_{ij} is the distance between electrons i and j. From the classical interaction energy we can extract the operator accounting for the electron–electron pair interaction $g(i, j)$ via the corresponding principle (c.p.) (*21*),

$$g^{CG}(i,j) = q_{\mathrm{e}}\phi_j - \frac{q_e}{c}\dot{\boldsymbol{r}}_i \cdot \boldsymbol{A}_j \xrightarrow{\text{c.p.}} \frac{q_{\mathrm{e}}^2}{r_{ij}}(1 - \boldsymbol{\alpha}_i\boldsymbol{\alpha}_j), \tag{19}$$

where we chose the velocity operator to be the Dirac velocity operator $c\boldsymbol{\alpha}$. The first term in Eq. (19) is the Coulomb operator and the second term is the so-called Gaunt operator that couples the spin momenta of the interacting electrons.

So far, we considered only the unretarded electromagnetic field. However, for the correct expression, we have to include the retardation of the vector potential due to the finite speed of light. We may obtain from Darwin's classical electromagnetic interaction energy expression (*21*) (correct up to $O(c^{-2})$),

$$g(i,j) = \frac{q_e^2}{r_{ij}} - \frac{q_e^2}{2c^2}\left[\frac{(c\boldsymbol{\alpha}_i)(c\boldsymbol{\alpha}_j)}{r_{ij}} + \frac{(\boldsymbol{r}_{ij}\cdot c\boldsymbol{\alpha}_i)(\boldsymbol{r}_{ij}\cdot c\boldsymbol{\alpha}_j)}{r_{ij}^3}\right], \qquad (20)$$

where the last two terms denote the Breit interaction.

By inserting the equations defining the kinetic energy operators and the pairwise interaction operators into Eq. (8) we obtain the Dirac–Coulomb–Breit Hamiltonian, which is in chemistry usually considered the fully relativistic reference Hamiltonian.

Note that the Breit-type operators are often neglected in quantum chemistry because they yield small energy contributions in comparison to the instantaneous Coulomb interaction. However, the effects may not be negligible in highly accurate quantum chemical calculations or for spin- or magnetic-field-dependent properties such as those measured by magnetic resonance spectroscopies.

B. Relation to Current-Density Functional Theory

In the previous section we presented the semi-classical electron–electron interaction: we treated the electrons quantum mechanically but assumed that they interact via classical electromagnetic fields. The Breit retardation is only an approximate treatment of retardation and we shall now consider a more consistent treatment of the electron–electron interaction operator that also provides a bridge to relativistic DFT, which is current-density functional theory. For the correct description we have to take the quantization of electromagnetic fields into account (however, we will discuss only old, i.e., pre-1940 quantum electrodynamics). This means the two moving electrons interact via exchanged virtual photons with a specific angular frequency ω $|\omega_{nm}|$. Electron j is, hence, scattered by a virtual photon that was emitted by electron i. The frequency of the virtual photon is of

course related to the energy difference of the initial state n and final state m of electron i,

$$E_m - E_n = \hbar\omega_{mn}. \tag{21}$$

B.1. The electromagnetic interaction energy

In order to derive an expression for the electron–electron interaction, we shall recall that a one-electron wave function ψ ($\boldsymbol{r}$, t) can be expanded in a sum of basis functions ψ_n ($\boldsymbol{r}$) and a time-dependent pre-factor $\exp(-\mathrm{i}E_n t/\hbar)$,

$$\psi(\boldsymbol{r},t) = \sum_n a_n \psi_n(\boldsymbol{r}) e^{(-\mathrm{i}E_n t/\hbar)}. \tag{22}$$

Moreover, in a relativistic framework with moving charges, we do have to deal not only with the electron density $\rho(\boldsymbol{r},t)$ which describes the distribution of charges q_e in space and yields the total charge Q_v by integration over the complete volume V multiplied by the electron charge q_e, but also the current density $\boldsymbol{j}(\boldsymbol{r},t)$ that is generated by the moving electrons. An expression for the interaction of two electrons can then be derived from these quantities (*21*).

According to the correspondence principle the classical expression for the electron density $\rho(\boldsymbol{r},t)$ can be converted to the quantum mechanical description by taking into account that the particle density is calculated by integration of the product of the N-electron wave function Ψ_el and its complex conjugate $\Psi_\mathrm{el}^\dagger$. We introduce the charge-weighted density by multiplication of the electron density with the electron charge,

$$\rho_\mathrm{C}(\boldsymbol{r},t) = q_\mathrm{e}\rho(\boldsymbol{r},t) = -e\rho(\boldsymbol{r},t). \tag{23}$$

From the classical charge density for a collection of point particles, $\rho_\mathrm{C}(\boldsymbol{r},t)$,

$$\rho_C(\boldsymbol{r},t) = \sum_{i=1}^{N} q_\mathrm{e}\delta^{(3)}(\boldsymbol{r} - \boldsymbol{r}_\mathrm{i}(t)) \tag{24}$$

we arrive via the correspondence principle at the quantum mechanical expression for the charge-weighted density

$$\rho_\mathrm{C}(\boldsymbol{r}) = \int_{-\infty}^{+\infty} \mathrm{d}^3 r_1 \cdots \int_{-\infty}^{+\infty} \mathrm{d}^3 r_N \Psi^\dagger(\boldsymbol{r}_1,\boldsymbol{r}_2,\ldots,\boldsymbol{r}_N)\hat{\rho}_\mathrm{C}\Psi(\boldsymbol{r}_1,\boldsymbol{r}_2,\ldots,\boldsymbol{r}_N). \tag{25}$$

Note that in Eqs. (22), (23), and (25) $\boldsymbol{r}$ denotes spatial coordinates (integration over spin degrees of freedom has been omitted for the sake of brevity).

Accordingly, the classical current density $\boldsymbol{j}(\boldsymbol{r}, t)$ is a 3-vector and depends on the velocity of the moving electrons $\dot{\boldsymbol{r}}$,

$$\boldsymbol{j}(\boldsymbol{r},t) = \sum_{i=1}^{N} \dot{\boldsymbol{r}}_i(t)\delta^{(3)}(\boldsymbol{r} - \boldsymbol{r}_{\mathrm{i}}(t)). \tag{26}$$

By multiplication with the electron charge, we obtain the charge-weighted current-density,

$$\boldsymbol{j}_{\mathrm{C}}(\boldsymbol{r},t) = q_{\mathrm{e}}\boldsymbol{j}(\boldsymbol{r},t) = -e\boldsymbol{j}(\boldsymbol{r},t). \tag{27}$$

The quantum mechanical expression for the charge-weighted current density is obtained from Eq. (26) when we replace the classical velocity $\dot{\boldsymbol{r}}_i(t)$ by the Dirac velocity operator $c\boldsymbol{\alpha}_i$ and evaluate its expectation value (*21*),

$$\boldsymbol{j}_{\mathrm{C}}(\boldsymbol{r}) = q_{\mathrm{e}}c\int_{-\infty}^{+\infty} \mathrm{d}^3 r_1 \cdots \int_{-\infty}^{+\infty} \mathrm{d}^3 r_N \Psi^{\dagger}(\boldsymbol{r}_1,\ldots,\boldsymbol{r}_N)$$

$$\times \sum_{i=1}^{N} \boldsymbol{\alpha}_i \delta^{(3)}(\boldsymbol{r}_i - \boldsymbol{r})\Psi(\boldsymbol{r}_1,\ldots,\boldsymbol{r}_N). \tag{28}$$

Based on the quantum mechanical equation of motion, the continuity equation actually defines the relation between the charge density $\rho(\boldsymbol{r}, t)$ and the current density $\boldsymbol{j}(\boldsymbol{r},t)$ at a given time,

$$\frac{\partial \rho(\boldsymbol{r},t)}{\partial t} + \nabla \boldsymbol{j}(\boldsymbol{r},t) = 0, \tag{29}$$

which we may combine to give the 4-current j^{μ}. The charge weighted 4-current j^{μ}_{C} reads accordingly,

$$j^{\mu}_{\mathrm{C}} = q_{\mathrm{e}} j^{\mu} = (c\rho_{\mathrm{C}}, \boldsymbol{j}_{\mathrm{C}}). \tag{30}$$

When inserting Eq. (22) into Eq. (28), $j^{\mu}_{C}(\boldsymbol{r},t)$ reads for the case of a single electron

$$j^{\mu}_{\mathrm{C}}(\boldsymbol{r},t) = \left(cq_{\mathrm{e}} \sum_{nm} a^{*}_n a_m \, e^{(-\mathrm{i}\omega_{mn}t)} \psi^{\dagger}_n \psi_m, \; q_{\mathrm{e}}c \sum_{nm} a^{*}_n a_m \, e^{(-\mathrm{i}\omega_{mn}t)} \psi^{\dagger}_n \boldsymbol{\alpha} \psi_m \right). \tag{31}$$

The scalar and vector potentials created by one electron is related to its 4-current j^{μ}_{C},

$$\Box A^{\mu} = +\frac{4\pi}{c} j^{\mu}_{\mathrm{C}}. \tag{32}$$

In Eq. (32) we exploited the short-hand notation for the d'Alembert operator $\Box$ that contains the second derivatives with respect

to time and spatial coordinates (the latter abbreviated by the Laplacian Δ),

$$\Box = \partial_\mu \partial^\mu = \frac{1}{c^2}\frac{\partial}{\partial t^2} - \Delta. \tag{33}$$

The 4-potential is then obtained as

$$A^\mu(\boldsymbol{r},t) = \frac{1}{c}\int \mathrm{d}^3 r' \frac{j^\mu_{\mathrm{C}}(\boldsymbol{r}',t')}{|\boldsymbol{r}'-\boldsymbol{r}|} = \frac{1}{c}\int \mathrm{d}^3 r' \frac{j^\mu_{\mathrm{C}}(\boldsymbol{r}',t-|\boldsymbol{r}'-\boldsymbol{r}|/c)}{|\boldsymbol{r}'-\boldsymbol{r}|}. \tag{34}$$

Here, the retardation is accounted for in $j^\mu_{\mathrm{C}}(\boldsymbol{r}',t')$ that denotes the value of j^μ_{C} at the retarded time $t - |\boldsymbol{r}'-\boldsymbol{r}|/c$.

The components of the 4-potential may be written in the light of Eq. (31) as

$$\phi(\boldsymbol{r},t) = q_{\mathrm{e}} \sum_{nm} a_n^* a_m e^{(\mathrm{i}\omega_{nm}t)} \int \mathrm{d}^3 r' \psi_n^\dagger(\boldsymbol{r}') \frac{1}{|\boldsymbol{r}-\boldsymbol{r}'|} e^{(\mathrm{i}\omega_{mn}|\boldsymbol{r}-\boldsymbol{r}'|/c)} \psi_m(\boldsymbol{r}'), \tag{35}$$

$$\boldsymbol{A}(\boldsymbol{r},t) = q_{\mathrm{e}} \sum_{nm} a_n^* a_m e^{(\mathrm{i}\omega_{nm}t)} \int \mathrm{d}^3 r' \psi_n^\dagger(\boldsymbol{r}') \frac{\boldsymbol{\alpha}}{|\boldsymbol{r}-\boldsymbol{r}'|} e^{(\mathrm{i}\omega_{mn}|\boldsymbol{r}-\boldsymbol{r}'|/c)} \psi_m(\boldsymbol{r}'), \tag{36}$$

where the retardation is found in the exponential function under the integral. The unretarded potential is received if the frequency of the exchanged virtual photon ω_{mn} is set to zero.

In analogy to the classical expression for a continuous charge distribution $\rho_{\mathrm{C}}(\boldsymbol{r})$,

$$U = \frac{1}{2}\int \mathrm{d}^3 r \int \mathrm{d}^3 r' \frac{\rho_C(\boldsymbol{r})\rho_C(\boldsymbol{r}')}{|\boldsymbol{r}-\boldsymbol{r}'|} = \frac{1}{2}\int \mathrm{d}^3 r \rho_C(\boldsymbol{r})\phi(\boldsymbol{r}), \tag{37}$$

—where the pre-factor 1/2 prevents double counting the interactions—we can set up the quantum mechanical expression for the interaction energy of the two electrons i and j. When generalizing the charge distribution $\rho_{\mathrm{C}}(\boldsymbol{r})$ by the 4-current $j^\mu_{\mathrm{C}}(i)$ of electron i and inserting the 4-potential $A_\mu(i)$ generated by electron j instead of the scalar field ϕ in Eq. (37), we arrive at the following expression:

$$V(i,j) = \frac{1}{2c}\int \mathrm{d}^3 r_i j^\mu_{\mathrm{C}}(i) A_\mu(i) = \frac{1}{2c^2}\int \mathrm{d}^3 r_i \int \mathrm{d}^3 r_j \frac{j^\mu_{\mathrm{C}}(i) j_{\mathrm{C},\mu}(j)}{r_{ij}}. \tag{38}$$

After inserting Eqs. (35), (36), and (31) into Eq. (38), we may then rewrite the electron–electron interaction as

$$V(i,j) = \frac{1}{2} q_{\mathrm{e}}^2 \sum_{klmn} a_l^* a_n^* a_m a_k e^{(\mathrm{i}[\omega_{nm}+\omega_{lk}]t)} V_{lnkm}, \tag{39}$$

with the matrix element V_{lnkm} defined as

$$V_{lnkm} = \int \mathrm{d}^3 r_i \int \mathrm{d}^3 r_j \psi_l^\dagger(\boldsymbol{r}_i)\psi_n^\dagger(\boldsymbol{r}_j)\frac{1-\boldsymbol{\alpha}_i\boldsymbol{\alpha}_j}{r_{ij}} e^{(\mathrm{i}\omega_{nm} r_{ij}/c)}\psi_m(\boldsymbol{r}_j)\psi_k(\boldsymbol{r}_i). \tag{40}$$

If we now set the frequencies of the exchanged virtual photon to zero, $\omega_{nm} \rightarrow 0$, i.e., if we neglect retardation effects, the energy expectation value reduces to

$$V(i,j) = \frac{1}{2} q_\mathrm{e}^2 \sum_{klmn} a_l^* a_n^* a_m a_k \int \mathrm{d}^3 r_i \int \mathrm{d}^3 r_j \psi_l^\dagger(\boldsymbol{r}_i)\psi_n^\dagger(\boldsymbol{r}_j)\frac{1-\boldsymbol{\alpha}_i\boldsymbol{\alpha}_j}{r_{ij}}\psi_m(\boldsymbol{r}_j)\psi_k(\boldsymbol{r}_i), \tag{41}$$

where we recover the Coulomb plus Gaunt operators in the integral as in Ref. (21). This expression for the electromagnetic interaction energy is central to current-density functional theory.

B.2. Current-Density Functional Theory

The idea of density functional theory is that solely the electron density provides all necessary information about a system of electrons. As we have seen, when considering the interaction of moving charged fermions, it is the 4-current j^μ rather than the electron density ρ that has to be considered. In 1964, Hohenberg and Kohn (*24*) stated that in a non-relativistic framework the ground-state energy of a system can be calculated from its electron density and any trial density yields an energy that is an upper bound to the correct solution.

The Hohenberg–Kohn theorems were extended by Rajagopal and Callaway (*25*) to the more general relativistic case. Instead of the electron density they treated the 4-current in the same manner as Hohenberg and Kohn and obtained the energy expression,

$$E_\mathrm{el}[j^\mu] = T[j^\mu] + V_{\mathrm{el-nuc}}[j^\mu] + J[j^\mu] + E_\mathrm{XC}[j^\mu], \tag{42}$$

where T $[j^\mu]$ is the kinetic energy functional $V_{\mathrm{el-nuc}}$ $[j^\mu]$, is the external potential arising from the interaction of the electronic 4-current j^μ with all nuclei, $J[j^\mu]$ the classical electromagnetic interaction energy as given by Eq. (41), and E_XC $[j^\mu]$ the exchange–correlation current-density functional that contains all exchange and correlation effects. In accordance with density functional theory, we would obtain the exact solution for the system considered with respect to the relativistic framework, if the exact exchange–correlation current-density functional were

known. Unfortunately, up to date no such exact analytical expression for $E_{XC}\ [j^{\mu}]$ exists. Hence, the accuracy of current DFT depends on how well the functional can be approximated (*26–30*).

From a physical point of view it seems obvious that the electron density and the current density depending on only three spatial coordinates may be more eligible candidates for the calculation of physical observables rather than the wave function depending on $3N$ (plus spin) coordinates. Difficulties, however, may arise when constructing these densities. The idea of Kohn and Sham was to consider a surrogate system of non-interacting fermions that has the same ground state density as the fully interacting system. The advantage of this choice is that the wave function of the surrogate system is an antisymmetrized Hartree product, i.e., a Slater determinant. Rajagopal and Callaway (*25*) derived the corresponding relativistic Kohn–Sham DFT (KS-DFT) equations for the non-interacting fermionic particles,

$$\left[c\boldsymbol{\alpha}\cdot\left(p-\frac{q_{\mathrm{e}}}{c}\boldsymbol{A}_{\mathrm{eff}}(\boldsymbol{r})\right)+\beta m_{\mathrm{e}}c^2+q_{\mathrm{e}}\phi_{\mathrm{eff}}(\boldsymbol{r})\right]\psi_{\mathrm{i}}(\boldsymbol{r})=\epsilon_i\psi_i(\boldsymbol{r}),\quad(43)$$

which resemble the one-electron Dirac equation in an effective potential. The effective 4-potential $(\phi_{\mathrm{eff}}(\boldsymbol{r}),\boldsymbol{A}_{\mathrm{eff}}(\boldsymbol{r}))$ depends on the electronic 4-current j^{μ},

$$\phi_{\mathrm{eff}}(\boldsymbol{r})=\phi_{\mathrm{ext}}(\boldsymbol{r})+\frac{q_{\mathrm{e}}}{c}\int \mathrm{d}^3r'\frac{j^0(\boldsymbol{r}')}{|\boldsymbol{r}-\boldsymbol{r}'|}+c\frac{\delta E_{XC}[\mathrm{j}^{\mu}]}{\delta\, j^0(\boldsymbol{r})},\quad(44)$$

$$\boldsymbol{A}_{\mathrm{eff}}(\boldsymbol{r})=\boldsymbol{A}_{\mathrm{ext}}(\boldsymbol{r})+\frac{q_{\mathrm{e}}}{c}\int \mathrm{d}^3r'\frac{\boldsymbol{j}(\boldsymbol{r}')}{|\boldsymbol{r}-\boldsymbol{r}'|}+c\frac{\delta E_{XC}[\mathrm{j}^{\mu}]}{\delta\, j(\boldsymbol{r})}.\quad(45)$$

Note that already because of the approximate nature of present-day functionals it can be beneficial to introduce spin-dependent functionals as suggested, e.g., by MacDonald and Vosko (*31*).

C. Spin-Density Functional Theory

In 4-component KS-DFT spin is no longer a good quantum number because spin–orbit coupling arises. We could circumvent this problem employing an external axis of quantization for the spin, which is conveniently the z-axis. Such an approach is called collinear. The z-component of the spin operator leads to the spin density and can be calculated by subtracting the α- and β-spin densities, i.e., the sum of the absolute-squared α-orbitals minus the sum of the absolute-squared β-orbitals, from each other.

If we refrain from such a restriction and consider a spin-operator-dependent Hamiltonian, such as the 4-component KS Hamiltonian or the Dirac–Coulomb Hamiltonian, the Hamiltonian does not commute with the square of the spin operator. The square of the spin operator and the Hamiltonian then do not share the same set of eigenfunctions, and hence spin is no longer a good quantum number. In this noncollinear framework we must therefore find a different solution and may define a spin density equal to the magnetization vector (*32*).

Here, we should mention that there exists an extensive discussion in the literature on the capabilities of spin-DFT regarding, for instance, the question whether the Kohn–Sham spin density has to be equal to the spin density of the fully interacting system of electrons (and in the case of open-shell singlet broken-symmetry (BS) determinants (see below) for binuclear transition-metal clusters this is certainly not the case; see Ref. (*33*) for a more detailed discussion). But the situation is much more subtle and one may basically set up the variational procedure in a Kohn–Sham framework such that the spin density of the Kohn–Sham system of non-interacting fermions represents the true spin density. However, the frame of this review is not sufficient to present all details on this matter (*34,35*).

III. From Dirac–Breit to Breit–Pauli Hamiltonians

Up to this point, we have presented the fully relativistic Hamiltonian. Of course, we could set out to calculate energies of molecules employing this Hamiltonian. However, the various spin–spin interactions are easier described in terms of a perturbation picture rather than as excited states of the full-fledged Hamiltonian. Especially for the fully relativistic Dirac–Coulomb–Breit Hamiltonian, the latter calculations would be computationally very demanding.

Another approach is therefore to reduce the 4-component Hamiltonian to an electron-only one eliminating the negative-energy states in the spectrum of the one-electron operator. For this, we may block-diagonalize the 4×4 Dirac Hamiltonian by applying unitary transformations. Thus, we obtain a block-diagonal Hamiltonian and simultaneously decouple the negative-energy states and may proceed with the block describing the positive energy states. The unitary transformations are rather involved and based on the idea to expand each unitary transformation into a Taylor series with respect to an anti-Hermitian operator. While there exist different expansion parameters (*36,37*), only the Douglas–Kroll–Hess expansion yields the correct results, whereas the Foldy–Wouthuysen 1/c expansion is ill-defined (*38–40*).

Note that as long as the unitary transformation is exact, i.e., as long as the Taylor series is infinite and converges, the exact energy eigenvalues of the 4-component untransformed Hamiltonian are obtained.

A second approach to achieve a reduction of the 4-component Hamiltonian to an electrons-only Hamiltonian is to introduce approximations by eliminating the small components of the wave function (*41–53*). Also here, different protocols have been successfully exploited in quantum chemistry.

A. The Breit–Pauli Hamiltonian

The Breit–Pauli Hamiltonian is an approximation up to $1/c^2$ to the Dirac–Coulomb–Breit Hamiltonian obtained from a free-particle Foldy–Wouthuysen transformation. Because of the convergence issues mentioned in the preceding section, the Breit–Pauli Hamiltonian may only be employed in perturbation theory and not in a variational procedure. The derivation of the Breit–Pauli Hamiltonian is tedious (*21*).

The Breit–Pauli Hamiltonian with an external field contains all standard one- and two-electron contributions as well as the magnetic interaction of the electrons and their interactions with an external electromagnetic field. We may group the various contributions in the Breit–Pauli Hamiltonian according to one- and two-electron terms,

$$H_{\mathrm{BP}} = \sum_{i=1}^{N} h^{\mathrm{Pauli}}(i) + \sum_{i>j}^{N} g^{\mathrm{BP}}(i,j), \tag{46}$$

where we identify the one-electron terms as the one-particle Pauli Hamiltonians $h^{\mathrm{Pauli}}(i)$ in an external field $A^{\mu}(\phi, \boldsymbol{j})$, that has not been specified explicitly yet. We keep this simple form to derive the general terms arising from an interaction with such an external field, whereas the individual contributions are introduced at a later stage.

Because often only the field-free Pauli Hamiltonian is presented in literature, we shall briefly sketch the derivation of the Hamiltonian $h^{\mathrm{Pauli}}(i)$ within an external field. For this, we start with the elimination of the small component in the one-electron Dirac equation by substitution of the small component of Eq. (15) to obtain an expression of the large component only

$$(V + c\boldsymbol{\sigma} \cdot \boldsymbol{p}X)\psi^{\mathrm{L}} = \epsilon\psi^{\mathrm{L}}, \tag{47}$$

where X denotes the energy-dependent operator

$$X = X(\epsilon) = (\epsilon - V + 2m_e c^2)^{-1} c\boldsymbol{\sigma} \cdot \boldsymbol{p} \tag{48}$$

Inserting Eq. (48) into Eq. (47) then yields

$$(V - \epsilon)\psi^L + \frac{1}{2m_e c^2}[(c\boldsymbol{\sigma} \cdot \boldsymbol{\pi})\omega(c\boldsymbol{\sigma} \cdot \boldsymbol{\pi})]\psi^L = 0, \tag{49}$$

where we introduced the scalar operator ω that may be approximated by a Taylor series expansion

$$\omega = \omega(\epsilon) = \left[1 - \frac{V - \epsilon}{2m_e c^2}\right]^{-1} = \sum_{k=0}^{\infty}\left(\frac{V - \epsilon}{2m_e c^2}\right)^k \approx \left(1 + \frac{V - \epsilon}{2m_e c^2}\right). \tag{50}$$

Note that the non-relativistic Schrödinger equation is recovered when ω is set to 1.

If we employ the approximated ω up to the order of $O(c^{-2})$ as given in the previous equation and insert it into Eq. (49), we obtain

$$h^{\text{Pauli}}(i) = \frac{1}{2m_e c^2}\left[(c\boldsymbol{\sigma}_i \cdot \boldsymbol{\pi}_i)\left(1 + \frac{V_i - \epsilon}{2m_e c^2}\right)(c\boldsymbol{\sigma}_i \cdot \boldsymbol{\pi}_i)\right], \tag{51}$$

where we also introduced the index "i," which denotes all quantities corresponding to electron i. With Dirac's relation,

$$\frac{1}{2m_e}(\boldsymbol{\sigma} \cdot \boldsymbol{\pi})(\boldsymbol{\sigma} \cdot \boldsymbol{\pi}) = \frac{\boldsymbol{\pi}^2}{2m_e} + \mathrm{i}\boldsymbol{\sigma} \cdot (\boldsymbol{\pi} \times \boldsymbol{\pi}), \tag{52}$$

we obtain the non-relativistic contributions, i.e., the non-relativistic kinetic energy in an external field as well as the coupling of the spin to the external magnetic field $\boldsymbol{B}_i$,

$$h_{\text{ext}}^{\text{Pauli}}(i) = \frac{1}{2m_e}\left[\boldsymbol{\pi}_i^2 - \frac{\hbar q_e}{c}\boldsymbol{B}_i\boldsymbol{\sigma}_i\right] = \frac{(\boldsymbol{p}_i - \frac{q_e}{c}\boldsymbol{A}_i)^2}{2m_e} - \frac{q_e}{m_e c}\boldsymbol{B}_i \cdot \boldsymbol{s}_i, \tag{53}$$

where we also utilized the definition of the electron spin operator $\boldsymbol{s}$ that is $\frac{\hbar}{2}\boldsymbol{\sigma}$. The $O(c^{-2})$ term in Eq. (51) yields the relativistic energy contributions, which we denoted here as $h_{\text{rel}}^{\text{Pauli}}(i)$,

$$h_{\mathrm{rel}}^{\mathrm{Pauli}}(i) = \frac{\boldsymbol{\sigma}_i \cdot \boldsymbol{\pi}_i V_i \boldsymbol{\sigma}_i \cdot \boldsymbol{\pi}_i}{4m_{\mathrm{e}}^2 c^2} - \frac{\epsilon \boldsymbol{\pi}_i^2}{4m_{\mathrm{e}}^2 c^2} \,. \tag{54}$$

After some algebraic manipulation [see, for example, chapter 13.1 in Ref. (*21*)] these terms yield

$$h_{\mathrm{rel}}^{\mathrm{Pauli}}(i) = -\frac{\boldsymbol{\pi}_i^4}{8m_{\mathrm{e}}^3 c^2} - \frac{1}{8m_{\mathrm{e}}^2 c^2}\,(\boldsymbol{\pi}_i^2 V_i) + \frac{\mathrm{i}\boldsymbol{\sigma}_i}{4m_{\mathrm{e}}^2 c^2}\,[\boldsymbol{\pi}_i V_i \times \boldsymbol{\pi}_i]. \tag{55}$$

Without presenting a detailed derivation, it can easily be seen when re-substituting $\boldsymbol{\pi}_i$ with $\boldsymbol{p}_i - q_e/c\boldsymbol{A}_i$ that all terms containing the vector field $\boldsymbol{A}_i$ can be omitted as they contain a total pre-factor $\propto 1/c^3$. However, we only consider terms that are correct up to $O(c^{-2})$,

$$h_{\mathrm{rel}}^{\mathrm{Pauli}}(i) = \underbrace{-\frac{\boldsymbol{p}_i^4}{8m_{\mathrm{e}}^3 c^2}}_{\text{mass–velocity}} \underbrace{-\frac{1}{8m_{\mathrm{e}}^2 c^2}\,(\boldsymbol{p}_i^2 V_i)}_{\text{Darwin}} \underbrace{+\frac{i}{4m_{\mathrm{e}}^2 c^2}\boldsymbol{\sigma_i}[\boldsymbol{p}_{\mathrm{i}} \mathrm{V_i} \times \boldsymbol{p}_{\mathrm{i}}]}_{\text{spin–orbit}} \,. \tag{56}$$

In order to readily compare these terms to their expressions in the Breit–Pauli Hamiltonian given for example in Refs. (*21,54*), we insert the definition of the electric field strength $\boldsymbol{E}_i$ and the momentum operator $\boldsymbol{p}_i$ into Eq. (55),

$$\boldsymbol{E}_i = -\nabla_i \left(\frac{V_i}{q_e}\right) \quad \text{and} \quad \boldsymbol{p}_{\mathrm{i}} = -\mathrm{i}\hbar\nabla_{\mathrm{i}}, \tag{57}$$

Then we obtain with the definition of the electron spin operator $\mathbf{s} = \frac{\hbar}{2}\boldsymbol{\sigma}$,

$$h_{\mathrm{rel}}^{\mathrm{Pauli}}(i) = -\frac{\boldsymbol{p}_i^4}{8m_{\mathrm{e}}^3 c^2} - \frac{\mathrm{i}\hbar q_{\mathrm{e}}}{8m_{\mathrm{e}}^2 c^2}\boldsymbol{p}_i \cdot \boldsymbol{E}_i - \frac{q_{\mathrm{e}}}{2m_{\mathrm{e}}^2 c^2}\,(\boldsymbol{E}_i \times \boldsymbol{p}_i)\boldsymbol{s}_i. \tag{58}$$

Combining these results, the Pauli Hamiltonian $h^{\mathrm{Pauli}}(i)$ with an external field can be written as

$$\begin{aligned} h^{\mathrm{Pauli}}(i) = {} & \frac{1}{2m_{\mathrm{e}}}\left(\boldsymbol{p}_i - \frac{q_{\mathrm{e}}}{c}\boldsymbol{A}_{\mathrm{ext}}\right)^2 - \frac{q_{\mathrm{e}}}{m_{\mathrm{e}}c}(\boldsymbol{s}_i \cdot \boldsymbol{B}_i) + V_i - \frac{\boldsymbol{p}_i^4}{8m_{\mathrm{e}}^3 c^2} \\ & - \frac{\mathrm{i}\hbar q_{\mathrm{e}}}{8m_{\mathrm{e}}^2 c^2}\boldsymbol{p}_i \cdot \boldsymbol{E}_i - \frac{q_e}{2m_{\mathrm{e}}^2 c^2}\boldsymbol{s}_i \cdot (\boldsymbol{E}_i \times \boldsymbol{p}_i). \end{aligned} \tag{59}$$

It comprises the non-relativistic Hamiltonian of the form $\boldsymbol{p}_i^2/2m_{\mathrm{e}} + V$ and the relativistic correction terms, such as the mass–velocity operator $-\boldsymbol{p}_i^4/8m_{\mathrm{e}}^3 c^2$, the Darwin term proportional to $\boldsymbol{p}_i \cdot \boldsymbol{E}_i$, and the spin–orbit coupling term proportional

to $\boldsymbol{s}_i \cdot (\boldsymbol{E}_i \times \boldsymbol{p}_i)$. Note that the diamagnetic term (see Ref. (55)) of the form $q_e^2 \boldsymbol{A}_i^2 / 2m_e c^2$ is incorporated in the first term in Eq. (59), whereas it was neglected in Bethe and Salpeter's presentation Ref. (*54*, p. 181) of the Breit–Pauli Hamiltonian but added in a later step of the derivation in Ref. (*54*, p. *183*). Considering the mass–velocity term $-\boldsymbol{p}^4/8m_e^3c^2$, we chose the pre-factor of the one-electron Pauli Hamiltonian (see Ref. (*21*)) to be 1/8 rather than 1/4 as in Bethe and Salpeter's book (*54*). As each term of $h^{\text{Pauli}}(i)$ should have the unit of energy, e.g. Joule, we omitted an $\hbar$ in the spin–orbit coupling term proportional to $\boldsymbol{s}_i \cdot (\boldsymbol{E}_i \times \boldsymbol{p}_i)$ and in the term containing the magnetic field proportional to $(\boldsymbol{s}_i \cdot \boldsymbol{B}_i)$ in contrast to H_{BP} in Ref. (*54*). (Note that $\boldsymbol{s}$ differs from our definition here, i.e., $\boldsymbol{s} = \frac{1}{2}\boldsymbol{\sigma}$ in Ref. (*54*) and the spin operator is defined as $\boldsymbol{J}_{\text{spin}} = \hbar\mathbf{s}$.) In our expression each term of $h^{\text{Pauli}}(i)$ features a correct energy unit which may easily be checked.

In contrast to the one-electron terms, the reduction of the 4×4 Dirac–Breit Hamiltonian to the 2×2 Breit–Pauli Hamiltonian is very tedious for the two-electron terms as each interaction term has to be transformed according to the Foldy–Wouthuysen protocol. As the derivation can be found for example in Refs. (*56–58*) and in detail in Ref. (*21*), we only present here the transformed terms and discuss their dimension. The two-electron Breit–Pauli operator $g^{\text{BP}}(i, j)$ reads

$$
\begin{aligned}
g^{\text{BP}}(i,j) = & \underbrace{\frac{q_e^2}{r_{ij}} - \frac{q_e^2}{2m_e^2c^2}\left[\frac{\boldsymbol{p}_i \cdot \boldsymbol{p}_j}{r_{ij}} + \frac{(\boldsymbol{r}_{ij} \cdot \boldsymbol{p}_i)(\boldsymbol{r}_{ij} \cdot \boldsymbol{p}_j)}{r_{ij}^3}\right]}_{\text{I: electron–electron interaction}} \\
& + \underbrace{\frac{q_e^2}{2m_e^2c^2}\left[\frac{(\boldsymbol{r}_{ij} \times \boldsymbol{p}_j) \cdot \boldsymbol{s}_i}{r_{ij}^3} + \frac{(\boldsymbol{r}_{ji} \times \boldsymbol{p}_i) \cdot \boldsymbol{s}_j}{r_{ij}^3}\right]}_{\text{II: spin–orbit interaction}} \\
& + \underbrace{\frac{q_e^2}{m_e^2c^2}\left[-\frac{8\pi}{3}(\boldsymbol{s}_i \cdot \boldsymbol{s}_j)\delta^{(3)}(\boldsymbol{r}_{ij}) + \frac{\boldsymbol{s}_i \cdot \boldsymbol{s}_j}{r_{ij}^3} - 3\frac{(\boldsymbol{r}_{ij} \cdot \boldsymbol{s}_i)(\boldsymbol{r}_{ij} \cdot \boldsymbol{s}_j)}{r_{ij}^5}\right]}_{\text{III: spin–spin interaction}}.
\end{aligned}
\tag{60}
$$

Term I denotes the classical electron–electron interaction which is related to Darwin's classical expression when expressed in terms of momenta rather than velocities (*21*). It comprises Coulombic interactions, magnetic, and retardation terms. Term II in Eq. (60) accounts for spin–orbit interactions, whereas term III describes spin–spin interactions. Note that all interaction

energies have to be in Gaussian units [C^2m^{-1}]. The dimension of the three-dimensional Dirac delta distribution $\delta^{(3)}$ is a reciprocal volume and its unit is thus [m^{-3}]. In order to obtain the correct energy unit [C^2m^{-1}] no $\hbar$ occurs in the pre-factor of the second term in Eq. (60) and $\hbar^2$ in the third term in Eq. (31) when comparing our expression to Bethe and Salpeter's in Ref. (54).

So far, we have not specified the external vector field but summarized all individual contributions in $A^{\mu}_{ext} = (c\phi_{ext}, \boldsymbol{A}_{ext})$. Each (moving) nucleus also gives rise to a vector potential $\boldsymbol{A}_I$ (through translational and rotational motion as well as spin) in addition to a truly external vector field $\boldsymbol{A}_0$ applied in the laboratory setup,

$$\boldsymbol{A}_{\text{ext}} = \boldsymbol{A}_0 + \sum_{I=1}^{M} \boldsymbol{A}_I \quad \text{and} \quad \phi_{\text{ext}} = \phi_0 + \sum_{\text{I}=1}^{M} \phi_I. \tag{61}$$

These fields become important in magnetic resonance spectroscopies, where the interaction between electronic and nuclear spins is considered in phenomenological Spin Hamiltonians. Note that $q_{\text{e}} \sum_{I=1}^{M} \phi_{\text{I}}$ is nothing else but the scalar potential created by the nuclei, which we denoted as $V_{\text{el–nuc}}$ in previous sections.

IV. Phenomenological Spin Hamiltonians

A. The Effective Hamiltonian in Electron Spin Resonance

In magnetic resonance spectroscopy, such as Electron Spin Resonance (ESR), also called Electron Paramagnetic Resonance (EPR), it is common to define an effective Hamiltonian describing the interactions between effective electron spins $\boldsymbol{S}^{\text{eff}}$ and effective nuclear spins $\boldsymbol{I}^{\text{eff}}$. Effective spins may denote the spins of an individual electron or of groups of strongly interacting individual electron spins coupled to one effective spin. The interaction of the individual electron and nuclear spins (producing magnetic fields) results in an energy splitting of the unperturbed quantum mechanical states.

Though the ESR Hamiltonian is typically expressed in terms of effective electronic and nuclear spins, it can, of course, also be derived from the more fundamental Breit–Pauli Hamiltonian, when the magnetic fields produced by the moving nuclei are explicitly taken into account. In order to see this, we shall recall that in classical electrodynamics the magnetic dipole equation can be derived in a multipole expansion of the current density. For the lowest order term the expansion yields (*59*)

$$\boldsymbol{A}(\boldsymbol{r}) = \frac{\boldsymbol{\mu} \times \boldsymbol{r}}{r^3} \,. \tag{62}$$

In quantum mechanics this then becomes the vector product of the nuclear magnetic dipole moment $\boldsymbol{\mu}_I$ and the distance vector between an electron i and the field-creating nucleus I (*60*)

$$\boldsymbol{A}_I = \frac{1}{2}\boldsymbol{\mu}_I \times \frac{\boldsymbol{r}_i - \boldsymbol{R}_I}{|\boldsymbol{r}_i - \boldsymbol{R}_I|^3} \,. \tag{63}$$

In quantum theory, the nuclear dipole-moment operator is proportional to the nuclear spin, i.e., nothing else but the gyromagnetic ratio γ_I multiplied by the nuclear spin operator $\boldsymbol{I}_I$,

$$\boldsymbol{\mu}_I = \gamma_I \boldsymbol{I}_I. \tag{64}$$

The nuclear spins give rise to additional terms in the Breit–Pauli Hamiltonian due to the interaction of the electrons with the magnetic moment of the nuclei and the electrostatic interaction with the electric quadrupole interaction of the nuclei. The magnetic interaction term of the spins with the nuclei is of the same type as the spin–spin interaction and following Abragam and Pryce (*61*) can be written as

$$H_{Ii} = \gamma_I \gamma_e \sum_{i=1}^{N} \left[\frac{(\boldsymbol{l}_i - \boldsymbol{s}_i) \cdot \boldsymbol{I}_I}{r_{Ii}^3} + \frac{3(\boldsymbol{r}_{Ii} \cdot \boldsymbol{s}_i)(\boldsymbol{r}_{iI} \cdot I_I)}{r_{Ii}^5} + 8\frac{\pi}{3}\delta^{(3)}(\boldsymbol{r}_{Ii})(\boldsymbol{s}_i \cdot \boldsymbol{I}_I) \right] + \text{quadrupole interactions} \tag{65}$$

where γ_I is the nuclear gyromagnetic ratio, γ_e the electron gyromagnetic ratio, and q_I the charge of nucleus I, as well as I_I its spin quantum number. Similar expressions were later provided by McWeeny (*161*) and Harriman (*64*). Note that quadrupole interactions included in the Abragam and Pryce expression were neglected by McWeeny.

Finally, the nuclear spins interact with the external field resulting in

$$H_I = -\gamma_I \boldsymbol{B}_{\text{ext}} \cdot \boldsymbol{I}_I. \tag{66}$$

Hence, the effective Hamiltonian as relevant in ESR spectroscopy in terms of the occurring interactions (derived by Abragam and Pryce (*51*)) reads,

$$H_{\text{eff}}^{\text{ESR}} = H_0 + \text{spin}-\text{orbit} + \text{spin}-\text{spin} + \text{spin}-\text{nuclear spin} + \text{spin}-\boldsymbol{B}_{\text{ext}} + \text{nuclear spin}-\boldsymbol{B}_{\text{ext}}, \tag{67}$$

where H_0 denotes the non-relativistic energy of the N-electron system. Note that "spin" without any additional adjective shall always denote the electronic spin.

In ESR spectroscopy it is, however, common to rename these contributions in terms of phenomenological operators as for example given in the book of Schweiger and Jeschke (*62*). For an open-shell system with one effective electron spin $\boldsymbol{S}^{\text{eff}}$ and M nuclei the effective Hamiltonian comprises the interaction of the electron with the external field $\boldsymbol{B}_{\text{ext}}$ (electron–Zeeman interaction) H_{EZ}, the interaction of the electron spin in the absence of an external field (the so-called zero-field splitting) H_{ZFS}, the hyperfine coupling between the electron spin and the magnetic field generated by a nuclear spin H_{HF}, the interaction of the nuclei spins with the external magnetic field $\boldsymbol{B}_{\text{ext}}$ (here: nuclear Zeeman interactions) H_{NZ}, the nuclear quadrupole interactions for nuclear spins with spin quantum numbers larger than 1/2, H_{NQ}, and one may also consider the spin–spin interaction between two nuclear spins H_{NN} that is omitted in Abragam's expression. Hence, we obtain for $H_{\text{eff}}^{\text{ESR}}$

$$H_{\text{eff}}^{\text{ESR}} = H_{\text{EZ}} + H_{\text{ZFS}} + H_{\text{HF}} + H_{\text{NZ}} + (H_{\text{NQ}} + H_{\text{NN}}). \tag{68}$$

In ESR spectroscopy the terms in the effective Hamiltonian are typically expressed by virtue of effective coupling matrices or tensors, whereas in this review we shall relate them to their corresponding terms in the Breit–Pauli Hamiltonian. The effective coupling matrices parametrize the electronic structure of the molecule under study and can be calculated from the Breit–Pauli Hamiltonian by employing a suitable representation of the molecular wave function.

The zero-field splitting, representing the interaction of two (strongly) interacting effective electron spins, is phenomenologically given by

$$H_{\text{ZFS}} = \boldsymbol{S}^{\text{eff}} \cdot \boldsymbol{D} \cdot \boldsymbol{S}^{\text{eff}}, \tag{69}$$

where the tensor $\boldsymbol{D}$ denotes the coupling strength between these effective electron spins. It represents spin–spin and spin–orbit contributions (*63,64,161*). Clearly, the spin–spin contribution corresponds to term III in Eq. (60) of the Breit–Pauli Hamiltonian. The spin–orbit coupling terms also incorporated in the tensor $\boldsymbol{D}$ in Eq. (69) can be split into one- and two-electron contributions (*65*). The one-electron equivalent in the Breit–Pauli Hamiltonian is the last term in Eq. (59), whereas the two-electron contribution corresponds to the second term in Eq. (60).

The interaction of the effective electron spin with the external $\boldsymbol{B}_{\text{ext}}$ field gives rise to the Zeeman splitting,

$$H_{\text{EZ}} = \mu_{\text{B}} \boldsymbol{B}_{\text{ext}} \cdot \boldsymbol{g} \cdot \boldsymbol{S}^{\text{eff}}, \tag{70}$$

where $\boldsymbol{g}$ is a (3×3) matrix accounting for the dependence of the interaction on the orientation of the molecule with respect to the magnetic field and the Bohr magneton μ_{B}. The Zeeman splitting corresponds to the second term in the one-electron Pauli Hamiltonian Eq. (59).

The interaction between the effective spin $\boldsymbol{S}^{\text{eff}}$ and the nuclear spin of the M nuclei $\boldsymbol{I}_I^{\text{eff}}$ generates the hyperfine splitting,

$$H_{\text{HF}} = \sum_{I=1}^{M} \boldsymbol{S}^{\text{eff}} \cdot \boldsymbol{A}^{(I)} \cdot \boldsymbol{I}_I^{\text{eff}}, \tag{71}$$

where $\boldsymbol{A}^{(I)}$ denotes the hyperfine tensor that accounts for the orientational dependence of the magnetic field produced by the nuclei, which must not be confused with the electromagnetic vector potential. It can be divided into an orientational-independent (isotropic) part and an anisotropic part,

$$\boldsymbol{A}^{(I)} = \boldsymbol{A}_{\text{iso}}^{(I)} + \boldsymbol{A}_{\text{noniso}}^{(I)}, \tag{72}$$

and its values are the hyperfine coupling constants. As the isotropic part $\boldsymbol{A}_{\text{iso}}^{(I)}$ occurs due to the contact interaction at the nucleus, it is also called *Fermi contact term*. Since the Breit–Pauli Hamiltonian comprises only the electronic interactions the hyperfine splitting term cannot be found in Eqs. (59) and (60) but explicitly has to be included as outlined earlier.

The nuclear Zeeman term describes the interaction of the nuclear spins with the external magnetic field. Just as the hyperfine splitting, this term is not incorporated in the original purely electronic Breit–Pauli Hamiltonian as presented in Eqs. (59) and (60) but becomes relevant for ESR spectroscopy.

As all of the terms in the effective ESR Hamiltonian correspond to quantities observable experimentally through an energy splitting between quantum mechanical states, different quantum chemical protocols exist to calculate such splittings with *ab initio* wave-function methods or DFT (*63,65–79*).

B. The Heisenberg Spin Hamiltonian

The phenomenological Spin Hamiltonian widely applied in quantum chemistry—often also referred to as the Dirac–Heisenberg–Van

Vleck Hamiltonian—treats the interactions of effective electronic spins and dates back to the work of Dirac, Heisenberg, and Van Vleck (*80–83*).

Dirac (*81,84,85*) showed that the potential energy of two interacting electron spins in a non-relativistic framework depends on their spin operators $\boldsymbol{s}_1$ and $\boldsymbol{s}_2$,

$$V_{ij} \propto 2K_{ij}\langle \boldsymbol{s}_1 \cdot \boldsymbol{s}_2 \rangle. \tag{73}$$

Whereas $\boldsymbol{s}_1$ and $\boldsymbol{s}_2$ are true one-electron spin operators, K_{ij} is the exchange integral of electrons and in one-electron states i and j (independent particle picture of Hartree–Fock theory assumed). It should be stressed here that in the original work by Van Vleck (*80*) in 1932 the integral was denoted as J_{ij} but as it is an exchange integral we write it as K_{ij} in order to be in accordance with the notation in quantum chemistry, where J_{ij} denotes a Coulomb integral.

Van Vleck (*80*) illustrated how Eq. (73) can be identified in the energy expression of the two interacting electrons in a non-relativistic field-free framework. For such a system the contribution to the electron–electron interaction energy E_{ij} comprises the Coulomb energy J_{ij} and the exchange energy K_{ij},

$$E_{ij} = J_{ij} \pm K_{ij}, \tag{74}$$

where the "+" holds in the case of the singlet state while the "–" in the case of the triplet state. In order to demonstrate the relation to Eq. (*73*), he explicitly had to introduce the term $2K_{ij}\langle \boldsymbol{s}_1 \cdot \boldsymbol{s}_2 \rangle$ into this expression as we shall see now. For this purpose, he calculated the spin coupling term $\boldsymbol{s}_1 \cdot \boldsymbol{s}_2$ by employing the relation

$$(\boldsymbol{s}_1 \cdot \boldsymbol{s}_2)^2 = \boldsymbol{s}_1^2 + \boldsymbol{s}_2^2 + 2\boldsymbol{s}_1 \cdot \boldsymbol{s}_2 \tag{75}$$

and utilized the eigenvalue equation for the total squared spin operator with $\boldsymbol{S}^2 \rightarrow S(S + 1)$ with $\boldsymbol{S} = \boldsymbol{s}_1 + \boldsymbol{s}_2$. He found the two eigenvalues for $\boldsymbol{s}_1 \cdot \boldsymbol{s}_2$ to be $-3/4$ and $+1/4$. They describe the antiparallel and parallel alignment of the two electron spins and corresponding to the $(J_{ij} + K_{ij})$ singlet- and the $(J_{ij} - K_{ij})$ triplet-state energies. Hence, the triplet energy can be rewritten as

$$E_{ij} = J_{ij} - \frac{1}{2}K_{ij} - 2K_{ij}\langle \boldsymbol{s}_1 \cdot \boldsymbol{s}_2 \rangle, \tag{76}$$

which becomes equal to Eq. (74) after inserting the eigenvalue for $\boldsymbol{s}_1 \cdot \boldsymbol{s}_2$.

Dirac pointed out that the coupling energy proportional to $2K_{ij}\langle \boldsymbol{s}_i \cdot \boldsymbol{s}_j \rangle$ "*is much greater than that of the spin magnetic moments. Such models […] were in use before the justification by*

quantum mechanics was obtained" (see Ref. (*81*, p. 228)). Van Vleck further added that this coupling of the spins is a pure exchange effect arising from the antisymmetry of the wave function and not from magnetic interaction of the electrons: "*[…] the exchange effect has a partial [re]-semblance to a powerful magnetic coupling between the spins. This is not at all the same as saying that actually there is a real magnetic coupling of such magnitude, as the actual magnetic forces are so weak that we have neglected them entirely in the present connection*" (see Ref. (*80*, pp. 318–319)).

Though the true electron spin operators were employed here as well as in the Breit–Pauli Hamiltonian, the phenomenological Spin Hamiltonian, in which the spin coupling is an exchange effect, is in sharp contrast to the Breit–Pauli Hamiltonian, that is including the (magnetic) spin–spin interactions. Since the exchange effect is an effect introduced by the Pauli principle imposed on the wave function, we may write the electron–electron interaction as an expectation value,

$$E = \langle \Psi^{\mathrm{SD}} | \sum_{i>j} g(i,j) | \Psi^{\mathrm{SD}} \rangle \longrightarrow \langle \Psi^{\mathrm{HP}} | \sum_{i>j} g(i,j) (1 - \underbrace{P_{ij}}_{\text{Van Vleck}}) | \Psi^{\mathrm{HP}} \rangle, \qquad (77)$$

where for our purposes the wave function is approximated by a single Slater determinant Ψ^{SD} that we may denote in accordance with the definition in Eq. (4) in terms of a Hartree product Ψ^{HP} and a pair-permutation operator P_{ij}. Here, we recover Van Vleck's expression in P_{ij}. It should be emphasized that each two-electron term of the Breit–Pauli Hamiltonian, i.e., each term in Eq. (60), contributes to the exchange energy, whereas in Van Vleck's expression the exchange energy stems merely from the instantaneous Coulomb interaction, which is the very first term in Eq. (60).

Of course, the Spin Hamiltonian as given in Eq.(73) could also be directly derived from Eq. (77) for Dirac (*81*) pointed out that any permutation operator can be written in terms of vectors of Pauli spin matrices $\boldsymbol{\sigma}_i$ and $\boldsymbol{\sigma}_j$ as

$$P_{ij} = -\frac{1}{2}\{1 + \boldsymbol{\sigma}_i \cdot \boldsymbol{\sigma}_j\}. \qquad (78)$$

In present-day quantum chemistry the Heisenberg Spin Hamiltonian is widely applied for the description of magnetic coupling in transition-metal clusters and may read in the case of a many-electron system,

$$H = -\sum_{i>j} 2K_{ij}\boldsymbol{S}_i \cdot \boldsymbol{S}_j, \tag{79}$$

where instead of electron spins $\boldsymbol{s}_i$ effective spins $\boldsymbol{S}_i$ were employed. In theory, whether or not the coupling constant K_{ij} describes the exchange effects or also the (effective) magnetic spin–spin coupling depends on the calculation of the approximate wave function, i.e., it depends on the Hamiltonian chosen for the calculation of the wave function. In experiment, these effects can hardly be separated, of course.

However, magnetic coupling behavior may be more complex to model than possible with a simple isotropic Heisenberg Spin Hamiltonian as defined in Eq. (79) and several recent studies set out to improve this description by modification of this Hamiltonian (*86–89*).

While improved Heisenberg Hamiltonians containing anisotropic interactions have been employed for a long time in solid state physics (*90,91*) (and the correct description of magnetic anisotropy effects is still subject to investigation (*92–94*)) its importance for quantum chemical calculations has only been encountered recently when DFT calculations on large transition-metal clusters became feasible. For molecular systems, efforts have been made by Van Wüllen (*88,89*) to capture magnetic anisotropic effects in the Heisenberg Hamiltonian. For that he included phenomenological terms for the Zeeman interaction $H_{\mathrm{Z}} = \mu_{\mathrm{B}}\sum_i g_i \boldsymbol{B} \cdot \boldsymbol{S}_i$ and the zero-field splitting $H_{\mathrm{ZFS}} = \sum_i \boldsymbol{S}_i \cdot \boldsymbol{D}_i \cdot \boldsymbol{S}_i$ to Eq. (79).

C. Calculation of the Exchange Integral K_{ij}

The exchange parameter K_{ij} reflects the magnetic coupling type in a molecule. Its most accurate prediction is therefore important to understand and model the magnetic coupling in any kind of open-shell molecule. Hence, we shall present here a short historic survey toward the calculation of K_{ij} by means of quantum chemical methods.

It is important to note that when the phenomenological Spin Hamiltonian was developed it was not suited to predict the magnetic behavior of a molecule or alloy *a priori* but could only explain what was observed experimentally (*95*) regardless of some working rules that existed. Van Vleck (*80*) pointed out that ferromagnetism requires a positive coupling constant, whereas antiferromagnetism a negative coupling constant, although this was experimentally not always confirmed (*96*).

Later, efforts were made to qualitatively predict the sign of the coupling constant based on simple models: for example, Kramers and Anderson's (*97,98*) idea included not only the nearest-neighbor interaction resulting in the exchange energy but also the next-nearest-neighbor interaction giving rise to the so-called super exchange energy. On this basis, they predict that transition-metal crystals with less than half-filled *d*-orbitals will exhibit ferromagnetic coupling, whereas crystals with more than half-filled *d*-orbitals antiferromagnetic coupling. As their idea did not predict the correct coupling in every case, Goodenough and Kanamori developed a different model based on the symmetry relation of the *d*-orbital of the metal and the *p*- or *s*-orbital of the ligand (*96,99*). Their model was developed for crystals assuming a simple ligand field surrounding the metal atom resulting in an energy splitting of the atomic *d*-orbitals. Based on the orientation of the atomic orbitals toward each other and the number of electrons in the *d*-orbitals of the metal, generalized rules were found to predict the type of magnetic coupling.

The application of these rules may fail for the prediction of magnetic coupling in transition-metal clusters, where the molecular orbitals may be different from simple atomic *d*-orbitals and a simple ligand field analysis may not reflect the correct energy splittings.

Nevertheless, the calculation of K_{ij} is an important issue. In experiment, it is considered as an empirical parameter fitted to experimental data so that the corresponding Heisenberg Hamiltonian describes the experimentally observed magnetic behavior (*100,101*). Although it would be more desirable from a quantum chemical point of view to directly calculate experimentally accessible properties, e.g., the magnetic susceptibility (*102*), the quantum chemical calculation of K_{ij} provides a means to compare experimental and calculated results—though in a somewhat indirect fashion.

In single-determinant theories like Hartree–Fock and DFT different schemes exist for the calculation of K_{ij}. In all expressions, the coupling is typically described as the energy difference between a high-spin (hs) state representing the ferromagnetic coupling and the broken-symmetry (BS) state (*103–108*) with two interacting local high-spin centers with opposite sign describing the antiferromagnetically coupled state. Note that the BS state is an artificial state in the single-determinant approximation to the electronic wave function (*33*).

Because such local high-spin centers are often considered to be the metal atoms in a cluster, we shall study two such centers *A* and *B* for the sake of simplicity only implying that the interaction

of more than two such centers requires a summation over pairs of interacting centers or a more complex interaction scheme. The two states have the same local quantum numbers S_A and S_B but with inverted M_s values. (Note that we have to define what a *local* spin quantum number shall be, see next section.)

The first scheme was proposed by Noodleman (*103*),

$$K_{AB} = -\frac{^{\mathrm{hs}}E - {}^{\mathrm{BS}}E}{S^2_{\mathrm{hs}}}\,, \tag{80}$$

where S^2_{hs} denotes the total spin of the high-spin state. Bencini *et al.* (*109*) and Ruiz *et al.* (*110*) suggested a slight modification of Noodleman's expression for the energy difference between the high-spin and the singlet state,

$$K_{AB} = -\frac{^{\mathrm{hs}}E - {}^{0}E}{S_{\mathrm{hs}}(S_{\mathrm{hs}}+1)}. \tag{81}$$

Note that ^0E is the energy of a true singlet state, i.e., a state with the spin eigenfunction $S=0$, and Eq. (81) is strictly only valid if the latter condition is fulfilled.

A scheme for the description of "weak coupling" was presented by Mouesca *et al.* (*111*) also based on earlier work by Noodleman (*103*) to be

$$K_{AB} = -\frac{^{\mathrm{hs}}E - {}^{\mathrm{BS}}E}{4S_i \cdot S_j}\,. \tag{82}$$

Another expression was given by Yamaguchi (*100,112*),

$$K_{AB} = -\frac{^{\mathrm{hs}}E - {}^{\mathrm{BS}}E}{^{\mathrm{hs}}\langle S^2\rangle - {}^{\mathrm{BS}}\langle S^2\rangle}\,. \tag{83}$$

In a recent work, Marx and collaborators presented a protocol to calculate the dynamics of the coupling constant $K_{AB}(t)$ on the basis of an improved Yamaguchi expression that incorporated spin projection in a Hubbard-corrected two-determinant approach to obtain more accurate K_{AB} values (*86,87*).

A further idea to improve Yamaguchi's expression was introduced by Clark and Davidson (*113,114*) who suggested to replace total spins with local spin expectation values of surrogate spin operators localized at atomic centers,

$$K_{AB} = -\frac{^{\mathrm{hs}}E - {}^{\mathrm{BS}}E}{2\left(^{\mathrm{hs}}\langle \boldsymbol{S}_A \cdot \boldsymbol{S}_B\rangle - {}^{\mathrm{BS}}\langle \boldsymbol{S}_A \cdot \boldsymbol{S}_B\rangle\right)}\,. \tag{84}$$

This is a reasonable expression from a conceptual point of view since we are interested in the magnetic interaction of local metal centers resulting in either ferro- or antiferromagnetic coupling. Hence, we shall delve deeper into the concepts of local electronic spins in the next section.

Before closing this section we shall note that physicists study the interaction in more complex spin systems as occurring in solid states (*115–117*).

V. Concept of Local Electronic Spins

In molecules, the interaction of surrogate spins localized at the atomic centers is calculated describing a picture of "spin–spin interaction of atoms." This picture became prominent for the description of the magnetic behavior of transition-metal clusters, where the coupling type (parallel or antiparallel) of surrogate spins localized at the metal centers is of interest. Once such a description is available it is possible to analyze any wave function with respect to the coupling type between the metal centers. Then, local spin operators can be employed in the Heisenberg Spin Hamiltonian. An overview over wave-function analyses for open-shell molecules with respect to local spins can be found in Ref. (*118*).

For an interaction of two local spin centers in a transition-metal cluster, two spin states are of interest according to what has been said in the previous section: the high-spin (hs) state with a maximum number of unpaired electrons and maximum total spin quantum number describing the ferromagnetic coupling and the broken symmetry (BS) state with two interacting local high-spin centers with opposite sign which we—despite vivid discussions in the literature (*33,119–121*)—refer to as the antiferromagnetically coupled state.

A description in terms of local spins, however, raises the question of how to define these localized surrogate spins, where we have to move from one-electron spin operators $\boldsymbol{s}_i$ to multi-electron spin operators $\boldsymbol{S}_A$ that are located at one center and summarize all electronic contributions attributed to this center. This can be solved by the introduction of projection operators p_A (*33,113,114,122–124*). The projection operators do not alter any property of the molecule but divide it into local basins A. They add up to the identity operator,

$$\sum_A p_A = \hat{1}. \tag{85}$$

Then, the molecular total spin operator $\boldsymbol{S}$ defined as a sum over one-electron operators may be rewritten in terms of local spin operators $\boldsymbol{S}_A$,

$$\boldsymbol{S} = \sum_{i=1}^{N} \boldsymbol{s}_i = \sum_{i=1}^{N} \boldsymbol{s}_i \sum_A p_A = \sum_A \sum_{i=1}^{N} \boldsymbol{s}_{i,A} = \sum_A \boldsymbol{S}_A. \tag{86}$$

Note that capital letters indicate multi-electron operators and that—in contrast to the previous sections—all quantities are expressed in atomic units. (However, Gaussian units may easily be recovered if each squared spin expression is multiplied by $\hbar^2$ and each linear expression by $\hbar$.)

The local expressions obtained in the decomposition procedure can then conveniently be employed in a Heisenberg Spin Hamiltonian, which reads for a pair interaction

$$H_{AB} = -2K_{AB}\boldsymbol{S}_A \cdot \boldsymbol{S}_B. \tag{87}$$

It can be evaluated by calculation of its expectation value. For this purpose, we need to calculate the exchange integral K_{AB} as given by Clark and Davidson in Eq. (84) and then evaluate the local spin expectation values for the operators $\boldsymbol{S}_A \cdot \boldsymbol{S}_A$.

A. Calculation of Local Spin Expectation Values

In order to present the derivation of local spin expectation values, we shall briefly recall the foundations of spin eigenvalue equations in the non-relativistic framework. Information on the spin states of a molecule can be extracted from either the total spin operator $\boldsymbol{S}^2$ or its z-component S_z (i.e., from its projection on the z-axis),

$$\boldsymbol{S}^2\Psi_{\text{el}} = S(S+1)\Psi_{\text{el}}, \tag{88}$$

where S can have the values $S = \pm\frac{1}{2}, \pm 1, \ldots$ and the projected spin S_z features the eigenvalues $M_s = S, (S-1), \ldots 0, \ldots -S$,

$$S_z\Psi_{\text{el}} = M_s\Psi_{\text{el}}. \tag{89}$$

Hence, for a given total spin eigenvalue S there exist $2S + 1$ states that all yield the same energy but may split when magnetic fields described as spin interactions are important in the Hamiltonian. The individual spin states are referred to as the $S = 0$ singlet state with $2S + 1 = 1$, as doublet $S = \frac{1}{2}$ with $2S + 1 = 2$, as triplet $S = 1$ with $2S + 1 = 3$, and so on.

In this framework, we restrict ourselves to single-determinant wave functions employing one Slater determinant, but all derivations can be extended to multi-determinant wave functions (*125–127*).

For the total spin expectation value several definitions exist. Here, we choose Löwdin's representation (*128*)

$$\boldsymbol{S}^2 = -\frac{N(N-4)}{4} + \sum_{i>j} P_{ij}^{\sigma}, \tag{90}$$

where N denotes—as before—the total number of electrons of the molecule and P_{ij}^{σ} a pair-permutation operator for spin coordinates only. With this definition, we may reduce the total spin expectation value in the framework of a Slater determinant wave function to double sums over two-electron integrals involving the spin-dependent pair-permutation operator,

$$\begin{aligned}\langle \boldsymbol{S}^2 \rangle &= \langle \Psi^{\mathrm{SD}} | \boldsymbol{S}^2 | \Psi^{\mathrm{SD}} \rangle \\ &= -\frac{N(N-4)}{4} + \langle \Psi^{\mathrm{SD}} | \sum_{i>j} P_{ij}^{\sigma} | \Psi^{\mathrm{SD}} \rangle \\ &= -\frac{N(N-4)}{4} + \frac{1}{2} \sum_{i=1,j=1}^{N} [\langle ij | P_{12}^{\sigma} | ij \rangle - \langle ij | P_{12}^{\sigma} | ji \rangle].\end{aligned} \tag{91}$$

(A detailed analysis of $\langle \boldsymbol{S}^2 \rangle$ in DFT can be found in Refs. (*129,130*).) Note the change of meaning in the summation indices in Eq. (91): In the second line i, j label electronic (spin) coordinates, while they denote the indices of spin orbitals in the third line. For the study of open-shell transition-metal clusters, it is necessary to obtain an expression for the total spin expectation value, where the summation runs over the number of α- and β-electrons rather than over the total number of electrons N. Thus, the sum in Eq. (91) may be split into four sums over the various spin combinations,

$$\begin{aligned}\langle \Psi^{\mathrm{SD}} | \sum_{i>j} P_{ij}^{\sigma} | \Psi^{\mathrm{SD}} \rangle = &\frac{1}{2} \sum_{i\in\alpha, j\in\alpha}^{N^{\alpha},N^{\alpha}} [\langle ij | P_{ij}^{\sigma} | ij \rangle - \langle ij | P_{ij}^{\sigma} | ji \rangle] \\ &+ \frac{1}{2} \sum_{i\in\alpha, j\in\beta}^{N^{\beta},N^{\beta}} [\langle \bar{i}\bar{j} | P_{ij}^{\sigma} | \bar{i}\bar{j} \rangle - \langle \bar{i}\bar{j} | P_{ij}^{\sigma} | \bar{j}\bar{i} \rangle] \\ &+ \frac{1}{2} \sum_{i\in\alpha, j\in\beta}^{N^{\alpha},N^{\beta}} [\langle i\bar{j} | P_{ij}^{\sigma} | i\bar{j} \rangle - \langle i\bar{j} | P_{ij}^{\sigma} | \bar{j}i \rangle] \\ &+ \frac{1}{2} \sum_{i\in\beta, j\in\alpha}^{N^{\beta},N^{\alpha}} [\langle \bar{i}j | P_{ij}^{\sigma} | \bar{i}j \rangle - \langle \bar{i}j | P_{ij}^{\sigma} | j\bar{i} \rangle],\end{aligned} \tag{92}$$

where i represents a spin orbital with α-spin and $\bar{i}$ an orbital with β-spin and $N=N^\alpha+N^\beta$. If we now apply the spin permutation operator, the expectation value reads

$$\langle\Psi^{\mathrm{SD}}|\sum_{i>j}P_{ij}^{\sigma}|\Psi^{\mathrm{SD}}\rangle=\frac{1}{2}\sum_{i\in\alpha,j\in\alpha}^{N^\alpha,N^\alpha}[\langle ij|ij\rangle-\langle ij|ji\rangle]+\frac{1}{2}\sum_{i\in\beta,j\in\beta}^{N^\beta,N^\beta}[\langle\bar{i}\bar{j}\,|\bar{i}\bar{j}\rangle-\langle\bar{i}\bar{j}\,|\bar{j}\bar{i}\rangle]$$
$$+\frac{1}{2}\sum_{i\in\alpha,j\in\beta}^{N^\alpha,N^\beta}[\underbrace{\langle i\bar{j}\,|\bar{i}j\rangle}_{=0}-\langle i\bar{j}\,|j\bar{i}\rangle]+\frac{1}{2}\sum_{i\in\beta,j\in\alpha}^{N^\beta,N^\alpha}[\underbrace{\langle\bar{i}j|i\bar{j}\rangle}_{=0}-\langle\bar{i}j|\bar{j}i\rangle]. \tag{93}$$

Integration over spin functions simplifies this equation because the first two sums in Eq. (92) may be rewritten in terms of the number of α- and β-electrons $N^{\alpha\psi}$and N^β, respectively,

$$\frac{1}{2}\sum_{i\in\alpha,\,j\in\alpha}^{N^\alpha,N^\alpha}[\langle\phi_i|\phi_i\rangle\langle\phi_j|\phi_j\rangle-\langle\phi_i|\phi_j\rangle\langle\phi_j|\phi_i\rangle]=\frac{1}{2}\big((N^\alpha)^2-N^\alpha\big). \tag{94}$$

With the definition in Eq. (94) the individual terms in Eq. (93) reduce to

$$\langle\Psi^{\mathrm{SD}}|\sum_{i>j}P_{ij}^{\sigma}|\Psi^{\mathrm{SD}}\rangle=\frac{1}{2}\left((N^\alpha)^2-N^\alpha\right)+\frac{1}{2}\left((N^\beta)^2-N^\beta\right)-\sum_{i\in\alpha,j\in\beta}^{N^\alpha,N^\beta}\langle i\bar{j}\,|\bar{j}\,i\rangle, \tag{95}$$

which is equivalent to the evaluation of the second term in the definition of the total spin expectation value $\boldsymbol{S}^2$ [see Eq. (91)]. Thus, when rewriting the first term of Eq. (91) in terms of the numbers of electrons N^α and N^β we obtain for the total spin expectation value of $\boldsymbol{S}^2$

$$\langle\boldsymbol{S}^2\rangle=\frac{1}{2}\left(N^\alpha+N^\beta\right)+\frac{1}{4}\left(N^\alpha-N^\beta\right)^2-\sum_{i\in\alpha,j\in\beta}^{N^\alpha,N^\beta}\langle i\bar{j}|\bar{j}i\rangle, \tag{96}$$

In order to obtain expressions for the local spin expectation values, different decomposition schemes exist. One may either partition the total spin expectation value $\langle\boldsymbol{S}^2\rangle$ (*122,124*) as suggested by Mayer or the total spin operator $\boldsymbol{S}^2$ (*113,114*) as proposed by Clark and Davidson. The corresponding decomposition schemes for multi-determinant wave functions may be found in Refs. (*125–127*).

For the partitioning into expressions for S_{zA} both Mayer's and Clark and Davidson's schemes yield the same result, namely, that the expectation value is equal to half the difference between the number of α- and β-electrons attributed to basin A,

$$\langle S_{zA}\rangle = \frac{1}{2}\,(N_A^{\alpha} - N_A^{\beta}). \tag{97}$$

Note that the expectation value for a restricted, unrestricted, or restricted open-shell determinant is always given by $\langle S_z\rangle = \frac{1}{2}\,(N^{\alpha} - N^{\beta})$. However, the expressions for the local expectation values $\langle \boldsymbol{S}_{\mathrm{A}}^2\rangle$ and $\langle \boldsymbol{S}_A \cdot \boldsymbol{S}_B\rangle$ differ depending on whether we start with the partitioning of the total spin operator $\boldsymbol{S}^2$ or of its expectation value $\langle \boldsymbol{S}^2\rangle$. (Nevertheless, for both decomposition schemes the local expressions add up to the same result for the total expectation value $\langle \boldsymbol{S}^2\rangle$.) In particular, Clark and Davidson's decomposition assigns non-vanishing local spin values to closed-shell molecules (*114*). Although we have already shown in earlier work that Mayer's partitioning scheme cures these insufficiencies (*122,124*) by construction, a more detailed analysis could be provided. Hence, we shall here elaborate on the origin of these differences. Despite the fact that the decomposition of the expectation value yields the correct local expressions, we would also require to define proper local operator expressions for use in a phenomenological Spin Hamiltonian as in Eq. (79).

We start with the partitioning of the total spin operator, introduce then the decomposition of the expectation value, and discuss the differences between these results. In accordance with Eq. (86) the decomposition of $\boldsymbol{S}^2$ yields,

$$\boldsymbol{S}^2 = \sum_A \boldsymbol{S}_A^2 + \sum_{A\neq B} \boldsymbol{S}_A \cdot \boldsymbol{S}_B. \tag{98}$$

We may rewrite the scalar product $\boldsymbol{S}_A \cdot \boldsymbol{S}_B$ in terms of projection operators as an expectation value (*113*),

$$\langle \boldsymbol{S}_A \cdot \boldsymbol{S}_B\rangle = \sum_{ij} \langle ij|p_A(1)\boldsymbol{s}_1 p_B(2)\boldsymbol{s}_2|ij\rangle. \tag{99}$$

When we explicitly consider α- and β-spins in Eq. (99) and reorder the resulting terms according to one and two-electron contributions, we obtain double sums over the number of α- and the β-electrons, N^{α} and N^{β}, as well as over the mixed terms where one sum runs over N^{α} and the other over N^{β},

$$\begin{aligned}\langle \boldsymbol{S}_A \cdot \boldsymbol{S}_B \rangle &= \frac{3}{4}\delta_{AB}\left[\sum_{i}^{N^\alpha}\langle i|p_A|i\rangle + \sum_{i}^{N^\beta}\langle \bar{i}|p_A|\bar{i}\rangle\right] \\ &+ \frac{1}{4}\sum_{ij}^{N^\alpha N^\alpha}\langle i|p_A|i\rangle\langle j|p_B|j\rangle + \frac{1}{4}\sum_{\bar{i}\bar{j}}^{N^\beta N^\beta}\langle \bar{i}|p_A|\bar{i}\rangle\langle \bar{j}|p_B|\bar{j}\rangle \\ &- \frac{1}{4}\sum_{ij}^{N^\alpha N^\alpha}\langle i|p_A|j\rangle\langle j|p_B|i\rangle - \frac{1}{4}\sum_{\bar{i}\bar{j}}^{N^\beta N^\beta}\langle \bar{i}|p_A|\bar{j}\rangle\langle \bar{j}|p_B|\bar{i}\rangle \\ &- \frac{1}{4}\sum_{i\bar{j}}^{N^\alpha N^\beta}\langle i|p_A|i\rangle\langle \bar{j}|p_B|\bar{j}\rangle - \frac{1}{4}\sum_{i\bar{j}}^{N^\alpha N^\beta}\langle i|p_B|i\rangle\langle \bar{j}|p_A|\bar{j}\rangle \\ &- \sum_{i\bar{j}}^{N^\alpha N^\beta}\langle i|p_A|\bar{j}\rangle\langle \bar{j}|p_B|i\rangle,\end{aligned} \tag{100}$$

which also holds in the case of $A=B$ yielding $\langle \boldsymbol{S}_A^2\rangle$. Again, we indicated the β-spin orbital i by a bar as $\bar{\text{i}}$ and make use of the idempotency of the projection operator. Note that in the case of a closed-shell molecule this expression yields

$$\langle \boldsymbol{S}_A \cdot \boldsymbol{S}_B\rangle_{\text{closed-shell}} = \frac{3}{2}\delta_{AB}\sum_{i}^{\mathrm{N}/2}\langle i|p_A|i\rangle - \frac{3}{2}\sum_{ij}^{N/2}\langle i|p_A|j\rangle\langle i|p_B|j\rangle, \tag{101}$$

which is equal to zero only in the case of a complete basis set.

For the evaluation of Eq. (100), we expand the one-electron functions into a sum over M atom-centered basis functions $|\mu\rangle$ of Slater or Gauss type,

$$|i\rangle = \sum_{\mu}^{M} C_{i\mu}|\mu\rangle, \tag{102}$$

where $C_{i\mu}$ denote the basis-set coefficients (molecular orbital (MO) coefficients). The projection operators are not uniquely defined but several expressions exist, see, for example, the definition by Löwdin (*131*). Mulliken's definition (*132*) does not fulfill all properties of projection operators (*114*) and yields a pseudo-projector. It reads

$$p_A = \sum_{\mu\in A}|\mu\rangle S^{-1}_{\nu\mu}\langle\nu|. \tag{103}$$

Here, $S^{-1}_{\nu\mu}$ denotes the inverse overlap matrix element between basis functions μ and ν. With Eqs. (102) and (103) the one-electron terms in Eq. (100) reduce to

$$\begin{aligned}\sum_i^{N^\alpha}\langle i|p_A|i\rangle &= \sum_i^{N^\alpha}\langle i|\sum_{\mu\in A,\nu}|\nu\rangle S^{-1}_{\nu\mu}\langle\mu|i\rangle=\sum_i^{N^\alpha}\sum_{\mu\in A,\nu}\langle i|\nu\rangle S^{-1}_{\nu\mu}\langle\mu|i\rangle \\ &= \sum_i^{N^\alpha}\sum_{\mu\in A,\nu}\sum_{\rho,\pi}\langle\rho|\nu\rangle S^{-1}_{\nu\mu}\langle\mu|\pi\rangle C^{\alpha *}_{i\rho}C^{\alpha}_{i\pi} \\ &= \sum_{\mu\in A}\sum_{\rho,\pi}P^{\alpha}_{\rho\pi}\delta_{\rho\mu}\mathrm{S}_{\mu\pi} \\ &= \sum_{\mu\in A}\sum_{\pi}P^{\alpha}_{\mu\pi}S_{\pi\mu}=\sum_{\mu\in A}(\mathbf{P}^\alpha\mathbf{S})_{\mu\mu}=N^\alpha_A,\end{aligned} \tag{104}$$

where $\mathbf{P}^\alpha$ is the spin density matrix comprising the basis-set coefficients. As before, N^α_A denotes the number of α-electrons at basin A. In a similar fashion the terms containing the β-orbitals may be simplified. The two-electron terms in Eq. (100) may be reduced according to

$$\sum_{ij}^{N^\alpha,N^\alpha}\langle i|p_A|i\rangle\langle j|p_B|j\rangle=\sum_{\mu\in A,\nu\in B}(\mathbf{P}^\alpha\mathbf{S})_{\mu\mu}(\mathbf{P}^\alpha\mathbf{S})_{\nu\nu}. \tag{105}$$

Altogether the expectation value for $\langle \boldsymbol{S}_A\cdot\boldsymbol{S}_B\rangle$ can be rewritten in terms of sums over the spin density matrices $\mathbf{P}^\alpha$ and $\mathbf{P}^\beta$,

$$\begin{aligned}\langle \boldsymbol{S}_A\cdot\boldsymbol{S}_B\rangle^{CD} &= \frac{3}{4}\delta_{AB}\left[\sum_{\mu\in A}(\mathbf{P}^\alpha\mathbf{S})_{\mu\mu}+\sum_{\mu\in A}(\mathbf{P}^\beta\mathbf{S})_{\mu\mu}\right] \\ &+\frac{1}{4}\sum_{\mu\in A,\nu\in B}(\mathbf{P}^\alpha\mathbf{S})_{\mu\mu}(\mathbf{P}^\alpha\mathbf{S})_{\nu\nu}+\frac{1}{4}\sum_{\mu\in A,\nu\in B}(\mathbf{P}^\beta\mathbf{S})_{\mu\mu}(\mathbf{P}^\beta\mathbf{S})_{\nu\nu} \\ &-\frac{1}{4}\sum_{\mu\in A,\nu\in B}(\mathbf{P}^\alpha\mathbf{S})_{\mu\nu}(\mathbf{P}^\alpha\mathbf{S})_{\nu\mu}-\frac{1}{4}\sum_{\mu\in A,\nu\in B}(\mathbf{P}^\beta\mathbf{S})_{\mu\nu}(\mathbf{P}^\beta\mathbf{S})_{\nu\mu} \\ &-\frac{1}{4}\sum_{\mu\in A,\nu\in B}(\mathbf{P}^\alpha\mathbf{S})_{\mu\mu}(\mathbf{P}^\alpha\mathbf{S})_{\nu\nu}-\frac{1}{4}\sum_{\mu\in A,\nu\in B}(\mathbf{P}^\beta\mathbf{S})_{\mu\mu}(\mathbf{P}^\beta\mathbf{S})_{\nu\nu}.\end{aligned} \tag{106}$$

Note that again for $A=B$ the expression for $\langle \boldsymbol{S}^2_A\rangle$ is obtained here.

When adding the spin density matrices $\mathbf{P}^\alpha$ and $\mathbf{P}^\beta$ to yield the total density matrix $\mathbf{P}$, $\mathbf{P}=\mathbf{P}^\alpha+\mathbf{P}^\beta$, and the total spin density matrix $\mathbf{P}^{\mathrm{s}}$ being the difference of $\mathbf{P}^\alpha$ and $\mathbf{P}^\beta$, $\mathbf{P}^{\mathrm{s}}=\mathbf{P}^\alpha-\mathbf{P}^\beta$, we

arrive at a more compact expression. If we now evaluate the cases $A \neq B$ and $A = B$ separately, we obtain for $\boldsymbol{S}_A \cdot \boldsymbol{S}_B$,

$$\langle \mathbf{S}_A \cdot \mathbf{S}_B \rangle^{\mathrm{CD}}_{A \neq B} = \frac{1}{2} \sum_{\mu \in A, \nu \in B} (\mathbf{P}^{\mathrm{s}}\mathbf{S})_{\mu\nu} (\mathbf{P}^{\mathrm{s}}\mathbf{S})_{\nu\mu} + \frac{1}{4} \sum_{\mu \in A, \nu \in B} (\mathbf{P}^{\mathrm{s}}\mathbf{S})_{\mu\mu} (\mathbf{P}^{\mathrm{s}}\mathbf{S})_{\nu\nu} - \frac{3}{8} \sum_{\mu \in A, \nu \in B} \left[(\mathbf{PS})_{\mu\nu} (\mathbf{PS})_{\nu\mu} + (\mathbf{P}^{\mathrm{s}}\mathbf{S})_{\mu\nu} (\mathbf{P}^{\mathrm{s}}\mathbf{S})_{\nu\mu} \right], \tag{107}$$

whereas the corresponding equation for the local expectation value of $\boldsymbol{S}_A^2$ (case $A = B$) reads,

$$\langle \mathbf{S}_A^2 \rangle^{\mathrm{CD}} = \frac{1}{2} \sum_{\mu \in A, \nu \in A} (\mathbf{P}^{\mathrm{s}}\mathbf{S})_{\mu\nu} (\mathbf{P}^{\mathrm{s}}\mathbf{S})_{\nu\mu} + \frac{1}{4} \sum_{\mu \in A, \nu \in A} (\mathbf{P}^{\mathrm{s}}\mathbf{S})_{\mu\mu} (\mathbf{P}^{\mathrm{s}}\mathbf{S})_{\nu\nu} - \frac{3}{8} \sum_{\mu \in A, \nu \in A} \left[(\mathbf{PS})_{\mu\nu} (\mathbf{PS})_{\nu\mu} + (\mathbf{P}^{\mathrm{s}}\mathbf{S})_{\mu\nu} (\mathbf{P}^{\mathrm{s}}\mathbf{S})_{\nu\mu} \right] + \frac{3}{4} \left[\sum_{\mu \in A} (\mathbf{P}^{\alpha}\mathbf{S})_{\mu\mu} + \sum_{\mu \in A} (\mathbf{P}^{\beta}\mathbf{S})_{\mu\mu} \right]. \tag{108}$$

Note that we introduced the superscript "CD" in order to distinguish the expressions obtained by Clark and Davidson from those by Mayer, which will be given in the following marked by "Ma."

In a similar fashion, Mayer's partitioning of the total spin expectation value can be derived. Starting from Löwdin's expression for the total spin expectation value, Eq. (96), a one-electron basis set is introduced as in Eq. (102) and the numbers of α- and β-electrons, N^{α} and N^{β}, respectively, are replaced by sums over diagonal matrix elements $\sum_{\mu} (\mathbf{P}^{\alpha}\mathbf{S})_{\mu\mu}$ and $\sum_{\mu} (\mathbf{P}^{\beta}\mathbf{S})_{\mu\mu}$ [cf. Eq. (104)],

$$\langle \mathbf{S}^2 \rangle = \frac{1}{2} \left[\sum_{\mu} (\mathbf{P}^{\alpha}\mathbf{S})_{\mu\mu} + \sum_{\mu} (\mathbf{P}^{\beta}\mathbf{S})_{\mu\mu} \right] + \frac{1}{4} \left[\sum_{\mu} (\mathbf{P}^{\alpha}\mathbf{S})_{\mu\mu} - \sum_{\mu} (\mathbf{P}^{\beta}\mathbf{S})_{\mu\mu} \right]^2 - \sum_{\mu} (\mathbf{P}^{\alpha}\mathbf{S}\mathbf{P}^{\beta}\mathbf{S})_{\mu\mu}. \tag{109}$$

As each basis function is located at an atomic center A, we may reorder the sums in Eq. (109) and summarize all basis functions attributed to one center A so that sums over basis functions assigned to center A are obtained

$$\langle \mathbf{S}^2 \rangle = \sum_A \underbrace{\left[\frac{1}{2} \sum_{\mu \in A, \nu \in A} (\mathbf{P}^{\mathrm{s}}\mathbf{S})_{\mu\nu} (\mathbf{P}^{\mathrm{s}}\mathbf{S})_{\nu\mu} + \frac{1}{4} \sum_{\mu \in A, \nu \in A} (\mathbf{PS})_{\mu\mu} (\mathbf{PS})_{\nu\nu} \right]}_{\langle \boldsymbol{S}_A^2 \rangle^{\mathrm{Ma}}}$$
$$+ \sum_{A \neq B} \underbrace{\left[\frac{1}{2} \sum_{\mu \in A, \nu \in B} (\mathbf{P}^{\mathrm{s}}\mathbf{S})_{\mu\nu} (\mathbf{P}^{\mathrm{s}}\mathbf{S})_{\nu\mu} + \frac{1}{4} \sum_{\mu \in A, \nu \in B} (\mathbf{PS})_{\mu\mu} (\mathbf{PS})_{\nu\nu} \right]}_{\langle \boldsymbol{S}_A \cdot \boldsymbol{S}_B \rangle^{\mathrm{Ma}}_{A \neq B}}. \tag{110}$$

B. Comparison of Mayer's and Clark and Davidson's Local $\langle \boldsymbol{S}^2 \rangle$ Decomposition Schemes

In order to understand the differences between the two decomposition schemes, we rewrite Clark and Davidson's expression for the local expectation value $\langle \boldsymbol{S}_A \cdot \boldsymbol{S}_B \rangle^{CD}$ in terms of Mayer's expression and establish the additionally arising terms, which are the number of electrons located on A only present in the case $A = B$ and further terms which are the so-called bond-order terms B_{AB},

$$\langle \mathbf{S}_A \cdot \mathbf{S}_B \rangle^{\mathrm{CD}} = \underbrace{\frac{3}{4} \delta_{\mathrm{AB}} \left[\sum_{\mu \in \mathrm{A}} (\mathbf{P}^{\alpha}\mathbf{S})_{\mu\mu} + \sum_{\mu \in \mathrm{A}} (\mathbf{P}^{\beta}\mathbf{S})_{\mu\mu} \right]}_{N_A}$$
$$+ \underbrace{\frac{1}{2} \sum_{\mu \in A, \nu \in B} (\mathbf{P}^{\mathrm{s}}\mathbf{S})_{\mu\nu} (\mathbf{P}^{\mathrm{s}}\mathbf{S})_{\nu\mu} + \frac{1}{4} \sum_{\mu \in A, \nu \in B} (\mathbf{P}^{\mathrm{s}}\mathbf{S})_{\mu\mu} (\mathbf{P}^{\mathrm{s}}\mathbf{S})_{\nu\nu}}_{\langle \mathbf{S}_A \cdot \mathbf{S}_B \rangle^{\mathrm{Ma}}}$$
$$- \underbrace{\frac{3}{4} \sum_{\mu \in A \nu \in B} (\mathbf{P}^{\alpha}\mathbf{S})_{\mu\nu} (\mathbf{P}^{\alpha}\mathbf{S})_{\nu\mu} - \frac{3}{4} \sum_{\mu \in A, \nu \in B} (\mathbf{P}^{\beta}\mathbf{S})_{\mu\nu} (\mathbf{P}^{\beta}\mathbf{S})_{\nu\mu}}_{B_{AB}}$$
$$= \langle \boldsymbol{S}_A \cdot \boldsymbol{S}_B \rangle^{\mathrm{Ma}} + \delta_{AB} \frac{3}{4} N_A - \frac{3}{8} B_{AB}. \tag{111}$$

Knowing both decomposition schemes yield the same squared total spin expectation value, we may write the expectation value of the total spin operator $\boldsymbol{S}^2$ in terms of Mayer's local expressions

for $\langle \boldsymbol{S}_A^2 \rangle$ and $\langle \boldsymbol{S}_A \cdot \boldsymbol{S}_B \rangle$ plus the additional terms arising in Clark and Davidson's decomposition scheme as

$$\begin{aligned}\langle \mathbf{S}^2 \rangle = & \underbrace{\sum_A \left[\frac{1}{2} \sum_{\mu \in A, \nu \in A} (\mathbf{P}^{\mathrm{s}}\mathbf{S})_{\mu\nu} (\mathbf{P}^{\mathrm{s}}\mathbf{S})_{\nu\mu} + \frac{1}{4} \sum_{\mu \in A, \nu \in A} (\mathbf{PS})_{\mu\mu} (\mathbf{PS})_{\nu\nu} \right]}_{\langle \boldsymbol{S}_A^2 \rangle^{\mathrm{Ma}}} \\ & + \frac{3}{4} \sum_A N_A - \frac{3}{8} \sum_{A,B} B_{AB} \\ & + \underbrace{\sum_{A \neq B} \left[\frac{1}{2} \sum_{\mu \in A, \nu \in B} (\mathbf{P}^{\mathrm{s}}\mathbf{S})_{\mu\nu} (\mathbf{P}^{\mathrm{s}}\mathbf{S})_{\nu\mu} + \frac{1}{4} \sum_{\mu \in A, \nu \in B} (\mathbf{PS})_{\mu\mu} (\mathbf{PS})_{\nu\nu} \right]}_{\langle \boldsymbol{S}_A \cdot \boldsymbol{S}_B \rangle_{A \neq B}^{\mathrm{Ma}}} \end{aligned} \tag{112}$$

Hence, Eq. (112) is fulfilled if the bond-order terms plus $\frac{3}{4}\sum_A N_A$ add up to zero,

$$\frac{3}{4} \sum_A N_A - \frac{3}{8} \sum_{A,B} B_{AB} \stackrel{!}{=} 0, \tag{113}$$

and both decomposition schemes, Clark and Davidson's and Mayer's, respectively, yield the same total spin expectation value $\langle \boldsymbol{S}^2 \rangle$.

Illustrating the consequences of the two different decomposition schemes for the local spin values obtained may best be accomplished at the example of Eq. (112): Clark and Davidson's partitioning yields larger terms for the expectation value of $\boldsymbol{S}_A^2$ because of the additional contribution from the $+\delta_{AB}\,\frac{3}{4}N_A$ and the $\frac{3}{8}B_{AA}$ terms, whereas the cross terms $\langle \boldsymbol{S}_A \cdot \boldsymbol{S}_B \rangle$ must be smaller in comparison to Mayer's decomposition scheme due to the $\frac{3}{8}B_{AB}$ term. This is nicely illustrated in the case of closed-shell diatomic molecules, where $\langle \boldsymbol{S}_A \cdot \boldsymbol{S}_B \rangle^{\mathrm{CD}}$ and $\langle \boldsymbol{S}_A^2 \rangle^{\mathrm{CD}}$ add up to zero —as may be seen from Table I—when not only $\langle \boldsymbol{S}_A \cdot \boldsymbol{S}_B \rangle$ but also the cross term with inverted local spin centers $\langle \boldsymbol{S}_B \cdot \boldsymbol{S}_A \rangle$ is accounted for.

Furthermore, we showed in an earlier study (*124*) that Mayer's local expressions for $\langle \boldsymbol{S}_A^2 \rangle$ can be interpreted in terms of the eigenvalues as $\langle \boldsymbol{S}_A^2 \rangle = S_A(S_A+1)$.

TABLE I

LOCAL SPINS OF SELECTED DIATOMIC MOLECULES OBTAINED WITH THE MAYER (MA) AND THE CLARK AND DAVIDSON (CD) DECOMPOSITION SCHEME TAKEN FROM REF. (*124*)

Molecule	Method	$\langle S_A^2 \rangle$	$\langle S_B^2 \rangle$	$\langle S_A \cdot S_B \rangle$
H_2	CD	0.38	0.38	−0.38
	Ma	0.00	0.00	0.00
N_2	CD	1.05	1.05	−1.05
	Ma	0.00	0.00	0.00
CO	CD	0.84	0.84	−0.84
	Ma	0.00	0.00	0.00

VI. Technical Issues: Optimization of Broken-Symmetry Determinants

The local spin concept allows us to analyze a given wave function in terms of the local spin distributions needed for the description of the magnetic coupling. Applied in single-determinant approaches, one has to be able to converge Noodleman's broken-symmetry solution (*103,104,107*) in a self-consistent field (SCF) procedure that provides the basis-set coefficients. This presents a technical problem. Typically, the wave function is converged in a SCF algorithm when an initial guess for the molecular orbitals is provided. The SCF iterations may, however, converge to a stationary point that is close to the initial guess and may not represent the Slater determinant with the desired local spin distributions that describe antiferromagnetic coupling.

In order to circumvent this problem, one may either manipulate the initial guess or set up a constrained optimization, where the SCF iterations converge to predefined (constrained) properties. The latter was achieved in a protocol by Van Voorhis and coworkers (*133–135*). This approach suffers from the fact that the constrained Slater determinant may not represent a local energy minimum of the unconstrained potential energy surface.

To avoid the problems associated with a constrained optimization protocol "restrained optimization" has been considered in our group (*136*) as a straightforward and simple extension of Van Voorhis' work. Instead of fixed ideal local spin values a range of acceptable constrained values are defined and the optimization is guided toward the region of the preassigned values. As soon as the actual local spin values are sufficiently close to the ideal values, the constraints are relaxed and the optimization is allowed to converge to the energy minimum as illustrated in Fig. 1.

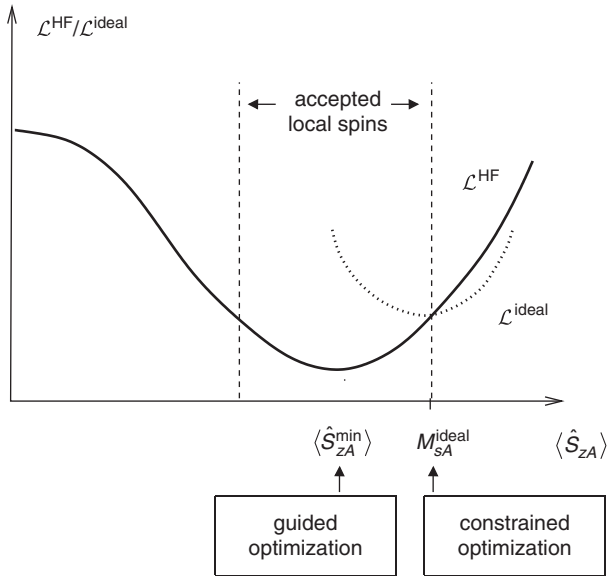

FIG. 1. Schematic representation of the restrained optimization scheme, where the set of MO coefficients is guided toward the region of acceptable local spin values. Reprinted with permission from Herrmann, C., Podewitz, M., Reiher, M. *Int. J. Quantum Chem.* **2009**, *109*, 2430–2446. Copyright 2009 John Wiley and Sons.

The advantage of such an optimization scheme is that the SCF iterations do not converge to a non-stationary energy on the unconstrained potential energy surface that may only represent an energy minimum on the constrained potential energy surface, but to a true energy minimum, where the final local spin values—within a certain threshold—may differ from the ideal ones.

Van Voorhis' constrained optimization is conveniently carried out with a Lagrange multiplier scheme (*137,138*), where the quantity to be optimized, i.e., the energy of the molecule, and the quantity to be constrained, here the local spins, were included as parameters in a Lagrangian functional. The multiplier is then updated after each SCF iteration step until the actual local spin values are in the predefined range of acceptable values. Of course, if the multiplier is then set to zero, a free optimization is performed allowing convergence to the true energy minimum of the unconstrained potential energy surface. To further guide this last optimization step by means of gradient information is, however, not that trivial.

The local spin values obtained in a decomposition scheme may either be local $\langle \boldsymbol{S}_A^2 \rangle$ or local $\langle S_{zA} \rangle$ expectation values as evident from the last section. Since we are interested merely in Slater determinants describing local high-spin centers, it is most suitable to employ local $\langle S_{zA} \rangle$ values as properties to be constrained in such a multiplier scheme. If we recall that the $\langle S_{zA} \rangle$ expectation values should be equal to the ideal M_{sA} and denote ideal values as M_{sA}^{ideal} values, the Lagrangian can be chosen to be (135,136)

$$\mathcal{L} = E - \sum_{i=1}^{N} \epsilon_i (\langle i|i \rangle - 1) - \sum_A \lambda_A \left(\langle S_{zA} \rangle - M_{sA}^{\text{ideal}} \right), \tag{114}$$

so that it ensures ideal local spin values M_{sA}^{ideal} on the fragments A. Here, λ_A is the Lagrangian multiplier. Now, we have to variationally optimize the Lagrangian $\mathcal{L}$ so that $\delta \mathcal{L} = 0$. This stationarity condition is only fulfilled if the imposed constraints are satisfied, i.e., if the actual $\langle S_{zA} \rangle$ value is in the accepted range so that $\langle S_{zA} \rangle$ and the ideal M_{sA}^{ideal} differ only within a certain threshold. As a side remark it should be noted that the constraints enter the one-electron Fock operator f' and give rise to an additional potential v_{add}

$$f' = -\frac{1}{2}\Delta + v_{\text{eff}} + v_{\text{add}} = f - \sum_A \lambda_A s_{zA}. \tag{115}$$

In the restrained optimization scheme, the SCF algorithm is employed with a fixed multiplier until convergence is achieved and subsequently the multiplier is updated, which is in our implementation (*134*) realized by a Newton-type optimization algorithm when employing the second derivatives of $\mathcal{L}$ with respect to λ_A as

$$\lambda_A^{\text{new}} = \lambda_A^{\text{old}} - \frac{\left(\frac{d\mathcal{L}}{d\lambda_A} \right)}{\left(\frac{d^2\mathcal{L}}{d\lambda_A^2} \right)}, \tag{116}$$

The expressions for the second derivatives may be obtained by perturbation theory (*134*) and can be calculated according to

$$\frac{d^2\mathcal{L}}{d\lambda_A^2} = -2 \sum_\sigma \sum_{i \in \sigma}^{\text{occ}} \sum_{a \in \sigma}^{\text{virt}} \frac{|\langle a|s_{zA}|i \rangle|^2}{\epsilon_i^\sigma - \epsilon_a^\sigma} \tag{117}$$

as a sum over S_{zA} expectation values of the occupied orbitals i and the virtual orbitals a divided by their energy difference, where σ indicates either α- or β-spin.

The advantage of such an optimization scheme is not only the convergence of a well-defined BS determinant but also the possibility to investigate *any* local spin distribution. Thus it is possible to estimate energy differences between various local spin distributions as long as it represents an energy minimum and employ them to study different magnetic coupling schemes.

VII. Studies on Open-Shell Polynuclear Transition-Metal Clusters

In this review, we presented the theoretical foundations of spin–spin interactions, the concept of local spins, and their convergence in a restrained optimization scheme. We shall now discuss the relevance and consequences for transition-metal clusters on the basis of new results.

In principle, transition-metal clusters may best be treated with multi-determinant wave-function methods (*139*), but in practice due to their size often only DFT calculations are feasible and method-inherent errors have to be taken care of, e.g., the problem of spin contamination and the approximate nature of the exchange–correlation functionals available.

In quantum chemistry, a number of different "recipes" for the investigation of such open-shell clusters exist. For example, it has been investigated which density functional performs best and which spin states should be considered to be relevant. We will point out here that it may not be sufficient to consider only selected spin states and more substantial investigations may be necessary.

A. Relevant Spin States in Transition-Metal Clusters

For transition-metal cluster studies, often only the ferromagnetically coupled high-spin (hs) state, the antiferromagnetically coupled broken-symmetry (BS) state, as well as the closed-shell state showing no magnetic coupling are investigated, whereas the spin state with the lowest relative energy is the desired one. However, to ensure that one of these selected spin states is of lowest energy and that there exists no intermediate spin state with lower energy, the energies of *all* potential spin states have to be investigated. In order to demonstrate the consequences of this, we present in Table II all possible spin states for a binuclear iron cluster **1**—synthesized in the Westerhausen group at the University of Jena (140)—with a maximum spin of S=4 corresponding to four unpaired electrons on each Fe center. In

TABLE II

SELECTED IDEAL TOTAL AND LOCAL SPIN EXPECTATION VALUES FOR THE [Fe_2] CLUSTER **1**, WHERE EACH METAL CENTER CARRIES FOUR UNPAIRED ELECTRONS RESULTING IN A TOTAL SPIN STATE OF S=4 FOR THE HIGH-SPIN STATE. LOCAL SPIN VALUES ON THE IRON ATOMS ARE DISPLAYED IN THE LAST COLUMN. UP-POINTING ARROWS INDICATE EXCESS OF α-SPIN AND DOWN-POINTING ARROWS EXCESS OF β-SPIN

Spin state	$S(S+1)$	M_{s1}	M_{s2}	$\langle S_{z_1} \cdot S_{z_2} \rangle$	
0	0	2	−2	−6	↑↑↑↑–↓↓↓↓
	0	1	−1	−3	↑↑–↓↓
	0	0	0	0	0–0
1	2	2	−1	−3	↑↑↑↑–↓↓
	2	1	0	0	↑↑–0
2	6	2	0	0	↑↑↑↑–0
	6	1	1	1	↑↑–↑↑
3	12	2	1	2	↑↑↑↑–↑↑
4	20	2	2	4	↑↑↑↑–↑↑↑↑

Table II up- and down-pointing arrows were chosen to illustrate the local spin distributions, where an up-pointing arrow represents an electron with α-spin and a down-pointing arrow an electron with β-spin. The ideal total spin expectation values are given in terms of the eigenvalues and local spins on the metal centers are indicated by ideal M_{sA}values.

Even in the simple case of a binuclear cluster, there exist nine relevant local spin distributions for the various spin states. It is obvious that the number of possible local spin distributions scales with the number of metal centers in the cluster and with the number of unpaired electrons at each center. Our restrained optimization tool can conveniently be employed to study any of these possible local spin distributions.

In practice, however, already with a comparatively small number of metal atoms it is no longer feasible to investigate all possible spin states with all potential realizations by various local spin distributions. Assumptions on the interaction of the metal centers on the basis of their structural arrangement and experimental susceptibility measurements have to be made. For example, for the BS state of a tetranuclear transition-metal cluster, one has to decide which of the four metal atoms couple in an antiferromagnetic fashion with each other. Prominent coupling schemes are, e.g., the dimer-of-dimers 2-plus-2-type or the 3-plus-1-type coupling scheme, whereas for a thorough discussion all possible interaction schemes need to be studied. This problem

is, for instance, vividly discussed in the literature in the case of the water-oxidizing complex of Photosystem II (*141–145*).

Even if the energies of all possible spin states were investigated, the conclusions might not be unambiguous as illustrated here at the example of binuclear [Fe_2] **1** and tetranuclear [Fe_4] **2**. (This second cluster has also been synthesized by Westerhausen and coworkers (*140*)). For both clusters we investigated all possible spin states. The structures were fully optimized for each spin state, but also single-point calculations on the optimized high-spin structures were carried out. Additionally, in the case of [Fe_2], we also studied the effect of different density functionals. The relative energy differences for the various spin states are presented in Fig. 2 for **1** and in Fig. 3 for **2**. For the solution of the BS state the question of how the four metal centers are coupled arises (as previously discussed) but is for the sake of simplicity not discussed here.

Note that in Figs. 2 and 3 the prime indicates that converged BS orbitals were provided as initial guess, whereas the double prime denotes that converged high-spin orbitals were employed. The energy of the closed-shell restricted state denoted as $S{=}R$ has been arbitrarily set to zero.

Depending on the initial guess Slater determinants with different energies were converged for one particular spin state, e.g., compare for $S{=}2$ of [Fe_2] **1** the BP86/RI/TZVP single-point results on the high-spin structure. These states with different energies exhibit distinct local spin distributions as may be seen from Table III and thus represent the various realizations of a total spin state. Instead of various initial guess orbitals, we may of course employ the restrained optimization tool (*136*), where we may converge any local spin distribution as long as it represents an energy minimum.

Note that in Table III local $\langle S_{zA}\rangle$, $\langle \boldsymbol{S}_A^2\rangle$, and $\langle \boldsymbol{S}_A \cdot \boldsymbol{S}_B\rangle$ expectation values for the [Fe_2] cluster **1** are listed. As shown in Section V the local expressions for the Mayer and the Clark and Davidson decomposition schemes differ. Hence, different values for the $\langle \boldsymbol{S}_A^2\rangle$, e.g., for $\langle \boldsymbol{S}_{\mathrm{Fe1}}^2\rangle$ located at the center Fe1, arise with these two partitioning schemes. The same argument holds for the cross terms $\langle \boldsymbol{S}_A \cdot \boldsymbol{S}_B\rangle$, here $\langle \boldsymbol{S}_{\mathrm{Fe1}} \cdot \boldsymbol{S}_{\mathrm{Fe2}}\rangle$. The total spin expectation value $\langle \boldsymbol{S}^2\rangle$ is shown to illustrate that spin contamination is fairly low for most spin states. The reader should not be confused by the fact that summation over the local spin values at the iron centers $\langle \boldsymbol{S}_{\mathrm{Fe1}}^2\rangle$, $\langle \boldsymbol{S}_{\mathrm{Fe2}}^2\rangle$, and $\langle \boldsymbol{S}_{\mathrm{Fe1}} \cdot \boldsymbol{S}_{\mathrm{Fe2}}\rangle$ does not yield the same value for Mayer and for Clark and Davidson data and that they do not sum up to $\langle \boldsymbol{S}^2\rangle$. The total spin expectation value $\langle \boldsymbol{S}^2\rangle$ is only obtained when summing all local spin values of all atoms of the [Fe_2] cluster **1**.

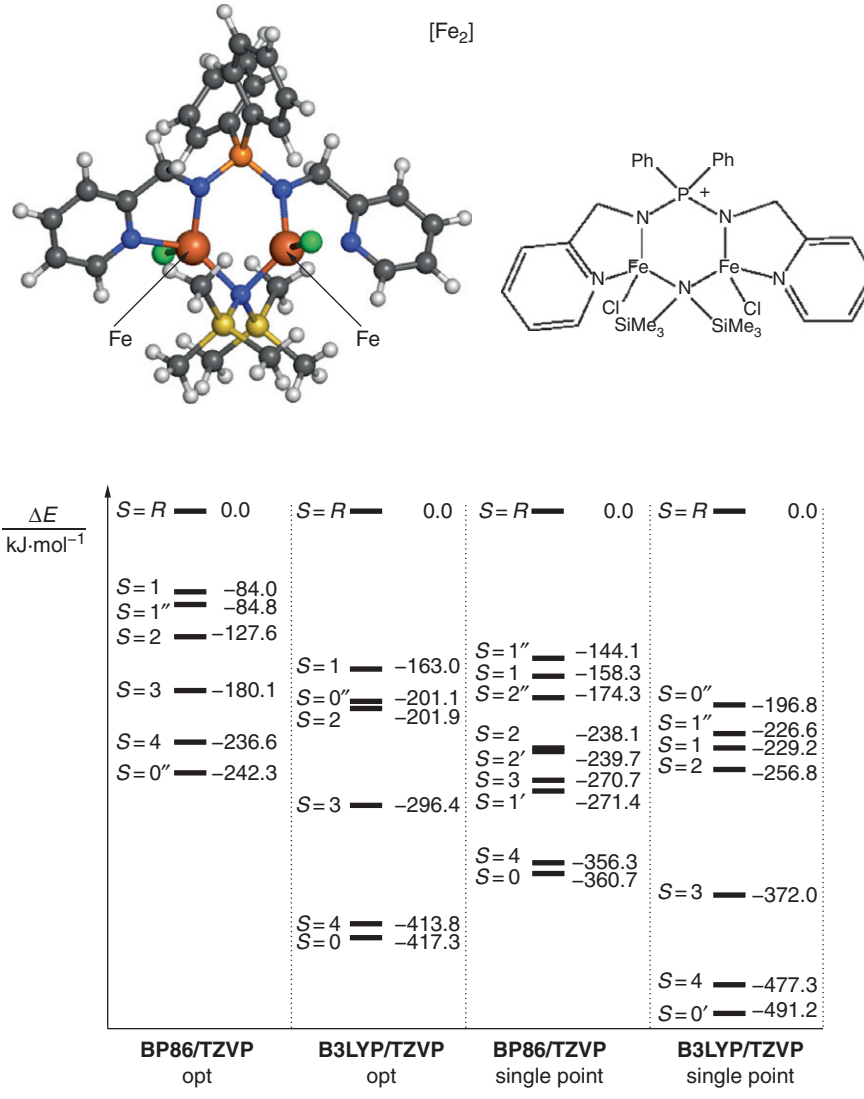

FIG. 2. Relative energy differences between the spin states of [Fe_2] **1**, for each spin state optimized structures denoted "opt" as well as for single-point calculations on the optimized high-spin structure denoted as "single point," where the energy of the closed-shell spin restricted state has arbitrarily been set to zero.

Considering [Fe_2] cluster **1**, although all calculations predict the S=0 broken-symmetry (BS) and the S=4 high-spin (hs) states to be most stable with the BS state slightly favored, the relative energy splittings may differ and the individual energy gaps may

depend on several criteria: like (i) on the density functional employed (the energy gap between the high-spin and the broken-symmetry state is sensitive to the amount of exact exchange energy in the functional (*33,136,146,147*)); and (ii) on whether single-point calculations or structure optimizations were performed. The latter effect is pronounced for the polynuclear cluster [Fe_4] **2**, which may be seen from Fig. 3. Here, we performed full structure optimizations for each spin state with relative energy differences displayed in the left energy ladder in Fig. 3 as well as single-point calculations on the optimized high-spin structure (right energy ladder in Fig. 3). For each calculation only the number of α- and β-electrons was specified. The relative energy gap between the most stable state, here the S=8 high-spin state, and the least stable closed-shell state is -370.4 kJ mol^{-1} for the single-point calculations, whereas for the structure optimizations the relative energy gap between the most stable spin state and the closed-shell state decreases to about -45 kJ mol^{-1}.

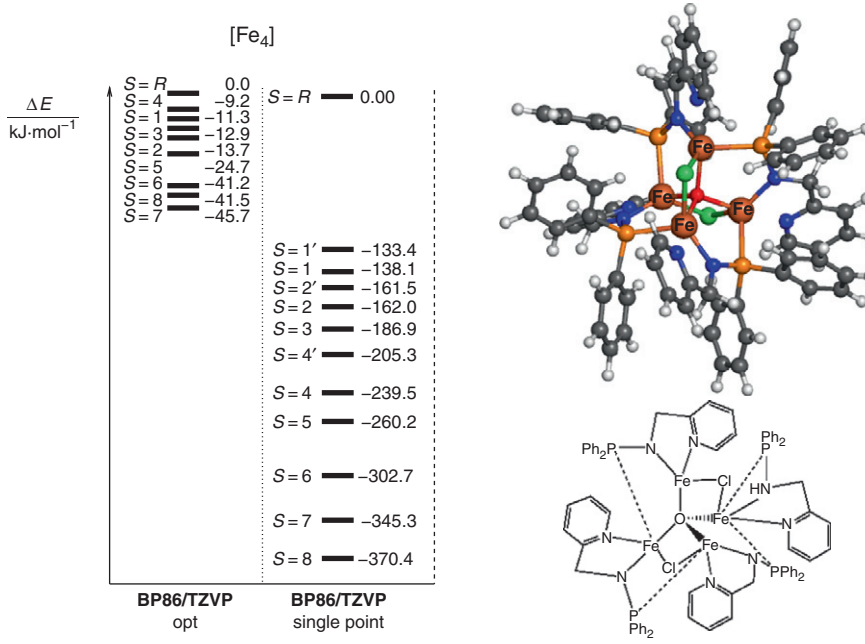

FIG. 3. Relative energies for spin states of the [Fe_4] cluster **2** on optimized structures of spin symmetry given (left panel) as well as single points at the high-spin structure (right panel). The BS solution is not displayed.

TABLE III

THE TOTAL SPIN EXPECTATION VALUE $\langle \boldsymbol{S}^2 \rangle$ AND SELECTED LOCAL $\langle S_{zA} \rangle$, $\langle \boldsymbol{S}_A^2 \rangle$, AND $\langle \boldsymbol{S}_A \cdot \boldsymbol{S}_B \rangle$ VALUES OF THE [Fe_2] CLUSTER **1** OBTAINED WITH MULLIKEN PROJECTION OPERATORS ARE GIVEN FOR LOCAL DECOMPOSITION SCHEMES ACCORDING TO MAYER AND TO CLARK AND DAVIDSON FOR SINGLE-POINT CALCULATIONS ON THE BP86/RI/TZVP OPTIMIZED HIGH-SPIN STRUCTURE

Mayer							Clark–Davidson		
M_s	$\langle \boldsymbol{S}^2 \rangle$	$\langle S_{zFe1} \rangle$	$\langle S_{zFe2} \rangle$	$\langle \boldsymbol{S}_{Fe1}^2 \rangle$	$\langle \boldsymbol{S}_{Fe2}^2 \rangle$	$\langle \boldsymbol{S}_{Fe1} \cdot \boldsymbol{S}_{Fe2} \rangle$	$\langle \boldsymbol{S}_{Fe1}^2 \rangle$	$\langle \boldsymbol{S}_{Fe2}^2 \rangle$	$\langle \boldsymbol{S}_{Fe1} \cdot \boldsymbol{S}_{Fe2} \rangle$
0″	3.98	1.80	−1.79	4.74	4.67	−3.20	5.81	5.73	−3.26
1	4.42	0.02	0.93	1.34	2.22	0.02	2.29	3.16	−0.01
1′	4.70	1.85	−1.05	4.86	2.18	−1.86	6.08	3.40	−2.01
1″	4.34	0.07	0.92	1.13	1.98	0.08	2.30	3.13	0.00
2	7.74	1.79	0.08	4.64	1.12	0.1	5.76	2.31	0.09
2′	7.81	1.80	0.01	4.71	1.16	0.06	5.82	2.33	−0.03
2″	7.35	1.02	0.96	2.12	2.05	1.02	3.35	3.25	0.90
3	12.71	1.73	1.09	4.38	2.30	1.93	5.54	3.54	1.79
4	20.24	1.81	1.83	4.73	4.38	3.35	5.84	5.94	3.26

Note that for each calculation we ensure that we optimize the spin state with the desired local spin distribution, which is straightforward for the high-spin state but difficulties may arise when determining the coupling schemes for the broken-symmetry state or any other intermediate spin state. As there are in principle many possible coupling schemes for the four iron atoms in the broken-symmetry state, we omitted the broken-symmetry solution here for the sake of brevity. In principle, we would have to evaluate *all* possible local spin distributions and determine the configuration that yields the lowest energy. However, it is neither our goal here to determine the magnetic coupling behavior nor to discuss spin crossover or the role of the bridging oxygen atom in this cluster. We merely sought to illustrate that it may not be sufficient to perform only single-point calculations for the various spin states on one specific structure (often on the high-spin structure or the crystal structure) but that the structures have to be optimized for each spin state. Moreover, it can also be seen from Fig. 3 that the structure optimization may alter the energetic order of the spin states and for the optimized structures (left panel) the high-spin state is no longer the most stable state but the S=7 state has a slightly higher stability.

The energy gaps between the various spin states are so small that they may be very well in the order of the error margin of DFT. Hence, we can no longer reliably predict which spin state is the most stable one. This may not be an issue when experimental results clearly characterize the type of magnetic coupling of such transition-metal clusters but one may run into trouble when experimental results do not allow for unambiguous conclusions on the magnetic coupling type. For example, it has been shown for a [Fe_6] cluster, where experimental susceptibility measurements did not clearly determine the magnetic coupling, that DFT calculations predict such small energy gaps between the hs and BS states that depending on the density functional employed and on whether single-point calculations or structure optimizations were performed the relative stability of the two states may be inverted (*148*).

B. Can Spin–Spin Interactions Be Structure Determining?

It has been long known that for a given transition-metal cluster the open-shell and the closed-shell species may differ. Typically, metal–ligand bond lengths are elongated for the open-shell structures, where the metal centers carry local spins and electrons occupy antibonding orbitals, in comparison to their closed-shell

analogs. However, in many cases these differences are very small due to a rigid scaffold of the cluster.

If, however, ligands are free to orientate, spin–spin interaction may be structure determining as for example in the case of the reactive intermediate of a [Ru_2] catalyst capable of oxidizing water to dioxygen (*149,150*). The active species with the sum formula $[(terpy)_2(H_2O)Ru(bpp)Ru(H_2O)(terpy)_2]^{3+}$ consists of two ruthenium centers with each *t*-pyridine ligands connected via a rigid 3,5-*bis*(2-pyridyl)pyrazole (bpp) ligand, whereas the two oxo-ligands are relatively free to orientate.

We studied the hs S=2, the triplet S=1, the BS S=0 as well as the closed-shell state for this reactive intermediate and present the BP86/RI/TZVP structure optimizations in Fig. 4. Local-spin distributions are given in Table IV for local expectation values.

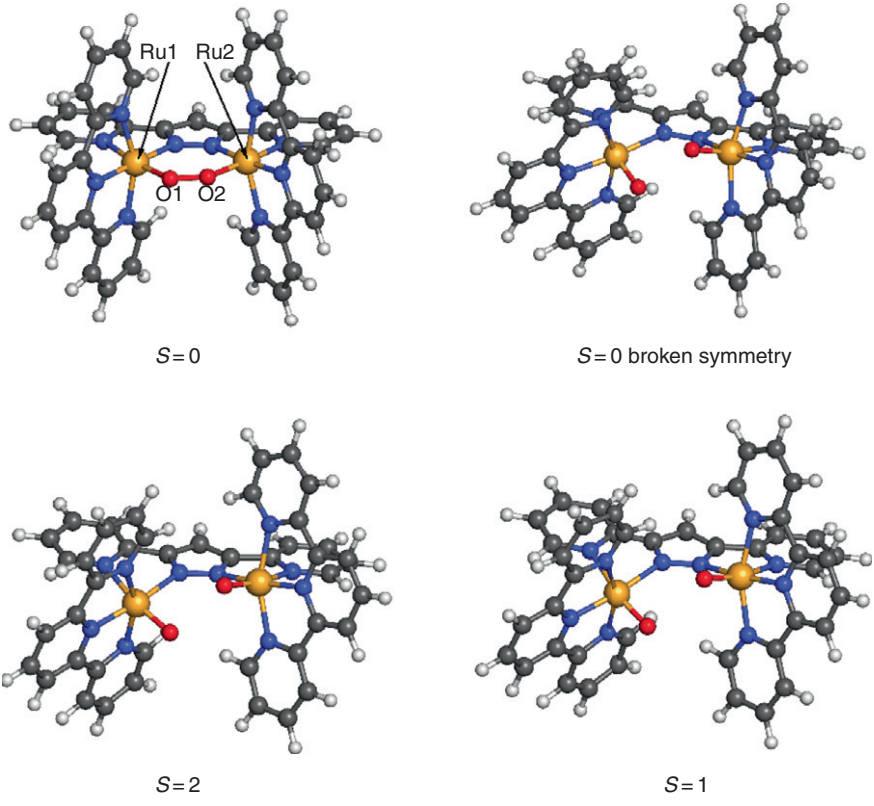

FIG. 4. Structures of the various spin states of a [Ru_2] catalyst intermediate. For the closed-shell species no Ru-oxo structure exists but all structure optimizations converge to the superoxo state.

TABLE IV

LOCAL SPIN DISTRIBUTIONS OBTAINED BY MODIFIED LÖWDIN PROJECTORS AS WELL AS THE TOTAL SPIN $\langle \boldsymbol{S}^2 \rangle$. THE ARROWS ARE GRAPHICAL REPRESENTATIONS OF THE UNPAIRED ELECTRONS

M_s	Local spins	$\langle \boldsymbol{S}^2 \rangle$	$\langle S_{zRu1} \rangle$	$\langle S_{zO1} \rangle$	$\langle S_{zRu2} \rangle$	$\langle S_{zO2} \rangle$
0 BS	↑↑–↓↓	1.964	0.44	0.45	−0.44	−0.45
1	00–↑↑	2.919	0.01	0.00	0.44	0.44
2	↑↑–↑↑	6.014	0.45	0.46	0.45	0.46

Our DFT studies on this intermediate clearly show that a [Ru_2] structure with two separate Ru-oxo groups could not be converged for the closed-shell state but requires a non-zero local spin on the oxygen atom(s) as can be understood from Table IV. All structure optimizations of the closed-shell state—even when the input structure is manipulated—converged to a superoxo species with a short oxygen–oxygen bond. Hence, phenomenologically speaking the local spin on the oxygen atoms prevents O–O bond formation and stabilizes a [Ru_2] cluster with two oxo-ligands.

VIII. Conclusions

Being able to accurately describe spin–spin interactions in transition-metal clusters is the first step en route to understand and model their molecular properties and chemical reactivities. This cannot be accomplished without a profound understanding of the fundamental quantum theory. As there exists hardly any presentation spanning basic theory to present-day quantum chemical applications, we aimed here to present such an overview with an emphasis on recent work carried out in our group. For this purpose, we reviewed the concepts of relativistic quantum chemistry starting from most fundamental Dirac–Coulomb–Breit Hamiltonian and subsequently presenting approximations to this fully relativistic Hamiltonian, namely the Breit–Pauli Hamiltonian and phenomenological Hamiltonians, i.e., the effective Spin Hamiltonian of ESR spectroscopy as well as the well-known Dirac–Heisenberg–Van Vleck Spin Hamiltonian.

Then, we focused on conceptual problems such as the definition of local spins that do hardly emerge naturally in holistic quantum theory. The local spin concept was rigorously introduced in quantum chemistry about 10 years ago by Clark and Davidson. We reviewed the most important contributions in this field and

pointed out problems that may arise from converging broken-symmetry determinants and how they can be solved.

In the last section of this review, we elaborated on the relevance and consequences of these concepts for transition-metal cluster chemistry on the basis of new results. We discussed problems and pitfalls that may arise in present-day quantum chemical DFT calculations on open-shell clusters. Clearly, these obstacles point to the necessity of developing improved density functionals and also new *ab initio* electron correlation methods, like, for example, the density renormalization group algorithm (*151*).

Computational Methodology

All electron calculations were carried out with the DFT program suite Turbomole (*152,153*). The clusters were treated as open-shell systems in the unrestricted Kohn–Sham framework. For the calculations we used the Becke–Perdew exchange–correlation functional dubbed BP86 (*154,155*) and the hybrid B3LYP functional (*156,157*). For BP86 we invoked the resolution-of-the-identity (RI) approximation as implemented in TURBOMOLE. For all atoms included in our models we employed Ahlrichs' valence triple-ζ TZVP basis set with polarization functions on all atoms (*158*). If not noted otherwise, initial guess orbitals were obtained by extended Hückel theory. Local spin analyses were performed with our local TURBOMOLE version, where either Löwdin (*131*) or Mulliken (*132*) pseudo-projection operators were employed. Broken-symmetry determinants were obtained with our restrained optimization tool (*136*). Pictures of molecular structures were created with PYMOL (*159*).

ACKNOWLEDGMENTS

This work has been financially supported by the Schweizer Nationalfonds and by ETH Zurich (TH Grant 0-20436-07).

REFERENCES

1. Benjamin, S. C.; Bose, S. *Phys. Rev. A* **2004**, *70*, 032314.
2. Carretta, S.; Santini, P.; Amoretti, G.; Troiani, F.; Affronte, M. *Phys. Rev. B* **2007**, *76*, 024408.
3. Schlegel, C.; van Slageren, J.; Manoli, M.; Brechin, E. K.; Dressel, M. *Phys. Rev. Lett.* **2008**, *101*, 147203.

4. Ardavan, A.; Rival, O.; Morton, J. J. L.; Blundell, S. J.; Tyryshkin, A. M.; Timco, G. A.; Winpenny, R. E. P. *Phys. Rev. Lett.* **2007**, *98*, 057201.
5. Hanson, R.; Kouwenhoven, L. P.; Petta, J. R.; Tarucha, S.; Vandersypen, L. M. K., *Rev. Mod. Phys.* **2007**, *79*, 1455.
6. Bertaina, S.; Gambarelli, S.; Mitra, T.; Tsukerblat, B.; Müller, A.; Barbara, B. *Nature* **2008**, *453*, 203–207.
7. Benjamin, S. C.; Ardavan, A.; Briggs, G. A. D.; Britz, D. A.; Gunlycke, D.; Jefferson, J.; Jones, M. A. G.; Leigh, D. F.; Lovett, B. W.; Khlobystov, A. N.; Lyon, S. A.; Morton, J. J. L.; Porfyrakis, K.; Sambrook, M. R.; Tyryshkin, A. M. *J. Phys. Condens. Matter* **2006**, *18*, S867–S883.
8. Gomez-Segura, J.; Diez-Perez, I.; Ishikawa, N.; Nakano, M.; Veciana, J.; Ruiz-Molina, D. *Chem. Commun*. **2006**, *27*, 2866–2868.
9. Leuenberger, M. N.; Loss, D. *Nature* **2001**, *410*, 789–793.
10. Childress, L.; Dutt, M. V. G.; Taylor, J. M.; Zibrov, A. S.; Jelezko, F.; Wrachtrup, J.; Hemmer, P. R.; Lukin, M. D. *Science* **2006**, *314*, 281–285.
11. Kahn, O. "*Molecular Magnetism*"; VCH: Weinheim, **1993**.
12. Behr, A. "*Angewandte Homogene Katalyse*"; Wiley-VCH: Weinheim, **2008**.
13. Chorkendorff, I.; Niemantsverdriet, J. W. "*Concepts of Modern Catalysis and Kinetics*"; Wiley-VCH: Weinheim, **2007**.
14. Hartwig, J. F. "*Organotransition Metal Chemistry: From Bonding to Catalysis*"; University Science books: Sausalito, CA, **2009**.
15. Thomas, J. M.; Thomas, W. J. "*Principles and Practice of Heterogeneous Catalysis*"; Wiley-VCH: Weinheim, **1996**.
16. Cornils, B.; Herrmann, W. A. "*Applied Homogeneous Catalysis with Organometallic Compounds: A Comprehensive Handbook in Three Volumes*"; Wiley-VCH: Weinheim, **2002**.
17. Miller, J. S.; Drillon, M. "*Magnetism: Molecules to Materials V*"; Wiley-VCH: Weinheim, **2005**.
18. Ribas Gispert, J. "*Coordination Chemistry*"; Wiley-VCH: Weinheim, **2008**.
19. Carretta, P.; Lascialfari, A. "*NMR-MRI, μSR and Mössbauer Spectroscopies in Molecular Magnets*"; Springer: Heidelberg, **2007**.
20. Boca, R. "*Theoretical Foundations of Molecular Magnetism (Current Methods in Inorganic Chemistry)*"; Elsevier Science: Amsterdam, **1999**.
21. Reiher, M.; Wolf, A. "*Relativistic Quantum Chemistry*"; Wiley-VCH: Weinheim, **2009**.
22. Cramer, C. J. "*Essentials of Computational Chemistry: Theory and Models*"; Wiley: Chichester, West Sussex, England, **2004**.
23. Jensen, F. "*Introduction to Computational Chemistry*"; Wiley: Chichester, West Sussex, England, **2007**.
24. Hohenberg, P.; Kohn, W. *Phys. Rev. B* **1964**, *136*, 864–971.
25. Rajagopal, A. K.; Callaway, J. *Phys. Rev. B* **1973**, *7*, 1912–1919.
26. Engel, E.; Dreizler, R. M. Relativistic density functional theory. In: "*Density Functional Theory II*", vol. 181; Ed. Nalewajski, R. F.; Springer: Berlin, **1996**, 1–80.
27. Engel, E.; Müller, H.; Speicher, C.; Dreizler, R. M. Density functional aspects of relativistic field theories. In: "*Density Functional Theory*", vol. 337; Eds. Gross, E. K. U, Dreizler, R. M.; Plenum Press: New York, **1995**, 65–118.
28. Engel, E.; Keller, S.; Bonetti, A.; Müller, H.; Dreizler, R. M. *Phys. Rev. A* **1995**, *52*, 2750–2764.
29. Engel, E.; Keller, S.; Dreizler, R. M. *Phys. Rev. A* **1996**, *53*, 1367–1374
30. Engel, E. Relativistic density functional theory: foundations and basic formalism. In: "*Relativistic Electronic Structure*

Theory—Fundamentals", vol. 11; Ed. Peter Schwerdtfeger, Elsevier: Amsterdam, **2002**, 523–621.
31. MacDonald, A. H.; Vosko, S. H. *J. Phys. Chem. C: Solid State Phys.* **1979**, *12*, 2977–2990.
32. van Wüllen, C. *J. Comput. Chem.* **2002**, *23*, 779–785.
33. Reiher, M. *Faraday Discuss.* **2007**, *135*, 97–124.
34. Jacob, C.R.; Reiher, M. "*poster presenation at DFT 2009*; Lyon, France. **2009**"
35. Jacob, C.R.; Reiher, M. **2010**, in preparation.
36. Hess, B. A. *Phys. Rev. A* **1986**, *33*, 3742–3748.
37. Douglas, M.; Kroll, N. M. *Ann. Phys.* **1974**, *82*, 89–155.
38. Wolf, A.; Reiher, M. *J. Chem. Phys.* **2004**, *121*, 2037–2047.
39. Wolf, A.; Reiher, M. *J. Chem. Phys.* **2004**, *121*, 10945–10956.
40. Reiher, M. *Theor. Chem. Acc.* **2006**, *116*, 241–252.
41. Chang, C.; Pelissier, M.; Durand, P. *Phys. Scr.* **1986**, *34*, 394–404.
42. Heully, J. L.; Lindgren, I.; Lindroth, E.; Lundqvist, S.; Mårtensson-Pendrill, A. M. *J. Phys. B: At. Mol. Phys.* **1986**, *19*, 2799–2815.
43. Durand, P. *C. R. Acad. Sci. II* **1986**, *303*, 119.
44. van Lenthe, E.; Baerends, E. J.; Snijders, J. G. *J. Chem. Phys.* **1993**, *99*, 4597–4610.
45. van Lenthe, E.; Baerends, E. J.; Snijders, J. G. *J. Chem. Phys.* **1994**, *101*, 9783–9792.
46. van Leeuwen, R.; van Lenthe, E.; Baerends, E. J.; Snijders, J. G. *J. Chem. Phys.* **1994**, *101*, 1272–1281.
47. van Leeuwen, R.; van Lenthe, E.; Baerends, E. J.; Snijders, J. G. *Int. J. Quantum Chem.* **1996**, *57*, 281–293.
48. Sadlej, A. J.; Snijders, J. G.; van Lenthe, E.; Baerends, E. J. *J. Chem. Phys.* **1995**, *102*, 1758–1766.
49. Ilias, M.; Saue, T. *J. Chem. Phys.* **2007**, *126*, 064102.
50. Liu, W.; Kutzelnigg, W. *J. Chem. Phys.* **2007**, *126*, 114107.
51. Kutzelnigg, W.; Liu, W. *J. Chem. Phys.* **2005**, *123*, 241102.
52. Kutzelnigg, W.; Liu, W. *Mol. Phys.* **2006**, *104*, 2225–2240.
53. Filatov, M.; Dyall, K. G. *Theor. Chem. Acc.* **2007**, *117*, 333–338.
54. Bethe, H. A.; Salpeter, E. E. "*Quantum Mechanics of One- and Two-Electron Atoms*"; Plenum/Rosetta: New York, NY, **1977**.
55. Luber, S.; Malkin-Ondik, I.; Reither, M. *Chem. Phys.* **2009**, *356*, 205–218.
56. Chraplyvy, Z. V. *Phys. Rev.* **1953**, *92*, 388–391.
57. Chraplyvy, Z. V. *Phys. Rev.* **1953**, *92*, 1310–1315.
58. Barker, W. A.; Glover, F. N. *Phys. Rev.* **1955**, *99*, 317–324.
59. Fliessbach, T. "*Elektrodynamik: Lehrbuch zur Theoretischen Physik II*"; Spektrum: Heidelberg, **2008**.
60. Kutzelnigg, W. Fundamentals of nonrelativistic and relativistic theory of NMR and EPR parameters. In: "*Theory of NMR and EPR Parameters*"; Eds. Kaupp, M.; Bühl, M.; Malkin, V. G.; Wiley-VCH: Weinheim, **2002**, 43–82.
61. Abragam, A.; Pryce, M.H.L. *Proc. R. Soc. Lond. A* **1951**, *205*, 135–153.
62. Schweiger, A.; Jeschke, G. "*Principles of Pulse Electron Paramagnetic Resonance*"; Oxford University Press: New York, **2001**.
63. Sinnecker, S.; Neese, F. *J. Phys. Chem. A* **2006**, *110*, 12267–12275.
64. Harriman, J. E. "*Theoretical Foundations of Electron Spin Resonance*"; Academic Press: London, **1978**.
65. Ganyushin, D.; Neese, F. *J. Chem. Phys.* **2006**, *125*, 024103.
66. Neese, F. *Coord. Chem. Rev.* **2009**, *253*, 526–563.
67. Neese, F. *J. Chem. Phys.* **2007**, *127*, 164112.

68. Zein, S.; Neese, F. *J. Phys. Chem. A* **2008**, *112*, 7976–7983.
69. Tatchen, J.; Kleinschmidt, M.; Marian, C. M. *J. Chem. Phys.* **2009**, *130*, 154106.
70. Gilka, N.; Taylor, P. R.; Marian, C. M. *J. Chem. Phys.* **2008**, *129*, 044102.
71. Kaupp, M.; Bühl, M.; Malkin, V. G. "*Calculation of NMR and EPR Parameters*"; Wiley-VCH: Weinheim, **2004**.
72. Autschbach, J. *Coord. Chem. Rev.* **2007**, *251*, 1796–1821.
73. Ziegler, T.; Autschbach, J. *Chem. Rev.* **2005**, *105*, 2695–2722.
74. Autschbach, J.; Ziegler, T. *Coord. Chem. Rev.* **2003**, *238*, 83–126.
75. Kaupp, M.; Köhler, F. H. *Coord. Chem. Rev.* **2009**, *253*, 2376–2386.
76. Bühl, M.; Kaupp, M.; Malkina, O. L.; Malkin, V. G. *J. Comput. Chem.* **1999**, *20*, 91–105.
77. Mawhinney, R. C.; Schreckenbach, G. *Magn. Reson. Chem.* **2004**, *42*, S88–S98.
78. Fukuda, R.; Hada, M.; Nakatsuji, H. *J. Chem. Phys.* **2003**, *118*, 1015–1026.
79. Fukuda, R.; Hada, M.; Nakatsuji, H. *J. Chem. Phys.* **2003**, *118*, 1027–1035.
80. Van Vleck, J. H. "*The Theory of Electric and Magnetic Susceptibilities*"; Oxford University Press: London, **1932**.
81. Dirac, P. A. M. "*The Principles of Quantum Mechanics*"; Clarendon Press, 2nd Edn: Oxford, **1935**.
82. Heisenberg, W. *Z. Phys.* **1928**, *49*, 619–636.
83. Heisenberg, W. *Z. Phys.* **1926**, *38*, 411–426.
84. Dirac, P. A. M. *Proc. R. Soc. Lond., Ser. A* **1926**, *112*, 661–677.
85. Dirac, P. A. M. *Proc. R. Soc. Lond., Ser. A* **1929**, *123*, 714–733.
86. Schreiner, E.; Nair, N. N.; Pollet, R.; Staemmler, V.; Marx, D. *Proc. Natl. Acad. Sci. USA* **2007**, *104*, 20725–20730.
87. Nair, N. N.; Ribas-Arino, J.; Staemmler, V.; Marx, D. *J. Chem. Theory Comput.* **2010**, *6*, 569–575.
88. van Wüllen, C. *J. Phys. Chem. A* **2009**, *113*, 11535–11540.
89. van Wüllen, C. *J. Chem. Phys.* **2009**, *130*, 194109.
90. Binder, K.; Landau, D. P. *Phys. Rev. B* **1976**, *13*, 1140–1155
91. Devlin, J. F. *Phys. Rev. B* **1971**, *4*, 136–146
92. Btoński, P.; Hafner, J. *Phys. Rev. B* **2009**, *79*, 224418.
93. Mankovsky, S.; Bornemann, S.; Minr, J.; Polesya, S.; Ebert, H.; Staunton, J. B.; Lichtenstein, A. I. *Phys. Rev. B* **2009**, *80*, 014422.
94. Waldmann, O.; Dobe, C.; Güdel, H. U.; Mutka, H. *Phys. Rev. B* **2006**, *74*, 054429.
95. Van Vleck, J. H. *Rev. Mod. Phys.* **1945**, *17*, 27–47.
96. Kanamori, J. *J. Phys. Chem. Solids* **1959**, *10*, 87–98.
97. Kramers, H. A. *Physica* **1934**, *1*, 182–192.
98. Anderson, P. W. *Phys. Rev* **1950**, *79*, 350–356.
99. Goodenough, J. B. *Phys. Rev.* **1955**, *100*, 564–573.
100. Soda, T.; Kitagawa, Y.; Onishi, T.; Takano, Y.; Shigeta, Y.; Nagao, H.; Yoshioka, Y.; Yamaguchi, K. *Chem. Phys. Lett.* **2000**, *319*, 223–230.
101. Boca, R. *Coord. Chem. Rev.* **2004**, *248*, 757–815.
102. Boca, R. *Coord. Chem. Rev.* **1998**, *173*, 167–283.
103. Noodleman, L. *J. Chem. Phys.* **1981**, *74*, 5737–5743.
104. Noodleman, L.; Case, D. A. *Adv. Inorg. Chem.* **1992**, *38*, 423.
105. Noodleman, L.; Peng, C. Y.; Case, D. A.; Mouesca, J. M. *Coord. Chem. Rev.* **1995**, *144*, 199–244
106. Noodleman, L.; Norman, J. G. Jr. *J. Chem. Phys.* **1979**, *70*, 4903–4906.

107. Noodleman, L.; Davidson, E. R. *Chem. Phys.* **1986**, *109*, 131–143.
108. Noodleman, L.; Baerends, E. J. *J. Am. Chem. Soc.* **1984**, *106*, 2316–2327.
109. Bencini, A.; Totti, F.; Daul, C. A.; Doclo, K.; Fantucci, P.; Barone, V. *Inorg. Chem.* **1997**, *20*, 5022–5030.
110. Ruiz, E.; Cano, J.; Alvalrez, S.; Alemany, P. *J. Comput. Chem.* **1999**, *20*, 1391–1400.
111. Mouesca, J. M.; Chen, J. L.; Noodleman, L.; Bashford, D.; Case, D. A. *J. Am. Chem. Soc.* **1994**, *116*, 11898–11914.
112. Yamaguchi, K.; Fukui, H.; Fueno, T. *Chem. Lett.* **1986**, 625–628.
113. Clark, A. E.; Davidson, E. R. *J. Chem. Phys.* **2001**, *115*, 7382–7392.
114. Herrmann, C.; Reiher, M.; Hess, B. A. *J. Chem. Phys.* **2005**, *122*, 034102.
115. Schollwöck, U.; Richter, J.; Farnell, D. J. J.; Bishop, R. F.; (Eds.) "*Quantum Magnetism*"; Springer: Berlin/Heidelberg, **2004**. Volume 645 of *Lecture Notes in Physics.*
116. Schollwöck, U. *Rev. Mod. Phys.* **2005**, *77*, 259–315
117. Dorogovtsev, S. N.; Goltsev, A. V.; Mendes, J. F. F. *Rev. Mod. Phys.* **2008**, *80*, 1275–1335
118. Davidson, E. R.; Clark, A. E. *Phys. Chem. Chem. Phys.* **2007**, *9*, 1881–1894.
119. Pople, J. A.; Gill, P.M.W.; Handy, N. C. *Int. J. Quantum Chem.* **1995**, *56*, 303–305.
120. Perdew, J. P.; Savin, A.; Burke, K. *Phys. Rev. A* **1995**, *51*, 4531–4541.
121. Illas, F.; Moreira, I. de P. R.; Bofill, J. M.; Filatov, M. *Phys. Rev. B* **2004**, *70*, 132414.
122. Mayer, I. *Chem. Phys. Lett.* **2007**, *440*, 357–359.
123. Davidson, E. A.; Clark, A. E. *Mol. Phys.* **2002**, *100*, 373–383.
124. Podewitz, M.; Herrmann, C.; Malassa, A.; Westerhausen, M.; Reiher, M. *Chem. Phys. Lett.* **2008**, *451*, 301–308.
125. Torre, A.; Alcoba, D. R.; Lain, L.; Bochicchio, R. C. *J. Phys. Chem. A* **2010**, *114*, 2344–2349.
126. Alcoba, D. R.; Lain, L.; Torre, A.; Bochicchio, R. C. *Chem. Phys. Lett.* **2009**, *470*, 136–139.
127. Mayer, I. *Chem Phys. Lett.* **2009**, *478*, 323–326.
128. Löwdin, P.-O. *Phys. Rev.* **1955**, *97*, 1474–1489
129. Wang, J. H.; Becke, A. D.; Smith, V. H. *J. Chem. Phys.* **1995**, *102*, 3477–3480.
130. Cohen, A. J.; Tozer, D. J.; Handy, N. C. *J. Chem. Phys.* **2007**, *126*, 214104.
131. Löwdin, P.-O. *J. Chem. Phys.* **1950**, *18*, 365–375.
132. Mulliken, R. S. *J. Chem. Phys.* **1955**, *23*, 1833–1840.
133. Wu, Q.; Yang, W. *J. Chem. Phys.* **2003**, *118*, 2498–2509.
134. Wu, Q.; Van Voorhis, T. *Phys. Rev. A* **2005**, *72*, 024502.
135. Rudra, I.; Wu, Q.; Van Voorhis, T. *J. Chem. Phys.* **2006**, *124*, 024103.
136. Herrmann, C.; Podewitz, M.; Reiher, M. *Int. J. Quantum Chem.* **2009**, *109*, 2430–2446.
137. Hybertsen, M. S.; Schlüter, M.; Christensen, N. E. *Phys. Rev. B* **1989**, *39*, 9028–9041
138. Dederichs, P. H.; Blügel, S.; Zeller, R.; Akai, H. *Phys. Rev. Lett.* **1984**, *53*, 2512–2515
139. Helgaker, T.; Jørgensen, P.; Olsen, J. "*Molecular Electronic-Structure Theory*"; John Wiley & Sons:, Chichester, **2000**.
140. M. Westerhausen, University of Jena, private communication.
141. Barber, J.; Murray, J. W. *Coord. Chem. Rev.* **2008**, *252*, 233–243.

142. Siegbahn, P. E. M. *Chem. Eur. J.* **2006**, *12*, 9217–9227.
143. Pantazis, D. A.; Orio, M.; Petrenko, T.; Zein, S.; Lubitz, W.; Messinger, J.; Neese, F. *Phys. Chem. Chem. Phys.* **2009**, *11*, 6788–6798.
144. Siegbahn, P. E. M. *Inorg. Chem.* **2008**, *47*, 1779–1786.
145. Siegbahn, P. E. M. *Acc. Chem. Res.* **2009**, *42*, 1871–1880.
146. Reiher, M. *Inorg. Chem.* **2002**, *41*, 6928–6935.
147. Herrmann, C.; Yu, L.; Reiher, M. *J. Comput. Chem.* **2006**, *27*, 1223–1239.
148. Malassa, A.; Agthe, C.; Görls, H.; Podewitz, M.; Yu, L.; Herrmann, C.; Reiher, M.; Westerhausen, M. *Eur. J. Inorg. Chem.* **2010**, *12*, 1777–1790.
149. Sens, C.; Romero, I.; Rodriguez, M.; Llobet, A.; Parella, T.; Benet-Buchholz, J. *J. Am. Chem. Soc.* **2004**, *126*, 7798–7799.
150. Romain, S.; Bozoglian, F.; Sala, X.; Llobet, A. *J. Am. Chem. Soc.* **2009**, *131*, 2768–2769.
151. Marti, K. H.; Malkin-Ondik, I.; Moritz, G.; Reiher, M. *J. Chem. Phys.* **2008**, *128*, 014104.
152. Ahlrichs, R.; Bär, M.; Häser, M.; Horn, H. C. Kölmel, *Chem. Phys. Lett.* **1989**, *162*, 165–169.
153. Ahlrichs, R., et al., http://www.cosmologic.de/turbomole.html
154. Becke, A. D. *Phys. Rev. A* **1988**, *38*, 3098–3100.
155. Perdew, J. P. *Phys. Rev. B* **1986**, *33*, 8822–8824.
156. Lee, C.; Yang, W.; Parr, R. G. *Phys. Rev. B* **1988**, *37*, 785–789.
157. Becke, A. D. *J. Chem. Phys.* **1993**, *98*, 5648–5652.
158. Schäfer, A.; Huber, C.; Ahlrichs, R. *J. Chem. Phys.* **1994**, *100*, 5829–5835.
159. DeLano, W. L. "*The PyMOL Molecular Graphics System*"; DeLano Scientific LLC: Palo Alto, CA, USA., http://www.pymol.org, **2008**.
160. Hanson, R.; Kouwenhoven, L. P.; Petta, J. R.; Tarucha, S.; Vandersypen, L. M. K. *Rev. Mod. Phys*. **2007**, *79*, 1217–1265.
161. McWeeny, R. "*Spins in Chemistry*"; Academic Press: London,**1970**.

INNER- AND OUTER-SPHERE HYDROGENATION MECHANISMS: A COMPUTATIONAL PERSPECTIVE

ALEIX COMAS-VIVES, GREGORI UJAQUE* and AGUSTÍ LLEDÓS*

Departament de Química, Universitat Autònoma de Barcelona, 08193 Bellaterra, Catalonia, Spain

I. Introduction

Hydrogenation is a canonical reaction in homogeneous catalysis besides being one of the most extensively studied processes within the entire research field (*1–3*). Moreover, metal-hydride intermediates are ubiquitous not only in homogeneous hydrogenation but they are at play also in several homogeneous catalytic processes. Hence, a fundamental understanding of hydrogenation reactions is of primary importance in order to further develop more efficient catalysts.

In homogeneous catalysis, hydrogenation refers to the addition of one or more hydrogen molecules into a substrate under the action of a homogeneous catalyst. When using molecular hydrogen

THEORETICAL AND COMPUTATIONAL INORGANIC CHEMISTRY
VOLUME 62 ISSN 0898-8838 / DOI: 10.1016/S0898-8838(10)62006-5

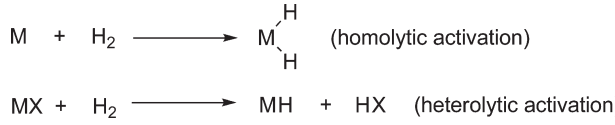

SCHEME 1. Activation routes of molecular hydrogen.

as a hydrogen source this species may be activated either homolytically or heterolytically such as shown in Scheme 1.

The interaction of dihydrogen with a transition metal fragment can lead to dihydrogen coordination, without breaking of the H–H bond, or to complete breaking of the H–H bond. In the past years, the key role of the initial coordination of H_2 to the transition metal complex (η^2–H_2 complexes) for both the homolytic and heterolytic activations has been recognized (*4–6*). Rupture of the H–H bond forms metal-hydride species, being key intermediates in several catalytic cycles (*7*). This is not a straightforward process since the H–H bond dissociation energy is 104 kcal mol^{-1}. Nevertheless, transition-metal complexes are able to activate molecular hydrogen in mild conditions. The homolytic activation involves a formal oxidative addition and it requires that the metal should be stable with a higher oxidation state by two formal units and two additional ligands. Conversely, in heterolytic activation there is no change in the oxidation state of the metal, implying an intramolecular (to a metal-ligand) or intermolecular (to an external base) proton transfer and the formation of a metal–hydride bond (*5,8*). Recently, mechanistic studies have shown that the heterolytic activation of molecular hydrogen may be assisted by protic solvents such as alcohols (*9–13*) and water (*14,15*). In these solvents heterolytic activation can occur through a chain of hydrogen-bonded solvent molecules connecting the H_2 proton with the basic center (for instance via a six-membered transition state) instead of an σ-bond metathesis [2+2] of the hydrogen molecule through a four-membered transition state (Scheme 2).

Molecular hydrogen is not the only source of hydrogen since other molecules such as alcohols can also be used as a hydrogen source. In that case, one refers to hydrogen-transfer reactions. In the hydrogen-transfer processes, a donor species DH_2 transfers two hydrogen molecules to an acceptor species A (Scheme 3).

These reactions are most common for polar double bond as reactants (carbonyls and imines) than for non-polar substrates (alkene and alkyne). Hence, hydrogen-transfer processes are a very interesting option in order to perform polar double bond hydrogenation since they allow mild conditions, high selectivity,

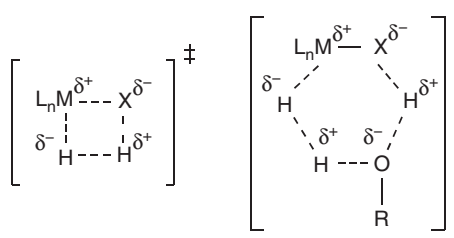

SCHEME 2. Schematic representation of the transition states for the heterolytic cleavage of the hydrogen molecule; non-assisted (left part) and assisted by one polar protic solvent molecule (right part).

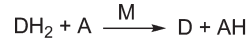

SCHEME 3. Hydrogen-transfer process.

and a high concentration of the reductant (*16–20*). Until now we have focused on the way H–H is broken, but a key point in hydrogenations is the placement of the substrate that will accept the hydrogen atoms. The classical mechanisms of transition metal homogeneous catalysis involve the reactants forming products while bonded to the central metal. However from Noyori's work on polar bond reduction (*21*) it has emerged that hydrogen transfer can also proceed with the substrate in the second coordination sphere, without direct coordination with the metal. Following this scheme, the next section describes the general reaction mechanisms for the hydrogenation processes from the substrate's perspective.

II. Reaction Mechanisms for Hydrogenation Reactions: The Substrate Viewpoint

The hydrogenation reaction mechanisms may be classified according to the role played by the substrate in the coordination sphere of the metal catalyst. Thus, those mechanisms proceeding with coordination of the substrate to the metal center can be labeled as inner-sphere mechanisms, whereas those with no direct coordination of the substrate to the metal center can be labeled as outer-sphere reaction mechanism (see Scheme 4). Hydrogenation reactions belonging to the so-called hydrogen transfer reactions (where the hydrogen source is usually an alcohol) can be also classified within these two families of reaction

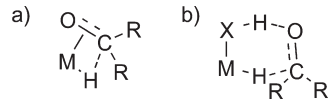

SCHEME 4. (a) Inner–sphere and (b) outer–sphere mechanisms for ketone hydrogenation.

pathways. In the next two subsections these two types of hydrogenation reaction mechanisms are described.

A. INNER-SPHERE MECHANISMS

Within the mechanisms proceeding with substrate coordination to the metal, we can distinguish between insertion mechanisms, being characterized by the substrate insertion into the M–H bond (Scheme 4a), and in the particular case of the hydrogen-transfer reactions, a mechanism where the substrate and the hydrogen source (usually an alcohol) are both coordinated to the metallic center, commonly named the Meerwein–Ponndorf–Verley (MPV) mechanism (Scheme 5) (*22–24*).

A.1. Insertion mechanisms

In homogeneous catalysis the classical hydrogenation catalysts are metal-transition based with metals such as Rh, Ir, Ru, and Os (*2*). Many of these catalysts operate through an insertion mechanism and depending on the number of hydrides in the metal complex one can distinguish between the monohydridic and the dihydridic routes. The monohydridic route, which goes through an intermediate initially containing one M–H bond, has the general catalytic cycle depicted in Scheme 6.

Thus, for alkene hydrogenation, after the coordination of the substrate a metal–alkyl intermediate is formed by insertion of

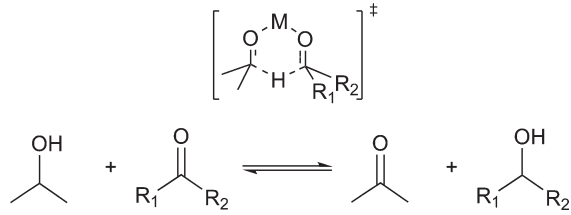

SCHEME 5. Metal-catalyzed hydrogen-transfer between ketones and 2-propanol through the Meerwein–Ponndorf–Verley (MPV) mechanism.

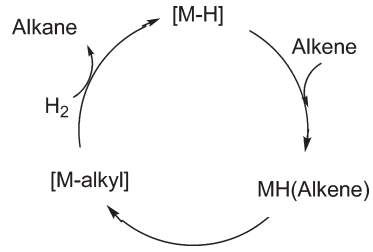

SCHEME 6. Monohydridic mechanism for alkene hydrogenation.

the alkene into the M–H bond. Finally, addition of a hydrogen molecule regenerates the metal–hydride species forming the final product, alkane. Alkene hydrogenation catalysts such as RhH(CO)$(PPh_3)_3$ and $RuCl_2(PPh_3)_3$ operates through this mechanism (*25,26*). Concerning the dihydridic route, the general reaction mechanism is shown in Scheme 7, where both the alkene and the hydrogen molecule are firstly incorporated into the metal complex.

The widely known Wilkinson catalyst is proposed to operate through this reaction mechanism. Computational evaluation of the full catalytic cycle showed that the rate-determining step implies the insertion and the subsequent isomerization process (*27*). Moreover, this catalyst has the particularity that the reaction mechanism depends on the hydrogen source since a monohydridic route has been proposed when 2-propanol is the hydrogen source (*28*).

In order to distinguish between the dihydridic and the monohydridic routes in hydrogen-transfer reactions, Bäckvall and coworkers developed an optically active α-deuterated alcohol. If the dihydridic route was occurring the deuterium would be scrambled between carbon and oxygen atoms whereas if the monohydridic

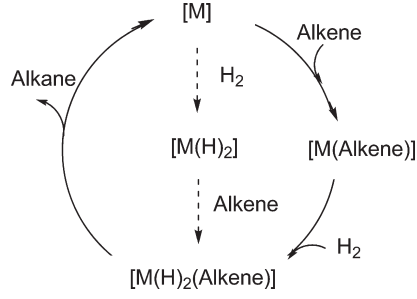

SCHEME 7. Dihydridic mechanism for alkene hydrogenation.

route was taking place the deuterium would end up in the α position of the racemized alcohol (*28*). Hydridic and dihydridic mechanisms in hydrogen-transfer reactions have been discussed in detail in other publications (*16,29*).

In aqueous hydrogenations, the pH has also been proposed to play a role in determining if the active species is either a monohydridic or a dihydridic species and also in the regioselectivity. Concerning the hydrogenation of other substrates such as carbonyls, imines, and alkynes, they may also operate through analogous mechanisms involving the insertion step. In the case of alkynes, for the $[OsHCl(CO)(PR_3)_2]$ catalysts ($PR_3 = PiPr_3$, $PtBu_2Me$), it has been proposed to go through alkenyl formation (*30*).

The reaction mechanisms in imine hydrogenation are by far the less studied since not many catalysts are active in this process (*31*). This is probably because imine hydrogenation is a less exothermic reaction (about 15 kcal mol^{-1}) than alkene hydrogenation (about 30 kcal mol^{-1}), that hydrogenation requires an η^2 coordination of imines although the most common coordination of imines is η^1, and that the resulting amine may poison the catalyst due to its strong binding to the metal center.

In hydrogen-transfer reactions, the inner-sphere mechanism has been by far less proposed than the outer-sphere mechanisms (*vide infra*). Nevertheless, there are some cases where it has been suggested to be the operating mechanism. In those cases leaving of one ligand has been proposed in order to allow substrate coordination. In the case of the $[RuH(i\text{-}PrOH)(CH_3\text{-}CONH)(CO)(PCy_3)_2]$ complex, the reaction showed inhibition with respect to PCy_3 concentration, in agreement with the requirement of PCy_3 leaving (*32*). For the [Rh(COD)(diamine)(hydride) the inner-sphere mechanism has been also proposed, being the β-elimination rate-limiting step due to the high stability of the previous alkoxide intermediate (*33*). There are other complexes such as [Ir(COD)(aminoalcohol)] and [Ir(COD)(aminosulfide)] where the lability of aminoalcohol and aminosulfide ligands was needed in order to allow the substrate coordination (*34*), hence the lability of the ligands is a key factor within the inner-sphere mechanism.

A.2. Meerweein-Ponndorf-Verley (MPV) mechanism

This particular reaction mechanism belongs to the family of hydrogen-transfer reactions. This pathway implies the direct transfer mechanism between the donor and the acceptor groups. The MPV mechanism is common for main group elements acting as Lewis acids catalysts such as aluminum isopropoxydes or

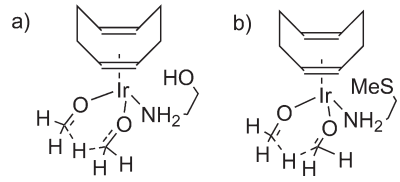

SCHEME 8. Direct hydrogen-transfer transition states for (a) Ir(COD)(amino alcohol) and (b) Ir(COD)(amino sulfide) complexes.

lanthanide salts; however, it has been also proposed for some transition-metal catalysts. The reaction pathway goes through a six-membered transition state, as previously shown in Scheme 5; thus, this mechanism needs the coordination of an alkoxide group and the substrate to the catalyst, therefore becoming an inner-sphere mechanism. For example, on the basis of computational calculations, Ir(COD)(aminoalcohol) and Ir(COD)(aminosulfide) were found to proceed through this reaction pathway (Scheme 8) (*34*). Analogously, the MPV mechanism was also found to be feasible for the $RhH(C_2H_4)_2[NCH_3)_3]_2$ complex as a catalyst (*35*).

B. Outer-Sphere Mechanisms

The previous section described a two-step mechanism. The first step is the coordination of the substrate into the metal coordination sphere. The second is the most characteristic step within the inner-sphere mechanism: the insertion of the substrate into the M–H bond. Nevertheless there are other mechanistic options that include neither substrate coordination nor M–H insertion. They are outer-sphere mechanisms and in turn can be classified as bifunctional and ionic mechanisms.

B.1. Bifunctional catalysts

Within the monohydridic route, apart from the already explained inner-sphere mechanisms, there is another possibility involving the concerted outer-sphere transfer of one hydride and one proton to the corresponding substrate (Scheme 4b). This mechanism is very common to the so-called bifunctional catalysts. This term was proposed by Noyori for those catalysts having one hydrogen with hydridic character directly bonded to the metal center of the catalyst, a hydride ligand, and another hydrogen with protic character bonded to one of the ligands of the metal complex (*20*). In Scheme 9, examples of bifunctional catalysts that are synthesized

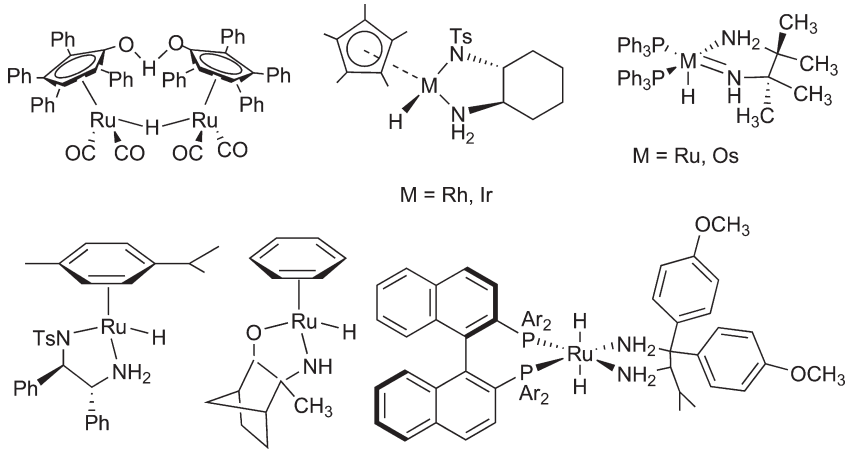

SCHEME 9. Examples of metal–ligand bifunctional catalysts.

by different research groups are shown (*10,36–41*). The metal center and one of the ligands are cooperatively acting in the hydrogen-transfer process (*42*).

In a pioneering work, Noyori and co-workers compared computationally the inner-sphere and the outer-sphere mechanisms for the Ru(η^6-benzene)(NCH_2CH_2Y) (Y=O,NH) catalyst (*43*). For the inner-sphere mechanism, the substrate coordination implied a large rearrangement of the metal coordination by changing the hapticity of the arene ring from η^6 to η^2, a fairly energy-demanding process. In comparison, the outer-sphere mechanism presented a relatively low-energy barrier, 10 kcal mol^{-1} (Scheme 10).

Several other bifunctional complexes containing different metals such as Ru, Rh, and Ir have been proposed to operate through the outer-sphere route (*44–49*). In some cases, this mechanism allowed to explain the observed enantioselectivity without substrate coordination (*48,49–52*).

Thus, in hydrogen-transfer reactions, most of the catalysts do prefer the outer-sphere mechanism instead of the MPV or the insertion mechanisms. For instance, the high stability of the intermediate formed, alkoxide in the case of carbonyl hydrogenation, is a major drawback for the inner-sphere mechanism. Nevertheless, in some particular cases, the inner-sphere mechanism may be competitive with the outer-sphere one. In these cases, some requirements must be accomplished, such as the high lability of one of the metal ligands in order to allow easily the substrate coordination or the formation of not very stable intermediates.

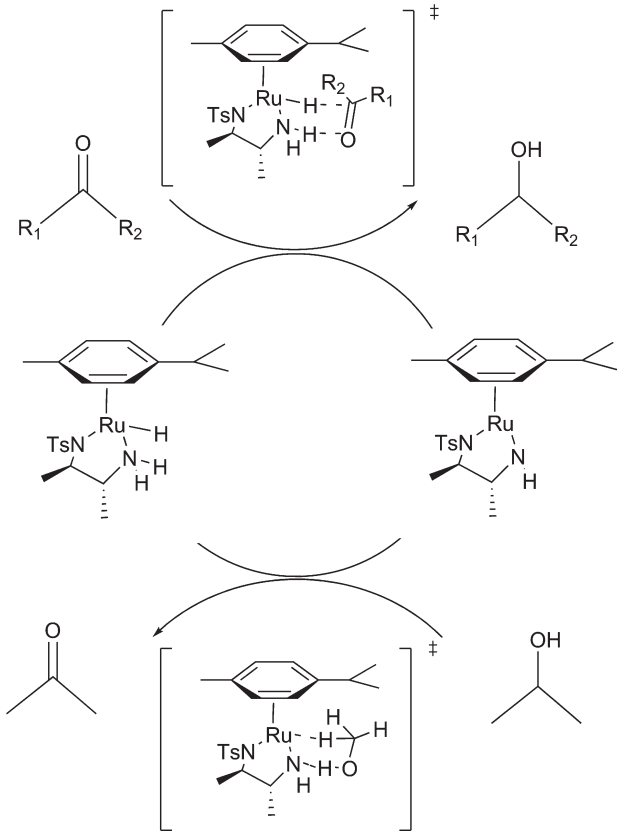

SCHEME 10. Concerted outer-sphere mechanism for the transfer hydrogenation using the Ru(η^6-arene)TsDPEN complex.

B.2. Ionic mechanisms

In the ionic mechanism, H_2 is added up to the substrate as the sum of one H^+ and one H^- in separated steps (*53,54*). A key feature of this reaction mechanism is that the insertion step of the substrate into the M–H bond is not needed. This mechanism takes place with the general scheme shown in Scheme 11. The first step of the ionic mechanism involves a proton transfer generating a neutral metallic intermediate. In the next step there is a hydride transfer giving rise to the hydrogenated product.

A family of molybdenum and tungsten complexes with the formula $[M(Cp)(CO)_2(PR_3)(O{=}CEt_2)]BAr_4'$ [Ar = 3,5-*bis*(trifluoromethyl)phenyl] are known to operate through this mechanism. In most of the cases, the rate-limiting step was the ketone displacement for H_2 in order to form the active dihydride (*55,56*). An

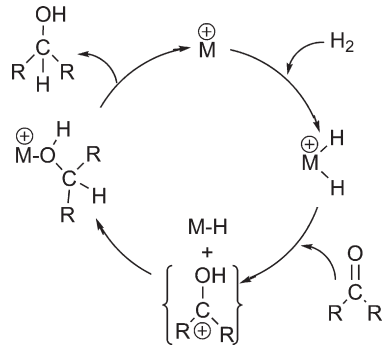

SCHEME 11. Proposed mechanism for catalytic ionic hydrogenation of ketones.

analogous mechanism was found for the hydrogenation of iminium cations by means of the Ru complexes with chiral phosphynes. In this case the hydride transfer was both the rate-limiting and the enantioselective step (*57*). Monometallic and bimetallic Ir-based imine hydrogenation catalysts have been also developed evolving through ionic mechanisms (*58,59*).

Note that this mechanism is closely related to that of the bifunctional catalysts. In fact, the latter is also said to work by means of an ionic mechanism since one proton and one hydride coming from the catalyst are added to the substrate. Note, however, that there is an important difference between both mechanisms: ionic mechanism takes place in two separated steps for the proton and hydride transfers, respectively, whereas in those involving bifunctional catalysts the H^+ and H^- transfers takes place concertedly.

III. Computational Investigation of Hydrogenation Mechanisms

The general mechanisms in homogeneous hydrogenation processes have been commented in the previous section. From experimental measurements, it is not easy discerning between inner- and outer-sphere pathways. Theoretical studies that give a detailed description of the process at the molecular level are very useful to study reaction mechanisms of homogeneous catalytic processes. The present section is devoted to illustrate with several examples of hydrogenation reaction mechanisms that have been studied by computational methods (*60*), most of them in our own group, the utility of such approach. The purpose of this contribution is to give an overview on theoretical studies of the

different hydrogenation mechanism, without actually going into computational details that can be found in the referenced articles.

The evaluation of the reaction mechanisms and their energy profiles has been generally performed by means of the DFT calculations using the B3LYP functional. Common pseudopotentials such as LANL2DZ were used for transition metals besides its associated double-ζ basis sets whereas double-ζ + polarization Pople basis sets (6-31g(d,p)) were taken for the main group elements. As far as the solvent effects are concerned, they have been generally included using continuum methods (either Polarizable Continuum Model, PCM, or Conductor-like Polarizable Continuum Model CPCM), which assume that the solvent is a continuum defined by a dielectric constant ε (see left part of Fig. 1). In order to take into account the direct participation of the solvent in the process, some explicit molecules have been included in some of our systems, combining both the implicit (continuum) and the explicit (discrete) solvation models (Fig. 1). When adding the Gibbs energy of solvation to the potential energy in gas phase, the energy profiles in solution are obtained. For more specific information about the theoretical approach used in every particular case we refer to the cited works.

By applying the above-mentioned methodology, deeper understanding of the essential steps and features in homogeneous hydrogenation reactions was obtained. Key issues such as the hydrogen activation step and the critical role played by the solvent in the heterolytic activation, the effect of the pH in regioselective hydrogenations in aqueous media, the role of the metal complex and its coordination sphere (ligands), the substrate–metal interactions, the specific hydrogenation mechanism in every case, and also the different ways from which the active

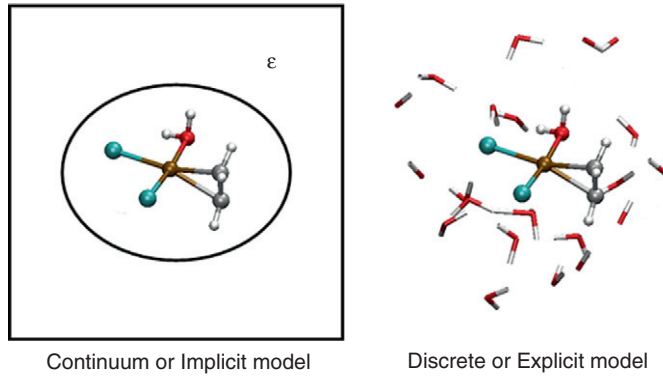

FIG. 1. Representation of the solvation models: continuum or implicit model and explicit model.

species of the transition-metal catalyst are generated could be evaluated. The following subsections have been divided according to the reaction mechanism following the classification described in the previous section.

A. Inner-Sphere Operating Catalysts

A.1. C=O vs. C=C Hydrogenation by Ru-Hydride in aqueous medium

In addition to organic solvents, hydrogenation catalysts in aqueous medium have been also developed, although to a lesser extent (*61*). The pH of the medium has proven to determine the active catalytic species in homogeneous hydrogenation reactions, eventually giving rise to regioselective reactions. One of the examples is the ruthenium(II) complex of *m*tppms (*m*tppms = *meta*-sulfonatophenyl-diphenylphosphine) developed by Joó and co-workers for the hydrogenation of cinnamaldehyde (3-phenylpropenal) in aqueous solution (*62,63*). The reactions were run at elevated temperatures (80 °C) and atmospheric hydrogen pressure, and selective reduction was obtained, depending on the pH of the reaction medium. In acidic medium, this catalyst promotes the C=C hydrogenation of unsaturated aldehydes giving rise to dihydrocinnamaldehyde. Conversely, it catalyzes the C=O hydrogenation in basic medium, yielding to cinnamyl alcohol (Scheme 12).

By means of potentiometric studies and MNR (^{1}H and ^{31}P) measurements, it was detected that the [RuHCl(mtppms)$_3$] was the majority species in acidic medium whereas [RuH$_2$(mtppms)$_4$] was the dominant species in neutral and basic medium. Despite the detection of the major species, the origin of the selectivity in the hydrogenation was not understood and the mechanistic features of the reaction remained unknown. Theoretical calculations starting from the postulated complexes as the active species in every case by means of B3LYP calculations (using PH_3 model phosphine ligands) and ONIOM(B3LYP:UFF) methodology (with the real PPh_3 ligands) were able to rationalize the origin of the regioselectivity (*64,65*).

In the case of the acidic medium, where C=C hydrogenation is taking place, an inner-sphere mechanism was proposed (*64*).

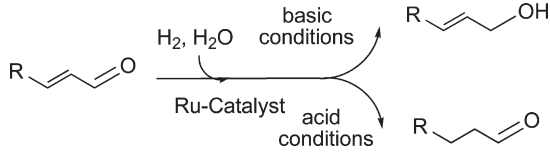

Scheme 12. Hydrogenation of unsaturated aldehydes in water.

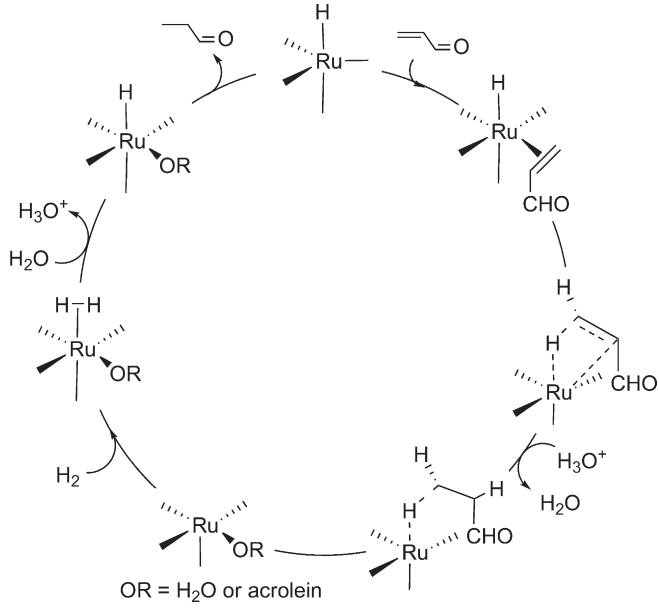

SCHEME 13. Reaction mechanism of the C=C reduction catalyzed by RuHCl(*m*tppms)$_3$] or [RuHCl(H_2O)(*m*tppms)$_2$] in acidic aqueous solution.

The energy profiles did not suggest a major difference in the catalytic activities of [RuHCl(*m*tppms)$_3$] and [RuH(H_2O)Cl (*m*tppms)$_2$]; thus, reactions through both pathways were possible; however, only the former was detected experimentally. After substrate's coordination (inner-sphere mechanism) its insertion into the Ru–H bond takes place followed by the proton-transfer from the medium to the substrate in order to complete the hydrogenation reaction. The proton-transfer from the medium is quite particular of aqueous solvent (*14*). In Scheme 13, the proposed reaction mechanism in acidic medium is depicted. In this study, the solvent effects were taken into account by combining explicit and implicit models. Theoretical calculations included a three-water-molecule cluster for the protonation step of the substrate and also for the hydride regeneration step, along with the continuum method. The latter step involves hydrogen coordination to the metal and a subsequent proton transfer to the three-water-molecule cluster regenerating the Ru–hydride catalyst. The step determining the selectivity is the substrate insertion into the M–H bond since the relative energy barriers for the insertion of C=C and C=O into the M–H bond are 5.3 and 17.3 kcal mol^{-1}, respectively, accounting for regioselectivity.

In basic medium the catalytic species was postulated to be a Ru–dihydride complex. In this case, the regioselectivity was determined by the proton-transfer step (*65*). The complete catalytic cycle in basic medium is depicted in Scheme 14. First the phosphine dissociation generating a vacant site for the substrate coordination takes place. Next step is the insertion of the substrate into the Ru–H bond (inner-sphere mechanism) followed by water coordination in order to occupy the vacant site. This step has the highest relative energy barrier for the overall process. To generate the final product this intermediate must be somehow protonated; however, in basic medium there are no easily available protons in solution. Thus, bulk water molecules are the only proton source. The transfer of a proton from a water molecule to the C=C bond requires at least 36.6 kcal mol^{-1}, which is much more than the highest barrier found for C=O hydrogenation

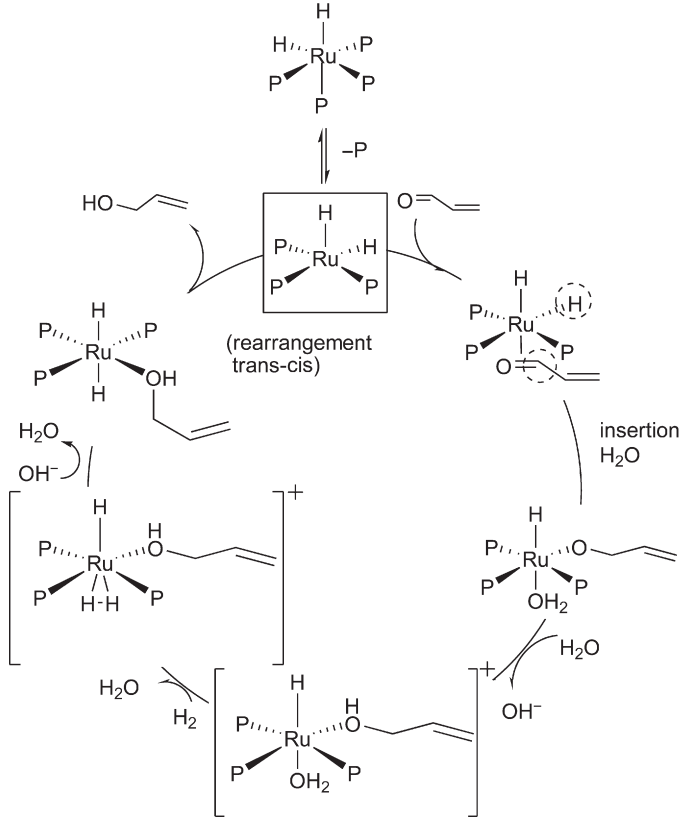

SCHEME 14. Proposed catalytic cycle for C=O selective hydrogenation by *cis*-[RuH_2(*m*tppms)$_4$] in basic aqueous media.

(16.1 kcal mol^{-1}). These energy differences account for the selectivity of the process. Replacing of the aquo ligand by a H_2 molecule and the subsequent heterolytic cleavage gives rise to the final alcohol product regenerating the initial dihydride catalytic species.

Delbecq and co-workers proposed the concerted transfer of the hydride and a proton from the aquo ligand to the C=O bond (*66*). Nevertheless, the main weakness of this mechanism is that it can not account for the change in regioselectivity when modifying the pH. The study in basic medium also addressed the problem of simulating a proton transfer coming from a water cluster giving rise to a hydroxide complex. By the cluster approach (three water molecules) a minimum is not obtained for the product since it is a charge separation process. However, an estimation of the stability of such complex could be made by fixing one coordinate. In the ongoing results of our group we have recently shown that *ab initio* molecular dynamics (CPMD) offers a very efficient framework to overcome such problems (*67*).

A.2. C=C Hydrogenation by gold and palladium–semisalen complexes

Despite its apparent noble character, gold catalysts have been recently found to be active in many homogeneous and heterogeneous catalytic processes such as oxidation reactions, nucleophilic additions, cross-coupling reactions, and alkene and imine hydrogenations (*69*–*71*). Corma and co-workers showed that Au (III) complexes were able to hydrogenate olefins with high turnover frequencies(TOFs) (*71*). Scheme 15 shows the structure of these gold complexes. The isoelectronic Pd(II) complexes were also synthesized, having a similar activity as its gold analogs.

Some of us addressed the mechanistic study of its intricate reaction mechanism (*71*) at B3LYP level coupled with PCM single-point calculations in order to take into account the solvent effects. The results of the computational study are summarized in

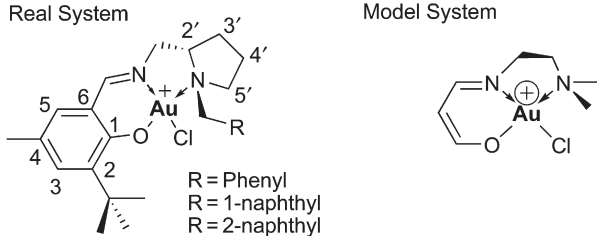

SCHEME 15. Gold catalysts used to hydrogenate olefins.

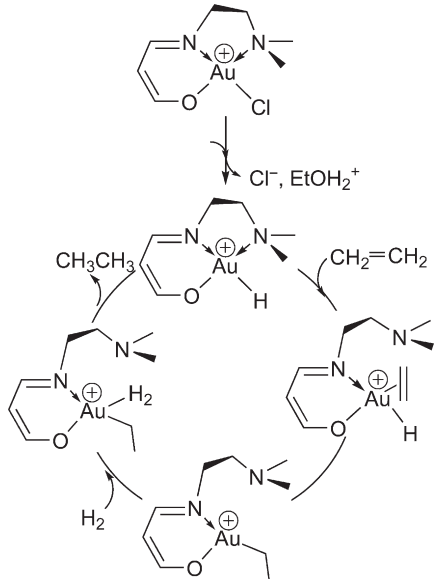

SCHEME 16. Proposed catalytic cycle for the Au(III)–Semisalen complexes.

the catalytic cycle depicted in Scheme 16. The initial H_2 activation was found to take place in the first step via a heterolytic cleavage over a chlorine ligand. This step generates a gold–hydride intermediate along with a proton release over the chlorine ligand. For this step, the assistance by one ethanol molecule plays a critical role by decreasing the energy barrier height by more than 10 kcal mol^{-1}. The related transition-state is depicted in Fig. 2. The presence of the solvent molecule (EtOH, a protic polar solvent) on one side polarizes the H_2 molecule helping the

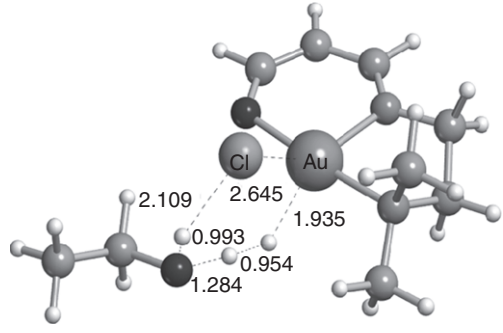

FIG. 2. Transition state for the heterolytic cleavage of hydrogen assisted by one ethanol molecule on the Au(III)–semisalen complex.

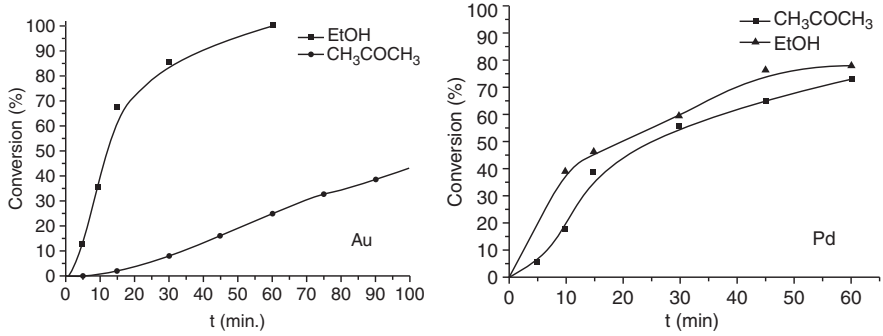

FIG. 3. Relative conversion in both ethanol and acetone in the case of gold (left) and palladium (right) complexes.

heterolytic cleavage of the H–H bond. Moreover, the solvent acts simultaneously as a proton-donor and proton-acceptor, therefore facilitating proton generation during the process.

The assistance of the solvent molecule was later confirmed experimentally: the reaction rate decreased significantly when changing a polar protic solvent such as ethanol by a polar aprotic solvent such as acetone (see left part of Fig. 3). This was a good example showing how computational calculations can be useful not only rationalizing experimental observations but also having predictive power.

The next step involves alkene coordination by means of an amine ligand substitution process (inner-sphere mechanism). This was found to be the rate-limiting step within the catalytic cycle with an energy barrier height of about 20 kcal mol^{-1}. The following step corresponds to the insertion of the olefin into the M–H bond. The subsequent coordination of H_2 to the generated vacant site gives rise to a σ-bond metathesis regenerating both the gold–monohydride and the final product (alkane).

An analogous catalytic pathway was found for palladium hydrogenation; however, conversely to gold complexes, the direct solvent assistance was not required (72). The energy barrier for the H_2 heterolytic cleavage was found to be similar for both in the presence and the absence of an explicit solvent (EtOH) molecule in the calculations. In this case, the role of the solvent was mostly electrostatic, by stabilizing the related transition state because of its polarity but not directly participating in the process. Again, the confirmation came by the experimental counterpart, by comparing the reaction rate for two solvents, finding similar reaction rates in both ethanol (polar protic) and acetone (polar non-protic); see right part of Fig. 3. Another difference between the gold and

palladium reaction mechanisms was that a trigonal bipyramid intermediate having the alkene coordinated to the palladium was located in the latter case, but not in the former one (*71,72*).

A.3. C≡C hydrogenation by means of palladium complexes

The reaction mechanism of palladium-catalyzed alkyne semihydrogenation was studied by means of *para*-hydrogen-based NMR investigation and DFT calculations at B3LYP level (*73,74*). The theoretical study explored the feasibility of two independent mechanisms, one based on the neutral species Pd(0)(P_2) (where P_2 = mono or bidentate phosphines) and the second based on cationic intermediates of the type $[Pd(II)(P_2)(H)]^+$. Experimentally, the main organic products detected were the corresponding *trans*-alkenes, and when a *cis*-alkene was used as substrate the isomerization proved to be facile even though only relatively small amounts of the corresponding alkane were detected. The DFT-derived scheme for the neutral mechanism is depicted in Scheme 17. In the neutral catalytic cycle, once the alkyne is coordinated (inner-sphere mechanism), a phosphine release is needed in order to coordinate an incoming hydrogen molecule to the palladium. Later, the σ-bond metathesis forming a Pd(κ^1P)(CH=CH_2)(H) intermediate takes place, after which transfer of the metal hydride to the vinyl ligand and phosphine recoordination leads to the alkene complex. Through an analogous pathway (left part of Scheme 17) we would obtain the resulting alkane.

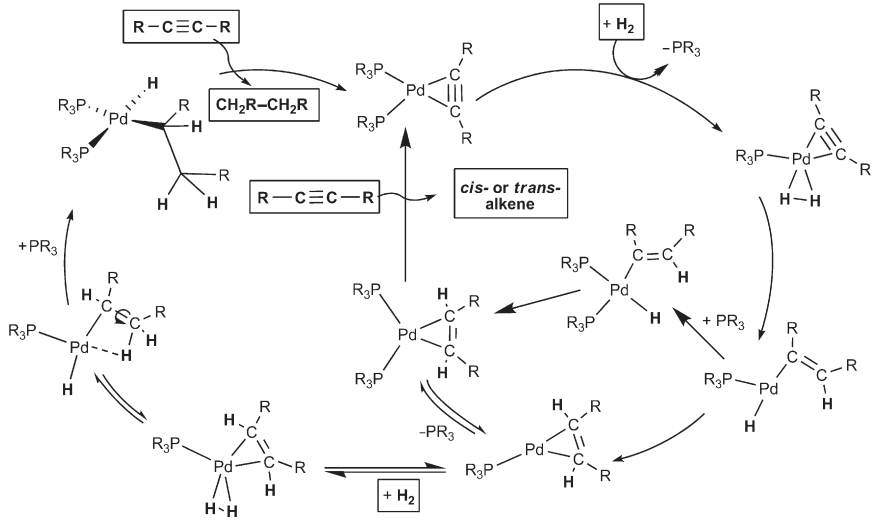

SCHEME 17. DFT-derived mechanism for the alkyne hydrogenation by a neutral palladium(0)–bisphospine complex .

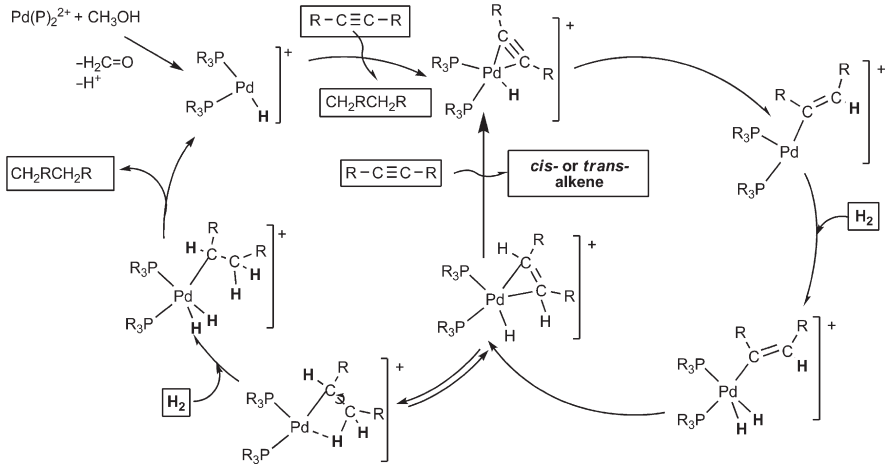

SCHEME 18. DFT-derived mechanism for the alkyne hydrogenation by a palladium monohydride bisphospine cation.

Concerning the cationic mechanism through the $[Pd(P_2)H]^+$ species, it gives rise to an alternative mechanism, shown in Scheme 18. As for the neutral cycle, the reaction starts with the coordination of the alkyne to the precursor (inner-sphere mechanism). In this case, since there is a vacant site in the metal coordination sphere the phosphine dissociation is not needed, thus avoiding this unfavorable step required in the neutral mechanism. The mechanism takes place also via an σ-bond hydrogen metathesis and with the subsequent insertion of the alkenyl into one of the M–H bonds. The neutral catalyst has an energy barrier height of 27 kcal mol^{-1} for the first hydrogenation step (leading to the alkene), whereas the subsequent hydrogenation to alkane presented an unaffordable energy barrier height of 45 kcal mol^{-1}. Conversely, for the cationic mechanism both the first and second hydrogenations have affordable energy barriers of only 11 kcal mol^{-1}. Besides being the most feasible reaction mechanism, the cationic mechanism fits well with all the experimental observations since palladium monohydrides were detected experimentally (*73,75*).

B. OUTER-SPHERE OPERATING CATALYSTS

B.1. The Shvo catalyst

The Shvo catalyst is one of the most paradigmatic hydrogen-transfer catalysts due to its great versatility. It is able to hydrogenate polar (ketones, imines) and non-polar bonds (alkenes,

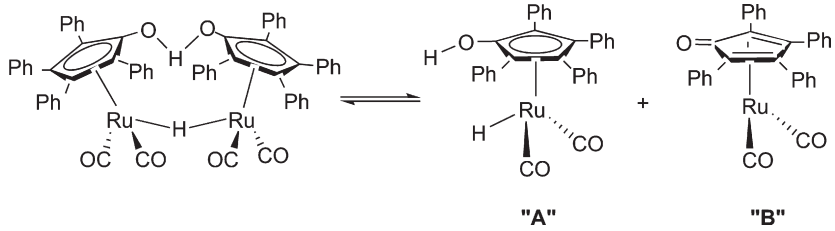

SCHEME 19. Equilibrium of the Shvo catalyst.

alkynes) and can use H_2 or alcohol (usually isopropanol) as a hydrogen source (*77*). Its versatility comes from the equilibrium shown in Scheme 19, generating two structures "A" and "B." These species are able to perform hydrogenation and oxidation processes leading to multiple applications in hydrogen-transfer reactions (*77–83*).

Nevertheless, the mechanism of the Shvo's catalyst has been one of the most controversial regarding the nature of the hydrogen-transfer process (*84*). The analysis of this reaction mechanism served as an example of comparison of both the inner- and outer-sphere reaction pathways for hydrogenation of polar, C=O (*85–87*) and C=N (*88–95*) and unpolar bonds (*95*). In the next subsections are presented the mechanistic studies we carried out for the hydrogenation of ketones, imines, alkenes, and alkynes (*29,87,95*).

B.1.a. Hydrogenation of ketones. The experimental work done by Casey's group analyzing the primary deuterium isotope effects on the hydrogenation of PhCHO using the the tolyl analog of the Shvo catalyst [2,5-Ph_2-3,4-Tol_2(η^5-C_4OH)]Ru$(CO)_2$H concluded that carbonyl hydrogenation was going through a concerted outer-sphere mechanism (*85*). The work by Bäckvall's group also supported a concerted mechanism, although taking place via an inner-sphere mechanism involving a $\eta^5 \rightarrow \eta^3$ ring slippage (*82*). We compared computationally the inner-sphere and outer-sphere mechanisms by means of the B3LYP calculations in solution (CPCM method) (*87*). MP2 and CCSD(T) single-point calculations were giving similar results, featuring the suitability of the DFT approach at B3LYP level for this particular system. In the theoretical study, several reaction mechanisms were analyzed besides the two previously commented. One involved a CO ligand leaving from the ruthenium coordination sphere. The high energy reported for this process (45.7 kcal mol^{-1} in THF) led us to discard this mechanism, in agreement with experimental results for the

CO by ^{13}CO exchange process (*81*). Another inner-sphere mechanism we analyzed involved the ring slippage of the CpOH ligand in order to generate a vacant site to coordinate the substrate as proposed in other systems (*96*). The computational analysis of the ligand exchange on other metal complexes showed the η^2 was the most favorable coordination mode (*97*). Although previous proposals suggested the η^3 ring slippage for the Shvo's catalyst (*79,80,86*) we were only able to characterize the η^2 intermediate. The same behavior was observed in other cases for transition states of the ligand coordination step (*98*). This so-called $\eta^5 \rightarrow \eta^2$ CpOH ring slippage mechanism had an overall barrier height of 33.0 kcal mol^{-1} in solution, being the hydride migration the rate-limiting step. Finally, an additional inner-sphere mechanism where the $\eta^5 \rightarrow \eta^3$ ring slippage was taking place concertedly to the hydride and proton transfers was found. This was the only case where a $\eta^5 \rightarrow \eta^3$ pathway could be theoretically characterized for the C=O reduction process. The energy barrier for this pathway in solution was 34.6 kcal mol^{-1} (Fig. 4).

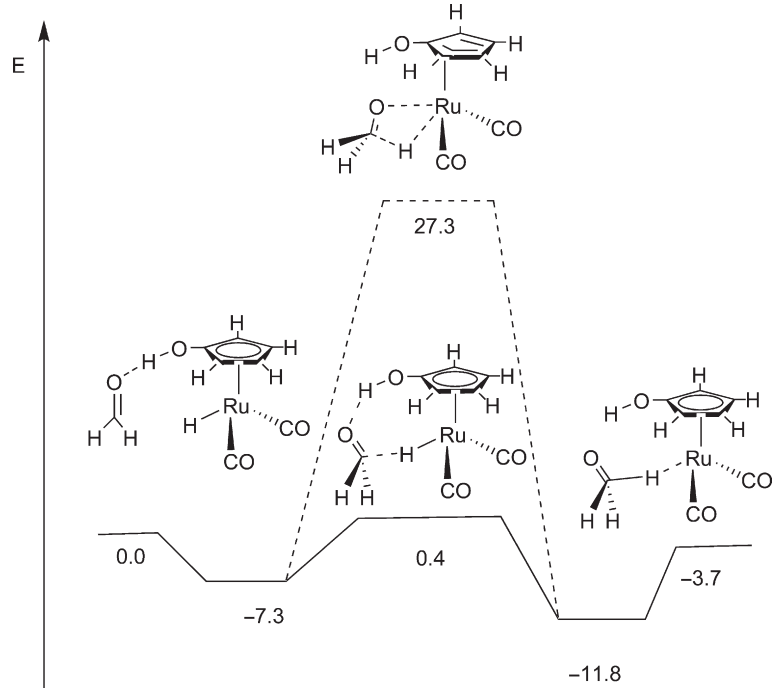

FIG. 4. Energy profiles in THF for both concerted pathways at B3LYP level for the hydrogenation of ketones by the Shvo's catalyst. Inner-sphere mechanism: dashed line; outer-sphere mechanism: solid line.

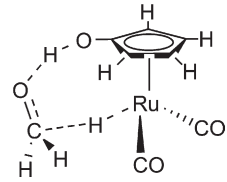

SCHEME 20. Concerted outer-sphere mechanism for carbonyl hydrogenation by the Shvo's catalyst.

The outer-sphere mechanism with the concerted H^+ and H^- transfer was also investigated (Scheme 20). The energy barrier in solution is 7.7 kcal mol^{-1}; therefore presenting by far the most favorable energy pathway among those theoretically evaluated, in agreement with a previous work (*88*). The energy profiles in THF for the inner- and outer-sphere mechanisms are depicted in Fig. 4.

The energy values obtained also agreed well with the experimental values for the reduction of PhCHO in THF-d_8: $\Delta H^{\ddagger} = 12.0 \pm 0.5$ kcal mol^{-1} using the Shvo's tolyl analog (*87*) and $\Delta H^{\ddagger} = 11.2 \pm 0.9$ kcal mol^{-1} for the analogous process in dry THF-d_8 (*99*). The inclusion of phenyl substituents groups into the model system did not change the energy profile; the energy barrier for the concerted outer-sphere mechanism with the complete catalyst (including the phenyl rings) was 8.0 kcal mol^{-1} in solution. The related transition states for both the model and the complete catalyst for the outer-sphere mechanism are depicted in Fig. 5. In addition, the theoretical calculation of kinetic isotope effects (KIEs) for the concerted outer-sphere mechanisms was also in agreement with the experimental values. Casey reported

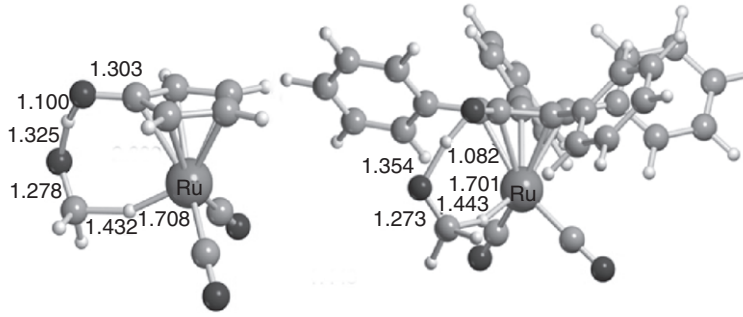

FIG. 5. Transition-states of the concerted outer-sphere mechanism for the hydrogenation of ketones in both the model (left) and complete (right) Shvo's catalysts.

combined KIEs by deuterating the Ru–D and C–D bonds of the Shv'o tolyl analog (where two phenyl groups were substituted by two tolyl groups). They reported a KIE of 3.6 ± 0.3 in the presence of a small amount of water (*85*) and a KIE of 3.38 ± 0.19 in dry THF (*99*) among other values in different solvents. The theoretical KIEs obtained by means of the Gibbs energy differences between initial reactants and the corresponding transition states were directly compared to the experimental values. The one more similar to the experimental value was the concerted outer-sphere one with a KIE value of 3.8 for the combined KIE arising from deuterating both the Ru–D and C–D bonds (e.g., the calculated KIE for the concerted inner-sphere mechanism was 0.8) (*87*).

In summary, the feasibility of the concerted outer-sphere mechanism was supported by the calculations because it has the lowest energy barrier among all the studied mechanisms and the closest calculated KIEs to those obtained experimentally.

B.1.b. Hydrogenation of Imines. For the hydrogenation of imines by the Shvo's catalyst, the analogous inner-(*93,94*) and outer-sphere mechanisms have been also theoretically investigated (*95*). The inner-sphere mechanism involving the $\eta^5 \rightarrow \eta^2$ CpOH ring slippage presented, in this case, an overall energy barrier height of 29.6 kcal mol^{-1} in solution, corresponding to the proton transfer to the iminic nitrogen. The $\eta^5 \rightarrow \eta^3$ concerted inner-sphere mechanism was computationally analyzed by Bäckvall and Privalov for an electron-donating imine and using the complete catalyst (including the phenyl rings) in the theoretical calculations (*93,94*). In their study, the solvent was taken into account by including explicit CH_2Cl_2 molecules and a polarized continuum method. The authors proposed a reasonable $\eta^5 \rightarrow \eta^3$ CpOH ring slippage coupled with an η^1 imine coordination, a fast proton transfer, followed by hydride transfer and a final $\eta^2 \rightarrow \eta^4$ ring slippage. All the steps presented similar energy barriers with an overall energy barrier of 15 kcal mol^{-1}(*94*).

In a parallel computational investigation both the inner- and outer-sphere mechanisms were analyzed (*95*). In this study the concerted outer-sphere mechanism showed an energy barrier of 9.6 kcal mol^{-1} in solution for the model system with the $H_2C{=}NH$ imine as a substrate (left of Fig. 6). The inclusion of the phenyl rings on the chemical model along with the geometry optimization in solution slightly decreased the energy barrier height to 6.8 kcal mol^{-1}. Hence, although there are some geometrical changes in the optimized structures, the energy profiles are not significantly changed when including phenyl rings (improving the

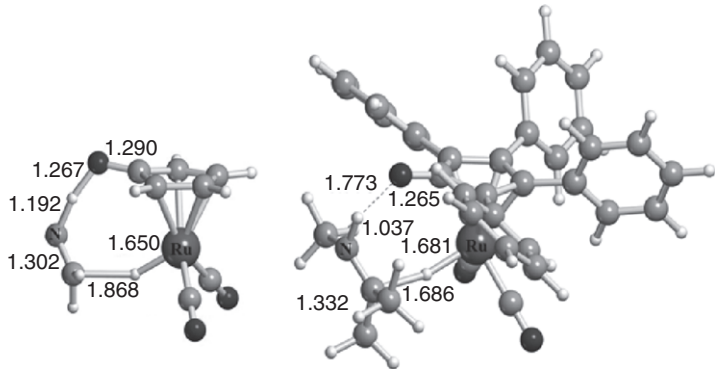

FIG. 6. Transition-states for the concerted outer-sphere mechanism for the hydrogenation of imines in both the model (left) and the complete Shvo catalysts (right); the former is for imine $H_2C{=}NH$, whereas the latter is for $(CH_3)_2C{=}N{-}CH_3$. Geometries optimized in solution (THF). Distances in Å.

model) and optimizing in solution. According to that, it represents a good compromise between accuracy and computational time to select a proper model for our catalyst and to perform single-point calculations in order to take into account solvent effects. Nevertheless, when the solvent is participating in the catalytic process some explicit solvent molecules (microsolvation) should be added to the common implicit solvation methods.

On the basis of the obtained results, the concerted outer-sphere mechanism seems to be more favorable than any of the inner-sphere evaluated mechanisms. The transition-state for the outer-sphere mechanism shows a certain degree of asynchronicity: the proton was relatively more transferred to the iminic nitrogen atom than the hydride to the iminic carbon atom.

In order to check if the concerted outer-sphere mechanism is also operating for electron-donating imines, the same authors evaluated imine ($(CH_3)_2C{=}N{-}CH_3$) hydrogenation including the phenyl substituents on the CpOH ligand and optimizing in solvent. The geometry of this transition-state is depicted in Fig. 6 (right). Concerning the energy barrier (4.0 kcal mol^{-1}) it was quite similar to that of the model imine (6.8 kcal mol^{-1}), being also in agreement with previous calculations by Casey and Cui (*88*). As expected, due to the increased basicity of a more electron-donating imine, the asynchronicity was higher than for the model imine, suggesting that outer-sphere stepwise mechanism could also be at play.

In summary, from the overall theoretical analysis it can be concluded that the concerted outer-sphere mechanism is near to 10 kcal mol^{-1} lower in energy than the lowest energy barrier reported for the inner-sphere mechanism. Therefore, theoretical analysis supports the concerted outer-sphere mechanism for the imine hydrogenation using the Shvo's catalyst. Finally, for the hydrogenation of non-polar multiple bonds (alkenes and alkynes) both inner- and outer-sphere mechanisms were also evaluated (*95*). The outer-sphere mechanism was found to be the preferred one in all the cases. When comparing the hydrogenation barriers between polar and non-polar bonds, the latter present energy barriers height approximately 10 kcal mol^{-1} higher in energy. This observation agreed with the observed chemoselectivity for polar double bond hydrogenation over multiple carbon–carbon bond hydrogenation.

IV. Concluding Remarks

In the present chapter, a classification of the hydrogenation reaction mechanisms according to the necessity (or not) of the coordination of the substrate to the catalyst is presented. These mechanisms are mainly classified between inner-sphere and outer-sphere mechanisms. In turns, the inner-sphere mechanisms can be divided in insertion and Meerweein–Ponndorf–Verley (MPV) mechanisms. Most of the hydrogenation reactions are classified within the insertion mechanism. The outer-sphere mechanisms are divided in bifunctional and ionic mechanisms. Their common characteristic is that the hydrogenation takes place by the addition of H^+ and H^- counterparts. The main difference is that for the former the transfer takes place simultaneously, whereas for the latter the hydrogen transfer is stepwise.

Theoretical calculations and in particular DFT calculations (mostly B3LYP) coupled with single-point PCM (or CPCM) calculations in solution and in some cases introducing some solvent molecules (microsolvation) when they are actively participating in the studied catalytic process are a suitable approach to analyze reaction mechanisms in the field of homogeneous catalysis. In our selected examples, calculations provide a structural description of all the intermediates and transition states involved in the catalytic cycle, and thus a clear sorting of a particular hydrogenation reaction as inner- or outer-sphere process. Their application to several hydrogenation reactions has allowed their classification into the general classes of hydrogenation reactions described in the first part of the chapter. Besides their classification,

theoretical analysis allowed a deeper understanding of the reaction mechanisms. Thus, the above-mentioned studies give insights on which could be the operating reaction mechanism by analyzing some factors that are subsequently summarized. In fact, although many factors may affect the hydrogenation mechanism, the general trend from these particular studies can be gathered as follows.

A. Catalyst and Substrate Structure

The sole catalyst structure gives valuable information on which could be the operating reaction mechanism: inner- (with substrate coordination to the metal) or outer-sphere (without substrate coordination to the metal). Hence, if the active form of the catalyst bears one or two hydrides (and no protic hydrogens) the insertion mechanism (inner-sphere mechanism) is more likely. Although an outer-sphere mechanism with one hydride transfer coming from the metal and one proton transfer coming from the medium should be also taken into consideration, mainly in aqueous medium at low pH values. If the catalyst is bifunctional containing two active hydrogens atoms with respective hydride and proton character, the outer-sphere reaction mechanism is expected to be the most probable operating mechanism. This trend is probably more accused in the case of polar double bond hydrogenation as, for instance, in the case of the Shvo's catalyst. Conversely, for non-polar double bonds hydrogenation (in the case where the media is not playing a role), it is usually completed by means of σ-bond metathesis of an incoming H_2 molecule, regenerating the metal–hydride species and forming the final hydrogenated product. The presence of ligands able to establish non-covalent interactions with the substrate, particularly hydrogen bonding, appears as an important factor in the outer-sphere mechanisms. They keep the substrate in the second coordination sphere allowing its ulterior reaction with the catalyst without requiring coordination to the metal.

B. Environmental Effects: Solvent and pH

The role of the solvent is crucial in some cases. For example, in the case of hydrogen activation it was actively participating in the heterolytic cleavage of the hydrogen in both the ruthenium and gold catalysts in water and ethanol, respectively. It must be noted that the so-called heterolytic activation of the hydrogen may be

operating in several catalytic hydrogenations and especially on those carried out in polar protic solvents since they are able to stabilize the resulting proton species. Moreover, these polar protic solvents (like water) can complete the hydrogenation by giving one proton to the insertion product.

Acknowledgements

Part of the computational work cited in this chapter was carried out in our group at the UAB in collaboration with experimental groups. We express our gratitude to our co-workers A. Corma (Universidad Politécnica de Valencia-CSIC), F. Joó (University of Debrecen), and J. López-Serrano and S. B. Duckett (University of York). We are grateful to the Spanish MICINN (Projects CTQ2008-06866-C02-01, Consolider Ingenio 2010 CSD2007-00006 and FPU fellowship to A.C.-V.) and to the Generalitat de Catalunya (2009/SGR/68 and "Distinció per a la Promoció de la Recerca Universitària") for financial support.

References

1. Klomp, D.; Hanefeld, U.; Peeters, J. A. In: *Handbook of Homogeneous Hydrogenation*; Eds. de Vries, J. G.; Elsevier, C. J.; Wiley-VCH: Weinheim, **2007**.
2. Chaloner, P. A.; Esteruelas, M. A.; Joó, F.; Oro, L. A. *Homogeneous Hydrogenation*; Kluwer Academic Publishers: Dordrecht, **1994**.
3. James, B. R. *Homogeneous Hydrogenation*; Wiley: New York, **1973**.
4. Kubas, G. J. *Metal Dihydrogen and σ-Bond Complexes*; Kluwer/Academic Plenum Publishers: New York, **2001**.
5. Kubas, G.J. *Adv. Inorg. Chem.* **2004**, *56*, 127.
6. Maseras, F.; Lledos, A.; Clot, E.; Eisenstein, O. *Chem. Rev.* **2000**, *100*, 601.
7. Peruzzini, M.; Poli, R.; (Eds.) *Recent Advances in Hydride Chemistry*; Elsevier SA: Amsterdam, **2001**.
8. Brothers, P. J. *Prog. Inorg. Chem*. **1981**, *28*, 1.
9. Ito, M.; Hirakawa, M.; Murata, K.; Ikariya, T. *Organometallics* **2001**, *20*, 379.
10. Sandoval, C. A.; Ohkuma, T.; Muñiz, K; Noyori R. *J. Am. Chem. Soc.* **2003**, *125*, 13490.
11. Rautenstrauch, V.; Hoang-Cong, X.; Churlaud, R.; Abdur-Rashid, K.; Morris, R. H. *Chem. Eur. J.* **2003**, *9*, 4954.
12. Casey, C. P.; Johnson, J. B.; Singer, S. W.; Cui., Q. J. *Am. Chem. Soc.* **2005**, *127*, 3100.
13. Hedberg, C.; Källström, K.; Arvidsson, P. I.; Brandt, P.; Andersson, P. G. *J. Am. Chem. Soc.* **2005**, *127*, 15083.
14. Rossin, A.; Gonsalvi, L.; Phillips, A. D.; Maresca, O.; Lledós, A.; Peruzzini, M. *Organometallics* **2007**, *26*, 429.

15. Friederich, A.; Drees, M.; der Günne, J. S. A.; Schneider, S. *J. Am. Chem. Soc.* **2009**, *131*, 17552–17553.
16. Gladiali, S.; Alberico, E. *Chem. Soc. Rev.* **2006**, *35*, 226.
17. Samec, J. S. M.; Bäckvall, J.-E.; Andersson, P. G.; Brandt, P. *Chem. Soc. Rev.* **2006**, *35*, 237.
18. Clapham, S. E.; Hadzovic, A.; Morris, R. H. *Coord. Chem. Rev.* **2004**, *248*, 2201.
19. Bäckvall, J.-E. *J. Organomet. Chem.* **2002**, *652*, 105.
20. Noyori, R.; Hashiguchi, S. *Acc. Chem. Res.* **1997**, *30*, 97.
21. Haack, K. J.; Hashiguchi, S.; Fujii, A.; Ikariya, T.; Noyori, R. *Angew. Chem. Int. Ed. Engl.* **1997**, *36*, 285.
22. Meerwein H.; Schmidt, R. *Justus Liebigs Ann. Chem.* **1925**, *444*, 221.
23. Verley, A. *Bull. Soc. Chim. Fr.* **1925**, *37*, 537.
24. Ponndorf, W. *Angew. Chem.* **1926**, *29*, 138.
25. Oro, L. A. *Fundamentos y aplicaciones de la Catálisis Homogénea*; INO Reproducciones, S.A., Zaragoza, **2000**.
26. Evans, D; Osborn, J. A.; Jardine, F. H.; Wilkinson, G. *Nature*, **1965**, *32*, 265.
27. Daniel, C.; Koga, N.; Han, J.; Fu, X. Y.; Morokuma, K. *J. Am. Chem. Soc.* **1988**, *110*, 3773.
28. Pàmies, O.; Bäckvall, J.-E. *Chem. Eur. J.* **2001**, *7*, 5052.
29. Comas-Vives, A.; Ujaque, G.; Lledós, A. *J Mol. Struct: THEOCHEM* **2009**, *903*, 123.
30. Andriollo, A.; Esteruelas, M. A.; Meyer, U.; Oro, L. A.; Sánchez-Delgado, R.; Sola, E.; Valero, C.; Werner, H. *J. Am. Chem. Soc.* **1989**, *111*, 7431.
31. Fabrello, A.; Bachelier, A.; Urrutigoïty, M.; Kalck, P. *Coord. Chem. Rev.* **2010**, *254*, 273.
32. Yi, C. S.; He, Z.; Guzei, I. A. *Organometallics* **2001**, *20*, 3641.
33. Guiral, V.; Delbecq, F.; Sautet, P. *Organometallics* **2000**, *19*, 1589.
34. Handgraaf, J.-W.; Reek, J.N.H.; Meijer, E.-V. *Organometallics* **2003**, *22*, 3150.
35. Guiral, V.; Delbecq, F.; Sautet, P. *Organometallics* **2001**, *20*, 2207.
36. Blum, Y.; Czarkie, D.; Rahamim, Y.; Shvo, Y. *Organometallics* **1985**, *4*, 1459.
37. Shvo, Y.; Czarkie, D.; Rahamim, Y. *J. Am. Chem. Soc.* **1986**, *108*, 7400.
38. Noyori, R.; Ohkuma, T. *Angew. Chem. Int. Ed.* **2001**, *40*, 40.
39. Fujii, A.; Hashiguchi, S.; Uematsu, N.; Ikariya, T.; Noyori, R. *J. Am. Chem. Soc.* **1996**, *118*, 2521.
40. Uematsu, N.; Fujii, A.; Hashiguchi, S.; Ikariya, T.; Noyori, R. *J. Am. Chem. Soc.* **1996**, *118*, 4916.
41. Wu, X.; Vinci, D.; Ikariya, T.; Xiao, J. *Chem. Commun.* **2005**, 4447.
42. Grützmacher, H. *Angew. Chem. Int. Ed.* **2008**, *47*, 1814.
43. Yamakawa, M.; Ito, H.; Noyori, R. *J. Am. Chem.* **2000**, *122*, 1466.
44. French, S. A.; Di Tommaso, D.; Zanotti-Gerosa, A.; Hancock, F.; Catlow, C.R.A. *Chem. Commun.* **2007**, 2381.
45. Casey, C. P.; Johnson, J. B. *J. Org. Chem.* **2003**, *68*, 1998.
46. Abdur-Rashid, K.; Clapham, S. E.; Hadzovic, A.; Harvey, J. N.; Lough, A. J.; Morris, R. H. *J. Am. Chem. Soc.* **2002**, *124*, 15104.
47. Di Tommaso, D.; French, S. A.; Catlow, C.R.A. *J. Mol. Struct.* **2007**, *812*, 39.
48. Yamakawa, M.; Yamada, I.; Noyori, R. *Angew. Chem. Int. Ed.* **2001**, *40*, 2818.
49. Alonso, D. A.; Brandt, P.; Nordin, S.J.M.; Andersson, P. G. *J. Am. Chem. Soc.* **1999**, *121*, 9580.
50. Petra, D. G. I.; Reek, J. N. H.; Handgraaf, J. -W.; Meijer, E. J.; Dierkes, P.; Kamer, P. C. J.; Brusse, J.; Schoemaker, H. E.; van Leeuwen, P. W. N. M. *Chem. Eur. J.* **2000**, *6*, 2818.

51. Di Tommaso, D.; French, S. A.; Zanotti-Gerosa, A.; Hancock, F.; Palin, E. J.; Catlow, C. R. A. *Inorg. Chem.* **2008**, *47*, 2674.
52. Leyssens, T.; Peeters, D.; Harvey, J. N. *Organometallics* **2008**, *27*, 1514.
53. Bullock, R. M. *Chem. Eur. J.* **2004**, *10*, 2366.
54. Guan, H.; Iimura, M.; Magee, M. P.; Norton, J. R.; Zhu. G. *J. Am. Chem. Soc*. **2005**, *127*, 7805.
55. Bullock, R. M.; Voges, M. H. *J. Am. Chem. Soc.* **2000**, *122*, 12594.
56. Voges, M. H.; Bullock, R. M. *J. Chem. Soc., Dalton Trans.* **2002**, 759.
57. Magee, M. P.; Norton, J. R. *J. Am. Chem. Soc.* **2001**, *123*, 1778.
58. Martin, M.; Sola, E; Tejero, S.; Andrés, J. L.; Oro, L. A. *Chem. Eur. J.* **2006**, *12*, 4043.
59. Martin, M.; Sola, E; Tejero, S.; López, J. A.; Oro, L. A. *Chem. Eur. J.* **2006**, *12*, 4057.
60. Maseras; F., Lledós, A., Eds. *Computational Modeling of Homogeneous Catalysis*; Kluwer Academic Publishers: Dordrecht, **2002**.
61. Joó, F. *Aqueous Organometallic Catalysis*; Kluwer: Dordrecht, The Netherlands, **2001**.
62. Joó, F.; Kovács, J.; Bényei, A. C.; Kathó, Á. *Angew. Chem., Int. Ed.* **1998**, *37*, 969.
63. Joó, F.; Kovács, J.; Bényei, A. C.; Kathó, Á. *Catal. Today* **1998**, *42*, 441.
64. Kovács, G.; Ujaque, G.; Lledós, A.; Joó, F. *Organometallics* **2006**, *25*, 862.
65. Rossin, A.; Kovács, G.; Ujaque, G.; Lledós, A.; Joó, F. *Organometallics* **2006**, *25*, 5010.
66. Joubert, J.; Delbecq, F. *Organometallics* **2006**, *25*, 854
67. Comas-Vives, A.; Stirling, A; Lledós, A.; Ujaque, G. *Chem. Eur. J.* **2010**, *16*, 8738.
68. Arcadi, A. *Chem. Rev.* **2008**, *108*, 3266.
69. Jiménez-Nuñez, E.; Echavarren, A. M. *Chem. Rev.* **2008**, *108*, 3326.
70. Hashmi, A.S.K.; Rudolph, M. *Chem. Soc. Rev.* **2008**, *37*, 1766.
71. Comas-Vives, A.; González-Arellano, C.; Corma, A.; Iglesias, M.; Sánchez, F.; Ujaque, G. *J. Am. Chem. Soc.* **2006**, *128*, 4756.
72. Comas-Vives, A.; González-Arellano, C.; Boronat, M.; Corma, A.; Iglesias, M.; Sánchez, F.; Ujaque, G. *J. Catal.* **2008**, *254*, 226.
73. López-Serrano, J.; Duckett, S. B.; Lledós, A. *J. Am. Chem. Soc.* **2006**, *126*, 9596.
74. López-Serrano, J.; Lledós, A.; Duckett, S. B. *Organometallics* **2008**, *27*, 43.
75. Clegg, W.; Eastham, G. R.; Elsegood, M.R.J.; Heaton, B. T.; Iggo, J. A.; Tooze, R. P.; Whyman, R.; Zacchini, S. *Dalton Trans.* **2002**, 3300.
76. Karvembu, R.; Prabhakaran, R.; Natarajan, K. *Coord. Chem. Rev.* **2005**, *249*, 911.
77. Menashe, N.; Salant, E.; Shvo, Y. *J. Organomet. Chem.* **1996**, *514*, 97.
78. Samec, J. S. M.; Bäckvall, J.-E. *Chem. Eur. J.* **2002**, *8*, 2955.
79. Shvo, Y.; Goldberg, I.; Czierke, D.; Reshef, D.; Stein, Z. *Organometallics* **1997**, *16*, 133.
80. Csjernyk, G.; Éll, A. H.; Fadini, L.; Pugin, B.; Bäckvall, J.-E. *J. Org. Chem.* **2002**, *67*, 1657.
81. Samec, J. S. M.; Éll, A. H.; Bäckvall, J.-E. *Chem.-Eur. J.* **2005**, *11*, 2327.
82. Éll, A. H.; Samec, J.S.M.; Brasse, C.; Bäckvall, J.-E. *Chem. Commun.* **2002**, 1144.
83. Choi, J. H.; Kim, N.; Shin, Y. J.; Park, J. H.; Park, J. *Tetrahedron Lett.* **2004**, *45*, 4607.
84. Conley, B. L.; Pennington-Boggio, M. K.; Boz, E.; Williams, T. J. *Chem. Rev.* **2010**, *110*, 2294.

85. Casey, C. P.; Singer, S. W.; Powell, D. R.; Hayashi, R. K.; Kavana, M. *J. Am. Chem. Soc.* **2001**, *123*, 1090.
86. Johnson, J. B.; Bäckvall, J.-E. *J. Org. Chem.* **2003**, *68*, 7681.
87. Comas-Vives, A.; Ujaque, G.; Lledós, A. *Organometallics* **2007**, *26*, 4135.
88. Casey, C. P.; Bikzhanova, G. A.; Cui, Q.; Guzei, I. A. (and Supporting Information therein) *J. Am. Chem. Soc.* **2005**, *127*, 14062.
89. Casey, C. P.; Bikzhanova, G. A.; Guzei, I. A. *J. Am. Chem. Soc.* **2006**, *128*, 2286.
90. Casey, C. P.; Johnson, J. B. *J. Am. Chem. Soc.* **2005**, *127*, 1883.
91. Samec, J. S. M.; Éll, A. H.; Bäckvall, J.-E. *Chem. Commun.* **2004**, 2748.
92. Éll, A. H.; Johnson, J. B.; Bäckvall, J.-E. *Chem. Commun.* **2003**, 1652.
93. Samec, J.S.M.; Éll, A. H.; Åberg, J. B.; Privalov, T.; Eriksson, L.; Bäckvall, J.-E. *J. Am. Chem. Soc.* **2006**, *128*, 14293.
94. Privalov, T.; Samec, J.S.M.; Bäckvall, J.-E. *Organometallics* **2007**, *26*, 2840.
95. Comas-Vives, A.; Ujaque, G.; Lledós, A. *Organometallics* **2008**, *27*, 4854.
96. Habib, A.; Tanke, R. S.; Holt, E. M.; Crabtree, R. H. *Organometallics* **1989**, *8*, 225.
97. Veiros, L. F. *Organometallics* **2000**, *19*, 5549.
98. Fan, H.-J.; Hall, M. B. *Organometallics* **2001**, *20*, 5724.
99. Casey, C. P.; Johnson, J. B. *Can. J. Chem.* **2005**, *83*, 1339.

COMPUTATIONAL STUDIES ON PROPERTIES, FORMATION, AND COMPLEXATION OF M(II)-PORPHYRINS

TATYANA E. SHUBINA

Computer-Chemie-Centrum and Interdisciplinary Center for Molecular Materials, Friedrich-Alexander-Universität Erlangen-Nürnberg, Nägelsbachstrasse 25 91052, Erlangen, Germany

I. Introduction

Organometallic compounds play an essential role in the development and production of new materials for industry, especially electronic materials. The role of metalloporphyrins as chemically interactive materials in chemical sensors has interested researchers for a long time (*1–4*). The rich coordination chemistry of porphyrins is responsible for their use in chemical-sensor

THEORETICAL AND COMPUTATIONAL INORGANIC CHEMISTRY
VOLUME 62 ISSN 0898-8838 / DOI: 10.1016/S0898-8838(10)62007-7

applications that use the changes induced in their physicochemical properties by the addition of axial ligands.

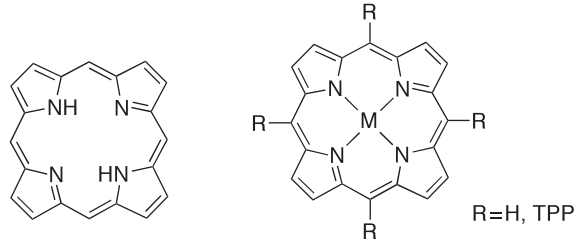

The basic structure of porphyrins (left) and metalloporphyrins (right).

The molecular skeleton of porphyrins consists of four pyrrole rings linked by methine bridges; the resulting molecule is fully conjugated and planar. This macrocycle is an aromatic system with a total of 22 π-electrons, of which only 18 are delocalized according to Hückel's rule of aromaticity ($4n + 2$ delocalized π-electrons, where $n = 4$). The extended aromatic system is also responsible for the high molar absorbance of the porphyrins and ultimately for the intense color. The nitrogen present in the core of the porphyrin represents a powerful coordinating system and almost all elements of the periodic table have been successfully coordinated to porphyrins.

Metalloporphyrins were formed early in the history of the prebiotic earth and played an important role in, for instance, catalyzing the disproportionation of hydrogen peroxide (*5–7*). Naturally occurring metalloporphyrins are among the most important prosthetic groups for oxygen storage and transfer (*8*), metabolism (*9,10*), photosynthesis (*11*), and many other redox reactions and small-molecule storage and transport purposes in biological systems (*12*). For example, heme proteins (which contain iron porphyrins) serve many roles, such as O_2 storage and transport (myoglobin and hemoglobin), electron transport (cytochromes b and c), and O_2 activation and utilization (cytochrome P450 and cytochrome oxidase). Chlorophylls (which have a central magnesium ion) and pheophytins (which are metal free) are found in the photosynthetic apparatus of plants and bacteria, whereas vitamin B12 (which contains cobalt) is present in bacteria and animals.

Synthetic porphyrins have been used extensively as model systems for investigating the complex biological functions of natural porphyrin-containing systems. Given the capabilities of porphyrins to bind and release gases and to act as the active center in catalytic reactions in biological systems, porphyrin-

based films on metal or semiconductor surfaces are extremely appealing as chemical and gas sensors as well as nanoporous catalytic materials in novel synthetic biomimetic devices. For example, the facile substitution of the periphery of various porphyrins has generated a series of unusual liquid crystalline materials. The porphyrin ligand serves as a platform on which one can achieve desirable molecular and materials properties, including very large dipole moments, polarizabilities, and hyperpolarizabilities (*13,14*). The nonlinear optical properties of these materials are of special interest, in part for energy transfer with molecular control, and in part for potential applications in optical communications, data storage, and electrooptical signal processing. The stability of mono- and dication porphyrin π-radicals makes these systems especially interesting for photoionization processes, closely related to the so-called special-pair reaction center of photosynthesis and the photogeneration of electron transfer. As another example, various polymeric porphyrins have been examined for their unusual low-dimensional conductivity.

For example, porphyrins have been proposed as active elements in gas-sensor devices. This field has become one of the fastest growing areas in both research and commercial respects. Several authors have proposed the use of some organic materials, e.g., phthalocyanine and porphyrin derivatives (*15–18*) to improve the device's performance characteristics, such as low operating temperature, selectivity, and so on.

The use of metalloporphyrin-based materials for detecting molecular oxygen is well developed. One approach that has been employed extensively involves the well-known phenomenon of quenching of metalloporphyrin phosphorescence by O_2. Due to their high phosphorescence quantum yields and short triplet lifetimes, platinum and palladium porphyrins were originally suggested as probes for oxygen by Eastwood and Gouterman (*19*). Porphyrin-based sensors have also been used for the detection of gases such as ammonia, hydrazine, and NO.

Zinc-5,10,15,20–tetraphenylporphyrin (ZnTPP) has been used as a coating material in ammonia sensors by immobilizing it on the surface of silicone rubber. Absorbance and fluorescence emission were the modes of detection. A spectral change is caused by the coordination of NH_3 molecules to the Zn^{II} ion in the immobilized metalloporphyrins. Sensing films made from the ZnTPP immobilized in silicone rubber were found to be the most sensitive for NH_3 sensing (*20*).

It has also been reported recently that metalloporphyrins have been introduced as coating materials of quartz microbalances to

obtain chemical sensors. The main features of such sensors' properties in terms of selectivity and sensitivity are extremely good. The nature of the central metal and the lateral groups is responsible for sensor properties. With only small variations in synthesis, it is possible to obtain sensors with different responses. This feature makes these compounds extremely attractive for sensor applications (*21*).

This review is intended to give an overview of the recent progress in the area of the formation of metalloporphyrins (the mechanism of the direct metalation reaction) and their reactions with small molecules (CO, NO, H_2O, O_2). Although the emphasis is on "less studied" examples, a selection of recent results on iron (II) porphyrin complexes with CO and NO is also included.

II. Models and Methods

A. Porphyrin Models

Generally, fourfold and fivefold coordination models are used to describe metalloporphyrins. In the fourfold coordination model, the metal atom is coordinated to the porphyrin nitrogen atoms and the lower coordination site remains free (Scheme 1b). The upper coordination site can later be occupied by ligands such as H_2O, CO, O_2, and NO.

This model represents a natural starting point for both experimental and theoretical studies. Crystal structures have been reported for a number of heme derivatives with different substituents in the ring (*22*). FeTPP (TPP = *meso*-tetraphenylporphyrin) has been particularly widely used. Its electronic state is known experimentally to correspond to a low-spin triplet ($S = 1$).

Coordination of a base (for example, the imidazole (Im) ligand) to the heme group leads to a five-coordinate species with a square

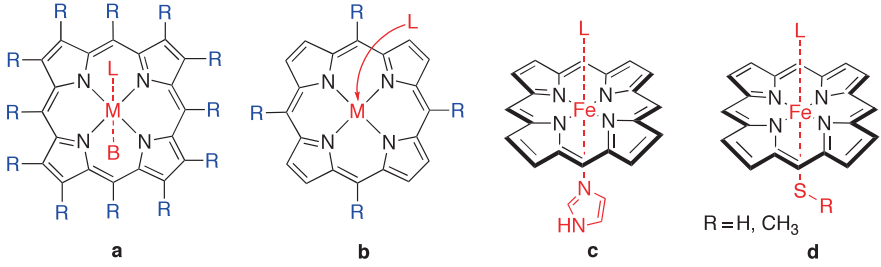

Scheme 1. Six- (a) and five-coordinate (b) complexes of metalloporphyrins. **B** can be any Lewis base. **L** = ligand.

pyramidal geometry. These compounds are good biomimetic models of myoglobine (Mb) and hemoglobin (Hb), with Im replacing the proximal histidine (His) of the biological systems (Scheme 1c). Additionally, coordination of cysteine to the heme group (or simply thiol or methanethiol) resembles cytochrome P450 (Scheme 1d).

Coordination of small organic molecules by porphyrin complexes gives rise to either five- or six-coordinate ligand–metalloporphyrin complexes (Eqs. (1) and (2)):

$$\mathrm{MP} + \mathrm{L} \rightleftarrows \mathrm{MP} - \mathrm{L} \tag{1}$$

$$\mathrm{MP(B)} + \mathrm{L} \rightleftarrows \mathrm{MP(B)} - \mathrm{L} \tag{2}$$

The data obtained in quantitative studies of these equilibria have been summarized in a review (*23*). These equilibria can easily be shifted in the desired direction by changing the concentrations of molecular ligands, the nature of the solvent, or the temperature. The coordination of additional ligands is accompanied by a shift of 5–35 nm of the absorption bands in the optical spectrum relative to those of the starting metalloporphyrin. The value and direction of the shift depend on the nature of the central atom and the molecular ligand and on the structure of porphyrin. The addition of the ligand leads to a bathochromic shift of the first absorption band, which corresponds to a low-frequency $\pi \rightarrow \pi^*$ transition, if the metalloporphyrin is planar and binds solvent molecules weakly.

Because of the diversity of polyhedral geometries found in porphyrin complexes with metal cations, additional ligands exhibit many different coordination modes. In Fe^{II}, Co^{II}, Mn^{II}, Zn^{II}, etc. complexes with one extra ligand, MP–L, the metal ion is pushed out of the N_4 plane, and the MN_4 coordination unit can be described as a pyramid with the M metal atom in the apical position.

B. Methods

Various theoretical methods and approaches have been used to model properties and reactivities of metalloporphyrins. They range from the early use of qualitative molecular orbital diagrams (*24,25*), linear combination of atomic orbitals to yield molecular orbitals (LCAO-MO) calculations (*26–30*), molecular mechanics (*31,32*) and semi-empirical methods (*33–35*), and self-consistent field method (SCF) calculations (*36–43*) to the methods commonly used nowadays (molecular dynamic simulations (*31,44,45*), density functional theory (DFT) (*35,46–49*), Moller–Plesset perturbation theory (MP*n*) (*50–53*), configuration interaction (CI) (*35,42,54–56*), coupled cluster (CC) (*57,58*), and CASSCF/CASPT2 (*59–63*)).

A large number of different types of DFT calculation have appeared over the years. Probably nearly all available DFT functionals have now been used to describe the properties and reactivity of metalloporphyrins, with the B3LYP (*64,65*) functional being the most popular choice.

III. Geometries and Electronic States of Metalloporphyrins

Consequently, there has been much interest in understanding the electronic structure of these molecules. Since the partial occupancy of the 3*d*-shell can yield a number of low-lying electronic states within a narrow energy range, it has long been debated as to what is the ground state for unligated, four-coordinate Fe(II) and Co(II) porphyrins (FeP and CoP, respectively).

Many studies have discussed the performance of various DFT functionals for metalloporphyrins. It is now generally accepted that the ground state of FeP is intermediate spin: only the $^3A_{2g}$ state arising from the $(d_z{}^2)^2(d_{xy})^2(d_\pi)^2$ configuration is compatible with Mössbauer, magnetic moment, and proton NMR data (*66–70*). The standard B3LYP functional suggests the ground state to be $^3A_{2g}$, in agreement with most experiments (*71*). For low-spin ($S = 1/2$) CoP, the ground-state configuration is known to be $^2A_{1g}$ $\{(d_{xy})^2(d_{xz})^2(d_{yz})^2(d_x{}^2{}_{-y}{}^2)^0(d_z{}^2)^1\}$. However, the ^2E_g state is only 0.2 eV higher in energy than the $^2A_{1g}$ ground state.

Detailed investigations of different spin states in metalloporphyrins have been performed by number of groups (*47,48,56,60,72–76*) and results relevant to Fe(II)P are summarized in the Table I.

Generally, it is agreed that CASPT2 provides much better accuracy than any DFT functionals. It is also necessary to use larger basis sets, since expanding the basis set and active space in a reference function provides a better description of each state. Second, relativistic corrections should be taken into account. As seen from Table I, the energies of several states exist in a small energy range, so that effects that may be neglected in calculations on other systems should be considered explicitly. Finally, the effect of geometry must be considered. Several authors (*53,77–79*) have reported the importance of geometry in elucidating the ground-state electronic structure of iron (II) porphyrin because the spin multiplicity of the molecule is very sensitive to the geometrical parameters chosen.

Additionally, the axial ligands influence the electronic structure of metalloporphyrins. It is known that axial ligation has a substantial influence on the redox (*80,81*) and photovoltaic (*82*) properties

TABLE I

SPIN MULTIPLICITIES AND RELATIVE ENERGIES, eV, OF Fe(II)P

Methods	$^1B_{2g}$	^1E_g	$^1A_{1g}$	$^3E_g(B)$	$^3B_{2g}$	$^3E_g(A)$	$^3A_{2g}$	$^5B_{2g}$	^5E_g	$^5A_{1g}$
CASSCF (*75*)	1.512	1.387	1.159	1.167	0.506	0.000	–0.026	–1.080	–1.192	–1.391
CASPT2 (*75*)	1.366	1.541	1.479	1.032	0.573	0.000	–0.018	–0.556	–0.708	–0.852
CASSCF (*76*)	1.568	1.350	1.263	1.115	0.518	0.000	–0.003	–1.076	–1.236	–1.347
MRMP (*76*)	1.270	1.508	0.171	0.632	0.177	0.000	0.229	–0.002	–0.180	–0.369
ZINDO (*56*)	1.76	0.93	0.98	1.03	0.39	0.000	–0.03	0.63	0.39	0.28
SCF (*78*)	1.58		1.36	1.41	0.51	0.000	–0.03	–1.05	–1.19	–1.40
CI (*78*)	1.6	1.33	1.06	1.12	0.20	0.000	0.47	0.09	–0.83	–0.10
CI (*87*)						0.000	–0.27			
DFT (*88*)			1.20	0.88	0.53	0.000	0.25	1.74	1.29	1.44
DFT (*89*)			1.24		0.58	0.000	0.19	1.76		1.52
PBE0/BSII (*60*)			1.59			0.00				–0.02
B3LYP/BSII (*60*)			1.50			0.00				0.19
OLYP/BSII (*60*)			1.56			0.00				0.27
BP86/BSII (*60*)			1.54			0.00				0.66
CASPT2 (*60*)			1.53			0.00				–0.28
CASPT2 (*60*)			1.51			0.00				–0.28
BLYP/6–31G(d) (*53*)			1.79			0.000				0.64
BLYP/6–311+G(d,p) (*53*)			1.43			0.000				0.63
B3LYP/6–31G(d) (*53*)			1.80			0.000				0.19
B3LYP/6–311+G(d,p) (*53*)			1.48			0.000				0.19
B3LYP/GEN (*53*)			1.37			0.000				0.17
B3PW91/6–31G(d) (*53*)			1.80			0.000				–0.11

(*Continued*)

TABLE I (*Continued*)

Methods	$^1B_{2g}$	^1E_g	$^1A_{1g}$	$^3E_g(B)$	$^3B_{2g}$	$^3E_g(A)$	$^3A_{2g}$	$^5B_{2g}$	^5E_g	$^5A_{1g}$
B3PW91/6–311+G(d,p) (*53*)			1.48			0.000				0.11
OLYP/6–31G(d) (*53*)			1.73			0.000				0.13
OLYP/6–311+G(d,p) (*53*)			–			0.000				0.13
M06L/6–31G(d) (*53*)			1.33			0.000				–0.10
M06L/6–311+G(d,p) (*53*)			1.15			0.000				–0.12
MP2/6–31G(d) (*53*)			1.88			0.000				–
MP2/cc–pVDZ (*53*)			1.54			0.000				–
DFT (*47*)			1.37	0.62	0.14	0.000	–0.12	0.93	0.73	0.59

of metal porphyrins. For example, iron porphyrins with coordinating axial ligands are diamagnetic ($S = 0$) in contrast to the four-coordinate species ($S = 1$) (*83,84*). Elucidating the electronic structure of metal porphyrins with axial ligands is also important for understanding their biological and catalytic functions (*85*).

There are generally two reasons why accurate prediction of MP–L (MP = metalloporphyrin, L = ligand) binding energies might be difficult, especially for DFT. First, the spin state of the metal ion might change during the ligand addition (i.e., FeP/FeP–NO or CoP/CoP–NO) (*86*), whereas the relative energies of different spin states for transition-metal complexes require a high-level description of electronic exchange and correlation. Second, the energy of a covalent M–L bond contains an important contribution from nondynamic correlation. Additional complications occur for the complexes with O_2, which suffer from a strong spin contamination in unrestricted single-determinant calculations.

IV. Metalation of Porphyrins

A. In Condensed Phases

Porphyrins in nature are usually synthesized in a metal-free form, the metal ions being inserted subsequently. This latter process is catalyzed by enzymes (*90*).

The reaction of a porphyrin molecule H_2P in solution with M^{2+} ions proceeds by release of two protons:

$$M^{2+} + H_2P \rightarrow MP + 2H^+ \tag{3}$$

Generally, two alternative mechanisms can be taken into account: (a) dissociation, which requires the porphyrin to be transformed to the mono- or dianion before reaction with the metal: and (b) displacement, requiring that a metal–porphyrin complex forms prior to the release of two protons (Eq. 3).

$$H_2P \rightarrow HP^- + H^+ \rightarrow P^{2-} + H^+$$
$$HP^- + M^{2+} \rightarrow PM + H^+$$
$$P^{2-} + M^{2+} \rightarrow PM$$

More than a half century ago, it was proposed (*91*) that reaction between zinc ion and solubilized porphyrin esters takes place via a displacement rather than a dissociation type of mechanism (Eq. 4).

$$Zn^{2+} + H_2P + 2H_2O \rightleftharpoons MP + 2H_3O^+ \tag{4}$$

Later, Fleischer and Wang (*92*) showed that such reaction indeed takes place via a displacement mechanism. The authors also showed that first the metal ion combines with the porphyrin to form a reactive intermediate, which subsequently decomposes to metalloporphyrin and two hydrogen ions. It was suggested that this intermediate has the metal atom sitting-atop (SAT) the porphyrin ring (Scheme 2). Notably, both hydrogen atoms of the pyrrole nitrogens are displaced toward the lower face of the porphyrin ring.

A number of authors have called the formation of SAT complex into question and instead suggested either (c) direct coordination between the metal ion and two pyrrolinine nitrogen atoms of the porphyrin to give H_2PM^{2+} or (d) ion pair formation between the porphyrin dication and solvated anion formed in solvents incapable of supporting separate charged species was proposed (*93*).

Finally, based on experimental studies many groups have reached a consensus that the mechanism of the direct metalation of porphyrins in solution consists of the following six steps:

– deformation of the porphyrin ring
– outer-sphere association of the solvated metal ion and the porphyrin
– exchange of a solvent molecule with the first pyrrolenine nitrogen atom
– chelate-ring closure with the expulsion of more solvent molecules
– first deprotonation of a pyrrole nitrogen atom
– final deprotonation of the second nitrogen atom and formation of the metalloporphyrin

Until now, only a few theoretical studies of porphyrin metalation by divalent metal ions in solution have been reported (*72,94,95*). In the first theoretical work (*94,96*) on this topic, insertion of Fe^{2+} and Mg^{2+} into the porphyrin ring was studied by DFT methods. The authors followed the reaction from the outer-sphere complex formation via stepwise displacement of the solvent molecules until

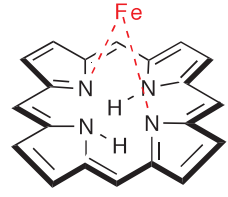

SCHEME 2. Schematic structure of the proposed SAT complex.

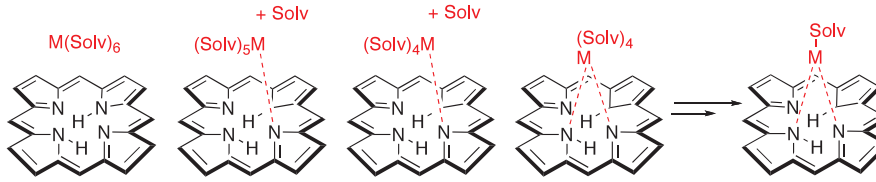

SCHEME 3. Stepwise formation of the SAT complex.

the metal ion is inserted into the porphyrin ring and only one solvent molecule remains (Scheme 3).

These results indicated that the reaction mechanism is, in fact, more complicated than normally assumed and should include nine (or optionally ten) steps:

1. Formation of an outer-sphere complex of the hydrated metal and the porphyrin.
2. Formation of the first metal–porphyrin bond by the exchange of one water ligand.
3. Exchange of the second water ligand.
4. Exchange of the third water ligand.
5. Formation of the second metal–porphyrin bond (going from a 1N to a 2N complex).
6. Exchange of the fourth water ligand.
7. Exchange of the fifth water ligand.
8. Deprotonation of the third pyrrole ring of the porphyrin.
9. Deprotonation of the fourth pyrrole ring of the porphyrin.
10. Formation of a second axial bond of the metal on the opposite side of the porphyrin ring.

The ligand exchange reactions were found to be almost thermoneutral (±5 kcal mol^{-1}) with barriers up to 13 kcal mol^{-1} (for Fe).

B. GAS-PHASE METALATION

The gas-phase formation of metalloporphyrin ions ($M(P)^+$) has been known for a long time, since the early mass-spectra studies of metalloporphyrins (*97,98*). Such gas-phase studies allow determination of the intrinsic properties of the species, unaffected by solvation, ion pairing, and other effects common to solution chemistry.

Wilkins and co-workers were first to report $M(P)^+$ (P = TPP, FTPP, and TpyP) in a trapped-ion spectrometer (*99*). Later, a similar procedure was reported by Irikura and Beauchamp (*100*). They studied the reaction of bare and ligated metal ions

with porphyrin vapor to produce metalloporphyrin cations and anions in good yield.

The authors showed that metal monocations react rapidly with gaseous neutral porphyrins to produce positively charged complexes metalloporphyrin$^+$ in such a way that H_2 is released from the central nitrogen of the H_2P molecule (Eq. 5):

$$M^+ + H_2P \rightarrow MP^+ + H_2 \quad (5)$$

The formation of anions requires the formation of cluster ions and electron transfers:

$$Ni(CO)_4 + e^- \rightarrow Ni(CO)_3^- + CO \quad (6)$$

$$Ni(CO)_3^- + nNi(CO)_4 \rightarrow\rightarrow Ni_{n+1}(CO)_m^- + (4n + 3 - m)CO \quad (7)$$

$$Ni_{n+1}(CO)_m^- + H_2P \rightarrow Ni(P)^- + [Ni_n, mCO,\ H_2] \quad (8)$$

Cases of $Fe(P)^+$, $Fe(P)^+$–(*solv*), $Fe(P)^+(H_2P)$, $Ni(P)^+$, $Ni(P)^-$, $Mn(P)^+$, $Cr(P)^+$, and $Cr(P)^-$ have been reported. When the ionization energy of the metal is larger than that of neutral porhyrin, the metal monocation may react with porphyrin by charge exchange to produce H_2P^+ ions.

Later, McGlynn *et al*. (*101*) reported an extensive study of the gas-phase reaction of octaethylporphyrin with 12 metal monocations, which were produced by laser ablation of Al, V, Cr, Fe, Ni, Nb, Mo, Hf, W, Re, Pt, and Au targets. Three different processes were suggested: charge transfer, metal-ion incorporation, and "dimerization."

In the first process, H_2P^+ is generated according to (Eq. 9):

$$M^+ + H_2P \rightarrow H_2P^+ + M \quad (9)$$

Out of 12 metal monocations studied, only Al^+ does not react via this route, which is the result of low IE of Al (IE(Al)< 6 eV, IE(H_2P) ≈6eV).

Metal incorporation proceeds according to Eq. (5) for all metal ions except Pt^+ and Au^+. Platinum and gold have very high IEs (8.96 and 9.23 eV, respectively) and charge exchange with H_2P thus proceeds much faster than ion incorporation.

"Dimerization" was observed only for M = Al, V, Cr, Fe, and Ni and proceeds according to Eq. (10):

$$MP^+ + H_2P \rightarrow (MP - H_2P)^+ \quad (10)$$

The reason for "dimerization" is not clear. None of these reactions has been studied theoretically.

C. Direct Porphyrin Metalation Under Ultra-High Vacuum Conditions

Although seemingly far removed from naturally occurring metalloporphyrins, ordered monolayers of porphyrins on inert surfaces (*102–111*) offer a unique opportunity to study the reactivity of porphyrin systems without the perturbing influences of solvation, counterions, protein environment, oxidizing atmosphere, or other environment effects. Generally, the influence of the surface on which the porphyrins are adsorbed is considerably better defined (especially in the case of a single crystal surface) than most other environment effects found in condensed-phase systems. In addition, metalloporphyrins are particularly suitable for surface functionalization on the nanoscale, which is the key to tailoring sensors, catalysts, and other devices whose functional principle is based on the interaction of an active solid surface with another (liquid or gaseous) phase. They combine a structure-forming element, the porphyrin framework, with an active site, the coordinated metal ion. Another particular advantage of these thin-film systems is that reactions such as coordination of metal atoms (*106–110*) or attachment of ligands (*103*) can be studied with surface-science techniques. The high thermal stability of many (metallo)porphyrins allows for film preparation by evaporation deposition despite the high molecular weight of the molecules (*112*). Alternatively, ordered monolayer films of metalloporphyrins can be obtained by the direct metalation of porphyrins adsorbed on an inert metal surface by bare transition-metal atoms under ultra-high vacuum (UHV) conditions (*107–109*). This approach allows the *in situ* synthesis of those metalloporphyrins that are too reactive to be synthesized in solution or not thermally stable enough for evaporation deposition.

Until recently, despite the number of the examples of the formation of cobalt(II)- and iron(II)-tetraphenylporphyrins (MTPP) (*107,108*) from the direct reaction of the bare metal atoms (Co or Fe) and adsorbed tetraphenylporphyrin molecules (2HTPP), it was only possible to speculate (*107–110*) about the reaction mechanism, since the reaction is fast at 300 K, and thus no intermediates could be observed.

The wealth of mechanistic pathways open to transition metals suggests such direct metallation reactions to be interesting candidates for mechanistic studies. However, only one theoretical study combined with experiment has been reported up to now (*113*).

As discussed in detail in Section III, in metalloporphyrins states of different spin multiplicities are close in energy in

many cases. Thus, the possibility of two-state reactivity (TSR) (*114*) in porphyrin reactions certainly exists. This concept has been used successfully to explain reactivity patterns in biological systems, usually containing iron-oxo species, and gas-phase chemistry of transition metal ions (*115*). A prerequisite for TSR is usually a high-spin ground state of the reactant and a low-lying low-spin excited state. Since the products of the direct metalation reaction have different spin states from the reactants, one would expect spin crossover to occur in the course of the reaction.

The question arises as to whether the metalation is a one-step reaction or whether one or more intermediate species exist. The complexity of the reaction (insertion of the metal atom (M), oxidation to M^{2+} and parallel reduction of hydrogen, release of H_2) makes a multistep reaction probable.

In order to obtain insight into possible reaction mechanisms, DFT calculations of the reaction of Co, Fe, and other transition metal atoms with the porphyrin molecule (2HP) were performed (*113*).

Figure 1 shows the lowest-energy reaction profile for the reaction of a bare Co atom with 2HP at different levels of theory. The first stage of the reaction is the barrierless formation of the novel 2H–metallaporphyrin complex **1** (denoted the *initial complex* in the following). This reaction is found to be exothermic with respect to the ground-state Co atom and 2HP at infinite separation by −46.3 and −52.2 kcal mol^{-1} at the B3LYP/6-31G(d,p) +LANL2DZ level for the high- (HS, spin $^3/_2$) and low-spin (LS, spin ½) states, respectively. The reaction is even more exothermic at two other levels of theory {B3LYP/6-31G(d) and B3LYP*/6-31G (d)}. However, the separation between the ^{4}Co and ^{2}Co states becomes somewhat too large (up to 40 kcal mol^{-1}, Fig. 1). The quartet HS and doublet LS states, ^{4}**1** and ^{2}**1**, have similar geometries with a distorted porphyrin core and differ in energy by only 0.1 kcal mol^{-1} at both B3LYP/6-31G(d,p)+LANL2DZ and B3LYP/6-31G(d) levels. At the B3LYP*/6-31G(d) level, ^{2}**1** was found to be more stable than ^{4}**1** by 10.2 kcal mol^{-1}. Therefore, a ground-state multiplicity cannot be assigned with certainty from the results of these calculations.

The geometry of this initial complex **1** can be described in terms of a "sitting-atop" complex (SAT) (Fig. 2), the formation of which has been proposed for a variety of reactions between porphyrins and metal ions in solution (See Section IV.A) (*92*).

The reaction can proceed from the initial complex **1** by two pathways. ^{2}**1** and ^{4}**1** form intermediates ^{2}**2** and ^{4}**2** via the late transition states ^{2}**TS1** and ^{4}**TS1**, which describe a hydrogen-atom transfer from the nitrogen to the metal atom. We were unable to

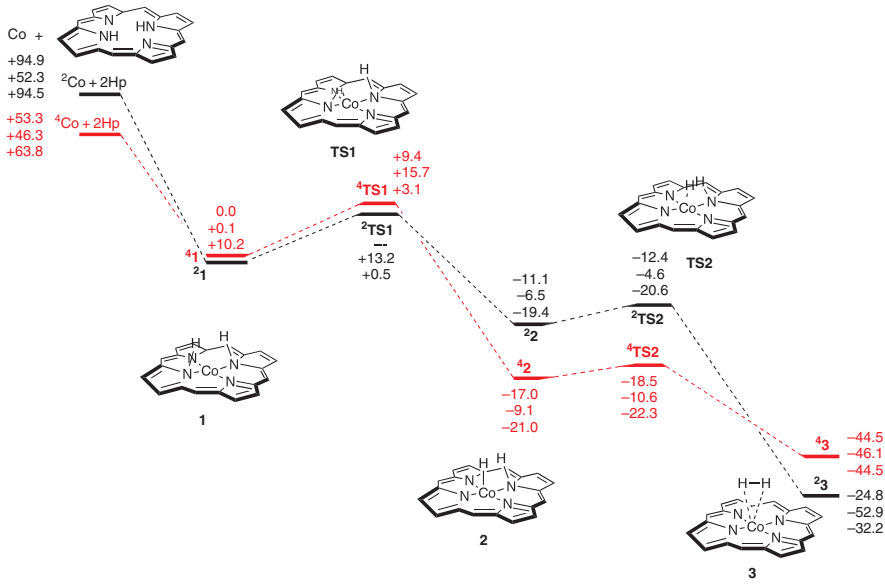

FIG. 1. Schematic energy profile for Co atom insertion into 2HP {ΔE +ZPE in kcal mol^{-1} at B3LYP/6–31G(d) (first entry), B3LYP/6–31G(d,p) +LANL2DZ (second entry), and B3LYP*/6–31G(d) (third entry)} (*113*).

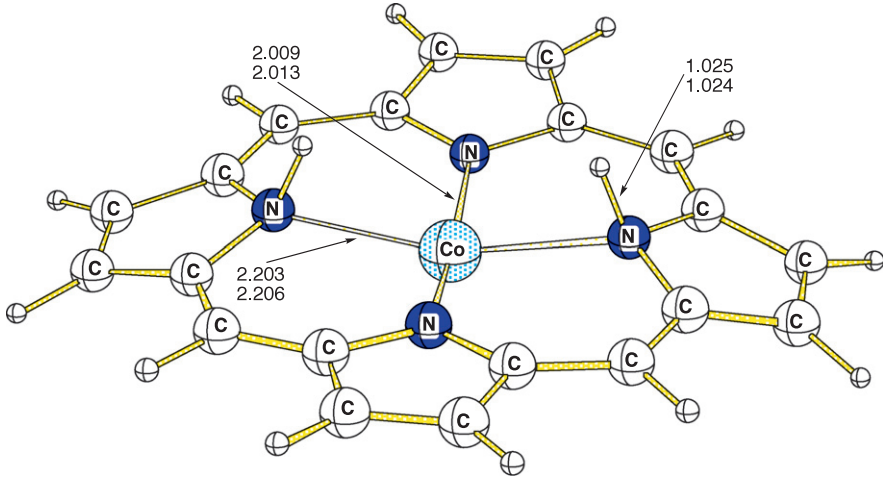

FIG. 2. Optimized geometries (B3LYP/6–31G(d,p)+LANL2DZ) of the initial complexes ^{2}**1** (first entry) and ^{4}**1** (second entry). Bond lengths are in Å (*113*).

find the LS transition state ^{2}**TS1** for this rearrangement at the B3LYP/6-31G(d) level, despite many attempts. However, the computed barrier for the high-spin reaction via transition state ^{4}**TS1** was found to be 9.4 kcal mol^{-1}. The computed barriers at the B3LYP/6-31G(d,p)+LANL2DZ level are 13.2 and 15.7 kcal mol^{-1} for high and low spins, respectively. The energy difference between the two transition states is 1.5 kcal mol^{-1}, with LS ^{2}**TS1** being the more stable. Similar trends in relative stability, but far lower barriers were found at the B3LYP*/6–31G(d) level (barriers for the rearrangement are 3.1 and 0.5 kcal mol^{-1} for high and low spins, respectively, so that LS transition state ^{2}**TS1** is 2.6 kcal mol^{-1} more stable than ^{4}**TS1**). However, the energy difference is once more too small for us to be able to assign a ground-state multiplicity for the transition state.

The formation of intermediate **2** is exothermic for both the HS and LS pathways. However, the computed values of ΔE depend on the choice of functional and basis set (Fig. 1). Nevertheless, the high-spin state ^{4}**2** was found to be somewhat more stable than ^{2}**2**.

The next reaction step is the very exothermic (up to 53 kcal mol^{-1}) formation of the CoP$\cdots$H$_2$ complex **3** via the transition state ^{4}**TS2** (high-spin pathway) or via the transition state ^{2}**TS2** (low spin). Both transition states ^{4}**TS2** and ^{2}**TS2** occur early and describe synchronous hydrogen abstraction from the pyrrolic nitrogen and formation of H$_2$. The reaction barrier for this process is calculated to be only 1.9 kcal mol^{-1} for the low-spin pathway (B3LYP/6-31G(d,p)+LANL2DZ) and is virtually absent at the B3LYP/6-31G(d) and B3LYP*/6-31G(d) levels of theory (Fig. 1).

The final complex **3** can be described as Co(II)P with a loosely bound H$_2$ molecule. Thus, one would expect **3** to have properties similar to Co(II)P. The results obtained at the B3LYP/6–31G(d,p) +LANL2DZ level predict **3** to have a doublet ground state, whereas calculations with the B3LYP and B3LYP* functionals with the 6–31G(d) basis set predict it to be high spin. The difference between spin states, however, is about 6 kcal mol^{-1} at the B3LYP/6–31G(d,p)+LANL2DZ level and much larger (ca. 12–20 kcal mol^{-1}) at the other two levels. Earlier calculations of Co(II)P identified LS as the ground state and HS was found to lie 16.9 kcal mol^{-1} above the ground state (*116*).

Thus, the overall reaction starting from the high-spin state for the Co atom and ending with the formation of Co(II)P can presumably be described as a two-state reactivity process.

The situation described above for the reaction of Co with 2HP is reproduced with some minor changes for the corresponding reactions of Fe and Ni (*113*).

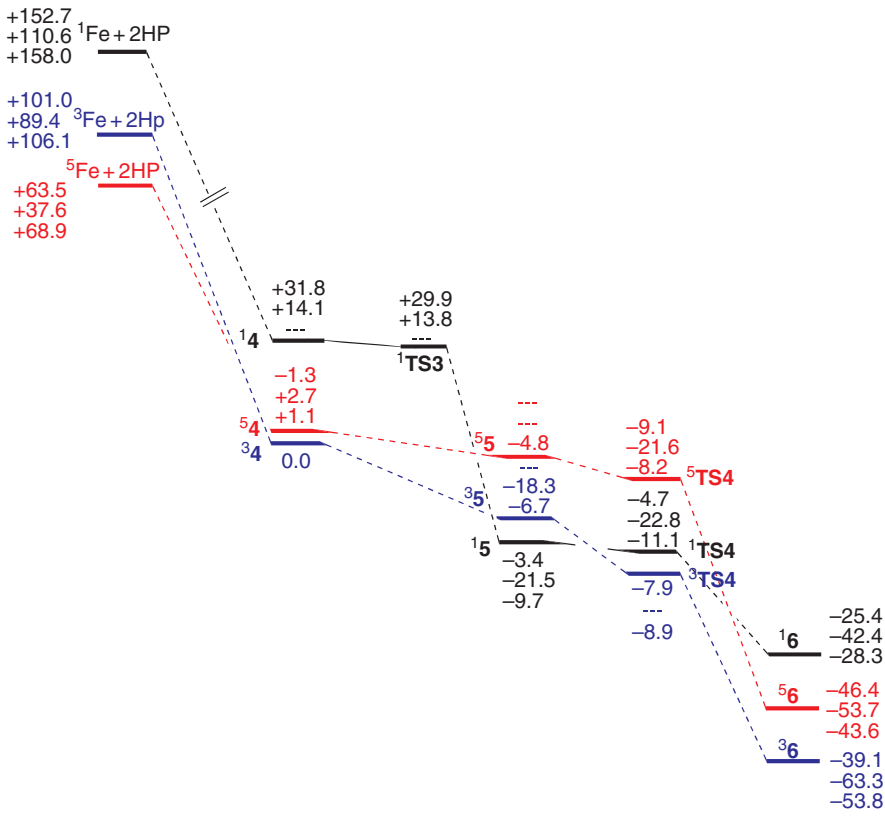

FIG. 3. Energy profile for Fe atom insertion into 2HP {ΔE+ZPE in kcal mol^{-1} at B3LYP/6–31G(d) (first entry), B3LYP/6–31G(d,p) +LANL2DZ (second entry), and B3LYP*/6–31G(d) (third entry)} (*113*).

The reaction with Fe (Fig. 3) is somewhat more complicated as it also involves participation of an intermediate-spin (IS, $S = 1$) state between the LS ($S = 0$) and the HS ($S = 2$) states in the course of the reaction. From the initial complex **4**, the reaction proceeds virtually without barriers until the final complex **6** is formed. In the cases of both ^{1}**TS3** and ^{1}**TS4**, the activation energies with respect to ^{1}**4** and ^{1}**5** were found to be 2.9 and 0.5 kcal mol^{-1}, respectively, without zero-point vibrational energy (ZPVE) correction. With ZPVE, both ^{1}**TS3** and ^{1}**TS4** become lower on the potential energy surface than the corresponding complexes ^{1}**4** and ^{1}**5** by 0.3 and 1.3 kcal mol^{-1}, respectively. In some cases, we were unable to locate transition states and local minima at all three levels of theory.

Again, similar to the situation with Co, the final complex **6** can be described as Fe(II)P$\cdots H_2$. Thus, one would expect **6** to have properties similar to the free Fe(II)P porphyrin.

The experimental value of the energy separation between triplet and the lowest quintet for FeTPP is 14.3 kcal mol^{-1} (*117*). Both B3LYP/6–31G(d,p)+LANL2DZ and B3LYP*/6–31G(d) predict ^{3}**6** to be more stable than ^{5}**6** by ca. 10 kcal mol^{-1}, whereas at the B3LYP/6–31G(d) level ^{5}**6** is more stable than ^{3}**6** by 7.3 kcal mol^{-1}.

Nevertheless, the overall reaction with the Fe atom can also be described as a two-state reactivity process, in which IS and HS states are competitive in energy and may cross.

In contrast to these reactions with the earlier transition metals, the reaction with Zn (Fig. 4) is calculated to proceed on a single singlet potential energy surface.

In the case of Zn metalation of 2HP, formation of intermediate **8** from the SAT complex **7** is associated with the activation barrier (Fig. 4, +32.6 and +34.8 kcal mol^{-1}, B3LYP/6-31G(d) and B3LYP/6–31G(d,p)+LANL2DZ, respectively). For metalation with Zn, the overall experimental activation energy was estimated to be 31 kcal mol^{-1}(*113*), which is in good agreement with the computed value.

The results obtained at the B3LYP/6–31G(d) level appear to be more reliable for the later transition metals (Zn) than those at the

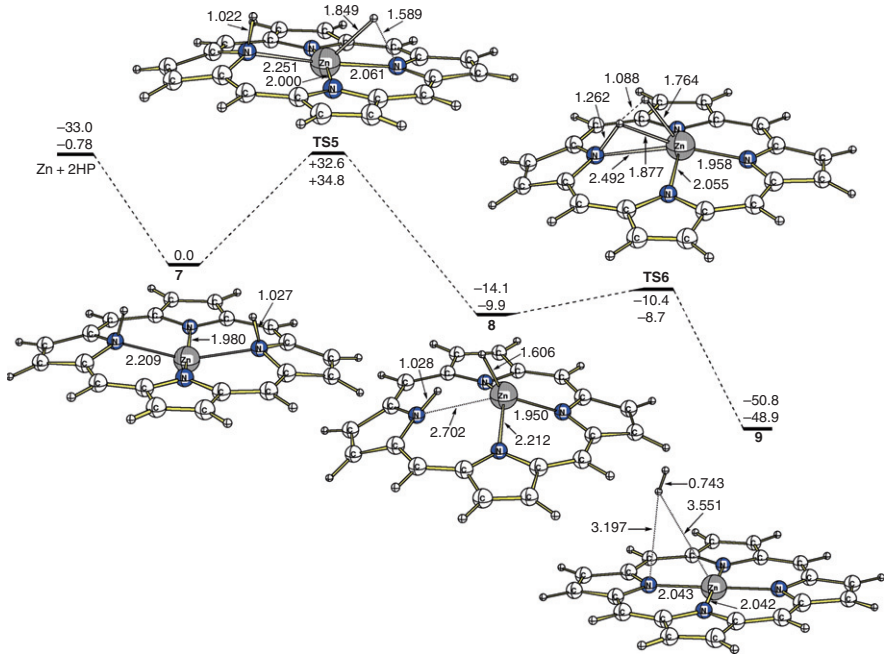

FIG. 4. Schematic energy profile for Zn atom insertion into 2HP {ΔE+ZPE in kcal mol^{-1} at B3LYP/6–31G(d) (first entry) and B3LYP/6–31G (d,p)+LANL2DZ (second entry)}. Bond lengths are in Å (*113*).

B3LYP/6–31G(d,p)+LANL2DZ level because the latter predict that the formation of the initial complex for zinc is endothermic, which disagrees with the experimental observations.

V. Binding of Small Molecules

The interaction of small molecules such as O_2, NO, and CO with hemoglobin and myoglobin play a central role in living cells and is important for the respiration and regulation processes. It is thus very important and challenging to understand and predict/reproduce binding energies of these ligands reliably by quantum-chemical calculations. Additionally, the accuracy of such calculations serves as a good benchmark for the modeling of similar bioinorganic processes.

Despite the increasing number of theoretical studies (*44,57,118–127*) on this topic, the results still remain inconsistent and somewhat puzzling.

Generally, the geometry of MP–XO complexes (X = C, N, O) can be rationalized in terms of the degeneracy of the MXO π^* orbitals (*128*). While carbonyl complexes are approximately linear (CO π^* orbital is empty), both NO and O_2 complexes are bent (the π^* orbital is singly (NO) or doubly (O_2) occupied) (see Fig. 5).

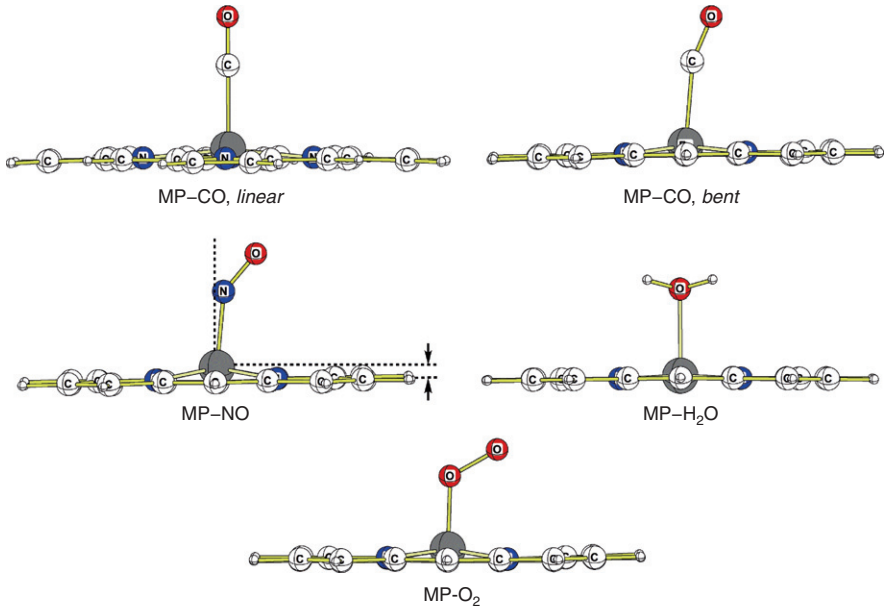

FIG. 5. Typical arrangement of CO, NO, H_2O, and O_2 units in MP–XO complexes.

An overview of the most important and recent results on MP–XO complexes follows.

A. Binding of CO to Fe(II) and Co(II) Porphyrins

Early reports on CO binding to the myoglobin led to the assumption that the CO unit in Mb–CO is bent. For example, Collman *et al*. (*129*) suggested on the basis of X-ray (*130*) and neutron (*131–135*) crystal structure data a Fe–C–O angle of 120–140°. Later, Ray *et al*. (*136*) concluded that the Fe–C–O angle must be uncertain to at least ±25°. Other (*137–139*) Mb–CO X-ray studies revealed much less CO displacement.

Now it is generally agreed that CO binding to the Fe in FeP system leads to a linear orientation of the M–C–O unit (C_{4v}, Fig. 5). In a protein matrix, the geometry of the Fe–C–O unit is somewhat distorted, but this is mainly because of the electrostatic perturbation from the distal environment (*140–142*).

There is much disagreement on the Fe–CO bond length and binding energy. The experimental value of 1.77(2) Å was observed for the six-coordinated FeTPP(Py)–CO complex (*143*). A much shorter bond length of 1.714 Å (Fe–C) was reported for five-coordinated Fe(OEP)–CO (*144*). Earlier, in a Car–Parrinello molecular dynamics study, the Fe–CO distance was found to be 1.69 Å, and a CO binding energy of 26 kcal mol^{-1} was reported (*145–147*). In other DFT studies, the reported binding energies are between +1.0 and −26.5 kcal mol^{-1} (*148*). Calculated binding energies for the six-coordinate FeP(Im)–CO system lie between +1.0 and −40.6 kcal mol^{-1} (B3LYP) (*148*). Gromacs MD simulations of CO binding to solvated myoglobin gave an activation enthalpy of 7–11 kcal mol^{-1} (*149,150*).

Experimental values of −18.1 and −19.5 kcal mol^{-1} have also been reported for a six-coordinate myoglobin complex (*151,152*).

Recently, we also have found that optimized geometries and binding energies depend very strongly on the functional and basis set used (*53*). For example, the Fe–CO bond length varies from 1.676 Å {OLYP/6-31G(d)} to 1.746 Å {B3LYP/6–311+G(d,p)} (Table II). CO binding energies were calculated to be in the range of −4.4 kcal mol^{-1} (B3LYP/6–311+G(d,p) to −26.6 (BLYP) kcal mol^{-1} (Table II). We also noted that while the MP2/cc–pVDZ computed geometry is close to those obtained with DFT functionals, the CO binding energy was found to be +4 kcal mol^{-1} (Table II).

An equivalent linear structure of CoP–CO was found to be a second-order saddle point (N_i = 2) when the 6-31G(d) basis set

TABLE II

BINDING ENERGY (ΔE+ ZPE, kcal mol^{-1}) AND KEY STRUCTURAL PARAMETERS (Fe–CO AND C–O BOND LENGTHS (Å) AND Fe–C–O ANGLE, °) OF FeP–CO UNIT (*53*)

Method	E_{bind}, kcal mol^{-1}	Fe–C, Å	C–O, Å	<Fe–C–O, °
BLYP/6–31G(d)	–26.6	1.699	1.176	180.0
BLYP/6–311+G(d,p)	–22.7	1.723	1.167	180.0
B3LYP/6–31G(d)	–6.8	1.717	1.154	180.0
B3LYP/6–311+G(d,p)	–4.4	1.746	1.144	180.0
B3LYP/GEN	–6.7	1.736	1.151	180.0
B3PW91/6–31G(d)	–9.6	1.699	1.154	180.0
B3PW91/6–311+G(d,p)	–8.4	1.724	1.144	180.0
OLYP/6–31G(d)	–23.8	1.676	1.173	180.0
OLYP/6–311+G(d,p)	–20.3	1.694	1.165	180.0
M06L/6–31G(d)	–29.1/ (–26.7)[a]	1.697	1.162	180.0
M06L/6–311+G(d,p)	–25.1/ (–22.3)[a]	1.719	1.154	180.0
MP2/6–31G(d)	1.6	1.645	1.168	180.0
MP2/cc–pVDZ	4.0	1.748	1.155	180.0
B3LYP (*148*) (BSI/BSII)[b]	0.7 (–2.8)	–	–	–
OLYP (*148*) (BSI/BSII)[b]	–11.4 (–16.7)	–	–	–
CASPT2 (*148*)	–11.4 (–16.0)	–	–	–
Car-Parinello MD (*145–147*)	–26	1.69	1.17	180.0
Exp FeTPP(Py)–CO (*143*)	–	1.77(2)	1.12(2)	179(2)
Exp (Fe(OEP)–CO) (*144*)	–	1.7140	1.1463	177.2
Exp (*151,152*)	–18.1…–19.5	–	–	–

[a] With respect to ^{5}FeP.
[b] Basis sets I and II.

was used (*53*). Re-optimization of this complex without symmetry restrictions leads to the energetically almost equivalent complex with a bent Co–CO moiety (Fig. 5 and Table III). Optimization of C_{4v}–linear complexes with the 6-311+G(d,p) basis set gives minima and optimization of bent starting geometries results in linear structures. The same preference for a bent CoP–CO structure is found with MP2.

The reaction of cobalt(II) porphyrins with CO has been studied by Wayland *et al*. (*153–156*) in some detail by electron paramagnetic resonance (EPR) in frozen solutions. They conclude that Co(II)TPP forms an axially symmetric weakly bonded 1:1 adduct with CO (*153–156*). To the best of our knowledge, there are no other studies on CoP–CO complexes, neither experimental nor theoretical.

As in the case with FeP–CO, the calculated CO binding energy, Co–CO and C–O bond lengths vary significantly. CoP–CO bond lengths vary from 1.838 Å (OLYP) to 1.949 Å (B3LYP) using the 6–31G(d) basis set. An even longer Co–CO bond length was found at the B3LYP/6–31G(d,p)+LANL2DZ and MP2/6–31G(d) levels

TABLE III

NUMBER OF IMAGINARY FREQUENCIES (N_i), BINDING ENERGY (ΔE+ ZPE, kcal mol^{-1}), AND KEY STRUCTURAL PARAMETERS (Co–CO, AND C–O BOND LENGTHS (Å) AND M–C–O ANGLE, °) OF CoP–CO UNIT (*53*)

Method	N_i	E_{bind}, kcal mol^{-1}	Co–C, Å	C–O, Å	<Co–C–O, °
BLYP/6–31G(d), C_{4v}	2	–19.6	1.852	1.164	180.0
BLYP/6–31G(d)	0	–19.6	1.862	1.166	158.1
BLYP/6–311+G(d,p)C_{4v}	0	–10.1	1.907	1.153	180.0
BLYP/6–311+G(d,p)	0	–10.1	1.905	1.153	179.9
B3LYP/6–31G(d) C_{4v}	2	–9.1	1.949	1.142	180.0
B3LYP/6–31G(d)	0	–9.2	1.959	1.143	158.4
B3LYP/6–31G(d,p)+LANL2DZ C_{4v}	2	–4.2	2.231	1.136	180.0
B3LYP/6–31G(d,p)+LANL2DZ	0	–4.2	2.245	1.136	167.4
B3LYP/6–311+G(d,p) C_{4v}	0	–2.7	2.054	1.131	180.0
B3PW91/6–31G(d) C_{4v}	2	–9.9	1.921	1.141	180.0
B3PW91/6–31G(d)	0	–9.8	1.917	1.141	180.0
B3PW91/6–311+G(d,p) C_{4v}	0	–4.5	1.999	1.131	180.0
B3PW91/6–311+G(d,p)	0	–4.5	2.001	1.131	179.9
OLYP/6–31G(d)C_{4v}	2	–14.3	1.838	1.161	180.0
OLYP/6–31G(d)	0	–14.3	1.844	1.163	159.6
OLYP/6–311+G(d,p)C_{4v}	0	–6.4	1.883	1.152	180.0
M06L/6–31G(d) C_{4v}	2	–18.1	1.894	1.150	180.0
M06L/6–31G(d)	0	–18.0	1.904	1.153	152.9
M06L/6–311+G(d,p) C_{4v}	0	–11.3	1.968	1.140	180.0
M06L/6–311+G(d,p)	0	–11.3	1.975	1.141	161.7
MP2/6–31G(d) C_{4v}	3	–11.6	2.193	1.148	180.0
MP2/6–31G(d)	0	–12.4	2.200	1.150	149.1
MP2/cc–pVDZ C_{4v}	0	–	2.308	1.145	180.0

(up to 2.245 Å, Table III). Using a larger basis set {6-311+G(d,p)} leads to a lengthening of the M-CO bond (by 0.05 Å, relative to the 6–31G(d) results) and to shortening of the C–O bond (Table III).

The CO binding energy to CoP varies from –9.2 kcal mol^{-1} (B3LYP) to −19.6 kcal mol^{-1} (BLYP) with the 6–31G(d) basis set, and from −2.7 (B3LYP) to −11.3 (M06L) with the 6–311+G (d,p) basis set. The MP2 calculated binding energy was found to be −12.4 kcal mol^{-1}.

In the complete absence of experimental data on the geometries of CoP–CO, it is difficult to validate the results obtained with different DFT functionals. However, the EPR spectra suggest linearity of Co-C-O unit, so that this system should be described at least with a triple-ξ quality basis set.

For coordination of CO to FeP and CoP, the interaction can be rationalized in terms of a "traditional" σ–donation/π–back-donation

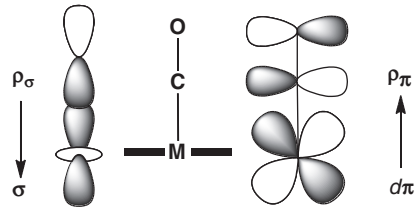

FIG. 6. Schematic representation of σ– (left) and π–bonding (right) interactions of CO with metals.

mechanism. This simple model considers the metal–CO bonding to consist of two main components (Fig. 6):

1. an σ–bonding interaction due to overlap of the CO HOMO (5σ) with empty metal orbitals of the correct symmetry—this leads to electron density transfer from the CO molecule to the metal center
2. π-bonds formed by back-donation from the FeP d_π and p_π orbitals to the π^*-antibonding orbitals of CO.

The major contributions arise from combination of $3d_{xz}$ (0.35e) with the $2p_x$ orbitals of the carbon (0.45e) and oxygen (0.65e) atoms and $3d_{yz}$ (0.35e) with the $2p_y$ orbitals of the carbon (0.45e) and oxygen (0.65e) atoms. The Mulliken charges are +0.47e for Fe and +0.17e for the CO moiety.

Compared to FeP–CO $\{d^6$–CO$\pi^{*0}\}$, the CoP–CO complex has an additional single unpaired electron $\{d^7$–CO$\pi^{*0}\}$ in the $3d_z{}^2$ orbital (0.5 e), which is used in σ bonding with CO (C 2*s*, 0.44e) (Fig. 7).

The π-back-donation from the CoP d_π orbitals is much less pronounced than for FeP and is mainly determined by a combination of four orbitals: $3d_{xz}$ (–0.98e) + C $2p_x$ (0.1e); $3d_{yz}$ (0.98e) + C $2p_y$ (–0.1e); $3d_{xz}$ (–0.1e) + C $2p_x$ (–0.4e) + O $2p_x$ (–0.8e); and $3d_{yz}$ (0.1e) + C $2p_y$ (0.4e) + O $2p_y$ (0.8e) (Fig. 7). The charge on the Co atom was found to be 0.68e and on the CO moiety −0.17e. Previously (*155,156*), CO was estimated to carry 0.13e. It should also be noted that there is a much higher contribution of the *d*-orbitals from the second *d*-shell.

B. Fe(II)P and Co(II)P Complexes with NO

Nitric oxide (NO) has profound biological significance and was named "Molecule of the Year" by *Science* magazine in 1992 (*157*). This also has resulted in the appearance of an increasing number of experimental and theoretical studies on metal–NO complexes (*158–161*).

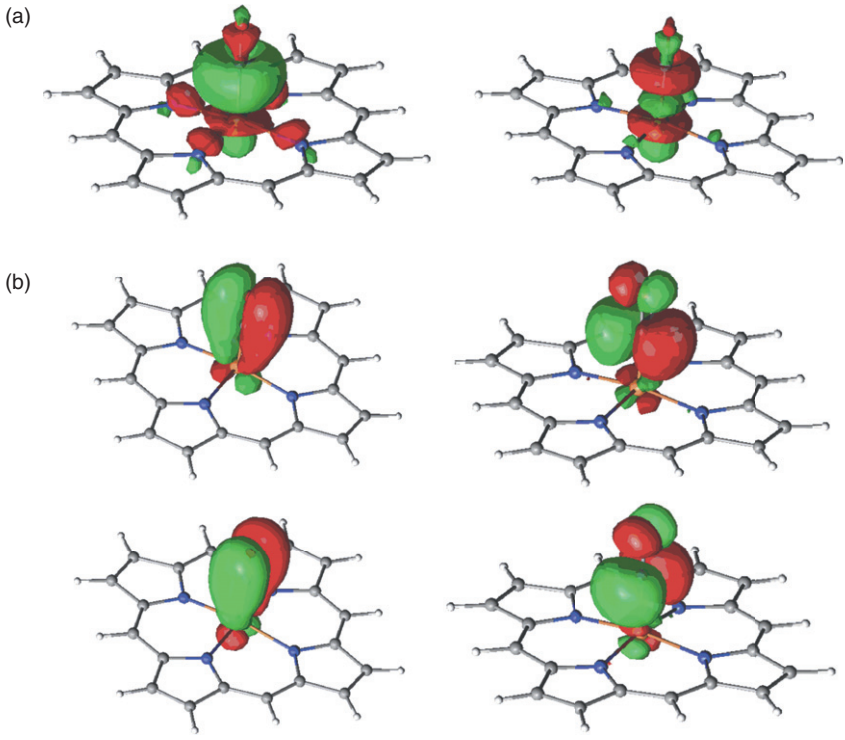

FIG. 7. Bonding (left) and antibonding (right) orbitals for the FeP–CO σ bond (a) and FeP–CO π bond (b).

The usual notation for the nitrosylmetalloporohyrins is $\{MNO\}^n$ after Enemark and Feltham (*162*). Thus, $\{FeNO\}^7$ stands for Fe(II)P–NO (six electrons from the 3*d* orbitals of Fe(II) and one electron from NO) and $\{CoNO\}^8$—for CoP–NO complexes. These two complexes are characterized by different M–N–O angles of approximately 140° and 120°, respectively.

In the case of FeP, NO is attached in the so-called "end-on" configuration, and the complex has C_s symmetry. The Fe atom is displaced (between 0.2 and 0.3 Å) with respect to the N_4 plane, and the Fe-N bond is displaced 6°–8° from what would be the C_4 symmetry axis in the linear structure (Fig. 5).

The NO tilting is believed to have its origin in the specific $d_z{}^2$ (Fe) and π^* (NO) orbital interactions (Fig. 8): the $d_z{}^2$ (Fe)–π^*(NO) interaction involves both lobes of the d_z^2 orbital and is facilitated by tilting.

The experimental values (*164*) based on X-ray data for FeTPP–NO are 1.71(1) Å and 149(1)°, respectively. The computed Fe–NO

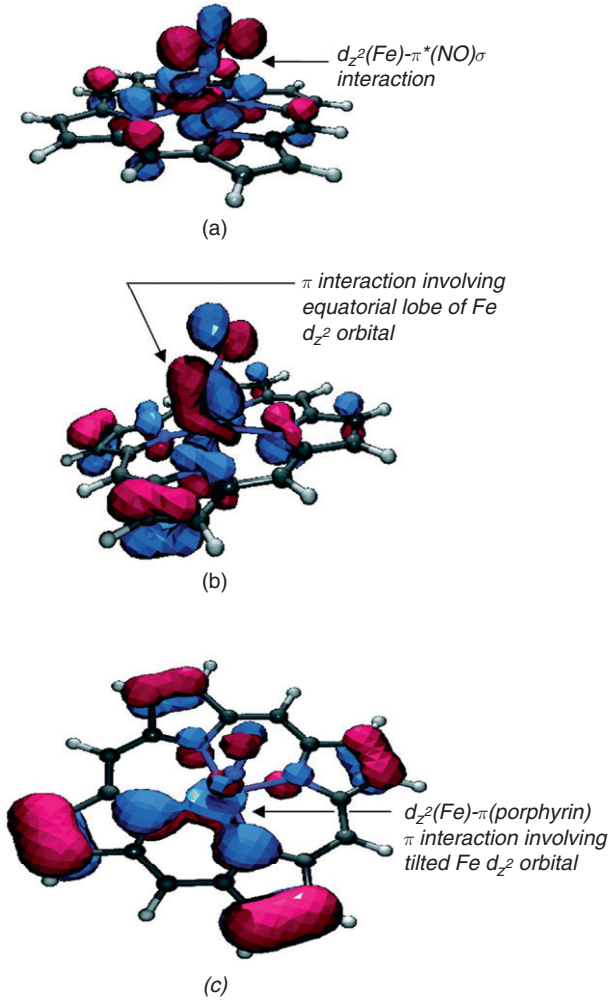

FIG. 8. Some MOs relevant to NO tilting (from (*163*)).

bond length was found to lie between 1.69 Å (OLYP) and 1.81 Å (B3LYP/6–311+G(d,p)); the Fe-N-O angle between 139.6° and 146.2° (Table IV). These values are reproduced well by BLYP/6–311+G(d,p), OLYP/6–311+G(d,p), and M06L/6–31G(d). On the other hand, MP2 gives in a very long Fe–NO bond length (2.25 Å) and predicts a Fe–N–O angle of only 124.5°. Based on this and the computed NO binding energy, the FeP–NO complex can be described as being unbound at the MP2 level. Binding energies obtained with DFT range from -6.5 kcal mol^{-1} (B3LYP/6–31G(d,p) +LANL2DZ) to -41.4 (M06L). Values reported in previous

TABLE IV

BINDING ENERGY (ΔE+ ZPE, kcal mol^{-1}) AND KEY STRUCTURAL PARAMETERS (Fe–NO AND N–O BOND LENGTHS (Å) AND Fe–N–O ANGLE, °) OF Fe–NO SYSTEM (*53*)

	E_{bind}, Kcal mol^{-1}	Fe–NO, Å	N–O, Å	<Fe–N–O, °
BLYP/6–31G(d)	–39.8	1.703	1.198	143.2
BLYP/6–311+G(d,p)	–35.1	1.719	1.187	144.6
B3LYP/6–31G(d,p) +LANL2DZ	–6.5	1.731	1.169	139.9
B3LYP/6–31G(d)	–14.4	1.796	1.182	139.6
B3LYP/6–311+G(d,p)	–10.6	1.809	1.169	142.2
B3PW91/6–311+G(d,p)	–13.7	1.782	1.164	144.4
OLYP/6–31G(d)	–36.3	1.688	1.185	144.8
OLYP/6–311+G(d,p)	–32.0	1.701	1.175	146.2
M06L/6–31G(d)	–41.4/ (–39.0)[a]	1.707	1.181	140.6
M06L/6–311+G(d,p)	–37.4/ (–34.6)[a]	1.726	1.169	141.6
MP2/cc–pVDZ	7.59	2.249	1.135	124.5
tape-FeTPP (*165,166*)	–39.6			148
PW91 (*163*)		1.692	1.184	143.75
Exp (*151,152,167*)	–26.6, –28.9, –22.8			
Exp (*164*)		1.71(1)	1.12(1)	149(1)

[a] With respect to ^{5}FeP.

theoretical studies range from -0.9 to -38 kcal mol^{-1} for five-coordinated complexes (*147,148*) and from +5.3 to –43 kcal mol^{-1} for six-coordinated complexes (*148*). Experimental binding energies are -26.6 and -28.9 kcal mol^{-1} for five-coordinated complexes (*151,152*), -39.6 kcal mol^{-1} (tape-FeTPP–NO) (*165,166*), and -22.8 kcal mol^{-1} (for a six-coordinated complex) (*167*).

Depending on the computational or experimental methods and models used, various resonance structures have been proposed for {FeNO}^{7} complexes, such as Fe(II)–NO^0, Fe(III)–NO$^-$ (metal-to-ligand charge transfer) or Fe(I)–NO$^+$ (ligand-to-metal charge transfer). It has been pointed out previously that DFT-computed spin densities of {FeNO}^{7} complexes are extremely sensitive to the choice of functional. The reported values are summarized in Table V.

According to CASSCF (and nonhybrid functionals), the spin population on the Fe atom is close to 1.0, whereas the NO moiety does not carry a significant amount of spin density. Based on that, the Fe(I)–NO$^+$ electronic structure was assigned to the FeP–NO complex. Earlier, (*147*) based on Car–Parinello MD simulations, the Fe(III)–NO$^-$ electronic structure was suggested for the FeP–NO complex. Additional complications came from the comparison of N–O bond length: while the experimentally measured bond

TABLE V

REPORTED SPIN DENSITIES FOR FeP–NO COMPLEX

Method	Spin density on the Fe atom	Spin density on the NO moiety
PBE0 (*148*)	0.31	0.71
B3LYP (*148*)	0.49	0.53
BP86 (*148*)	0.97	0.05
OLYP (*148*)	1.19	–0.15
CASSCF (*148*)	1.02	–0.01
CASSCF	0.96	0.03
CASSCF (*53*)	1.06	–0.08

length is 1.12 Å, all calculations predict value of 1.16–1.2 Å (Table IV). This has led to the alternative explanation that in FeTPP–NO the bond is of the Fe(II)–NO^+ type.

Very recent sophisticated CASSCF/CASPT2 calculations (*61*) shed some light on this problem. Radoń *et al*. (*61*) performed an analysis of the number of configurations and calculated the weight of the given resonance structures. Consequently, FeP–NO can best be characterized as mixture of Fe(II)–NO^0 and Fe(III)–NO^- resonance structures. The Fe(I)–NO^+ electronic structure participates only with a few %.

Only few (*63,148,163*) theoretical studies have been reported so far on nitrosyl–Co(II)P. In contrast to FeP–NO, the direction of the Co–N in CoP–NO bond is nearly perpendicular to the porphyrin plane (we found a tilt of the Co–N bond of only 0.4°) and the Co atom is displaced from the N_4–plane by only 0.1–0.2 Å. These findings are in good agreement with X-ray data on Co(OEP)–NO (*168*) and CoT(*p*-OCH_3)PP–NO (Table VI).

Once again, the geometries and NO binding energy depend strongly on the method used. The Co-NO bond length was found to lie between 1.77 Å (B3PW91) and 1.88 Å (MP2/6-31G(d)) and the Co–N–O angle between 116.2° and 123.8° (Table VI). Zhu *et al*. (*169*) estimated the homolytic Co^{II}–NO bond dissociation energy to be 20.8–24.6 kcal mol^{-1} in benzonitrile solution. Our computed NO binding energy ranges from −2.2 (B3LYP/6–31G(d, p)+LANL2DZ) to −36.7 kcal mol^{-1} (BLYP) (see Table VI). Both the OLYP/6-311+G(d,p) and M06L/6-311+G(d,p) methods agree well with the experimental values. Interestingly enough, in the case of CoP–NO, MP2/6–31G(d) performs reasonably well in describing geometry and binding energy in comparison to various DFT functionals (Table VI). However, it still underestimates the binding energy.

TABLE VI

BINDING ENERGY (ΔE+ ZPE, kcal mol^{-1}) AND KEY STRUCTURAL PARAMETERS (Co–NO AND N–O BOND LENGTHS (Å) AND Co–N–O ANGLE, °) OF THE Co–NO SYSTEM

	E_{bind}, Kcal mol^{-1}	Co–NO, Å	N–O, Å	<Co–N–O, °
BLYP/6–31G(d)	–36.7	1.795	1.195	123.2
BLYP/6–311+G(d,p)	–28.3	1.834	1.182	122.7
B3LYP/6–31G(d,p) +LANL2DZ	–2.2	1.839	1.169	118.7
B3LYP/6–31G(d)	–11.5	1.790	1.175	120.5
B3LYP/6–311+G(d,p)	–3.6	1.828	1.161	120.2
B3PW91/6–31G(d)	–12.9	1.773	1.171	120.7
B3PW91/6–311+G(d,p)	–5.1	1.809	1.157	120.3
OLYP/6–31G(d)	–30.3	1.780	1.183	123.8
OLYP/6–311+G(d,p)	–23.6	1.814	1.172	123.3
M06L/6–31G(d)	–30.8	1.786	1.181	120.7
M06L/6–311+G(d,p)	–25.5	1.822	1.167	120.4
MP2/6–31G(d)	–13.8	1.878	1.137	116.2
PW91 (*163*)		1.817	1.178	122.33
tape-CoTPP–NO (*165,166*)	–39.6			123
Exp (*169*)	*ca* –21 to –25			
Co(OEP)–NO (*168*)		1.8444	1.1642	122.7
CoT(p-OCH_3)PP–NO		1.855(6)	1.159(8)	120.6

C. Fe(II)P AND Co(II)P COMPLEXES WITH O_2

One of the simplest biological reactions involving molecular oxygen is the binding of O_2 to the Fe(II) center in a heme group. Taking into account that molecular oxygen is a triplet ($^1O_2$ is ca. 22 kcal mol^{-1} higher in energy than $^3O_2$) with two unpaired electrons and Fe(II) in heme group (deoxyheme) has four unpaired electrons (it is a quintet) the resulting Fe(II)–O_2 adduct should have either a triplet or a septet state. However, experimentally, this complex is a single state, thus making this reaction to be formally spin-forbidden.

Normally, the Fe–O_2 unit is bent and has the so-called asymmetric end-on configuration (Fig. 5, Scheme 4). However, in some cases for FeP-based systems, the symmetric side-on configuration has been suggested (Scheme 4). This configuration has been trapped (*170*) at low temperature upon photoexcitation of FeTPP–O_2. Additionally, Mb–O_2 adduct at low temperatures also shows a nonphotolyzable fraction, which has been suggested to arise from isomerization to the side-on structure (*171,172*).

De Angelis *et al*. (*173*) reported Fe–O and O–O bond lengths of 1.91 Å and 1.38 Å, respectively, and Fe–O–O angle of 69.8° for the side-on FeP(Im)–O_2 complex. This complex appears to be only

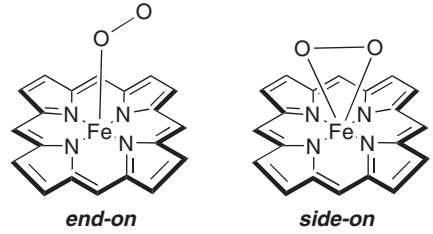

SCHEME 4. End-on and side-on complexes of $FeP–O_2$.

10.7 kcal mol^{-1} higher than end-on isomer. In the theoretical work of Tsuda *et al*. (*174*) $FeP–O_2$ side-on complex is 14.4 kcal mol^{-1} higher than $FeP–O_2$ end-on complex. Computed (B3PW91/LANL2DZ) Fe–O and O–O bond lengths and Fe–O–O angle are 1.904 Å, 1.416 Å, and 68.18°, respectively.

The lowest energy state of end-on $FeP–O_2$ is open-shell singlet; the closed-shell singlet with the same occupation numbers is 1.2 kcal mol^{-1} higher in energy (*175*). This is in agreement with the experimental observation that the O_2 adduct is silent in EPR experiments (*176*).

The main discussion is about the nature of Fe–O bond. Pauling suggested a closed-shell $^1FeP^{II}–^1O_2$ description with both moieties in the singlet state (*177–179*). The second model, introduced by Weiss (*180*), describes an electron transfer from iron to O_2 upon binding, i.e., $^2FeP^{III}–^2O_2^-$ structure. Finally, McClure (*181*) and later Goddard and Olafson (*182,183*) suggested an ozone model, $^3FeP^{II}–^3O_2$. Mossbauer spectroscopy indicates unpaired electron density on Fe–O moiety, thus giving support to the Weiss model (*184*). A later experiment suggests a ground state with mixed ferrous (Pauling model) and ferric (Weiss model) character with the ratio of 0.357:0.643 (*185*).

Many theoretical calculations on the $FeP–O_2$ electronic structure support various descriptions: HF calculations support either Pauling model (*29*) or the Weiss model (*186*). The Weiss model is also supported by molecular mechanics (*32*) and semi-empirical INDO (*187*) calculations. DFT calculations either fully support Weiss description (*127,147*) or predict a 75–80% weight of the Weiss configuration (*57,188*), with the Pauling configuration providing the remaining 20–25% (*147,189*). Additionally, strong basis set and functional dependence on electron transfer (and thus on $FeP–O_2$ configuration) were found by Radon *et al*. (*60*). Early CASPT2 calculations predict multi-configuration state consisting of a closed-shell configuration ($^1FeP^{II}–^1O_2$) 50% and $FeP^{III}–^2O_2^-$ (50%). (*121,184*).

TABLE VII

BINDING ENERGY (ΔE+ ZPE, kcal mol^{-1}) AND KEY STRUCTURAL PARAMETERS (Fe–O_2 AND O–O BOND LENGTHS (Å) AND Fe–O–O ANGLE, °) OF THE Fe–O_2 (*END-ON*) SYSTEM

Structure (method)	E_{bind}, kcal mol^{-1}	Fe–O, Å	Fe–O–O, °	O–O, Å
^{1}FeP–O_2 BP86 (*147*)	–9	1.74	123	1.28
^{1}FeP(Im)–O_2 LSD (*44*)	–15	1.77	121	1.30
^{1}FeP(Im)–O_2 PBE (*190*)		1.78	121.0	1.28
^{1}FeP(Im)–O_2 … His PBE (*190*)		1.77	118.8–119.8	1.30
^{1}FeP(Im)–O_2 B3LYP/6 –31G(d) (*191*)		1.85	118.1	1.29
^{3}FeP(Im)–O_2 B3LYP/6 –31G(d) (*191*)	8.4 kcal mol^{-1} higher than ^{1}FeP(Im)–O_2	2.91	119.7	1.22
^{1}FeP(Im)–O_2 (BP86/SVP) (*118*)	CASPT2 (*16,14*)–14.9	1.82	120.6	1.27
^{1}FeP–O_2 (CASPT2) (*60*)	–9.9			
^{1}FeP(Im)–O_2 (CASPT2) (*60*)	–9.9			
^{1}FeP–O_2 (UB3LYP/LANL2DZ (6–31G(d)) (*192*)	–7.8	2.252	121.5	1.272
^{1}FeP(SH)–O_2 (*192*)	–17.87	1.940	118.2	1.356
^{1}FeP(Im)–O_2 (*192*)	–8.37	1.891	117.9	1.345
Tape-FeP–O_2 pw-DFT (*193*)	–12.8	1.78	122	1.28
Exp. FeMb–O_2 (*194*)	–12 ··· –18 (*195*)	1.81	122	1.24

All results on the FeP–O_2 systems are collected in the Table VII.

It was observed early that replacement of iron by cobalt in hemoglobin results in the protein (CoMb) that binds oxygen reversibly (*196,197*). In contrast to the native iron system, little data are available on cobalt-substituted heme proteins. The only high-resolution crystal structure of $CoMbO_2$ was reported by Brucker *et al*. in 1996 (*198*). In particular, authors showed that the CoO_2 moiety exhibits the same end-on type of structure as the FeO_2 in HbO_2. However, the Co–O bond (2.01 Å) was found to be longer than the Fe–O bond (1.86 Å) and the Co–O–O angle is smaller (109° ± 5°) than in Fe–O–O (119°) (Fig. 5).

Early EPR measurements on a nonheme Co–O_2 complex concluded that the O_2 ligand jumps between two bent structures (*199*). Later, this was confirmed for $CoHbO_2$ (*200*).

The theoretical work on Co–O_2 complexes resembling $CoMbO_2$ structure is also limited to only a few papers.

Degtyarenko *et al*. (*190,201*) reported static and dynamic calculations on CoP(Im)–O_2 complexes. The authors found that the rotation of the oxygen around the metal–oxygen bond is six times faster for the cobalt analog than for its native counterpart and is practically barrierless (0.5 kcal mol^{-1}). This suggests that the oxygen ligand in cobalt heme analogs will always be more flexible.

Shi and Zhang studied dioxygen binding to a variety of transitional metal macrocycles and reported an O_2 binding energy to the CoP and CoTPP of –10.8 and –9.9 kcal mol^{-1}, respectively (*202*). Only the end-on structure was found to be stable.

Tsuda and Kasai studied the interaction of O_2 (*203*) with metalloporphyrins and the effect of imidazole on it (*204*) and concluded that in the O_2 adducts, an imidazole ligand induces a strong electron donation to O_2, resulting in the weak O–O bond.

Steiger *et al*. (*205*) suggested the Co^{III}–O_2^- structure based on femtosecond dynamics. Molecular orbital diagrams (*24,25*) and earlier LCAO-MO-SCF calculations (*29*) support this assignment. No *ab initio* or DFT results on the electronic structure of CoP–O_2 have been reported so far.

All results on the CoP–O_2 systems are collated in Table VIII. Once again, the geometries and binding energy depend strongly on the method and model used.

TABLE VIII

BINDING ENERGY (ΔE+ ZPE, KCAL MOL^{-1}) AND KEY STRUCTURAL PARAMETERS (CO–O_2 AND O–O BOND LENGTHS (Å) AND CO–O–O ANGLE, °) OF THE CO–O_2 SYSTEM

Structure (method)	E_{bind}, kcal mol^{-1}	Co–O, Å	Co–O–O, °	O–O, Å
^{2}CoP–O_2 (BP/DNP) (*202*)	–10.8	1.876	–	1.264
^{2}CoP–O_2 (B3PW91) (*204*)	–13.77	2.358	–	1.263
^{4}CoP–O_2 (B3PW91) (*204*)	–2.49	2.510	–	1.266
^{6}CoP–O_2 (B3PW91) (*204*)	–1.68	1.893	–	1.258
^{2}CoP(Im)–O_2 (B3PW91) (*204*)	–15.24	2.049	–	1.297
^{2}CoP(Im)–O_2 (PBE) (*190,201*)	–	1.94	117.7	1.28
^{2}CoTPP–O_2 (BP/DNP) (*202*)	–9.9	1.873	–	1.166
Exp. CoMb–O_2 (*198*)	–11.3 (*197*),–13.3 (*206*)	2.03	109° ± 5°	1.18
Exp. CoTPP–O_2 (*207*)	–12.2	–	–	–

D. Fe(II)P Complexes with H_2O

Cytochrome P450 is another family of biologically important enzymes, which mainly catalyze the oxidation of organic substances. The active site of the enzymes is composed of the Fe (III) protoporphyrin(IX) moiety, and in the resting state a water molecule is bound as the second ligand. Understandably, there have been many experimental and theoretical studies on Fe(III) P–H_2O systems. However, only two computational articles were published on Fe(II)–H_2O.

In 2005, Groenhof *et al.* (*208*) studied the resting state of P450 and reported that the FeP–H_2O ground state is intermediate spin (triplet), with the singlet being 19.2 kcal mol^{-1} higher in energy (OPBE/TZP). Unfortunately, no data on geometries and H_2O binding energy were reported.

Strickland and Harvey later studied (*57*) water binding to the model Fe(II) compounds. The authors reported an ^{1}Fe(II)Im–H_2O binding energy of –12.7 and –8.1 kcal mol^{-1} (B3LYP and B3PW91, respectively). The triplet and quintet states were found to be more weakly bound that the singlet (–5.3 and –4.9 kcal mol^{-1}, respectively (B3LYP) and –1.3 and 2.7 kcal mol^{-1} (B3PW91)). The computed Fe–O bond length is 2.107 Å (B3LYP) and 2.087 Å (B3PW91). Despite the fact that water usually does not bind to the ferrous iron of deoxy-myoglobin, these calculations agree with the laser photolysis of the Fe–H_2O bond, where a weakly bound water complex with myoglobin was observed (*209,210*).

VI. Summary and Conclusions

This chapter has reviewed certain experimental results and computational studies involving some of the metalloporphyrins (Fe(II)P, Co(II), and others). The present investigation also explored the accuracy of several DFT methods. The geometries of MP–XO complexes and XO binding energy were found to depend very strongly on the functional and basis set used. In many cases, model systems should be described at least with a triple-ξ quality basis set.

Although relatively expensive and difficult to use, CASSCF/CASPT2 methods often provide meaningful chemical descriptions. This, coupled with the continuing increase in computational power, suggests that the study of properties and reactions involving metalloporphyrins should be pursued with these accurate methods.

Acknowledgements

First of all, I would like to express my gratitude to the institutions that facilitated this work. Studies related to the formation, properties, and reactivity of metalloporphyrins were supported by grants from the Alexander von Humboldt Stiftung (fellowship 2005–2006), by the Deutsche Forschungsgemeinschaft through SFB 583, "*Redox-Active Metal Complexes; Control of Reactivity via Molecular Architectures*" and by a grant of computer time on the Höchstleistungsrechner in Bayern II (HLRB II).

Secondly, I thank Prof. Tim Clark and acknowledge collaborative studies with Prof. Hans-Peter Steinrück, Dr. Michael Gottfried, Dr. Hubertus Marbach (Lehrstuhl für Physikalische Chemie II, Universität Erlangen-Nürnberg), Prof. Rudi van Eldik (Lehrstuhl für Anorganische Chemie, Universität Erlangen-Nürnberg), and Prof. Laura Gagliardi (University of Minnesota, USA).

References

1. Di Natale, C.; Paolesse, R.; Alimelli, A.; Macagnano, A.; Pennazza, G.; D'Amico, A. *Proc. IEEE Sens. 2003. IEEE Int. Conf. Sens. 2nd* **2003**, *1*, 120–123.
2. Paolesse, R.; Mandoj, F.; Marini, A.; Di Natale, C. *Encyclopedia Nanosci. Nanotechnol.* **2004**, *9*, 21–42.
3. Pimenta, A. M.; Araujo, A. N.; Montenegro, M.C.B.S.M.; Pasquini, C.; Rohwedder, J.J.R.; Raimundo, I. M.*J. Pharm. Biomed. Anal.* **2004**, *36* (1), 49–55.
4. Harmon, H. J. *Methods* **2008**, *46*(1), 18–24.
5. Hodgson, G. W.; Ponnamperuma, C. *Proc. Natl. Acad. Sci. USA* **1968**, *59*(1), 22–28.
6. Kamaluddin;, M. S.; Singh;, M.; Deopujari, S. W. *Origins Life Evol Biospheres* **2005**, *17*, 59.
7. Barone, G.; Silvestria, A.; Roos, B. O. *Phys. Chem. Chem. Phys.* **2005**, *7*, 2126.
8. Chapman, S. K.; Daff, S.; Munro, A. W. *Struct. Bonding (Berlin)* **1997**, *88*, (Metal Sites in Proteins and Models: Iron Centres), 39–70.
9. Greenwoord, D. M. "*Metabolic Pathways*"; Academic Press: New York, NY, **1969**; Vol. 3 of Amino Acids and Tetrapyrroles.
10. Lewis, D. F. V. "*Cytochromes P450: Structure, Function and Mechanism*"; Taylor and Francis: London, **1996**.
11. Beale, S. I. Tetrapyrrole photoreceptors in photosynthetic organisms. **2002**, 74.
12. Dolphin, D.; Felton, R. H. *Acc. Chem. Res.* **1974**, *7*(1), 26–32.
13. Suslick, K. S.; Chen, C. T.; Meredith, G. R.; Cheng, L. T. *J. Am. Chem. Soc.* **1992**, *114*, 6928.
14. Suslick, K. S.; Rakow, N. A.; Kosal, M. E.; Chou, J. -H. *J. Porph. Phthalocyan.* **2000**, *4*, 407–413.

15. Azad, A. M.; Akbar, S. A.; Mhaisalkar, S. G.; Birkelfeld, L. D.; Goto, K. S. *J. Electrochem. Soc.* **1992**, *139*, 3690.
16. Kowel, S. T.; Selfridge, R.; Eldering, C.; Matloff, N.; Stroeve, P.; Higgins, B. G.; Srinivasan, M. P.; Coleman, L. B. *Thin Solid Films* **1987**, *152*, p. 377.
17. Arnold, M. A. *Anal. Chem.* **1992**, *64*, 1015A.
18. Bauer, S. J. *Appl. Phys.* **1996**, *80*, 5531.
19. Eastwood, D.; Gouterman, M. *J. Mol. Spec.* **1970**, *35*, 359.
20. Lee, S.; Okura, I. *Analyst* **1997**, *122*, 81–84.
21. Natale, C. *Mater. Sci. Eng.* **1998**, *C5*, 209–215.
22. Scheidt, W. R.; Ellison, M. K. *Acc. Chem. Res.* **1999**, *32*, 350–359.
23. Berezin, B. D.; Koifman, O. I. *Usp. Khimii, Rus. Chem. Rev.* **1980**, *49*, 2389.
24. Bytheway, I.; Hall, M. B. *Chem. Rev.* **1994**, *94*, 639–658.
25. Wayland, B. B.; Minkiewicz, J. v.; Abd-Elmageed, M. E. *J. Am. Chem. Soc.* **1974**, *96*, 2795–2801.
26. Matlow, S. L. *J. Chem. Phys.* **1955**, *23*, 673–680.
27. Gouterman, M.; Wagnière, G. H.; Snyder, L. C. *J. Mol. Spectrosc.* **1963**, *11*, 108–127.
28. Mathur, S. C.; Singh, J.; Kumar, B. *Phys. Stat. Sol. B* **1971**, *48*, 843–849.
29. Dedieu, A.; Rohmer, M.-M.; Viellard, A. *J. Am. Chem. Soc.* **1976**, *98*, 5789–5800.
30. Vysotskii, Y. B.; Kuz'mitskii, V. A.; Solov'ev, K. N. *J. Struct. Chem.* **1981**, *22*, 497–503.
31. Marques, H. M.; Brown, K. L. *Coord. Chem. Rev.* **2002**, *225*, 123–158.
32. Torrens, F. *Molecules* **2004**, *9*, 632–649.
33. Zandler, M. E.; D'Soud, F. *J. Mol. Struct. (Theochem)* **1997**, *401*, 301–314.
34. Gouterman, M. In: *"The Porphyrins"*; vol. III; Ed. Dolphin, D.; Academic Press: New York, NY, **1978**, pp. 1–165.
35. Linnanto, J.; Korppi-Tommola, J. *Phys. Chem. Chem. Phys.* **2006**, *8*, 663–687.
36. Almlof, J. *Int. J. Quantum Chem.* **1974**, *8*(6), 915–924.
37. Spangler, D.; McKinney, R.; Christoffersen, R. E.; Maggiora, G. M.; Shipman, L. L. *Chem. Phys. Lett.* **1975**, *36*(4), 427–431.
38. Spangler, D.; Maggiora, G. M.; Shipman, L. L.; Christoffersen, R. E. J.*Am. Chem. Soc.* **1977**, *99*(23), 7478–7489.
39. Spangler, D.; Maggiora, G. M.; Shipman, L. L.; Christoffersen, R. E. *J. Am. Chem. Soc.* **1977**, *99*(23), 7470–7477.
40. Kashiwagi, H.; Takada, T.; Obara, S.; Miyoshi, E.; Ohno, K. *Int. J. Quantum Chem.* **1978**, *14*(1), 13–27.
41. Kashiwagi, H.; Obara, S. *Int. J. Quantum Chem.* **1981**, *20*(4), 843–859.
42. Rohmer, M.-M. *Chem. Phys. Let.* **1985**, *116*, 44–49.
43. Zwaans, R.; van Lenthe, J. H.; den Boer, D.H.W. *J. Mol. Struct (Theochem)* **1995**, *339*, 153–160.
44. Rovira, C.; Kunc, K.; Hutter, J.; Ballone, P.; Parinello, M. *Int. J. Quantum Chem.* **1998**, *69*, 31–35.
45. Rovira, C.; Parrinello, M. *Int. J. Quantum Chem.* **2000**, *80*(6), 1172–1180.
46. Ghosh, A. *Acc. Chem. Res.* **1998**, *31*(4), 189–198.
47. Liao, M.-S.; Scheiner, S. *J. Comput. Chem.* **2002**, *23*(15), 1391–1403.
48. Liao, M.-S.; Scheiner, S. *J. Chem. Phys.* **2002**, *117*(1), 205–219.
49. Scherlis, D. A.; Estrin, D. A. *Int. J. Quantum Chem.* **2002**, *87*(3), 158–166.
50. Jewsbury, P.; Yamamoto, S.; Minato, T.; Saito, M.; Kitagawa, T. *J. Phys. Chem.* **1995**, *99*, 12677.
51. Weigend, F.; Häser, M. *Theor. Chem. Acc.* **1997**, *97*, 331–340.

52. Ghosh, A.; Almloef, J. *J. Phys. Chem.* **1995**, *99*, 1073–1075.
53. Shubina, T. E.; Clark, T. *J. Coord. Chem.* **2010**, DOI: 10.1080/00958972.2010.503346.
54. Zwaans, R.; van Lenthe, J. H.; den Boer, D. H. W. *J. Mol. Struct. (Theochem)* **1996**, *367*, 15–24.
55. Parusel, A. B. J.; Grimme, S. *J. Porph. Phthalocyan.* **2001**, *5*, 225–232.
56. Edwards, W. D.; Weiner, B.; Zerner, M. C. *J. Am. Chem. Soc.* **1986**, *108*(9), 2196–2204.
57. Strickland, N.; Harvey, J. N. *J. Phys. Chem. B* **2007**, *111*(4), 841–852.
58. Johansson, M. P.; Sundholm, D. *J. Chem. Phys.* **2004**, *120*, 3229–3236.
59. Radon, M.; Broclawik, E. *J. Chem. Theory Comput.* **2007**, *3*(3), 728–734.
60. Radon, M.; Pierloot, K. *J. Phys. Chem. A* **2008**, *112*(46), 11824–11832.
61. Radon, M.; Broclawik, E.; Pierloot, K. *J. Phys. Chem. B 114*(3), 1518–1528.
62. Vancoillie, S.; Zhao, H.; Radon, M.; Pierloot, K. *J. Chem. Theory Comput.* **2010**, *6*(2), 576–582.
63. Jaworska, M. *Chem. Phys.* **2007**, *332*, 203–210.
64. Becke, A. D. *Phys. Rev. A* **1988**, *38*, 3098.
65. Lee, C.; Yang, W.; Parr, R. G. *Phys. Rev. B* **1988**, *37*, 785.
66. Collman, J. P.; Hoard, J. L.; Kim, N.; Lang, G.; Reed, C. A. *J. Am. Chem. Soc.* **1975**, *97*, 2676.
67. Lang, G.; Spartalian, K.; Reed, C. A.; Collman, J. P. *J. Chem. Phys.* **1978**, *69*, 5424.
68. Boyd, P. D. W.; Buckingham, A. D.; McMecking, R. F.; Mitra, S. *Inorg. Chem.* **1979**, *18*, 3585.
69. Goff, H.; La Mar, G. N.; Reed, C. A. *J. Am. Chem. Soc.* **1977**, *99*, 3641.
70. Mispelter, J.; Momenteau, M.; Lhoste, J. M. *J. Chem. Phys.* **1980**, *72*, 1003.
71. Kozlowski, P. M.; Spiro, T. G.; B´erces, A.; Zgierski, Z., *J. Phys. Chem. B* **1998**, *102*, 2603.
72. Liao, M.-S.; Watts, J. D.; Huang, M.-J. *J. Phys. Chem. A* **2005**, *109*(35), 7988–8000.
73. Liao, M.-S.; Watts, J. D.; Huang, M.-J. *J. Comput. Chem.* **2006**, *27*(13), 1577–1592.
74. Liao, M.-S.; Watts, J. D.; Huang, M.-H. *J. Phys. Chem. A* **2007**, *111*, 5927–5935.
75. Choe, Y.-K.; Nakajima, T.; Hirao, K.; Lindh, R. *J. Chem. Phys.* **1999**, *111*(9), 3837–3845.
76. Choe, Y.-K.; Hashimoto, T.; Nakano, H.; Hirao, K. *Chem. Phys. Let.* **1998**, *295*(4), 380–388.
77. Sontum, S. F.; Case, D. A.; Karplus, M. *J. Chem. Phys.* **1983**, *79*(6), 2881–2892.
78. Rawlings, D. C.; Gouterman, M.; Davidson, E. R.; Feller, D. *Int. J. Quantum Chem.* **1985**, *28*(6, Pt. 1), 773–796.
79. Khvostichenko, D.; Choi, A.; Boulatov, R. *J. Phys. Chem. A* **2008**, *112*, 3700–3711.
80. Cocolios, P.; Kadish, K. M. *Isr. J. Chem.* **1985**, *25*, 138.
81. Takahashi, K.; Komura, T.; Imanaga, H. *Bull. Chem. Soc. Jpn.* **1989**, *62*, 386.
82. Langford, C. H.; Seto, S.; Hollebone, B. R. *Inorg. Chim. Acta* **1984**, *90*, 221.
83. Kobayashi, H.; Yanagawa, Y. *Bull. Chem. Soc. Jpn.* **1972**, *45*, 450.
84. Peng, S. M.; Ibers, J. A. *J. Am. Chem. Soc.* **1976**, *98*, 8032.
85. Que, J. L.; Tolman, W. B. *Nature* **2008**, *455*, 333.

86. Gibson, G. G.; Tamburini, P. P. *Xenobiotica* **1984**, *14*, 27.
87. Rohmer, M. M. *Chem. Phys. Lett.* **1985**, *116*(1), 44–49.
88. Delley, B. *Physica B (Amsterdam)* **1991**, *172*(1–2), 185–193.
89. Matsuzawa, N.; Ata, M.; Dixon, D. A. *J. Phys. Chem.* **1995**, *99*(19), 7698–7706.
90. Dailey, H. A.; Jones, C. S.; Karr, S. W. *Biochim. Biophys. Acta* **1999**, *99*, 7–11.
91. Dempsy, B.; Lowe, M. B.; Phillips, J. N. In: "*Haematin Enzymes*"; Eds. Falk, J. E.; Lemberg, R.; Morton, R. K.; Pergamon Press, Ltd: Oxford, **1959**, pp. 29–40.
92. Fleischer, E. B.; Wang, J. H. *J. Am. Chem. Soc.* **1960**, *82*, 3498–3502.
93. Burnham, B. F.; Zuckermann, J. J. *J. Am. Chem. Soc.* **1970**, *92*, 1547.
94. Shen, Y.; Ryde, U. *J. Inorg. Biochem.* **2004**, *98*(5), 878–895.
95. Hsiao, Y.-W.; Ryde, U. *Inorg. Chim. Acta* **2006**, *359*(4), 1081–1092.
96. Shen, Y.; Ryde, U. *Chem. Eur. J.* **2005**, *11*(5), 1549–1564.
97. Budzikiewicz, H. In: "*The Porphyrins*"; vol. III; Ed. Dolphin, D.; Academic Press: New York, NY, **1978**.
98. Smith, K. M. In: "*Porphyrins and Metalloporphyrins*"; Ed. Smith, K. M.; Elsevier: Amsterdam, **1975**, pp. 3–58.
99. Forest, E.; Marchon, J.-C.; Wilkins, C. L.; Yang, L. C. *Org. Mass. Spectrom.* **1989**, *24*, 197–200.
100. Irikura, K. K.; Beauchamp, J. L. *J. Am. Chem. Soc.* **1991**, *113*(7), 2767–2768.
101. Kazazić, S.; Klasinc, L.; McGlynn, S. P.; Srzić, D.; Vicente, M. G. H. *J. Phys. Chem. A* **2004**, *108*, 10997–11000.
102. Barlow, D. E.; Scudiero, L.; Hipps, K. W. *Langmuir* **2004**, *20*(11), 4413–4421.
103. Williams, F. J.; Vaughan, O. P. H.; Knox, K. J.; Bampos, N.; Lambert, R. M. *Chem. Commun. (Cambridge, UK)* **2004**, *15*, 1688–1689.
104. Vaughan, O. P. H.; Turner, M.; Williams, F. J.; Hille, A.; Sanders, J. K. M.; Lambert, R. M. *J. Am. Chem. Soc.* **2006**, *128*(30), 9578–9579.
105. Vaughan, O. P. H.; Williams, F. J.; Bampos, N.; Lambert, R. M. *Angew. Chem. Int. Ed.* **2006**, *45*(23), 3779–3781.
106. Katsonis, N.; Vicario, J.; Kudernac, T.; Visser, J.; Pollard, M. M.; Feringa, B. L. *J. Am. Chem. Soc.* **2006**, *128*(48), 15537–15541.
107. Gottfried, J. M.; Flechtner, K.; Kretschmann, A.; Lukasczyk, T.; Steinrueck, H.-P. *J. Am. Chem. Soc.* **2006**, *128*(17), 5644–5645.
108. Buchner, F.; Schwald, V.; Comanici, K.; Steinrueck, H. -P.; Marbach, H. *ChemPhysChem* **2007**, *8*(2), 241–243.
109. Auwarter, W.; Weber-Bargioni, A.; Brink, S.; Riemann, A.; Schiffrin, A.; Ruben, M.; Barth, J. V. *ChemPhysChem* **2007**, *8*(2), 250–254.
110. Kretschmann, A.; Walz, M.-M.; Flechtner, K.; Steinrueck, H.-P.; Gottfried, J. M. *Chem. Commun. (Cambridge, UK)* **2007**, *6*, 568–570.
111. Lukasczyk, T.; Flechtner, K.; Merte, L. R.; Jux, N.; Maier, F.; Gottfried, J. M.; Steinrueck, H. -P. *J. Phys. Chem. C* **2007**, *111*(7), 3090–3098.
112. Scudiero, L.; Barlow, D. E.; Mazur, U.; Hipps, K. W. *J. Am. Chem. Soc.* **2001**, *123*(17), 4073–4080.
113. Shubina, T. E.; Marbach, H.; Flechtner, K.; Kretschmann, A.; Jux, N.; Buchner, F.; Steinrueck, H. -P.; Clark, T.; Gottfried, J. M. *J. Am. Chem. Soc.* **2007**, *129*, 9476–9483.
114. Schroeder, D.; Shaik, S.; Schwarz, H. *Acc. Chem. Res.* **2000**, *33*(3), 139–145.
115. Shaik, S.; Danovich, D.; Fiedler, A.; Schroeder, D.; Schwarz, H. *Helv. Chim. Acta* **1975**, *78*(6), 1393–1407.

116. Rovira, C.; Kunc, K.; Hutter, J.; Parrinello, M. *Inorg. Chem.* **2001**, *40*(1), 11–17.
117. Boyd, P. D. W.; Buckingham, D. A.; McMeeking, R. F.; Mitra, S. *Inorg. Chem.* **1979**, *18*(12), 3585–3591.
118. Ribas-Ario, J.; Novoa, J. J. *Chem. Comm.* **2007**, *30*, 3160–3162.
119. Sigfridsson, E.; Ryde, U. *J. Biol. Inorg. Chem.* **1999**, *4*, 99–110.
120. Olah, J.; Harvey, J. N. *J. Phys. Chem. A* **2009**, *113*(26), 7338–7345.
121. Jensen, K. P.; Roos, B. O.; Ryde, U. *J. Inorg. Biochem.* **2005**, *99*(4), 978.
122. Jensen, K. P.; Roos, B. O.; Ryde, U. *J. Inorg. Biochem.* **2005**, *99*(1), 45–54.
123. Sigfridsson, E.; Ryde, U. *J. Inorg. Biochem.* **2002**, *91*(1), 101–115.
124. Blomberg, L. M.; Blomberg, M. R. A.; Siegbahn, P. E. M. *J. Inorg. Biochem.* **2005**, *99*(4), 949–958.
125. Rovira, C.; Kunc, K.; Hutter, J.; Ballone, P.; Parrinello, M. *J. Phys. Chem. A* **1997**, *101*(47), 8914–8925.
126. Harvey, J. N. *J. Am. Chem. Soc.* **2000**, *122*(49), 12401–12402.
127. Rutkowska-Zbik, D.; Witko, M.; Stochel, G. *J. Comput. Chem.* **2007**, *28*(4), 825–831.
128. Hoffman, R.; Chen, M. M.-L.; Thorn, D. *Inorg. Chem.* **1977**, *16*, 503.
129. Collman, J. P.; Fu, L. *Acc. Chem. Res.* **1999**, *32*(6), 455–463.
130. Kuriyan, J.; Wilz, S.; Karplus, M.; Petsko, G. A. *J. Mol. Biol.* **1986**, *192*(1), 133–154.
131. Cheng, X.; Schoenborn, B. P. *Acta Crystallogr. Sect. B: Struct. Sci.* **1990**, *B46*(2), 195–208.
132. Cheng, X.; Schoenborn, B. P. *J. Mol. Biol.* **1991**, *220*(2), 381–399.
133. Norvell, J. C.; Nunes, A. C.; Schoenborn, B. P. *Science (Washington, DC, 1883)* **1975**, *190*(4214), 568–570.
134. Hanson, J. C.; Schoenborn, B. P. *J. Mol. Biol.* **1981**, *153*(1), 117–146.
135. Phillips, S. E.; Schoenborn, B. P. *Nature* **1981**, *292*(5818), 81–82.
136. Ray, G. B.; Li, X. Y.; Ibers, J. A.; Sessler, J. L.; Spiro, T. G. *J. Am. Chem. Soc.* **1994**, *116*(1), 162–176.
137. Quillin, M. L.; Arduini, R. M.; Olson, J. S.; Phillips, G. N., Jr. *J. Mol. Biol.* **1993**, *234*(1), 140–155.
138. Kachalova, G. S.; Popov, A. N.; Bartunik, H. D. *Science (Washington, DC)* **1999**, *284*(5413), 473–476.
139. Young, F.; Phillips, G. N., Jr. *J. Mol. Biol.* **1996**, *256*, 762.
140. Spiro, T. G.; Kozlowski, P. M. *Acc. Chem. Res.* **2001**, *34*, 137–144.
141. Vogel, K. M.; Kozlowski, P. M.; Zgierski, M. Z.; Spiro, T. G. *J. Am. Chem. Soc.* **1999**, *43*, 9915–9921.
142. Lash, T. D. *J. Porph. Phthalocyan.* **2001**, *5*, 313–314.
143. Peng, S. -M.; Ibers, J. A. *J. Am. Chem. Soc.* **1976**, *25*, 8032–8036.
144. Silvernail, N. J.; Noll, B. C.; Schulz, C. E.; Scheidt, W. R. *Inorg. Chem.* **2006**, *45*, 7050–7052.
145. Rovira, C.; Ballone, P.; Parinello, M. *Chem. Phys. Let.* **1997**, *271*, 247–250.
146. Rovira, C.; Parinello, M. *Chem. Eur. J.* **1999**, *5*, 250–262.
147. Rovira, C.; Kunc, K.; Hutter, J.; Ballone, P.; Parinello, M. *J. Phys. Chem. A* **1997**, *101*, 8914–8925.
148. Radon, M.; Pierloot, K. *J. Phys. Chem. A* **2008**, *112*, 11824–11832.
149. D'Abramo, M.; Di Nola, A.; Amadei, A. *J. Phys. Chem. B* **2009**, *113*, 16346–16353.
150. Goldbeck, R. A.; Bhaskaran, S.; Ortega, C.; Mendoza, J. K.; Olson, J. S.; Soman, J.; LKlinger, D. S.; Esquerra, R. M. *PNAS* **2006**, *103*, 1254–1259.
151. Olson, J. C.; Phillips, G. N. *J. Biol. Inorg. Chem.* **1997**, *2*, 544–552.

152. Springer, B. A.; Egeberg, K. D.; Slighar, S. G.; Rohlfs, R. J.; Matthews, A. J.; Olson, J. C. *J. Biol. Chem.* **1989**, *264*, 3057–3060.
153. Cui, W.; Li, S.; Wayland, B. B. *J. Organomet. Chem.* **2007**, *692*, 3198–3206.
154. Wayland, B. B.; Sherry, A. E.; Bunn, A. G. *J. Am. Chem. Soc.* **1993**, *115*, 7675–7684.
155. Wayland, B. B.; Minkiewicz, J. V.; Abd-Elmageed, M. E. *J. Am. Chem. Soc.* **1974**, *96*, 2795–2801.
156. Wayland, B. B.; Mohajer, D. *J. Am. Chem. Soc.* **1971**, *93*, 5296–5296.
157. Cullota, E.; Kpshland, D. E., *Science (Washington, DC)* **1992**, *258*, 1862.
158. Westcott, B. L.; Enemark, J. H. *Inorg. Electron. Struct. Spectrosc.* **1999**, *2*, 403–450.
159. Chiavarino, B.; Crestoni, M. E.; Fornarini, S.; Rovira, C. *Inorg. Chem. (Washington, DC, USA)* **2008**, *47*(17), 7792–7801.
160. Tangen, E.; Svadberg, A.; Ghosh, A. *Inorg. Chem.* **2005**, *44*(22), 7802–7805.
161. Ghosh, A. *JBIC, J. Biol. Inorg. Chem.* **2006**, *11*(6), 712–724.
162. Enemark, J. H.; Feltham, R. D. *Coord. Chem. Rev.* **1974**, *13*, 339.
163. Ghosh, A.; Wondimagegn, T. *J. Am. Chem. Soc.* **2000**, *122*, 8101–8102.
164. Scheidt, W. R.; Frisse, M. E. *J. Am. Chem. Soc.* **1975**, *97*, 17–21.
165. Nguen, T. Q.; Escano, M.C.S.; Shimoji, N.; Nakanishi, H.; Kasai, H. *Surf. Interface. Anal.* **2008**, *40*, 1082–1084.
166. Nguen, T. Q.; Escano, M.C.S.; Tanako, R.; Nakanishi, H.; Kasai, H. *J. Phys. Soc. Jpn.* **2009**, *78*, 014706.
167. Chen, O.; Groh, S.; Liechty, A.; Ridge, D. P. *J. Am. Chem. Soc.* **1999**, *121*, 11910–11911.
168. Ellison, M. K.; Scheidt, W. R. *Inorg. Chem.* **1998**, *37*, 382–383.
169. Zhu, X.-Q.; Li, Q.; Hao, Q.-F.; Cheng, J.-P. *J. Am. Chem. Soc.* **2002**, *124*, 9887–9893.
170. Watanabe, T.; Ama, T.; Nakamoto, K. *J. Phys. Chem.* **1984**, *88*, 440.
171. Chance, M. R.; Courtney, S. H.; Chavez, M. D.; Ondrias, M. R.; Friedman, J. M. *Biochemistry* **1990**, *29*, 5537.
172. Miller, L. M.; Patel, M.; Chance, M. R. *J. Am. Chem. Soc.* **1996**, *118*(19), 4511–4517.
173. De Angelis, F.; Car, R.; Spiro, T. G. *J. Am. Chem. Soc.* **2003**, *125*, 15710–15711.
174. Tsuda, M.; Dy, E. S.; Kasai, H. *Eur. Phys. J. D* **2006**, *38*, 139–141.
175. Jensen, K. P.; Ryde, U. *J. Biol. Chem.* **2004**, *279*(15), 14561–14569.
176. Momenteau, M.; Reed, C. A. *Chem. Rev. (Washington, DC, USA)* **1994**, *94* (3), 659–698.
177. Pauling, L.; Coryell, C. D. *Proc. Natl. Acad. Sci. USA* **1936**, *22*, 210–216.
178. Pauling, L. *Stanford Med. Bull.* **1948**, *6*, 215–217.
179. Pauling, L. *Nature (London)* **1964**, *203*(4941), 182–183.
180. Weiss, J. J. *Nature* **1964**, *202*, 83–84.
181. McClure, D. S. *Radiat. Res. Suppl.* **1960**, *2*, 218–242.
182. Goddart, W. A.; Olafson, B. D. *Proc. Natl. Acad. Sci. USA* **1975**, *72*, 2335–2339.
183. Olafson, B. D.; Goddart, W. A. *Proc. Natl. Acad. Sci. USA* **1977**, *74*, 1315–1319.
184. Jensen, K. P.; Roos, B. O.; Ryde, U. *J. Inorg. Biochem.* **2005**, Erratum, *99*, 978.
185. Tsai, T. E.; Groves, J. L.; Wu, C.S.J. *Chem. Phys.* **1981**, *74*, 4306–4314.

186. Nozawa, T.; Hatano, M.; Nagashima, U.; Obara, S.; Kashiwagi, H. *Bull. Chem. Soc. Jpn.* **1983**, *56*(6), 1721–1727.
187. Herman, Z.; Loew, G. H. *J. Am. Chem. Soc.* **1980**, *102*, 1815–1821.
188. Koch, W.; Holthausen, M. C. *"A Chemist Guide to Density Functional Theory"*; Wiley-VCH: Weinheim, **2000**.
189. Franzen, S. *Proc. Natl. Acad. Sci. USA* **2002**, *99*(26), 16754–16759.
190. Degtyarenko, I.; Nieminen, R. M.; Rovira, C. *Biophys. J.* **2006**, *91*(6), 2024–2034.
191. Nakashima, H.; Hasegawa, J. y.; Nakatsuji, H. *J. Comp. Chem.* **2006**, *27*(4), 426–433.
192. Sun, Y.; Hu, X.; Li, H.; Jalbout, A. F. *J. Phys. Chem. C* **2009**, *113*, 14316–14323.
193. Nguen, T. Q.; Escano, M. C. S.; Shimoji, N.; Nakanishi, H.; Kasai, H. *Phys. Rev. B* **2008**, *77*, 195307.
194. Vojtechovsky, J.; Chu, K.; Berendzen, J.; Sweet, R. M.; Schlichting, I. *Biophys. J.* **1999**, *77*(4), 2153–2174.
195. Johnson, C. R.; Ownby, D. W.; Gill, S. J.; Peters, K. S. *Biochemistry* **1992**, *31*, 10074.
196. Hoard, J. L.; Scheidt, W. R. *Proc. Natl. Acad. Sci. USA* **1973**, *70*(12, Pt. 2), 3919–3922.
197. Spilburg, C. A.; Hoffman, B. M.; Petering, D. H. *J. Biol. Chem.* **1972**, *247* (13), 4219–4223.
198. Brucker, E. A.; Olson, J. S.; Phillips, G. N., Jr.; Dou, Y.; Ikeda-Saito, M. *J. Biol. Chem.* **1996**, *271*(41), 25419–25422.
199. Getz, D.; Melamud, E.; Silver, B. L.; Dori, Z. *J. Am. Chem. Soc.* **1975**, *97*(13), 3846–3847.
200. Walker, F. A.; Bowen, J. *J. Am. Chem. Soc.* **1985**, *107*(25), 7632–7635.
201. Degtyarenko, I.; Biarnes, X.; Nieminen, R. M.; Rovira, C. *Coord. Chem. Rev.* **2008**, *252*(12–14), 1497–1513.
202. Shi, Z.; Zhang, J. *J. Phys. Chem. C* **2007**, *111*(19), 7084–7090.
203. Tsuda, M.; Sy Dy; Kasai, H. *J. Chem. Phys.* **2005**, *122*, 244719.
204. Tsuda, M.; Kasai, H., *Surf. Sci.* **2007**, *601*, 5200–5206.
205. Steiger, B.; Baskin, J. S.; Anson, F. C.; Zewail, A. H. *Angew. Chem. Int. Ed.* **2000**, *39*(1), 257–260.
206. Yonetani, T.; Yamamoto, H.; Woodrow, G. V. *J. Biol. Chem.* **1974**, *249* 682.
207. Collman, J. P.; Brauman, J. I.; Doxsee, K. M.; Halbert, T. R.; Hayes, S. E.; Suslick, K. S. *J. Am. Chem. Soc.* **1978**, *100*(9), 2761–2766.
208. Groenhof, A. R.; Swart, M.; Ehlers, A. W.; Lammertsma, K. *J. Phys. Chem. A* **2005**, *109*(15), 411–3417.
209. Lamb, D. C.; Prusakov, V.; Engler, N.; Ostermann, A.; Schellenberg, P.; Parak, F. G.; Nienhaus, G. U. *J. Am. Chem. Soc.* **1998**, *120*, 2981–2982.
210. Lamb, D. C.; Kriegl, J.; Kastens, K.; Nienhaus, G. U. *J. Phys. Org. Chem.* **2000**, *13*, 659–663.

DEALING WITH COMPLEXITY IN OPEN-SHELL TRANSITION METAL CHEMISTRY FROM A THEORETICAL PERSPECTIVE: REACTION PATHWAYS, BONDING, SPECTROSCOPY, AND MAGNETIC PROPERTIES

FRANK NEESE, WILLIAM AMES, GEMMA CHRISTIAN, MARIO KAMPA, DIMITRIOS G. LIAKOS, DIMITRIOS A. PANTAZIS, MICHAEL ROEMELT, PANIDA SURAWATANAWONG and SHENGFA YE

Institut für Physikalische und Theoretische Chemie, Universität Bonn, Wegelerstr. 12, D-53115 Bonn, Germany

I. Introduction

Open-shell transition metal ions play central roles in many modern research fields such as catalysis, molecular magnetism, or bioinorganic chemistry, to name only a few. Central to this

THEORETICAL AND COMPUTATIONAL INORGANIC CHEMISTRY
VOLUME 62 ISSN 0898-8838 / DOI: 10.1016/S0898-8838(10)62008-9

importance is that transition metals are redox active, stereochemically fairly flexible, and through the many open-shell states display a puzzling variety of magnetic properties. Thus, transition metal ions display highly complex reactivities in the active sites of enzymes or catalysts. Tailor-made building blocks of mononuclear transition metal complexes act as building blocks for the design of single-molecule magnets or switchable spin-crossover complexes.

The multifaceted behavior of transition metal complexes calls for not only theoretical explanations within a common conceptual framework but also theoretical tools that are powerful enough to predict the chemical and magnetic behavior of open-shell transition metal ions. Specifically, one looks for theoretical methods to calculate geometries and relative energies for stable species and transition states as well as for methods that allow one to determine spectroscopic parameters with sufficiently predictive accuracy.

For quantum chemistry, first-row transition metal complexes are perhaps the most difficult systems to treat. First, complex open-shell states and spin couplings are much more difficult to deal with than closed-shell main group compounds. Second, the Hartree–Fock method, which underlies all accurate treatments in wavefunction-based theories, is a very poor starting point and is plagued by multiple instabilities that all represent different chemical resonance structures. On the other hand, density functional theory (DFT) often provides reasonably good structures and energies at an affordable computational cost. Properties, in particular magnetic properties, derived from DFT are often of somewhat more limited accuracy but are still useful for the interpretation of experimental data.

In this short review, we will touch upon several subjects that our group has recently investigated and that illustrate the challenges that are met in theoretical transition metal chemistry: (a) reactivity of high-valent iron-oxo sites and the challenge of multiple spin-state channels, (b) the treatment of magnetic spectroscopic observables in the case of (near) orbital degeneracy, (c) the experimentally validated description of transition metal complexes with coordinated ligand radicals, and (d) the calculation of the magnetic properties of oligonuclear transition metal clusters with applications to Photosystem II. Clearly, each of these areas would warrant a review on its own right. It is nevertheless hoped that this chapter will provide an instructive first overview of the theoretical challenges. The reader who is more interested in technical and theoretical aspects is referred to two recent reviews dealing with multireference wavefunction-based methods and DFT methodology, both applied to transition metal chemistry (*1,2*).

II. Calculation of Reaction Pathways

In this section we highlight some of the issues that are frequently encountered in theoretical studies of reactivity at open-shell transition metal centers. The principal methods and techniques are best demonstrated by example, and for this purpose we will draw on recent computational studies of alkane C−H bond activation by oxo-iron(IV). Oxo-iron(IV) intermediates are key intermediates in the catalytic cycles of heme and non-heme iron enzymes functionalizing unactivated C−H bonds using the green oxidant molecular dioxygen (*3*). Hence, there is considerable interest in understanding their reactivity in order to design and prepare low-molecular-weight catalysts to achieve these transformations. The most intensively studied systems are the so-called compounds I and II in the cytochrome P450 enzyme family, which catalyze the biodegradation of xenobiotics (*4*). Likewise, oxo-iron(IV) intermediates have been detected in four non-heme iron enzymes (*5*). Simultaneously, a series of non-heme oxo-ferryl model complexes has been synthesized and spectroscopically characterized (*6,7*) whereas in some cases they were even crystallized (*8*).

Taurine, α-ketoglutarate dioxygenase (TauD), is a member of the family of non-heme iron enzymes. TauD catalyzes the hydroxylation of alkane C−H bonds in the substrate taurine (2-aminoethane-1-sulfonic acid), which enables *Escherichia coli* to use the aliphatic sulfonate taurine as a sulfur source during periods of sulfate starvation (*9*). The enzyme is proposed to activate O_2 using a high-spin Fe(II) active site along with α-ketoglutarate as a cosubstrate to generate an Fe(IV)=O intermediate (*10*). The high-valent ferryl-oxo species, which was suggested for TauD, is the first iron(IV) intermediate that has been unambiguously identified experimentally.

Quantum chemical calculations have made many valuable contributions to this field. One major advantage of theoretical calculations is that they can be used to study reactive species, which may be difficult to study experimentally, and to explore the electronic structure of the system in detail. This approach is illustrated here for our studies of the reactivity of the TauD oxo-Fe(IV) center C−H bond activation.

A. Construction of a Model

The first step in a theoretical study of an enzyme is the construction of a model. Depending on the computational equipment and the desired accuracy of the calculations, geometry

optimizations of systems containing up to 200 atoms can be handled by DFT methods (*2,11,12*). Hence, the quantum-mechanical treatment of whole enzymes is out of question. One way of overcoming this dilemma is to use molecular mechanics, which can easily handle several thousand atoms. However, electronic structure and reactivity are completely inaccessible through classical molecular mechanics. A different approach is to use a cluster model. Within this approach, only the region of interest is studied by a quantum mechanical method such as DFT, usually up to 200 atoms including the active center. The rest of the enzyme can be modeled using a solvation model (such as the conductor-like screening model (COSMO) (*13*) or the polarizable continuum model (PCM) (*14,15*). This gives satisfying results as long as no directed hydrogen bonds are present (*16*). Modeling the active site by electronic structure methods and the protein bulk together with the solvent by molecular mechanics is a method referred to as QM/MM (*17,18*). The two approaches have recently been compared by Himo and Siegbahn (*19*).

The creation of a cluster model requires a suitable X-ray structure of the protein. Smaller cluster models include the first coordination sphere, whereas larger and more accurate models should encompass the second coordination sphere as well. For structural and electrostatic reasons, residues forming hydrogen or salt bridges to the first coordination sphere or the substrate are considered the most important. The residues included in the model then have to be cut off from the rest of the protein, and to avoid the presence of unsaturated atoms, methyl groups or hydrogen atoms have to be added. Truncation should be done in a way that the chemical characteristics of the residues are retained. For instance, if a histidine residue is part of the enzyme active site, the imidazole ring is best completely included in the model. The degrees of freedom of the active site residues in an enzyme are reduced due to covalent and non-covalent bonds with the protein environment. In order to take this into account, constraints must be applied to some atoms during geometry optimization of a cluster model (*20*).

Figure 1 shows the TauD enzyme and two models for the active site. The smallest model includes the iron center with only the first coordination sphere and the substrate. The histidines are modeled by imidazole rings, whereas the aspartate is included in the form of an acetic acid molecule. The larger model includes the cofactor, α-ketoglutarate, and the second coordination sphere of the site. Larger models are also used for histidine and aspartate.

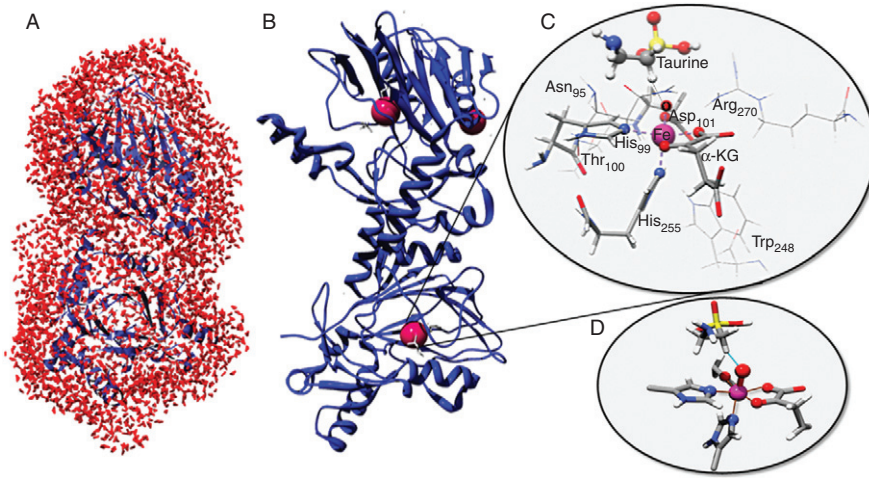

FIG. 1. Construction of a computational model for TauD. (A) the solvated TauD enzyme (PDB code 1GY9, solvating water molecules in red); (B) the desolvated enzyme; (C) the active site with the substrate and α-ketoglutarate bound to the iron centre, and the most important amino acids in the first and second coordination sphere; (D) a minimal model for TauD including only the first coordination sphere and the substrate.

B. REACTION PATHWAYS

Once the model has been constructed, the reaction pathway can be investigated. Reaction schemes are usually constructed using information available from experiment, such as the spectroscopic properties of trapped key intermediates, or comparisons with established pathways for similar reactions. The proposed reaction pathways can then be explored by calculating energy minima for reactants, intermediates, and products (see reference (*21*) for an overview of available computational techniques).

Locating minima is not always straightforward since a reaction surface is usually complex, and a geometry optimization calculation will only locate minima close to the starting point. It is usually not feasible to systematically explore all possible conformers, so chemical intuition and corroborative evidence from experiment play important roles. A nice example is the identification of the coordination geometry of oxo-iron(IV) intermediate in TauD (*22*). As mentioned above, during optimization of enzyme active sites, key atoms are sometimes fixed to mimic the constraints that the protein environment exerts on the active site (*20*).

After the minima have been located, the search is extended to the transition states that connect them. Transition state searches are more involved than the location of minima and, given the complexity of potential energy surfaces, chemical intuition is again the key, since the search usually requires the investigator to have a reasonable idea of what type of structure it is searched for. Once the reaction profile has been explored, the lowest energy pathway is chosen. The calculated reaction profiles can be checked through comparison with available experimental data, for example, geometrical parameters from X-ray crystallography, kinetic data, kinetic isotope effects, and spectroscopy.

The calculated reaction profile for H abstraction for the TauD Fe(IV)=O model is shown in Fig. 2 (*23*). The calculations were carried out with the ORCA package (*24*), using the B3LYP density functional (*25,26*) and Karlsruhe basis sets for all atoms (*27–29*) in combination with the RIJONX (*30*) or RIJCOSX approximations (*31*) and appropriate auxiliary basis sets (*32–34*). The protein environment was modeled by the COSMO solvation model with a dielectric constant of 4.0 (*12*). The reaction follows the consensus mechanism for aliphatic C–H activation by oxyl-ferryl compounds (*35*) in which the first step is H-atom abstraction via TS1 to give a hydroxo-Fe(III) complex with a C-centered alkyl radical, labeled IN. This is followed by a rebound step via TS2 to give the final product, ethanol and the ferrous active site. Overall, this is a two-electron oxidation process where the σ_{C-H} bonding orbital serves as the electron donor and the H-atom abstraction is rate limiting.

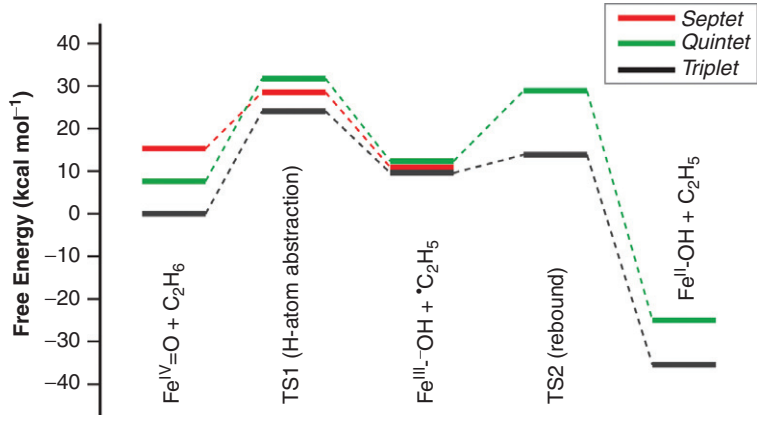

FIG. 2. Calculated reaction profile for the TauD model system.

This reaction profile also illustrates one of the other important challenges in the study of transition metal systems, namely that the metal-containing active site often has several accessible spin states. Specifically in the case of Fe(IV)=O, the triplet, quintet, and septet spin states. Consequently, the reaction can, in principle, proceed on different electronic potential energy surfaces and it is necessary to test all possibilities when exploring a reaction surface. This has been labeled "two-state reactivity" and has been elaborated by Shaik, Schwarz, Schröder, and co-workers (*36–40*). In the case of TauD, the results show that the reaction is only feasible on the quintet surface, in agreement with earlier DFT studies (*11,41–45*).

Detailed electronic structure studies, including insights gained from ligand field theory (*46*), can be especially useful in interpreting the reaction profiles and understanding the reactivity and selectivity of these systems. The exploration of two-state reactivity and the value of detailed electronic structure analysis are illustrated by our studies of the H atom abstraction step catalyzed by TauD (*23,47*), which are presented here for each spin-state surface: the hypothetical septet, the quintet, and the triplet.

A.1. Septet pathway

The lowest-energy septet state of the $(FeO)^{2+}$ core has the orbital occupation pattern $(\sigma(Op_z))^2(\pi(Op_{x,y})^3(d_{xy})^1(\pi^*(d_{xz,yz}))^2(\sigma^*(d_{x2\text{-}y2}))^1(\sigma^*(d_{z2}))^1$, as shown in Fig. 3. This bonding pattern is best described as a high-spin ferric center ($S_{Fe} = 5/2$) ferromagnetically coupled to an oxyl ($S_O = ½$) radical. Compared to the quintet ground state, this represents an oxo-to-iron $\pi(Op_{x,y})\rightarrow\sigma^*(d_{z2})$ charge transfer state accompanied by a spin flip, reducing the bond order from 2 to 1. Accordingly, the $^7(FeO)^{2+}$ reactant is over 16 kcal mol^{-1} higher in energy than the $^5(FeO)^{2+}$ ground state and therefore the septet surface is not a viable pathway for C–H activation. However, of the three spin states, the septet $(FeO)^{2+}$ core is the most reactive toward C–H bond activation with the lowest barrier to H-atom abstraction.

As the substrate approaches the $^7(FeO)^{2+}$ core, the Op_x orbital, which is singly occupied, interacts with the C–H σ–bonding orbital to form two three-centered molecular orbitals (MOs), σ_{CHO} and σ^*_{CHO}, as shown in Fig. 3 (right). Therefore, Op_x acts as the electron acceptor orbital. Since it is a π-bonding orbital this pathway is referred to as the "π pathway."

Once the system passes through ^{7}TS1, it forms a high-spin (HS) Fe(III) ion that is ferromagnetically coupled to a substrate alkyl radical. Thus, the second electron transfer from the substrate to

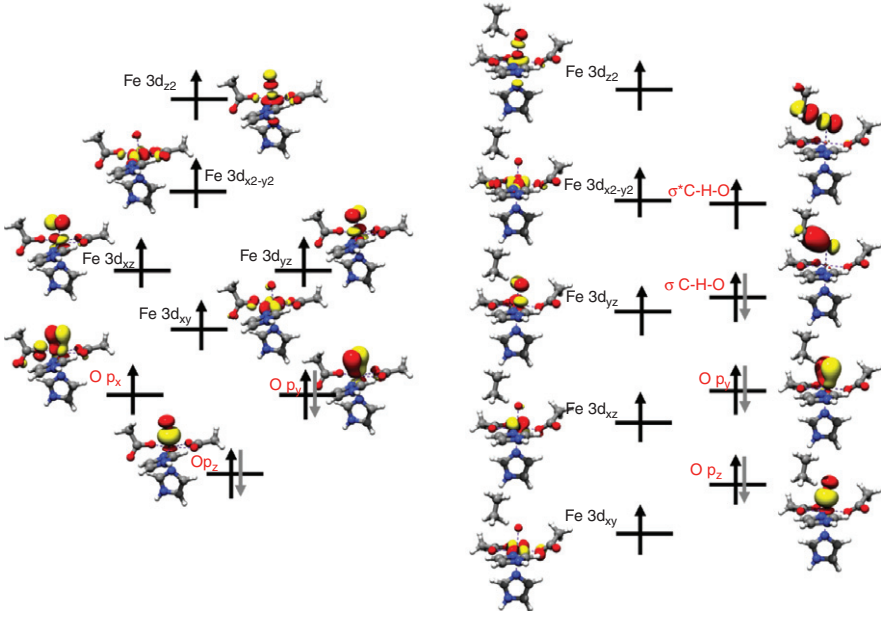

FIG. 3. The MO diagrams for the septet reactant (left) and ^{7}TS1 (right).

the iron center is spin forbidden. It follows that the reaction cannot go further on the septet surface.

A.2. Quintet pathway

The quintet is the ground state of the $(FeO)^{2+}$ reactant and is best described as an oxo-Fe(IV) species, with four electrons singly occupying the Fe d_{xz}, d_{yz}, d_{x2-y2}, and d_{z2} orbitals (as shown in Fig. 4). Quintet $(FeO)^{2+}$ has a very covalent metal–oxygen bond with two half π-bonds (involving the Fe d_{xz}, d_{yz} and O p_x, p_y orbitals) and one σ bond (Fe d_{z2} and O p_z orbitals).

Upon approach of the substrate, the system forms ^{5}TS1 (Fig. 4, right), which has a similar electronic structure to ^{7}TS1 except for a few key differences. First, HS Fe(III) is antiferromagnetically rather than ferromagnetically coupled to an alkyl radical, and secondly, it is the Op_z orbital rather than the Op_x orbital that forms the three-centered MOs with the incoming substrate. It can be then simply argued that in the transition state one electron has been transferred from the C–H bond to the metal d_{z2} orbital. Based on the bonding picture of the reactant, the Fe-d_{z2} MO would be expected to be antibonding with respect to the

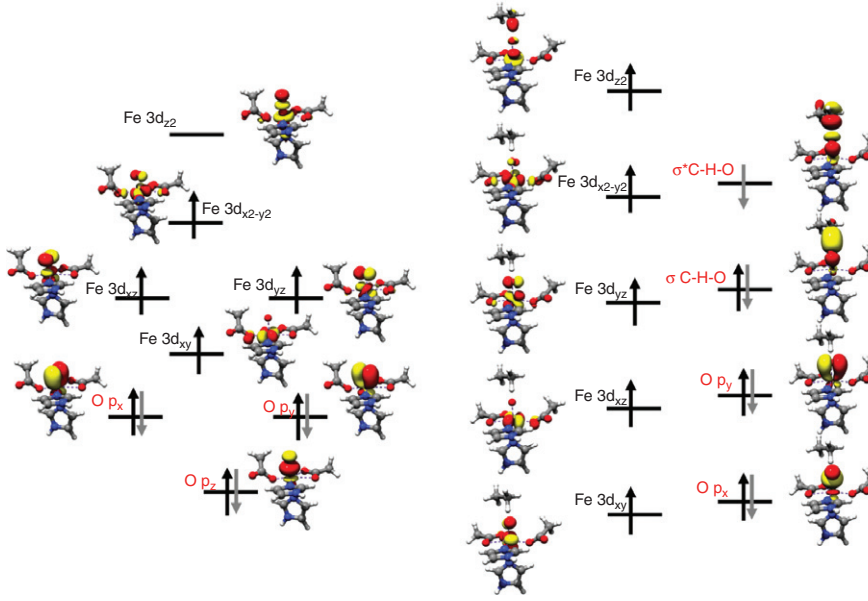

FIG. 4. Molecular orbital diagrams for the quintet reactant (left) and ^{5}TS1 (right).

Op_z orbital. However, on closer inspection, it becomes clear that it is the bonding combination between the Fe-d_{z2} and Op_z fragment orbitals. Therefore, significant rearrangement of the electronic structure must have occurred in the formation of the transition state.

Accordingly, constrained optimizations of the $(FeO)^{2+}$ core were carried out to study the bonding as the Fe–O bond changes. These calculations showed that as the Fe–O bond lengthens, the electron distribution changes from that of the Fe(IV)=O to a broken symmetry solution with five singly occupied Fe-3d orbital-based MOs and a spin-down SOMO, which is essentially a p_z orbital on the oxo-ligand, see Fig. 5. The electronic structure is best interpreted as antiferromagnetic coupling between a high-spin Fe(III) and an oxyl radical.

Importantly, oxyl oxygen is more reactive than oxo due to its higher electrophilicity. The oxyl formation also enhances the ability of the $(FeO)^{2+}$ to react with the bonding C–H σ-orbital since the O-based p_z SOMO overlaps more efficiently with the C–H σ-orbital of the substrate, compared to the Fe-d_{z2} based orbital, which has little Op_z character. This facilitates the electron transfer and formation of the three centered MOs observed in ^{5}TS1. The overall H-atom abstraction step can be described as

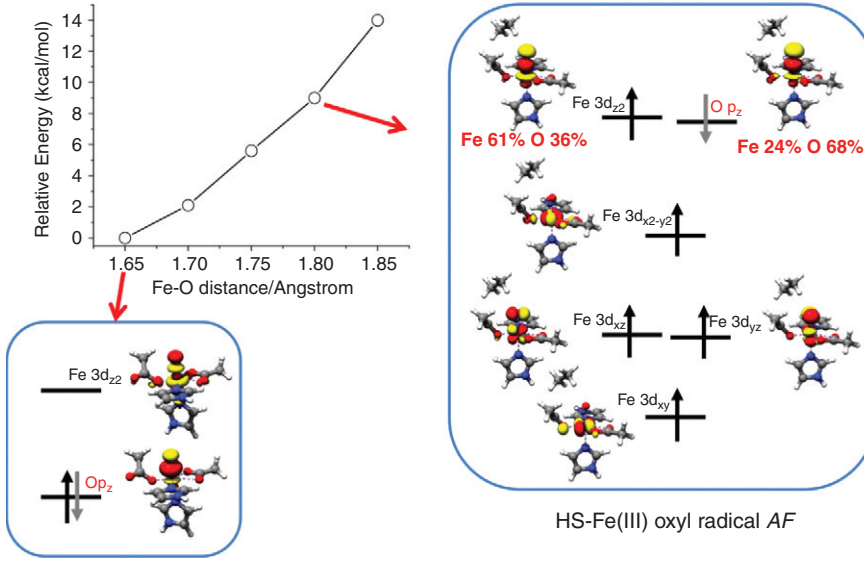

FIG. 5. Evolution of the quintet oxo–iron(IV) as a function of the Fe–O_{oxo} distance.

a relay process where the oxo group first delivers an electron to the metal center before accepting an electron from the σ_{C-H} bond. In this scheme, the electron acceptor is the Op_z orbital and not the Fe-d_{z2} orbital proposed in earlier studies (*41,42,44,45,48*). Since the Op_z orbital has Fe–O σ character, this is referred to as the "σ-pathway." After passing over the ^{5}TS1, the system forms ^{5}IN which is essentially identical to ^{7}IN, since they have the same orbital occupation patterns except that the ferric center is antiferromagnetically coupled with the alkyl radical.

The final step in the reaction is the rebound, which takes place via an "early" transition state, ^{5}TS2, which has a long C–O bond (2.68 Å). The early transition state is in agreement with the small rebound barrier. Upon formation of the C–O bond, the second electron is transferred to the metal center giving a high-spin ferrous ($S_{Fe} = 2$) ion bound to the product, ethanol.

A.3. Triplet pathway

Triplet $(FeO)^{2+}$ lies about 7 kcal mol^{-1} above the quintet ground state in energy. It is calculated to have the orbital occupation $(\sigma(Op_z))^2(\pi(Op_{x,y})^4(d_{xy})^2(\pi^*(d_{xz,yz}))^2$, in which the Fe–O bond order is formally 2, as for the quintet. The transition state for H-abstraction, ^{3}TS1, is best described as a low-spin (LS) Fe(III)

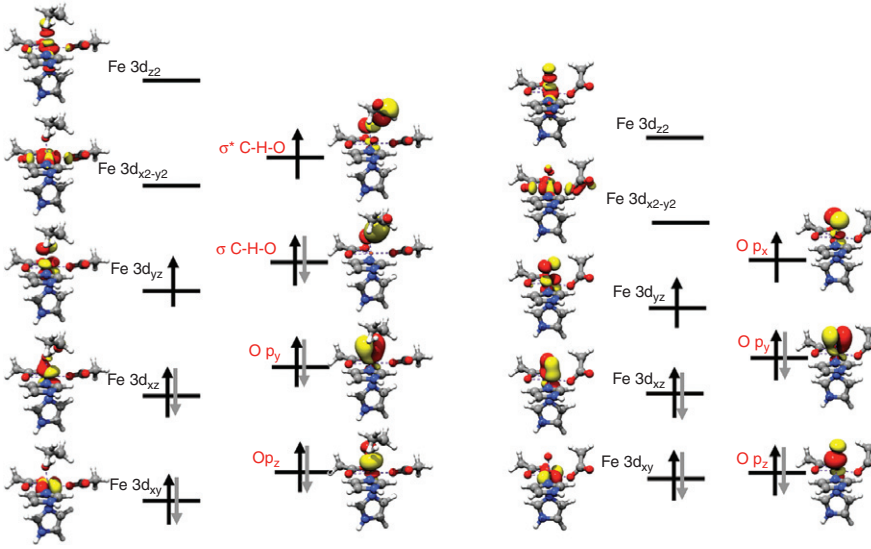

FIG. 6. Molecular orbital diagrams for ^{3}TS1 (left) and the constrained model of the triplet reactant with the Fe–O bond distance at 1.80 Å (right).

ion ferromagnetically coupled with a three centered C–H–O radical, see Fig. 6. Again, the bonding nature in the Fe-3d_{xz}-based MO is not what would be expected from the reactant, being an antibonding instead of bonding combination. Following the same reasoning, this indicates that the triplet $(FeO)^{2+}$ core also requires a preparatory step before reaction with the substrate.

Constrained optimizations at different Fe–O bond lengths confirmed this, showing that as the Fe–O bond lengthens, the triplet $(FeO)^{2+}$ species undergoes a change from intermediate-spin (IS) oxo-ferryl ($S_{Fe} = 1$) to an LS ferric ion ($S_{Fe} = ½$) ferromagnetically coupled to an oxyl radical, shown in Fig. 6. The oxyl-radical-based SOMO in this case is the Op_x orbital, which then interacts with the σ_{C-H} bonding orbital, forming three-centered MOs similar to those found for the septet case. Analogous to the septet case, this can be called a π mechanism since O-p_x is a π-bonding orbital. Passing over the ^{3}TS1 gives the ^{3}IN, which is an LS ferric ($S_{Fe} = ½$) ion ferromagnetically coupled to an alkyl radical ($S_c = ½$). The rebound step on the triplet surface involves a relatively high barrier of 16.5 kcal mol^{-1}, compared to that calculated for the quintet, and so the quintet surface is clearly favored.

The different reactivity of the quintet and triplet oxo-Fe(IV) species can be understood by dividing the barrier to C–H bond activation into three contributions: (a) the geometric rearrangement required to reach the transition state; (b) the Pauli repulsion between the incoming substrate and the iron species; and (c) the orbital interactions between the donor and the acceptor. The main geometrical rearrangements required to reach the transition state are the elongation of the Fe–O bond in the ferryl-oxo species and the breaking of the C–H bond in the substrate. Lengthening the Fe–O bond from its equilibrium bond length in the $(FeO)^{2+}$ species to that found in the TS1 is calculated to be only slightly less favorable for the quintet ($9.4\,kcal\,mol^{-1}$) than for the triplet ($8.1\,kcal\,mol^{-1}$). Therefore, the cost associated with the formation of the oxyl-ferric species on the two surfaces does not explain their different reactivity.

Additional insight comes from considering the geometrical requirements for interaction with the substrate in the transition states. On the quintet surface, the reaction proceeds via the "σ-mechanism" where the Op_z orbital is the electron acceptor, requiring a vertical attack of the C–H bond on the $(FeO)^{2+}$ core in order to maximize orbital overlap. This leads to a nearly colinear Fe–O–H arrangement. More importantly, such an attack geometry substantially reduces the Pauli repulsion between the substrate and the oxo-iron(IV) reactant. Along the triplet surface, the reaction proceeds via the π-mechanism where the $O\text{-}p_x$ orbital is the electron acceptor. Maximum orbital overlap favors a horizontal approach of the substrate (Fe–O–H angle close to 90°), which would involve considerable Pauli repulsion. Consequently, there must be a compromise between maximizing the orbital interactions and minimizing the Pauli repulsion, leading to a Fe–O–H angle close to 120° in ^{3}TS1. This trade-off also leads to an increase in energy of ^{3}TS1 compared to ^{5}TS1 and hence explains the lower reactivity of the triplet species towards C–H bond activation.

The insights from the H-atom transfer step can also be extended to the rebound step. In the quintet rebound step, the final electron acceptor is the weakly π-antibonding $Fe\text{-}3d_{xz,yz}$ orbital, consistent with its low barrier. In the triplet rebound, however, the strongly σ-antibonding $Fe\text{-}3d_{z2}$ orbital is the electron acceptor and so it may not come as a surprise that this is accompanied by a higher barrier.

Given the advantages of the σ-pathway for H-atom abstraction mentioned above, it seems sensible to ask whether a σ-pathway could be operative on the triplet surface as well. This possibility was explored for model iron(IV)–oxo complexes involving

NH_3 and OH ligands, $[Fe(IV)(O)(NH_3)_5]^{2+}$, $[Fe(IV)(O)(OH)_{(axial)}(NH_3)_4]^{+}$, and $[Fe(IV)(O)(OH)_{2(eq)}(NH_3)_3]$ (*49*). For these systems, the σ- and π- pathways were investigated on both the triplet and quintet surfaces. The $^5\sigma$ and $^3\pi$ pathways were similar to those calculated for TauD, with $^5\sigma$ the lowest in energy of the four alternatives. The π-pathways were next in energy, where the triplet and quintet surfaces were found to have comparable barriers for H-atom abstraction. The triplet σ pathway could only be located for $[Fe(IV)(O)(NH_3)_5]^{2+}$ and had the highest barrier at 20.3 kcal mol^{-1}. The large barrier to $^3\sigma$ H-atom abstraction can be attributed to the fact that the final acceptor orbital σ* (FeO) is much higher in energy than for the quintet counterpart. Moreover, the IS Fe(III) center, which is generated on the triplet surface, is also higher in energy compared to the HS Fe(III) center, which evolves on the quintet surface because of reduced spin polarization. For the rebound step, the triplet barriers (σ-type) were higher than those of the quintet, therefore the reactivity of the oxo−iron(IV) complexes toward alkane C−H bond hydroxylation decreases in the order of $\sigma^5 > \pi^5 > \pi^3 > \sigma^3$.

In summary, our studies of C−H bond activation by oxo-iron (IV) species have shown that the quintet oxo-iron(IV) species is the most reactive form. The detailed analysis suggests that this arises because the different spin states have different requirements for the optimal approach of the substrate. Thus, the already complex nature of the reactivity of open-shell systems is further complicated by the fact that the preferred spin state may be different depending on which angle the substrate approaches the metal center. This is clearly a feature that applies more generally than to just high-valent oxo-iron(IV) sites.

III. EPR of Degenerate Systems

Magnetic resonance experiments are usually parameterized by a phenomenological spin Hamiltonian (SH) that only contains spin degrees of freedom. This Hamiltonian only describes the energetics of the magnetic sublevels of the electronic ground state. However, it leads to relatively simple equations that often can be solved by hand and thus serves as an invaluable tool in the analysis of magnetic data. The price to pay for the apparent simplicity of the SH is the introduction of phenomenological parameters such as the *g*-tensor, the zero-field splitting tensor, the hyperfine tensor, or the quadrupole tensor. For orbitally non-degenerate systems, there is an unambiguous relationship between the magnetic sublevels of the electronic ground state

$|\Psi_0^{SM}\rangle$ and the fictitious spin-only basis states $|SM\rangle$ for the solution of the SH eigenvalue equations. This relationship has been extensively reviewed elsewhere and the associated computer programs are widely used (*50,51*).

Electronically degenerate systems, as they arise, for example, from certain d^N configurations in higher than rhombic point groups, exhibit a number of interesting properties related to their degeneracy. First, the number of accessible magnetic sublevels is larger than just $2S+1$, which would be the degeneracy of an orbitally non-degenerate system. Consequently, the energy levels in the presence of relativistic perturbations and external magnetic fields are not well described by the usual SH concept. In particular, if the different spatial members of the degenerate multiplet interact by spin–orbit coupling (SOC), the magnetic effects become exceedingly large (in the literature, this situation is frequently referred to as "in-state SOC" or also as "first-order SOC"). Secondly, since orbitally degenerate systems are subject to Jahn–Teller distortions, there are remarkable effects of vibronic coupling. Both effects have a significant influence on the EPR spectra of such compounds. The following section is devoted to the investigation of the subject for zero-field-splitting parameters.

A. Theory

As indicated above, the SH concept only relates to spin degrees of freedom. It does not refer to the geometric or electronic structure of the system under consideration. The goal of quantum chemistry is to somehow connect the geometric and electronic structure of a given molecular system to its SH parameters. We will present two ways of calculating the *D*-tensor, once a proper description of the electronic structure is given. In order to do so, it is inevitable for (nearly) degenerate cases to use multireference methods. Some of the fundamentals of these methods will be provided below. Subsequently, the Jahn–Teller effect on degenerate transition metal complexes will be discussed.

A.1. Zero-Field Splitting

In the absence of an external magnetic field, orbitally non-degenerate levels with spin multiplicity greater than 2 split due to direct electron spin–spin coupling (in first order) and spin–orbit coupling (in second and higher orders of perturbation theory). This phenomenon is called zero-field splitting (ZFS). The SH that describes this phenomenon can be formulated in

the form $\vec{S}D\vec{S}$ where **D** is a 3×3 tensor and $\vec{S}$ is the spin vector in Cartesian coordinates. In principle, the D-tensor contains six unique components. By passing through its principal axis system and observing that the trace of D just shifts all magnetic sublevels equally, one only needs two values to parameterize the SH: the axial ZFS parameter D, defined as $D = D_{zz} - \frac{1}{2}(D_{xx} + D_{yy})$ and the rhombicity E defined as $E = \frac{1}{2}(D_{xx} - D_{yy})$. The usual convention implies a choice of axis system which guarantees that $0 \leq E/D \leq 1/3$.

One way to calculate the ZFS parameters is through ligand field theory (*52,53*) but for quantitative calculations it is nowadays possible to use accurate correlated *ab initio* methods. It is known that the direct spin–spin contribution (SSC) is dominant for organic molecules, and for a long time it was assumed that for inorganic complexes exclusively the SOC dominates. Nevertheless, exceptions to this rule have been identified (*54,55*).

The spin-orbit mean field (SOMF) operator (*56–58*) is used to approximate the Breit–Pauli two-electron SOC operator as an effective one-electron operator. Using second-order perturbation theory (*59*), one can end up with the working equations:

$$D_{kl}^{SOC-(0)} = -\frac{1}{S^2} \sum_{b(S_b=S)} \Delta_b^{-1} \left\langle 0SS \middle| \sum_i z_{k;i}^{SOMF} \hat{S}_{i;z} \middle| bSS \right\rangle \times \left\langle bSS \middle| \sum_i z_{l;i}^{SOMF} \hat{s}_{i;z} \middle| 0SS \right\rangle \quad (1)$$

$$D_{kl}^{SOC-(-1)} = -\frac{1}{S(2S-1)} \sum_{b(S_b=S-1)} \Delta_b^{-1} \left\langle 0SS \middle| \sum_i z_{k;i}^{SOMF} \hat{s}_{i;+1} \middle| b(S-1)(S-1) \right\rangle \times \left\langle b(S-1)(S-1) \middle| \sum_i z_{l;i}^{SOMF} \hat{s}_{i;-1} \middle| 0SS \right\rangle \quad (2)$$

$$D_{kl}^{SOC-(+1)} = -\frac{1}{(S+1)(2S+1)} \times \sum_{b(S_b=S+1)} \Delta_b^{-1} \left\langle 0SS \middle| \sum_i z_{k;i}^{SOMF} \hat{s}_{i;-1} \middle| b(S+1)(S+1) \right\rangle \times \left\langle b(S+1)(S+1) \middle| \sum_i z_{l;i}^{SOMF} \hat{s}_{i;+1} | 0SS \right\rangle \quad (3)$$

where the first term describes contributions from excited states with the same spin multiplicity as the ground one ($S' = S$), whereas the second and third terms account for contributions from excited states with total spins of $S' = S-1$ and $S' = S+1$, respectively. Here

k and l denote Cartesian components x, y, z, and Δ_b is the energy difference between the ground state and excited state b in the absence of the SOC interaction. The effective one-electron operator $z_{k:i}^{SOMF}$ is described in detail elsewhere (*60*). As an alternative to the perturbation sum truncated at a given number of excited states, one can use quasi-degenerate perturbation theory (QDPT)(*61*). This treats spin–orbit coupling to infinite order, which is more accurate in the case of strong SOC, but at the same time suffers from the same truncation error as a finite sum-over-states.

The spin–spin coupling (SSC) contribution can be calculated directly without imposing any approximation to the integrals or coupling coefficients (*60,61*) using the following formulas:

$$\left\langle aSM\middle|D^{(0)}_{\mathrm{pqrs}}Q^{(0)}_{\mathrm{pqrs}}\middle|a'SM'\right\rangle = \frac{\sqrt{(S+1)(2S+3)}}{\sqrt{S(2S-1)}}\begin{pmatrix} S' & 2 & S \\ M' & 0 & M \end{pmatrix} \times\left\langle aSS\middle|D^{0}_{\mathrm{pqrs}}Q^{0}_{\mathrm{pqrs}}\middle|a'SS\right\rangle \tag{4}$$

Here

$$Q^{(0)}_{\mathrm{pqrs}} = \frac{1}{4\sqrt{6}}\left\{\hat{E}_{\mathrm{pq}}\delta_{\mathrm{sr}} - \hat{S}^{\mathrm{z}}_{\mathrm{ps}}\hat{S}^{\mathrm{z}}_{\mathrm{rq}} + \frac{1}{2}(\hat{S}^{\mathrm{z}}_{\mathrm{ps}}\hat{S}^{\mathrm{z}}_{\mathrm{rq}} - \hat{E}_{\mathrm{pq}}\hat{E}_{\mathrm{rs}})\right\}$$

represents a special two-electron spin density and

$$D^{(0)}_{\mathrm{pqrs}} = \frac{1}{\sqrt{6}}\iint\varphi_{\mathrm{p}}(\mathrm{r}_1)\varphi_{\mathrm{r}}(\mathrm{r}_2)\frac{3r_{1z}r_{2z} - \mathrm{r}_1\mathrm{r}_2}{r_{12}^5}\varphi_q(\mathrm{r}_1)\varphi_s(\mathrm{r}_2)\mathrm{dr}_1\mathrm{dr}_2$$

denotes the two-electron field gradient integrals. Within this second quantization approach, we define the excitation operators $\hat{E}_{\mathrm{pq}}$ and $\hat{S}_{\mathrm{pq}}$ through $\hat{E}_{\mathrm{pq}} = \hat{a}^{\dagger}_{\mathrm{p}}\hat{a}_{\mathrm{q}} + \hat{b}^{\dagger}_{\mathrm{p}}\hat{b}_{\mathrm{q}}$ and $\hat{S}_{\mathrm{pq}} = \hat{a}^{\dagger}_{\mathrm{p}}\hat{a}_{\mathrm{q}} - \hat{b}^{\dagger}_{\mathrm{p}}\hat{b}_{\mathrm{q}}$. The operators $a^{\dagger}_{\mathrm{p}} = a^{\dagger}_{\mathrm{p}\alpha}$and $b^{\dagger}_{\mathrm{p}} = a^{\dagger}_{\mathrm{p}\beta}$, in turn, are creation operators for alpha and beta spin orbitals, respectively. Likewise, $a_{\mathrm{p}} = a_{\mathrm{p}\alpha}$and $b_{\mathrm{p}} = a_{\mathrm{p}\beta}$are the alpha and beta annihilation operators. Analogous to the SOC contribution, the SSC terms can be included either by finite order (in this case, first order) or by QDPT. Similarly, magnetic fields can be included in the QDPT procedure in a straightforward way, which allows one to calculate g-tensors of nearly orbitally degenerate systems.

A.2. Multireference configuration interaction (MR-CI)

It has become apparent that for certain systems the ground-state wavefunction is of genuine multiconfigurational nature and cannot be described qualitatively correctly by a single

configuration as it is done in Hartree–Fock theory. For the present purposes, the most important example of genuine multiconfigurational wavefunctions is transition metal complexes with (nearly) degenerate states. These systems have to be approached with a multiconfigurational ansatz. Here the calculation is divided into two steps. In the first step, one constructs a qualitatively correct approximation to the states of interest and in the second step refines the model as far as possible (or desired) to obtain accurate energies or spectroscopic properties.

In order to build up a reasonable zeroth-order approximation, one needs to include a limited set of configuration state functions (CSFs) that is necessary to describe most of the physics of the system. A point of major importance is the selection of CSFs that are chosen to build up the zeroth-order approximation. There is no best answer to this question and thorough consideration of the system under investigation is crucial in order to gain reasonable results. The most widely used approach is the "complete active space" (CAS) method. Its basic idea is the following: one defines the "active" orbital subset, which should contain most of the physics of the system, and includes m electrons in n active orbitals. All other orbitals have fixed occupations of either 2 or 0. These orbital subspaces are called the internal (doubly occupied) and external (empty) space. Then one constructs all possible CSFs with m electrons in n active orbitals with the desired total spin and performs a full-configuration interaction (CI) calculation within this set of CSFs. Since the set of functions is complete in this many-electron space and the problem is solved iteratively, the method is referred to as "complete active space self consistent field" method, CAS-SCF(m,n). It yields qualitatively correct wavefunctions and energies for multiconfigurational systems.

The second step of the calculation involves the treatment of dynamic correlation effects, which can be approached by many-body perturbation theory (*62*) or configuration interaction (*63*). Multireference coupled-cluster techniques have been developed (*64–66*) but they are computationally far more demanding and still not established as standard methods. At this point, we will only focus on configuration interaction approaches. What is done in these approaches is to regard the entire zeroth-order wavefunction $|\Psi_I^0\rangle$ or its constituent parts $|\phi_J\rangle$ and to perform single and double excitations relative to these "reference" functions. This produces a set of "excited" CSFs $\{|\Omega\rangle\}$ that are used as expansion space for the "configuration interaction" (CI) procedure. The resulting wavefunction may be written as

$$\left|\Psi_I\right\rangle = \sum_J B_{JI}\left|\Omega_J\right\rangle \tag{5}$$

The parameters B_{JI} are determined variationally during the CI step. Since the set of $\{|\Omega\rangle\}$ may include the set of $\{|\phi_J\rangle\}$, one does not write $|\Psi_I\rangle = |\Psi_I^0\rangle + \sum_J B_{JI}|\Omega_J\rangle$ but we will not go into detail here.

The set of $|\Omega\rangle$s may become very large with hundreds of millions of members not being unusual. Due to the huge expansion space, the CI step may become immensely expensive and we will shortly introduce two approaches that address this problem. The first one is the difference-dedicated CI (DDCI) scheme, which was proposed in the 1990s by Malrieu and co-workers (*67,68*). Basically it features a physically motivated *a priori* truncation of the expansion space. It has been shown that up to second order in quasi-degenerate perturbation theory the most numerous classes of excitations that contain configurations with two holes in the internal space and two particles in the virtual space do not enter the expression for energy differences. Thus, if one is interested in state energy difference as, for example, in the calculation of spectroscopic parameters, this scheme provides a considerable speed-up at almost no loss of accuracy. In quantum chemical terminology, these excitations are said to have four degrees of freedom, where a degree of freedom is either a hole in the internal space or a particle in the virtual space. It is possible to further reduce the expansion space by avoiding all excitations that have more than two degrees of freedom. Corresponding to the number of allowed degrees of freedom, the methods are referred to as MR-DDCI2 and MR-DDCI3. A more recent variant of this approach is the spectroscopy-oriented CI (SORCI) (*69*), which makes use of the DDCI truncation scheme. Briefly summarized, it first performs a MR-DDCI2 calculation in order to set up a reduced molecular orbital space with a set of approximately optimal orbitals. Subsequently, an MR-DDCI3 calculation is performed within this reduced orbital space giving the final results.

In summary, it can be said that multireference CI methods provide a balanced description of static and dynamic correlation effects. This comes at the cost of a considerably increased computational demand compared to single-reference methods. Nevertheless, a multireference approach is inevitable for systems with a genuine multiconfigurational character such as symmetric transition metal compounds.

A.3. The Jahn–Teller effect

Jahn and Teller introduced in 1937 their famous theorem (*70*) stating that any non-linear molecule with symmetry high enough to produce a degenerate electronic ground state would

spontaneously distort in order to lower the symmetry and lift the degeneracy. The idea behind the Jahn–Teller theorem is that in the case of degenerate electronic states the adiabatic approximation does not hold any more. Thus, a separation of the electronic and nuclear Schrödinger equation is not possible, which means that the electronic and nuclear motions have to be coupled in some way, resulting in what is called vibronic coupling.

Even though the motion of the nuclei is not negligible any more, its effect on the electrons is still smaller than the interactions among the electrons themselves. Hence, the vibronic coupling can be treated perturbatively, with the unperturbed system being the purely electronic problem and the vibronic coupling being the perturbing potential. Accordingly, the dynamic energy potential involving the interactions between nuclei and electrons is expanded around a minimum observed from the pure electronic problem.

$$V(r,Q) = V(r,0) + \sum_a \left(\frac{\partial V}{\partial Q_a}\right)_0 Q_a + \frac{1}{2}\sum_{a,b}\left(\frac{\partial^2 V}{\partial Q_a \partial Q_b}\right)_0 Q_a Q_b + \ldots \tag{6}$$

with Q_a, Q_b being some normal modes of vibration of the right symmetry. Since the first derivative of the potential is equivalent to the force acting on the molecule, it has to vanish for the equilibrium geometry. In order to calculate the force for a specific electronic state, we will have to calculate the matrix element

$$\left\langle \Phi_{el} \middle| \frac{\partial V}{\partial Q_a} \middle| \Phi_{el} \right\rangle = \left\langle \Phi_{el} \middle| F_a \middle| \Phi_{el} \right\rangle \tag{7}$$

and if this is non-zero, the molecule will spontaneously distort. Instead of explicitly calculating the matrix elements, group theory can already tell if they will be zero or not just by calculating the direct product: $\Gamma^{el} \otimes \Gamma^{F_a} \otimes \Gamma^{el} = \Gamma^{el} \otimes \Gamma^{el} \otimes \Gamma^{F_a}$. For this term not to vanish, the direct product $\Gamma^{el} \otimes \Gamma^{el}$ must have a common non-reducible representation with Γ^{F_a}. In the case of an E_g ground state, it has been shown (*71,72*) that the potential energy surface for the two degenerate electronic states will split with energy eigenvalues given by the equations

$$\varepsilon_{\pm}^{v}(\rho,\phi) = \frac{1}{2}K_E\rho^2 \pm \rho[F_E^2 + G_E^2\rho^2 + 2F_E G_E \rho \cos(3\phi)]^{\frac{1}{2}} \tag{8}$$

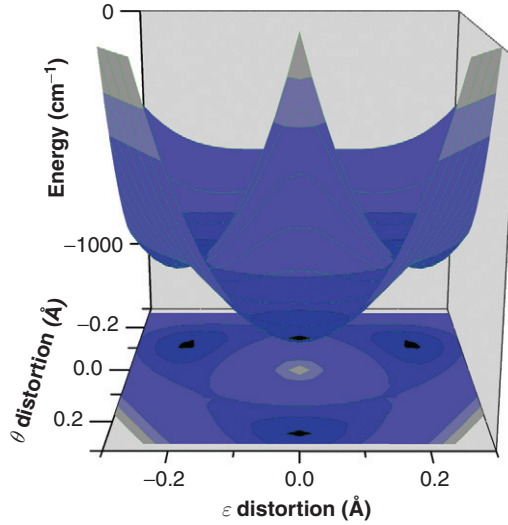

FIG. 7. The potential energy surface for the two E_g normal modes of vibration calculated at the CASSCF(4,5)/TZVPP level of theory.

With $\rho = (Q_\theta^2 + Q_\epsilon^2)^{\frac{1}{2}}$ being the Jahn–Teller radius, F_E the linear vibronic coupling constant, G_E the quadratic vibronic coupling constant, K_E the force constant for the E_g normal mode of vibration, and Q_θ, Q_ε the two degenerate vibrations of e_g symmetry.

Accordingly, the energy surface should have three equal and symmetric minima that belong to the D_{4h} symmetry point group and, of course, one maximum at the point of O_h symmetry. This was confirmed by calculations, using the CASSCF (*4,5*) method, for the $Cr(H_2O)_6^{2+}$ complex. In this complex, Cr^{2+} has a d^4 electronic configuration that leads to an E_g electronic ground state and hence exhibits strong vibronic coupling. Figure 7 shows the calculated potential energy surface with three equidistant minima around a central maximum at the O_h symmetric point.

B. APPLICATIONS

Detailed analysis of the components of the ZFS parameters was performed in a recent study (*55*). Through the use of multireference SORCI (*69*) and CASSCF methods, the contribution of direct SSC was calculated over the previously mapped Jahn–Teller potential energy surface. Figure 8 shows the decomposition of the total D value into contributions from spin–orbit and direct spin–spin terms, across the e_θ normal mode of vibration.

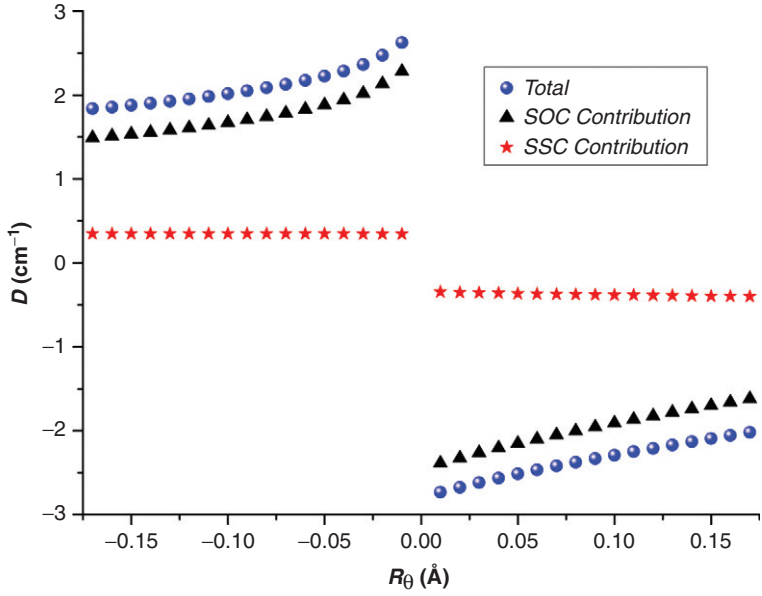

FIG. 8. Decomposition of the total D value to spin–orbit (SOC) and spin–spin (SSC) contributions for $Cr(H_2O)_6^{2+}$.

The plot of the direct SSC reveals that the value of the direct SSC does not depend on the molecular geometry. This fact demonstrates that this is mainly a first-order effect, thus justifying the use of first-order perturbation theory for its description. Moreover, it becomes obvious that the SSC contribution to the ZFS is significant and cannot be neglected in a quantitative description.

Another issue in the calculation of D is the treatment of SOC effects. Due to the orbital degeneracy, those effects are potentially large and perturbation theory may not be appropriate for their description. This subject was investigated by comparing the values of D and E gained by second-order perturbation theory (Eqs. (1)–(3)) with the results of quasi-degenerate perturbation theory (QDPT) calculations, which account for SOC effects to infinite order. In Fig. 9 we present a plot of both results for the value of D versus displacement along the Jahn–Teller active e_θ mode of vibration. The deviation sums up to 1.4% or 0.033 cm^{-1}, showing that second-order perturbation theory is fully adequate for the calculation of these values.

Finally, it is interesting to compare the contributions from states with the same spin multiplicity with the ground state

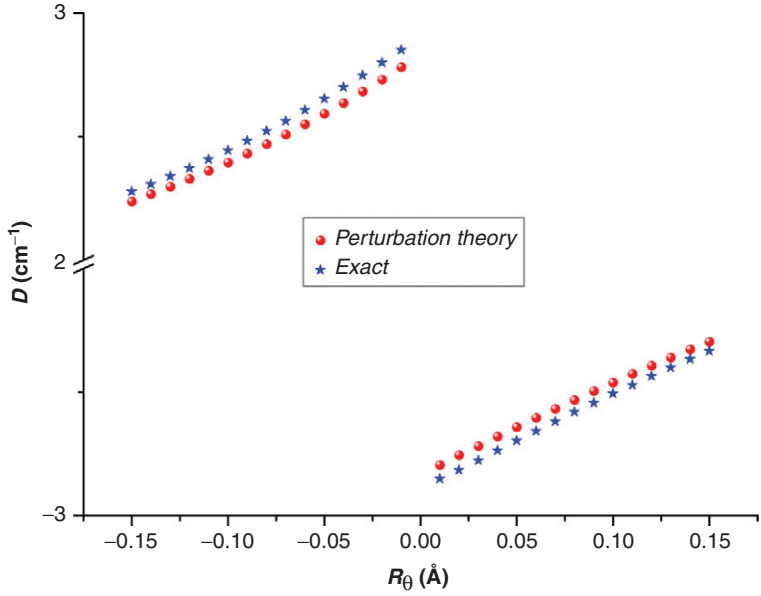

FIG. 9. Comparison between the second-order perturbation theory and quasi-degenerate perturbation theory for the D value of $Cr(H_2O)_6^{2+}$.

and contributions from triplet excited states. In Fig. 10 the calculated energy spectrum for the lower electronic states of the complex along the e_g normal mode of vibration is presented. All quintet states and the lower triplet states have been included. Here the splitting of the degenerate states due to the lowering of the symmetry can nicely be seen.

Table 1 contains the contributions from each of the previously calculated electronic states to the spin–orbit component of the calculated D value for the ground electronic state, both in the elongation and in compression cases. It can be seen that the quintet states have the largest contribution. Nevertheless, these data clearly demonstrate the importance of the triplet states. Taken together, their contribution to the total D value is almost as large as the quintet contribution. It is also noteworthy that the excited triplet-state $^3T_{2g}$ contributes considerably with $0.25\,cm^{-1}$. For a total D value of $-2.4\,cm^{-1}$ calculated using the SORCI method, $1.020\,cm^{-1}$ is due to in-state SOC, whereas $1.068\,cm^{-1}$ arises from SOC to excited triplet states. Of course, the remaining $0.360\,cm^{-1}$ is due to direct SSC effects. In summary, these results reveal that both spin–flip transitions for SOC contributions and

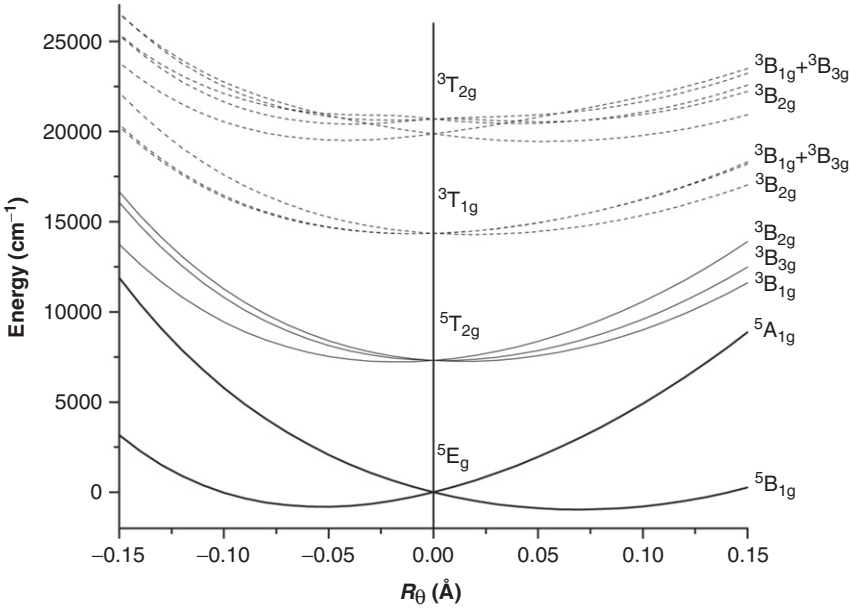

FIG. 10. Energy spectrum for the lower electronic states of $Cr(H_2O)_6^{2+}$, along the path of the e_θ normal mode of vibration, calculated using the CASSCF(4,5) method and the TZVPP basis set.

TABLE I

CONTRIBUTION OF DIFFERENT EXCITED STATES TO THE SPIN–ORBIT COMPONENT OF THE D VALUE

State in O_h	State in D_{2h}	Contribution to D (cm^{-1}) Elongation	Compression
$^3T_{2g}$	$^3B_{3g}$	0.12	−0.07
	$^3B_{2g}$	−0.12	−0.09
	$^3B_{1g}$	0.01	0.08
	Sum:	−0.25	−0.08
$^3T_{1g}$	$^3B_{3g}$	−0.37	1.04
	$^3B_{2g}$	−0.40	−0.10
	$^3B_{1g}$	0.00	0.00
	Sum:	−0.77	0.94
$^5T_{2g}$	$^5B_{3g}$	0.17	0.58
	$^5B_{2g}$	0.15	0.65
	$^5B_{1g}$	−1.40	0.00
	Sum:	−1.24	1.23

direct SSC effects play an important role for the calculation of ZFS tensors in orbitally degenerate transition metal complexes.

IV. Metal–Radical Interactions

Metal–radical complexes play an important role in inorganic and bioinorganic chemistry (*73*). These complexes contain metal ions bound to non-innocent ligands, which often are open-shell organic radicals. To understand their role in biological systems and their catalytic activity, quantum chemical calculations can be applied in complement to spectroscopy. Due to the complicated bonding situation, a proper description of the electronic structure for this kind of complex can be challenging. This section provides practical guidelines for the calculation of electronic structures and spectroscopic properties along with some examples for the study of metal–radical interactions. A more detailed description of the theoretical background can be found in the literature (*74–76*).

A. Geometry Optimization

An accurate molecular geometry is of major importance for the calculation of the electronic structures and spectroscopic properties. The geometry optimization always needs to be performed before the calculation of other properties. Considering the size of most metal–radical systems (100–200 atoms), DFT is a suitable method for quantum chemical calculations as it is reliable and economical. "Pure" density functionals, for example, BP86, PBE, TPSS, may take advantage of the use of density fitting to speed up the calculation, which is particularly efficient for the geometry optimizations. However, one has to use them with some caution as they are known to overestimate the covalency of chemical bonds and tend to display a bias toward low-spin states (*77*). Hybrid functionals include a fraction of Hartree–Fock (HF) exchange, which strongly favors high-spin states. Hence, these functionals benefit from this error compensation and yield more reliable spin-state energetics. B3LYP is by far the most commonly used hybrid functional whereas other functionals with different extent of HF exchange, such as PBE0 and TPSSh, can be considered as alternatives.

In general, DFT calculations are known to converge fast with the size of the basis set. Although polarized double-zeta basis sets are a minimum requirement, polarized triple-zeta basis sets are

recommended to obtain more reliable results, especially for the transition metals. In addition, relativistic effects can become important for first row transition metals and heavier elements so that at least scalar relativistic effects should be included in the calculations. The use of effective core potentials (ECPs), which replace a large number of core electrons with an effective one-electron operator, is usually an adequate way of approximately accounting for these effects in the geometry optimizations (*78*). However, ECPs have several limitations and have often been shown to yield less than optimal results for the calculation of spin-state energetics and magnetic properties (*79,80*). Besides, explicit treatment of all electrons is imperative for the determination of spectroscopic parameters and any other properties that require a correct description of the electronic density (*81*). Therefore, employing a scalar relativistic all-electron approach is always recommended, using, for example, the zeroth-order regular approximation (ZORA) (*82,83*) along with appropriately constructed basis sets (*84–86*).

B. Broken Symmetry and Corresponding Orbital Transformation

The spin in a metal–radical complex can be grouped into two local sites (A and B), which can be ferromagnetically or antiferromagnetically coupled to each other. Special attention is paid to the case of antiferromagnetic coupling, in which a single determinant wave function is no longer an appropriate description. *Ab initio* multireference methods would be necessary, but the required number of active space orbitals to generate the configuration state functions makes these methods extremely expensive and limits their applicability to small molecules. An alternative method based on DFT and known as "broken symmetry" approach was proposed early on by Noodleman (*87*) and becomes helpful when one needs to identify a spin-coupled metal–radical system from a classical coordination compound with closed-shell ligands.

The broken symmetry (BS) wavefunction consists of a single determinant that contains all doubly occupied orbitals but two singly occupied orbitals, with opposite spin localized on separated fragments of the molecule (referred to as magnetic orbitals φ_A and φ_B). The magnetic orbitals are spin orthogonal but spatial non-orthogonal and the shape of the magnetic orbitals is determined by the variational principle. For a system exhibiting antiferromagnetic coupling, only a weak interaction between the two

fragments is expected. If the interaction between the two fragments is strong and the spatial overlap between the two magnetic orbitals ($S_{AB} = \langle \varphi_A | \varphi_B \rangle$) becomes unity, the two magnetic orbitals have converged to one delocalized orbital and a closed-shell determinant is obtained.

Due to the spin polarization effect, the magnetic orbitals can be difficult to identify from a spin-unrestricted calculation. Since the total energy of a Kohn–Sham determinant is invariant under unitary transformations between the spin-up orbitals among each other and spin-down orbitals among each other, one can arrange each spin-up orbital to overlap at most with each spin-down orbital on the basis of the corresponding orbital transformation (COT) (*88–90*). Then, the molecular orbitals (MOs) are ordered into pairs of maximum similarity between spin-up and spin-down orbitals and can be separated into three groups: (i) the MOs with spatial overlap close to one (doubly occupied MOs), (ii) the MOs with spatial overlap significantly different from zero or one (spin-coupled pair MOs), and (iii) the spin-up MOs that are unmatched with the spin-down MOs for a state with $M_S > 0$ (singly occupied MOs). Through the corresponding orbital transformation, one can visualize the spin-coupled pair of the BS wavefunction. The abbreviation BS(m,n) is introduced to represent a broken symmetry calculation with m unpaired spin-up and n unpaired spin-down electrons.

A point of concern is the spin density of the BS wavefunction. While the electron density optimized in the BS method is of high quality—as is the electron density of DFT for closed-shell systems—the spin density is more problematic. If one considers a case with just two unpaired electrons in a singlet state (e.g., a biradical), the BS method would provide large positive spin density on one fragment and large negative spin density on the other. This is clearly unphysical, since for a singlet state the spin density is precisely zero at each and every point in space. The shortcoming arises from the fact that the BS method only makes use of a single determinant whereas for a true singlet state with two unpaired electrons a two-determinant wavefunction is mandatory. Analogous arguments hold for higher spin states of course. The BS spin density is nevertheless still not completely unphysical—if one ignores the sign, one might look at it as a density of effectively unpaired electrons. However, spectroscopic observables should not be calculated directly from the BS spin density but instead from equations that contain some spin projection (*2*).

A comparison between BS and closed-shell calculations was shown for diamagnetic $[Fe(CN)_2(L)]^-$ (L = pentane-2,4-dione-bis(*S*-alkylisothiosemicarbazonato)) (**1**) (*91,92*). Through the

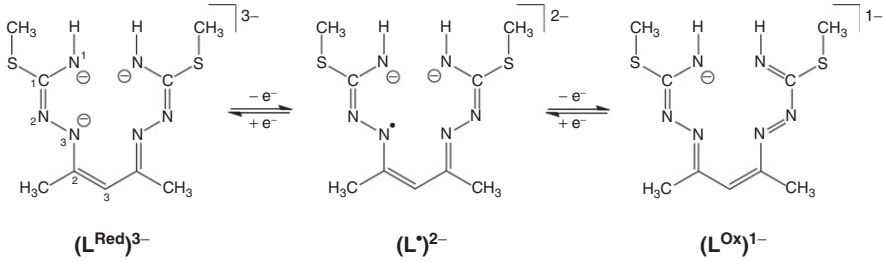

FIG.11. Three redox states of ligand L (pentane-2,4-dione-bis(S-alkylisothiosemicarbazonato).

π-conjugated structure, the electron transfer to or from ligand L generates three redox states (Fig. 11). Two electronic structures are possible for complex **1**: (i) a low-spin ferrous ($S_{Fe} = 0$) and a monoanionic diamagnetic ligand $(L^{Ox})^{1-}$ and (ii) a low-spin ferric ($S_{Fe} = 1/2$) antiferromagnetically coupled with a dianionic π-radical ligand $(L^{\cdot})^{2-}$ ($S_L = 1/2$). The geometry optimizations carried out for a closed-shell and a BS(1,1) state revealed the BS(1,1) solution to be lower in energy than the closed-shell solution by 3 kcal mol^{-1}.

The DFT calculations of the hypothetical molecules, $Na^{I}(L^{Ox})$, $Zn^{II}(L^{\cdot})$, and $Ga^{III}(L^{Red})$, show the increase of N1–C1 and N2–N3 bond distances and the decrease of the C1–N2 bond distance upon reduction of the ligand (by about 0.03 Å). The bond distances in the ligand L in $Zn^{II}(L^{\cdot})$ are close to the BS(1,1) structure, which is in agreement with the crystal structure of complex **1**. Figure 12 shows the MO scheme of the BS(1,1) solution for **1** containing two doubly occupied Fe d-orbitals, two unoccupied Fe d-orbitals, and a spin-coupled pair between a singly occupied Fe d-orbital and a ligand orbital. The respective spin density plot shows opposite sign between the iron center and the ligand with an equal amount of spin.

The geometric parameters of the ligand L, in addition to the calculated total energy, confirm the electronic structure of complex **1** as a low-spin Fe(III) ($S_{Fe} = 1/2$) antiferromagnetically coupled with a dianion π-radical ligand $(L^{\cdot})^{2-}$ ($S_L = 1/2$) in a total spin $S_t = 0$ ground state. One should always compare calculated structures with, if available, the crystal structure to ensure that the electronic structure is obtained for the right geometry. Other experimental data are also significant for the study of electronic structures of metal–radical complexes, as will be discussed in the following sections.

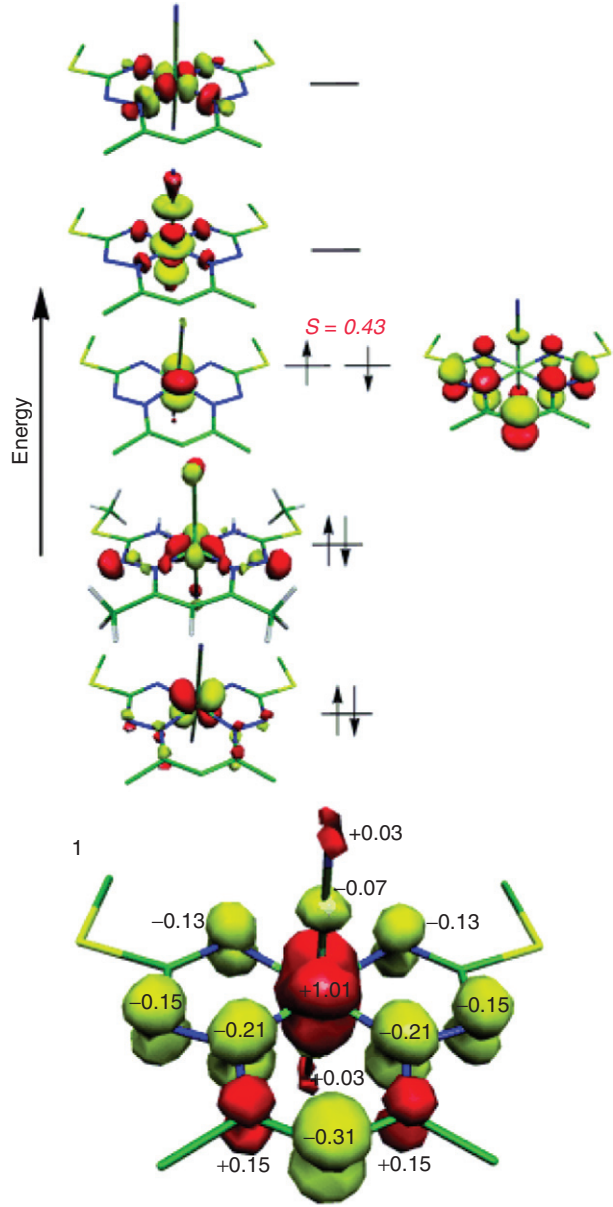

FIG.12. Qualitative MO scheme for complex **1** ($S_t = 0$, BS(1,1)) (top) and spin density plot with Mulliken spin populations (bottom).

C. Mössbauer Parameters

Several possible electronic structures may be obtained from spectroscopic data and geometry calculations. The common way to determine the most likely structure is the total energy. However, sometimes, the calculated energy differences of possible electronic states are within the error limits of the calculations (an optimistic error bar is $2-5\,\mathrm{kcal\,mol^{-1}}$ (*93*)). In this situation, it becomes difficult to identify the proper electronic structure description on the basis of the total energies alone. Thus, the calculation of spectroscopic properties can lead to a better understanding and verification of the calculated geometric and electronic structures of the compound being studied.

Since iron is abundant in biological systems and several oxidation states are possible depending on the influence of the geometry of iron coordination and ligands (*94*), iron complexes constitute a large group among the known metal–radical systems. ^{57}Fe Mössbauer spectroscopy is an important analytical tool to study these complexes since the primary Mössbauer parameters, the isomer shift δ and the quadrupole splitting ΔE_q, provide information about the valence and spin states of the iron centers (*76,95*). Comparison of calculated and experimental Mössbauer parameters may confirm or invalidate an electronic structure description.

The isomer shift is the shift of the transition energy of the sample ^{57}Fe nuclei from spin state $I = 1/2$ to $I = 3/2$ relative to the transition energy measured for ^{57}Fe foil. It has been shown that the isomer shift is proportional to the total electron density at the iron nucleus ρ_0, which in turn is dependent on, among other factors, the binding ligands. A linear regression of calculated ρ_0 values and a set of experimentally obtained isomer shifts for known compounds give linear fit parameters that can be used to estimate an isomer shift of other unknown iron compounds from the calculated electron density (*96–98*). It is noteworthy that each combination of density functional and basis set requires its own set of fitting parameters (*98*).

Due to the electric quadrupole interaction, the $M_I = \pm 1/2$ and $M_I = \pm 3/2$ components of the $I = 3/2$ state of ^{57}Fe split up, giving rise to the quadrupole splitting. Derived from the interaction of the nuclear quadrupole moment with the electric field gradient at the iron nuclei, ΔE_Q provides information about the asymmetry of the electron density around the iron nucleus. The electric field gradient at the iron nucleus can be calculated to obtain ΔE_Q (*97*). Since both δ and ΔE_Q are related to the electron density at the nucleus, basis sets with an enlarged flexibility at the core region

are required for Mössbauer calculations. Inclusion of relativistic effect by the ZORA formalism may also be considered (*97*).

An example of using calculated Mössbauer parameters to verify electronic structures has been shown for the oxidation of $[Fe(py)(S_2C_6H_4)_2]^{1-}$ (**2**) (*91*). Complex **2** is well characterized as containing two closed-shell dianions (benzene-1,2-dithiolate), an apical pyridine, and an intermediate-spin Fe(III) ($S_{Fe} = S_t = 3/2$). Upon one-electron oxidation, $[Fe(py)(S_2C_6H_4)_2]^0$ (**3**) is obtained (*91*). Whereas the $[Fe(PR_3)(S_2C_6H_4)_2]^0$ analog has been described as a Fe(IV) species(*99*) ($S_{Fe} = S_t = 1$) with two closed-shell dianionic dithiolates and a neutral phosphine, the $[Fe(py)(S_2C_6H_4)_2]^0$ (**3**), on the other hand, is shown by spectroscopic data to contain a Fe(III) ($S_{Fe} = 3/2$) center antiferromagnetically coupled to mixed valence ligands (dithiolate^{2-}/dithiolate^{1-}, $S_L = 1/2$) giving a total spin $S_t = 1$.

The spin-unrestricted $S_t = 3/2$ structure for complex **2** was calculated (*91*), and the MO scheme in Fig. 13 shows one doubly occupied, three singly occupied, and one unoccupied Fe d-orbital. Moreover, the spin density plot reveals that all unpaired electrons are mainly located at the iron center. The calculated Mössbauer parameters are in good agreement with the experimental data ($\delta^{calc} = 0.39$ and $\Delta E_Q^{calc} = 3.43$; $\delta^{exp} = 0.33$ and $\Delta E_Q^{exp} = 3.03$) (*91*), thus confirming that the electronic structure description is correct. For complex **3**, a standard spin-unrestricted DFT calculation with $S_t = 1$ was performed, but it converged to a BS(3,1) solution (*91*). Analysis of the wavefunction showed that the spin-coupled pair consists of a Fe d-orbital and a ligand π-orbital (Fig. 13) having a spatial overlap of 0.61. The spin density plot of **3** represents three α-spin on the Fe and one β-spin distributed over dithiolate ligands. Again the calculated and experimental Mössbauer parameters are in good agreement ($\delta^{calc} = 0.34$ and $\Delta E_Q^{calc} = 3.17$; $\delta^{exp} = 0.29$ and $\Delta E_Q^{exp} = 3.02$).

The calculated Mössbauer parameters are consistent with the experiment and confirm the proposed electronic structures of both complexes. The results explain the similar Mössbauer parameters observed for both **2** and **3** despite their different ground spin states ($S_t = 3/2$ for **2** and $S_t = 1$ for **3**) since they both contain Fe(III) in an intermediate spin state, binding to closed-shell dithiolate ligands for **2** and open-shell π-radical ligand for **3**. Hence, the oxidation of **2** is concluded to be ligand based.

In addition to the isomer shift and the quadrupole splitting, it is possible to obtain the hyperfine coupling tensor from a Mössbauer experiment if a magnetic field is applied. This additional parameter describes the interactions between unpaired electrons and the nuclear magnetic moment. Three terms contribute to the hyperfine coupling: (i) the isotropic Fermi contact, (ii) the spin−dipole

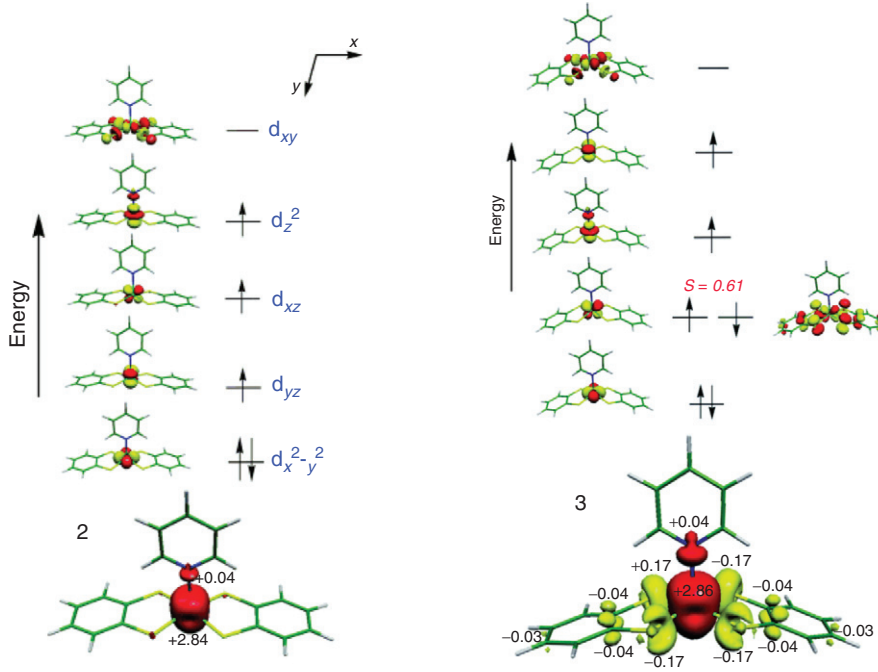

FIG. 13. Qualitative MO schemes for complex **2** ($S = 3/2$) and **3** ($S = 1/2$, BS(3,1)) (top), and spin density plots with Mulliken spin populations (bottom).

interaction, and (iii) the spin–orbit interaction. Whereas the first two terms are first-order properties, the last term is a response property and has to be determined by solving a set of coupled-perturbed equations (*74,100*). Hyperfine coupling tensors can also be extracted from EPR experiments, as will be discussed in more detail below.

D. IR Spectra and Vibrational Frequencies

Vibrational frequencies measured in IR experiments can be used as a probe of the metal–ligand bond strength and hence for the variation of the electronic structure due to metal–radical interactions. Theoretical estimations of the frequencies are obtained from the molecular Hessian, which can be straightforwardly calculated after a successful geometry optimization. "Pure" density functionals usually give accurate vibrational frequencies due to an error cancellation resulting from the neglect of

anharmonicity and compensating deviations from the true harmonic frequency (*101*). Hybrid functionals, on the other hand, exhibit an improved accuracy for the calculation of harmonic frequencies. However, if the effect of anharmonicity is taken into account, frequency calculations with hybrid functionals suffer from a systematic error compared to experimental values. One way to overcome this deficiency is to use scaling factors that shift uniformly the computed frequencies so that they are closer to experimental values. However, instead of trying to predict the absolute frequency, it is often more desirable to predict the relative trend within a series of similar compounds.

E. Study of the $\{FeNO\}^{6-8}$ Series

The electron transfer series of $[Fe(NO)(cyclam\text{-}ac)]^{x}$ ($x = +2, +1$, and 0) (*102*) (Fig. 14) that composes the $\{FeNO\}^{n}$ ($n = 6$, 7, and 8) complex series in the convenient notation suggested by Enemark and Feltham (*103*) is a good example that clearly shows the value of DFT calculations applied together with experimental Mössbauer and IR spectroscopy to gain insight into the electronic structure of metal–radical complexes.

The calculated NO stretching frequencies, in good agreement with experiment, decrease significantly, going from $\{FeNO\}^{6}$ to $\{FeNO\}^{8}$ (ν_{calc}(NO): 1871, 1600, and 1331 cm^{-1}; ν_{exp}(NO): 1904, 1607, and 1271 cm^{-1}, respectively), as the nitrosyl ligand is reduced and the NO bond becomes weaker. The changes in the electronic and geometric structure also affect the *trans*-carboxylate group. An increase of the electron density on the NO ligand along the $\{FeNO\}^{6}$ to $\{FeNO\}^{8}$ series leads to the loss of Fe–NO back-bonding, which reduces the electron donation from the carboxylate group. Therefore, more electronic charge is delocalized in the C=O π^* orbital. This results in a decrease of the observed and calculated C=O stretching frequency going from

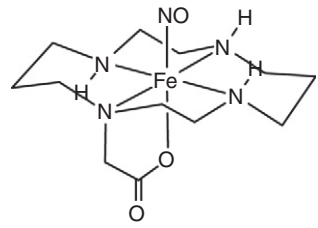

Fig.14. Structure of the complex Fe(NO)(cyclam-ac).

$\{FeNO\}^6$ to $\{FeNO\}^8$ (ν_{calc}(CO): 1758, 1706, and 1659 cm^{-1}; ν_{exp}(CO): 1713, 1657, and 1619 cm^{-1}, respectively).

Mössbauer isomer shifts are strongly related to the back-bonding ability of the ligand known from a comparative study of NO, CO, PR_3, and SR_2 ligands in six-coordinate iron complexes (*104*), which explains the change in the observed isomer shifts of the $[Fe(NO)(cyclam\text{-}ac)]^x$ compound series ($\delta^{exp} = 0.02$, 0.28, and 0.41 mm s^{-1} for $x = +2$, +1, 1, and 0, respectively). The DFT calculations of the isomer shift suggest that all compounds are low-spin Fe(II) species (within an error of 0.05 mm s^{-1}). Reduction of the ligand from NO^+ to NO· and NO^- decreases its π-acceptor strength such that the isomer shift increases from $\{FeNO\}^6$ to $\{FeNO\}^8$ species with no change of the iron oxidation state. Briefly summarized, Mössbauer and IR spectroscopy together with DFT calculations confirm the idea that the electron reduction of $[Fe(NO)(cyclam\text{-}ac)]^{2+}$ occurs at the NO ligand and not at the low-spin Fe(II) center.

V. Magnetic Properties of Oligonuclear Clusters

In this part we focus on current theoretical approaches to the magnetic properties of transition metal clusters, extending the metal–radical spin coupling discussed in Section IV to the more complex and general case of metal–metal spin coupling. First we provide an outline of the necessary theoretical framework based on DFT and the BS formalism. Emphasis is placed on recently developed methods that allow for the calculation of hyperfine coupling parameters in systems containing more than two exchange-coupled centers (*105*). Specific literature examples of importance to the oxygen evolving complex (OEC) of Photosystem II (PSII) are also highlighted (*106,107*).

A. Theory

The calculation of magnetic parameters such as the hyperfine coupling constants and *g*-factors for oligonuclear clusters is of fundamental importance as a tool for the evaluation of spectroscopic data from EPR and ENDOR experiments. The hyperfine interaction is experimentally interpreted with the spin Hamiltonian (SH) $H = \hat{S} \cdot \tilde{A} \cdot \hat{I}$, where $\hat{S}$ is the fictitious electron spin operator related to the ground state of the cluster, $\tilde{A}$ is the hyperfine tensor, and $\hat{I}$ is the nuclear spin operator. Consequently, it is

possible to experimentally assign the ground-state S_t of an oligonuclear cluster. However, the apparent ground state of the system does not arise from well-defined unpaired spins in well-characterized molecular orbitals, but is typically described in terms of the magnetic coupling between N spin subsystems interacting via $N(N-1)/2$ Heisenberg exchange couplings J_{ij} according to the phenomenological Heisenberg–Dirac–van Vleck Hamiltonian:

$$H_{\mathrm{HDvV}} = -2\sum J_{ij}\hat{S}_i\hat{S}_j \qquad (9)$$

As an example, it is helpful to consider the case of $Mn^{III}Mn^{IV}$ dimers for which experimentally the ground state has been determined to be $S_t = ½$, arising from an antiferromagnetic coupling between the four unpaired electrons of Mn^{III} and the three unpaired electrons of Mn^{IV} (*106*).

While theoretical models for the exchange interaction in transition metal dimers are well- understood (*108*), the electronic structure of oligonuclear open-shell transition metal systems still poses significant challenges to quantum chemistry. The principal reason is that the calculation of the ground-state wavefunction in these systems is an inherently multideterminental problem. Therefore, the contemporary Kohn–Sham formulation of DFT is inadequate for an accurate representation of such states (*2,75,109–111*). Fortunately, however, this problem can be usually circumvented by an effective description of the antiferromagnetic states through the use of the BS formalism (*87,112–114*). Within the BS approach, the antiferromagnetic state is represented by a single unrestricted determinant where the singly occupied opposite-spin "magnetic orbitals" are variationally allowed to assume spatial parts that are largely localized on the different magnetic centers. It has been noted previously in the literature (*90,115*) and should be further stressed that the BS approach gives a good description of the electron density of the antiferromagnetic ground state, even though it provides a qualitatively incorrect spin density. Therefore, computed properties that do not depend on the spin density are typically as reliable as any straightforward DFT calculation can afford. On the other hand, calculations of spin-dependent parameters require the use of spin-projections to extract values that can be meaningfully compared to experiment values (*2*).

The Heisenberg exchange coupling constants J can be calculated from the BS DFT solutions utilizing the approaches of Noodleman (*87*), Ruiz (*116*), or Yamaguchi (*117–119*), which differ in the assumptions made regarding the strength of the

exchange interaction. From the three approaches the expression of Yamaguchi is preferred, because it consistently covers the full range of weak to strong exchange coupling limits. For a dimer the corresponding formula is

$$J = -\frac{E_{\mathrm{HS}} - E_{\mathrm{BS}}}{\langle \hat{S}^2 \rangle_{\mathrm{HS}} - \langle \hat{S}^2 \rangle_{\mathrm{BS}}} \tag{10}$$

and the exchange coupling constants thus obtained determine the levels of the spin−state ladder:

$$E(S) = -JS(S+1) \tag{11}$$

The comparison of the calculated spin energy levels with the levels probed experimentally has proven to be a useful tool in the comparison of theory and experiment. Of course, the complexity of the problem increases considerably with increasing number of magnetically interacting nuclei, because the number of distinct spin configurations and the associated number of BS solutions that must be considered scale as 2^N. For $N \geq 4$, a further complication arises owing to the overdetermined nature of the problem, in the sense that the number of possible BS solutions exceeds the number of unknown J values. As we have shown recently, this situation can be most efficiently dealt with using a singular value decomposition scheme (*105*), which ensures that the values obtained represent the optimal least-squares fit. This approach also accounts for the non-orthogonality between the high-spin and the individual BS solutions (*120*). Nevertheless, great care should be taken when comparing computed and experimentally fitted J values; the appropriate course of action is to obtain the spectrum of eigenvalues by direct diagonalization of the Hamiltonian (*105*) and directly base any comparisons with experiment on physically meaningful energy levels.

Once a description of the electronic structure has been obtained in these terms, it is possible to proceed with the evaluation of spectroscopic properties. Specifically, the hyperfine coupling constants for oligonuclear systems can be calculated through spin projection of site-specific expectation values. A full derivation of the method has been reported recently (*105*) and a general outline will only be presented here. For the calculation of the hyperfine coupling constants, the total system of N transition metal centers is viewed as composed of N subsystems, each of which is assumed to have definite properties. Here the isotropic hyperfine is considered, but similar considerations apply for the anisotropic hyperfine coupling constants. For the nucleus K in subsystem A, it can be

shown that the general equation that connects the BS solution to experimentally comparable hyperfine values has the form

$$A_{\mathrm{iso}}^{(K)} = A_{\mathrm{iso,site}}^{(K)} \left(\frac{\langle S_z^{(A)} \rangle}{S_t} \right) \tag{12}$$

where $\langle S_z^{(A)} \rangle$ is the site spin expectation value and S_t is the fictitious spin of the system, as discussed previously. The intrinsic site-specific value $A_{\mathrm{iso,site}}^{(K)}$ is determined from the appropriate BS solution by the following equation:

$$A_{\mathrm{iso,site}}^{(K)} = \pm A_{\mathrm{iso,BS}}^{(A)} \left(\frac{\langle S_z \rangle_{\mathrm{BS}}}{S_A} \right) \tag{13}$$

Here S_A is the specific spin on site A and the positive or negative sign is applied depending on the larger proportion of α or β spin at the site, respectively. From the preceding analysis it becomes obvious that the key component for calculating hyperfine coupling constants that are comparable to experiment is the site spin expectation $\langle S_z^{(A)} \rangle$. Assuming the strong exchange coupling limit and the validity of the effective Heisenberg–Dirac–van Vleck Hamiltonian, the eigenstates $|I\rangle$ of he Hamiltonian for N spin subsystems are

$$\left| I \right\rangle = \left| S_A, S_B, \ldots, S_N, S M_S \right\rangle = \sum C_I^{S_A M_{S_A} \ldots S_N M_{S_N}} \left| S_A M_{S_A}, \ldots, S_N M_{S_N} \right\rangle \tag{14}$$

Once these eigenstates have been determined, the individual site spin expectation values can be obtained as

$$\left\langle S_z^{(A)} \right\rangle = \sum \left| C_I^{S_A M_{S_A} \ldots S_N M_{S_N}} \right|^2 M_{S_A} \tag{15}$$

where $\left| C_I^{S_A M_{S_A} \ldots S_N M_{S_N}} \right|^2$ g gives the weight of the basis state $\left| S_A M_{S_A}, \ldots, S_N M_{S_N} \right\rangle$ in the ground-state eigenfunction $|I\rangle$ describing the Kramers doublet of lowest energy.

The method described above is of general validity and can be applied to transition metal clusters of arbitrary shape, size, and nuclearity. It should be noted that in the specific case of a system comprising only two interacting exchanged coupled centers, our general treatment yields the same result as that of Bencini and Gatteschi (*121*), which was specifically formulated for dimers. In this case, the relation between the spin-projection coefficient and the on-site spin expectation value is simply given by

$$c_A = \frac{\langle S_z^{(A)} \rangle}{S_t} \tag{16}$$

In the weak coupling limit, the effect of ZFS must be accounted for in the effective Hamiltonian:

$$H_{\text{eff}} = -2\sum J_{ij}\hat{S}_i \cdot \hat{S}_j + \sum \hat{S}_i \cdot \tilde{D}^{(i)} \cdot \hat{S}_i \tag{17}$$

The local ZFS tensor for site i is given by $\tilde{D}^{(i)}$. In extreme cases where the ZFS is very large or the J coupling is very small the ground state may not be describable by the standardSH. If the ground state remains a doublet upon the inclusion of the ZFS, then the approximation of $S_{eff}=S_t$ is still valid even though the ground state is no longer an eigenstate of $\hat{S}^2$. The effect of ZFS on magnetic and spectroscopic properties has been studied in detail for specific mixed-valence manganese dimers (*106*), although the extension to oligonuclear systems has not been firmly established at this point. Regarding the evaluation of the g-tensor, for systems with two strongly interacting centers, the g-tensor can be assumed to be made up of contributions from both the high-spin and broken-symmetry solutions, with localized site contributions from centers A and B:

$$\begin{aligned} g_A &= \frac{1}{2S_A}(g_{\text{HS}}M_{\text{S}}^{\text{HS}} + g_{\text{BS}}M_{\text{S}}^{\text{BS}}) \\ g_B &= \frac{1}{2S_B}(g_{\text{HS}}M_{\text{S}}^{\text{HS}} - g_{\text{BS}}M_{\text{S}}^{\text{BS}}) \end{aligned} \tag{18}$$

These g-tensor site matrices g_A and g_B are subsequently employed for the computation of the total molecular g-tensor of the antiferromagnetic state by multiplication with the respective spin projection coefficients $c_i = \langle S_z^{(i)} \rangle / S_t$. Applications of this approach have been successfully demonstrated on dinuclear $Mn^{III}Mn^{IV}$ models of the manganese catalases (*122,123*). To date, the calculation of the molecular g-tensor for an oligonuclear system of $N>2$ exchange-coupled spin subsystems has not been fully developed.

B. Applications

Several recent studies have been devoted to understanding and predicting the magnetic and spectroscopic properties of oligonuclear transition metal clusters, concentrating particularly on

manganese compounds (*105,106,122–125*). Here, we will highlight selected applications on complexes containing four metal centers, since these better demonstrate both the novel theoretical aspects of the current approach and its potential to probe systems of increasing size and complexity.

The first case study focuses on the tetranuclear complex $[Mn_4O_6(bpy)_6]^{4+}$ (Fig. 15), synthesized and characterized by Girerd and co-workers (*126,127*). This compound was selected because its well-characterized structural and magnetic properties serve as an ideal platform for the theoretical treatment of magnetic exchange interactions in tetranuclear clusters that resemble the OEC. Additionally, the all-Mn^{IV} form of the complex is readily reduced by γ-ray irradiation to a mixed-valence $Mn^{III}Mn^{IV}_3$ form that exhibits a spin-doublet ground state (*127*), corresponding exactly to the S_2 state of the OEC in Photosystem-II (*128*). Detailed EPR studies of the reduced form of the complex have yielded accurate manganese hyperfine coupling constants, thus enabling the reliable evaluation and validation of the new theoretical approach previously outlined.

The electronic structure of the complex was determined in the framework of the BS approach, obtaining the six possible exchange coupling constants J from a set of one high-spin and seven BS solutions. The results confirm that $[Mn_4O_6(bpy)_6]^{4+}$ adopts a singlet ground state with three dominant antiferromagnetic exchange pathways (J_{AB}, J_{BC}, and J_{CD}), whereas the molecular symmetry is clearly reflected in the calculated J parameters, with $J_{AB} = J_{CD}$. Significant variations in the absolute

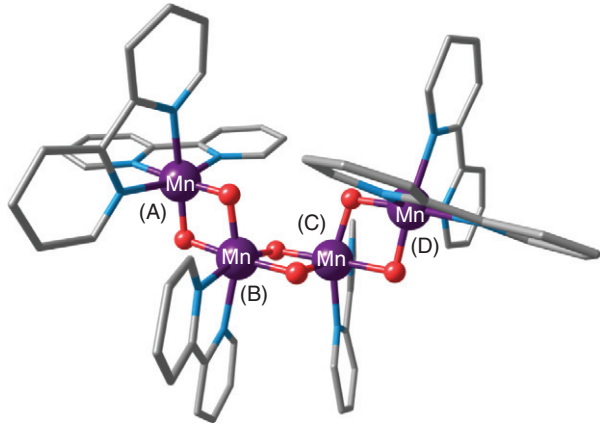

FIG. 15. Structure of the tetranuclear manganese cluster $[Mn_4O_6(bpy)_6]^{4+/3+}$.

J values were observed using different types of functional, usually deviating significantly from the experimentally fitted parameters. It must be emphasized that comparison between computed and experimental J values is complicated not simply because of the variable performance of the density functionals themselves; the fitting of the experimental data is an equally important parameter of the problem. Specifically, since only a few energy levels are probed in thermal depopulation experiments (up to approximately $3kT$), the fitting process is often under-determined and can lead to several possible sets of exchange coupling constants that reproduce the observed behavior equally well. By carefully analyzing the dependence of the first few energy levels on the J values for the present case, we have established that there is indeed a whole range of J values that produce an essentially identical spectrum of low-energy levels (Fig. 16), with the experimentally reported set being only one of the possibilities.

Thus, as pointed out previously, any comparisons with experiment must rely on energy levels obtained by full diagonalization of the Heisenberg Hamiltonian. Following this approach, we have contrasted experimental and theoretical results for the lowest energy levels as well as the resulting Boltzmann populations that directly relate to observable quantities such as the magnetic susceptibility. These comparisons led to the conclusion that the hybrid meta-GGA functional TPSSh (*129*) best matches

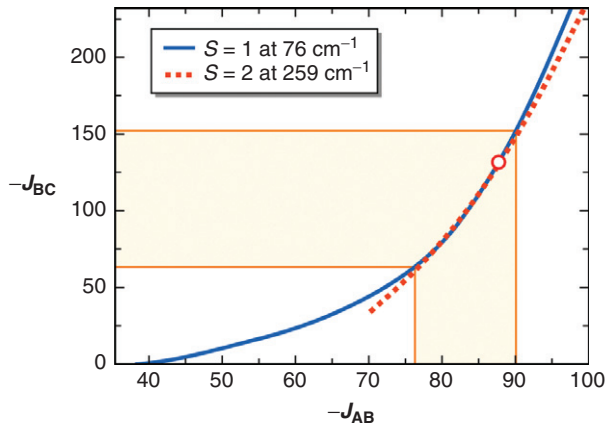

FIG. 16. Range of J values (cm^{-1}) that reproduce the first two energy levels at the experimentally deduced separations for $[Mn_4O_6(bpy)_6]^{4+}$. The shaded area represents the range of coincidence and the circle indicates the pair of experimentally fitted J parameters.

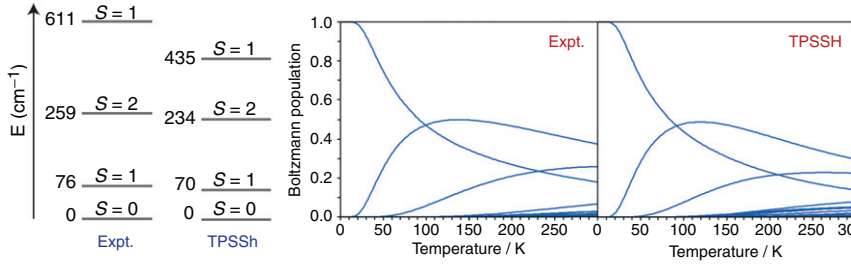

FIG.17. Comparison of lowest energy levels (cm^{-1}) and Boltzmann populations between experimental and computed (TPSSh) values.

experiment (Fig. 17) and hence can be safely assumed to afford the most accurate description of the electronic structure of the tetranuclear complex. It is worth noting that the superior performance of TPSSh has been evidenced in several recent studies (*85,130–132*) for a wide range of properties of transition metal systems.

Moving to the evaluation of the hyperfine parameters for the reduced $Mn^{III}Mn^{IV}_3$ form of the complex, $[Mn_4O_6(bpy)_6]^{3+}$, a fundamental prerequisite involves the calibration of the method with reference to a set of reliable experimental data. This is necessary because the currently available density functional methods significantly underestimate the isotropic hyperfine coupling constants because of the inadequate description of spin polarization (*100,133*). The deviations from experiment are systematic and can be compensated for by inclusion of a scaling factor that is specific for a given combination of functional and basis set (the CP(PPP) basis sets are recommended for the transition metal atoms) (*96*). For the TPSSh functional, an extensive calibration study on a set of manganese monomers and dimers led to a scaling factor of 1.49 for the non-relativistic case (*106*). Inclusion of scalar relativistic effects was shown to reduce the scaling factor to 1.24 but not to make the results more systematic. Therefore, the use of the non-relativistic approach seems preferable on practical grounds, keeping in mind that the TPSSh scaling factor of 1.49 accounts in approximately equal parts for spin polarization effects and scalar relativistic corrections.

The computed exchange couplings again reveal antiferromagnetic coupling between neighboring Mn ions, yielding an $S_t = ½$ ground state. Thus, the appropriate spin configuration (BS state) to use in the calculation of the ^{55}Mn hyperfine coupling constants (HFCs) is the one described $|2, -3/2, 3/2, -3/2\rangle$, where the components of the state correspond to the M_S values of individual Mn

centers. Following the theoretical procedure outlined in the preceding section, the site spin expectation values $\langle S_z^{(K)} \rangle$ were first calculated and found to be in fair agreement with the literature values that can be deduced by correlating measured and given constant site HFCs (*105,127*). Having the values of the site spin expectation coefficients, it is then straightforward to calculate the HFCs of the relevant BS state $A_{\mathrm{iso,BS}}^{(K)}$ and convert these quantities into site values, $A_{\mathrm{iso,site}}^{(K)}$. Multiplying the site values with the corresponding $\langle S_z^{(K)} \rangle / S_t$ ratio yields the final projected isotropic and anisotropic ^{55}Mn HFCs. A summary of all computed results and their comparison with experiment is provided in Table 2.

From the anisotropic contributions to the HFCs, it is confirmed that the reduced Mn_A^{III} site is the main source of anisotropy in the system. The computed values reproduce the rhombicity of all anisotropic hyperfine tensors, but there is a clear tendency of overestimation. In any case, since the anisotropic components are at least an order of magnitude smaller than the isotropic contributions to the HFC, it is more appropriate and useful to focus on the latter. All isotropic HFCs have the correct signs with respect to the

TABLE II

CALCULATED (SCALED TPSSH) ^{55}MN HYPERFINE PARAMETERS (MHZ): SITE VALUES AND SPIN-PROJECTED ISOTROPIC AND ANISOTROPIC HFCS FOR $[Mn^{III}Mn^{IV}{}_3(Bpy)_6]^{3+}$; COMPARED WITH EXPERIMENT

	Mn_A(III)	Mn_B(IV)	Mn_C(IV)	Mn_D(IV)
Calc.				
$A_{iso,site}^{(K)}$	−205.9	−249.0	−246.5	−199.2
$\langle S_z^{(K)} \rangle$	0.930	−0.500	0.509	−0.440
$A_{iso}^{(K)}$	−383.0	249.0	−251.0	175.3
A_x	−25.8	−10.6	9.3	1.3
A_y	90.0	13.9	4.0	7.7
A_z	−64.2	−3.3	−13.3	−9.0
Expt.				
$\langle S_z^{(K)} \rangle$	0.989	−0.521	0.432	−0.392
$\lvert A_{iso}^{(K)} \rvert$	449.2	228.3	189.4	171.5
A'_x	14.3	4.0	7.2	6.6
A'_y	−41.1	−1.4	0.1	−2.0
A'_z	26.8	−2.5	−7.3	−4.6

majority or minority spin population carried by each fragment. Interestingly, the site values display a useful and informative correlation with the local coordination environment of each center, as seen from the fact that the Mn ions display similar site values for identical environments: about −200 MHz for N_4O_2 ligation and −250 MHz on average for N_2O_4 ligation. As for the final projected isotropic HFCs, the magnitudes as well as the trends of the calculated values are in good agreement with the experimental data, thus confirming the validity of the approach.

The present theoretical scheme is also useful in isolating, analyzing, understanding, and ultimately predicting the effect of individual parameters on particular observables. For example, using the present tetramanganese cluster as a test case, it is possible to quantify the influence of the J_{BC}/J_{AB} ratio on the site-spin expectation values and the isotropic ^{55}Mn hyperfine coupling constants. Assuming $J_{BC} = J_{CD}$, which is to be expected from the calculated values of the exchange coupling constants, treatment of both antiferromagnetic ($J_{BC}/J_{AB} \geq 0$) and ferromagnetic ($J_{BC}/J_{AB} \leq 0$) situations results in the correlation plot illustrated in Fig. 18. The plot demonstrates the strong dependence of the computed values on the J_{BC}/J_{AB} ratio and their abrupt change when the ratio approaches zero. For the entire antiferromagnetic branch, the HFCs of the Mn_A^{III} and Mn_C^{IV} sites are particularly sensitive to the ratio of exchange coupling constants with a variation that reaches 100 MHz.

Another example of detailed insight into the behavior of calculated ^{55}Mn HFCs comes from investigating the dependence of these quantities on the secondary (not nearest-neighbor) exchange coupling constants. Such a study would test, for example, the validity of simplifications that exclude the secondary

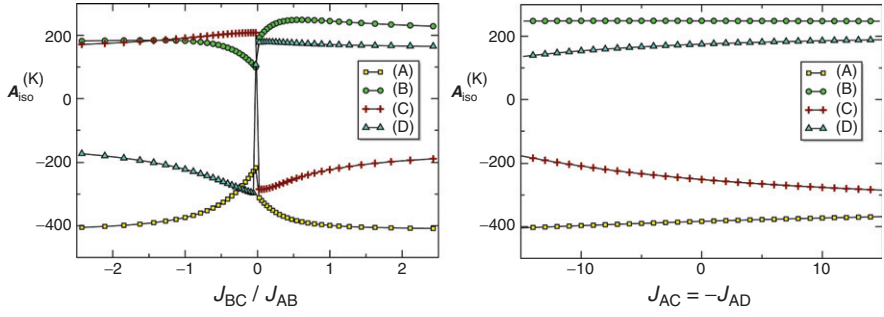

FIG. 18. Dependence of isotropic ^{55}Mn hyperfine parameters (MHz) on the J_{BC}/J_{AB} ratio (left) and the magnitude of the secondary exchange coupling constants J_{AC}, J_{AD} (right) for $[Mn^{III}Mn^{IV}{}_3(bpy)_6]^{3+}$.

exchange couplings from the theoretical treatment. Thus, focusing on the influence of the J_{AC} and J_{AD}, we can consider the two possible configurations $J_{AC} = J_{AD}$ and $J_{AC} = -J_{AD}$. When the two exchange coupling constants have the same sign, the calculated on-site coefficients and the isotropic HFCs remain practically unchanged for the entire range of J values. This is in stark contrast to the case of two J constants having opposite signs. Figure 18 shows the strong sensitivity of computed HFCs for both Mn_C^{IV} and Mn_D^{IV} sites, with variations reaching 100 MHz and 50 MHz, respectively. On the contrary, Mn centers A and B remain practically unaffected by the J_{AC} values for the entire range studied. We note at this point that the dependence of the calculated site expectation values and ^{55}Mn HFCs on the secondary set of J constants can be rationalized in terms of the intrinsic tilting displayed by the four site-spin vectors for each metal ion with respect to the total spin of the system. The modification of the tilt angle upon variation of individual exchange coupling constants can indeed offer an additional perspective on the behavior of the system (*105*).

The case study of the tetranuclear manganese complex presented above and the specific examples of structure/spectroscopy correlations have established the validity of the proposed methods and set the stage for more ambitious applications. The first such application has been the recent evaluation of several structural models of the OEC in the S_2 state ($Mn^{III}Mn^{IV}_3$) of the Kok cycle (*107*). Twelve structural models were considered, 10 of which were based on Mn_4O_5Ca core topologies derived by polarized EXAFS spectra. Figure 19 shows one of the models included in the set.

The study first of all identified the ligation environments that cause localization of the unique Mn^{III} center at a particular site. Subsequently, through the calculation of exchange coupling constants with the BS approach described previously and subsequent diagonalization of the Heisenberg Hamiltonian, the complete spectrum of magnetic sublevels was obtained. This led to a classification of the models in those that display a doublet ground state and correspond to the multiline signal (MLS) of the S_2 state of the OEC and those that display a sextet ground state and could be related to the $g = 4.1$ signal of the S_2 state. Following the description of the electronic structure, the ^{55}Mn hyperfine coupling constants were computed for the S_2 MLS state models and the quantities involved in the individual steps of the procedure (site-spin expectation values, intrinsic site isotropic hyperfine parameters, and projected ^{55}Mn isotropic hyperfine constants) were analyzed with respect to the geometry and electronic structure of each model. Importantly, the ^{55}Mn HFCs were

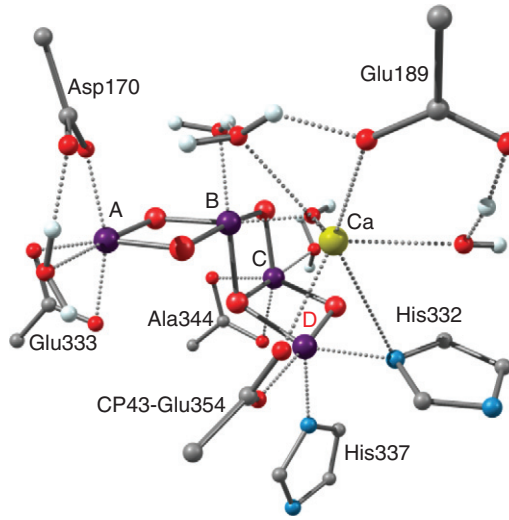

FIG. 19. One of the structures included in an extensive evaluation study of magnetic and spectroscopic properties for models of the S_2 state of the oxygen evolving complex.

shown to react sensitively to structural distortions and hence may serve to distinguish between different structural proposals. Therefore, the present approach emerges as a useful contributor to the effort of maximizing the information content of contemporary EPR and ENDOR experiments and, ultimately, of relating the available spectroscopic data for the various oxidation states of the OEC with actual geometric features (*107*).

It should be clear from the preceding examples that theoretical studies of this type serve not simply to validate computational predictions by detecting potential sources of error, but also to identify the origins of particular spectroscopic characteristics, establish trends, and uncover correlations between structural or electronic features and spectroscopic observables. It remains to be seen in future applications how far this approach can take us in establishing reliable connections between structural parameters and spectroscopic properties for larger and more complex oligonuclear transition metal systems.

VI. Concluding Remarks

In this chapter we have covered some topics of current interest in theoretical inorganic and bioinorganic chemistry. In one way or

another all of the subjects treated in this chapter are related to the fact that open-shell transition metals display a high degree of electronic complexity. This shows up in their reaction pathway that will frequently show multistate reactivity. Likewise, the magnetic and electronic properties of open-shell transition metals can be very complicated, as in the case of Jahn–Teller systems, and special techniques need to be employed to successfully model them. The intricate bonding situations that are created by exchange coupling (in essence, nothing but a very weak chemical bond) in metal–radical systems and oligonuclear metal clusters are another area that is highly challenging to theory. We hope that it became evident that DFT in its present form is already able to deal with many of the subtleties of open-shell transition metals, their reactions, and their properties. DFT is, however, neither perfectly accurate nor universally reliable. Specifically, the calculations on the complicated systems covered here are not of "black-box" character, and it is considered unlikely that this can be achieved in the future. Hence, insight into the actual chemistry and electronic structure of the systems on the side of the theoretician is required. Second, it is of utmost importance to seek feedback from experiments wherever and whenever possible. In our opinion, high-resolution spectroscopy is a very good way to obtain that feedback. Methods to directly link spectroscopy and electronic structure theory have been developed and will continue to be developed to the benefit of a happy marriage between experimentalists and theoreticians.

References

1. Neese, F.; Petrenko, T.; Ganyushin, D.; Olbrich, G. *Coord. Chem. Rev.* **2007**, *251*, 288.
2. Neese, F. *Coord. Chem. Rev.* **2009**, *253*, 526.
3. See the special issue High valent iron intermediates in biology; *J. Inorg. Biochem.* **2006**, *100*, 419–880.
4. Ortiz de Montellano, P. R. *Cytochrome P450: Structure, Mechanism and Biochemistry*; 3rd ed.; Kluwer Academic/Plenum Publisher: New York, **2004**.
5. Krebs, C.; Fujimori, D. G.; Walsh, C. T.; Bollinger, J. M., Jr. *Acc. Chem. Res.* **2007**, *40*, 484.
6. Costas, M.; Mehn, M. P.; Jensen, M. P.; Que, L., Jr. *Chem. Rev.* **2004**, *104*, 939.
7. Que, L., Jr. *Acc. Chem. Res.* **2007**, *40*, 493.
8. Rohde, J. U.; In, J. H.; Lim, M. H.; Brennessel, W. W.; Bukowski, M. R.; Stubna, A.; Munck, E.; Nam, W.; Que, L., Jr. *Science* **2003**, *299*, 1037.
9. van der Ploeg, J. R.; Weiss, M. A.; Saller, E.; Nashimoto, H.; Saito, N.; Kertesz, M. A.; Leisinger, T. *J. Bacteriol.* **1996**, *178*, 5438.

10. Hanauske-Abel, H. M.; Günzler, V. *J. Theor. Biol.* **1982**, *94*, 421.
11. Siegbahn, P. E. M.; Borowski, T. *Acc. Chem. Res.* **2006**, *39*, 729.
12. Siegbahn, P. E. M. *J. Biol. Inorg. Chem.* **2006**, *11*, 695.
13. Klamt, A.; Schüürmann, G. *J. Chem. Soc., Perkin Trans.* **1993**, *2* 799.
14. Miertus, S.; Scrocco, E.; Tomasi, J. *Chem. Phys.* **1981**, *55*, 117.
15. Cammi, R.; Tomasi, J. *J. Comput. Chem* **1995**, *16*, 1449.
16. Sinnecker, S.; Rajendran, A.; Klamt, A.; Diedenhofen, M.; Neese, F. *J. Phys. Chem A.* **2006**, *110*, 2235.
17. Senn, H. M.; Thiel, W. *Angew. Chem., Int. Ed.* **2009**, *48*, 1198.
18. Senn, H. M.; Thiel, W. In: *Atomistic Approaches to Modern Biology. From Quantum Chemistry to Molecular Simulations*; *Vol. 268*; Ed. Reiher, M.; Springer: Berlin, Germany, **2007**, pp 173−290.
19. Siegbahn, P. E. M.; Himo, F. *J. Biol. Inorg. Chem.* **2009**, *14*, 643.
20. Siegbahn, P. E. M. *Q. Rev. Biophys.* **2003**, *36*, 91.
21. Jensen, F. *Introduction to Computational Chemistry*; John Wiley & Sons: New York, **1999**
22. Sinnecker, S.; Svensen, N.; Barr, E. W.; Ye, S.; Bollinger, J. M., Jr.; Neese, F.; Krebs, C. *J. Am. Chem. Soc.* **2007**, *129*, 6168.
23. Ye, S.; Neese, F. *submitted*.
24. Neese, F.; *ORCA - version 2.6*; Universität Bonn: Bonn, Germany, **2008**.
25. Becke, A. D. *J. Chem. Phys.* **1993**, *98*, 5648.
26. Lee, C. T.; Yang, W. T.; Parr, R. G. *Phys. RevB.* **1988**, *37*, 785.
27. Schafer, A.; Huber, C.; Ahlrichs, R. *J. Chem. Phys.* **1994**, *100*, 5829.
28. Schafer, A.; Horn, H.; Ahlrichs, R. *J. Chem. Phys.* **1992**, *97*, 2571.
29. Weigend, F.; Häser, M.; Patzelt, H.; Ahlrichs, R. *Chem. Phys. Lett.* **1998**, *294*, 143.
30. Neese, F.; Olbrich, G. *Chem. Phys. Lett.* **2002**, *362*, 170.
31. Neese, F.; Wennmohs, F.; Hansen, A.; Becker, U. *Chem. Phys.* **2009**, *356*, 98.
32. Eichkorn, K.; Treutler, O.; Ohm, H.; Häser, M.; Ahlrichs, R. *Chem. Phys. Lett.* **1995**, *242*, 652.
33. Eichkorn, K.; Weigend, F.; Treutler, O.; Ahlrichs, R. *Theor. Chem. Acc.* **1997**, *97*, 119.
34. Weigend, F.; Köhn, A.; Hättig, C. *J. Chem. Phys.* **2002**, *116*, 3175.
35. Groves, J. T.; Mcclusky, G. A. *J. Am. Chem. Soc.* **1976**, *98*, 859.
36. Shaik, S.; Hirao, H.; Kumar, D. *Acc. Chem. Res.* **2007**, *40*, 532.
37. Fiedler, A.; Schroder, D.; Shaik, S.; Schwarz, H. *J. Am. Chem. Soc.* **1994**, *116*, 10734.
38. Schröder, D.; Schwarz, H. *Angew. Chem., Int. Ed.* **1995**, *34*, 1973.
39. Shaik, S.; Danovich, D.; Fiedler, A.; Schroder, D.; Schwarz, H. *Helv. Chim. Acta* **1995**, *78*, 1393.
40. Shaik, S.; Kumar, D.; de Visser, S. P.; Altun, A.; Thiel, W. *Chem. Rev.* **2005**, *105*, 2279.
41. de Visser, S. P. *J. Am. Chem. Soc.* **2006**, *128*, 9813.
42 de Visser, S. P. *J. Am. Chem. Soc.* **2006**, *128*, 15809.
43. Ensing, B.; Buda, F.; Gribnau, M. C.M.; Baerends, E. J. *J. Am. Chem. Soc.* **2004**, *126*, 4355.
44. Bernasconi, L.; Baerends, E. J. *Eur. J. Inorg. Chem*. **2008**, 1672.
45. Bernasconi, L.; Louwerse, M. J.; Baerends, E. J. *Eur. J. Inorg. Chem.* **2007**, 3023.
46. Griffith, J. S. *The Theory of Transition Metal Ions*; Cambridge University Press: Cambridge, **1964**.
47. Ye, S.; Neese, F. *Curr. Opin. Chem. Biol.* **2009**, *13*, 89.

48. Michel, C.; Baerends, E. J. *Inorg. Chem.* **2009**, *48*, 3628.
49. Geng, C.; Ye, S.; Neese, F. *Angew. Chem. Int. Ed.* **2010**, *49*, 5717.
50. Kaupp, M.; Bühl, M.; Malkin, V. G. (Eds.) *Calculation of NMR and EPR parameters. Theory and Applications*; Wiley-VCH: Weinheim, Germany, **2004**.
51. Neese, F.; Solamon, E. I. In: *Magnetoscience – From Molecules to Materials*; Vol. IV; Eds. Miller, J. S., Drillom, M.; Wiley: New York, **2003**, pp. 345–466.
52. Figgis, B.N.; Hitchman, M.A. *Ligand Field Theory and its Applications*; Wiley-VCH: New York, **2000**.
53. Ballhausen, C.J. *Introduction to Ligand Field Theory*; McGraw-Hill: New York, **1962**.
54. Neese, F. *J. Am. Chem. Soc.* **2006**, *128*, 10213.
55. Liakos, D.G.; Ganyushin, D.; Neese, F. *Inorg. Chem.* **2009**, *48*, 10572.
56. Berning, A.; Schweizer, M.; Werner, H.J.; Knowles, P.J.; Palmieri, P. *Mol. Phys.* **2000**, *98*, 1823.
57. Neese, F. *J. Chem. Phys.* **2005**, *122*, 034107.
58. Hess, B.A.; Marian, C.M.; Wahlgren, U.; Gropen, O. *Chem. Phys. Lett.* **1996**, *251*, 365.
59. Neese, F.; Solomon, E.I. *Inorg. Chem.* **1998**, *37*, 6568.
60. Ganyushin, D.; Neese, F. *J. Chem. Phys.* **2006**, *125*, 024103.
61. Ganyushin, D.; Neese, F. *J. Chem. Phys.* **2008**, *128*, 114117.
62. Andersson, K.; Roos, B.O. In; *Modern Electronic Structure Theory*; Ed. Yarkony, D.; World Scientific: Singapore, **1995**, p. 55.
63. Buenker, R.; Peyerimhoff, S. *Theor. Chem. Acc.* **1974**, *35*, 33.
64. Pal, S.; Rittby, M.; Bartlett, R.J.; Sinha, D.; Mukherjee, D. *J. Chem. Phys.* **1988**, *88*, 4357.
65. Szalay, P.G.; Bartlett, R.J. *Chem. Phys. Lett.* **1993**, *214*, 481.
66. Mahapatra, U.S.; Datta, B.; Mukherjee, D. *J. Chem. Phys.* **1999**, *110*, 6171.
67. Miralles, J.; Castell, O.; Caballol, R.; Malrieu, J.-P. *Chem. Phys.* **1993**, *172*, 33.
68. Miralles, J.; Daudey, J.-P.; Caballol, R. *Chem. Phys. Lett.* **1992**, *198*, 555.
69. Neese, F. *J. Chem. Phys.* **2003**, *119*, 9428.
70. Jahn, H.A.; Teller, E. *Proc. R. Soc. Ser. A* **1937**, *161*, 220.
71. Bersuker, I.B. *Chem. Rev.* **2001**, *101*, 53.
72. Bersuker, I.B. *The Jahn-Teller Effect*; Cambridge University Press; Cambridge, **2006**.
73. Ray, K.; Petrenko, T.; Wieghardt, K.; Neese, F. *Dalton Trans.* **2007**, 1552.
74. Piligkos, S.; Slep, L.D.; Weyhermüller, T.; Chaudhuri, P.; Bill, E.; Neese, F. *Coord. Chem. Rev.* **2009**, *253*, 2352.
75. Neese, F. *J. Biol. Inorg. Chem.* **2006**, *11*, 702.
76. Neese, F. *Curr. Opin. Chem. Biol.* **2003**, *7*, 125.
77. Fouqueau, A.; Casida, M.E.; Daku, L.M.L.; Hauser, A.; Neese, F. *J. Chem. Phys.* **2005**, *122*, 044110.
78. Frenking, G.; Antes, I.; Böhme, M.; Dapprich, S.; Ehlers, A.W.; Jonas, V.; Neuhaus, A.; Otto, M.; Stegmann, R.; Veldkamp, A.; Vyboishchikov, S.F. *Rev. Comp. Chem.* **1996**, *8*, 63.
79. Güell, M.; Luis, J.M.; Solà, M.; Swart, M. *J. Phys. Chem. A* **2008**, *112*, 6384.
80. Cirera, J.; Ruiz, E. *C. R. Chim.* **2008**, *11*, 1227.
81. Vyboishchikov, S.F.; Sierraalta, A.; Frenking, G. *J. Comput. Chem.* **1997**, *18*, 416.
82. van Lenthe, E.; Snijders, J.G.; Baerends, E.J. *J. Chem. Phys.* **1996**, *105*, 6505.
83. van Wüllen, C. *J. Chem. Phys.* **1998**, *109*, 392.

84. Pantazis, D.A.; Chen, X.Y.; Landis, C.R.; Neese, F. *J. Chem. Theory Comput.* **2008**, *4*, 908.
85. Bühl, M.; Reimann, C.; Pantazis, D.A.; Bredow, T.; Neese, F. *J. Chem. Theory Comput.* **2008**, *4*, 1449.
86. Pantazis, D.A.; Neese, F. *J. Chem. Theory Comput.* **2009**, *5*, 2229.
87. Noodleman, L. *J. Chem. Phys.* **1981**, *74*, 5737.
88. Amos, A.T.; Hall, G.G. *Proc. R. Soc. Ser. A* **1961**, *263*, 483.
89. King, H.F.; Stanton, R.E.; Kim, H.; Wyatt, R.E.; Parr, R.G. *J. Chem. Phys.* **1967**, *47*, 1936.
90. Neese, F. *J. Phys. Chem. Solids* **2004**, *65*, 781.
91. Chlopek, K.; Muresan, N.; Neese, F.; Wieghardt, K. *Chem- Eur. J.* **2007**, *13*, 8390.
92. Knof, U.; Weyhermüller, T.; Wolter, T.; Wieghardt, K.; Bill, E.; Butzlaff, C.; Trautwein, A.X. *Angew. Chem. Int. Ed. Engl.* **1993**, *32*, 1635.
93. Grimme, S. *J. Phys. Chem. A* **2005**, *109*, 3067.
94. Crichton, R.R. *Inorganic Biochemistry of Iron Metabolism*; Ellis Horwood Limited: West Sussex, **1991**.
95. Gütlich, P.; Link, R.; Trautwein, A. *Mössbauer Spectroscopy and Transition Metal Chemistry*; Springer: Heidelberg, **1978**.
96. Neese, F. *Inorg. Chim. Acta* **2002**, *337*, 181.
97. Sinnecker, S.; Slep, L.D.; Bill, E.; Neese, F. *Inorg. Chem.* **2005**, *44*, 2245.
98. Römelt, M.; Ye, S.; Neese, F. *Inorg. Chem.* **2009**, *48*, 784.
99. Sellmann, D.; Geck, M.; Knoch, F.; Ritter, G.; Dengler, J. *J. Am. Chem. Soc.* **1991**, *113*, 3819.
100. Neese, F. *J. Chem. Phys.* **2003**, *118*, 3939.
101. Neugebauer, J.; Hess, B.A. *J. Chem. Phys.* **2003**, *118*, 7215.
102. Serres, R.G.; Grapperhaus, C.A.; Bothe, E.; Bill, E.; Weyhermuller, T.; Neese, F.; Wieghardt, K. *J. Am. Chem. Soc.* **2004**, *126*, 5138.
103. Enemark, J.H.; Feltham, R.D. *Coord. Chem. Rev.* **1974**, *13*, 339.
104. Li, M.; Bonnet, D.; Bill, E.; Neese, F.; Weyhermüller, T.; Blum, N.; Sellmann, D.; Wieghardt, K. *Inorg. Chem.* **2002**, *41*, 3444.
105. Pantazis, D.A.; Orio, M.; Petrenko, T.; Zein, S.; Bill, E.; Lubitz, W.; Messinger, J.; Neese, F. *Chem.-Eur. J.* **2009**, *15*, 5108.
106. Orio, M.; Pantazis, D.A.; Petrenko, T.; Neese, F. *Inorg. Chem.* **2009**, *48*, 7251.
107. Pantazis, D.A.; Orio, M.; Petrenko, T.; Zein, S.; Lubitz, W.; Messinger, J.; Neese, F. *Phys. Chem. Chem. Phys.* **2009**, *11*, 6788.
108. Ceulemans, A.; Chibotaru, L.F.; Heylen, G.A.; Pierloot, K.; Vanquickenborne, L.G. *Chem. Rev.* **2000**, *100*, 787.
109. Parr, R.G.; Yang, W. *Density-Functional Theory of Atoms and Molecules*; Oxford University Press: Oxford, **1989**.
110. Koch, W.; Holthausen, M.C. *A Chemist's Guide to Density Functional Theory*; 2nd ed.; Wiley-VCH: Weinheim, , **2001**.
111. Orio, M.; Pantazis, D.A.; Neese, F. *Photosynth. Res.* **2009**, *102*, 443.
112. Noodleman, L.; Post, D.; Baerends, E. *J. Chem. Phys.* **1982**, *64*, 159.
113. Noodleman, L.; Davidson, E.R. *Chem. Phys.* **1986**, *109*, 131.
114. Noodleman, L.; Case, D.A. *Adv. Inorg. Chem.* **1992**, *38*, 423.
115. Kirchner, B.; Wennmohs, F.; Ye, S.; Neese, F. *Curr. Opin. Chem. Biol.* **2007**, *11*, 134.
116. Ruiz, E.; Cano, J.; Alvarez, S.; Alemany, P. *J. Comput. Chem.* **1999**, *20*, 1391.
117. Yamaguchi, K.; Takahara, Y.; Fueno, T. In *Applied Quantum Chemistry*; Eds. Smith Jr., V.H., Scheafer III, H.F., Morokuma, K., D. Reidel: Boston, **1986**, p 155.

118. Yamanaka, S.; Kawakami, T.; Nagao, H.; Yamaguchi, K. *Chem. Phys. Lett.* **1994**, *231*, 25.
119. Shoji, M.; Koizumi, K.; Kitagawa, Y.; Kawakami, T.; Yamanaka, S.; Okumura, M.; Yamaguchi, K. *Chem. Phys. Lett.* **2006**, *432*, 343.
120. Bencini, A.; Totti, F. *J. Chem. Theory Comput.* **2009**, *5*, 144.
121. Bencini, A.; Gatteschi, D. *EPR of Exchange Coupled Systems*; Springer Verlag: Berlin, **1990**.
122. Sinnecker, S.; Neese, F.; Noodleman, L.; Lubitz, W. *J. Am. Chem. Soc.* **2004**, *126*, 2613.
123. Sinnecker, S.; Neese, F.; Lubitz, W. *J. Biol. Inorg. Chem.* **2005**, *10*, 231.
124. Baffert, C.; Orio, M.; Pantazis, D.A.; Duboc, C.; Blackman, A.G.; Blondin, G.; Neese, F.; Deronzier, A.; Collomb, M.-N. *Inorg. Chem.* **2009**, *48*, 10281.
125. Pantazis, D.A.; Krewald, V.; Orio, M.; Neese, F. *Dalton Trans.* **2010**, *39*, 4959.
126. Philouze, C.; Blondin, G.; Girerd, J.-J.; Guilhem, J.; Pascard, C.; Lexa, D. *J. Am. Chem. Soc.* **1994**, *116*, 8557.
127. Blondin, G.; Davydov, R.; Philouze, C.; Charlot, M.-F.; Styring, S.; Åkermark, B.; Girerd, J.-J.; Boussac, A. *J. Chem. Soc., Dalton Trans.* **1997**, 4069.
128. Kulik, L.V.; Epel, B.; Lubitz, W.; Messinger, J. *J. Am. Chem. Soc.* **2007**, *129*, 13421.
129. Staroverov, V.N.; Scuseria, G.E.; Tao, J.; Perdew, J.P. *J. Chem. Phys.* **2003**, *119*, 12129.
130. Kossmann, S.; Kirchner, B.; Neese, F. *Mol. Phys.* **2007**, *105*, 2049.
131. Pantazis, D.A.; McGrady, J.E.; Maseras, F.; Etienne, M. *J. Chem. Theory Comput.* **2007**, *3*, 1329.
132. Jensen, K.P. *Inorg. Chem.* **2008**, *47*, 10357.
133. Munzarová, M.; Kaupp, M. *J. Phys. Chem. A* **1999**, *103*, 9966.

VIBRONIC COUPLING IN INORGANIC SYSTEMS: PHOTOCHEMISTRY, CONICAL INTERSECTIONS, AND THE JAHN–TELLER AND PSEUDO-JAHN–TELLER EFFECTS

RUSSELL G. MCKINLAY, JUSTYNA M. ŻUREK
and MARTIN J. PATERSON

Department of Chemistry, School of Engineering and Physical Sciences, Heriot-Watt University, Edinburgh, EH14 4AS Scotland

I. Introduction

The interaction of light with matter gives rise to many varied and fascinating phenomena. Molecular photochemistry at the most basic level deals with interactions of molecules and photons to generate different electronic configurations, which may show substantially different chemical reactivity than ground-state species (*1*). Photochemical reactions may involve many electronic states, each of different character, which may be coupled strongly

THEORETICAL AND COMPUTATIONAL INORGANIC CHEMISTRY
VOLUME 62 ISSN 0898-8838 / DOI: 10.1016/S0898-8838(10)62009-0

at certain geometrical arrangements of the nuclei. In these regions, the so-called vibronic coupling allows vibrational motion of nuclei to change the nature of electronic wavefunctions. Such regions therefore involve a breakdown of the Born–Oppenheimer approximation, which is a cornerstone of modern computational chemistry. Experimental advances using femtosecond laser pulses have seen detailed studies of fundamental molecular processes occurring on an ultrafast (sub-picosecond) timescale (*2–8*). Concomitant with experimental spectroscopic advances have been the development of computational methods to explore the nature of the electronic states involved (*9, 10*), and the subsequent dynamical motion of nuclei across multiple potential energy surfaces (*11*).

The development of experimental techniques such as time-resolved femtosecond spectroscopy allows us to follow in "real time" photochemical reactions, resulting in greater insight into the mechanisms of light-induced chemistry. However, the chemistry investigated can be very complex and the analysis of data sets can be very challenging. Computational organic photochemistry has seen tremendous advances (*12–18*), and a wide variety of organic systems have been investigated (see, for example, Refs. (*19–24*) for a range of the organic photo-processes studied). The photochemistry of such systems often involves only a few electronic states and can now be modelled with a high degree of accuracy. The photochemical reactions in biological systems have become one of the primary subjects of investigation by both theory and time-resolved spectroscopy in recent years. For example, photosynthesis has been the subject of many studies because it connects a wide range of light-induced processes, many involving mechanisms of action that are still relatively poorly understood at the molecular level. Sundström in a recent review article has presented the main ideas of these processes in femtobiology, including light harvesting, energy transfer between pigments in purple bacterias, and the quenching of dangerous radicals by carotenoids or reactions in green plants (*25*). Time-resolved spectroscopic studies on the pigment rhodopsin, which is present in the retina of the eye, suggested that the *cis* to *trans* photoisomerization reaction of the retinal chromophore occurs on an ultrafast timescale, and results in a chain of other reactions to form different photoproducts. Subsequent *ab initio* calculations on this photoisomerization revealed the existence of conical intersections between the S_0 and S_1 electronic states of rhodopsin, and explained the experimentally observed ultrafast timescale of the photoreaction (*26,27*). A similar mechanism was reported for the bacterial photoreceptor Photoactive Yellow Protein (PYP) (*28–30*). Experimental studies using a fluorescence up-conversion technique, and sub-picosecond

transient absorption or gain spectroscopy also report the ultrafast timescale of *cis* to *trans* photo-isomerization of this chromophore. These studies show that the absorption of a photon by the PYP molecule causes the subsequent formation of red-shifted and blue-shifted intermediates before the system returns back to its original ground-state form. The formation of these photoproducts can be rationalized via different non-adiabatic radiationless decay paths. Many recent studies have focused on the influence of vibronic coupling on the photochemical behavior of DNA and RNA bases (*31,32*). Such studies on biological systems show how advanced experimental techniques have come to increasingly rely on computational studies to rationalize and interpret data when several vibronically coupled electronic states are involved. Similarly advanced spectroscopic investigations of inorganic systems have also taken place (*2–8,33,34*), and therefore the computational modelling of vibronic coupling in inorganic chemistry is a very timely subject for review.

Such inorganic photochemical reactions often present considerably more challenges to the computational chemist than their organic counterparts discussed above. In part, this can be due to the density of low-lying electronic states, relativistic effects including spin–orbit coupling, heavy atom dynamics, and real and quasi-degeneracies among states. However, the photochemistry of transition metal complexes is of tremendous importance and intersects many branches of science and technology, including semi-conductors (*35,36*), and biochemistry (*37–39*). Therefore, the application of the state-of-the-art computational methodologies to inorganic photochemical problems is of prime importance in order to unravel and explain such fundamental yet complex photochemistry.

This review is concerned primarily with the issue of vibronic coupling and the non-adiabatic breakdown of the Born–Oppenheimer approximation in inorganic molecules. Here the well-known Jahn–Teller, and pseudo-Jahn–Teller effects are of paramount importance. In the next section we introduce some of the theoretical background on the computational treatment of such phenomena, followed by a brief review of some important results in computational inorganic photochemistry from other groups in the field, while in the final section we discuss some case studies from our group that highlight many of the salient points. These examples are *the Jahn–Teller effect in the photodissociation and ultrafast relaxation of transition metal carbonyls, the pseudo-Jahn–Teller effect in ammonia and a bimetallic system*, and *a photochemical stereochemical transformation involving a general conical intersection*.

II. Theoretical and Computational Background

A. The Born–Oppenheimer Approximation

The Born–Oppenheimer separation of electronic and nuclear motion is one of the cornerstones of modern chemistry. Conceptually, the lightest nucleus (the proton) is around 1836 times heavier than an electron and we can imagine that the electronic dynamics is much faster than the nuclear dynamics. We can therefore think of the nuclei moving in a potential over the averaged electronic motion and that any displacement of the nuclei will elicit an almost instantaneous response from the electrons. However, also of crucial importance to the successful separation of these degrees of freedom are the energy differences between the generated electronic energy levels, and when they become close the Born–Oppenheimer approximation begins to break down regardless of the mass disparity.

Symbolically, the full Hamiltonian (nuclei and electrons) can be written as

$$\hat{H}_T(\mathbf{R},\mathbf{r}) = \hat{T}_N(\mathbf{R}) + \hat{H}_e(\mathbf{R};\mathbf{r}) \tag{1}$$

where $\hat{T}_N$ is the nuclear kinetic energy operator acting on nuclear coordinates ($\mathbf{R}$), and $\hat{H}_e(\mathbf{R};\mathbf{r})$ is defined as the electronic Hamiltonian. This is generated by "clamping" the nuclei in fixed positions, and solving the resulting eigenvalue equations

$$\hat{H}_e \Psi_i^e(\mathbf{r};\mathbf{R}) = V_i(\mathbf{R})\Psi_i^e(\mathbf{r};\mathbf{R}) \tag{2}$$

for the so-called adiabatic electronic wavefunctions $\Psi_i^e(\mathbf{r};\mathbf{R})$ (which now depend parametrically on the nuclear coordinates), with nuclear-coordinate-dependent eigenvalues $V_i(\mathbf{R})$ called the adiabatic potential energy surface for state i. Note that there are an infinite number of adiabatic eigenfunctions and eigenvalues, which we associate with the ground and excited electronic states of the molecule.

The Born–Oppenheimer approximation may then be thought of as keeping the electronic eigenfunctions independent and not allowing them to mix under the nuclear coordinates. This may be seen by expanding the total molecular wavefunction using the adiabatic eigenfunctions as a basis

$$\Phi_T(\mathbf{r},\mathbf{R}) = \sum_{i=1}^{\infty} \chi_i^n(\mathbf{R})\Psi_i^e(\mathbf{r};\mathbf{R}) \tag{3}$$

Inserting this expression into the total molecular Schrödinger equation, and using the fact that the electronic eigenfunctions are

orthonormal $\int \Psi_i^{e*} \Psi_j^e d\mathbf{r} = \delta_{ij}$ (since they are eigenfunctions of a Hermitian operator) leads to the following (using rectilinear Cartesian coordinates for the nuclear kinetic energy operator $\hat{T}_N$)

$$\nabla_n^2 \chi_i^n + V_j \chi_i^n + \sum_{i=1}^{\infty} -\frac{1}{M} \left[\langle \Psi_j^e | \nabla_n | \Psi_i^e \rangle (\nabla_n \chi_i^n) + \langle \Psi_j^e | \nabla_n^2 | \Psi_i^e \rangle \right] \chi_i^n = E_{\text{tot}} \chi_i^n \tag{4}$$

where M is some suitable mass scale (e.g., the ratio of nuclear to electronic masses). The Born–Oppenheimer approximation is obtained by neglecting nondiagonal terms $(i \neq j)$ and the diagonal term $\langle \Psi_i^e | \nabla_n^2 | \Psi_i^e \rangle$ in Eq. (4) above to obtain the nuclear Schrödinger equation

$$\nabla_n^2 \chi_i^n + V_i \chi_i^n = E_{\text{tot}} \chi_i^n \tag{5}$$

where it can be seen that the expansion coefficients are the nuclear wavefunctions, and the electronic energy enters as a potential for the nuclei. The nondiagonal terms are called the first- and second-order non-adiabatic coupling terms respectively. They can be seen to couple different electronic states through motion of the nuclei. The second-order non-adiabatic coupling can be written in terms of the first-order coupling so it is this first-order term that is of paramount importance in nonadiabatic problems (*11*). One can see how the inverse mass dependence will make the coupling terms very small (the conceptual Born–Oppenheimer approximation), but crucially the first-order non-adiabatic coupling can also be written as (*11*),

$$\langle \Psi_j^e | \nabla_n | \Psi_i^e \rangle = \frac{\left\langle \Psi_j^e \left| \frac{\partial \hat{H}_e}{\partial \mathbf{R}} \right| \Psi_j^e \right\rangle}{V_j - V_i} \tag{6}$$

such that this coupling term depends inversely on the difference between electronic eigenvalues (i.e., the difference in energy between electronic states i and j). When the difference approaches zero, the non-adiabatic coupling term diverges and has a singularity at a point of degeneracy between electronic states. As we shall see below, it is the calculation of the term in the numerator on the right of Eq. (6) above that is crucial in finding conical intersections, and obtaining the magnitude of Jahn–Teller and pseudo-Jahn–Teller couplings. For further details see, for example, Refs. (*11, 42*).

B. Conical Intersections

Conical intersections occur whenever there is an electronic degeneracy. These were predicted on a mathematical basis by von-Neumann and Wigner in 1929 (*40*). They worked out that two independent parameters need to be varied to achieve a degeneracy of eigenvalues of a real symmetric matrix (such as a real Hamiltonian matrix). The key idea was that the parameters were independent: if one thinks of these as geometrical parameters then one arrives at the noncrossing rule for diatomics. Namely, that with only one vibrational degree of freedom (the internuclear distance) the two electronic states cannot cross if they are of the same symmetry. Teller realized that this does not hold for polyatomic molecules and consequently the potential energy surfaces of polyatomic molecules may cross in a space of dimension n–2 (*41*), where n is the number of vibrational degrees of freedom (3N-6 for nonlinear polyatomic molecules composed of N atoms). Following von-Neumann and Wigner, the two degrees of freedom that need to be independently varied to achieve a degeneracy are conventionally called the gradient difference vector ($\mathbf{x}_1$), and the derivative coupling vector ($\mathbf{x}_2$) (*16,42*)

$$\mathbf{x}_1 = \frac{\partial(E_1 - E_2)}{\partial \mathbf{R}} \tag{7}$$

$$\mathbf{x}_2 = \left\langle C_2^t \middle| \left(\frac{\partial \hat{H}_e}{\partial \mathbf{R}} \right) \middle| C_1 \right\rangle \tag{8}$$

where E_1 and E_2 are the two electronic eigenvalues, $\mathbf{R}$ is a vector of nuclear Cartesian displacements, and C_1 and C_2 are solutions of the electronic Schrödinger equation in a configuration interaction problem, i.e., any standard representation of electronic states expanded in a basis of electron configurations.

An alternative way of thinking of these two vectors are that if one is at a degeneracy then (infinitesimal) movement in the plane spanned by these vectors (the so-called branching space) will lift the degeneracy (*42*). When the electronic energy is plotted against these two vectors, one obtains the famous double-cone potential energy surfaces (Fig. 1 top). Such regions represent photochemical funnels that drive the system from the upper to the lower surfaces on the timescale of a single vibrational period. The cone may be circular in shape (Fig. 1, top left), or possibly elliptic when the $\mathbf{x}_1$ and $\mathbf{x}_2$ vectors have different lengths (both representing the so-called peaked intersections)

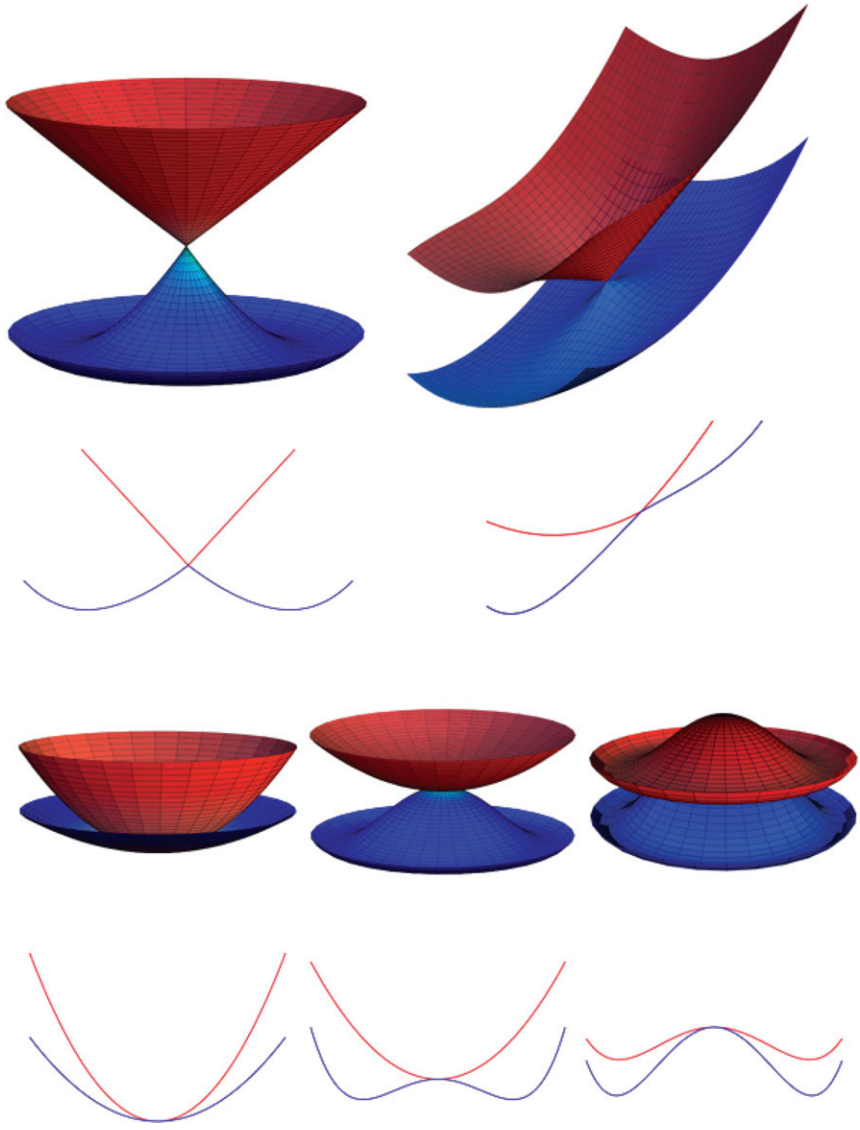

FIG. 1. Conical intersection surface topologies (top), and Renner–Teller surface topologies (bottom). Top left is a generic circular cone, such as is obtained from a Jahn–Teller problem involving only the linear vibronic coupling. Top right is a sloped conical intersection obtained in a general vibronic coupling problem where all three linear vibronic coupling constants are different. Bottom left to right show type-I, -II, -III Renner–Teller surfaces. These are obtained when only second-order vibronic coupling is included.

(*42*). In Fig. 1 (top right) we show a sloped conical intersection in the terminology of Ruedenberg *et al* (*29*). Here the cone is tilted due to the fact that the force (gradient) vectors on both the upper and lower surfaces point in the same direction. The first-order topology (sloped vs. peaked) controls the nature of the photochemical reaction dynamics, and whether reactants are regenerated or photoproducts are formed (*23,24*).

The space orthogonal to the branching space is called the intersection space, is of dimension 3N–8, and has received much attention in recent years (*23,24,43*). In rectilinear Cartesian displacements in this space the upper and lower surfaces look like one of the three shown in Fig. 1 (bottom). Note that the degeneracy is lifted quadratically via direct displacement along one of these rectilinear coordinates. These are formally the same as the well-known Renner–Teller degeneracies in linear molecules. Type-I involves destabilizing on both the upper and lower surfaces with respect to the vibration, whereas type-II involves stabilization on the lower surface and destabilization on the upper one, while type-III involves stabilization on both. The importance of such second-order degeneracy lifting is seen in high-resolution spectroscopy (*42*), and in understanding the complex nature of the conical intersection seam. A point of conical intersection is but a single point on an n–2 dimensional degenerate seam, which is highly curved through the nuclear configuration space. The second-order effects, combined appropriately with the first-order ones, allow a description of the curved seam (*43,44*). Thus, although from Fig. 1 it might appear that all nuclear motion lifts the degeneracy, in fact only first-order motion does but the intersection space is curved so that it cannot be described by rectilinear displacements. However, in Jahn–Teller problems (introduced below), one almost always uses a fixed set of Cartesian nuclear displacements for convenience. The parameters quantifying the non-adiabatic coupling then are a measure of the extent to which the potential energy surfaces split at first and second order as in Fig. 1.

C. The Jahn–Teller Effect

The Jahn–Teller effect has been the subject of intense study in solid-state physics and molecular sciences for almost 80 years (*45,46*). In their seminal paper, Jahn and Teller proved that all systems in orbitally degenerate states are unstable with respect to non-totally symmetric vibrations which cause a

stabilization on the lower adiabatic potential energy surface (*47*). These Jahn–Teller geometries can of course be understood as conical intersections between the components of the degenerate electronic states (*42*). The symmetry of the vibrational modes that lift the Jahn–Teller degeneracy can be found from the symmetric square of the degenerate electronic state irreducible representation with itself (*47*). Jahn and Teller worked this out exhaustively for all point groups but more general aesthetic proofs have since appeared (*46*). The upshot is that there is always a nontotally symmetric vibration that removes the Jahn–Teller degeneracy and lowers the symmetry of the molecule. The standard nomenclature for this is, for example, $E \otimes e$, meaning that a degenerate electronic state of E symmetry interacts with a degenerate pair of vibrational modes of e symmetry. If one calculates the gradient difference and derivative coupling vectors ($\mathbf{x_1}$ and $\mathbf{x_2}$ above) then one obviously finds that they have the correct symmetry as predicted by the Jahn–Teller theorem (as they must since they lift the degeneracy at first order). However, if a general set of symmetry adapted vibrational normal modes is used (a standard rectilinear set, for example as obtained from a harmonic frequency analysis) then the $\mathbf{x_1}$ and $\mathbf{x_2}$ vectors are linear combinations of all modes with the Jahn–Teller symmetry (*42*), e.g., if there are five modes of e symmetry then the branching space vectors are linear combinations of all five of these and are not, in general, parallel to any particular e pair. Furthermore, symmetry may also be used to determine which modes display second-order Jahn–Teller activity (discussed in the appendix of Ref. (*42*)), and these fixed modes generate potential energy surfaces as depicted in Fig. 1 bottom.

Although the Jahn–Teller effect has been traditionally used to explain observed molecular structures or spectral data, in recent years it has been used to connect time-resolved spectroscopy with inorganic photochemistry, as we discuss in section 4 below. In essence, such Jahn–Teller geometries can be reached by driving an excited-state chemical reaction (such as a photodissociation) toward a region of configuration space where such degeneracies exist (*2,5–7,34*). These regions contain nonclassical structures for inorganic chemistry. Such Jahn–Teller geometries then provide natural funnels for ultrafast radiationless decay to the ground electronic state (*48*). In this respect, the Jahn–Teller conical intersection is no different from the accidental ones found in organic photochemistry discussed in the introduction above, but its presence may be more readily inferred due to the often higher symmetry of unsaturated coordination complexes that can be generated via an inorganic photochemical reaction.

D. The Pseudo-Jahn–Teller Effect

The pseudo-Jahn–Teller (pJT) effect is a very useful tool for the explanation of the local curvature of adiabatic potential surfaces. It has been successfully applied in many areas of organic and inorganic chemistry (*45,46,49,50*), and it provides information of why a particular system in a nondegenerate state undergoes symmetry breaking. Further, the pJT effect informs which states mix together under certain vibrations. There is however an unfortunate ambiguous terminology regarding the pseudo-Jahn–Teller effect. In some circles it is called the second-order Jahn-Teller effect. We mean the second-order Jahn–Teller effect to be true Jahn–Teller coupling at second-order in nuclear displacements to give potentials as in Fig 1 bottom, i.e., second-order displacements from a point of electronic degeneracy (*42*). We reserve pseudo-Jahn–Teller coupling to be a vibronic coupling between two nondegenerate electronic states via a nontotally symmetric (non-degenerate or degenerate) vibrational mode. Still other authors use the term pseudo-Jahn–Teller coupling to describe the coupling between degenerate and non-degenerate states (*11*).

In fact, as we discuss in section 4 below, pJT coupling gives surfaces resembling the type-II Renner–Teller surfaces shown in Fig. 1, but separated by a finite energy difference. Many theoretical formulations of the pseudo-Jahn–Teller effect have been proposed. The simplest is perhaps the perturbative expansion originally due to Pearson (*51*)

$$E(Q_i) = E_0 + Q_i \left\langle \Psi_0 \left| \frac{\partial V}{\partial Q_i} \right| \Psi_0 \right\rangle + \frac{Q_i^2}{2} \left\langle \Psi_0 \left| \frac{\partial^2 V}{\partial^2 Q_i} \right| \Psi_0 \right\rangle$$

$$+ Q_i^2 \sum_j \frac{\left[\left\langle \Psi_0 \left| \frac{\partial V}{\partial Q_i} \right| \Psi_j \right\rangle \right]^2}{E_0 - E_j} + \ldots \qquad (9)$$

where E represents the energy of an electronic state (Ψ_0) as a function of a vibrational normal coordinate Q_i, E_0 represents the energy at the optimized geometry from which the distortion occurs, V is the electronic potential, Ψ_0 and Ψ_j are electronic wavefunctions (typically ground and excited), and E_j is the energy of the j-th excited state. The first of these terms is the gradient of an electronic state and will be zero for the optimized structure of a non-degenerate state by definition. The second term is always positive as proved by Bersuker *et al.* (*49*) and may be conceptually thought of as the energy

increase due to distortion using the fixed (unrelaxed) wavefunction optimized at the reference geometry, whereas the third term is the mixing of adiabatic electronic states under a nuclear perturbation. This last term allows the electronic wavefunction to relax at distorted geometries and is always negative. For example, for the mixing of the ground and j-th excited electronic state we have

$$\left\langle \Psi_0 \left| \frac{\partial V}{\partial Q_i} \right| \Psi_j \right\rangle \tag{10}$$

The relative magnitude of both second-order terms determines whether the molecule is stable with respect to distortion along the vibrational coordinate Q_i. If the relaxation term is of larger magnitude than the distortion term then the geometry is unstable and the potential energy surface has negative curvature for mode Q_i.

Much work on the theory of Jahn–Teller and pseudo-Jahn–Teller effects has been reported by Bersuker and co-workers. They have proved that the pJT effect is the only possible source of instabilities of high symmetry molecular systems in non-degenerate states. These researchers have investigated the pJT effect in many systems, including planar BH_4^-, CH_4, BH_3, CH_3^-, NH_3, octahedral metal complexes MH_6 (M = Sc^{3-}, V, Cr), and a series of octahedral hexafluoride systems (*45, 46, 49, 50*).

Simple models of when there is pJT activity may be gained by examining the excited-state proximities and potential surface curvatures of constrained species, see, for example, a recent study relating to bridging hydride ligands in Mn–Si hydrosilane complexes (*52*). More extensive investigations of pseudo-Jahn–Teller activity require multiconfigurational electronic structure methods, for example, the CASSCF force constant diagnostic devised by Bearpark (*53*). Here one explicitly calculates the second-order vibronic mixing terms in Eq. (10) in a CASSCF second-derivative computation (as part of the coupled perturbed multiconfiguration self-consistent field (CP-MCSCF) equations). One can control the inclusion of certain couplings via symmetry constraints on the CASSCF wavefunction. This method allows the switching on and off of negative pJT couplings between wavefunctions belonging to different irreducible representations of the point group, and the pJT coupling is manifest when the potential surface has a negative curvature along one mode when the pJT terms are switched on, and a positive curvature along the same mode when they are switched off. This method has seen several applications in organic chemistry (*42, 53, 54*), and we have begun applying it to inorganic problems as highlighted in section 4 (*55*).

III. Important Computational Results in Inorganic Photochemistry

We briefly review some of the most relevant theoretical studies of inorganic photochemistry in recent years. Due to the previously discussed complexity of these processes, and the consequent theoretical tools required to model them, such reports are less common than for organic systems discussed in the introduction above. The group of Daniel and co-workers has performed by far the majority of investigations into inorganic spectroscopy and photochemical reactivity. An impressive body of results highlights what can be achieved by using the state-of-the-art computational techniques, including multiconfigurational *ab initio* wavefunction methods, density functional, and *ab initio* response methods, in conjunction with coupled-state wave packet dynamics simulation of appropriate reduced dimensionality (typically one- or two-dimensional simulations) (*56–74*).

The photochemistry of the transition metal complex HMn(CO)(1,4-diaza-1,3-butadiene) was investigated in Ref. (*60*). The lowest energy structures of the complex for both the ground and lowest triplet metal to ligand charge-transfer (MLCT) excited states were determined, in addition to the role that MLCT states play in the photochemistry of such systems. Previous CASSCF-CCI calculations of the potential energy curves had already been carried out where it was believed that under low-energy photoexcitation at 500 nm, a singlet MLCT state was populated, which would then undergo fast intersystem crossing to a long-lived triplet MLCT state (*59*). The system could then undergo emission, or a small fraction of the molecules may dissociate hydrogen. Alternatively, it was proposed that if the system was excited at higher energies around 300 nm then a different singlet state would be populated that was not of MLCT character, but rather d-d or σ-π^* character. Via this excited pathway, the system would undergo intersystem crossing to another triplet state, from which the system could dissociate hydrogen, after further internal conversions, or become trapped in another long-lived triplet MLCT state and undergo emission. The presence of σ-π^* and σ-σ^* states and their positions in the electronic spectrum of this species was believed to be important as avoided crossings between such photodissociative states and MLCT states prevents the photodissociation of hydrogen. The upshot of this is that the system will either undergo fast CO loss or just undergo internal conversion relaxation to the ground electronic state. The system will also undergo emission if the lowest triplet MLCT state is populated. In the later study CASSCF was again used to optimize the structures of both the ground state and the lowest triplet MLCT state

and to study the changes in structure when going from the former state to the latter. It was concluded that there is a small structural change in going from the ground state to the MLCT state, which involves a slight elongation of the metal–CO axial bond, and a shortening of the M–H bond, and it was also discussed that care must be taken when selecting orbitals for the CASSCF active space, a common potential pitfall when using this method (*vide infra*). In a later paper (*74*), the potential energy curves along the Mn–H bond for the ground state and the first three triplet states using CASSCF-CCI was reported. This degree of freedom was the only one investigated. Two avoided crossings were predicted between two of the triplet states, which are bound, and the third, which is repulsive. Ligand to ligand charge transfer (LLCT) states have also been reported, and the UV/vis spectrum was investigated using wave packet dynamics in a diabatic representation (*75*). It was concluded from this that the non-adiabatic coupling in the system between the bound and repulsive triplet states could influence the reactivity of the bound states. This study continued with a paper reporting the CASSCF/MR-CCI study of the potential energy surfaces of this species, this time for both Mn–H and Mn–CO axial bond cleavage deactivation channels, where hydrogen loss is homolytic. The states involved ranged from the ground state to low-lying MLCT, the so-called sigma-bond to ligand charge transfer (SBLCT), and metal-centered (MC) states. Wave packet dynamics were once again used to simulate this photochemistry using CASSCF/MR-CCI potentials. It was predicted that upon excitation in the visible region the CO ligand was ejected in under 500 fs after initial excitation into a singlet MLCT state. It was believed that no other processes such as intersystem crossing to a triplet state were competitive with this ultrafast process.

Another study was performed on a similar system, this time $HCo(CO)_4$, highlighting the rich and complex photochemistry of such organometallic complexes (*58*). Here it was described how the CASSCF-CCI method was used to produce potential energy surfaces corresponding to homolytic Co–H bond cleavage, and the ejection of a carbonyl ligand. The ground and first few electronic excited states were investigated. Wave packet propagation dynamics studies were then performed on these surfaces in order to discover the nature of the initial photochemical reaction dynamics. The resulting mechanism for photodissociation that was proposed involved initial excitation at 229 nm into a singlet E state, which is of d-σ^* character. There is believed to be a competing process between ultrafast loss of hydrogen in under

10 fs and a redistribution of vibrational energy around the molecule before Co–H bond homolysis. After vibrational energy redistribution intersystem crossing to either triplet $A_1(\sigma\text{-}\sigma^*)$ or E $(3d_\delta\text{-}\sigma^*)$ states is possible. Then CO loss or Co–H bond homolysis can occur from the triplet E or A_1 states respectively. After this the fraction of molecules in the triplet E state that did not undergo CO loss can redistribute the remaining vibrational energy, and then it was postulated that the molecule would then phosphoresce to the ground state. A later study by Ambroksek *et al* (*72*) again looked at the photoreactivity of $HCo(CO)_4$, along with $H_3CCo(CO)_4$. This time wave packet dynamics were used to study two-dimensional potential energy surfaces, which related to the four low-lying singlet excited states of the system, two of metal to sigma-bond charge-transfer (MSBCT) character and two of MLCT character. Triplet states that correspond to the products of H or CH_3 loss were also investigated. Compared with previous studies already reported, the authors looked in detail at these four excited electronic states to obtain a converged UV absorption spectrum with wave packet dynamics, whereas previously only two states had been looked at in detail. It was found that the upper MLCT states do not contribute to the photoreactivity and that the singlet MSBCT states cause the dissociation of CO and CH_3. The b^1E state is thought to be the initiator of ultrafast CO loss and M–H/CH_3 bond homolysis. A similar study was also performed on the $Cr(CO)_4$(2,2′-bipyridine) system (*66*).

The photochemistry of rhenium-containing complexes has also been investigated using multiconfigurational *ab initio* methods. For methyltrioxorhenium (CH_3ReO_3), an organometallic species with catalytic applications, CASSCF/MS-CASPT2 and TD-DFT (various functionals) were used to study the UV-vis absorption spectrum and subsequent photochemistry. Good agreement was found with experiment with the lowest state predicted to be an LMCT state between oxygen and rhenium. A later paper built on this study using wave packet propagation dynamics to study the rhenium–methyl bond homolysis, investigating both singlet and triplet low-lying excited states (*76*). CASSCF calculations were used to construct potential energy curves as a function of Re–C distance. The initial state populated is the b^1A_1 state followed by population of the a^1E and a^3A_1 states a few femtoseconds later, where the first two states are non-adiabatically coupled. The latter two states show spin–orbit coupling and it was believed that this spin–orbit coupling between these states controls the dissociation of about 20% of the molecules by Re–C bond homolysis. The remaining 80% of molecules are believed to remain in the potential wells of the two singlet states.

Ben Amor *et al.* (*73*) used a similar methodology in the study of the Sn–I bond elongation in trimethyltin iodide. The aim was to study a one-dimensional potential energy surface along the Sn–I bond elongation to establish the branching ratio between ionic and radical initial products of the photodissociation. The favored channel to be produced via photodissociation is the ionic one with a branching ratio of 5:1 over the radical products when irradiated at 207 nm. Non-adiabatic couplings were not included in the dynamics simulations, only spin–orbit couplings, although non-adiabatic couplings are believed to influence the process of photodissociation as the gA' and gA'' states were found to be close in energy, pointing to a possible conical intersection in the area where the wave packet would arrive on the former state.

The selective examples discussed above hopefully highlight the range of multistate inorganic problems involving vibronic coupling that have been studied using advanced computational methodologies. In the next section we will focus on recent results in our group by giving a selection of case studies highlighting salient aspects of such computational modelling in inorganic chemistry.

IV. Case Studies

A. Metal Carbonyl Photodissociation and Ultrafast Relaxation

We shall now discuss our ongoing interests regarding the photodissociation and relaxation pathways of binary transition metal carbonyls (*48*). These are paradigm complexes in inorganic chemistry and have found many uses, for example, as reactive precursors in catalysis (*77*). They are also interesting as model complexes to study M–CO dative bonding. Recently intriguing experimental data on such complexes have shown that they possess a rich photochemistry (*2,5–7,34*), which is only now beginning to be understood thanks to modern pump-probe laser experiments in combination with multiconfigurational electronic structure methods (*48*) and quantum dynamics simulations (*78,79*).

The electronic spectra of these species have been extensively investigated in the past using both theory and experiment (*64,65,80,81*). The experimental spectra are generally poorly resolved and contain a high density of coupled vibronic states (*34*), which severely complicates the assignments (*82*). For example, there has been considerable debate about the nature of the initially populated state in $Cr(CO)_6$ photodissociation (*83–86*). It was until recently believed to be of ligand field (LF) nature, but

recent computational investigations have shown that the MLCT state is in fact populated and a crossing (real or avoided) between this state and a LF state along an asymmetric stretch induces population transfer to the directly dissociative LF state (*85,86*). Accurate quantum dynamics simulations are currently being undertaken to simulate the vibronic spectra in the vertically excited region, but this is extremely challenging due to the number of electronic states and non-adiabatic couplings that need to be included in suitable model Hamiltonians.

To get the complete picture of the photoreactivity of metal carbonyls, essentially a "three-pronged attack" is needed. The first is to accurately compute the electronic spectrum, assigning all the coupled vibronic states within the appropriate spectral energy range. As discussed above, this is very difficult, although progress has been made on the purely electronic nature of the transitions using variants of response theory. It is now possible to model the correlated response of frequency-dependent electromagnetic perturbations using coupled cluster theory (*87,88*). Recent work using the equation-of-motion (EOM) approach has proven very useful in the assignment of the electronic spectrum of $Cr(CO)_6$ (*81*). The efficacy of coupled cluster response techniques is due to the fact that they are capable of treating all excited states in a balanced manner, and allow for mixing of excited electronic configurations at the correlated level. For $Cr(CO)_6$, $Fe(CO)_5$, and $Ni(CO)_4$ electronic spectra have also been obtained from high-level CASPT2 computations (*84*). The results here can be very accurate, although one must be cautious as often different zeroth-order active spaces must be used to model different types of excited state, and thus it may be difficult to get a balanced treatment of all states within a given spectral range. We have recently applied linear response coupled cluster theory, including a perturbative treatment of triple excitations to the electronic absorption of $Fe(CO)_5$ (*48*). An advantage of using response theory is that both single- and multi-photon transition moments may be calculated (*89*). For example, the one- and two-photon absorption spectra of $Fe(CO)_5$ have sufficiently small spectral overlap that photochemistry initialized via such different absorptions can be quite different (*90*). Understanding these alternative photochemical paths is of particular interest in $Fe(CO)_5$ and should help to understand the nature of the different electronic states contributing to each broad spectral band. We shall not focus any further on the electronic spectroscopy of metal carbonyls, although it should be noted in passing that time-dependent density functional theory (TD-DFT) has seen extensive use in this area (*68,70,82*). For accurate computation of electronic spectra in larger complexes,

particularly with modern functionals designed to better describe charge transfer states (e.g., the Coulomb attenuated version of the popular B3LYP functional: CAM-B3LYP(*91*)), TD-DFT should see continued extensive application to such problems.

The second "prong" of attack mentioned above is to map the excited-state reactive potential energy surfaces, including regions of strong non-adiabatic coupling such as conical intersections. Multiconfigurational methods are appropriate here, including CASSCF, CASPT2, and MRCI. CASSCF evaluation of analytical first and second derivatives of the energy with respect to nuclear displacements is now commonplace, and further the analytical computation of non-adiabatic coupling matrix elements is also routinely performed (e.g., within the Gaussian program (*92*)). Thus, with a judicious choice of active space one can map the potential energy surfaces from reactants to photochemical products in a smooth and continuous fashion (*78*). An incomplete accounting of dynamical correlation of electron pairs in CASSCF means that often state-orderings may be different and relative energetics between excited critical points must be treated cautiously. Extended methods such as CASPT2 may be used to determine more accurate energetics, although analytical derivatives for CASPT2 have only very recently appeared, and while numerical derivatives may sometimes be useful, caution again must be exercised as these often miss small features on the potential energy surfaces of unsaturated metal carbonyl complexes (*48*). MRCI gradients and non-adiabatic couplings are possible but at present are limited to relatively small systems and are too expensive to see general use in inorganic problems. Below we detail CASSCF investigation of $Cr(CO)_5$, $Fe(CO)_4$, and $Mn(CO)_5$ potential energy surfaces. These species are the reactive products that appear on an ultrafast timescale in the photodissociation of $Cr(CO)_6$, $Fe(CO)_5$, and $Mn_2(CO)_{10}$ respectively.

Understanding the potential energy surfaces for photodissociation and subsequent radiationless decay leads to the third "prong" of attack: simulation of the nuclear dynamics on these coupled potential energy surfaces. One has a choice of how to accomplish this, each with pros and cons, and associated computational expense. The essential features one has to decide on are (i) how to treat the electronic potential energy surfaces: analytically via some suitable fit to (global) multidimensional functions for some or all vibrational degrees of freedom, or on-the-fly (local) surfaces obtained from electronic structure energies, gradients, and possibly also Hessians, (ii) how to describe the nuclear motion on those surfaces: via quantum wave packets, or as semi-classical particles with well-defined trajectories. All combinations of these two

choices are, in principle, possible; however, quantum wave packet simulations on local on-the-fly surfaces is very challenging, and the first developments in this direction have only recently appeared (*93–95*). After a discussion of the potential energy surfaces below, we shall then return to dynamics and review the results of using on-the-fly trajectory surface hopping (*78*), and multidimensional wave packet dynamics, using a model diabatic vibronic coupling Hamiltonian (*79*), for the case of $Cr(CO)_5$ radiationless deactivation following photodissociation of $Cr(CO)_6$.

A.1. Jahn–Teller potential energy surfaces

We shall now focus on our results of modelling the potential energy surfaces for photodissociation for three metal carbonyls, $Cr(CO)_6$, $Mn_2(CO)_{10}$, and $Fe(CO)_5$. One common feature of these carbonyls from experiment is that they are known to eject one CO ligand on an ultrafast timescale (*2,4–7,34*). Although the nature of the initial states that lead to this are still under discussion (*vide supra*), the mechanism of relaxation of the unsaturated metal carbonyl that remains has also been the subject of much investigation (*2,5–7,34,48,78,79*).

After photodissociation of a single carbonyl ligand, the resulting unsaturated complex may be capable of achieving a geometry of nonabelian symmetry (and degenerate irreducible representations of the point group). Such degenerate states are Jahn–Teller active, the geometry being on a conical intersection seam as discussed above. Two aspects need to be considered: (i) Are there Jahn–Teller geometries that connect the excited and ground electronic states? (ii) If there are, are they accessible on the excited reaction path following the photodissociation?

Multiconfigurational methods are required to describe different geometries with partial orbital occupancies and possible degenerate states. CASSCF is the method of choice to model reactive potential energy surfaces as degeneracies and quasi-degeneracies are automatically taken care of, and by virtue of the orbital optimization, the mixing of metal and ligand orbitals as the geometry is changed is also accounted for. In considering what orbitals are needed in the CASSCF active space, the metal 3d orbitals are perhaps the most obvious choice, as the different arrangements of electrons in these orbitals gives rise to the textbook examples of Jahn–Teller instabilities (*96*). This gives active spaces of (6,5), (7,5), and (8,5) for the $Cr(CO)_5$, $Mn(CO)_5$, and $Fe(CO)_4$ unsaturated complexes, respectively. However, such active spaces do not converge well, and the wavefunctions obtained are prone to spurious symmetry breaking, which can cause inaccurate

energetics and geometries. What is needed is to realize that metal carbonyls are paradigm systems for dative bonding involving electron pair donation from the ligand. Thus, in an active space only including a single set of orbitals, the electrons are unable to dynamically correlate their respective motions and are on average much too close together. A successful technique to handle this is to augment the active space with a set of empty orbitals with an extra node in the internuclear M–L region. These orbitals are notionally the 4d counterparts to the occupied 3d orbitals. For example, for $Cr(CO)_5$, the active space would increase from (6,5) to (6,10). Such active spaces now give accurate barrier heights relative to correlated single-configuration methods (*48*), but crucially are also capable of treating excited states and degeneracies as well in a balanced manner. A related active-space augmentation has been successfully used in CASPT2 calculations of metal carbonyl bonding in the ground state (*97*) and for the electronic spectroscopy of metal carbonyls (*84*). What is found from the optimized CASSCF wavefunctions is that the occupancy of the 4d orbitals (as obtained from the diagonal elements of the one-electron-density matrix) are non-negligible: about 0.1 in the ground electronic state relative to their occupied counterparts (~1.9). For $Cr(CO)_5$, a smaller active space is actually possible by dropping both a 3d orbital and its 4d counterpart. This is because there is one unoccupied 3d orbital at all geometries for $Cr(CO)_5$ in the ground and lowest electronic excited states (*78,79*). For further discussion see Ref. (*48*).

The work of Fuβ and co-workers (*2,5–7,34*) has shown that $Cr(CO)_5$, $Mn(CO)_5$, and $Fe(CO)_4$ return to the lowest electronic states of the initially excited multiplicity within several hundred femtoseconds of the photodissociation of the parent carbonyl. This timescale precludes a spin–orbit induced change from the low-spin manifold and anticipates the accessibility of a conical intersection seam to facilitate radiationless population transfer to the ground state.

For $Cr(CO)_6$ ejection of a CO ligand leaves a $Cr(CO)_5$ fragment in an almost square-pyramidal geometry on the S_1 state (*78*). There is a possible Jahn–Teller geometry at trigonal bipyramid (TBP) geometries as can be seen from the electronic configurations in Fig. 2, $\left((d_{xz})(d_{yz})\right)^4\left((d_{xy})(d_{x^2-y^2})\right)^2$ which leads to the following possible electronic states: $e' \otimes e' = {}^1E' \oplus {}^1A'_1 \oplus {}^3A'_2$. The triplet is a stable minimum at TBP geometries $\left(\left((d_{xz})(d_{yz})\right)^4\left((d_{xy})^1(d_{x^2-y^2})^1\right)\right)$ but is inaccessible on the ultrafast timescales considered here. Therefore, one needs to consider the ${}^1E'$ and ${}^1A'_1$ states. The only way to determine the lower

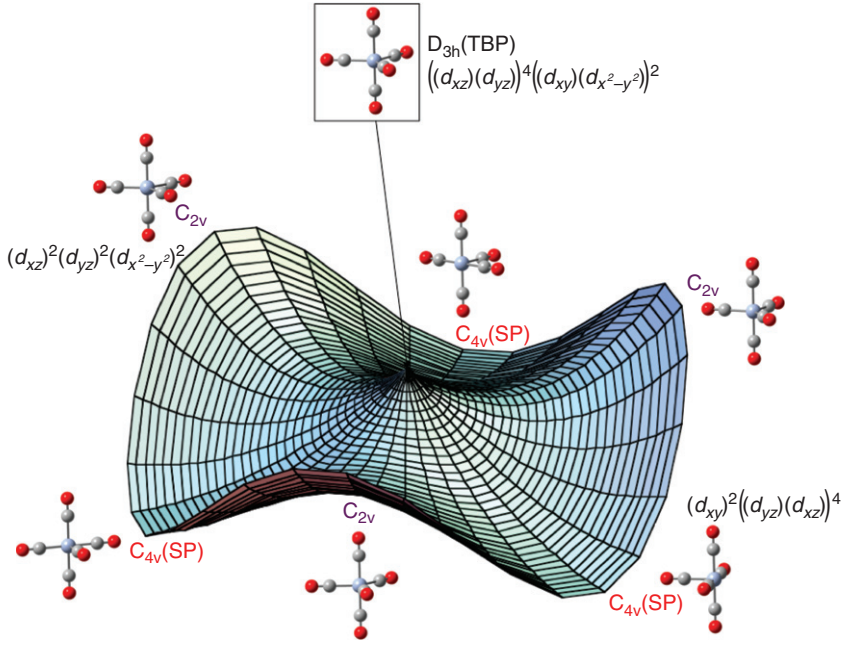

FIG. 2. $Cr(CO)_5$ Jahn–Teller surface around trigonal bipyramid (TBP) geometry (D_{3h}), which has a doubly degenerate electronic state. There are three equivalent square-pyramidal (SP) minima (C_{4v}), connected via three equivalent transition structures (C_{2v}). The barrier is about 12 kcal mol^{-1}.

energy of these is to perform a high-level computation. CASSCF shows that the $^1E'$ is the lowest, and thus this degenerate state connects the S_0 and S_1 photochemical states via a Jahn–Teller conical intersection (how this intersection is reached is the subject of the next subsection). The Jahn–Teller surface for the $^1E'$ state is shown in Fig. 2. The two geometrical coordinates are the degenerate symmetric and asymmetric CMC bends (*78,79*).

A very useful tool to predict suitable stable geometries around the point of a Jahn–Teller conical intersection is the epikernel principle of Ceulemans and Vanquickenbourne (*98*). This states that highest-ranking epikernels are the point groups of minima, and that lower-ranking epikernels, and kernels will be point groups for saddle points for any Jahn–Teller distortion. Kernels are the groups of symmetry elements that are preserved when distorting along a vector spanning an irreducible representation of a given point group. Epikernels are groups of higher symmetry that are selectively preserved in part of the distortion space (*98*).

For example, in $Cr(CO)_5$, we find that the branching space of the Jahn–Teller intersection has e' symmetry (i.e., the symmetric and asymmetric bending that define Fig. 2). The epikernel of this irreducible representation in the point group D_{3h} is $E(D_{3h}, e') = C_{2v}$. Thus the Jahn–Teller "trough" will have C_{2v} symmetry. Note that at some points the C_{2v} symmetry accidently becomes C_{4v} (of which it is an abelian subgroup). These points are the stable square-pyramidal mimima (electronic configuration $(d_{xy})^2((d_{yz})(d_{xz}))^4$), whereas the transition structures connecting them have C_{2v} symmetry. This highlights two important considerations in applying the epikernel principle, first it is only applicable to first-order Jahn–Teller distortions, and second it cannot predict any accidental alignments of a subgroup with a larger nonabelian group. However, it is an excellent starting point for examining the Jahn–Teller surface. It is also worth noting that the number of equivalent epikernel distortion directions is given by the quotient between the order of the nonabelian point group of the Jahn–Teller geometry and the epikernel subgroup. This tells us how many equivalent minima and saddle points around the lower "trough" there are for a given carbonyl. See Ref. (*48*) for a more detailed discussion of the application of the epikernel principle to unsaturated metal carbonyls.

The surface shown in Fig. 2 highlights the geometrical changes that take place in this system. Initially in a nondegenerate excited state at SP geometries, the molecule approaches the Jahn–Teller TBP geometry, via symmetric bending of the ligands. At this geometry the ground and excited states are degenerate and the system crosses to the ground-state surface. The continued symmetric bending takes the system along a C_{2v} ridge where it begins to move downhill in the orthogonal asymmetric bending coordinate toward a stable SP minimum. This will be further expounded upon in the dynamics discussion in the following subsection.

The photodissociation of $Mn_2(CO)_{10}$ is a much more challenging system than $Cr(CO)_6$ because there are two dissociation channels possible, namely M–M bond homolysis or ejection of a carbonyl ligand. Again the $Mn(CO)_5$ or $Mn_2(CO)_9$ fragments are experimentally found to return to their electronic ground state on an ultrafast timescale, which precludes a spin–orbit spin–change (from singlet to triplet for the bimetallic, and doublet to quartet for the $Mn(CO)_5$ radical) (*4,5*). So far we have only studied the metal–metal homolysis in detail, using CASSCF with a (7,8) active space to study the Jahn–Teller surface. This surface for $Mn(CO)_5$ is very similar to that discussed above for $Cr(CO)_5$ (Fig. 2). At TBP geometries the electronic configuration is

$\left((d_{xz})(d_{yz})\right)^4\left((d_{xy})(d_{x^2-y^2})\right)^3$. Therefore, there is a single hole in a doubly degenerate set of orbitals, and the electronic state is assigned straightforwardly as $^1E'$. The Jahn–Teller surface is therefore almost identical to that shown in Fig. 2, and the dynamics of the $Mn(CO)_5$ radical are expected to be similar to $Cr(CO)_5$ on a short timescale. The primary difference in the Jahn–Teller surface between these systems is that the barrier to pseudorotation is much smaller in $Mn(CO)_5$ than in $Cr(CO)_5$, which we believe to be due to a smaller pseudo-Jahn–Teller coupling to a third upper non-degenerate state (*48,79*).

The final carbonyl Jahn–Teller surface discussed is for $Fe(CO)_4$, formed from the photodissociation of trigonal bipyramidal $Fe(CO)_5$, whose photochemistry is one of the most investigated of the binary transition metal carbonyls (*90*). Again this photoproduct has been found to form on an ultrafast timescale with a Jahn–Teller conical intersection inferred at a tetrahedral geometry (*5*). This species presents further challenges: either an axial or an equatorial ligand may be initially ejected (and although the axial path is likely to be favored both need to be considered and modelled), and the tetrahedral geometry has triply degenerate irreducible representations leading to possible three-state Jahn–Teller conical intersections and associated five-dimensional branching spaces (*40*). We have studied the $Fe(CO)_4$ Jahn–Teller surface using CASSCF with an (8,10) active space.

$Fe(CO)_4$ at tetrahedral geometries is $d^8(e^4t_2^4)$, which leads to the following electronic states: $t_2 \otimes t_2 = {}^1A_1 \oplus {}^1E \oplus {}^1T_2 \oplus {}^3T_1$. Again we can discard the $^3T_1$ state due to the timescales involved in the radiationless relaxation (*5*). Similarly to $Cr(CO)_5$ above, the only way to determine the energetic ordering of the singlet states is via high-level computation. In their spectroscopic analysis, Fuß *et al.* (*2,5*) proposed a pathway through a Jahn–Teller conical intersection imposed by the $^1T_2$ state. Furthermore, this intersection explains the nature of the photoproduct, which was previously determined using ultrafast electron diffraction by Zewail *et al.* (*3,33*) as C_{2v} $Fe(CO)_4$ in a singlet electronic state. Geometrically, they find that one of the pair of CFeC angles is 169 ± 2°, and the other 125 ± 3° (see below and Fig. 3 for our CASSCF results).

In Fig. 3 we show a cross section of the Jahn–Teller surface around the tetrahedral geometry. The simplest Jahn–Teller intersection is of $T \otimes t_2$ type (i.e., a triply degenerate electronic state whose components are coupled via a triply-degenerate vibration). Optimization of a triply degenerate conical intersection is not routinely possible at present. The vibrational modes of T_d $Fe(CO)_4$ span $Q_{3N-6} \in 2A_1 \oplus 2E \oplus T_1 \oplus 4T_2$, so there are clearly several candidate vibrations. This $T \otimes t$ type of

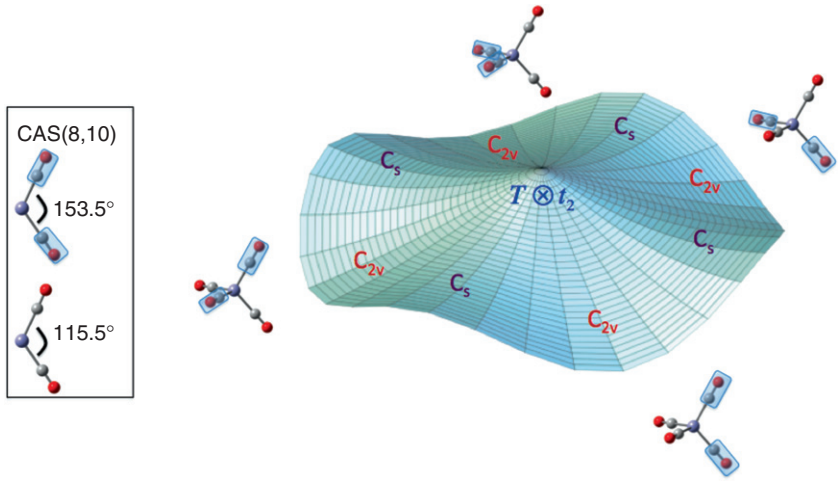

FIG. 3. $Fe(CO)_4$ cross section of the Jahn–Teller surface around a tetrahedral geometry (T_d), which has a triply degenerate singlet electronic state. The surface is a two-dimensional cross section through the three-dimensional Jahn–Teller surface. There are four equivalent C_{2v} minima connected via four equivalent C_s transition structures. The CASSCF CFeC angles are given to the left. Further C_{2v} minima and C_s transition structures exist in the remaining orthogonal coordinate.

intersection has received a lot of attention in the triplet manifold ($T \otimes t_1$ in this case) (*99–101*), as this corresponds to the global minimum of $Fe(CO)_4$. Bending of the CO ligands in a pairwise fashion leads from T_d to C_{2v}, and both the triplet and singlet Jahn–Teller surfaces are similar (*48*). The epikernel principle predicts that the number of equivalent C_{2v} minima will be given by the quotient of the size of the T_d group and the C_{2v} group $\left(= \frac{|n_{T_d}|}{|n_{C_{2v}}|} = \frac{24}{4} = 6\right)$. In Fig. 3 we show a two-dimensional cross section of the full three-dimensional surface, using a pair of orthogonal bending coordinates, each obtained as a linear combination of the three triply degenerate CFeC bending modes. Note that the full triply degenerate Jahn–Teller problem is $T \otimes (t_2 \oplus e)$, where the branching space is five dimensional in keeping with the von Neumann Wigner theorem. To our knowledge only the $T \otimes t_2$ interaction has been considered in any detail for $Fe(CO)_4$ in either the singlet or triplet manifolds. In the 2D cross section of this shown in Fig. 3 there are four C_{2v} minima (two per bending coordinate), connected by four C_s transition structures. In the

third orthogonal bending coordinate, there are a further two C_{2v} minima (each of these is connected to each of the others via C_s transition structures – the total number of these is given by the quotient of the size of the T_d group and the C_s group $\left(=\frac{|n_{T_d}|}{|n_{C_{2v}}|}=\frac{24}{2}=12\right)$ (*48*). The best visual representation of this is given by the octahedral model of Poliakoff *et al.* (*99*) in which each minimum is placed at the vertex of an octahedron. As depicted in Fig. 3, the barrier to pseudo-rotation between C_{2v} minima is quite small (about 4 kcal mol^{-1}).

Although the CASSCF Jahn–Teller surface in the singlet manifold helps to explain the experimental data relating to the ultrafast relaxation of $Fe(CO)_4$, (*3,5,33*) there is a problem which highlights the complexity of this system. CASSCF and MRCI predict that the $^1T_2$ state is in fact not the lowest singlet electronic state at T_d geometries. For example, CASSCF predicts that the ^1E state is in fact 5 kcal mol^{-1} lower than the $^1T_2$ state. However, an $E\otimes e$ Jahn–Teller intersection does not correctly give the observed photoproduct. We expect that in fact a complete Jahn–Teller model will involve both Jahn–Teller and pseudo-Jahn-Teller coupling: $(T\oplus E)\otimes(t_2\oplus e)$– a five-state, five-mode model. This is due to the proximity of the ^1E and $^1T_2$ states; the components of these states can strongly pseudo-Jahn–Teller couple via the same vibrations that are separately Jahn–Teller active within each degenerate manifold. This is reminiscent of the vibronic coupling in the P_4^+ cation (*102*). We are currently constructing such a model for use in quantum dynamics simulations of this system.

A.2. Multi-state dynamics simulation

Having established that conical intersections are accessible to connect excited state with ground-state potential energy surfaces, the next stage in modelling the reactive photochemistry is to simulate the dynamical motion of the nuclei on those coupled potential energy surfaces. As discussed above in section 3, Daniel *et al.* have performed the vast majority of dynamics simulations in inorganic photochemistry, via quantum wave packet approaches (*58,63,66,67,72,73,76*). The majority of these studies used reduced mode one- or two-dimensional simulations that are appropriate for the problems studied (e.g., direct photodissociation). As we discuss below the radiationless relaxation of unsaturated binary metal carbonyls requires a multimode treatment. Such approaches are still in their infancy in inorganic photochemistry and we now review two somewhat complementary approaches to

the relaxation of excited $Cr(CO)_5$: semi-classical trajectory surface hopping, and MCTDH wave packet simulation via a model vibronic coupling Hamiltonian.

In Ref. (*78*) a semi-classical trajectory study was performed. Here CASSCF potentials (using the (6,8) active space discussed above) were evaluated on-the-fly, and local surface information in the form of energies, gradients, and Hessians were used to drive classical trajectories on a single (ground or excited) potential energy surface. Non-adiabatic transitions between potential energy surfaces were determined using solutions to the time-dependent electronic Schrödinger equation. In basic terms, the probability that the system will hop from one potential surface to another is given by solution of the time-dependent Schrödinger equation for the time-dependent configuration interaction coefficients of the CASSCF wavefunction (these are propagated using a short-time propagator when the electronic states are sufficiently close in energy). If there is a hop from a higher to a lower surface then energy is added to the nuclei (in the direction of the non-adiabatic coupling vector) to account for energy conservation.

The trajectory studies in Ref. (*78*) were initiated by running a single-state trajectory on the S_1 surface of $Cr(CO)_6$. Dissociation of a CO ligand was observed within 90 fs, and this ligand was noted to leave in a rotationally excited fashion, consistent with the measured rotational temperature observed in the similar $W(CO)_6$ (*103*). Although the ejection of the ligand was the dominant nuclear motion, a subtle initialization of the in-plane symmetric L-M-L bending was also observed.

The positions and velocities of the nuclei in the $Cr(CO)_5$ fragment were then used as initial conditions in a surface-hopping trajectory started on S_1 (see Fig. 4 left). The system quickly (within 80 fs) reaches the TBP Jahn–Teller geometry where the CCrC angles are equal to 120º. The molecule travels briefly along the ground state C_{2v} ridge before hopping back up to the upper surface, spending a further 20 fs there until finally hopping to the ground state. During this last phase of the dynamics, energy is partially transferred from the symmetric to the asymmetric bending (remember that together these two motions define the branching space for the Jahn–Teller intersection in Fig. 2). The dynamics then evolves on the ground-state potential energy surface. Essentially, the asymmetric bending becomes excited as the molecule oscillates in the square-pyramidal well of the Jahn-Teller "moat". The Fourier transform of the dynamics corresponding to bending motion shown in Fig. 4 gives a vibrational frequency of 98 cm^{-1}, which corresponds to an observed vibrational coherence in the photoproduct of 96 cm^{-1} (*6,7*).

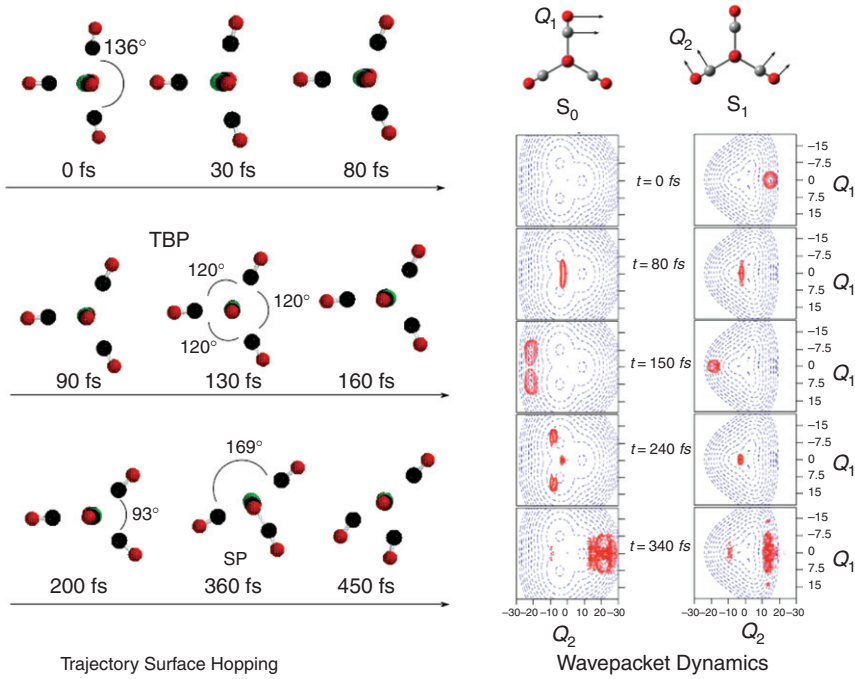

FIG. 4. $Cr(CO)_5$ excited state relaxation dynamics: comparison of semi-classical trajectory surface hopping (left), and MCTDH wave packet dynamics (right). Trajectory shows molecule passing through TBP Jahn–Teller geometry within 130 fs, then oscillating in SP potential well afterward. Wave packet dynamics plotted for the S_1 and S_0 adiabatic states in the space the symmetric and asymmetric CCrC bending coordinates.

The surface hopping study was rather expensive in terms of CPU time, and consequently large numbers of trajectories could not be run. This is important to obtain statistically converged dynamical properties. The main goal of the surface hopping study was thus not to obtain such information but to provide mechanistic insight into the photodissociation and subsequent relaxation processes. The semi-classical work in the full space of nuclear coordinates provides the important vibrational degrees of freedom that one needs to include in any quantum model of the nuclear motion. This will now be described.

A vibronic coupling model Hamiltonian was constructed using CASSCF (active space and basis set as discussed above for the semi-classical study) (*79*). The vibrational modes were obtained from a Hartree–Fock frequency calculation of the dianion, and it

was found that fitting the vibronic coupling diabatic potentials to the adiabatic CASSCF data required at least a three- state, five-mode model. The three states can be thought of as the degenerate the $^1E'$ and $^1A'_1$ adiabatic states obtained from the d^6 singlet electron configuration of TBP $Cr(CO)_5$: the diabatic states being linear combinations of these adiabatic ones. The vibrational modes required were linear combinations of the CCrC and OCrO degenerate pairs of symmetric and asymmetric bending vibrations. The final mode required was the totally symmetric breathing mode. The final model contained nine parameters to be obtained from fitting to the adiabatic CASSCF potentials, although this model Hamiltonian was non-intuitive, and required extensive experimentation with fitting. The model thus captures the essentials of the coupled Jahn–Teller surfaces, but cautions that the adiabatic potentials in the semi-classical work may hide pseudo-Jahn–Teller couplings required in a diabatic model vibronic Hamiltonian (*79*).

Wave packet dynamics simulations using this model vibronic coupling Hamiltonian were then carried out using the multiconfiguration time-dependent Hartree (MCTDH) method (*104*). The wave packet probability density is plotted for the S_1 and S_0 states in Fig. 4 right for the most important degenerate pair of bending vibrations. Population transfer to the ground state takes place after 80 fs and the wave packet bifurcates symmetrically at the Jahn–Teller geometry (center of surfaces). The wave packet motion is primarily radial, reaching the outer Jahn–Teller wall after 150 fs, returning to the conical intersection after 240 fs, and crosses through to the other side of the potential wall after 340 fs. Also notice that some population returns to the excited states after this passage across the intersection region. A time of 340 fs corresponding to radial motion back and forth across the Jahn–Teller intersection matches well the experimental timescale for the coherent vibration observed. This motion should be contrasted with the circular motion observed in the semi-classical dynamics.

Each of the semi-classical trajectory surface hopping and quantum wave packet dynamics simulations has its pros and cons. For the semi-classical trajectory surface hopping, the lack of coherence and phase of the nuclei, and total time per trajectory are cons; whereas inclusion of all nuclear degrees of freedom, the use of potentials direct from electronic structure theory, the ease of increasing accuracy by running more trajectories, and the ease of visualization of results are pros. For the quantum wave packet dynamics, the complexity of setting up an appropriate model Hamiltonian, use of approximate fitted potentials, and the

inclusion of only selected vibrational modes are cons; whereas full quantum treatment of nuclei, speed once the model Hamiltonian is set up, and gaining a more detailed understanding of the vibronic coupling when setting up the model Hamiltonian are all pros.

B. Computational Studies of the Pseudo-Jahn–Teller Effect

B.1. Ammonia

As an introduction to modern computational treatments of the pseudo-Jahn–Teller effect, we will briefly discuss the well-known pseudo-Jahn–Teller effect in ammonia using CASSCF force constants. Ammonia displays an interesting balance between competing internal forces and has interested the theoretical community for decades (*105*). In Fig. 5(a), we show the potential energy curve via the inversion coordinate. At a highly correlated level the inversion barrier is about 5 kcal mol^{-1}. Interestingly, the expectation value of the electronic wavefunction with the electronic Hamiltonian is lower at planar geometries than at pyramidal ones (Fig. 5(a)). However, the nuclear repulsion is larger at the optimal planar geometry, with the net result slightly favoring the pyramidal structure.

CASSCF analysis of the planar structure is shown in Fig. 5(b). The active space was built by distributing eight electrons in seven orbitals forming 490 configuration state functions (CSFs). All electrons of the system were included, excluding the nitrogen core $1s^2$ pair. A frequency calculation that includes all CSFs in the solution of the CP-MCSCF equations gives $\upsilon = 750.6i\ cm^{-1}$ for the vibrational wavenumber of the inversion mode. Thus the planar D_{3h} geometry is a first-order saddle point. As discussed above, the CP-MCSCF equations correspond to the quadratic terms in Eq. (9), and include both orbital and configuration mixing under the second-order nuclear perturbation. Restricting the CASSCF frequency calculation to CSFs of only ground-state symmetry (A_1 in the C_{2v} subgroup of D_{3h}) switches off the quadratic pJT term contribution between states of different symmetries. Thus, performing the CASSCF frequency with and without CSFs of different symmetries will inform if a pseudo-Jahn–Teller mixing is responsible for a given distortion via a vibrational coordinate. The pJT effect is demonstrated by a change from an imaginary frequency, when all CSFs are included, to a real frequency when CSFs of a particular symmetry type are excluded. Now, a frequency calculation including CSFs of all symmetry except B_2 gives no imaginary vibrational

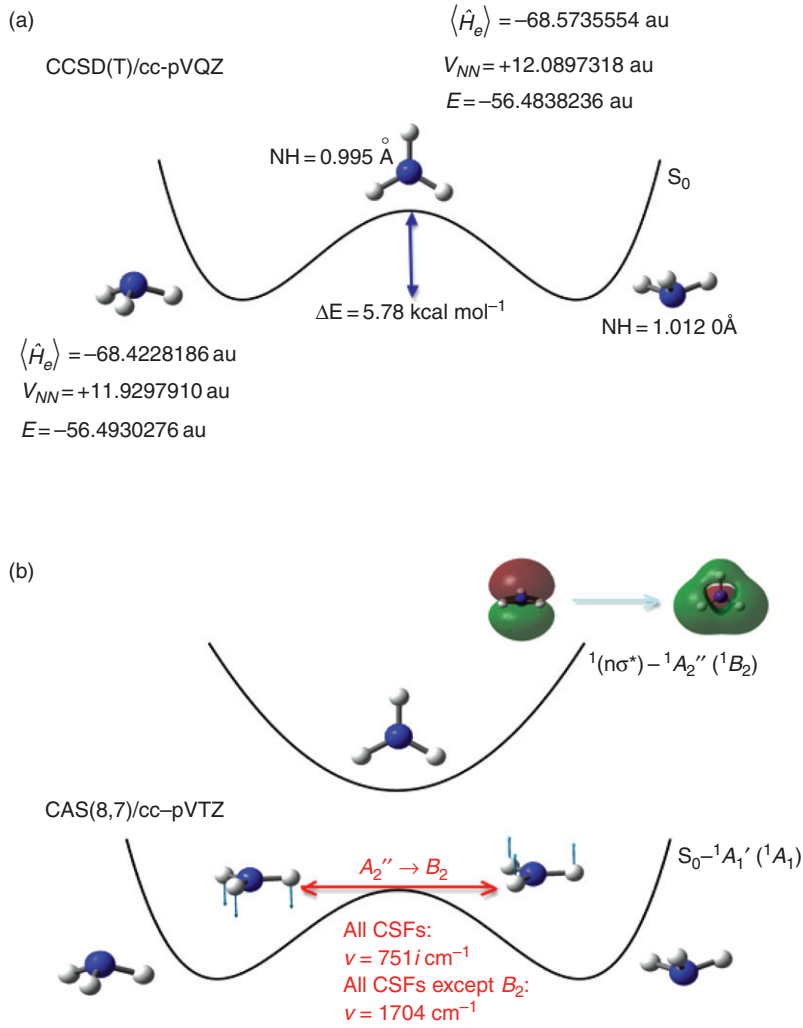

FIG. 5. The pseudo-Jahn–Teller effect in ammonia (NH_3). (a) CCSD(T) ground state potential energy curve; breakdown of energy into expectation value of electronic Hamiltonian $\langle \hat{H}_e \rangle$, and nuclear–nuclear repulsion V_{NN}. (b) CASSCF frequency analysis of pseudo-Jahn–Teller effect showing the effect of including CSFs of B_2 symmetry is to couple the ground and $^1(n\sigma^*)$ states to give a negative curvature to the adiabatic ground state potential energy surface for the inversion mode.

frequencies, and the vibrational wavenumber for inversion is now $\upsilon = 1703.8\ cm^{-1}$. The lowest excited state of ammonia is a $^1(n\boldsymbol{\sigma}^*)$ (HOMO to LUMO transition shown in Fig. 5(b)). This state has

symmetry A_2'' in D_{3h} and symmetry B_2 in the C_{2v} subgroup. This state lies about 6.05 eV above the ground adiabatic state at the planar geometry. The CASSCF frequency results clearly show that this state pJT couples to the ground state to change the curvature of the lower adiabatic potential energy surface and give a lower energy stable pyramidal C_{3v} minimum. Also note that since the S_1 state is nominally antibonding between the N and Hs, this pJT mixing also explains the NH bond elongation from the optimal D_{3h} to C_{3v} structures to allow for a reduction of nuclear–nuclear repulsion.

B.2. The edge-sharing bioctahedral complex $Mo_2(DXylF)_2(O_2CCH3)_2(\mu_2\text{-}O)_2$

We will now detail our work on understanding if a pseudo-Jahn–Teller mechanism is responsible for the observed geometry of a bimetallic system: $Mo_2(DXylF)_2(O_2CCH_3)_2(\mu_2\text{-}O)_2$, where DXylF is N,N'-di(2,6-xylylformamidine) (*55*). It is well known that vibronic coupling effects are one of the sources of distortions in crystal lattices (*46,106*). Cotton *et al*. presented studies on the edge-sharing bioctahedral complex $Mo_2(DXylF)_2(O_2CCH_3)_2(\mu_2\text{-}O)_2$ in which the main ring $Mo_2(\mu_2\text{-}O)_2$ displays rhomboidal C_{2h} symmetry rather than the expected D_{2h} square-shaped geometry (*107*). The authors postulated that this distortion could be due to pseudo-Jahn–Teller effects rather than crystal packing distortions.

We have applied the CASSCF frequency test to this system (*55*). With the associated expense of CASSCF Hessian evaluation we developed a model complex with the xylyl and methyl groups replaced by hydrogens (see Fig. 6). The basic active space for CASSCF studies included four electrons distributed in six orbitals (the three σ, π, δ metal–metal bonding orbitals, and their antibonding counterparts shown in Fig. 6). We note that the issue of "orbital doubling" discussed above for the metal carbonyls does not cause problems here: this is due to the different bonding mode involved, and the fact that the metal–metal anti-bonding orbitals provide correlation to the metal–metal bonding orbitals as further discussed below.

We also performed extensive DFT studies on both the full target system and the model for calibration purposes. For details of one-electron basis sets used please consult Ref. (*55*). We used the B3LYP functional but found the ground-state potential energy surface to be relatively insensitive to the chosen functional (note though that this does not mean that DFT gives the correct surfaces, as important nondynamical correlation effects are

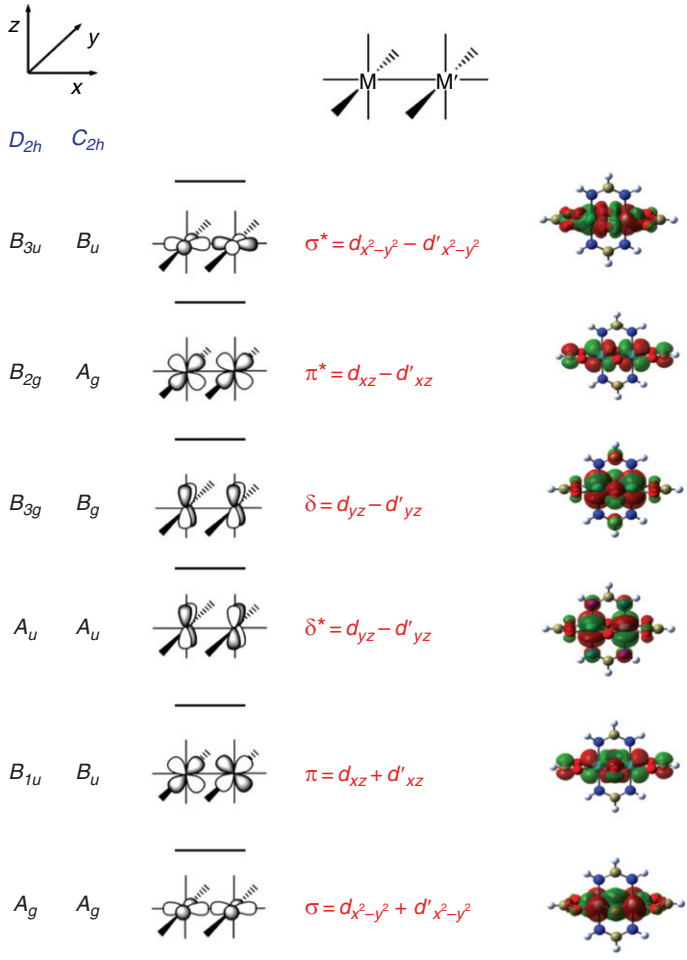

FIG. 6. Metal-metal orbitals in edge-sharing bioctahedral complex $Mo_2(DXylF)_2(O_2CCH_3)_2(\mu_2\text{-}O)_2$: schematic M-M interactions left, CASSCF optimized orbitals of model complex right [Adapted from Ref. 55 with permission].

missing – *vide infra*). DFT frequency calculations show for both the full and the model system that the rhomboidal C_{2h} structure is the ground-state minimum. The model system with D_{2h} symmetry of the main $Mo_2(\mu_2\text{-}O)_2$ structural motif is a transition state using both DFT and CASSCF (with all CSFs included in the computation). The vibrational mode responsible for D_{2h} to C_{2h} distortion (the rhomboidal distortion) has b_{1g} symmetry, and for CASSCF calculations including all possible CSFs (total = 105) is imaginary with wavenumber $\nu = 452.91i$ cm^{-1}. When we restrict the calculations

to CSFs of only ground-state symmetry A_g (total = 21) this vibration is no longer imaginary and has $\upsilon = 37.70\ \mathrm{cm}^{-1}$, which proves that there is a pseudo-Jahn–Teller effect in operation. Since the ground state is totally symmetric, the state it couples to via a b_{1g} vibration is a B_{1g} state. The lowest state of this symmetry is a $^1(\pi\delta*)$ state, which is also the S_1 state. This state is of course a dark state to standard one-photon absorption. The ground electronic state S_0 can be written as $\sigma^2\pi^2$; however, CAS calculations reveal that there is significant correlation between the σ bonding and σ* antibonding orbitals, and also correlation between π bonding and π* antibonding orbitals (*55*). This is manifested in the CASSCF one-electron density matrix where there is significant population of the antibonding orbitals (about 0.1 – 0.2 electrons). Thus, the CASSCF wavefunctions should sound warning bells on the applicability of DFT here. The CASSCF S_1 state is nominally $\sigma^2\pi^1\delta*^1$ but again there is significant correlation across the σ, π, δ systems. Note that this (lowest) excited state has the δ* orbital occupied before the δ orbital. This is not uncommon, and often the energetic ordering of these orbitals in bimetallic systems depends very subtlety on any bridging atoms present (*108*). The $^1(\pi\delta^*)$ state has B_{1g} symmetry so we can see that since $\Gamma_{S_0}(A_g)\otimes\Gamma_{Q_{Rd}}(b_{1g})\otimes\Gamma_{S_1}(B_{1g})\supset A_g$ these states can couple through the rhomboidal b_{1g} vibration. The potential energy surfaces for the ground and first excited states of the model complex are shown in Fig. 7. One can see that the square D_{2h} geometry is a first-order saddle point on S_0, whereas it is a minimum on S_1. The two states are separated by about 1.05 eV at this geometry. The pseudo-Jahn–Teller coupling allows the ground state to mix with the $^1(\pi\delta*)$ state causing a change from positive to negative curvature on S_0 and an increase in the S_0–S_1 energy gap. From the potential energy surfaces shown in Fig. 7, it is hopefully clear that such pseudo-Jahn–Teller coupling very closely resembles the type-II Renner–Teller coupling discussed above (Fig. 1); the only difference is the fact that there is a finite energy gap between the coupled states at the reference geometry.

C. GENERAL CONICAL INTERSECTIONS: MER–FAC PHOTOIZOMERIZATION IN A PT–AMIDO PINCER COMPLEX

In our final case study we shall focus on the photoinduced *mer* to *fac* isomerization reaction recently observed by Harkins and Peters (*109*). We have investigated this system in detail (*110*), and it provides a nice example of a general conical intersection in an inorganic photochemical problem, i.e., one that is not imposed by symmetry via a Jahn–Teller degeneracy.

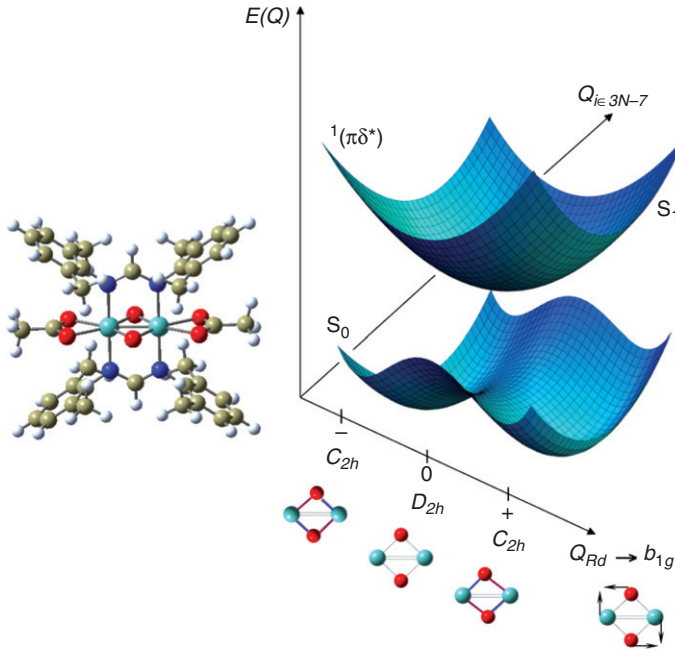

FIG. 7. Potential energy surfaces for ground and first excited state of $Mo_2(DXylF)_2(O_2CCH_3)_2(\mu_2\text{-}O)_2$ complex. The pseudo-Jahn-Teller effect results from a coupling between S_0 and the excited $^1(\pi\delta*)$ state, causing the central $Mo_2(\mu_2\text{-}O)_2$ motif to be rhomboidal (C_{2h}), rather than square (D_{2h}) [Adapted from Ref. (*55*) with permission].

The intriguing experimental result from Harkins and Peters was that they found that (BQA)$PtMe_2I$ (BQA=bis (8-quinolinyl)amine) (see Fig. 8) exposed to visible light irradiation resulted in an unexpected stereochemical transformation from the *mer* form (all coordinating nitrogens and metal being coplanar), to the *fac* form (all coordinating nitrogens *cis* to each other). DFT predicts both the *mer* and *fac* isomers to have a very similar stability (*110*). Such complexes are very important in inorganic chemistry and photochemistry as the BQA ligand belongs to the robust group of "pincer-type" amido ligands, which undergo a rich variety of chemistry, including applications in catalysis (*111–113*), electrochemical devices (*114*), and in the activation of small molecules (*115,116*). These ligands also have potential uses in organic light emitting diode devices (OLEDs) (*117,118*). One common feature of the BQA ligand is its tendency to adopt planar geometries with the central amide nitrogen having sp^2 hybridization.

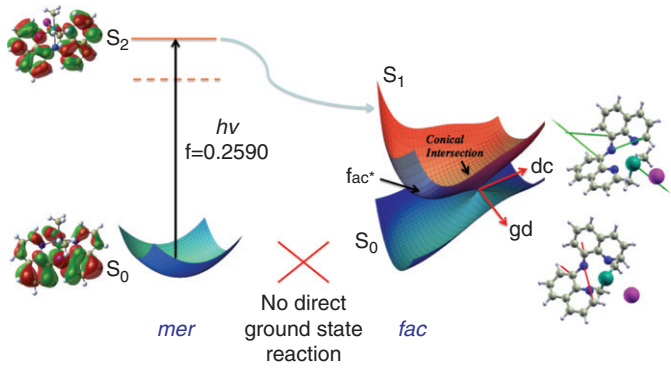

FIG. 8. Schematic representation of the potential surfaces leading to photoisomerisation of (BQA)$PtMe_2I$ from *mer* to *fac* isomer via a sloped conical intersection at *fac*-like geometries. Shown to the right are the branching space vectors: the gradient difference (gd=$\mathbf{x}_1$), and the derivative coupling (dc=$\mathbf{x}_2$). The primary orbitals involved in the electronic transition are shown to the left [Adapted from Ref. (*110*) with permission].

Both the *mer* and *fac* have one broad intense absorption band at lower energies: 534 nm for the *mer*, and 422 nm for the *fac* (*109*). Time-dependent density functional theory (B3LYP), in conjunction with the polarizable continuum model (PCM) of solvation, closely reproduces these values. For further analysis of the effect of different functionals and basis sets see Ref. (*110*). The main conclusion of TD-DFT is that the populated states are of localized $\pi\pi^*$ character, with very little involvement of the central metal orbitals. It was previously postulated that the populated states were of LMCT character but TD-DFT shows that the low energy band of the absorption spectrum arises predominately from localized $\pi\pi^*$ states that reduce the conjugation across the amide linker. This is important as the reduction in conjugation allows the BQA ligand to fold in. TD-DFT geometry optimization (recently available in Gaussian (*92*)) shows that upon photoexcitation of the *mer* form the system can relax in the S_1 adiabatic state to an excited *fac*-like geometry (see geometries in Ref. (*110*)). Whether the photoexcited state is actually S_1 or S_2 depends sensitively on the functional used, although regardless of this an S_1 *fac*-like geometry is reached.

It is on the *fac* (product) side that we find a non-adiabatic radiationless decay channel back to the ground state via a sloped conical intersection (Fig. 8) that connects the excited and ground state *fac* species. To investigate this region we have used CASSCF. The shear system size here presents difficulties

in choosing an appropriate active space. The approach adopted was to use natural orbitals obtained from unrestricted Hartree–Fock calculations. Such approximate natural orbitals have eigenvalues that are occupation numbers and give an indication of each orbitals importance in a multi-configurational wavefunction. Occupation numbers (diagonal elements of the one-electron density matrix) that differ significantly from zero or two should be included in the complete active space (see the discussion above of the importance of orbital occupations in the bimetallic example). From a more qualitative point of view, the natural orbitals were compared with the orbitals involved in the TD-DFT response eigenvectors. Finally an active space consisting of 14 electrons distributed in 12 orbitals to generate 314028 singlet CSFs was obtained. This was checked for stability by reoptimizing to the same electronic state after switching pairs of weakly correlated orbitals into and out of the active space.

A sloped conical intersection was found that was about 10 kcal mol^{-1} above the excited *fac* minimum (also optimized with CASSCF and very similar to the TD-DFT optimized geometry). The conical intersection is shown schematically to the right in Fig. 8, along with the gradient difference ($\mathbf{x}_1$: Eq. (7)) and derivative coupling ($\mathbf{x}_2$: Eq. (8)) vectors. For the bare BQA ligand we found an extended seam of conical intersection, which has a global minimum with the two quinoline arms twisted at about 90º to each other. The seam also extends to geometries similar to that found in the complex at folded *fac*-like geometries (found via constrained optimization of the intersection seam). Thus the degeneracy between the ground and first excited state is a feature of bare ligand itself.

The photochemical pathway can therefore be thought of as excitation on the BQA ligand, leading to reduced conjugation across the amide linkage, a downhill driving force toward the *fac* region by folding of the BQA, and a loose rearrangement of the other ligands around the metal. Here there is an excited *fac* minimum that is connected to the ground electronic state via a sloped conical intersection. Radiationless decay here generates the stable *fac* photoproduct. Interestingly, the role of the metal seems to be as a scaffold, which clips the BQA in place in both geometries, but which does not participate directly in the observed photochemistry. The non-adiabatic pathway from excited species to ground species also seems to only exist in the *fac* region, meaning the photochemical isomerization is essentially a one-way process. Note that the sloped topology of the intersection (Fig. 8) means that excitation on the *fac* side will regenerate the S_0 *fac*.

V. Conclusions and Outlook

We have presented a necessarily biased and non-exhaustive review of recent work on the application of computational chemistry to vibronic coupling problems in inorganic chemistry. Given the capabilities of modern time-resolved spectroscopy, such computational studies are becoming increasingly important. The methods of excited-state quantum chemistry, in conjunction with appropriate treatment of the dynamical motion of nuclei, gives ever more detailed information. As hardware continues to improve, larger inorganic systems will be investigated. Continued software advances will allow for unprecedented inclusion of more coupled electronic states and vibrational degrees of freedom. Thus the field has matured to the point where accurate multi-state, multi-mode computational treatment of inorganic photochemical problems can routinely be contemplated.

Acknowledgments

We thank the EPSRC for funding through grant EP/F01709X.

References

1. Turro, N. J.; Ramamurthy, V.; Scaiano, J. C. *Principles of Molecular Photochemistry: An Introduction*. University Science Books: Sausalito, CA, **2009**.
2. Fuss, W.; Trushin, S. A.; Schmid, W. E. *Res. Chem. Intermed.* **2001**, *27*(4–5), 447–457.
3. Ihee, H.; Cao, J.; Zewail, A. H. *Angew. Chem. Int. Ed.* **2001**, *40*(8), 1532–1536.
4. Kim, S. K.; Pedersen, S.; Zewail, A. H. *Chem. Phys. Lett.* **1995**, *233*(5–6), 500–508.
5. Trushin, S. A.; Fuss, W.; Kompa, K. L.; Schmid, W. E. *J. Phys. Chem. A* **2000**, *104*(10), 1997–2006.
6. Trushin, S. A.; Fuss, W.; Schmid, W. E. *Chem. Phys.* **2000**, *259*(2–3), 313–330.
7. Trushin, S. A.; Fuss, W.; Schmid, W. E.; Kompa, K. L. *J. Phys. Chem. A* **1998**, *102*(23), 4129–4137.
8. Zewail, A. H. *Pure Appl. Chem.* **2000**, *72*(12), 2219–2231.
9. Roos, B. O.; Andersson, K.; Fülscher, M. P.; Malmqvist, P. A.; Serrano-Andrés, L.; Pierloot, K.; Merchan, M. *Adv. Chem. Phys.* **1996**, *93*, 219–331.
10. Roos, B. O. Multiconfigurational quantum chemistry. In *Theory and Application of Computational Chemistry: The First Forty Years*, Eds. Dykstra, C.; Frenking, G.; Kim, K.; Scuseria, G.; Elsevier: Amsterdam, **2005**, p. 725.
11. Worth, G. A.; Cederbaum, L. S. *Annu. Rev. Phys. Chem.* **2004**, *55*, 127–158.

12. Robb, M. A.; Bernardi, F.; Olivucci, M. *Pure Appl. Chem.* **1995**, *67*(5), 783–789.
13. Bernardi, F.; Olivucci, M.; Robb, M. A. *Chem. Soc. Rev.* **1996**, *25*(5), 321–328.
14. Yarkony, D. R. *Rev. Mod. Phys.* **1996**, *68*(4), 985–1013.
15. Garavelli, M.; Bernardi, F.; Olivucci, M.; Vreven, T.; Klein, S.; Celani, P.; Robb, M. A. *Faraday Discuss.* **1998**, *110*, 51–70.
16. Robb, M. A.; Garavelli, M.; Olivucci, M.; Bernardi, F. *Rev. Comput. Chem.* **2000**, *15*, 87–146.
17. Yarkony, D. R. *J. Phys. Chem. A* **2001**, *105*(26), 6277–6293.
18. Garavelli, M. *Theor. Chem. Acc.* **2006**, *116*(1–3), 87–105.
19. Palmer, I. J.; Ragazos, I. N.; Bernardi, F.; Olivucci, M.; Robb, M. A. *J. Am. Chem. Soc.* **1993**, *115*(2), 673–682.
20. Sanchez-Galvez, A.; Hunt, P.; Robb, M. A.; Olivucci, M.; Vreven, T.; Schlegel, H. B. *J. Am. Chem. Soc.* **2000**, *122*(12), 2911–2924.
21. Blancafort, L.; Jolibois, F.; Olivucci, M.; Robb, M. A. *J. Am. Chem. Soc.* **2001**, *123*(4), 722–732.
22. Paterson, M. J.; Blancafort, L.; Wilsey, S.; Robb, M. A. *J. Phys. Chem. A* **2002**, *106*(47), 11431–11439.
23. Paterson, M. J.; Robb, M. A.; Blancafort, L.; DeBellis, A. D. *J. Am. Chem. Soc.* **2004**, *126*(9), 2912–2922.
24. Paterson, M. J.; Robb, M. A.; Blancafort, L.; DeBellis, A. D. *J. Phys. Chem. A* **2005**, *109*(33), 7527–7537.
25. Sundström, V. *Annu. Rev. Phys. Chem.* **2008**, *59*, 53–77.
26. Kandori, H.; Shichida, Y.; Yoshizawa, T. *Biochem. (Moscow)* **2001**, *66*(11), 1197–1209.
27. Kim, J. E.; McCamant, D. W.; Zhu, L. Y.; Mathies, R. A. *J. Phys. Chem. B* **2001**, *105*(6), 1240–1249.
28. Chosrowjan, H.; Mataga, N.; Nakashima, N.; Imamoto, Y.; Tokunaga, F. *Chem. Phys. Lett.* **1997**, *270*(3–4), 267–272.
29. Groenhof, G.; Schafer, L. V.; Boggio-Pasqua, M.; Grubmuller, H.; Robb, M. A. *J. Am. Chem. Soc.* **2008**, *130*(11), 3250.
30. Groenhof, G.; Bouxin-Cademartory, M.; Hess, B.; De Visser, S. P.; Berendsen, H. J. C.; Olivucci, M.; Mark, A. E.; Robb, M. A. *J. Am. Chem. Soc.* **2004**, *126*(13), 4228–4233.
31. Barbatti, M.; Lischka, H. *J. Am. Chem. Soc.* **2008**, *130*(21), 6831–6839.
32. Blancafort, L.; Cohen, B.; Hare, P. M.; Kohler, B.; Robb, M. A. *J. Phys. Chem. A* **2005**, *109*(20), 4431–4436.
33. Ihee, H.; Cao, J.; Zewail, A. H. *Chem. Phys. Lett.* **1997**, *281*(1–3), 10–19.
34. Trushin, S. A.; Kosma, K.; Fuss, W.; Schmid, W. E. *Chem. Phys.* **2008**, *347* (1–3), 309–323.
35. Hoffman, M. R.; Martin, S. T.; Choi, W.; Bahnemann, D. W. *Chem. Rev.* **1995**, *95*, 69–96.
36. Potje-Kamloth, K. *Chem. Rev.* **2008**, *108*(2), 367–399.
37. Haas, K. L.; Franz, K. J. *Chem. Rev.* **2009**, *109*(10), 4921–4960.
38. McMillin, D. R.; McNett, K. M. *Chem. Rev.* **1998**, *98*, 1202–1219.
39. Szacilowski, K.; Macyk, W.; Drzewiecka-Matuszek, A.; Brindell, M.; Stochel, G. *Chem. Rev.* **2005**, *105*, 2647–2694.
40. Von Neumann, J.; Wigner, E. Z. *Phys.* **1929**, *30*, 467–470.
41. Teller, E. *Isr. J. Chem.* **1969**, *7*, 227–235.
42. Paterson, M. J.; Bearpark, M. J.; Robb, M. A.; Blancafort, L.; Worth, G. A. *Phys. Chem. Chem. Phys.* **2005**, *7*(10), 2100–2115.
43. Sicilia, F.; Blancafort, L.; Bearpark, M. J.; Robb, M. A. *J. Chem. Theory Comput.* **2008**, *4*(2), 257–266.

44. Paterson, M. J.; Bearpark, M. J.; Robb, M. A.; Blancafort, L. *J. Chem. Phys.* **2004**, *121*(23), 11562–11571.
45. Bersuker, I. B. *Chem. Rev.* **2001**, *101*(4), 1067–1114.
46. Bersuker, I. B. *The Jahn-Teller Effect*. Cambridge University Press: Cambridge: **2006**, p. 616.
47. Jahn, H. A.; Teller, E. *Proc. Roy. Soc. Lond. A* **1937**, *161*, 220–235.
48. Mckinlay, R. G.; Paterson, M. J. The Jahn-Teller Effect in Binary Transition Metal Carbonyl Complexes. In: "*The Jahn-Teller Effect: Fundametals and Implications for Physics and Chemistry*", Eds. Köppel, H.; Yarkony, D. R.; Barentzen, H.; Springer: Heidelberg, **2009**, p 311–344.
49. Bersuker, I. B.; Balabanov, N. B.; Pekker, D.; Boggs, J. E. *J. Chem. Phys.* **2002**, *117*(23), 10478–10486.
50. Garcia-Fernandez, P.; Bersuker, I. B.; Boggs, J. E. *J. Chem. Phys.* **2006**, *124*(4), 044321.
51. Pearson, R. G. *Proc. Nat. Acad. Sci. U.S.A.* **1975**, *72*(6), 2104–2106.
52. Paterson, M. J.; Chatterton, N. P.; McGrady, G. S. *New J. Chem.* **2004**, *28* (12), 1434–1436.
53. Bearpark, M. J.; Blancafort, L.; Robb, M. A. *Mol. Phys.* **2002**, *100*(11), 1735–1739.
54. Blancafort, L.; Bearpark, M. J.; Robb, M. A. *Mol. Phys.* **2006**, *104*(13–14), 2007–2010.
55. Żurek, J. M.; Paterson, M. J. *Inorg. Chem.* **2009**, *48*(22), 10652–10657.
56. Daniel, C. *J. Am. Chem. Soc.* **1992**, *114*(5), 1625–1631.
57. Marquez, A.; Daniel, C.; Sanz, J. F. *J. Phys. Chem.* **1992**, *96*(1), 121–123.
58. Daniel, C.; Heitz, M. C.; Lehr, L.; Manz, J.; Schröder, T. *J. Phys. Chem.* **1993**, *97*(48), 12485–12490.
59. Finger, K.; Daniel, C. *J. Am. Chem. Soc.* **1995**, *117*(49), 12322–12327.
60. Guillaumont, D.; Daniel, C. *Chem. Phys. Lett.* **1996**, *257*(1–2), 1–7.
61. Heitz, M. C.; Ribbing, C.; Daniel, C. *J. Chem. Phys.* **1997**, *106*(4), 1421–1428.
62. Hachey, M. R. J.; Daniel, C. *Inorg. Chem.* **1998**, *37*(6), 1387–1391.
63. Guillaumont, D.; Daniel, C. *J. Am. Chem. Soc.* **1999**, *121*(50), 11733–11743.
64. Rubner, O.; Engel, V.; Hachey, M. R.; Daniel, C. *Chem. Phys. Lett.* **1999**, *302*(5–6), 489–494.
65. Kuhn, O.; Hachey, M. R.D.; Rohmer, M. M.; Daniel, C. *Chem. Phys. Lett.* **2000**, *322*(3–4), 199–206.
66. Guillaumont, D.; Vlcek, A.; Daniel, C. *J. Phys. Chem. A* **2001**, *105*(7), 1107–1114.
67. Daniel, C. *Coord. Chem. Rev.* **2003**, *238*, 143–166.
68. Ambrosek, D.; Villaume, S.; Gonzalez, L.; Daniel, C. *Chem. Phys. Lett.* **2006**, *417*(4–6), 545–549.
69. Ben Amor, N.; Villaume, S.; Maynau, D.; Daniel, C. *Chem. Phys. Lett.* **2006**, *421* (4–6), 378–382.
70. Costa, P. J.; Calhorda, M. J.; Bossert, J.; Daniel, C.; Romao, C. C. *Organometallics* **2006**, *25*(22), 5235–5241.
71. Gonzalez, L.; Daniel, C. *J. Comput. Chem.* **2006**, *27*(15), 1781–1786.
72. Ambrosek, D.; Villaume, S.; Daniel, C.; Gonzalez, L. *J. Phys. Chem. A* **2007**, *111*(22), 4737–4742.
73. Ben Amor, N.; Ambrosek, D.; Daniel, C.; Marquardt, R. *Chem. Phys.* **2007**, *338*(2–3), 81–89.
74. Finger, K.; Daniel, C.; Saalfrank, P.; Schmidt, B. *J. Phys. Chem.* **1996**, *100*(9), 3368–3376.
75. Finger, K.; Daniel, C. *J. Chem. Soc., Chem. Commun.* **1995**, (14), 1427–1428.

76. Costa, P. J.; Calhorda, M. J.; Villaume, S.; Daniel, C. *New J. Chem.* **2008**, *32*(11), 1904–1909.
77. Walter, T. D.; Casey, S. M.; Klein, M. T.; Fole, H. C. *Energy Fuels* **1994**, *8*, 470–473.
78. Paterson, M. J.; Hunt, P. A.; Robb, M. A.; Takahashi, O. *J. Phys. Chem. A* **2002**, *106*(44), 10494–10504.
79. Worth, G. A.; Welch, G.; Paterson, M. J. *Mol. Phys.* **2006**, *104* (5–7), 1095–1105.
80. Kotzian, M.; Rosch, N.; Schroeder, H.; Zerner, M. C. *J. Am. Chem. Soc.* **1989**, *111* (20), 7687–7696.
81. Villaume, S.; Strich, A.; Daniel, C.; Perera, S. A.; Bartlett, R. J. *Phys. Chem. Chem. Phys.* **2007**, *9*, 6115–6122.
82. Ben Amor, N.; Villaume, S.; Maynau, D.; Daniel, C. *Chem. Phys. Lett.* **2006**, *421*(4–6), 378–382.
83. Beach, N. A.; Gray, H. B. *J. Am. Chem. Soc.* **1968**, *90*(21), 5713–5721.
84. Pierloot, K.; Tsokos, E.; Vanquickenborne, L. G. *J. Phys. Chem.* **1996**, *100* (41), 16545–16550.
85. Pollak, C.; Rosa, A.; Baerends, E. J. *J. Am. Chem. Soc.* **1997**, *119*(31), 7324–7329.
86. Rosa, A.; Baerends, E. J.; van Gisbergen, S. J.A.; van Lenthe, E.; Groeneveld, J. A.; Snijders, J. G. *J. Am. Chem. Soc.* **1999**, *121*(44), 10356–10365.
87. Christiansen, O.; Jørgensen, P.; Hättig, C. *Int. J. Quantum Chem.* **1998**, *68*(1), 1–52.
88. Christiansen, O.; Koch, H.; Jørgensen, P.; Olsen, J. *Chem. Phys. Lett.* **1996**, *256*, 185–194.
89. Paterson, M. J.; Christiansen, O.; Pawłowski, F.; Jørgensen, P.; Hättig, C.; Helgaker, T.; Sałek, P. *J. Chem. Phys.* **2006**, *124*(5), 054322.
90. Leadbeater, N. *Coord. Chem. Rev.* **1999**, *188*, 35–70.
91. Yanai, T.; Tew, D. P.; Handy, N. C. *Chem. Phys. Lett.* **2004**, *393*(1–3), 51–57.
92. Frisch, M. J.T.G.W.; Schlegel, H. B.; Scuseria, G. E.; Robb, M. A.; Cheeseman, J. R.; Scalmani, G.; Barone, V.; Mennucci, B.; Petersson, G. A.; Nakatsuji, H.; Caricato, M.; Li, X.; Hratchian, H. P.; Izmaylov, A. F.; Bloino, J.; Zheng, G.; Sonnenberg, J. L.; Hada, M.; Ehara, M.; Toyota, K.; Fukuda, R.; Hasegawa, J.; Ishida, M.; Nakajima, T.; Honda, Y.; Kitao, O.; Nakai, H.; Vreven, T.; Montgomery, Jr., J. A.; Peralta, J. E.; Ogliaro, F.; Bearpark, M.; Heyd, J. J.; Brothers, E.; Kudin, K. N.; Staroverov, V. N.; Kobayashi, R.; Normand, J.; Raghavachari, K.; Rendell, A.; Burant, J. C.; Iyengar, S. S.; Tomasi, J.; Cossi, M.; Rega, N.; Millam, N. J.; Klene, M.; Knox, J. E.; Cross, J. B.; Bakken, V.; Adamo, C.; Jaramillo, J.; Gomperts, R.; Stratmann, R. E.; Yazyev, O.; Austin, A. J.; Cammi, R.; Pomelli, C.; Ochterski, J. W.; Martin, R. L.; Morokuma, K.; Zakrzewski, V. G.; Voth, G. A.; Salvador, P.; Dannenberg, J. J.; Dapprich, S.; Daniels, A. D.; Farkas, Ö.; Foresman, J. B.; Ortiz, J. V.; Cioslowski, J.; Fox, D. J. *Gaussian 09, Revision A.02*, Gaussian, Inc.: Wallingford CT, **2009**.
93. Lasorne, B.; Robb, M. A.; Worth, G. A. *Phys. Chem. Chem. Phys.* **2007**, *9*, 3210–3227.
94. Worth, G. A.; Robb, M. A.; Burghardt, I. *Faraday Discuss.* **2004**, *127*, 307–323.
95. Worth, G. A.; Robb, M. A.; Lasorne, B. *Mol. Phys.* **2008**, *106*(16), 2077–2091.
96. Jean, Y. *Molecular Orbitals of Transition Metal Complexes*. OUP: Oxford, **2005**.
97. Persson, B. J.; Roos, B. O.; Pierloot, K. *J. Chem. Phys.* **1994**, *101*(8), 6810–6821.

98. Ceulemans, A.; Vanquickenborne, L. G. *Struct. Bond.* **1989**, *71*, 125–159.
99. Poliakoff, M.; Ceulemans, A. *J. Am. Chem. Soc.* **1984**, *106*(1), 50–54.
100. Poliakoff, M.; Turner, J. J. *Angew. Chem. Int. Ed.* **2001**, *40*(15), 2809–2812.
101. Poliakoff, M.; Weitz, E. *Acc. Chem. Res.* **1987**, *20*(11), 408–414.
102. Meiswinkel, R.; Köppel, H. *Chem. Phys. Lett.* **1993**, *201* (5–6), 449–457.
103. Holland, J. P.; Rosenfeld, R. N. *J. Chem. Phys.* **1988**, *89*, 7217–7225.
104. Beck, M. H.; Jäckle, A.; Worth, G. A.; Meyer, H. D. *Phys. Rep.* **2000**, *324* (1), 1–105.
105. Kettle, S. F. A. *Symmetry and structure: Readable Group Theory for Chemists*. (3rd ed.),; Wiley: Chichester, **2007**.
106. Köppel, H.; Yarkony, D. R.; Barentzen, H. *The Jahn-Teller Effect: Advances and Perspectives, Springer Series in Chemical Physics*. Springer; Heidelberg, **2009**.
107. Cotton, F. A.; Daniels, L. M.; Murillo, C. A.; Slaton, J. G. *J. Am. Chem. Soc.* **2002**, *124*(12), 2878–2879.
108. Cotton, F. A.; Walton, R. A. *Multiple bonds Between Metal Atoms*. Clarendon Press: Oxford, **1993**.
109. Harkins, S. B.; Peters, J. C. *Inorg. Chem.* **2006**, *45* (11), 4316–4318.
110. Żurek, J. M.; Paterson, M. J. *J. Phys. Chem. Lett.* **2010**, *1*, 1301–1306.
111. Huang, M. H.; Liang, L. C. *Organometallics* **2004**, *23* (11), 2813–2816.
112. Sun, K.; Wang, L.; Wang, Z. *Organometallics* **2008**, *27*, 5649–5656.
113. Weng, W.; Guo, C. Y.; Çelenligil-Çetin, R.; Foxman, B. M.; Ozerov, O. V. *Chem. Commun.* **2006**, (2), 197–199.
114. Harkins, S. B.; Peters, J. C. *J. Am. Chem. Soc.* **2005**, *127* (7), 2030–2031.
115. Harkins, S. B.; Peters, J. C. *Organometallics* **2002**, *21*(9), 1753–1755.
116. Van Koten, G. *Pure Appl. Chem.* **1989**, *61*(10), 1681–1694.
117. Humbs, W.; van Veldhoven, E.; Zhang, H.; Glasbeek, M. *Chem. Phys. Lett.* **1999**, *304*(1–2), 10–18.
118. van Veldhoven, E.; Zhang, H.; Glasbeek, M. (Sub)picosecond Time-Resolved Fluorescence Depolarization of OLED Compounds Alq_3, Gaq_3, and Inq_3. In: "*Ultrafast Phenomena XII*, Ed. Elsaesser", T.; Springer: New York, **2001**; p 482–484.

ELEMENTARY REACTIONS IN POLYNUCLEAR IONS AND AQUEOUS–MINERAL INTERFACES: A NEW GEOLOGY

JAMES R. RUSTAD

Department of Geology, University of California, One Shields Ave, Davis, CA 95616, USA

I. Molecular Geology

Since they first puzzled over the geometric regularity of faceted crystals, geologists have been striving for a molecular-level understanding of the processes that control the transformation of earth materials. The relative lack of success in this endeavor can be revealed by asking why, if everyone knows what a "molecular biologist" is, there is no such corresponding occupation as a "molecular geologist." That this should be so is even more surprising considering the vast amount of effort devoted over the 20th century to the determination of thousands of crystal structures of minerals of geological importance. Up through the 1970s every geology department in a major research university had at least

THEORETICAL AND COMPUTATIONAL INORGANIC CHEMISTRY
VOLUME 62 ISSN 0898-8838 / DOI: 10.1016/S0898-8838(10)62010-7

one specialist in X-ray mineralogy and crystallography. Roughly contemporaneous with the understanding of plate tectonics, geology had completed a remarkably comprehensive database of the crystal structures of thousands of minerals making up the Earth's crust and the more remote mineral assemblages making up the Earth's mantle. Uncovering the fundamental atomic structures of earth materials should have had the same transformational effect on geology that, for example, protein crystallography had on biology. The most basic and most interesting questions, such as the motions of tectonic plates, the rates of dissolution and weathering of rocks at the earth's surface into primary oxides and clay minerals, the process of replacing and preserving biological materials with minerals on deep time-scales, and the fractionation of isotopes during establishment of the earth's rock record have a molecular component that is no less central or less fascinating than those underpinning biological processes.

Many of these questions are not purely academic. For example, it is well known that ice bubbles trapped in ice sheets such as the one covering Greenland and Antarctica can be used to reconstruct the composition of earth's atmosphere over the past 750,000 years (*1*). Because atmospheric CO_2 levels have never exceeded 300 ppm during that time, society is now concerned with the 380 ppm CO_2 levels found in the atmosphere today. However, a million years is a relatively short time scale for geological processes. There are techniques that can probe, indirectly using carbon and boron isotopes, atmospheric CO_2 concentrations on much longer 10–100 million-year timescales and indicate that PCO_2 levels may have been 10–15 times higher over a significant fraction of the past 650 million years of earth history during which complex life has evolved (*2*). Effective use of such methods depends on increasingly detailed molecular-level knowledge of how the carbon and boron isotope signatures are imprinted in minerals.

Beginning with a pioneering paper by Gibbs (*3*), computational chemistry and computational mineral physics have been used extensively in the geosciences. Computational chemistry is much more central to molecular-level geology than it is in molecular biology. Of course, computational chemistry has made important contributions to molecular biology, but molecular biology could, and did, evolve without the field of computational chemistry. It is not clear that this is the case in molecular geology, where the entire context of a molecular-level understanding is often based on computational models of processes that are thought to occur at mineral–water interfaces, grain boundaries, or dislocation cores. Partly this is because

molecular geology evolved somewhat later than molecular biology, and happened to coincide with the rise of computational chemistry in the 1970s and 1980s. More importantly, the central role of computational chemistry in the earth sciences arises because molecular-level characterization of interfaces, where much of the action takes place in geological phenomena, is a more difficult problem than determination of the molecular structure of, for example, proteins. Obviously, both proteins and minerals can be crystallized. In fact, one of the earliest studies in protein crystallography was a collaborative effort between a physiologist and a mineralogist, resulting in a remarkable collection of hemoglobin crystals collected from hundreds of different species (*4*). That a physiologist should seek aid from a mineralogist in searching for a more fundamental molecular understanding of biological processes seems ironic now, and pointedly highlights the divergence of research directions in each of these fields since that time.

Because mineral transformations are often governed by surface phenomena, geologists are only now beginning to resolve surface structures at a sufficiently fine scale to think about potential molecular-level processes. When structural details are resolved, after great effort, it is often difficult to connect this detail to any mechanistic understanding of a geological process, because only a static picture of the process is achieved. Part of the reason for the difference in focus on molecular processes in geology and biology may reflect the fact that because the whole point of protein structure is function, the structures are often much more directly suggestive of function. For proteins and nucleic acids, the need computational chemistry to guide the connection between structure and function may not be as crucial as it is for earth materials. Furthermore, geological processes often operate on much longer timescales than those that are of interest to biology, ultimately meaning that the long-term evolution of geological micro or nano structure could depend on small structural details whose consequences only become apparent on long time scales. Progress in understanding earth materials at a molecular level is strongly dependent on advances in computational chemistry.

II. Modeling Tools for Geochemical Systems

While there is a long history of using parameterized force fields to study minerals (*5*), molecular modeling of reactive processes, involving coupled ligand, proton, and electron-exchange reactions

in aqueous media requires flexible capabilities. Since Car and Parrinello's paper in 1985 (*6*), there has been rapid progress in direct dynamics with forces calculated from electronic structure calculations, but these techniques are still computationally too expensive for routine modeling tasks on polynuclear ions and surfaces. Progress on practical research problems in geochemistry is much faster if there is a parameterized model with sufficient flexibility to simulate these coupled processes at a reasonably accurate level. By "conventional" molecular dynamics (MD) it is meant that the interatomic interactions can be expressed as distances, angles, torsions, etc., between pairs, triplets, quadruplets, etc., of atoms. Many, or even most, definitive, quantitative calculations will still require electronic structure calculations; however, design of expensive "*ab initio*" numerical experiments can be much more effective if there exists a molecular modeling capability for large systems and, maybe even more important, rapid simulations for small systems, which can be completed on time-scales that are nearly interactive.

For interfacial systems, potential functions should ideally be transferrable from the gas-phase to the condensed phase. Aqueous–mineral interfaces are not in the gas phase (although they may be close, see (7)), but both the water molecules and the atoms/ions in the substrate are in contact with an environment that is very different from their bulk environment. The easiest "different environment" to test, especially when comparing with electronic structure calculations, is a vacuum, so there is likely to be a great deal of information available on either the surface of the solid or the gas-phase polynuclear ion or the gas-phase aquo complex (i.e., $Fe(H_2O)_6^{3+}$, $CO_3(H_2O)_6^{2-}$). The gas-phase transferability requirements on potential functions are challenging, but it is difficult to imagine constructing "effective" potential functions for such systems without using gas-phase systems in the construction process. This means that any water molecules used on these complexes must also "transfer" from the gas phase to the condensed phase. A fundamental aspect of this transferability is polarization.

A. Potential Energy Functions

The potential model for water used in our work is taken from the work of Stillinger and David (8) (SD) as modified by Halley and co-workers (9) (HRR). Models for water that are capable of heterolytic dissociation into ions OH^- and H^+ could take two different approaches. Probably the best approach, promising but not yet

broadly applied to aqueous systems, is to assign environment-dependent charges governed by the principle of electronegativity equalization (10). An earlier approach, the one taken by Stillinger and David, is to treat the water molecule as having formal +1 and –2 point charges on the proton and oxide ions, respectively, essentially creating an ionic model for water of the type that is used to model molten salts and oxide minerals (11). The oxide ion is polarizable, and, unlike many polarizable water models, the dipole moment of the oxide ion responds to the electric field of the protons within the molecule. If the oxide ion is assigned a polarizability of 1.444 $Å^3$ and experiences the full-charge dipole interaction of a +1 proton at 1 Å, the induced dipole moment will be too large, and the overall moment too small, compared to the known dipole moment of a gas-phase water molecule (1.85 D). Stillinger and David therefore introduced a smooth cutoff function, which multiplies the charge–dipole interaction and reduces it at short range. The parameters are chosen such that the gas-phase dipole moment is exactly 1.85 D. Halley and co-workers implemented a short-ranged angle-dependent potential to recover the gas-phase vibrational frequencies for the isolated water molecule. The potential expressions are given as follows:

$$\Phi_{OO}(r_{OO'},\vec{\mu}_O,\vec{\mu}_{O'})=\frac{1}{2}\sum_O\sum_{O}{}'\frac{A_{OO}}{r'^{12}_{OO}}+\frac{B_{OO}}{r'^{6}_{OO}}+\frac{q_O q'_O}{r'_{OO}}+\frac{q_O(\vec{\mu}\cdot\vec{r})}{r'^{3}_{OO}}$$
$$+\frac{1}{2}\vec{\mu}_O\left(\overleftrightarrow{I}-\frac{3\vec{r}_{OO'}\vec{r}_{OO'}}{r^2_{OO'}}\right)\vec{\mu}'_O \qquad (1)$$

where $\vec{r}_{ij}=\vec{r}_i-\vec{r}_j$, $\overleftrightarrow{I}$ is the 3×3 unit matrix, and $\vec{\mu}_0$ is the dipole vector on the oxygen. The functional form of the O–H interaction is

$$\Phi_{OH}(r_{OH},\vec{\mu}_O)=\sum_O\sum_H a_{OH}\frac{e^{-b_{OH}r_{OH}}}{r_{OH}}$$
$$+\left\{c_{OH}(r_{OH}-r_{0_{OH}})^2-d_{OH}(r_{OH}-r_{0_{OH}})\right\}e^{-e_{OH}(r-r_{0_{OH}})}$$
$$+\frac{q_O q_H}{r_{OH}}+\frac{q_H(\vec{\mu}_O\cdot\vec{r}_{OH})}{r^3_{OH}}S_{OH} \qquad (2)$$

where

$$S(r)=\frac{r^3}{r^3+f(r)} \qquad (3)$$

and

$$f(r) = \frac{f_{OH}(r - r_{0_{OH}})e^{-g_{OH}(r - r_{0_{OH}})} + h_{OH}e^{-p_{OH}r}}{1 + e^{S_{OH}(r - t_{OH})}} \tag{4}$$

H–H interactions are purely coulombic

$$\Phi_{HH}(r'_{HH}) = \frac{1}{2}\sum_{H}\sum_{H}{}' \frac{q_H q'_H}{r'_{HH}} \tag{5}$$

For water molecules, there is a three-body term of the form

$$\Phi_{HOH}(r_{OH}, r_{OH'}, \theta_{HOH})\sum_{O}\sum_{H}\sum_{H'}\{\phi(r_{OH}, r_{OH'}, \theta_{HOH})\} \times \exp\left(-e_{HOH}\left[(r - r_{0_{OH}})^{2+}(r - r_{0_{OH'}})^{2}\right]\right) \tag{6}$$

$$\phi(r, r', \theta) = a_{HOH}(r - r_{0_{OH}})(r' - r_{0_{OH}}) + \frac{1}{2}b_{HOH}(\theta - \theta_0) + c_{HOH}(r + r' - 2r_{0_{OH}})(\theta - \theta_0) + d_{HOH}(\theta - \theta_0) \tag{7}$$

where $r_{0_{OH}}$ and θ_0 are the desired bond length and bond angle in the water molecule. These parameters are chosen such that the isolated water molecule has the correct vibrational frequencies.

TABLE I

POTENTIAL PARAMETERS FOR WATER MODEL

A_{OO}	2.02	a_{HOH}	–0.640442
B_{OO}	1.35	b_{HOH}	0.019524
		c_{HOH}	–0.347908
a_{OH}	10.173975	d_{HOH}	–0.021625
b_{OH}	3.69939	e_{HOH}	16.0
c_{OH}	–0.473492	θ_0	104.45
d_{OH}	0.088003		
e_{OH}	16.0	q_H	1+
f_{OH}	1.3856	q_O	2–
g_{OH}	0.01		
h_{OH}	48.1699	α	1.444 Å^3
p_{OH}	3.79228		
s_{OH}	3.0		
t_{OH}	5.0		
r_0	0.9584		

When used in conjunction with Equations (1 through 6), energies in e^2/Å are generated. For reference, the water molecule at equilibrium geometry has an energy of 3.11595 e^2/Å

Table I lists the potential parameters in units of e (charge), Å (length), and e^2/Å (energy).

In the HRR model, O–O interactions were chosen to reproduce as closely as possible the O–O radial distribution function (12), the oxygen–oxygen distance in the water dimer, and the water dimer binding energy. For the HRR model, the ambient pressure at room temperature is about 0.7 GPa. It can be adjusted to zero pressure by changing the B_{OO} coefficient to –1.35; however, the dimer binding energy is then too high (11.7 kcal/mol) and the O–O distance in the water dimer is then too close (2.75 Å). This is, in a sense, the price that must be paid for insisting on gas-phase to condensed-phase transferability. The average water dipole moment at 300 K in pure water is close to 3.0 debye, in good agreement with estimates from density functional methods (13); thus the model passes probably the most important test of gas-phase to liquid-phase transferability. The proton in water yields a mixture of Eigen and Zundel $H_5O_2^+$ structures, whereas the hydroxide ion yields a subequal mixture of $OH(H_2O)_3^-$ and $OH(H_2O)_4^-$ species (14).

The next step was to extend the model, keeping the same oxide ion as used in the water, but adding other cations beyond H^+. The goal was to find a sufficiently flexible metal–oxygen interaction function for the potential to describe both the aquo ion in aqueous solution and the bulk metal oxide structure as accurately as possible. Following (15), the first extension was to iron oxide fitted to quantum mechanical calculations on the Fe^{3+}–H_2O potential surface. The functional form allows for polarization of bound water molecules by the M^{3+} ion. This polarization opposes the contribution of the protons to the induced dipole moment of bound water molecules. The total dipole moments of the bound water molecules are thus larger than that of unbound water molecules. In (*15*) it was shown that the enhanced (repulsive) dipole–dipole interaction among bound water molecules is an important many-body effect in stabilizing octahedral coordination for Fe^{3+}(aq). The functional form of the M–O interaction is

$$\Phi_{FeO}(r_{FeO},\vec{\mu}_O)=\sum_{Fe}\sum_{O}A_{FeO}e^{-B_{FeO}r_{FeO}}-\frac{C_{FeO}}{r_{FeO}^6}+\frac{D_{FeO}}{r_{FeO}^{12}}+\frac{q_{Fe}q_O}{r_{FeO}}+\frac{q_{Fe}(\vec{\mu}_O\cdot\vec{r}_{FeO})}{r_{FeO}^3}S_{FeO}(r_{FeO}) \quad (7)$$

where

$$S_{FeO}(r)=1-\frac{1}{e^{E_{FeO}(r-F_{FeO})}+1} \quad (8)$$

TABLE II

Potential Parameters for Cations

Ions	A_{MO}	B_{MO}	C_{MO}	D_{MO}	E_{MO}	F_{MO}
Fe(2+/3+)	1827.7	4.925	–2.136	–74.680	1	1.8
Na(+)	450.0	3.600	17.0		3.2	1.9
C(4+)	4933.9	6.35	8.52	1.5	2.738	1.20664
Si(4+)	220.0	4.17			4	1.4
P(5+)	120.0	3.75			4	1.35
Nb(5+)	638.39	3.94	1.84		3.63	1.78
S(6+)	85	3.6			4	1.35
Cr(6+, 5+, 4+)	248.05	3.678			1.234	1
Cl(7+)	85	3.6			4	1.35

Parameters for Fe, as well as some other cations discussed below, are given in Table II. The parameters may be applied to either Fe^{2+} or Fe^{3+} simply by changing the charge.

B. Obtaining Model Parameters

It has also been possible to make reasonable models for oxyacids $HClO_4$, H_2SO_4, H_2CrO_4, H_3PO_4, H_4SiO_4, and H_2CO_3 by treating these species as having central cations with the full +7 (Cl), +6 (S, Cr), +5(P), and +4(Si,C) formal charges. Since common reactivity trends for these acids are directly related to the "cation" charge, the relative acidities of the species will be at least qualitatively correct when building the potential functions around an ionic framework. The parameters for these species, along with those for $Fe^{3+/2+}$ and Na^+, are given in Table II. For the oxyanions ions, we carry out quantum mechanical calculations for protonated, deprotonated, hydroxylated, and dehydroxylated forms of these ions, and fit the parameters to the structures and energies determined from quantum mechanics. A typical set of test molecules relevant to the carbonate system is shown in Fig. 1.

The "gas-phase" model would then be tested on condensed phases. In the case of the carbonate ion, the parameters can be used to examine the structure of CO_2(aq), CO_3^{2-}(aq), and HCO_3(aq) as well as the structure of, for example, siderite $FeCO_3$ and nahcolite $Na(HCO_3)$. For the aqueous species, the most instructive comparisons are with the results of *ab initio* molecular dynamics studies of solvated ions, where the radial distribution functions can be used to check the extent of solvation. Fig. 2, for

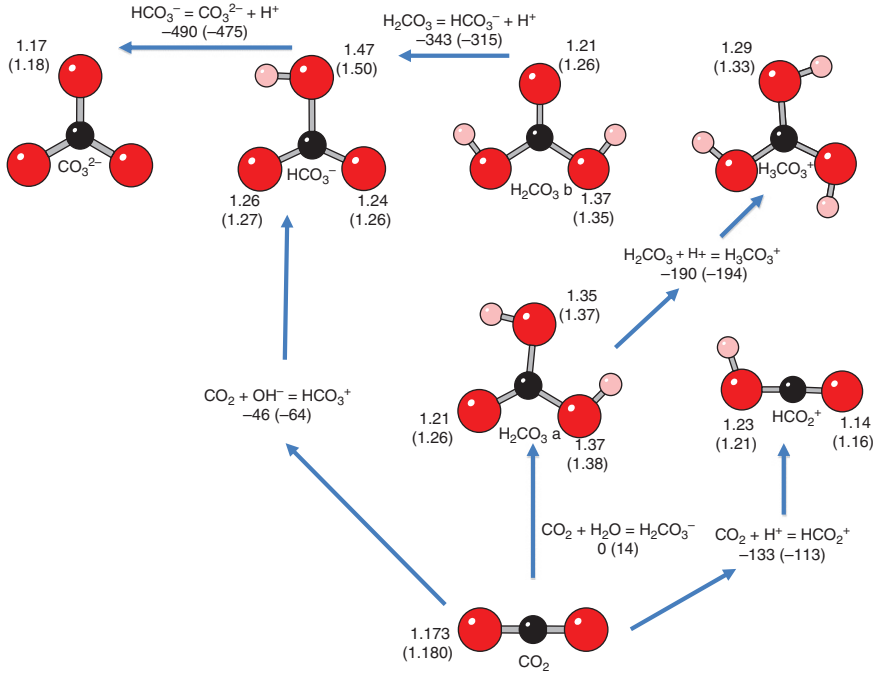

FIG. 1. Molecule training set for fitting potential function parameters for the carbonate system. Red atoms are O^{2-}, black atoms are C^{4+}, and pink atoms are H^{+}. Bond lengths from C^{4+} to O^{2-} are given in angstroms. Energies for transformations between the different species are given in kcal/mol.

example, shows the radial distribution functions obtained with the parameterized model compared with AIMD in the CO_2, HCO_3^-, CO_3^{2-} systems. It is important to keep in mind the purpose for which the potential function is designed. For example, for the perchlorate ion, the goal may be only to create a large, poorly complexing, highly acidic anion with the appropriate charge. Creating a model for the carbonate ion could be much more challenging, as one needs to account as correctly as possible for the relative energies of multiple protonation states as well as conversion between CO_2 and CO_3^{2-} carbon coordination states.

The strategy for fitting parameters can obviously vary from system to system. The task is to produce a model that is capable of describing the wide variety of protonation and coordination states experienced at surfaces and in polynuclear ions. It makes sense to start with structures having coordination environments that may be very different from the regular environments

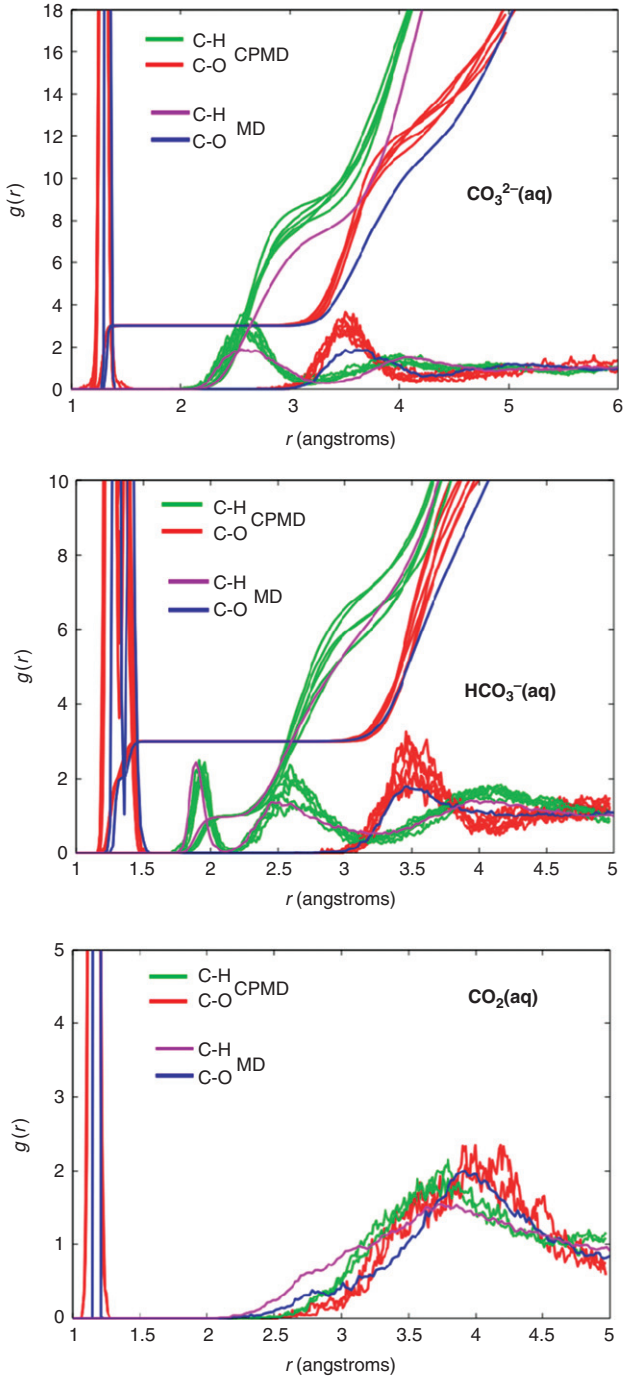

FIG. 2. Radial distribution functions compared between *ab initio* molecular dynamics (CPMD) and the parameterized molecular dynamics model (MD). Multiple traces for the CPMD calculations represent repeated molecular dynamics calculations.

experienced in bulk condensed phases, and then checking that these models also give reasonable results for the more regular coordination environments. For this purpose, the structures and energies of quantum mechanical calculations on small molecules provide a manageable, unbiased data set from which to start when fitting the model. Evaluation of model predictions for these quantities is very rapid, so an investigator can get at least a preliminary model in one or two working days.

The choice of the exchange correlation functional in the density functional theory (DFT) calculations is not very important, so long as a reasonable double-zeta basis set is used. In general, the parameterized model will not fit the quantum mechanical calculations well enough for improved DFT calculations to actually produce better-fitted parameters. In other words, the differences between the different DFT functionals will usually be small relative to the errors inherent in the potential model. A robust way to fit parameters is to use the downhill simplex method in the parameter space. Having available an initial set of parameters, taken from an analogous ion, facilities the fitting processes.

As an example application, the fitting of parameters for the Nb^{5+}–O^{2-} interaction is described. This model has been used to find potential oxygen exchange pathways in polyoxoniobate anions (16). Fig. 3 shows the molecules used to fit the potential function parameters and gives the model parameters, as well as those calculated using DFT with the BP86 functional and the DZVP basis set. The resulting model is then used to predict the structure of the $Nb_{10}O_{28}^{6-}$ ion in solution, shown in Fig. 4, which also provides a comparison between the model bond lengths and bond lengths calculated quantum mechanically in continuum solvent. Other than the terminal oxo bonds being too long, the overall structure of the $Nb_{10}O_{28}^{6-}$ (decaniobate) ion is well reproduced by the ionic model.

Even if it is decided that large-scale AIMD or QM/MM studies are required for a particular system (for example, to obtain a more accurate description of the terminal oxo bonds in the decaniobate anion above), the ionic model produced using the above techniques can often serve as a baseline for a better understanding of the more accurate calculations. For example, there is no point in calling on complex rehybridization schemes to "explain" the difference in bond length between the Nb_1– $\mu^{12}O$ (1.87 Å) and Nb_2–$\mu^{12}O$ (2.12 Å) bonds if these same features can be reproduced with the simple ionic model. If, for example, the "rattling" of the Nb^{5+} ion in an octahedral oxygen coordination geometry that is slightly too large for the ion is a key aspect of the reaction

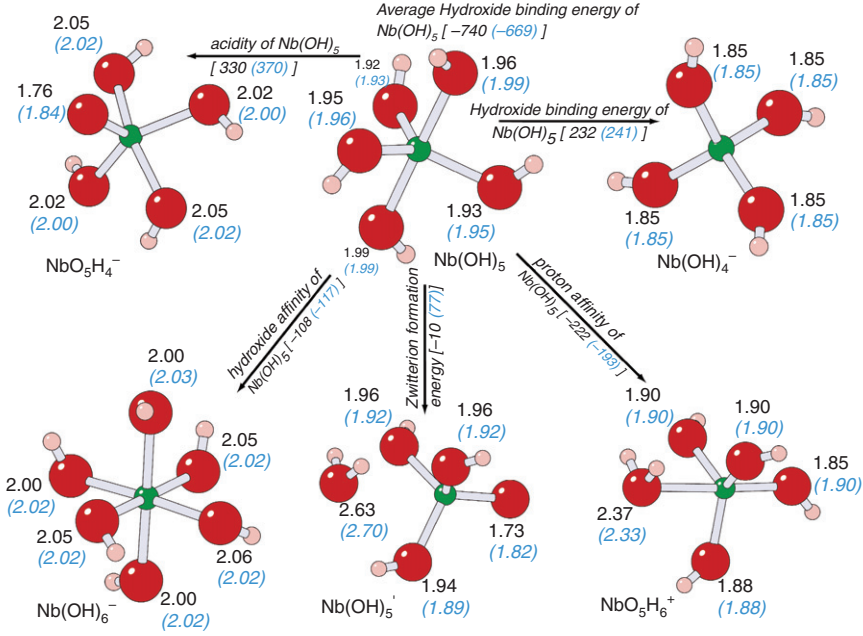

FIG. 3. Molecules used to fit potential parameters for Nb^{5+}-O^{2-} interactions. Atoms are as in Figure 1, except that the small green atom is Nb^{5+}. DFT calculations are compared with model predictions. Model predictions are given in parenthesis in blue text. Bond lengths are given in angstroms, and reaction energies are given in kcal/mol.

pathways for oxygen exchange, the parameterized model, which can account accurately for the relative radius ratios, should be capable of revealing these pathways. Comparing an electronic structure calculation with the simpler model can often make the advantages of the electronic structure approach more immediately apparent.

III. Example Systems

A. Broensted Acid–Base Reactions

A.1. Ion hydrolysis

Hydrolysis of water molecules induced by ions in aqueous solution or at the surfaces of minerals or polynuclear ions is a fundamental aspect of most dynamic processes taking place at

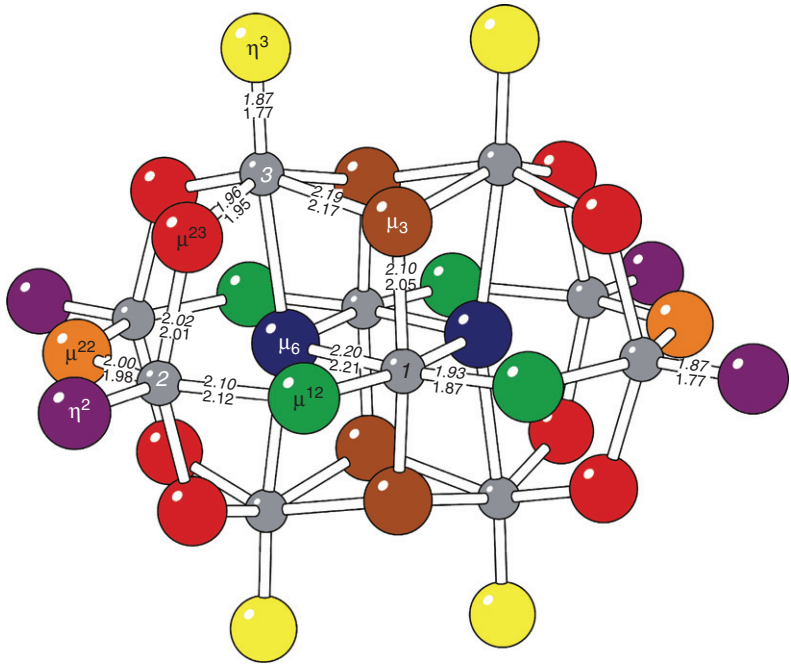

FIG. 4. Decaniobate $Nb_{10}O_{28}^{6-}$ ion. Symmetrically equivalent oxygen atoms are shown in different colors. The niobium ions are labeled 1, 2, 3, as shown in the Figure. The oxygen atoms are then labeled with respect to the numbers on the niobium atoms, and whether they are bridging (μ) or terminal (η). Bond lengths are compared for density functional theory in continuum solvent versus model predictions as averaged over a molecular dynamics simulation in water. DFT-calculated bond lengths are above, and model predictions are below, given in angstroms.

oxide–water interfaces. Trivalent cations are often extensively hydrolyzed in aqueous solution according to the reaction:

$$M(H_2O)_n^{3+} \leftrightarrow M(OH)_n^{(3-n)+} + nH^+ \qquad (9)$$

In dilute solutions, these reactions produce a series of $M(OH)_n$ ($n = 1$–4) hydrolysis species with populations that depend on solution pH (17). Hydrolysis chemistry is fundamental to the behavior of trivalent metal ions in water as the extent of hydrolysis governs the polymerization of metal ions into extended structures that eventually crystallize into secondary oxide and oxyhydroxide minerals and clays. When building a general capability to simulation geochemical reaction mechanisms, hydrolysis is the place to begin. If the hydrolysis equilibria of

the cations are not qualitatively correct, the utility of the molecular model will be extremely limited. Note that in constructing the model, the gas-phase proton affinity of the $M(OH)^{2+}$ ion can be checked against electronic structure calculations. For example, for the $M=Fe^{3+}$ model referenced above, the gas-phase proton affinity is 40 kcal/mol. This is quite a bit higher than the range of values calculated for $Fe(OH)^{2+}$ from ab initio theory 20–30 kcal/mol (*18,19*) but very close to the value calculated for $Al(OH)^{2+}$. The correlation with size-charge ratio for these ions is known to be poor (witness the lesser acidity of the smaller Al^{3+} ion). Despite the fact that DFT calculations were shown to correlate very well with acidities, the electronic structural reasons for the trends observed in the acidities of the trivalent ions are unclear. Until the underlying reasons for these trends are better understood, the Al^{3+}-like value of 40 kcal/mol must be accepted, realizing that we are not now really talking about "iron" but a model trivalent ion. Such disagreement may result, from using the same oxygen properties, for example, polarizability, in both the aluminum and iron aquo ions.

In (*20*) the titration of a model Fe^{3+} ion in solution was simulated with the Fe^{3+}–O–H MD model described above. Because of the way the model is designed, allowing hydrolysis reactions to occur spontaneously, the distribution of the $M(OH)_n$ species can simply be recorded as a function of the amount of protons and hydroxide ions added to the solution. The simulations are used to find the distribution of hydrolysis species in a neutral solution and to determine how this distribution responds to added protons or hydroxide ions in solution.

To adopt such an approach, there must be a sufficient number of proton exchanges on molecular dynamics timescales for the complexes to provide meaningful averages. Characteristic exchange times for the Fe^{3+} aquo ion are given in Table III. As expected, there is a strong dependence on the protonation state of the aquo ion. The characteristic time is expected to decrease with increasing pH, as exchange from a hydrolyzed species would be

TABLE III

Characteristic Timescales for Proton Exchange

Conc. ([H+] or [OH–])	τ picoseconds
0.022[H+]	133
0.003[H+]	175
0.0007[H+]	106
0.014[OH–]	57

expected to be more rapid than from the fully protonated ion. The results show a slight maximum between hydrogen mole fractions $X_{H+} = 0.022$ and $X_{H+} = 0.0007$, that is, the rate of proton exchange actually increases with decreasing pH. A similar maximum in proton exchange rate as a function of pH has been observed in ^{1}H NMR spectroscopy on rhodium(III) in aqueous solutions (*21*).

The apparent pH of the neutral solution, in this case $Fe(OH)_3$ in 878 water molecules, can be obtained by taking the observed ratios of the hydrolysis species, for example, for the iron system, the pK_a for the first hydrolysis reaction

$$Fe^{3+} = Fe(OH)^{2+} + H^+ \qquad (10)$$

is 2.2. If, for example, we observe in a solution to which n protons have been added, that the ratio of $Fe(OH)^{2+}/Fe^{3+}$ is nearly unity, then the apparent pH would be nearly 2.2.

Each of the pK_{1n} pairs can be used to estimate pH* separately: pK_{11} = 2.19, pK_{12} = 3.48, pK_{13} = 6.33, and pK_{14} = 9.6. From the observed ratios of each pair of hydrolysis species, pH* can be defined:

$$pH^* = pK_{1n} + \log \left\{ M(OH)_n^{(3-n)} / M(OH)_{(n-1)}^{(3-n+1)} \right\} \qquad (10)$$

For the neutral systems, over the eight runs, the pH* estimated from pK_{12} and the $\log[M(OH)^{2+}/M(OH)_2^+]$ varies from 5.26 to 6.29 (average value ≈ 5.5); pH* estimated from pK_{13} and $\log [M(OH)_2^+/M(OH)_3]$ ranges from 6.13 to 6.93 (average value ≈ 6.6); and the pH* estimated from pK_{13} and $\log (M(OH)_3)/(M(OH)_4^-)$ ranges from 6.5 to 7.6 (average value ≈ 7.1). These ratios should ideally indicate neutral pH = 7.

When excess protons or excess hydroxide ions are added to the solution, we expect the ratios of the hydrolysis species to shift to more acidic or basic values. In Fig. 5, we plot the apparent pH of the solution, as inferred from, on the acid side (where protons are added to the solution), the logarithm of the ratio of the number of counts of the $Fe(OH)^{2+}$ configurations to the number of counts of the hexaaquo complex, and, on the base side (where hydroxide ions are added to the solution), the logarithm of the ratio of the number of counts for $Fe(OH)_4^-$ to the number of counts of the $Fe(OH)_3$ complex.

A.2. Effect of hydrolysis on electron-exchange between ferrous and ferric iron in aqueous solution

The capability of the dissociating water model, augmented to include metal–water interactions, to qualitatively describe the process of ion hydrolysis can be applied to the problem of electron

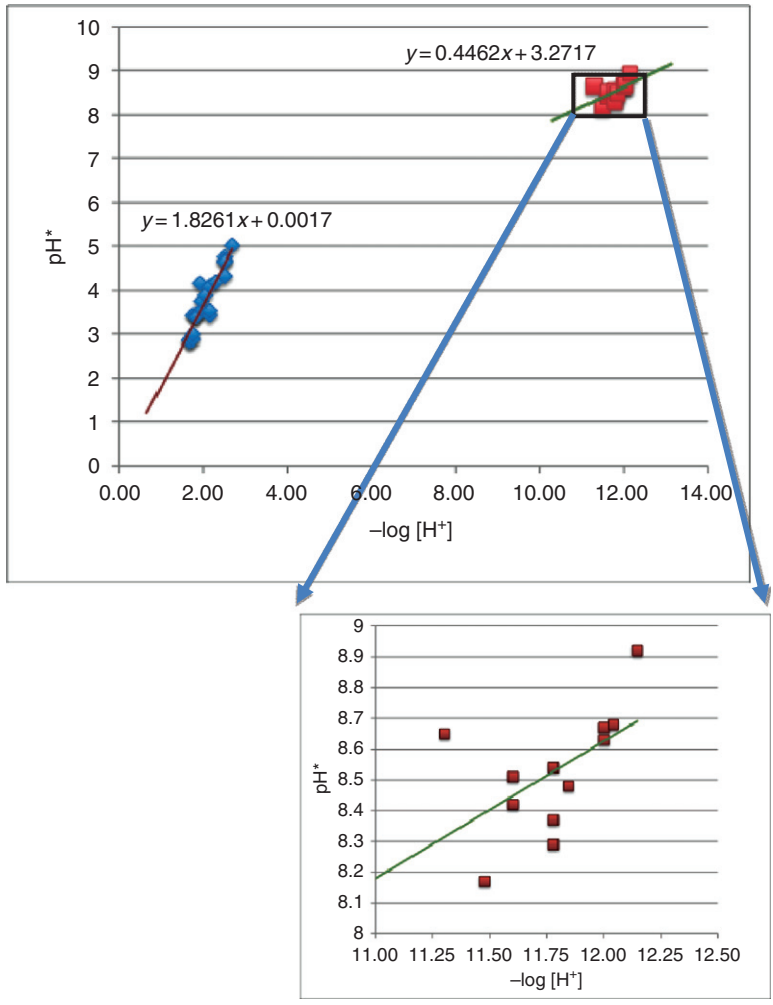

FIG. 5. Apparent pH* calculated through distributions of $Fe(OH)^{2+}$/Fe^{3+} (blue diamonds) and $Fe(OH)_4^-$/$Fe(OH)_3$ (brown squares), versus the -log[H^+] computed from the number of protons added to the solution on the acid side, or from the amount of added hydroxide, taking K_w=14, on the base side.

transfer between ferrous and ferric iron in aqueous solutions. Early studies showed that self-exchange rates increase by a factor of 4– 5 as pH increased from 0 – 2 and the fraction of hydrolyzed ferric iron approaches half of the total ferric iron in solution (*22*). The hydrolysis of the iron could affect the rate of electron exchange in several ways. First, the reduced charge of the

$Fe(OH)^{2+}$ species should lower the potential of mean force between the ferrous and ferric ions. Because it is easier for the ferrous Fe^{2+} aquo ion to approach the hydrolyzed ferric iron (perhaps even forming an inner-sphere complex), electron exchange between the two species should be facilitated. On the other hand, in the absence of formation of an inner-sphere Fe(III)–OH–Fe(II) bridge, the presence of hydroxide in the coordination shell of the ferric iron should make it more difficult for the ferric iron to accept an electron because of the increased reorganization energy of the hydrolyzed complex. Finally, the hydrolyzed ferric complex has a more open pathway for accepting a hydrogen atom into the structure, for example, via formation of a H_3O_2 bridge that could facilitate a hydrogen atom electron transfer mechanism.

In (*23*) the importance of the effects of increasing reorganization energies and decreasing potential of mean force with increasing pH was evaluated using previously developed computational methods (*24,25*) and the hydrolyzing model for ferric iron described above. A molecular dynamics calculation was carried out for ferrous Fe_A^{2+} and ferric Fe_B^{3+} ions in aqueous solution. During the simulation, account is kept of the usual potential energy for the "normal" Fe_A^{2+} and Fe_B^{3+} state, as well as the "reversed" Fe_A^{3+} and Fe_B^{2+} state. The potential energy difference for a given configuration between the normal and reversed states can be identified with the reorganization energy for electron transfer. On average, the water molecules are more strongly polarized around the ion, so the potential energy of the reversed charge state will be, on average, unfavorable due to the reorganization energy. By keeping track of the probability distribution of reorganization energies, the free energy of electron transfer can be computed. For example, a Gaussian distribution of reorganization energies would correspond to a parabolic free energy surface for electron transfer because the negative logarithm of a Gaussian is a concave-upward parabola. By finding the probability or, equivalently, the free energy for configurations with zero reorganization energy (i.e., zero potential energy difference between the normal and reversed states), the free energy of electron transfer can be estimated.

How would the distribution of hydrolysis species fit into the general picture of solvent fluctuations? Would the reorganization energies, when resolved into contributions from Fe^{3+}, $FeOH^{2+}$, $FeOH_2^{+}$, form separate distributions, or would the hydrolysis fluctuations be part of a "continuum" of solvent fluctuations? In other words, is it more correct to regard the phenomenon of hydrolysis, as far as its effect on electron transfer, from the point of view of contributions from separate hydrolysis "species"

or is it more correct to imagine the process in terms of a continuum of states, but with an increasing overall tendency to "trap" the electron on the ferrous iron as the [OH] concentration increases, analogous, in a sense, to the effect that would result from increasing the dielectric constant of the solution in which the transfer was taking place?

The results of the calculations, shown in Fig. 6, show widely overlapping reorganization energy distributions for the different hydrolysis species, and strongly support the idea that hydrolysis should more properly be viewed is just another kind of solvent fluctuation on a continuum of types of solvent fluctuations. In other words, there are many Fe^{3+} configurations having reorganization energies exceeding those of, for example, $Fe(OH)_2^+$; in fact, it is not easy to see any difference at all in the average reorganization energies of each hydrolysis species. In terms of the overall effect of pH on the self-exchange rate, the reduction of the potential of mean force with increasing pH was balanced by the increased reorganization energy due to hydroxide-induced stabilization of the Fe^{3+} ion. If the reduction of the potential of mean force exceeds the increase in the reorganization energy, the self-exchange rate would increase with increasing pH. This view contrasted with the existing view that the observed increase in

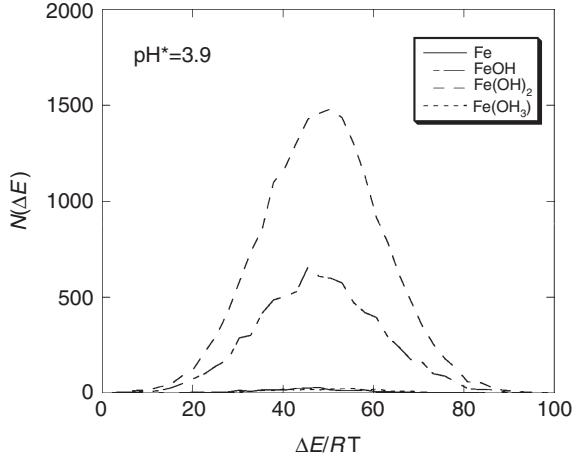

FIG. 6. Distribution of Fe^{2+}/Fe^{3+} reorganization energies found in the MD simulation of electron transfer in a hydrolyzing solution of Fe^{3+} (the Fe^{2+} could hydrolyze, but never does) at an apparent pH near 3.9. The strongly overlapping distributions show almost no shift in reorganization energy as a function of hydrolysis, indicating that the hydrolysis fluctuations lie on a continuum with all other solvent fluctuations.

electron transfer rate with increasing pH was the result of a particularly efficient hydrogen atom transfer pathway for exchange between $Fe(OH)^{2+}$ and Fe^{2+}.

A.3. Titration of a polyoxocation in solution

The extent of protonation of oxide surfaces has a fundamental influence on virtually every aspect of their chemical behavior in aqueous systems, governing dissolution/precipitation, sorption, and redox reactions, and controlling the mobility and aggregation state of colloidal-sized particles. The earliest approach to describing surface charging employed an effective "2-pK" model describing the pH of zero charge of the surface (*26*). In conjunction with assumptions about charge densities and surface capacitances, the pH–surface charge relationship could be calculated from the two pK_as of the model surface functional group (surface–OH_2^+, surface–OH, and surface–O^-). Many investigators have supposed that a better model of the surface could be obtained by explicitly taking into account the crystallographic heterogeneity of the surface sites, using the so-called "multisite" models (*27*). A molecular-level understanding of surface protonation reactions begins with some knowledge of which crystal facets define typical crystallite morphologies for a given mineral. The crystals are then cleaved parallel to these surfaces, several possible schemes for termination of the crystal structure are identified and guesses are made concerning the various types of oxide sites that will define the cleavage surface given a certain surface termination recipe. The pK_a for each type of oxide site is estimated, and, given the relative surface areas of the facets defining the idealized crystal, the surface proton uptake and release can be estimated as a function of pH.

Here again, quantum chemical calculations can be used to check the performance of the parameterized model on more complex molecules, used as surrogates for surface sites on oxides. Consider the $Fe_3(OH)_7(H_2O)_6{}^{2+}$ molecule in Fig. 7. The deprotonation energy for the μ_3-OH site in this model molecule was calculated using the generalized gradient approximation in density function theory (DFT) and also with the conventional Fe^{3+}–O–H force field (*28*). Both calculations gave 179 kcal/mol, showing that the model is capable of giving accurate results and is properly accounting for the influence of multiple Fe–O bonds on the acidity of the OH functional group.

The multisite surface complexation model (MS-SCM) by Hiemstra, Van Riemsdijk, and Bolt (*27*) was the first effort directed at understanding the reactivity of an oxide surface in terms of heterogeneous array individual surface functional groups. These authors

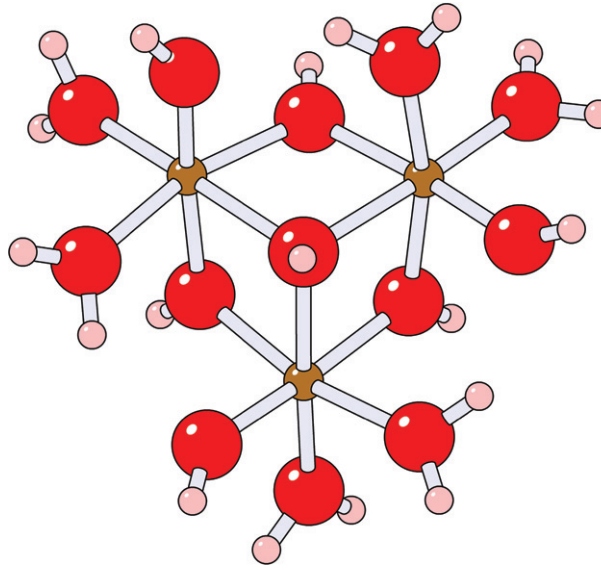

FIG. 7. $Fe_3(OH)_7(H_2O)_6^{2+}$ trimer used to compare gas-phase acidities of m_3-OH, groups between density functional theory and the MD model. The MD model and GGA DFT calculations both predict a gas-phase acidity of 179 kcal/mol.

used the concept of total "bond valence" as governing the pK_as of individual oxide sites on an oxide mineral surface. A simple definition of bond valence could be the sum of the formal charge divided by the coordination number (sometimes called the Pauling bond strength) over all cations attached to the oxide ion plus the –2 formal charge on the oxide ion. Roughly, the greater the Pauling bond strength contributed to the surface oxide ion, the more positive the bond valence at the oxide ion, and the greater the acidity. Parameterization of their MS-SCM model was based on an empirical relationship between the Pauling bond strength and pK_a for oxo ions with known structure and pK_a. An early molecular modeling approach to this problem (*29*) used a parameterized molecular model constructed for the aqueous Fe^{3+} ion, showed that it gave reasonable predictions for the crystal structures of α-, β-, and γ-FeOOH, and used the model to calculate the gas-phase proton affinities of individual sites on several surfaces of goethite (α-FeOOH). Using an empirical relationship between the gas-phase acidities of $Fe(H_2O)_6^{3+}$ and $Fe(OH)_3$ and the solution pK_a. they were able to produce an MS-SCM by relating the calculated gas-phase proton affinities to solution pK_a.

Although both of these approaches produced reasonable results, there was no real control on the types of functional groups present on the surface at the time, leading to difficulties in evaluating the sensitivity to different surface terminations that are to some extent chosen arbitrarily in the model. Early work attempting to search spectroscopically for the existence of η-H_2O, μ-OH, and μ_3-OH groups on iron oxide and oxyhydroxide surfaces (*30,31*) were difficult to interpret, because there was no convincing separation of the hydroxyl stretch frequencies that would allow identification of the different surface functional groups. Recent electronic structure calculations (*32*) show that the stretching frequencies of the η-H_2O, μ-OH, and μ_3-OH groups are all within a few wave numbers of one another and would have been impossible to see with the resolution available using spectroscopic techniques in the 1970s.

The situation has improved with the advent of high-resolution X-ray reflectivity studies (*33*) and high-resolution infrared spectroscopic methods (*34*) but most surface X-ray reflectivity studies are interpreted using fractional site occupancies, indicating a high density of defects on these surfaces giving rise to functional groups of unknown local structure and mutual arrangement. Knowledge of aqueous–mineral interfacial structures at the functional group level remains a difficult and elusive problem that may only be definable in a statistical sense. Even on simple oxides like TiO_2, which has been extensively studied both theoretically and experimentally, the populations of functional groups on ultra-high vacuum systems with a single monolayer of water molecules have not been determined unequivocally (*35*).

These difficulties created an incentive to focus theoretical investigations on polynuclear ions, which were structurally well characterized, and, though innovative experimental studies using NMR to follow the dynamics of oxygen-isotope exchange processes were beginning to yield unprecedented details of elementary reactions in aqueous solutions (*36*).

One of the first computational tasks was to simulate the deprotonation of the surface of the $Al_{30}O_8(OH)_{56}(H_2O)_{26}^{18+}$ (Al_{30}) ion and the $Al_{13}O_4(OH)_{24}(H_2O)_{12}^{7+}$ (Al_{13}) ion using the techniques similar to those used on the Fe^{3+} ion described above. The structure of the Al_{30} ion, shown in Fig. 8, has been determined through X-ray diffraction studies on the sulfate hydrate salt (*37,38*). A fully protonated Al_{30} ion was immersed in a solution of 18 perchlorate ions and brought to an equilibrium protonation state, where, in the neutral solution, it lost two protons, one from each of the S4 waters, illustrated in Fig. 8. Addition of hydroxide ions to the surrounding solution induced further deprotonation of the

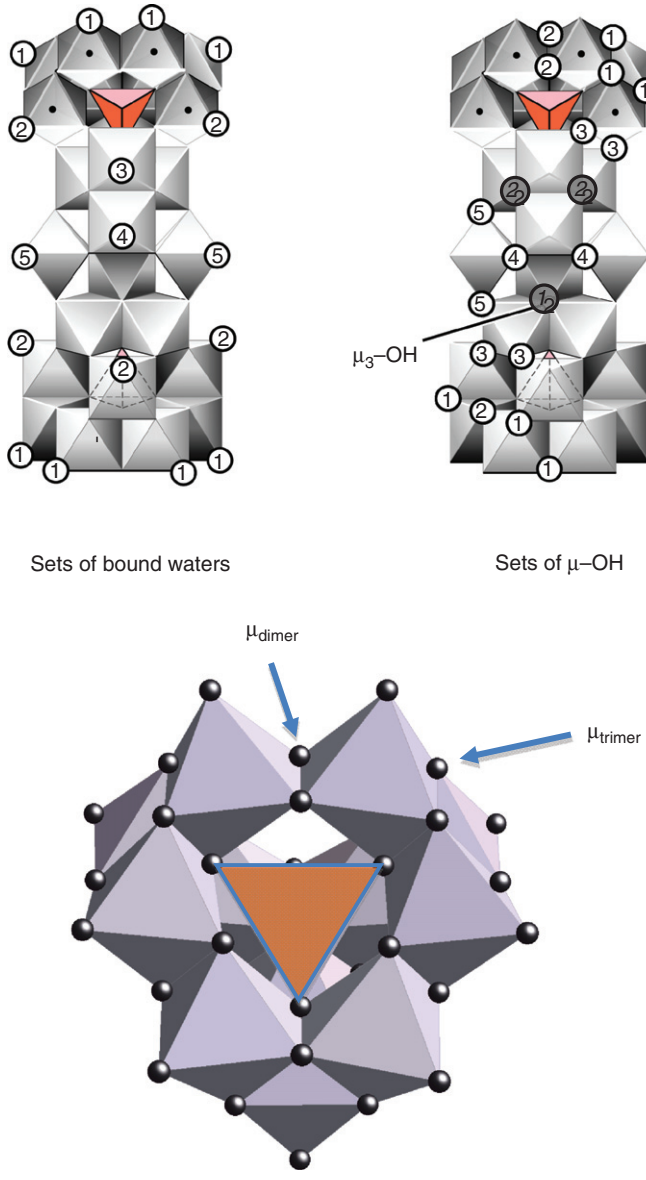

FIG. 8. $Al_{30}{}^{18+}$ (a) and $M_{13}{}^{7+}$ (b) polynuclear clusters. Sets of different oxygen sites (some are not shown) grouped together for identification. In the representation of the bridging hydroxide ions on the right, the doubly bridging sites (μ–OH) are shown with white circles and the triply bridging sites (μ_3–OH) are shown in gray with identifying numbers in italics. The tetrahedral metal in the center of each δ-13 unit is shown in orange.

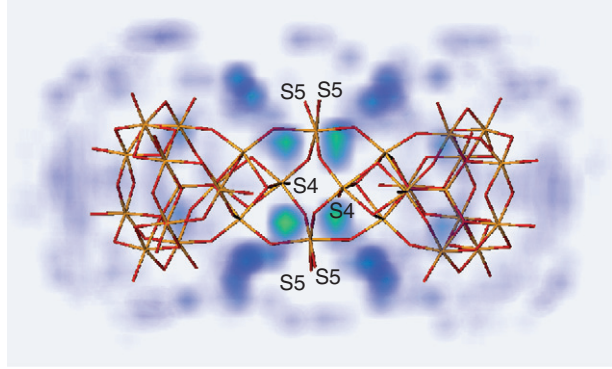

FIG. 9. Variation of water density around the M_{30}^{18+} cation. Sites labeled S5 and S4 use the same numbers as used in Figure 8.

ion. The next sites to deprotonate were the four S5 waters, followed by the S1 and S2' sites. From an experimental point of view, the major problem is that these ions cannot deprotonate very much before they become unstable to flocculation, so the titrations can only take place over a limited range of pH. Experimental measurement of the acidometric titration of the Al_{30} ion was reported in (*39*). Increasing pH above pH=4 led to two protons being lost by pH 5, with loss of an additional six protons by pH=5.5, followed by a plateau with little proton loss until flocculation occurs near pH 6.5. Comparison of the simulation results with the measured titration curve indicated that the first plateau could be explained by relatively high acidities of the S4 and S5 sites. The major factor determining the relative acidities of the functional groups was the disposition of the hydrating waters in the central region of the molecule, as shown in Fig. 9. None of the μ-hydroxo groups lost or gained a proton during the course of the simulation, despite the fact that these groups had relatively high gas-phase proton binding energies. The μ_3-hydroxo functional groups did exchange protons with the solution on the timescale of the simulation, but because of their isolation from the solvent, and, hence, the difficulty of hydrating the deprotonated μ_3-oxo site, were not a significant source of acidity for the Al_{30} ion. These calculations conclusively highlighted the importance of hydration forces and solvent accessibility in determining the relative acidities of the surface functional groups.

A.4. Surface charge accumulation on α-FeOOH nanoparticles

Molecular dynamics simulations were used to compute proton distributions on faceted α-FeOOH particles 3–8 nm in size (*40*).

Model crystallites of α-FeOOH were created with systematic variations in the ratio of the two commonly developed (021) and (110) facets. The model particles for the two extreme cases in large (long thin particle) and small (short fat particle) (110)/(021) surface area ratios are illustrated in Fig. 10. These particles were protonated to

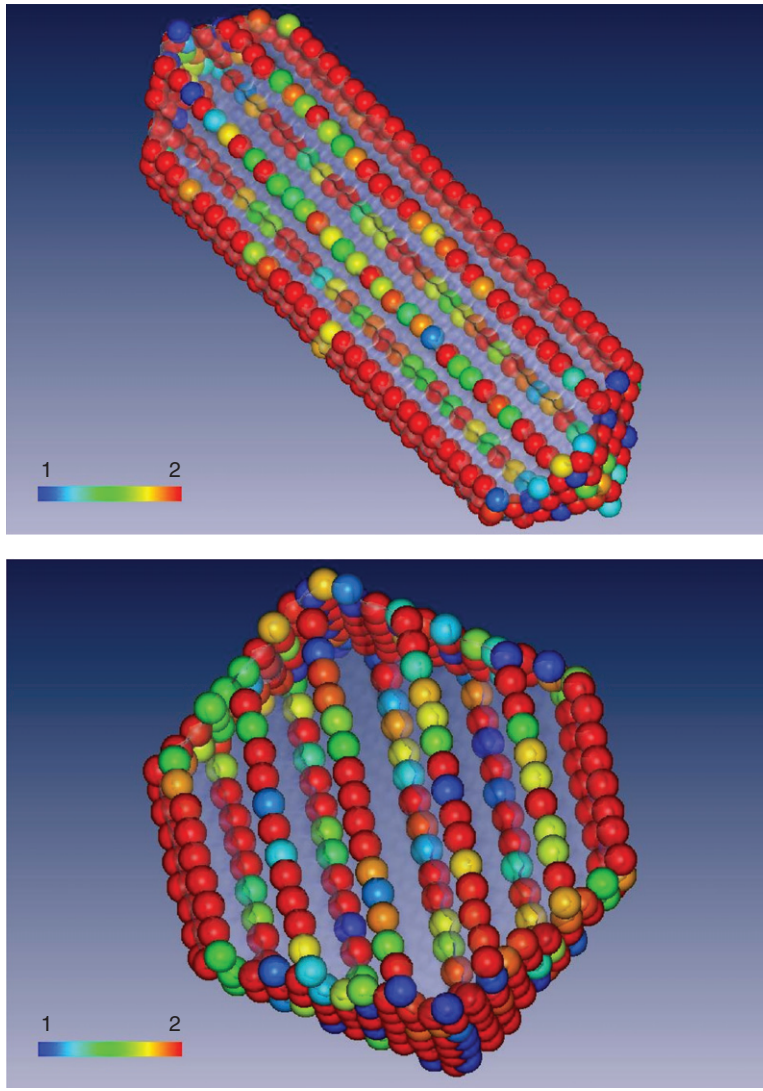

FIG. 10. Average protonation states of terminal η-H_2O groups on model α-FeOOH nanoparticles having high (a) and low (b) ratios of (110)/(021) surfaces. Blue corresponds to an average protonation state of 1 (FeOH) and red to an average protonation state of 2 ($FeOH_2$).

neutrality and immersed in water (without counterions). The protonation states of the surface oxide ions was computed and indicated by the color coding in Fig. 10, with a protonation state of 2 corresponding to red and a protonation state of 1 corresponding to blue. Green would correspond to an average protonation state of 1.5. To provide a baseline for understanding the effect of crystal shape in governing the proton uptake, simulations were also carried out on idealized two-dimensional slabs representing the (021) and (110) crystal faces. The major finding is that, at these length scales, the simulated proton distributions do not at all reflect the sum of contributions from individual crystal faces. Instead protons accumulate preferentially at edge regions defined by the acute intersections of the $(110)-(\bar{1}0)$ surfaces. The effect was explained as resulting from the more effective solvation of excess charge at the acute edges of the particles and the tendency for surface charge to accumulate at sharp edges (*41*).

Studies of proton uptake on goethite have noted that surface roughness appears to have a noticeable effect on the total proton uptake, but little effect on the pH of zero charge (*42*). Variations in the amount of proton uptake on a suite of goethite particles were interpreted as being the result of variability in surface roughness (42,*43*). The roughest surfaces were shown to have the largest proton uptake. The cause of this behavior was interpreted as a closer association of protons with the rough surfaces. The simulations on the model particles may indicate that the higher uptake of the rough surfaces is due to dielectric effects favoring proton accumulation in edge regions. In a system with background electrolyte, the electrolyte contribution to polarization around the surface charge would presumably also be enhanced in the edge region. Inhomogeneous proton accumulation on colloidal particles and rough surfaces would have broad implications for ligand exchange and electron transfer reactions. Because sites at acute edges are more accessible to protons, and have longer Fe–O bonds to bound water sites, they should be preferentially reduced in oxidation–reduction reactions involving electron transfer from the solution phase to the solid phase. Similarly, electrons will be more mobile in edge regions for the same reason that decreasing pH increases ferrous–ferric exchange rates in homogeneous solution (*23*). Ligand exchange kinetics would be similarly enhanced due to the swelling effects and increased M–O bond lengths at edge sites (*44*). The heterogeneity in the proton distributions will also influence the aggregation behavior of colloidal particles and provide a possible mechanism for electrostatic complementarity, allowing interparticle attachment pathways away from the point of zero charge.

At some larger size, the behavior of the system overall must be predictable from the slabs; however, a detailed study of the mesoscale crystallography of goethite indicates the presence of pores on the (110) faces bounded by (021) surfaces (*45*). Any real system will likely have significant roughness on 10-nm length scales, and hence, the edge effects highlighted in the simulations would still influence the charging behavior of the material. Thus, the calculations have some degree of generality and are not necessarily limited to the small length scales accessible through the simulations.

B. Water, Hydroxide, and Oxide Exchange Kinetics

B.1. Polyoxocations

The exchange of oxygen between water molecules in bulk solution and individual functional groups at a mineral surface is one of the most fundamental expressions of water–rock interaction. These reactions are central to a wide variety of geochemical processes, including dissolution, sorption, and colloid formation, yet little is known about the actual molecular pathways for exchange or even about the relative exchange rates at different coordination sites. Because there is so little information about mineral surface reactions at the molecular scale, the mechanisms have always been interpreted using ideas derived from studies of simple octahedral substitutions in monomeric aqueous complexes (*46*).

The coordination chemistry of oxygen atoms at a mineral surface would be expected to be much more complicated than that of a simple monomeric ion. Studies of oxygen isotope-exchange reactions in small aqueous clusters using nuclear magnetic resonance (NMR) spectroscopy provide a foundation for understanding ligand exchange kinetics in extended structures (*36*). Because the structures of the aqueous clusters are known, these studies allow reactions to be followed at individual sites. Rates of exchange of water molecules and hydroxyl bridges bound to metal ions with water molecules in the bulk solution were separately measured in these clusters. The clusters are 1–2 nm in size and were chosen because they have functional groups similar to those thought to be present at aluminum-hydroxide mineral surfaces.

B.1.a. Water exchange rates. Water-exchange rates are key guides of chemical reactivity in aqueous coordination compounds. Aqueous metal–ligand complexation reactions take place through the diffusion-limited formation of an electrostatic ion pair,

followed by slow elimination of a water molecule bound to the metal center. This rate of the slow step is governed by the intrinsic water-exchange rate for the metal ion. Once the rate of water detachment is known, the rates of other ligand-exchange reactions usually can be estimated to within a factor of 10. Rates of surface complexation reactions at solid–water interfaces are intimately involved in diverse phenomena such as adsorption, electron transfer, and surface charging. There is no doubt that water-exchange rates are as fundamental to the reactivity of these systems as they are to coordination compounds, but, thus far, experimental determination of rates has been possible only for the simplest polynuclear systems.

Water-exchange rates for the Al^{3+} aquo ion, the Al_{13} and Al_{30} polynuclear ions discussed above, and models of clay mineral surfaces (gibbsite $Al(OH)_3$, kaolinite $Al_2Si_2O_5(OH)_4$, and boehmite AlOOH) were determined computationally using molecular dynamics methods (*44*). Like the mineral surfaces, the polycations have water molecules bound at active sites that are separated by sets of relatively rigid hydroxyl bridges. Unlike the mineral surfaces, the polyoxocations have active sites whose arrangements are known from X-ray diffraction studies on hydrated salts of these ions. The molecular dynamics calculations were able to link these structurally diverse systems together into a simple structure–reactivity trend based on $Al–OH_2$ bond lengths and highlight the role of the Al_{13} and Al_{30} ions in systematically bridging the structural gap between the hexaaquo ion and the oxide surfaces.

As a general rule it should be expected that, in a series of polynuclear ions made from the same cation, the water molecules should exchange faster than they do for the monomeric aquo complex of the cation. The relevant experimental data for these clusters have been summarized in a recent review (*36*). Because the $Al(H_2O)_6^{3+}$ ion has the highest average charge per aluminum, the monomer should be the least reactive complex in the series. At 298 K, the $Al(H_2O)_6^{3+}$ ion exchanges waters with a characteristic time of 1.2 seconds. The 12 bound waters on the Al_{13} class of complexes are all equivalent and, in keeping with this general rule, have characteristic exchange times between 0.0009 seconds and 0.005 seconds, depending on the identity of the central tetrahedral ion (aluminum, gallium, and germanium). For Al_{30}, there are six distinct types of bound waters. Separate values cannot be assigned from the ^{17}O NMR experiments, although, overall, the timescales are consistent with a few milliseconds to tenths of milliseconds. Four of the bound waters, however, react so quickly that they

could not be detected in ^{17}O NMR, which means that they exchange at least a factor of 10 more rapidly than the others.

Molecular dynamics calculations were carried out to estimate water exchange rates for surface sites on each of these species. The CLAYFF force field was used to do the calculations (*47*). This force field operates in conjunction with the SPC/E water model and was developed for simulating aluminum hydroxide minerals and clays. The authors used this force field because it was much less expensive than the Stillinger–David type force field described above, and, with long simulations, the temperature dependence of the rate could be obtained directly from rate calculations carried out at several temperatures, and, hence, the activation enthalpies and entropies, ΔH^* and ΔS^*, could be determined. The measurements of water exchange rates take place in a pH region where acid–base reactions probably do not couple strongly with ligand exchange processes. For the Al_{13}^{7+} and Al_{30}^{18+} ions, charges on each of the aluminum ions were adjusted to reproduce the net charge on the complex. Water-exchange rates were calculated for each species using the reactive-flux method (*48*). In this method, an arbitrary reaction coordinate is expressed between the outgoing/incoming water molecule and the aluminum site to which it is attached. The potential of mean force along the reaction coordinate, W(r), was calculated using umbrella sampling, with 20–30 windows and a harmonic biasing potential. The rate constant is taken as $k_{RF}=\kappa k_{TST}$, where k_{TST} is the transition-state rate constant calculated from the potential of mean force and κ is the transmission coefficient that accounts for barrier recrossing associated with the choice of reaction coordinate. The transmission coefficient is obtained by starting a series of simulations with the Al–H_2O distance balanced (and equilibrated) at the maximum in the potential of mean force, integrating forward and backward in time and counting the fraction of successful barrier crossings (*49*). The calculated rates are in reasonable agreement with the measured rates and, as shown in Fig. 11a, correlate well with calculated Al–OH_2 bond lengths on the exchanging sites. The slow rate of water exchange around the $Al(H_2O)_6^{3+}$ is consistent with the short Al–O bond length calculated for the hexaaquo complex (1.83 calculated versus 1.88 measured). Calculations on the Al_{30} molecule reflect the site heterogeneity present in the Al_{30} ion. The slowest rates are for S3 and S4 (see Fig. 8), which have very short Al–OH_2 bond lengths both in the simulation and in the X-ray structure. There is no experimental evidence for exchange rates as slow as those calculated; however, given the very short bond lengths observed for these sites, it is perhaps surprising that the NMR studies do

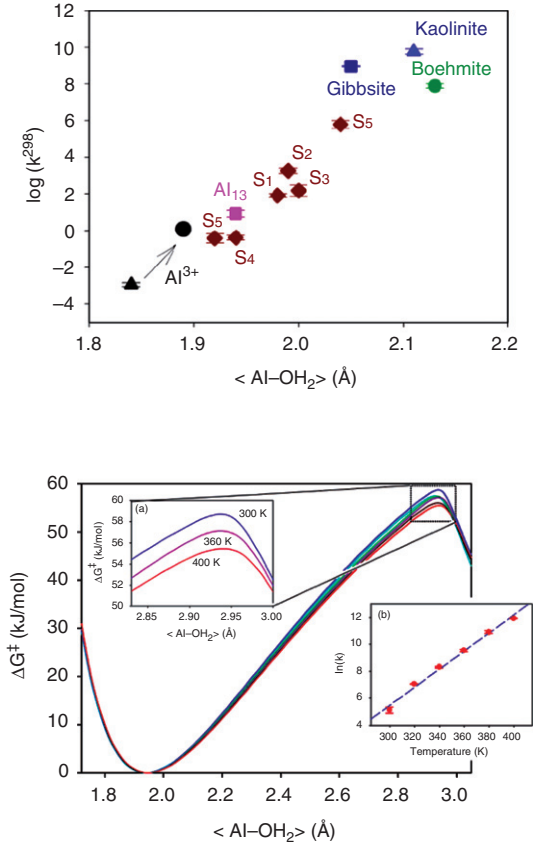

FIG. 11. (a) Correlation of calculated rate constant k at 298 K versus average Al–O bond length on a series of polynuclear clusters and minerals. S1–S5 sites correspond with the notation given in Figure 8. (b) Temperature dependence in calculated potential of mean force and (inset) temperature dependence of the rate computed by integration of the potential of mean force.

not resolve two very slowly exchanging sites. The four symmetrically equivalent S5 sites exchange much faster than the other sites, consistent with the experimental observation that four waters are too reactive to measure with ^{17}O NMR.

The temperature dependence of the rate constants was used to determine the activation parameters (Figure 11b). Activation parameters have been measured for both $Al(H_2O)_6^{3+}$ and Al_{13}. The calculated value of ΔH^* for the $Al(H_2O)_6^{3+}$ ion (101.5 ± 2.6 kJ mol^{-1}) is larger than the experimental value of 85 ± 3 kJ mol^{-1}, which again reflects the short Al-OH_2 bond length predicted by

our modified CLAYFF force field for the Al^{3+} aquo ion. The ability of the umbrella-sampling approach to relate ΔH^* to both the reaction coordinate and its associated transmission coefficient provides information complementary to the quantum mechanical studies, which neglect the transmission contribution. The relationship between ΔH^* and the temperature dependence of the exchange rate is much clearer in the umbrella-sampling reactive-flux approach. The ΔH^* of 64 kJ mol^{-1} calculated for the Al_{13} ion agrees well with the experimental values of 53 ± 12, 63 ± 7, and 56 ± 8 kJ mol^{-1} for the Al_{13}, $GaAl_{12}$, and $GeAl_{12}$ ions, respectively (*36*). Activation volumes for water exchange could be obtained through the pressure dependence of the calculated rate constant, analogous to Fig. 11. This has not been done for any of the polynuclear species discussed above, but the activation volume for water exchange around Li^+(aq) has been calculated in this way (*50*).

Overall, the estimates of the characteristic exchange times for the aluminous minerals are surprisingly short, falling within the range of 10^{-8}– 10^{-10} s, close to those for alkali and alkaline-earth metal ions. Waters bound at the edges of the minerals will exchange rapidly with bulk waters and with other ligands. The fast rates for these surface sites are consistent with the long Al–OH_2 bond lengths and also follow the general trend that rates increase, and ΔH^* values decrease, with increasing size and decreasing charge per aluminum ion of the complex. This framework provides, for the first time, a means for estimating kinetic parameters for sites at aqueous polynuclear ions and oxyhydroxide surfaces. This result is an important step forward for environmental chemistry, where treatment of reaction kinetics at the aqueous–mineral interface is a long-standing problem.

B.1.b. Hydroxide bridge exchange on (Al, Ga, Ge)$Al_{12}O_4(OH)_{24}(H_2O)_{12}^{7+}$. In a series of groundbreaking experimental studies of single-site reactivity in polyoxocations, Casey and co-workers [see (36) for a review] determined the relative rates of hydroxide bridge exchange in a series of isostructural chemically substituted $MAl_{12}^{7+/8+}$ ions. These ions have the ε-Keggin structure shown in Fig. 8. There are two symmetrically unique hydroxide bridges, one connecting trimeric $Al_3(OH)_3$ structures and another connecting the four trimers together with dimeric $Al_2(OH)_2$ structures. The measurements showed that rates of exchange of the two hydroxide bridges in each Keggin ions were found to be independent of pH and to differ dramatically from one another by as much as a factor of 1000, with the dimeric bridges reacting faster.

Moreover, the rates were extremely sensitive to a single metal substitution in the tetrahedral site at the center of the ion. These substitutions cause rates to differ by at least a factor of 10^5 with bridge replacement rates increasing in the order $GaAl_{12} < AlAl_{12} < GeAl_{12}$. Because the central tetrahedral metal is three bonds away from the exchanging oxygen, it is surprising that the effect of substitution at the tetrahedral site is so strong.

Molecular dynamics simulations and electronic structure calculations showed that the observed reactivity trend arises because the central metal in the Keggin ion controls the formation of a hydrated metastable intermediate through polarization of the fourfold coordinated oxygen atoms (μ_4-O) in each ε-Keggin structure (*51*). The mechanism involves bond rupture at two metal centers, partially releasing one of the "dimer" bridges, and allowing it to take on two waters of hydration to replace the broken Al–μ_4-O bonds and the resulting surface structure is stabilized by H_3O_2 bridges. This metastable intermediate then undergoes replacement of one of the μ-OH functional groups with an H_3O_2 bridge. Exchange takes place as the metastable intermediate relaxes back to the ε-Keggin structure; each oxygen in the H_3O_2 structure has a 50% probability of being exchanged back out of the complex as it relaxes. The mechanism is illustrated in Fig. 12. The reason for the observed reactivity trend is simply that the stronger the tetrahedral M–μ_4O bond, the weaker the bond from the same μ_4–O to the outer aluminum atoms, facilitating formation of the metastable intermediate. This idea is supported by the trends in (Ga, Al, Ge)–μ_4O and μ_4O–Al bond lengths observed in X-ray diffraction studies on the ε-Keggin structures.

The reaction to form the hydrated intermediate has a high positive reaction volume (ΔV_{rxn}) relative to the stable ε-Keggin structure. This (ΔV_{rxn})includes removal of two water molecules from the bulk solution that return the five-coordinated aluminums to their six-coordinated state. An additional water molecule is required to form the H_3O_2 bridge where the oxygen exchange takes place. The volume of the Al_{13} hydrated intermediate is 479 cm^3/mol (using a probe radius of 1.4 Å in the Connolly excluded volume calculation). This exceeds the volume of the stable Al_{13} ion by 78 cm^3/mol. Subtracting the volume of the three water molecules (54 cm^3/mol), a net +24 cm^3/mol is estimated for the activation volume of the reaction. The experimentally measured activation volume is +7.1 cm^3/mol (*52*). While an exact correspondence between the activation volume estimated from the pressure dependence of the rate constant and the approximate calculation based on Connolly

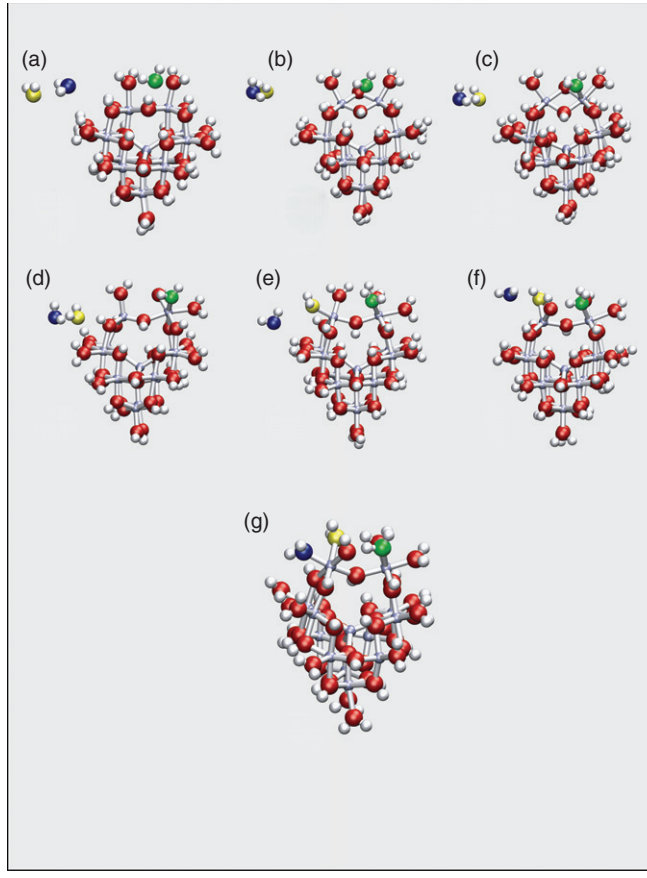

FIG. 12. Process of hydroxide exchange on dimer-bridging OH groups on the ε-Keggin ion through formation of a metastable intermediate. Oxygen atoms are red, protons are white, and trivalent metal atoms are gray. The green, blue, and yellow oxygen atoms progressively associate themselves in moving from (a–g) onto the metastable intermediate. Formation of the H_3O_2 bridge involving the green oxygen atom results in hydroxide exchange with 50% probability as the structure relaxes from (g) back to (a).

solvent-excluded volume would not be expected, the proposed mechanism predicts that rates of oxygen exchange at the μ-O bridges in the Al_{13} will decrease with increased pressure and will be dominated by the large increase in volume to form the intermediate, consistent with the measured sign of the activation volume.

A corollary of the proposed mechanism is that solvation forces are important in stabilizing the hydrated intermediate. If the

electrolyte distribution around the highly charged ion ties up water molecules needed for the stabilization of the intermediate, activation of the stable Keggin ion into the expanded intermediate will be inhibited. Therefore, a reduction in water activity should directly affect the formation of the intermediate complex facilitating the exchange. Any mechanism facilitated by the dissociative loss of a water molecule from the ε-Keggin structure would be consistent in sign with the measured activation volume, but should have an opposite response to an increase in ionic strength of the solution, as this effect should enhance the tendency for water loss from the complex. The concepts of dissociative and associative reactions, and the traditional interpretation of activation volumes in water exchange reactions, on simple aquo ions need to be revised when considering exchange in extended structures.

C. Polyoxoanions

Recent experimental studies on substituted decaniobate ions having the general formula $H_nNb_{10-m}Ti_mO_{28}^{-(6+m-n)}$ provide an opportunity to better understand the effect of protonation on oxygen exchange kinetics. While the solution stabilities of the polyoxocations discussed above decrease rapidly as they deprotonate, oxygen exchange reactions in the decaniobate and mono-titano and di-titano-substituted versions of the decaniobate ion can be followed over a range of pH conditions (*16,53*). The experimental studies reveal substantial differences in the isotope exchange rates between the different oxygen atom types. The reactivity differences change with pH. At pH 5.5 where the molecule is ~80% protonated, the rates are $\mu^{22}\text{-O} \approx \eta^2\text{-O} \approx \eta^3\text{-O} \gg \mu^{23}\text{-O} > \mu^{12}\text{-O} > \mu_3\text{-O} > \mu_6\text{-O}$ with the fastest reacting sites showing decreasing rates with increasing pH. From pH 7 to 9.5, the overall rates increase, and the relative values change somewhat becoming $\mu^{22}\text{-O} \approx \eta^3\text{-O} > \eta^2\text{-O} \approx \mu^{23}\text{-O} > \mu^{12}\text{-O} \approx \mu_3\text{-O} \approx \mu_6\text{-O}$. This "amphoteric" behavior suggests the existence of both proton and hydroxide enhanced pathways in the exchange reactions.

The Nb^{+5} ion is unusual in that it appears to exhibit a degree of coordination frustration, in the sense of being too large for tetrahedral coordination, about also too small for optimal octahedral coordination, leading to structures, like those of V^{5+}, where the "rattling" of the ion in an octahedral cage can have an important influence on bonding (*54*). These effects are evident in Fig. 4, showing the coordination structure of the decaniobate ion.

It seems reasonable to suppose that the rattling of the small Nb^{5+} ion in its mismatched coordination sphere would figure prominently in governing the mechanism of oxygen isotope exchange. Fluctuations in the local coordination geometry of the Nb^{5+} would be expected to give rise to a marked time dependence of coordination number with instantaneous configurations closer to five-fold or four-fold coordination. During such fluctuations, the bond to the sixth oxygen atom would be stretched and vulnerable to attack. It is also during these excursions that the rattling Nb^{5+} might reopen its coordination sphere to an incoming nucleophile (hydroxide or water).

To better understand the possible weak links in the decaniobate ion that might give rise to oxygen exchange, a molecular dynamics calculation was carried out with the PQS quantum chemistry code (www.pqs-chem.com) of the decaniobate ion embedded in the COSMO continuum solvent model (*55*) (dielectric constant = 80, probe radius = 1.4 Å). The time step was set at 0.001 picoseconds, and the simulation was run for 3000 time steps. The kinetic energy of the system was equivalent to 1000 K in temperature. During the dynamics, several excursions of the type shown in Fig. 13 were observed, where the Nb_3–μ_3O bond would break, the Nb_3 niobium would pass through a five-fold coordinate intermediate in Fig. 13(b), and become tetrahedrally coordinated as illustrated in Fig. 13(c). The average bond lengths and the fractional average fluctuations are given in Table IV. The calculation confirms that the bonds most susceptible to breaking are the Nb_3–μ_3-O bonds on the top of the molecule. That the η_3–O exchanges should be relatively fast fits in well with this finding. However, the fastest oxygen atoms to exchange over most of the pH range are the η_2–O and μ^{22}–O oxygen atoms and these have the smallest RMS bond fluctuations during the simulation. Based on Table IV, it might be guessed that the μ^{12}–O and μ_3-O would exchange more quickly than the μ^{22}–O.

Molecular dynamics simulations of the decaniobate ion were carried out using the conventional MD model described above with 250 solvating waters (*16*). With no added hydroxide or protons, the molecule was stable over 10 ns simulation times. Average bond lengths and fluctuations are given in Table IV, and, in a relative sense, compare well with the DFT direct dynamics, given that the RMS fluctuations in bond length are smaller because of the much lower temperature. Thus the same general conclusions/expectations discussed for the direct dynamics calculation would hold for the conventional MD calculation.

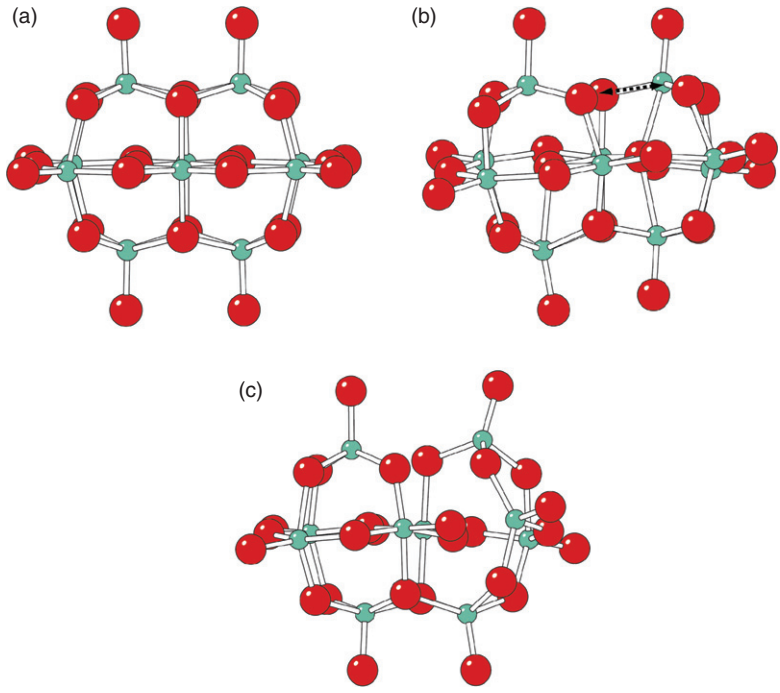

FIG. 13. Coordination fluctuations of Nb^{5+} in the decaniobate ion during a molecular dynamics calculation of the decaniobate ion in continuum solvent. Oxygen atoms are red, and niobium atoms are green. The dynamics are characterized by frequent Nb–μ_3-O bond ruptures, as shown in (b), followed by instantaneous tetrahedral coordination for the Nb_3, shown in (c). See Figure 4 for description of notation.

To obtain more information on the hydroxide-enhanced pathway at high pH, a single hydroxide ion was added to the solution. After several nanoseconds of simulation time, the ion began to break down by the process illustrated in Fig. 14. This is initiated by hydroxide attack on Nb_1 in the region where the two μ^{12}-O and μ_3-O atoms come together on one of the outer octahedral faces of Nb_1. At this point, Nb_1 becomes disconnected from the μ_3-O atom at the top of the decaniobate ion as well as the two μ_6-O atoms at the center of the ion as shown in Fig. 14b. The Nb_1 ion is tetrahedrally coordinated at this point and begins to hydrate with water molecules shown in blue, increasing its coordination number. Nb–OH_2 functional groups are highly acidic, and as the hydration waters are progressively attached to the "pulled out" Nb_1 they lose protons. These protons then become available to protonate other oxygen sites on the

TABLE IV

Bond Lengths and Their Root Mean Square Fluctuations for the Decaniobate Ion in Figure 4 as Predicted From Molecular Dynamics Calculations

	DFT COSMO (1000 K)			Parameterized MD model Explicit Water (300 K)		
	<r>	RMS	RMS/<r>	<r>	RMS	RMS/<r>
Nb_3-μ_3	2.28	0.347	0.152	2.19	0.071	0.033
Nb_3- μ^{23}	1.96	0.087	0.045	1.96	0.030	0.015
Nb_2- μ^{23}	2.05	0.115	0.056	2.02	0.036	0.018
Nb_2- μ^{22}	2.01	0.114	0.056	2.00	0.036	0.018
Nb_3- η^3	1.78	0.042	0.024	1.87	0.021	0.011
Nb_2-η^2	1.79	0.063	0.035	1.88	0.021	0.011
Nb_1- μ^{12}	1.89	0.067	0.036	1.93	0.025	0.013
Nb_2- μ^{12}	2.18	0.177	0.082	2.10	0.048	0.023
Nb_1- μ_6	2.25	0.171	0.076	2.21	0.071	0.032
Nb_1- μ_3	2.07	0.131	0.063	2.11	0.050	0.024

decaniobate ion and can be quickly transferred to other surface sites through the Grothuss mechanism. As shown in Fig. 14d, the η^2-O groups become protonated in the conventional MD model. The parameterized model does not do very well on the terminal oxygen atoms, giving Nb_2–η^2-O and Nb_3–η^3-O bonds that are too long, and probably have too high of a proton affinity. It is difficult to even check how inaccurate the proton affinities might be for the model decaniobate ion because the COSMO continuum solvation model has not been implemented in the MD force field. Therefore, unlike the hexaaquo cation and oxyanion systems described above, there is no possibility of a direct comparison between the gas-phase proton affinities of the decaniobate ion; the anions are not even stable in the absence of solvation, which must be taken into account by a continuum solvent model in the DFT studies and by using real water molecules in the conventional molecular dynamics. This is where the theoretical disadvantages of working on large anions become particularly inconvenient, as it is hard to compare these methods quantitatively.

It remains difficult to understand how this sequence of events would lead to a particularly fast exchange rate of the μ^{22}-O and η^2-O sites. If anything, the pathway indentified by the MD simulations would suggest that the η^3-O and μ_3-O exchange the most rapidly. A working hypothesis is that perhaps the proton affinity of the μ^{22}-O site is large relative to the other sites, and if this site

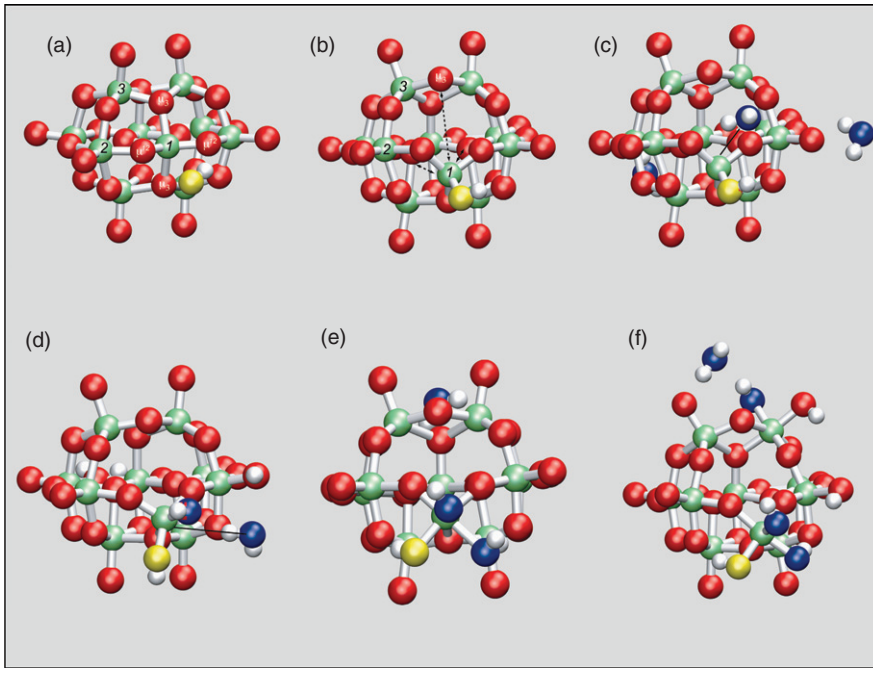

FIG. 14. Formation of metastable intermediate revealed in a classical molecular dynamics simulation of the decaniobate ion under basic conditions. Oxygen atoms are red, niobium atoms are green, and protons are white. The added hydroxide ion is represented by the yellow oxygen. Nb_1 is nucleophilically attacked by the hydroxide ion in (b), and the upper bond to the m_3 and the bonds to the m_6 oxygen atoms in the center of the ion are broken. The displaced niobium atom then proceeds to hydrate, with the waters represented by the blue oxygen atoms becoming progressively attached, and then hydrolyzing to release protons that can bind to other oxygen atoms on the decaniobate. Water molecules also hydrate the top Nb_3 atoms as they become detached from the central m_6 oxygen atoms after the Nb_1–m_3O bond is ruptured.

receives protons emitted by the water molecules hydrating the intermediate state in Fig. 14, or some other analogous intermediate state, the exchange rate of these bridges would be accelerated. But there is no direct evidence of this in the calculations, and it is also possible that there exists a completely unrelated pathway that has not been identified in the MD simulations. At this point, the parameterized model has taken the theoretical work as far as it can, and the problem becomes a good task for AIMD.

The system is a large one for AIMD and using AIMD to search for reaction paths in such systems is a very computationally intensive process. It is possible that the structures located with the parameterized model might prove to be good starting points for finding reaction pathways in the AIMD studies.

However, the fact that the weak bonds in the decaniobate ion are distant from the most rapidly exchanging ions echoes the mechanism of hydroxide exchange identified for the ε-Keggin ion strongly suggests that, again, a metastable intermediate plays a governing role in the pathways of oxygen exchange. If the mechanism were purely a local one, it seems almost certain that the η_3-O and μ_3-O sites would exchange faster than the others, since, as indicated in both the DFT studies and the conventional MD model, this is where the direct action seems to take place in the decaniobate ion in its unperturbed state.

IV. Geological Problems with Molecular Level Solutions

The term "molecular geochemistry" is easier on the ear than "molecular geology". The reason for this is probably that applications of the physical chemistry of interfaces to real geological problems are few. Most of the justification for building a better understanding of mineral–water interfacial processes has come from the standpoint of contaminant fate and transport in the Earth's subsurface. Such applications are societally important but will never have a transformative influence on our understanding of the history and behavior of the earth. Is there any indication that molecular-level knowledge of mineral–water interface geochemistry will have an influence on our ability to read the rock record more accurately and with greater precision?

A. Boron Isotopes in Marine Minerals

One example where computational chemistry has made a remarkable contribution to understanding the history of the earth is in the field of boron isotope geochemistry. Boron exists in the oceans as both $B(OH)_3$ and $B(OH)_4^-$. The pK_a of boric acid ($\sim$8.8) is such that both boric acid and borate are present in the pH ranges near that of seawater (7.5–8.5). Carbonate minerals forming in marine environments incorporate trace amounts of boron into their structures during growth, presumably through incorporation of the charged $B(OH)_4^-$ species. Because boric acid

and borate should have different affinities for ^{11}B and ^{10}B, it has been proposed that measurement of the isotopic composition of boron trapped in ancient carbonate minerals, which is assumed to give the boron isotopic composition of only borate, could conceivably be used to estimate the pH of ancient seawater (*56*). Since the pH of seawater is directly related to atmospheric PCO_2, the technique can be used to estimate the PCO_2 of the atmosphere over time scales corresponding to the residence time of boron in the oceans, roughly 15 million years (we need to know the overall boron isotopic composition of the entire ocean to apply the method). Given concerns over rising levels of atmospheric CO_2 concentrations, the history of PCO_2 of the atmosphere on geological timescales is an important geological problem.

To carry out such an estimate, the equilibrium constant K_{34} for the reaction given in Equation (11) must be known:

$$^{10}B(OH)_3 + ^{11}B(OH)_4^- = ^{11}B(OH)_3 + ^{10}B(OH)_4^- \qquad (11)$$

Until recently, the only value available for K_{34} was estimated from the measured vibrational frequencies of the boric acid and borate ions (*57*). These frequencies were used to build a valence force field for borate and boric acid, which was then used to calculate the vibrational partition functions for both ions, and, hence, K_{34}, yielding a value of 1.019 (in other words, boric acid is enriched in ^{11}B relative to borate under equilibrium conditions). This approach was used to infer more acidic ocean pH values (pH<7.5) 20 million years in the geologic past. More recent quantum-mechanical calculation of the vibrational partition functions (*58,59,60,61*) indicated that the equilbrium constant is near 1.025–1.030, much higher than previously thought. The quantum chemical calculations motivated, and were corroborated by careful experiments in which the small shift in pK_a of $B(OH)_3$ with boron-isotope substitution was used to determine K_{34} (*62*). More recently, ab initio molecular-dynamics calculations (*63*) showed that the reason for the discrepancy with the small K_{34} value was because the strongly fractionating asymmetric stretching vibration had been incorrectly assigned and, thus, completely missed. The new value for K_{34} (1.028) implied that the pH of the Miocene oceans was not 7.5, but closer to 8.5. In an ironic illustration of an interdisciplinary "house of cards", interpretation of 20 million years of the earth history was called into question because of the misassignment of a single vibrational frequency for $B(OH)_4^-$. It is even more remarkable that the discrepancy was initially discovered through computational chemistry. Interestingly, the geological community had managed to mold their interpretations

around a completely erroneous estimate of the equilibrium constant, causing some vigorous discussion in the geochemical literature as the basis for the boron-isotope pH proxy began to unravel (*64,65,66*).

Building a more accurate boron-based paleo pH meter requires a much more detailed knowledge of the crystallographic structure of boron incorporated into calcite (*67*) and a more complete knowledge of how the boron actually passes from aqueous solution into the mineral. For example, it might not be true that all the boron incorporated into the structure comes from $B(OH)_4^-$. or, it may be that the isotopic composition of $B(OH)_4^-$ in calcite differs systematically from that of $B(OH)_4^-$(aq). In other words, successful application of such "geoforensics" involves molecular-level tools that have to be well understood from a physicochemical point of view. Conversely, the vastness of geologic time has a way of making inadequacies in our understanding of physicochemical laws evident, sometimes at a very fundamental level (Kelvin's estimate of the age of the earth in the absence of radioactive heating being the classic example). The earth can be regarded as a vehicle for exploring reaction dynamics on immense timescales unavailable to direct experiment (*68,69*). Thus the interdisciplinary conversation between physical chemistry and geology may be more of an exchange than a lecture.

B. Carbon Isotopes In Soil Minerals

Another geochemically based technique for reconstructing the PCO_2 of the earth's atmosphere involves the determination of the mixing profile of atmospheric and microbial CO_2 sources in soils (*70,71*). It has been known for a long time that CO_2(g) is enriched in ^{13}C relative to organic matter (*72*). This can be understood in terms of the weaker bonding environment present in, for example, proteins, relative to inorganic forms of carbon (*73,74*). However, atmospheric CO_2(g) is heavier than microbial CO_2(g) because the microbial CO_2 can be thought of as fresh from the reservoir of isotopically light organic reservoir. During periods of high PCO_2 in the atmosphere, the soil is more strongly dominated by the isotopically heavy atmospheric signature. If atmospheric PCO_2 is small, the soil is more strongly dominated by the isotopically light microbial signature. Some of the CO_2(g) is taken up by carbonate and oxide/oxyhydroxide minerals forming in soils. The carbon isotope profile imprinted in the minerals forming in the soil, and the shape of the isotopic profile have been used to estimate atmospheric PCO_2 (*70,71*).

A key question is then the relationship between the isotopic composition of the CO_2(g) in the soil and the CO_2 "dissolved" in the mineral species growing in the soils. The equilibrium carbon isotope fractionations between CO_2(g) and carbonate minerals ($CaCO_3$ (both calcite and aragonite polymorphs), $MgCO_3$ (magnesite)) are known experimentally and can be accurately calculated from quantum chemistry (*75*). Overall, carbon in carbonate minerals is isotopically heavier than carbon in CO_2(g) by about 0.1% (10 per mil, in the usual units used by isotope geochemists) with smaller variations among the individual carbonate minerals. For oxide/oxyhydroxide mineral species, such as goethite (α-FeOOH), the fractionations were not known and initially assumed to be close to zero (i.e., the equilibrium constant for isotope exchange was assumed to be close to 1.000) (*71*). Later, it was found that a positive fractionation of 0.25%(with the goethite heavier in ^{13}C than the CO_2) appeared to fit best within geologic constraints (*76*). There has to be some degree of circularity in using geological evidence to infer *both* the extent of the isotope fractionation *and* the PCO_2 level. Quantum mechanical calculations of the equilibrium constant were carried out to gain additional insight into the issue (*77*).

In contrast to the carbonate minerals, where all the carbon is in the form of carbonate ions in a known arrangement, the structure of the dissolved CO_2 component of goethite is not known. Knowledge of the structure is needed to carry out vibrational calculations to estimate the isotopic fractionations. Early studies, based on infrared vibrational spectroscopy, suggested that the carbonate was located in the open channels that are a prominent feature of the goethite structure (*78*). Later studies, using higher-resolution 2-D correlation methods, indicated a more complex speciation (*79*). To locate potential structures for CO_2 dissolved in carbonate (CO_2(m); m for mineral), *ab initio* molecular dynamics simulations were carried out for a variety of possible initial configurations representing substitutions (a) $C^{4+} = 4H^+$ and (b) $C^{4+} = M^{3+} + H^+$, as a sort of "conformer searching" procedure. These calculations were carried out in α-AlOOH, because treating FeOOH with the plane-wave density functional theory is very expensive, especially when including exact exchange in the functionals (which is required if it is desired that FeOOH be nonmetallic). As shown in Fig. 15, two basic structures were identified: one for starting configuration (a), in which the carbon occupied the open channel site, as envisioned in the early spectroscopy work, and another for starting configuration (b), in which the carbon was embedded in one of the faces of the vacant octahedron created by removing the Al^{3+}.

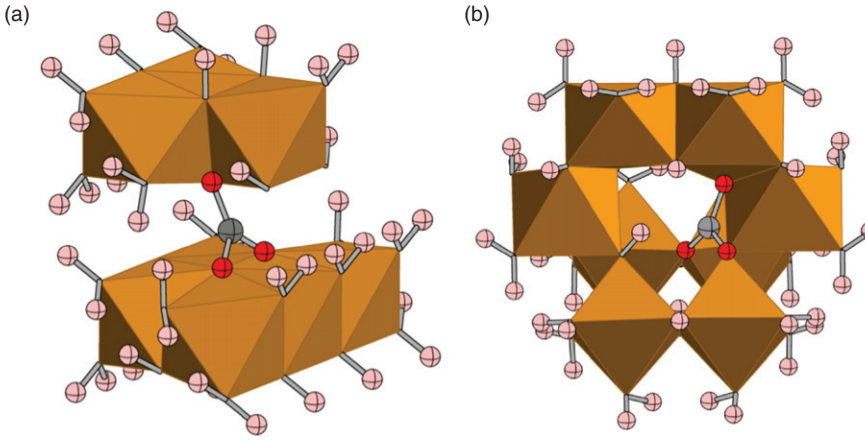

FIG. 15. Two possible configurations of carbon dioxide dissolved in goethite. Brown octahedra are Fe^{3+} centered octahedra making up the goethite structure, C^{4+} is shown in gray, oxygen atoms attached to C^{4+} are shown in red. Configurations are shown as (a) as a carbonate-like ion straddling the open channels, replacing three protons parallel to the **b** crystallographic axis in the goethite structure (b) embedded in the face of a vacant octahedron resulting from a Fes^{3+} vacancy. Each of the structures requires the removal of an additional proton.

Using the defect structures observed for CO_2(a) and CO_2(b) in AlOOH, structural models of these species were constructed for goethite from the known X-ray structure. The estimated isotopic compositions of the CO_2(a) and CO_2(b) species differed dramatically from each other in both AlOOH and FeOOH. For FeOOH, according to the quantum mechanical calculations, the open channel site CO_2(a) should harbor a highly isotopically light population of carbon atoms, depleted in ^{13}C by nearly 2 ‰ relative to CO_2(g), whereas the CO_2(b) site was predicted to have an isotopic composition similar to that of CO_2(g). One way to interpret the results of the calculations would be to infer that most of the CO_2(m) was in the form of CO_2(a). This is supported by the lower energy of the CO_2(b) configuration relative to CO_2(a) in diaspore (the energy difference for goethite could not be estimated from the calculations).

On the other hand, given the accessibility of the open channels, it is difficult to believe that the speciation of CO_2(m) in the solid does not end up being heterogeneous, with both types of defects being represented, and possibly more, given that some configurations would probably be missed in the *ab initio* molecular dynamics conformer searching procedure. Furthermore, the

relative energies of the two structures may not be the same in FeOOH as in AlOOH. If some of the CO_2(m) sites were structurally located within the open channels, the mineral could have a highly ^{13}C-depleted isotopic signature relative to CO_2(g). The predicted compositional contrast is almost great enough that the isotopic composition of CO_2(a) species could be mistaken for organic carbon. A depth-dependent variation in the fraction of CO_2(a) and CO_2(b) could have a strong effect on the carbon isotope compositions of goethite crystals as a function of depth, interfering with the recording of the primary microbial-atmospheric profile.

C. Final Remarks

These examples, dealing with the history of the PCO_2 of the Earth's atmosphere, one of the most pressing scientific problems of our time, show why geology must become focused more strongly at the molecular level. Exploration of the molecular-level details of the record of isotopes preserved in minerals and, ultimately, being able to sample isotope distributions at a site-specific level will require application of the best experimental and computational tools available. Moreover, it seems almost inevitable that solution of the energy problem must ultimately come from discovering effective ways to chemically trap solar energy on a large scale (*80*). Such traps must be made from geologically common materials because of the diffuse nature of the solar energy source, and their successful design will require a molecular-level understanding of these geological materials. Thus, there is no shortage of urgent, high-stakes geological problems. Paradoxically, priorities in geology remain focused on fieldwork, much like our sister science of biology was 100 years ago when geologists and biologists collaborated on the beginnings of structural investigations of hemoglobin (*4*). This focus must change as the plate-tectonic revolution fades into the annals of the history of science, and we anticipate a new century of geological discoveries.

References

1. Alley, R. B. *The Two Mile Time Machine* Princeton University Press: Princeton, **2000**.
2. Royer, D. L.; Berner, R. A.; Montañez, I. P.; Tabor, N. J.; and Beerling, D. J. *GSA Today* **2004**, *14*, 4.

3. Gibbs, G. V. *Am. Mineral.* **1982**, *67*, 421.
4. Reichert, E. T.; Brown, A. P. *The Crystallography of Hemoglobin*. Carnegie Institute of Washington, Publication No. 116, **1909**
5. Catlow C. R. A.; Thomas J. M.; Parker S. C.; Jefferson D. A. *Nature*, **1982**, *295*, 658.
6. Car, R.; Parrinello, M. *Phys. Rev. Lett.* **1985**, *55*, 2471.
7 Chandler, D. *Nature* **2002**, *417*, 491.
8. Stillinger, F. H.; David, C. W. *J. Chem. Phys.***1978**, *69*, 1473.
9. Halley, J. W.; Rustad, J. R.; Rahman A. *J. Chem. Phys.* **1993**, *98*, 4110.
10 Mortier, W. J.; Van Genechten, K.; Gasteiger, J. *J. Am. Chem. Soc.***1985**, *107*, 829.
11. Aguado, A.; Bernasconi, L.; Jahn, S.; Madden, P. A. *Faraday Discuss.* **2003**, *124*, 171.
12. Soper, A. K.; Phillips, M. G. *Chem. Phys.* **1986**, *107*, 47
13. Silvestrelli, P. L.; Parrinello, M. *Phys. Rev. Lett*. **1999**, *82*, 5415.
14. Tuckerman, M. E.; Laasonen, K.; Sprik, M.; Parrinello, M. *J. Chem. Phys.* **1995**, *103*, 150.
15. Curtiss, L. A.; Halley, J. W.; Hautman, J.; Rahman, A.*J. Chem. Phys.* **1987**, *86*, 2319.
16. Villa, E. M.; Ohlin, C. A.; Rustad, J. R.; Casey, W. H. J. Am. Chem. Soc. **2009**, *131*, 16488.
17. Baes, C. F.; Mesmer, R. E. *The Hydrolysis of Cations*; Wiley: New York, **1976**.
18. Rustad, J. R.; Dixon, D. A., Rosso, K. M.; and Felmy, A. R. *J. Am. Chem. Soc*. **1999**, *121*, 3234.
19. Martin, R. L.; Hay, P. J.; Pratt, L. R. *J. Chem. Phys. A*, **1998**, *102*, 3565.
20. Rustad, J. R.; Casey, W. H. *Theor. Chem. Acc.* **2006**, *115*, 136.
21. Banyai I.; Glaser J.; Read M. C.; Sandstrom M. *Inorg. Chem.* **1995**, *34*, 2423.
22. Silverman, J.; Dodson, R. W. *J. Phys. Chem.* **1952**, *56*, 846.
23. Rustad, J. R.; Felmy, A. R.; Rosso, K. M. *J. Chem. Phys.* **2004**, *120*, 7607.
24. Kuharski R. A.; Bader, J. S.; Chandler, D.; Sprik M.; Klein, M. L.; Impey, R. W. *J. Chem. Phys.* **1988**, *89*, 3248.
25. Huang, J. K.; Warshel, A. *J. Am. Chem. Soc.* **1987**, *109*, 715.
26. Parks, G. A.; de Bruyn, P. L. *J. Phys. Chem.* **1962**, *66*, 967.
27. Hiemstra, T.; Van Reimsdijk, W. H.; Bolt, G. H. *J. Colloid. Interface Sci.* **1989**, *133*, 91.
28. Rustad, J. R.; Dixon, D. A.; Felmy A. R. *Geochim. Cosmochim. Acta.* **2000**, *64*, 1675.
29. Rustad, J. R.; Felmy A. R.; and Hay, B. P. *Geochim. Cosmochim. Acta.* **1996**, *60*, 1553.
30. Russel, J. D.; Parfitt, R. L.; Fraser, A. R.; Farmer, V. C. *Nature*, **1974**, *248*, 220.
31. Rochester, C. H.; Topham, S. A. *J. Chem. Soc. Faraday Trans.* **1979**, *75*, 591.
32. Rustad, J. R.; Boily, J. F. *Am. Mineral.* **2010**, *95*, 414.
33. Catalano, J. G.; Fenter, P.; Park, C. Geochim. *Cosmochim. Acta.* **2009**, *73*, 2242.
34. Boily, J. F.; Felmy, A. R. Geochim. *Cosmochim. Acta.* **2008**, *72*, 3338.
35. Kowalksi, P. M.; Meyer, B.; Marx, D. *Phys. Rev. B* **2009**, *79*, art. no 115410.
36. Casey, W. H. *Chem. Rev*. **2006**, *106*, 1.
37. Rowsell, J.; Nazar, L. J. *Am. Chem. Soc*. **2000**, *122*, 3777.
38. Allouche, L.; Gerardin, C.; Loiseau, T., Taullele, F. Angew. Chem. Int. **2000**, *39*, 511.

39. Casey, W. H.; Rustad, J. R.; Banerjee, D.; Furrer, G. J. *Nanopart. Res*. **2005**, *7*, 377.
40. Rustad, J. R. and Felmy, A. R. Geochim. Cosmochim. Acta.**2005**, *69*, 1405.
41. Feynman, R. P. Leighton R. B. and Sands M.*The Feynman Lectures on Physics vol II*, Addison-Wesley: Reading, MA
42. Boily, J. F. Colloids and Surfaces. *Phys. Eng. Aspects* **2001**, *179*, 11.
43. Venema P. Charging and ion adsorption behaviour of different iron (hydr) oxides PhD. Thesis, Wageningen Agricultural University: Wageningen, The Netherlands.
44. Wang, J. W.; Rustad J. R.; Casey, W. H. *Inorg. Chem*. **2007**, *46*, 2962.
45. Weidler, P. G.; Hug, S. J., Wetche, T. P.; Hiemstra, T. Geochim. *Cosmochim. Acta.* **1998**, *62*, 3407.
46. Langford, C. H.; Gray, H. B. *Ligand Substitution Processes*; W. A. Benjamin: New York, **1966**.
47. Cygan, R. T.; Liang, J. J.; Kalinichev, A. *J. Phys. Chem. B* **2004**, *108*, 1255.
48. Chandler, D. *Introduction to Modern Statistical Mechanics* Oxford University Press: Oxford, **1987**.
49. Bennett, C. H., Exact Defect Calculations in Model Substances, In: "*Diffusion in Solids: Recent Developments*"; Eds. Nowick, A. S.; Burton, J. J.; Academic Press, New York, **1975** p. 73.
50. Rustad, J. R.; Stack, A. G. *J. Am. Chem. Soc*. **2006** , *128*, 14778.
51. Rustad, J. R.; Loring, J. S.; Casey, W. H. *Geochim. Cosmochim. Acta.* **2004**, *68*, 3011.
52. Loring, J. S.; Yu, P.; Phillips, B. L.; Casey W. H. *Geochim. Cosmochim. Acta.* **2004**, *68*, 2791
53. Villa, E. M.; Ohlin, C. A.; Balogh, E.; Anderson, T. M.; Nyman, M. D.; Casey, W. H. *Am. J. Sci.* **2008**, *308*, 942.
54. Dunitz, J. D.; Orgel, L. E. *Adv. Inorg. Chem.* **1960**, *2*, 1.
55. Klamt A.; Schuurmann, G. J. *Chem. Soc. Perkin Trans.* **1993**, *2*, 799.
56. Hemming, N. G.; Hanson, G. N. *Geochim. Cosmochim. Acta.* **1992**, *56*, 537.
57. Kotaka, M.; Kakihana, H. Nucl. *Reactors* **1977**, *2*, 1–12.
58. Oi, T. *J. Nucl. Sci. Technol.* **2000**, *37*, 166.
59. Oi T.; Yanase S. *J. Nuc. Sci. Tech.* **2001**, *38*, 429.
60. Zeebe, R. E. *Geochim. Cosmochim. Acta*. **2005**, *69* 2753–2766.
61. Liu, Y.; Tossell J. A. *Geochim. Cosmochim. Acta.* **2005**, *69*, 3995.
62. Klochko, K.; Kaufman, A. J.; Yao, W. S.; Byrne, R. H.; Tossell, J. A. Earth and Planet. *Sci. Lett.* **2006**, 248–276.
63. Rustad, J. R.; Bylaska E. J. *J. Am. Chem. Soc.* **2007**, *129*, 2222.
64. Pagani, M.; Lemarchand, D.; Spivack, A.; Gaillardet, J. *Geochim. Cosmochim. Acta.* **2005**, *69*, 953–961.
65. Hönisch, B.; Hemming, N. G.; Loose, B. *Geochim. Cosmochim. Acta.* **2007**, *71*, 1636.
66. Pagani, M.; Spivack, A. *Geochim. Cosmochim. Acta.* **2007**, *71*, 1642.
67. Sen, S.; Stebbins, J. F.; Hemming N. G.; Ghosh, B. *Am. Mineral.* **1994**, *79*, 819.
68. Lemarchand, D.; Wasserburg, G. T.; Papanastassiou, D. A. *Geochim. Cosmochim. Acta*. **2004**, *68*, 4665
69. Fantle, M; DePaolo, D. J. *Geochim. Cosmochim. Acta*. **2007**, *71*, 2524.
70. Cerling T. E. *Am. J. Sci*. **1991**, *291*, 377.
71. Yapp, C. J.; Poths H. Nature **1992**, *355*, 342.
72. Nier, A. O.; Gulbransen, E. A. *J. Am. Chem. Soc*. **1939**, *61*, 697.
73. Galimov, E. M. *The Biological Fractionation of Isotopes*. Academic Press, New York, **1985**.

74. Rustad, J. R. *Org. Geochem*. **2009**, *40*, 720.
75. Rustad, J. R., Nelmes, S. L.; Jackson, V. E.; Dixon, D. A. *J. Phys. Chem. A* **2008**, *112*, 542.
76. Yapp, C. J.; Poths, H. *Geochim. Cosmochim. Acta*. **1993**, *57*, 2599.
77. Rustad, J. R.; Zarzycki, P. *Proc. Natl. Acad. Sci. USA* **2008**, *105*, 10297.
78. Russell, J. D.; Paterson, E., Fraser, A. R.; Farmer, V. C. *J. Chem. Soc. Faraday Trans.* **1975**, *71*, 1623.
79. Boily, J. F.; Szanyi, J., Felmy, A. R. *Geochim. Cosmochim. Acta.* **2006**, *70*, 3613.
80. Lewis, N. S.; Nocera, D. G. *Proc. Natl. Acad. Sci. USA* **2006**, *103*, 15729.

THE AROMATIC AMINO ACID HYDROXYLASE MECHANISM: A PERSPECTIVE FROM COMPUTATIONAL CHEMISTRY

ELAINE OLSSON[a], KNUT TEIGEN[b], AURORA MARTINEZ[b] and VIDAR R. JENSEN[a]

[a]Department of Chemistry, University of Bergen, Allégaten 41, N-5007 Bergen, Norway
[b]Department of Biomedicine, University of Bergen, Jonas Lies vei 91, N-5009 Bergen, Norway

I. Introduction

The aromatic amino acid hydroxylases (AAHs) are a family of pterin-dependent enzymes comprising phenylalanine hydroxylase (PAH), tyrosine hydroxylase (TH), and tryptophan hydroxylase (TPH, with two gene products TPH1 and TPH2). The AAHs perform the hydroxylation of aromatic amino acids and play an important role in mammalian metabolism and in the biosynthesis of

THEORETICAL AND COMPUTATIONAL INORGANIC CHEMISTRY
VOLUME 62 ISSN 0898-8838 / DOI: 10.1016/S0898-8838(10)62011-9

monoamine neurotransmitters and hormones, vital for proper neuroendocrine functions (for previous reviews see *(1–6)*). The AAHs are metalloenzymes and possess a non-heme iron atom in the active site. Such non-heme iron active sites are less accessible to spectroscopic investigation than the better understood heme counterparts because they do not exhibit the clear spectral features of the porphyrin ligand (*7*). Molecular-level computational studies may thus complement experiment and play a particularly important role as provider of mechanistic insight for this class of enzymes. This review gives an overview of the molecular-level computational studies performed to date, with a particular focus on density functional theory (DFT) investigations of the AAH reaction mechanism performed by our group in recent years. Our results are discussed and compared with experimental results and with other computational modeling studies of the same enzyme family and also with other iron-containing enzymes. The first two chapters contain a thorough review of biological and structural issues of the AAH enzymes. The two last chapters contain a brief discussion of the computational methods used in studies of metalloenzyme reactivity in general followed by the review of the computational results obtained so far for the AAH enzymes.

PAH is mainly found in the liver and in the kidneys and converts L-phenylalanine (L-Phe) to L-tyrosine (L-Tyr) (Scheme 1), which is the rate-limiting step in the catabolism of L-Phe to carbon dioxide and water. TH is present in the central nervous system (CNS),

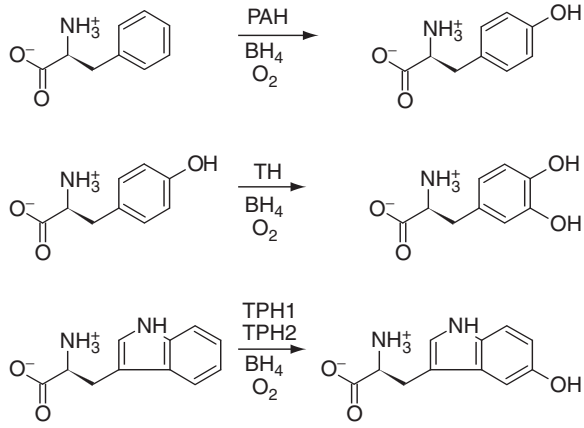

SCHEME 1. Hydroxylation of the aromatic amino acids (L-Phe, L-Tyr, and L-Trp) as catalyzed by their respective hydroxylase enzymes (PAH, TH, TPH1, and TPH2) using the cofactor BH_4 and dioxygen as additional substrates.

peripheral sympathetic neurons, and the adrenal medulla where it catalyzes the hydroxylation of L-Tyr to L-dihydroxyphenylalanine (L-DOPA), which is the rate-limiting step in the synthesis of the catecholamines dopamine, noradrenaline, and adrenaline. The TPHs convert L-tryptophan (L-Trp) into 5-hydroxytryptophan, which is the rate-limiting step in the biosynthesis of serotonin. Serotonin can be further metabolized to yield melatonin (*8,9*).

The AAHs are functionally and structurally similar, which is reflected in a high sequence similarity (Fig. 1). Phylogenetic and functional analyses place a protozoan PAH close to the ancestor sequence of the AAHs, thus aiding to define the evolutionary history of this enzyme family (*10*). While bacterial PAH is monomeric, the mammalian AAHs are tetrameric enzymes that consist of three domains: an N-terminal regulatory ACT domain, a central catalytic domain that includes a non-heme iron at the active

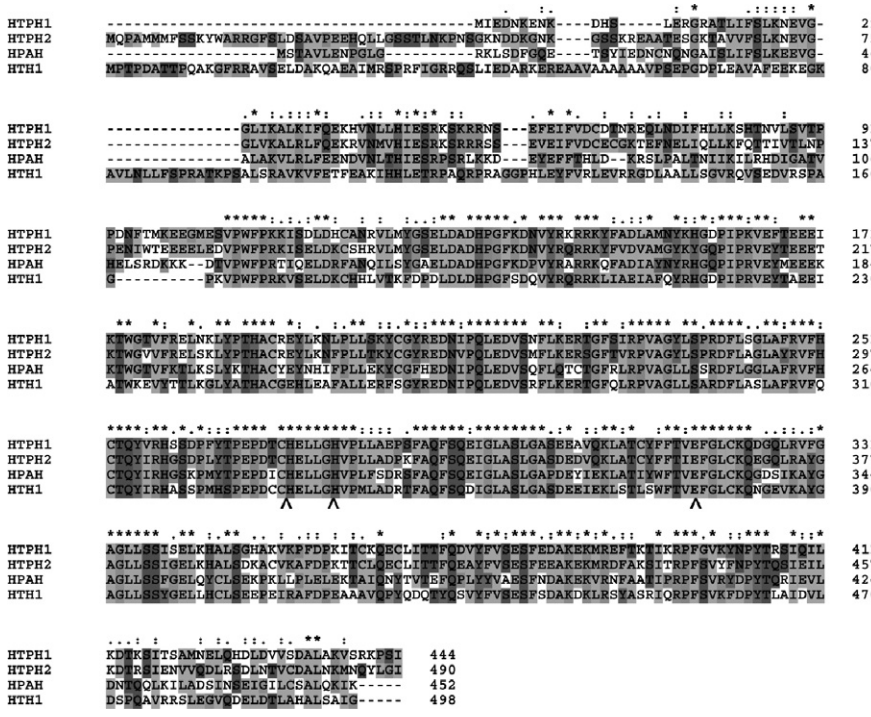

FIG. 1. Sequence alignment of human TPH1 (SWISS-PROT P17752), human TPH2 (TrEMBL Q8IWU9), human PAH (SWISS-PROT P00439), and human TH1 (SWISS-PROT P07101). The asterisks above the sequences indicate identity, while homolog properties of the residues are indicated with two dots or one dot, depending on the degree of similarity. The conserved 2-His-1-Glu motif is also marked by "^."

site and presents the highest sequence similarity (Fig. 1), and a C-terminal oligomerization domain (Fig. 2; see also Section II). The AAHs use a tetrahydropterin cofactor and dioxygen as additional substrate, and the atoms of the latter are incorporated into the amino acid substrate and the cofactor. The reduced form of the physiological cofactor (6R)-L-erythro-5,6,7,8-tetrahydrobiopterin (BH_4) donates two electrons during the catalytic reaction and is oxidized to tetrahydrobiopterin-4a-carbinolamine (4a-OH-BH_4) (*11–16*). BH_4 is sometimes referred to as a cosubstrate

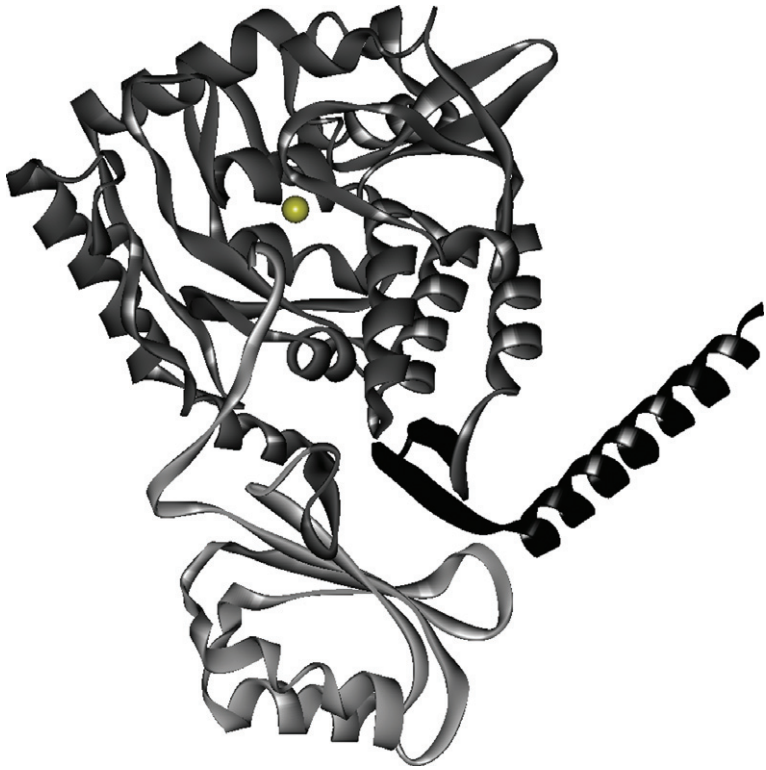

FIG. 2. Structural model of the PAH subunit showing the domain organization in ribbon representation. The regulatory ACT domain (residues 19–110) is shown in light gray, the catalytic domain (residues 111–410) in dark gray, with the iron as a sphere, and the oligomerization domain (residues 411–452) in black. The oligomerization domain consists of a dimerization motif (411–425) and a tetramerization helix (426–452). The truncated forms lacking the tetramerization helix exist as dimers in solution. Composite model created using the structures PDB 2PHM (rat PAH) and PDB 2PAH (human PAH).

(instead of cofactor), remarking that in the catalytic cycle it is hydroxylated together with the amino acid substrate and has to leave the enzyme in order to be regenerated. Whether BH_4 is referred to as a cofactor or cosubstrate has implications for the definition of enzyme type to which the AAHs belong. If BH_4 is defined as a cofactor the AAHs are referred to as monooxygenases (as is usually the case) or mixed function dioxygenases, as only one of the oxygen atoms is transferred to the substrate, while the other oxygen atom is finally reduced to water. If BH_4 is referred to as a (co)substrate, then, in a strict sense, the AAHs are dioxygenases. The ferrous form (Fe^{II}) of the iron atom is required for catalytic activity (*17–19*), and the inactive ferric form (Fe^{III}) is prereduced by the cofactor (*20–22*). The iron atom is anchored in the active site by two histidines and one glutamic acid (*4*) (Fig. 1). This so-called 2-His-1-Glu motif is seen also for other non-heme iron-dependent enzymes (*23,24*). The mechanisms by which the AAHs perform their catalytic reactions are generally considered to be very similar, taking into account (i) the high sequence identity in the catalytic domain; (ii) the dependence of Fe^{II}, dioxygen, and BH_4; and (iii) the similarity of their aromatic substrates and the reactions that they perform (*3,25*). The generally accepted reaction mechanism for the AAHs is a two-step mechanism in which a Fe^{IV}=O species is formed in the first step and which is responsible for the hydroxylation of the amino acid substrate in the second step (*15,26–28*). A high-valent Fe^{IV} species has been detected in the TH reaction using Mössbauer and electron paramagnetic resonance (EPR) spectroscopy on the ternary complex TH-Fe^{II}-6-methyl-5,6,7,8-tetrahydropterin ($6MPH_4$)-Tyr and was proposed to be the above-mentioned Fe^{IV}=O hydroxylating intermediate (*29*). Most structural and mechanistic information on AAHs has been derived from PAH and TH. The TPHs have been shown to be rather unstable and hard to isolate in large amounts, which complicates experimental investigations (*19,30*). The substrate specificity of the AAHs is determined by the catalytic domain and modulated by the regulatory domain (*2,6*). The strictness of the substrate specificity depends on the enzyme and the aromatic amino acid substrate. Only TH can hydroxylate L-Tyr and all four AAHs can hydroxylate L-Phe. PAH and the TPHs can hydroxylate L-Phe and L-Trp. Human (h) TPH2 shows a higher catalytic efficiency toward L-Trp (vs. L-Phe) than TPH1 (*30*). The molecular basis for the increased catalytic efficiency of PAH with L-Phe and of TPH1 with L-Trp has been investigated and associated with residue Trp326 (hPAH)/Phe313 (hTPH1) (*31*). This position, however, does not seem to determine the preference of TH for L-Tyr vs. L-Trp (*32*).

A. Phenylalanine Hydroxylase

Mammalian PAH is a cytoplasmic enzyme mainly located in the liver and in the kidneys. A dysfunctional PAH, usually due to mutations in the gene coding for the enzyme, is associated with the disorder Følling's disease or phenylketonuria (PKU; [Mendelian Inheritance in Man number 261600]), an inherited metabolic disease, which if left untreated can lead to severe mental retardation. If L-Phe fails to be metabolized by PAH, it accumulates in the blood reaching toxic levels. Alternative pathways for the breakdown of L-Phe give rise to toxic phenylketones (phenylpyruvate, phenylacetate, and phenyllactate) that are secreted in the urine (hence PKU). Both too high levels of phenylalanine and presence of phenylketones in the blood give rise to neurotoxicity and lead to severe, progressive mental retardation (*33*). Phenylalanine competes with the transport of other aromatic amino acids and catecholamines to pass the blood–brain barrier. Thus, the level of important neurotransmitters in the brain can be dramatically reduced in PKU patients (*34*). At present, the majority of PKU patients are diagnosed within days of birth by effective neonate screening so that treatment, based on diet very low in L-Phe, can be started early and clinical symptoms are not developed. More than 500 mutations in the *PAH* gene have been reported and registered in the PAH locus knowledgebase [PAHdb] (*35,36*). Expression, characterization, and computational analyses of mutation impact in a large number of these mutants have aided to establish the genotype–phenotype relationships and have revealed that decrease in protein stability is the main molecular pathogenic mechanism in PKU, though some catalytic mutations and other factors also contribute to the phenotypic outcome (*37*). Recently, there have been important developments of novel and promising therapeutic strategies aiming to alleviate or substitute the strict diet (*38*). Of those the supplementation with the cofactor BH_4 is already successfully used in the treatment of a large number of PKU patients (*39*).

It was early established that at least for PAH, which as isolated contains the catalytic iron in the ferric high-spin ($S = 5/2$) state, the Fe^{III} is reduced to Fe^{II} by BH_4. This is termed reductive activation of PAH and *in vitro* this reduction is an obligate step that occurs in the pre-steady-state period (*20*). A midpoint potential at pH 7.25 (E_m (Fe^{III}/Fe^{II})) of $+207 \pm 10$ mV was calculated for the iron in hPAH, which seems to be adequate for a thermodynamically feasible electron transfer from BH_4 (E_m (q-BH_2/BH_4) = +174 mV) (*40*).

There is no consensus about the order of substrate and cofactor binding for formation of the quaternary complex (PAH-L-Phe-BH_4-O_2) during the catalytic cycle, probably because different studies have used different experimental approaches and a variety of cofactors (*3*), as well as PAH from different sources. Volner *et al.* (*41*) have proposed a sequential-ordered mechanism with pterin binding first followed by L-Phe and then O_2 as the last substrate to the PAH from *Chromobacterium violaceum*. Using several spectroscopic techniques, Kemsley *et al.* (*42*) showed that binding of both L-Phe and BH_4 is required to change the coordination properties of the Fe^{II} at the active site of the human enzyme. The binding results in a loss of coordinated water and a change in the electronic structure of the iron atom, allowing the binding of dioxygen and the formation of the catalytic-competent PAH-L-Phe-BH_4-O_2 quaternary complex (see Section IV, where the mechanistic investigations are discussed in more detail). The requirement of PAH for a tetrahydropterin cofactor is absolute, but several analogues of BH_4, such as $6MPH_4$ and 6,7-dimethyl-5,6,7,8-tetrahydropterin ($DMPH_4$), can effectively substitute the natural cofactor in catalysis, although with lower affinity (*5*). The K_m of PAH for BH_4 is in the range 15–40 μM, while the substrate, L-Phe, binds with lower affinity ($S_{0.5} \gtrsim 150$ μM for the eukaryotic PAH) and typically manifests positive cooperativity (Hill coefficient, $h \sim 2$) (*6,43*). The positive cooperative activation of PAH is in fact a major regulatory mechanism, also accompanied by phosphorylation at Ser16, which acts synergistically with L-Phe activation, and inhibition by the cofactor BH_4 (*43*). The positive cooperative binding of L-Phe by mammalian PAH is believed to represent a protection mechanism that safeguards L-Phe homeostasis in blood in order to both avoid PKU and provide a continuous supply of tyrosine for protein synthesis. The inhibitory effect of BH_4 is manifested in the absence of L-Phe as a way to protect the enzyme from unfolding and degradation in the resting state (*44*), constituting an important molecular mechanism for the understanding of BH_4-responsive PKU (*45*).

B. Tyrosine Hydroxylase

TH is present in the CNS, peripheral sympathetic neurons, and the *adrenal medulla*, where human TH exists in at least four isoforms created by alternative splicing (hTH1–4), hTH1 being the predominant form in the *adrenal medulla* and in the *locus coeruleus* and *substantia nigra* of the brain and in the adrenal medulla (*46,47*). Dysfunctions in the enzymatic activity are

related to Parkinson's and cardiovascular diseases, and mutations in the *TH* gene are associated with juvenile parkinsonism and autosomal recessively inherited forms of DOPA-responsive dystonia as well as progressive infantile encephalopathy with L-DOPA-nonresponsive dystonia (for a recent review see (*48*)). L-DOPA is precursor to the catecholamines dopamine, noradrenaline, and adrenaline, functioning as neurotransmitters and hormones.

TH shows comparable affinity for BH_4 ($K_m = 13–27$) and L-Tyr ($K_m = 7–37$ μM) (for summarized values of K_m see Teigen *et al.* (*6*)). Fe^{II} is required for catalytic activity of TH and like PAH, TH can be (pre)reduced by the cofactor (*12*). Studies on the steady-state kinetic mechanism of rat (r) TH revealed an ordered binding of the three substrates to the active site, with BH_4 binding first, O_2 second, and L-Tyr last (49). ^{18}O kinetic isotope effect measurements on TH indicate that a one-electron transfer from the cofactor to dioxygen is the rate-limiting step in the overall reaction and that the amino acid substrate is not taking part in this step (*50*). By Mössbauer spectroscopy, direct evidence has been obtained for a high-valent Fe^{IV} species, which might be the proposed Fe^{IV}=O hydroxylating intermediate (*29*) (see Section IV).

TH is a cytoplasmic enzyme, but association to membranes has also been reported, the N-terminal sequence being important for this association (*51*). The physiological relevance of membrane association is not totally understood, but it might be a way to regulate L-DOPA and dopamine synthesis at the sites of neurotransmission, e.g., catecholamine secretory granules in chromaffin cells, brain synaptic vesicles, and synaptosomal membranes. The N-terminal is also the site for several phosphorylation sites, i.e., Ser/Thr8, Ser19, Ser31, and Ser40 (numeration in both hTH1 and rTH), which are phosphorylated both *in vitro* and *in situ* by various kinases and reversibly dephosphorylated by phosphatases (*2*). Phosphorylation at Ser19 controls the interaction with 14-3-3 proteins, which stabilizes and increases TH activity and in the case of 14-3-3γ also the interaction with membranes (*51*). A major regulation of TH activity is associated with the feedback inhibition by catecholamines, which tightly coordinate to the non-heme iron forming a high-spin ($S = 5/2$) Fe^{III}-catecholamine complex at the active site (*52*). This inhibition is relieved by phosphorylation at Ser40 by cAMP-dependent protein kinase (PKA), providing synergetic short-term regulatory mechanisms (*2,53*). The effect and physiological relevance of phosphorylation by other kinases at the other sites is less understood, but it is becoming increasingly clear that there is an interrelation between sites. Thus, phosphorylation at Ser19 (*54*) or Ser31 (*55*) in TH can also indirectly activate the enzyme

via a hierarchical mechanism by increasing the rate of phosphorylation of Ser40. Additional regulatory mechanisms for TH are substrate inhibition, which appear to act allosterically, involving the regulatory domain (*56*) and negative cooperativity for the natural cofactor BH_4 ($h = 0.5–0.6$) (*57*). While the physiological significance of substrate inhibition is not totally clear, the negative cooperativity for BH_4 might provide a high regulation of activity in a very narrow concentration range of cofactor, corresponding with the low physiological concentrations of BH_4 (<5 μM) within dopaminergic neurons of the *basal ganglia* (*57*).

C. Tryptophan Hydroxylase

Mammalian TPH exists as two gene products or isoforms: TPH2, which was relatively recently discovered (*58*) and since then identified as the main neuronal isoform, and the previously known TPH1, considered primarily as a peripheral isoform, abundant in the pineal gland and gut (*8,59*). The human TPH1 and TPH2 show an overall sequence identity of 71%, with the major difference being the longer sequence at the N-terminus of TPH2 (see Fig. 1). Although TPH1-mRNA is even more abundant than TPH2-mRNA in several areas of the brain (*60,61*), the use of monospecific antibodies has revealed that TPH2 is the predominant enzyme form expressed in brain extracts from *mesencephalic tegmentum, striatum*, and *hippocampus*, with a molecular weight of 56 kDa, while TPH1 is the predominant form in pineal gland and P815 mastocytoma cells, with a molecular weight of 51 kDa (*59*). Both TPHs catalyze the hydroxylation of L-Trp to 5-hydroxytryptophan, which is the rate-limiting step in the synthesis of serotonin (5-hydroxytryptamine). This neurotransmitter is associated with complex control of the CNS as well as regulating sleep, food intake, mood, and sexual behavior (*62,63*). Serotonin is further metabolized to melatonin mainly in the pineal gland and skin. Dysfunction of the serotonergic system and mutations and polymorphisms in the *TPH1* gene have been associated with various neurological and psychiatric disorders including depression, suicidal behavior, anxiety, alcoholism, and drug abuse (*64–66*), while mutations in *TPH2* have been proposed to give susceptibility to unipolar depression (Zhang *et al.* 2005 (*67*)), bipolar disorder (Cichon *et al.* 2008 (*68*)), and attention-deficit hyperactivity disorder (McKinney *et al.* 2008 (*69*)), among others.

Though being the focus of extensive psychiatric disorder association studies, the TPHs are the members of the AAH family for which less functional, molecular, and regulatory information has

been obtained. Some comparative studies of the isolated isoforms have been, however, undertaken (*30*). This study revealed different kinetic properties for TPH2, including lower V_{max} and lower affinity for L-Trp than TPH1 and also a reduced catalytic efficiency with L-Phe (relative to L-Trp) as substrate (*30*). Contrary to the rate-limiting step in PAH and TH which is indicated to occur before oxygen transfer into the amino acid substrate, the incorporation of oxygen to tryptophan is suggested to be the rate-limiting step for TPH1 (*70*).

Some regulatory mechanisms have been revealed for the TPHs, such as activation by phosphorylation-dependent interaction with 14-3-3 proteins (*71,72*). Catecholamines are also reported to be inhibitors of TPH (*73*). L-DOPA and L-DOPA-quinone derivatives, but not the end product serotonin, have also been shown to be inhibitors of TPH activity (see Martinez *et al.* 2001 (*74*) for the physiological and pharmacological implications of the inhibitory effects by catechol derivatives).

D. Other Dioxygen Activating Mononuclear Non-Heme Iron Enzymes

The 2-oxoacid-dependent dioxygenase family of non-heme iron enzymes requires dioxygen and the cofactor α-ketoglutarate (α-KG) for catalytic activity. As for the AAHs, they have an active ferrous iron anchored in the active site with the 2-His-1-carboxylate (the carboxylate being Glu or Asp) binding motif that can be seen in many metalloenzymes (*23*) and three ligating water molecules to give a hexacoordinate Fe^{II} complex (*75*). The generally accepted reaction mechanism for 2-oxoacid-dependent dioxygenases is very much similar to that of the AAHs, starting with the α-KG cofactor coordinating to iron in a bidentate manner, replacing two ligating water molecules. Next the binding of the substrate to the active site triggers the dissociation of the last water molecule, creating a vacant position on iron where subsequently dioxygen binds. Attack of dioxygen on α-KG and heterolytic cleavage of the O–O bond forms a Fe^{IV}=O species, which is believed to be responsible for hydroxylation of the substrate (*75*). This Fe^{IV}=O species has been isolated and identified (*76–79*).

Other non-heme enzymes that use dioxygen are 4-methoxybenzoate *O*-demethylase, extradiol catechol dioxygenases, the oxidoreductase isopenicillin *N* synthase, and α-keto acid-dependent enzymes (*28*). Moreover, the BH_4-dependent glyceryl-ether monooxygenase (GEM) also appears to be dependent on non-heme iron for catalysis (see also Section I.E).

E. (6R)-L-ERYTHRO-5,6,7,8-TETRAHYDROBIOPTERIN

The natural cofactor of the AAHs, BH_4 (Scheme 2), is a heterocyclic compound chemically classified as a pteridine that includes a fused pyrimidine and pyrazine rings. As many other naturally occurring pteridines BH_4 has a pterin structure, which includes an amino substituent in position 2 and an oxo group in position 4 of the pyrimidine ring. The term biopterin is reserved for pterins with a dihydroxypropyl group in position 6.

BH_4 is essential for the AAHs to carry out their respective catalytic reactions and, at least for PAH, the prereductive activation, which appears to produce dihydrobiopterin quinonoid (q-BH_2) directly (*20*). After the PAH catalytic cycle an oxygen atom is incorporated into the cofactor, providing 4a-OH-BH_4 which dissociates from the active site. In order to regenerate the functional tetrahydro form of BH_4 pterin carbinolamine dehydratase catalyzes the dehydration of 4-OH-BH_4 to q-BH_2, which is reduced back to BH_4 by dihydropteridine reductase (Scheme 2). q-BH_2 can also be converted to 7,8-dihydropterin (BH_2) which can be regenerated to BH_4 by dihydrofolate reductase (DHFR).

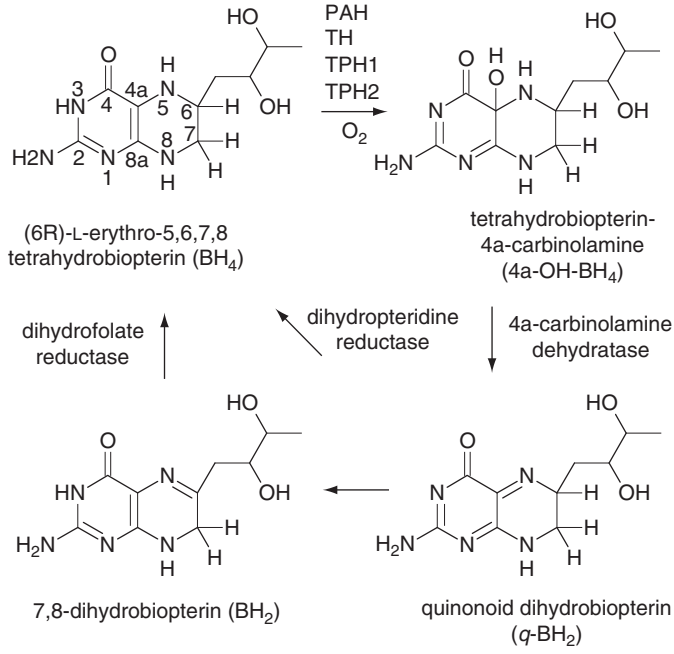

SCHEME 2. Oxidation and regeneration of the cofactor (6R)-L-erythro-5,6,7,8-tetrahydrobiopterin (BH_4).

Intracellular BH_4 levels are maintained in mammals by *de novo* synthesis from GTP, involving several enzymes (for a review on the biosynthesis and regeneration of BH_4, see Ref. (*11*)). A defect in one of the enzymatic steps in this complex L-Phe hydroxylating system in humans usually leads to hyperphenylalaninemia and, more severely, to PKU.

Under structural and functional investigations of the AAHs the inactive oxidized cofactor analogue BH_2 has often been used instead of BH_4, due to the instability of the natural cofactor (*80–85*). Nuclear magnetic resonance (NMR) and crystallographic studies have provided important information on the structure of binary and ternary complexes of the AAHs. The cofactor binds close to the active site iron making stacking interactions with an invariant Phe (e.g., Phe254 in hPAH). The amino group at C2 and N3 in BH_4 hydrogen bonds with the carboxylic group of a conserved glutamate residue (Glu286 in hPAH) (*80,86*). In the crystal structures of the enzymes complexed with the cofactor, these hydrogen bonding interactions are water-mediated for BH_2 and BH_4, but occur without water mediation for BH_4 in the crystal structures of the enzymes complexed with both cofactor and substrate analogue. In addition to the functional catalytic role of the cofactor in the AAH reaction, BH_4 has a regulatory role both for PAH, as an inhibitor and stabilizer of the enzyme, and for TH, eliciting negative cooperativity (see Sections I.A and I.B). These regulatory properties seem dependent on the presence of the dihydroxypropyl side chain at C6 of the cofactor, and functional cofactor analogues, such as the commonly used $6MPH_4$, support the hydroxylation reaction but do not elicit the regulatory properties (*57,87*).

Other pterin-dependent enzymes include GEM, mandelate 4-monooxygenase, benzoate-4-hydroxylase, anthranilate 2,3-dioxygenase, and the nitric oxide synthases (NOS), which all use dioxygen as additional substrate (*1,5,25,88*). Very little is known of the structure and function of these enzymes, except the NOS which are the focus of extensive functional and pharmacological investigations. NOS also do use BH_4 as a redox cofactor, but as opposed to the AAHs, the oxidized cofactor does not dissociate at every catalytic turnover but is reduced back *in situ* by the reductase domain. Moreover, in the catalytic reaction of NOS the participation of a pterin radical has been established (*89,90*). GEM, on the other hand, was a puzzling enzyme for many years because no sequence was assigned to this activity, until very recently, when it has been finally associated to transmembrane protein 195 (*91*). This sequence shows no homology to AAHs or NOS, but contains the fatty acid hydroxylase motif, found in enzymes which contain

a diiron center and which, like GEM, carry out hydroxylations of lipids at aliphatic carbon atoms.

II. Structural Information

Several X-ray crystal structures have been solved for the AAHs (see Table I), and the only member of the family for which no crystal structure has been reported is TPH2. However, the high sequence identity of TPH1 and TPH2 (see Fig. 1) indicates that the two isoforms are very similar in structure and reliable homology models of TPH2 are feasible. In fact, the homology-based model of the catalytic domain of TPH1, based on PAH that was reported by McKinney *et al.* (*31*) in 2001, has a root mean square deviation for atomic positions of 2.6 Å when compared with the first TPH1 crystal structure published in 2002 (*85*). The high structural and functional resemblance of the catalytic domain within the AAH family implies that mechanistic information based on one of the family members can in favorable cases be extrapolated to be valid for the family in general. The AAH crystal structures reveal information about the active site and the iron environment. The non-heme active site iron atom is anchored by two histidines (His285 and His290 in hPAH, His331 and His336 in rTH, and His272 and His277 in hTPH1) and one glutamic acid (Glu330 in hPAH, Glu376 in rTH, and Glu317 in hTPH1) (Fig. 1). In addition to this 2-His-1-Glu triad, up to three water molecules are coordinated to the metal, i.e. these are ligating water molecules. Binary crystal structures of the cofactor or cofactor analogue in complex with TH, PAH, and TPH1 are available and the cofactor is placed in the second coordination sphere with the carbonyl oxygen located 3.67–4.18 Å from iron in these complexes. The ternary complex of PAH with cofactor and substrate analogues has also been solved and the cofactor carbonyl oxygen is placed at a distance of 3.12–3.53 Å from the iron in these complexes (Table I). The ternary complexes contain none or one ligating water molecule and have a bidentate Glu. This implies that when the cofactor and substrate enter the active site, dissociation of water molecules is triggered and the cofactor is placed closer to the iron. This is also in agreement with the results obtained by NMR that shows displacement of water coordinated to the active site iron upon substrate binding (*92*). In fact, in one of the most recently reported crystal structures of the ternary complexes of PAH (*93*) the cofactor is actually placed at a distance (Fe–O4(BH_4) distance of 3.12 Å) approaching that of the first coordination sphere, and there are no water molecules coordinated to the metal. The latter result suggests that formation of an iron-cofactor bond during catalysis cannot be

TABLE I

Overview of AAH crystal structures deposited in the protein databank from human (h), rat (r), *Chromobacterium violaceum* (cv), *Colwellia psychrerythraea* (cp), and chicken (c). The number of iron-coordinated water molecules (Lig. H_2O) as well as interatomic active site iron to BH_4 carbonyl oxygen distances (Fe–O4 (BH_4), where applicable) are tabulated

Complex	PDBid	Domains included	Fe–O4 (BH_4)[a]	Lig. H_2O	Ref.
cvPAH	1LTU	Catalytic	–	No iron	(*83*)
cpPAH	2V28	Catalytic	–	No iron	(*94*)
hPAH	2PAH	Catalytic and oligomerization	–	No crystal water	(*95*)
cvPAH-Fe^{III}	1LTV	Catalytic	–	2	(*83*)
rPAH-Fe^{III}	2PHM	Regulatory ACT, catalytic and dimerization motif	–	3	(*96*)
hPAH-Fe^{III}	1PAH	Catalytic and dimerization motif	–	3	(*97*)
hPAH-Fe^{II}	1J8T	Catalytic and dimerization motif	–	1	(*98*)
cpPAH-Fe^{III}-SO_4	2V27	Catalytic	–	2	(*94*)
rPAH-Fe^{III}-Ser_{16}-PO_4	1PHZ	Regulatory ACT, catalytic and dimerization motif	–	1	(*96*)
cvPAH-Fe^{III}-BH_2	1LTZ	Catalytic	4.18	2	(*83*)
hPAH-Fe^{III}-BH_2	1DMW	Catalytic and dimerization motif	3.82	3	(*82*)
hPAH-Fe-BH_2	1LRM	Catalytic and dimerization motif	3.67	3	(*81*)
hPAH-Fe^{II}-BH_4[b]	1J8U	Catalytic and dimerization motif	3.81	3	(*98*)
hPAH-Fe^{II}-BH_4-NLE[c]	1MMT	Catalytic and dimerization motif	3.53	1	(*93*)
hPAH-Fe^{II}-BH_4-THA[d, e]	1MMK	Catalytic and dimerization motif	3.12	0	(*93*)
hPAH-Fe^{II}-BH_4-THA[e]	1KW0	Catalytic and dimerization motif	3.37	1	(*81*)
rTH-Fe^{III}	1TOH	Catalytic and oligomerization	–	2	(*99*)
rTH-Fe^{III}-BH_2	2TOH	Catalytic and oligomerization	3.64	2	(*84*)
hTPH1-Fe^{III}-LXO[f]	3HF6	Catalytic	–	3	(*100*)
hTPH-Fe^{III}-BH_2	1MLW	Catalytic and dimerization motif	3.63	3	(*85*)
cTPH-Trp	3E2T	Catalytic	–	0	(*101*)

[a] Distances are given in angstroms.
[b] The active site of this X-ray crystal structure is shown in Fig. 3.
[c] NLE = norleucine.
[d] The active site of this X-ray crystal structure is shown in Fig. 4.
[e] THA = thienylalanine.
[f] LXO = 4-(4-amino-6-{[(1R)-1-naphtalene-2-ylethyl]amino}-1,3,5-triazin-2-yl)-L-phenylalanine.

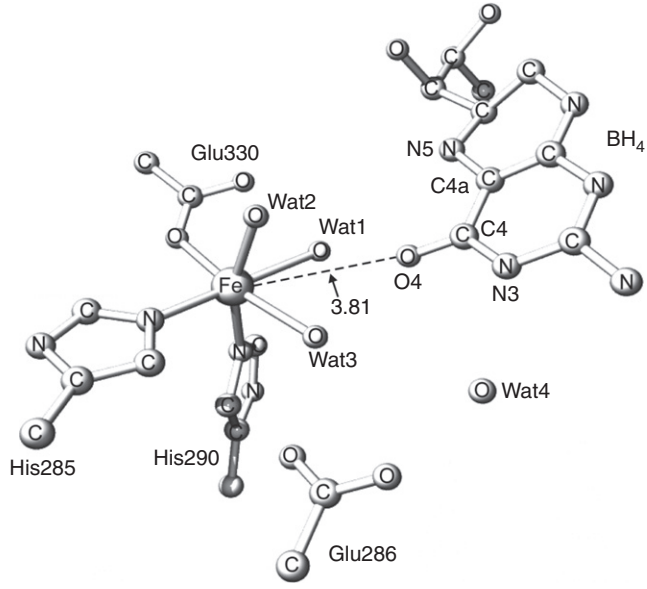

FIG. 3. The iron complex in the X-ray crystal structure of the catalytic domain of hPAH in binary complex with the cofactor. Distances are given in angstroms.

excluded. The position of the cofactor and the possibility of bond formation to the metal during catalysis are questions that have been addressed in recent quantum chemical studies of the AAH mechanism (see the next sections).

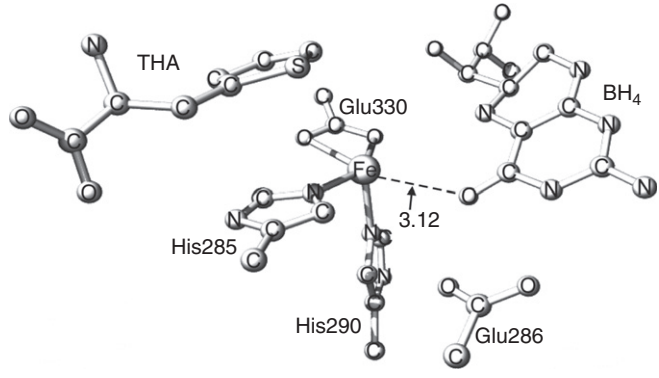

FIG. 4. Active site in the X-ray crystal structure of the catalytic domain of hPAH in ternary complex with BH_4 and substrate analogue thienylalanine (THA). Distances are given in angstroms.

III. The Cluster Model Approach to Quantum Chemical Studies of Enzyme Reactions

Quantum chemical modeling can offer insight into reaction mechanisms and in particular locate transition states and short-lived intermediates which can be problematic or impossible to observe by experimental techniques. The usefulness of quantum chemical methods even extends to enzymatic reactions, i.e., for reacting systems containing thousands of atoms. This may seem a paradox since the computational effort involved in quantum chemical calculations grows rapidly with the size of the system. There are two main approaches to overcome the size problem and making quantum chemical-based studies of enzymatic reaction mechanisms possible, namely the cluster model approach and the hybrid quantum mechanics (QM)/molecular mechanics (MM) approach. Both approaches are based on the fact that the central reacting part of the overall system is described by a quantum chemical method, the formal difference being that, in the QM/MM approach, a surrounding, less-central part of the system, described using classical mechanics, is included. The MM regions frequently extend to encompassing a single domain, or even the complete enzyme. Thus, due to the overall computational cost of the QM/MM approach, the QM parts of the latter are often smaller than the QM models employed in cluster model studies, and it is not always obvious which approach should be trusted the most (*102*).

The highest possible level at which QM descriptions of enzymatic reactions can be performed routinely is DFT based on the generalized gradient approximation (GGA). The most common functional used in both QM and QM/MM studies of enzymatic reactions is the hybrid-GGA functional B3LYP (*103,104*), which incorporates some exact (Hartree–Fock) exchange. This functional has been shown to give satisfactory results for transition metal reactions, with a typical error range of 3–5 kcal mol^{-1} (*105*). More specifically, this functional has been used extensively also in studies involving dioxygen activation (see below). Moreover, in a recent validation study, B3LYP was found to offer a dissociation curve for hydrogen peroxide of even higher quality than UCCSD (T) (unrestricted coupled cluster including singles and doubles and a perturbative estimate of triples, one of the most accurate *ab initio* methods available) (*106*), lending further credibility to the studies of O–O activation using this functional.

Even though the QM models of the reacting core of an enzyme often involve a significant number of atoms, the underlying GGA

does not account for noncovalent dispersion-type interactions (*107*). However, this deficiency can be ameliorated by inclusion of an empirical term describing long-range dispersion. In general, GGA-based methods including such an empirical term (termed DFT-D) show substantial improvement in accuracy over the parent DFT functionals and in particular reduce the systematic tendency to underbinding seen for B3LYP and similar functionals, in main group as well as in transition metal chemistry (*108–114*). Promising tests in which empirical dispersion corrections have improved upon relative energies that are difficult to obtain by standard DFT alone have also started to appear for metalloenzymes (*115*).

In the cluster model approach, polarization effects involving the surrounding protein are often taken into account in an approximate manner by placing the cluster model in a dielectric cavity with a low dielectric constant, typically using the polarizable continuum model (PCM) in single-point energy calculations following the geometry optimizations. A large number of studies of enzyme reaction mechanisms have involved B3LYP calculations on relatively small cluster models (from 20 to 30 atoms and upward (*105,116*)), with effects of the surrounding protein added from the PCM model. In recent years it has been possible to explore the effects of larger cluster models, i.e., with more of the protein included, and the effects of increasing the size of the cluster have been studied, among other things, by monitoring the magnitude of the calculated solvent corrections. It has been shown that the results converge surprisingly rapidly with increasing cluster size, with vanishing PCM solvent corrections already at a cluster size of 150–200 atoms in challenging cases (*102*). However, large models require significant computational effort and the conformational flexibility may represent a severe problem. Thus, a cluster model containing only the parts of the enzyme that play a significant role in the reaction mechanism at hand is usually employed (*102*).

A series of mechanistic investigations of the AAH reaction by means of the B3LYP functional in combination with cluster models have been performed in recent years (*117–123*). One such model used to investigate the formation of the Fe^{IV}═O hydroxylating intermediate was based on the X-ray crystal structure of the catalytic domain of hPAH containing inactive Fe^{III} in binary complex with the cofactor analogue BH_2 (PDBid: 1DMW (*82*)) (*118*) (Table I). The model included the hexacoordinate iron complex with the 2-His-1-Glu binding motif and three ligating water molecules together with the cofactor analogue, Glu286, and a water molecule. The three latter groups were

taken from the second coordination sphere in the X-ray crystal structure. In the model building, imidazole was used as a model for histidine, whereas glutamate was modeled by formate. Also, 5,6,7,8-tetrahydropterin was used instead of the (6R)-erythro-5,6,7,8-tetrahydrobiopterin (BH_4), i.e., the $(CH(OH))_2CH_3$ substituent in position C6 was replaced by a hydrogen atom for reasons of computational efficiency. A single water molecule was dissociated prior to dioxygen binding. The $Fe^{IV}{=}O$ complex arrived at in the first reaction step, with one water molecule and one hydroxyl group coordinating iron in addition to the 2-His-1-Glu binding motif, was used, with some modifications, as a model for the active site also in the second part of the reaction, the substrate hydroxylation (*117*). Whereas benzene was taken to model phenylalanine, indole was used for tryptophan. Glu286 and the oxidized cofactor were omitted from the second coordination sphere and two water molecules were used instead to maintain a hydrogen bonding network and to facilitate the tautomerization. The hydroxylation of these two substrates was also investigated using a positively charged model in which the hydroxyl group in the above neutral model was protonated to give $[H_2O{-}Fe^{IV}{=}O]^+$ (*117*).

In another DFT study devoted to the reaction mechanism of $Fe^{IV}{=}O$-catalyzed hydroxylation of L-Phe, the gas-phase cluster model was based on the X-ray crystal structure of the catalytic domain of hPAH containing ferric iron (hPAH-Fe^{III}) (PDBid: 1PAH (*97*)) (*119*). The water molecule distal to His290 was replaced by the oxo-ligand and only ligands of the first coordination sphere were included in the model. The amino acid residues were truncated in the model to include the side chains only. This model was also used as the QM part in a QM/MM study of the hydroxylation of L-Phe. In the latter study, the MM part included the complete catalytic domain (*119*).

A few years ago we performed a brief study of the iron–dioxygen complex using a cluster model based on the ternary complex of PAH with the substrate analogue THA and BH_4 (hPAH-Fe^{II}-BH_4-THA) (PDBid: 1MMK (*93*)) (*120*). No ligating water molecules were retained on the iron atom in the refinement of the crystal structure, cf. Fig. 4 (Table I). The same strategy with respect to model building as described for Ref. (*118*) was followed.

Our recent DFT investigations of the AAH catalytic cycle (*121–123*) will be the main focus of the discussion to come. The gas-phase cluster model that constitutes the starting point for these studies is based on the X-ray crystal structure of the catalytic domain of hPAH in binary complex with the cofactor (hPAH-Fe^{II}-BH_4) (PDBid: 1J8U) (*98*). The active site iron and the six ligands,

His285, His290, Glu330, H_2O1250 (Wat1), H_2O1251 (Wat3), and H_2O1253 (Wat2), were extracted from the X-ray crystal structure, cf. Fig. 3. In addition, the cofactor, Glu286, and H_2O1142 (Wat4), all placed in the second coordination sphere of iron in the crystal structure, were also included in the model. The simplifications followed the strategy described earlier. Histidine was modeled as imidazole and glutamate as formate, and the diol chain on the cofactor was substituted by a hydrogen atom, i.e., 5,6,7,8-tetrahydropterin was used to model BH_4. The models used when investigating the formation of the $Fe^{IV}{=}O$ complex in the first part of the reaction mechanism did not include the substrate (*121,122*). However, in the second part, where the amino acid substrate is hydroxylated by the $Fe^{IV}{=}O$ intermediate, benzene was used as a model for Phe (*123*). Since all AAHs can hydroxylate L-Phe, benzene appears to be an appropriate substrate model (*6*).

We have followed a modeling strategy close to that recommended by Siegbahn *et al.* for quantum chemical cluster model studies of catalytic centers of metalloenzymes in general (*102,105,116*), and as applied in particular by his research group also in studies of the title enzymatic reaction (*117,118*), resulting in models containing 50–75 atoms. The hybrid B3LYP functional (*103,104*) as implemented in the Gaussian 03 program package was used for all calculations (*124*). All minima and transition states were fully optimized without any constraints, using algorithms involving the first and second derivatives of the energy. Basis sets of valence double-ζ quality (termed LANL2DZ) were used, with an effective core potential for the 10 inner electrons of iron (*125,126*). Single-point (SP) energy evaluations were performed in the optimized geometries using improved basis sets compared to those of the geometry optimizations and vibrational analyses, with polarization and diffusion functions added. In the SP calculations, polarization effects involving the surrounding protein were taken into account using PCM (*127*) with the dielectric constant set to a value, $\varepsilon = 4$, typical for studies of proteins and with a temperature of 298 K. The Bondi set of atomic radii (*128*), with explicit hydrogen atoms, was used to construct the solute cavity. Only the electrostatic terms of the solvation energies were used. Finally, an empirical term accounting for long-range dispersion was added to the B3LYP energies, meaning that our final energy evaluations were those of B3LYP-D (*108*).

QM modeling is a useful tool with which to obtain insight into reaction mechanisms. In particular, it is possible to study the structure and properties of transient intermediates and transition states not easily accessed by experimental methods.

However, one should keep in mind that simplified models of the actual physical systems are routinely used and that molecular-level modeling techniques involve various levels of approximations. In principle, computational chemistry can only disprove, and never prove, a particular reaction mechanism. In practice, however, a computational investigation may still, in many cases, be a useful guide as to the likeliness of a given reaction pathway. Comparison to experimental information and to computational studies of alternative reaction mechanisms will help establish the kind of trust (or lack thereof) that should be put into a particular reaction mechanism obtained by computational chemistry.

IV. DFT Investigations of the AAH Mechanism

The structural similarity of the catalytic domains of the enzymes of the AAH family, together with the identical reaction that they catalyze (i.e., hydroxylation of aromatic substrates) and the common dependency on BH_4 and O_2 (Section I), suggests that the mechanisms by which these enzymes operate are similar. It is assumed that the general AAH reaction mechanism follows a two-step reaction route in which a high-valent iron–oxo ($Fe^{IV}{=}O$) complex is formed in the first step, and that this intermediate is responsible for the hydroxylation of the aromatic amino acid substrate in the second step (*15,26–28,50*). The first step starts with O_2 binding and activation and proceeds via a Fe–O–O–BH_4 bridge and a subsequent heterolytic cleavage of the O–O bond to form the $Fe^{IV}{=}O$ species, concomitant with cofactor oxidation. The hydroxylation of the amino acid substrate by the $Fe^{IV}{=}O$ intermediate in the second step is suggested to occur via an electrophilic aromatic substitution, involving a carbocation intermediate. A 1,2-hydride migration (NIH shift) to give a dienone and a subsequent tautomerization of the ketone to the phenol form conclude the hydroxylation of the substrate.

So far, molecular-level computational studies of the AAH reaction have followed the general two-step mechanism. The results from these studies are discussed in the following.

A. Step I—Formation of the $Fe^{IV}{=}O$ Hydroxylating Intermediate

The X-ray crystal structures of the AAHs in binary complexes with the cofactor or cofactor analogue contain three or two water ligands in addition to the 2-His-1-Glu binding motif (*84,85,98*).

However, the binding of both cofactor and substrate to the active site seems to trigger the dissociation of all water molecules prior to binding of dioxygen and formation of the active quaternary complex (e.g., PAH-Fe^{II}-BH_4-L-Phe-O_2 in the case of PAH) (*6*). Modeling of dioxygen in the active site of the X-ray crystal structure of the catalytic domain of hPAH in ternary complex with the cofactor and THA (hPAH-Fe^{II}-BH_4-THA) (PDBid: 1KW0 (*81*)), featuring only one ligating water molecule (Table I), showed that the best position of dioxygen to probe formation of the suggested Fe–O–O–BH_4 bridge was that of the single remaining ligating water molecule (*81*). A reaction mechanism was suggested in which two water molecules dissociate, triggered by the binding of BH_4 and L-Phe, and the last water molecule is replaced by dioxygen (*81*). Furthermore, EPR and UV-Vis spectroscopy studies of bacterial PAH showed that the last ligating water molecule is dissociated upon binding the dioxygen mimic nitric oxide to the enzyme in complex with the cofactor analogue and L-Phe (cPAH-Fe^{II}-$DMPH_4$-Phe-NO), resulting in a pentacoordinate iron complex (*129*). This implies a similar reaction mechanism to that proposed for 2-oxoacid-dependent dioxygenase, which starts by dissociation of ligating water molecules, triggered by the presence of cofactor and substrate, to give a water-free Fe–O_2 complex (*75*).

The binding of dioxygen to a water-free iron model complex of the active site of PAH was the subject of an initial DFT study by some of us (*120*). The model was based on the X-ray crystal structure of the catalytic domain of hPAH in ternary complex with the cofactor and THA (hPAH-Fe^{II}-BH_4-THA) (PDBid: 1MMK (*93*)) (Table I). The gas-phase cluster model contained the tetracoordinate iron complex with the 2-His-1-Glu binding motif, in which Glu330 coordinated in a bidentate fashion. O_2, Glu286, and the cofactor were placed in the second coordination sphere. Geometry optimization gave a structure containing the cofactor in the first coordination sphere, with a O4–Fe distance of 1.92 Å, see Fig. 5 (*120*). Glu330 was found to coordinate to iron in a monodentate fashion and to form a strong hydrogen bond with the pterin cofactor. The findings in this work, together with experimental data and structural information from X-ray crystallographic and NMR studies (*80,81,93,98,129*), form the basis for our subsequent DFT investigation of the complete catalytic cycle, to be discussed in the following. The study starts at the enzyme resting state, as found in crystal structures involving binary complexes of PAH with the cofactor (see above). In these complexes, iron is coordinated by three water molecules. All three water molecules are successively dissociated prior to binding and activation of dioxygen.

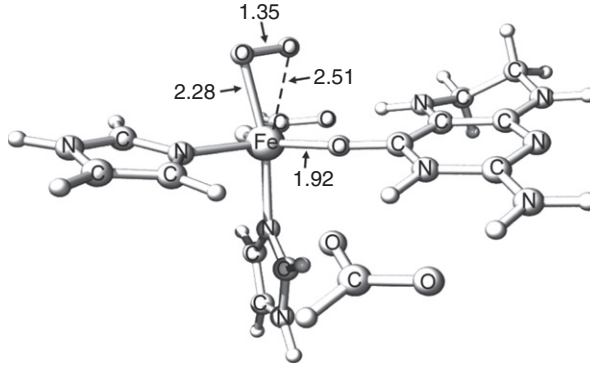

FIG. 5. The spin septet ground state of the iron–dioxygen complex as geometry optimized using DFT (B3LYP) (*120*). Distances are given in angstroms.

A.1. Dissociation of ligating water molecules

The optimized hexacoordinate complex (**1b**, Fig. 6) that constitutes the starting point of the DFT investigation has a spin quintet ground state with almost all the spin located on Fe (3.85). This structure could be superimposed with the iron complex of the X-ray crystal structure with a weighted root mean square deviation of 0.73 Å where the iron atoms of the two structures were constrained to coincide (*130*). The Fe–O4(BH_4) distance was reduced from 3.81 Å in the X-ray crystal structure to 3.52 Å in the optimized structure **1b**. Conformations in which the imidazole ring in His290 was rotated 180° compared to that of the X-ray crystal structure (and **1b**) were found to be of comparable, and often lower, energy than that of the conformation seen in the X-ray crystal structure. Both conformers were thus systematically monitored throughout the reaction pathway.

For the hexacoordinate starting complex (**1**) derived from the crystal structure of the binary complex, the most stable conformer (**1a**, Fig. 6) was found to feature the imidazole ring in His 290 rotated 180° compared to that of the crystal structure, and this conformation of His290 was found to be preferred for all stationary points leading up to the Fe^{IV}=O intermediate. Unless otherwise noted, all energies in this study are given relative to **1a**.

To investigate the dissociation of the ligating water molecules from iron, the water molecules were sequentially removed from the gas-phase cluster model. In the X-ray crystal structure (PDB id: 1J8U (*98*), cf. Fig. 3), Wat1, distal to His285, and Wat2, distal to His290, are the ligating water molecules with highest

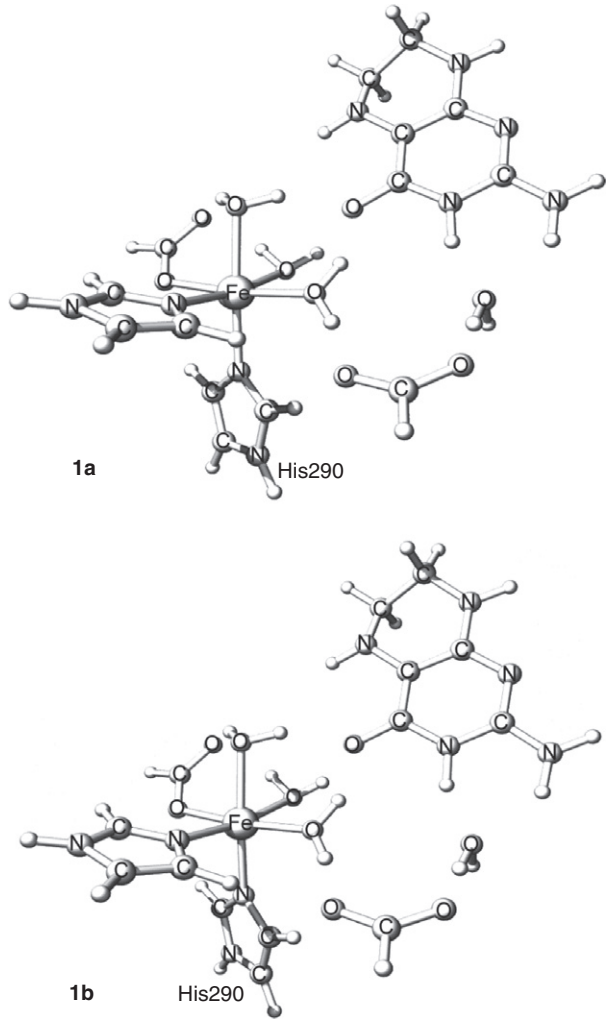

FIG. 6. The hexacoordinate complex (**1b**) optimized from a model of the X-ray crystal structure (PDBid: 1J8U). The conformer **1a** has the imidazole ring in His290 rotated 180° compared to that of the X-ray crystal structure (and **1b**) and is slightly more stable than **1b**. Distances are given in angstroms.

B-factors, indicating that these should be the ones most easily dissociated from iron. Our calculations show that the binding enthalpy of Wat1 in the hexacoordinate starting structure **1a** is 4.2 kcal mol^{-1}, compared to 10.0 kcal mol^{-1} for Wat2. The associated free energy barrier for the dissociation of Wat1 is 4.4 kcal

mol^{-1} (**TS[1a-2a]**‡, Figs. 7 and 8) and the barrier is reached at a Fe–O(Wat1) distance of 3.31 Å. Removing Wat1 from **1a** leads to a structure (**2a**, Fig. 8) 5.3 kcal mol^{-1} more stable than **1a** in free energy in which the cofactor is placed in the first coordination sphere of iron, coordinating via the carbonyl oxygen atom O4 (Fe–O4 distance of 2.13 Å). The successive water dissociations, and the accompanying cofactor coordination to the metal, are illustrated in Scheme 3.

The second water molecule to be dissociated is Wat2, with a reaction enthalpy for **2a** → **3a** + H_2O amounting to 9.2 kcal mol^{-1}. The pentacoordinate complex **3a** (Fig. 9), with Wat2 removed, is 1.6 kcal mol^{-1} more stable in free energy than **2a** and also binds the cofactor somewhat more tightly (Fe–O4 distance of 2.10 Å). For this iron complex (**3**), with only one ligating water molecule left, the cofactor position and orientation were manipulated to also probe a coordination to iron via N5, as observed for

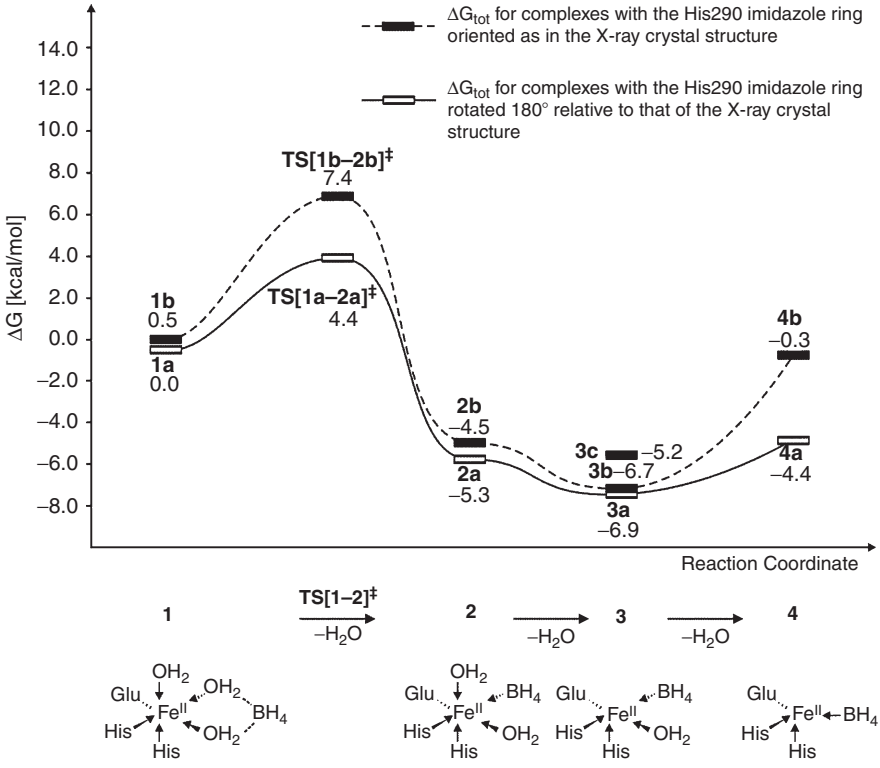

FIG. 7. Calculated relative free energies of water dissociation from the hexacoordinate iron complex **1a**.

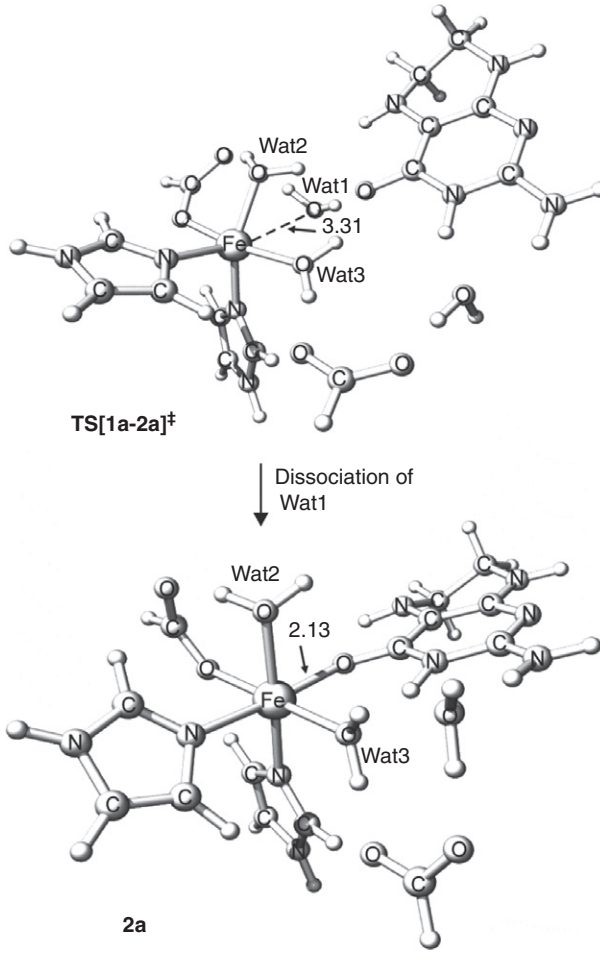

FIG. 8. Optimized transition state for dissociation of Wat1 (**TS[1a-2a]**‡) and the optimized product (**2a**) upon removal of Wat1 from the hexacoordinate starting structure. Distances are given in angstroms.

complexes of cofactor analogues and cvPAH (*131*). The most stable conformer found for a structure involving N5 coordination to the metal (**3c**, Fig. 9) turned out to be less stable than **3a** by close to 2 kcal mol^{-1}. The bond dissociation free energy for the cofactor in **3a** is close to 6 kcal mol^{-1}. In comparison, dissociation of Wat3 is thermodynamically preferred, with a dissociation free energy of 2.5 kcal mol^{-1}.

Dissociation of the last water molecule from **3a** leads to the water-free tetracoordinate iron complex **4a**, which is

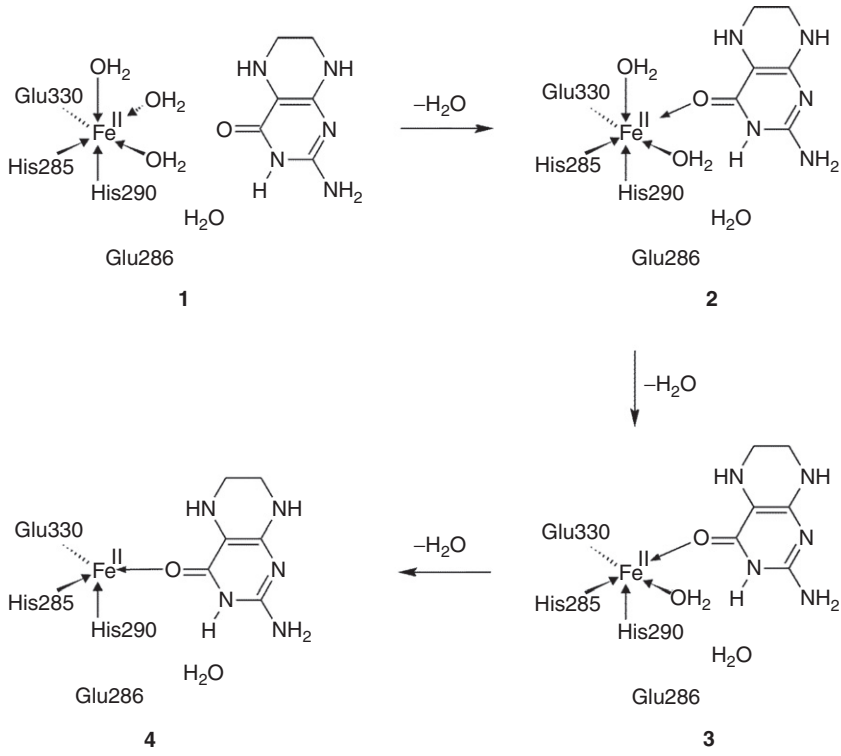

SCHEME 3. The initial dissociation of water molecules from the active site iron complex.

4.4 kcal mol^{-1} more stable than the hexacoordinate starting structure **1a**, cf. Fig. 7 and Scheme 3. As in the starting X-ray crystal structure (*98*), Glu330 coordinates to iron in a monodentate fashion (with Fe–O distances of 2.05 Å and 2.87 Å, respectively). In contrast, bidentate coordination of Glu330 is observed in an X-ray crystal structure in which no water molecules coordinate to iron (*93*). Instead, Glu330 in **4a** maintains a strong hydrogen bond with the hydrogen atom on N5 in the cofactor. The same hydrogen bond was also observed in the Fe–O_2 complex in our initial DFT study of dioxygen binding (*120*). The distance between Fe and the distal oxygen of Glu330 is reduced from 3.47 Å to 2.87 Å upon going from **3a** to **4a**. The iron complex is now void of water molecules and ready to capture a dioxygen molecule. The least hindered position for this task appears to be the position originally held by Wat2, cf. Fig. 3.

In the present work, water molecules dissociated from the iron center are assumed to adopt another protein-bound position and

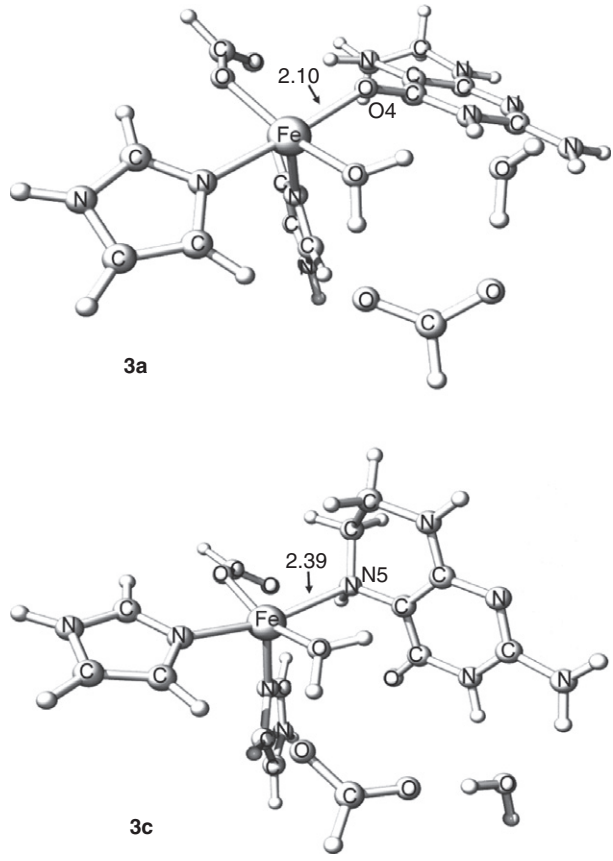

FIG. 9. The most stable optimized structure after dissociation of the second water molecule with a cofactor coordination via the carbonyl oxygen atom O4 (**3a**) and a less stable structure in which the cofactor coordinates via N5 (**3c**). Distances are given in angstroms.

are removed from the cluster model of the active center. The continuum description (PCM) of the protein environment used here (PCM, $\varepsilon = 4$) underestimates the interactions experienced by the dissociated water molecules, but this underestimation is partly canceled by the overestimated entropy of the single water molecules in the computation of their free energy. We assume that the overall effect is a slight underestimation of the stability of the dissociated states.

In the DFT investigation of Bassan *et al.* (*118*), only a single water molecule was dissociated prior to binding of dioxygen. The water molecule distal to His290 was believed to offer the best dioxygen position for the subsequent formation of the

Fe–O–O–BH_4 bridge and was thus selected for removal (*118*). However, a significantly higher dissociation enthalpy (22.5 kcal mol^{-1}) than our 10.0 kcal mol^{-1} was reported. Little information is available on the various optimized structures in Ref. (*118*). Thus, in order to investigate this discrepancy we dissociated the water molecule distal to His290 from a hexacoordinate complex based on the X-ray crystal structure used in Ref. (*118*). The geometry of the resulting pentacoordinate complex (for Cartesian coordinates see structure **2f** in the SI of Ref. (*121*)) appears to be very similar to the structure in Figure 2 in Ref. (*118*). Next we calculated the dissociation enthalpy (11.8 kcal mol^{-1}) using our methodology. Calculating the single-point energy using the approach described in Ref. (*118*) resulted in a dissociation enthalpy of 11.4 kcal mol^{-1}. However, omitting solvent effects increases this estimate to 19.5 kcal mol^{-1}, approaching the value reported in Ref. (*118*). In other words, most of the 12.5 kcal/mol discrepancy between the present estimate and that of Ref. (*118*) probably originates from differences with respect to inclusion of solvent and/or thermochemical corrections rather than the use of different cluster models (*121*). The difference between the two studies with respect to this dissociation reaction thus represents a rare case in which we have attributed a significant discrepancy between results of the quantum chemical studies on the hydroxylase mechanism to differences between the computational procedures.

A.2. Dioxygen binding and activation

All three AAH enzymes require iron in order to be catalytically active (*2,17–19*), and a vast amount of information has accumulated on the direct and extensive involvement of the metal in the catalytic reaction (*5*). A solid proof for a vacant position on Fe for coordination of dioxygen was obtained by Kemsley *et al.* (*42*) using circular dichroism and magnetic circular dichroism spectroscopy and suggested a direct involvement of the metal in the catalytic reaction.

Binding of dioxygen to the water-free iron complex **4a** leads to **5a** (Fig. 10), which has a septet ground state originating from the triplet dioxygen and the quintet iron complex **4a** and which is 2.9 kcal mol^{-1} less stable than **4a**. Dioxygen is placed above the cofactor, parallel to the N5–C4a bond, at a distance of ca. 4.7 Å from the iron atom. Coordination of dioxygen to iron from **5a** is associated with a free energy barrier of 2.6 kcal mol^{-1} (**TS[5a-6a]**‡, Fig. 10) and leads to a rather weakly bound complex, in which dioxygen coordinates in an end-on fashion with a Fe–Oa distance of 2.55 Å (**6a**, Figs. 11 and 12). Dioxygen is still in a

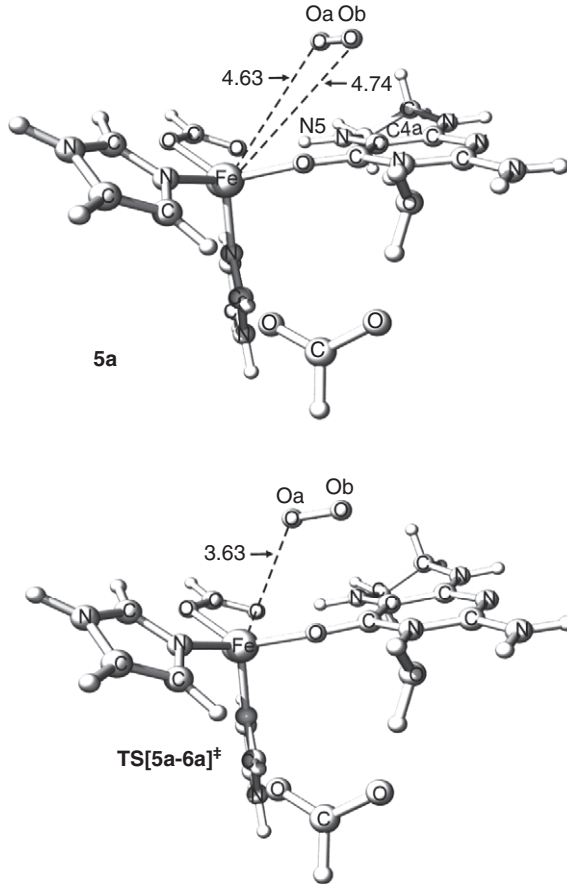

FIG. 10. Water-free iron complex with dioxygen placed above the cofactor (**5a**) and the transition state for dioxygen coordination to iron (**TS[5a-6a]**‡). Distances are given in angstroms.

triplet spin state with a spin population of 1.70. The iron complex is now pentacoordinate in agreement with spectroscopic results (*42,129*) and the Fe–Oa(BH_4) distance is 1.95 Å. The overall barrier associated with the binding of O_2 to the metal is calculated to be 8.4 kcal mol^{-1}, taken as the difference between structure **3a**, containing one ligating water molecule, and the pentacoordinate water-free Fe–O_2 complex (**6a**) (*121*). In comparison, Bassan *et al.* (*118*) calculated a free energy cost of 10.0 kcal mol^{-1} for binding of dioxygen, not including solvent effects. However, they assumed that this cost would be reduced by inclusion of the nonbonded interactions from the surrounding protein. Similar effects have been found in QM/MM studies of the binding of

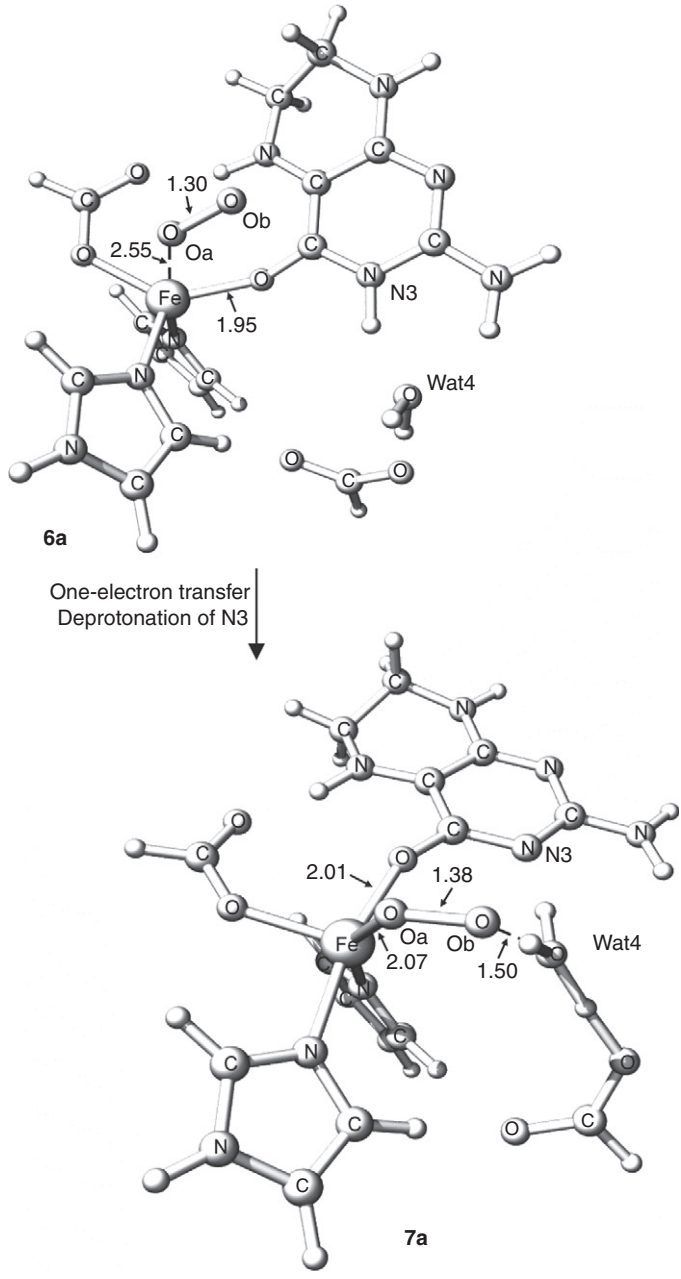

FIG. 11. Optimized structures of the weak Fe–O_2 complex (**6a**) and the Fe–O_2 complex located after the one-electron transfer from the cofactor to dioxygen and the simultaneous deprotonation of N3 by Wat4 (**7a**). Distances are given in angstroms.

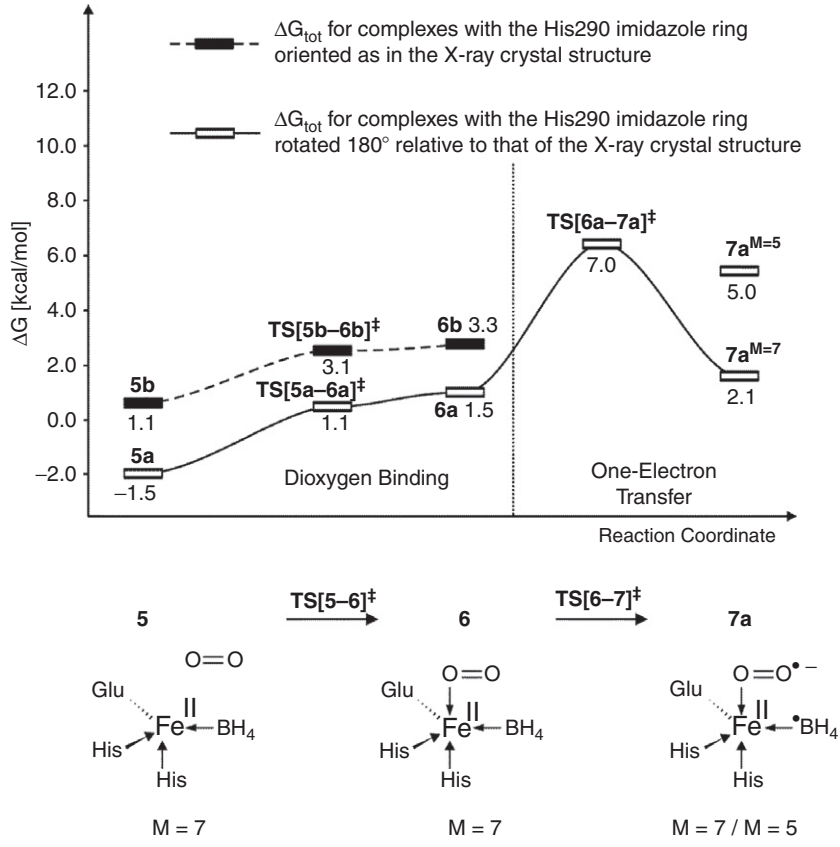

FIG. 12. Calculated relative free energies for dioxygen binding, one-electron transfer, and spin inversion.

dioxygen to hemerythrin (*118*) and isopenicillin *N* synthase (*132*). The relatively low barrier to dioxygen binding obtained in our study would probably be lowered even further by inclusion of nonbonded interactions to the surrounding protein, and this will be the subject in an upcoming QM/MM investigation.

The next step involves a strengthening of the Fe–Oa bond, leading to the 0.6 kcal mol^{-1} less stable **7a$^{M=7}$** (Fig. 11) which has a significantly shorter Fe–Oa distance (2.07 Å) than **6a** (Fig. 11). A decrease in spin population for O_2, from 1.70 in **6a** to 1.09 in **7a$^{M=7}$**, and a corresponding increase for the cofactor, from 0.43 in **6a** to close to unity in **7a$^{M=7}$**, confirm that a one-electron transfer from the cofactor to dioxygen has taken place. The involvement of a pterin radical has been established in the reaction catalyzed by NOS (*89*). For the AAHs, such a species has

been postulated, based on ^{18}O kinetic isotope measurements (*50*), but its involvement in the catalytic reaction has so far not been confirmed. Furthermore, starting from **6**, Wat4 deprotonates N3 of the cofactor and generates a neutral cofactor radical with a strong hydrogen bond to Wat4. The distal oxygen atom of dioxygen (Ob), in turn, forms a hydrogen bond to the protonated Wat4 (Ob–H(Wat4) = 1.50 Å in $\mathbf{7a}^{\mathbf{M=7}}$). Similar interactions involving the distal oxygen have been noted for the heme oxygenase HmuO using X-ray crystallography and resonance Raman spectroscopy (*133*) as well as in the modeling of the O_2-binding mode in tryptophan 2,3-dioxygenase (*134*). In structures $\mathbf{7a}^{\mathbf{M=7}}$, the third proton on Wat4 is almost equally shared with the negatively charged Glu286 (H–O(Wat4) = 1.17 Å and H–O(Glu286) = 1.24 Å). Glu286 also maintains hydrogen bonds to both His285 and His90, effectively reducing the negative charge (–0.73 e) on this residue. Moreover, the Glu side chain is acidic (p*K*a ~ 4 (*135*)). The acidity and reduced negative charge of this residue together with the interactions to N3 and Ob maintained by Wat4 thus explain why Glu286 does not fully deprotonate the latter. The availability of an additional proton in the vicinity of Wat4 means that this water molecule may act as a proton source at a later stage in the reaction (cf. Scheme 4). The one-electron transfer from the cofactor to dioxygen and the concerted deprotonation of the cofactor are associated with a free energy barrier of 5.5 kcal mol^{-1}, leading to an overall barrier of 13.9 kcal mol^{-1}, as measured from **3a**. This step is predicted to be rate limiting in our DFT investigation of the AAH catalytic cycle, which compares well with the fact that a one-electron transfer has already been proposed to be rate limiting in the reaction catalyzed by TH (*50*). In the DFT study of Bassan *et al.* (*118*), formation of a pterin radical was not observed.

A spin septet Fe–O–O–BH_4 bridge structure (described below) could not be obtained, and a spin inversion to the quintet state must take place prior to bridge formation. All attempts to stabilize a Fe–O–O–BH_4 bridge structure in a spin septet state resulted in rupture of the Ob–C4a bond and decay to the Fe–O_2 complex. Both the energies and the geometries of the spin septet and quintet states of the Fe–O_2 complexes are similar, indicating that the enthalpic cost of spin inversion should be small in this region of the reaction, i.e., on the section leading up to the Fe–O–O–BH_4 bridge formation. And indeed, minimum energy points for the crossing (MECP) between the potential energy surfaces of, for example, $\mathbf{7a}^{\mathbf{M=7}}$ and $\mathbf{7a}^{\mathbf{M=5}}$ could be located (*136*). This MECP was calculated to be 0.2 kcal mol^{-1} above the septet spin state ($\mathbf{7a}^{\mathbf{M=7}}$) in energy ($E_0$, i.e., total energies including zero-point corrections). The probability of spin inversion was not calculated, but this quantity depends on the

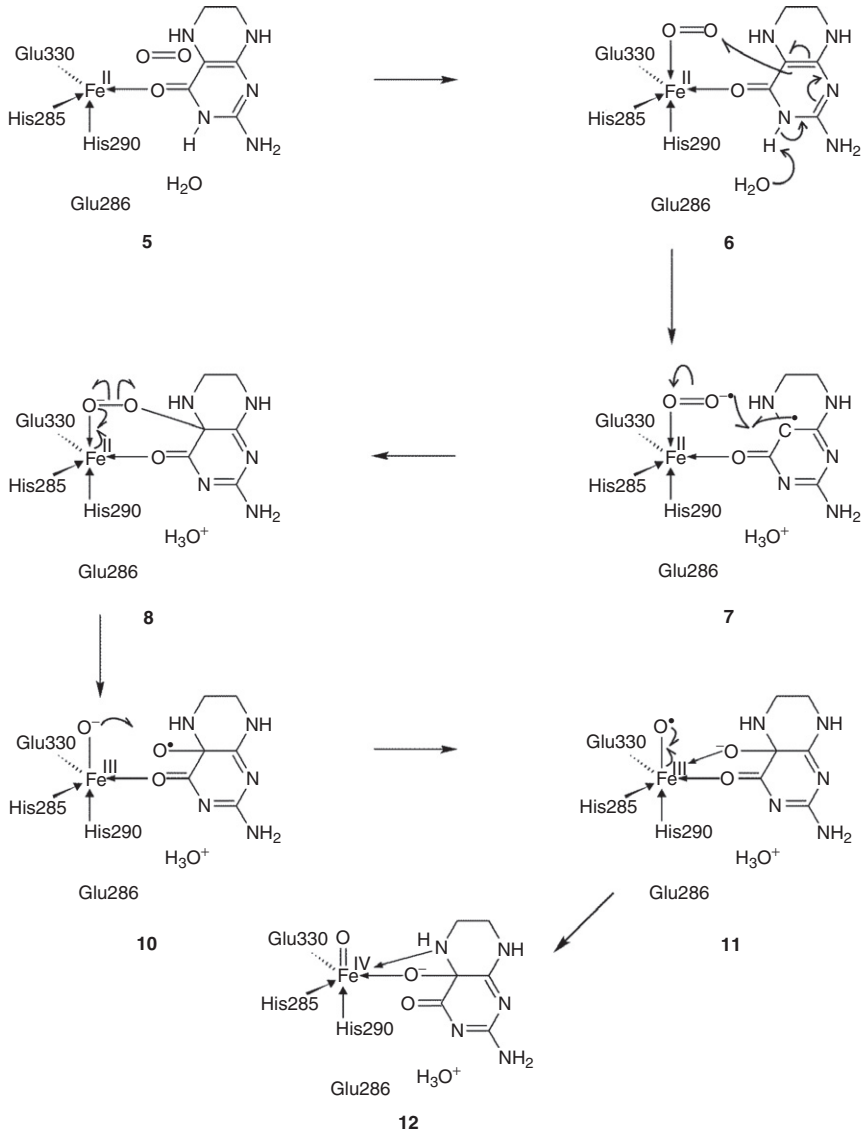

SCHEME 4. The electronic rearrangements involved in the binding of the dioxygen and the subsequent formation of the Fe^{IV}=O hydroxylating species.

spin orbit coupling which should be appreciable for a transition metal complex such as the present (*137*). This suggests that the overall probability of spin inversion must be expected to be high in this part of the reaction mechanism. In other words, spin inversion most likely does not represent a bottleneck in the catalytic reaction.

A.3. Formation of the Fe–O–O–BH_4 bridge

A Fe–O–O–BH_4 bridge structure has been proposed as an intermediate in the formation of the Fe^{IV}=O species in the AAHs (*15*). The Fe–O–O–BH_4 bridge structure **8a** (Fig. 13) in our study, involving C4a as the bridgehead atom in the cofactor, is formed as a result of bond formation between the two radical species

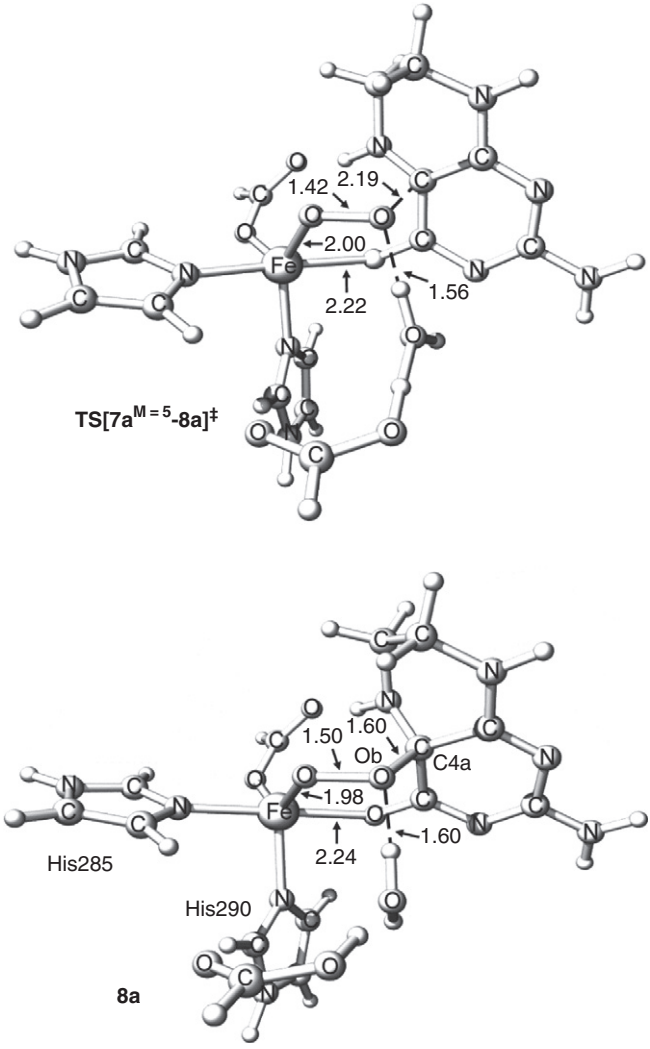

FIG. 13. Optimized transition state for formation of the Fe–O–O–BH_4 bridge structure **TS[7a$^{M=5}$-8a]**‡ and the accompanying product **8a**. Distances are given in angstroms.

($[BH_4]\cdot$ and $[O_2]^-$) in $\mathbf{7a^{M=5}}$. Once the one-electron transfer from the cofactor to dioxygen ($\mathbf{6a^{M=7}} \rightarrow \mathbf{7a^{M=7}}$) and the subsequent spin pairing from septet to quintet ($\mathbf{7a^{M=7}} \rightarrow \mathbf{7a^{M=5}}$) are completed, the Ob–C4a bond formation leading to the Fe–O–O–BH_4 bridge structure is facile, the activation barrier ($\mathbf{7a^{M=5}} \rightarrow \mathbf{TS[7a^{M=5}\text{-}8a]^{\ddagger}}$) vanishing at our final level of theory ($-2.6\,\mathrm{kcal\,mol^{-1}}$), while without correction for dispersion effects this barrier is $1.3\,\mathrm{kcal\,mol^{-1}}$. The reaction is exergonic by close to $8\,\mathrm{kcal\,mol^{-1}}$ and leads to the so far most stable structure in our study, $7.2\,\mathrm{kcal\,mol^{-1}}$ below **1a** in free energy. In contrast, Bassan *et al.* (*118*) calculated the barrier to bridge formation to be $16.6\,\mathrm{kcal\,mol^{-1}}$ from the Fe–O_2 complex, and this barrier turned out to be rate limiting. Furthermore, they calculated the Fe–O–O–BH_4 bridge structure to be less stable (by $2.9\,\mathrm{kcal\,mol^{-1}}$) than the quintet Fe–$O_2$ complex. The lower barrier to bridge formation in our study is probably to a large extent caused by the radical mechanism, which, in turn, may be the result of both the direct coordination of the cofactor and the deprotonation of the cofactor. Moreover, the higher stability of the bridge structures seen in our study is partly also the result of the inclusion of an empirical term accounting for long-range dispersion which stabilizes the structure by $5.2\,\mathrm{kcal\,mol^{-1}}$ from $\Delta G_{\text{tot-disp}} = -2.0\,\mathrm{kcal\,mol^{-1}}$ to $\Delta G_{\text{tot}} = -7.2\,\mathrm{kcal\,mol^{-1}}$.

Prior to the O–O bond rupture and the formation of the $Fe^{IV}{=}O$ species, a rotation of Wat4 leads to **9a** (Fig. 14), about $1\,\mathrm{kcal\,mol^{-1}}$ more stable than **8a** (cf. Fig. 15 for the relative free energies). The rotation results in establishment of a hydrogen bond between Wat4 and Oa that stabilizes the growing charge on the latter (–0.66 e) and facilitates the subsequent rupture of the O–O bond. The rotation is associated with a low activation barrier ($1.5\,\mathrm{kcal\,mol^{-1}}$). The following elongation of the O–O bond leads to an intermediate (**10a**, Fig. 14) with an Oa–Ob distance of 2.12 Å and which is close to $7\,\mathrm{kcal\,mol^{-1}}$ less stable than **9a**. An unpaired electron is located on Ob and iron is now oxidized to Fe^{III} (Scheme 4). The O–O bond elongation is associated with a free energy barrier amounting to ca. $9\,\mathrm{kcal\,mol^{-1}}$. The corresponding barrier in the study of Bassan *et al.* (*118*) is somewhat lower ($\Delta G^{\ddagger} = 4.8\,\mathrm{kcal\,mol^{-1}}$), probably due to favorable hydrogen bond interactions involving the ligating water molecules.

A.4. Formation of the $Fe^{IV}{=}O$ species

According to our DFT study the rupture of the O–O bond starts with a homolytic cleavage resulting in an unpaired electron on the oxygen atom (Ob) added to the cofactor (**10a**). The electronic

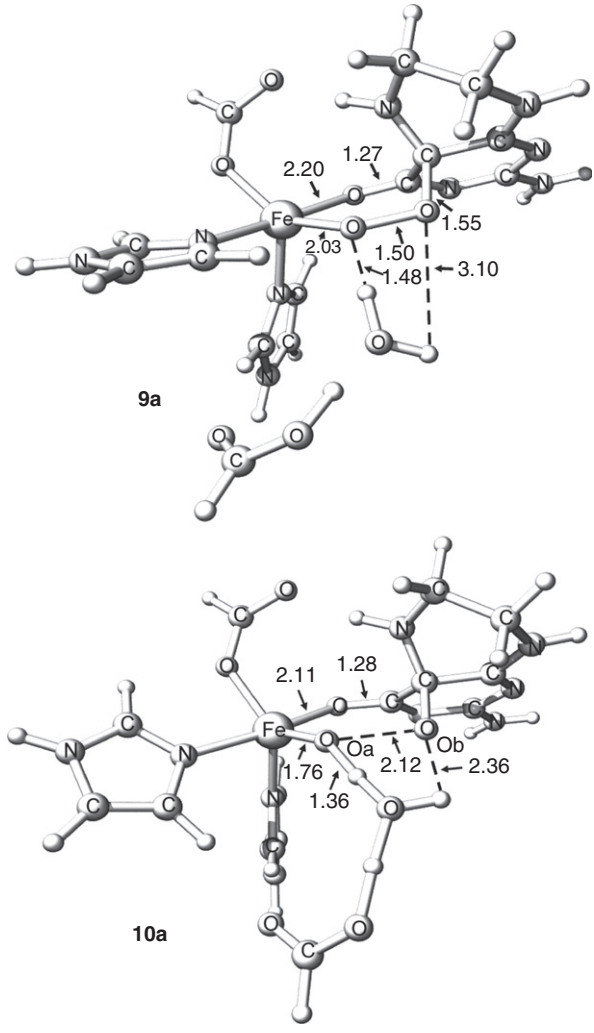

FIG. 14. Optimized Fe–O–O–BH_4 bridge structure after rotation of Wat4 (**9a**) and optimized structure with elongated O–O bond (**10a**).

structure of **10a** is, of course, more involved than that suggested by the Lewis structure in Scheme 4. For example, the bond between Oa and Ob is not yet entirely broken and consists of a single electron in a Oa–Ob σ bonding orbital and manifests itself in a Wiberg bond index of 0.28 (*122*). It appears that this bond must be completely broken prior to the second of the two iron atom oxidations and the Fe═O double bond formation. The breaking of the last of the Oa–Ob bond components consists of a transfer of the single electron from the σ bonding orbital to Ob,

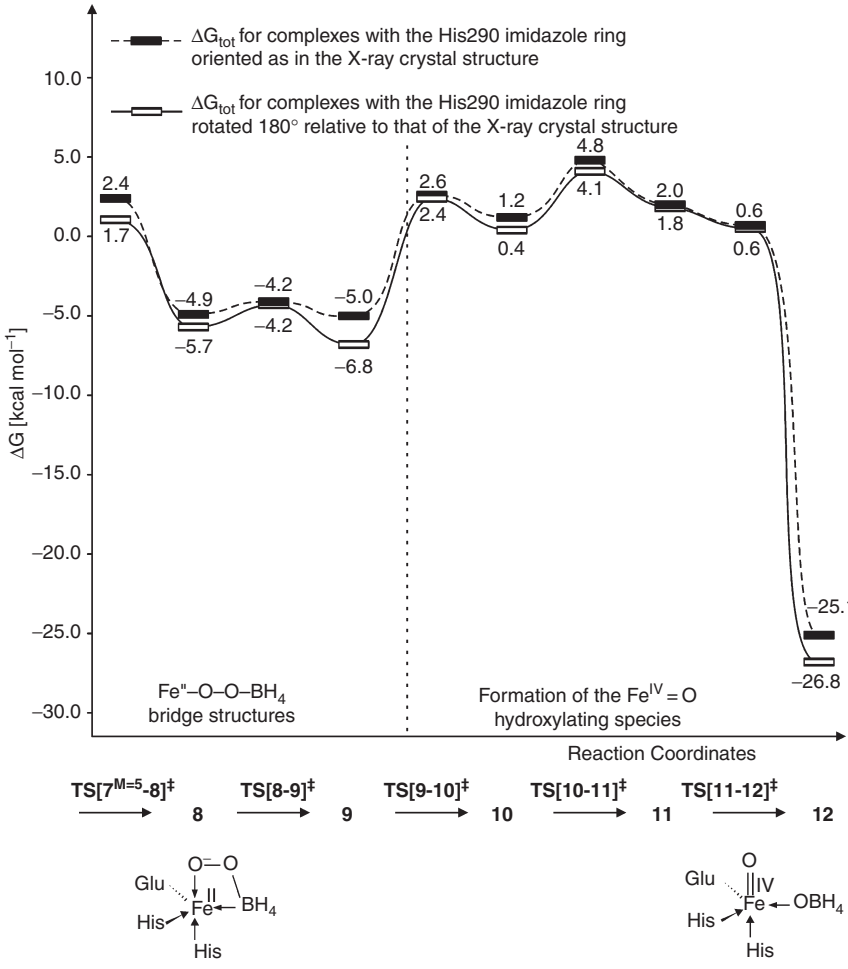

FIG. 15. Calculated relative free energies for formation of the Fe^{IV}=O intermediate. TS[8a-9a] and TS[11b-12b] could not be located, hence the ΔG_{tot} reported for these transition states are those of TS[8b-9b] (with His290 as in the X-ray crystal structure) and TS[11a-12a] (with His290 rotated), respectively (122).

resulting in the formation of the intermediate **11a** (cf. Fig. 16) in which Ob carries a negative charge (–0.92 e) and significant spin population is located on Oa (–0.60). The breaking of the Oa–Ob bond is accompanied by significant geometrical changes. The cofactor is now coordinating iron in a bidentate fashion via O4 (2.21 Å) and Ob (2.11 Å). The Fe–Oa bond is elongated, from 1.76 Å in **10a** to 1.91 Å in **11a**, and this step is associated with a free energy barrier of 3.7 kcal mol^{-1} (**TS[10a-11a]**‡, Fig. 16). An elongation of the Fe–Oa bond was also seen in the transition state

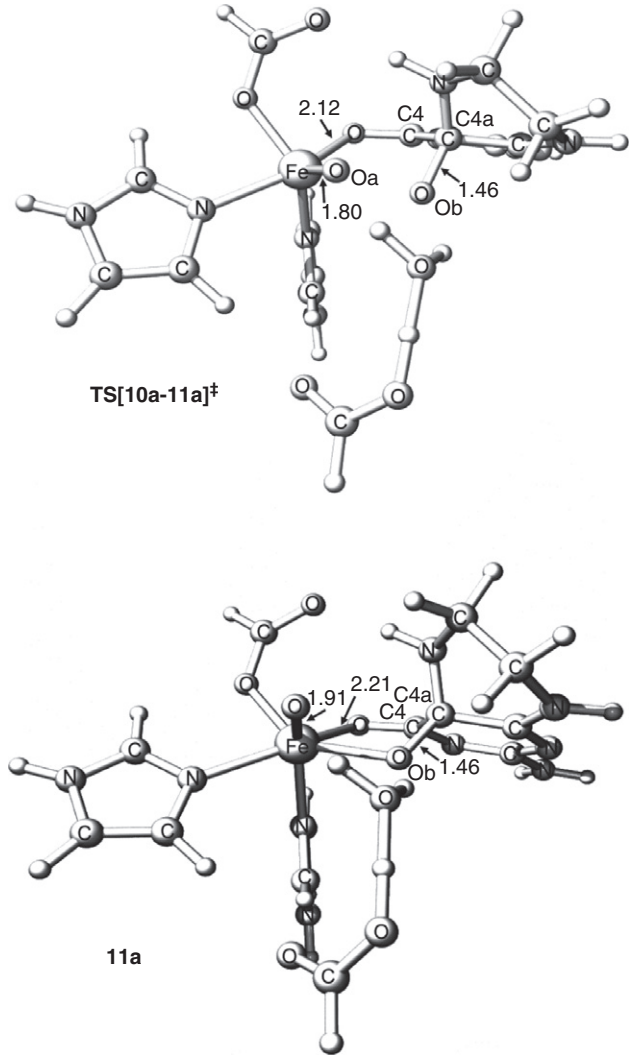

FIG. 16. Optimized transition state **TS[10a-11a]**‡ for the second electron transfer leading to **11a**. Distances are given in angstroms.

for formation of the Fe^{IV}=O species in the study of Bassan *et al.* (*118*). In **11a**, the Fe–Oa bond consists of a singly occupied σ bonding orbital. The final stage of the Fe^{IV}=O complex formation is initiated by the transfer of a second electron to this orbital from iron. The shortening of the Fe–Oa distance due to the presence of a complete σ bond, in turn, allows for significant Fe d_π–O p_π interaction, thus explaining the considerable shortening of the

Fe–Oa bond, to 1.65 Å in **12a**. The formation of a Fe=O bond is accompanied by a change in cofactor metal coordination from O4 (–0.67 e) to a more negatively charged and better donor, N5 (–0.76 e). The free energy barrier associated with this step is canceled out at the final level of theory (i.e., including dispersion, solvent, and thermochemical corrections), and the reaction is highly exergonic (by 27.2 kcal mol^{-1}) (**TS[11a-12a]**‡, Fig. 17).

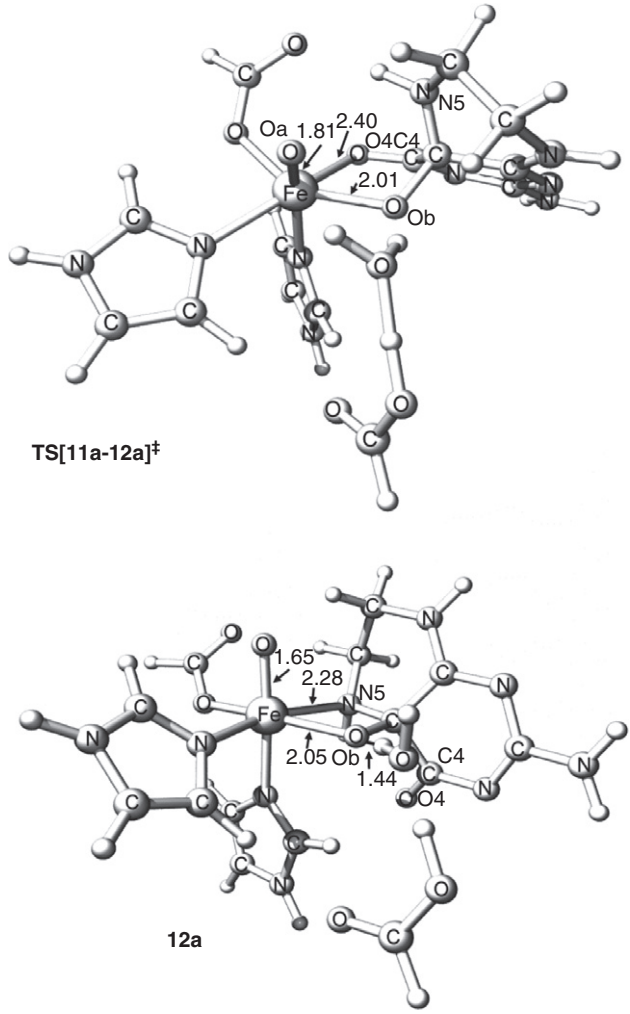

FIG. 17. Optimized transition state **TS[11a-12a]**‡ leading to the Fe^{IV}=O intermediate with a chelate cofactor **12a**. Distances are given in angstroms.

The overall barrier for the O–O bond breakage is 10.9 kcal mol^{-1} upon going from **9a** to **TS[10a-11a]**‡. In comparison, the calculated free energy barrier for this step in the study of Bassan *et al.* (*118*) was only 4.8 kcal mol^{-1}. However, their transition state was located 12.8 kcal mol^{-1} above the spin septet Fe–O_2 complex, partly as a result of the fact that dispersion was not accounted for. The oxygen atom added to the cofactor was protonated by one of the ligating water molecules. The positively charged cofactor (N3 remaining protonated throughout) was then removed from the model together with Glu286 and replaced by a water molecule, resulting in a HO–Fe^{IV}=O complex with two water molecules in the second coordination sphere. This model complex was then applied in the subsequent investigation of the hydroxylation of the amino acid substrate (*117*), i.e., the second main reaction step and the subject of the next section.

B. Step II—Fe^{IV}=O-Catalyzed Hydroxylation of the Aromatic Amino Acid

The Fe^{IV}=O species (**12a**) arrived at in the first part of the investigation was applied in the second part focusing on substrate hydroxylation (*123*). Starting by complex **13a** (Fig. 18), benzene was included as a model for the amino acid substrate. The model used by Bassan *et al.* (*117*) in the second reaction step was also based on the Fe^{IV}=O model arrived at in the first main step, but was simplified by removing the oxidized cofactor and Glu286 from the second coordination sphere and by adding one water molecule (see the previous section). The resulting model contained in total two water molecules in the second coordination sphere, thus offering possibilities for establishing hydrogen bonds and facilitating tautomerization.

B.1. Formation of the O–C bond

Information about the substrate binding site in PAH is available from X-ray crystal structures of PAH in complexes involving substrate analogues (*81,93*) (Table I) and from NMR spectroscopy of hPAH in complex with BH_2 and L-Phe (*80,120*), see Section II. In our study (*123*), benzene was initially placed above His285 in the Fe^{IV}=O complex in order to probe π-stacking interactions. However, geometry optimization led to an edge–face interaction between benzene and His285 (**13a**, Fig. 18), with one benzene hydrogen atom pointing toward the His285 imidazole ring and another toward O(Fe). The cluster model lacks interactions from

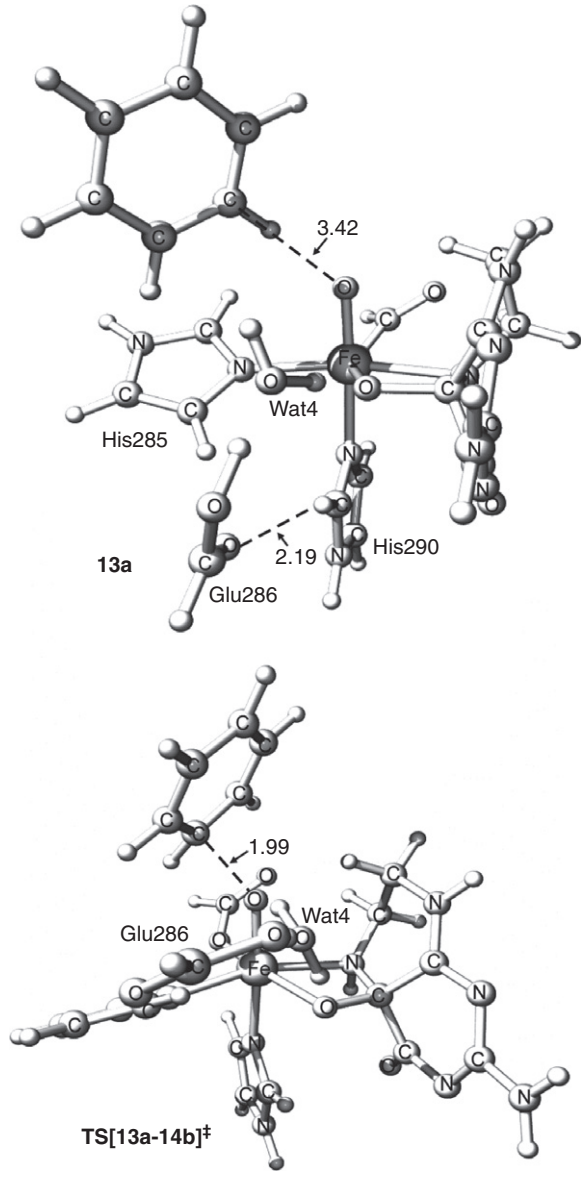

FIG. 18. Optimized structure of the Fe^{IV}=O complex with benzene (**13a**) and the transition state for the C–O bond formation (**TS[13a-14b]**‡). Distances are given in angstroms.

nearby residues and also involves a simplified substrate, which thus probably explains why the orientation of the substrate deviates from the experimentally determined structures.

In the direct electrophilic aromatic addition starting from **13a**, benzene approaches the oxo-ligand in an end-on fashion, resulting in a free energy barrier of 12.6 kcal mol^{-1} (**TS[13a-14b]**‡, Fig. 18) and a kinetic product (**14b**) with a stability similar to that of **13a**. The relative free energies of the substrate hydroxylation are presented in Fig. 19. Thus far in the reaction, the

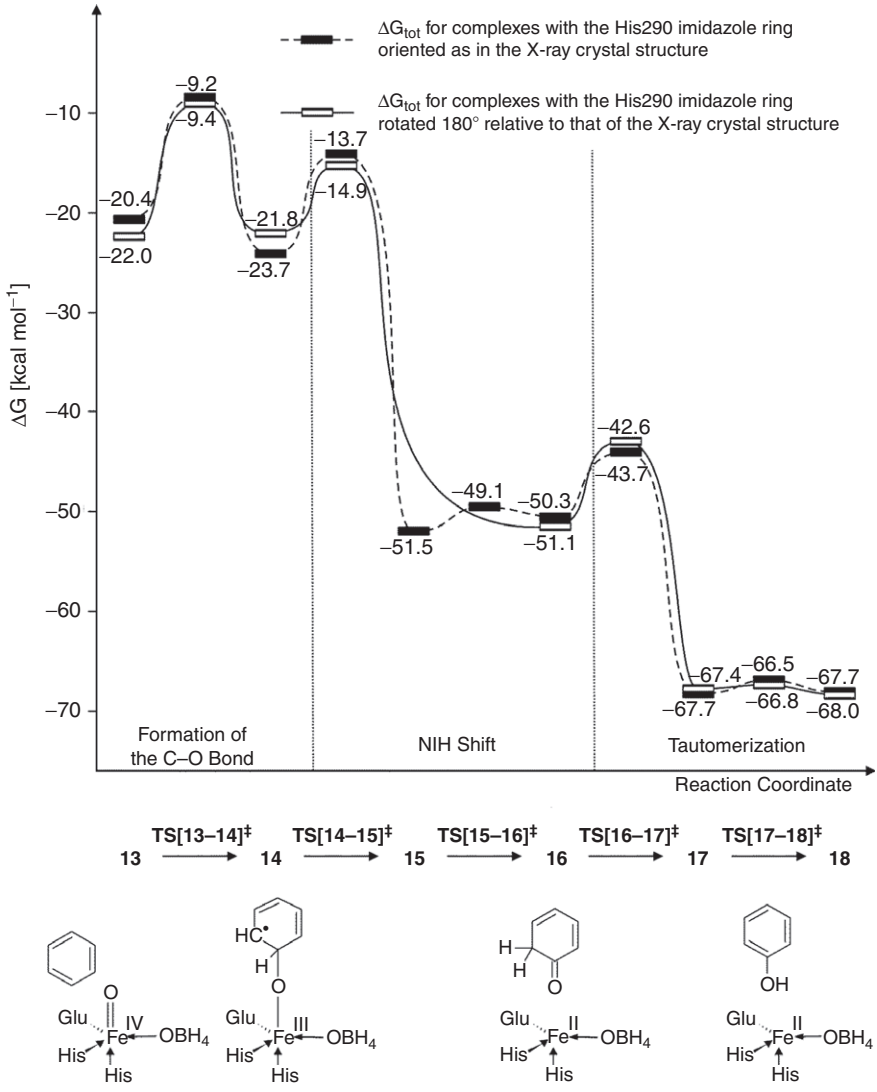

FIG. 19. Calculated free energy for the Fe^{IV}=O-mediated substrate hydroxylation.

conformation with the His290 imidazole ring rotated 180° compared to that of the crystal structure has been the most stable. For structure **14** however, the most stable conformer (**14a**, Fig. 20) has the same orientation of the His290 imidazole ring as the crystal structure, and hence this structure is discussed in

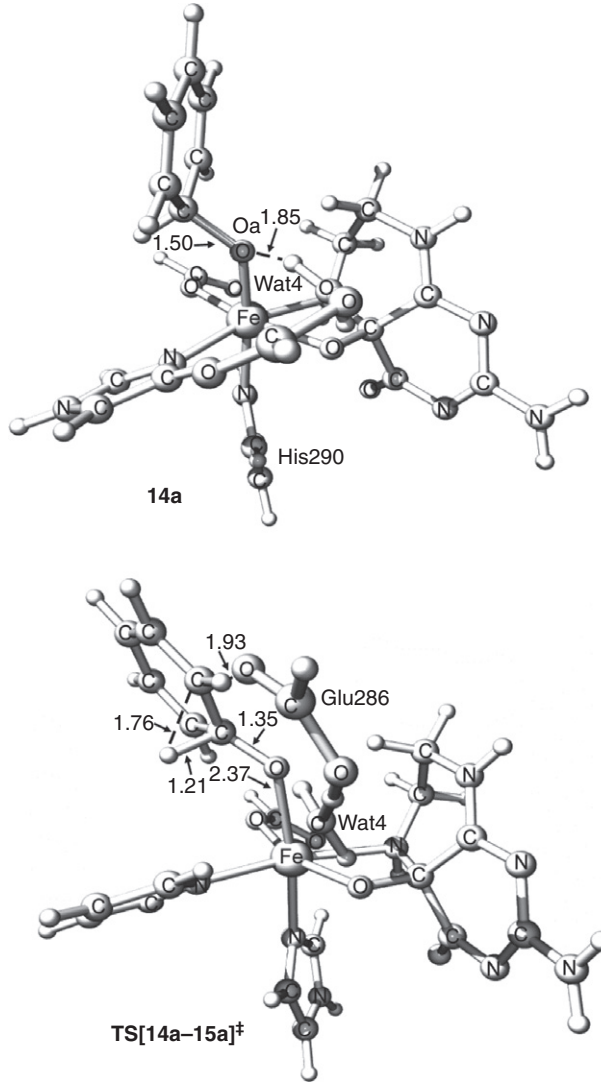

FIG. 20. Optimized structure of the arene radical **14a** and the transition state for NIH shift (**TS[14a-15a]**‡). Distances are given in angstroms.

the following. The benzene ring in **14a** has one unpaired electron antiferromagnetically coupled with the unpaired electrons on iron and its other ligands. This shows that the substrate oxidation proceeds over two steps, the first involving a one-electron transfer from benzene to iron, resulting in an arene radical and a reduction of Fe^{IV} to Fe^{III}, see Scheme 5 for an overview of the electronic rearrangements.

The formation of the C–O bond is rate limiting in the hydroxylation of the substrate, with a barrier only slightly lower than the overall free energy barrier associated with the one-electron transfer from the cofactor to dioxygen (13.9 kcal mol^{-1}, see Section II.A.2). The similar magnitudes of the two main barriers are in agreement with experimental evidence. Kinetic isotope effect measurements on PAH with ring-deuterated Phe and the cofactor analogue 6-methyltetrahydropterin show only a small effect, indicating that the overall barriers in the first and second main step of the reaction are of the same magnitude (*2,138*). Whereas for TH it was suggested that the rate-limiting step did not arise from a chemical reaction involving the substrate (*2,139*), the addition of an oxygen atom to the substrate has been suggested to, fully or partially, account for the rate-limiting step of TPH (*140*).

The C–O bond formation was also found to be rate limiting in the substrate hydroxylation, with barriers amounting to 16.2 kcal mol^{-1} for benzene and 16.3 kcal mol^{-1} for indole, in calculations involving a different cluster model (HO–Fe^{IV}=O) of the hydroxylating intermediate (*117*). For a positively charged active site model [H_2O–Fe^{IV}=O]$^+$, and with benzene as substrate model, the two-electron oxidation proceeded in one step, resulting in the formation of an arenium cation and a corresponding reduction of Fe^{IV} to Fe^{II} (*117*). The two-step oxidation found when using HO–Fe^{IV}=O was ascribed to the negatively charged ligands of that model, thus hampering the reduction of iron. Two negatively charged ligands are also seen in the water-free model of our study, the oxidized cofactor being the second negatively charged ligand, in place of the OH-group used in Ref. (*117*).

With the charged [H_2O–Fe^{IV}=O]$^+$ model and indole as substrate, the C–O bond formation was found to be remarkably facile (barrier of 6.8 kcal mol^{-1}). This is not consistent with experimental data showing that addition of an oxygen atom to the substrate is rate limiting, or partially rate limiting, in the hydroxylation of Trp by TPH (*140*). An insufficient model, lacking some structural features, was indicated as the explanation of this discrepancy with experiment (*117*).

An arene oxide could not be located for the water-free Fe^{IV}=O model used in our study. Attempts at symmetric attacks of two

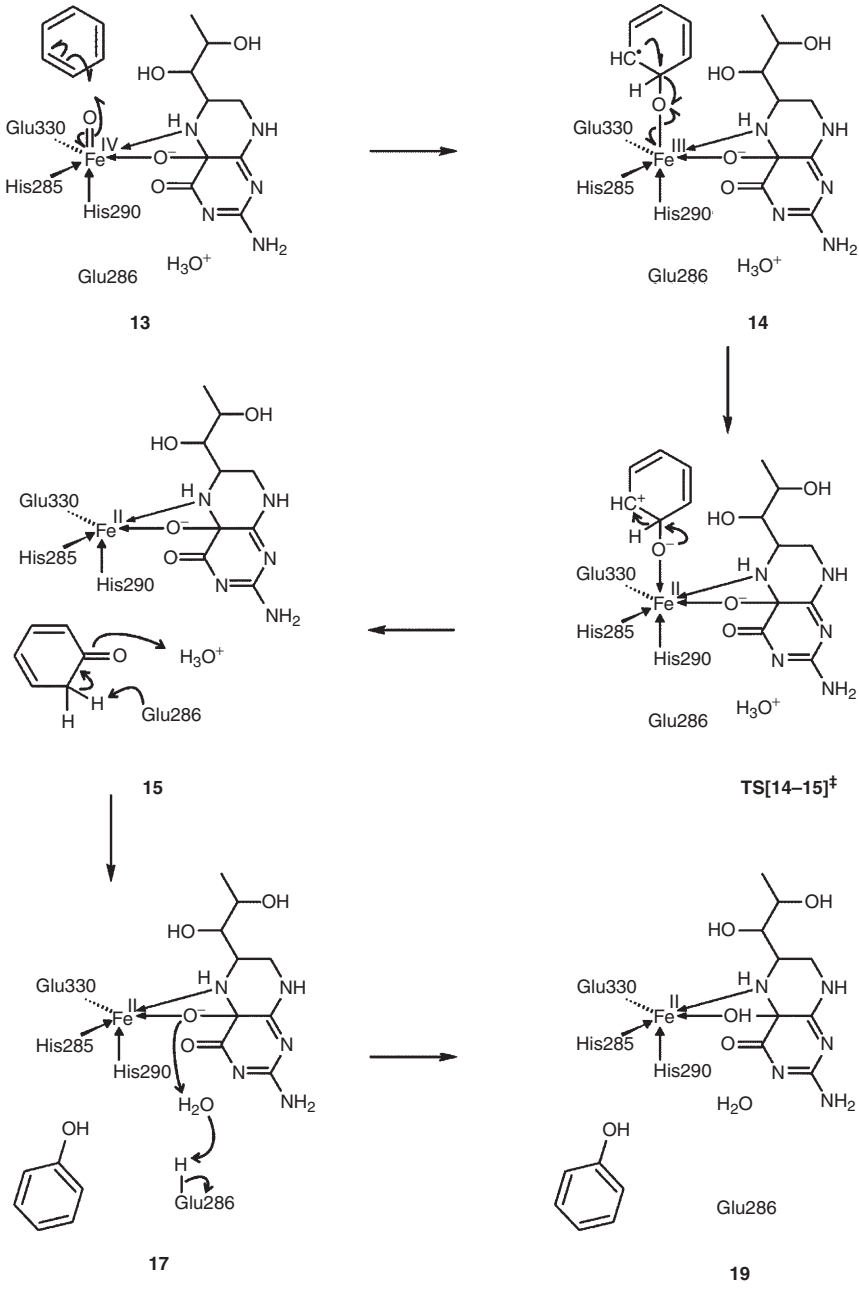

SCHEME 5. The electronic rearrangements of the aromatic amino acid substrate hydroxylation.

adjacent benzene carbon atoms onto the oxo-ligand resulted in rotation of the substrate and the formation of an arene radical product. For the HO–Fe^{IV}=O model, the simultaneous formation of two C–O bonds to give an epoxide was not observed (*117*). However, an arene oxide was formed from the arene radical, with an associated free energy barrier significantly larger than that of the subsequent NIH shift, the epoxide also being less stable than dienone resulting from the NIH shift. In a QM/MM study of hydroxylation of benzene by the human cytochrome P450 enzyme, Bathelt *et al.* calculated the barrier of epoxidation formation to be similar to the NIH shift barrier (*141*).

B.2. NIH shift

The second step of the overall two-electron oxidation of the substrate occurs early during the NIH shift, in which a second electron is transferred from the substrate to iron and which is accomplished already in the transition state of the NIH shift (**TS [14a-15a]**‡, Fig. 20). The benzene ring carries a positive charge (0.95 e) and a combined spin population reduced to almost zero, indicating the presence of an arenium cation and a reduced Fe^{II} in the transition state (Scheme 5). The NIH shift is a 1,2-hydride transfer in which the hydrogen atom on the oxidized carbon atom in the substrate migrates to an adjacent carbon atom. No preference with respect to the direction of migration from C(O) could be detected in the calculations, but to facilitate the subsequent tautomerization, the carbon atom closest to Glu286 and Wat4 was chosen as receiver of the migrating hydrogen atom. The NIH step is associated with a free energy barrier of 10.0 kcal mol^{-1} and is exergonic by 27.8 kcal mol^{-1}, leading to a structure (**15a**, Fig. 21) with the substrate placed in the second coordination sphere of iron, maintaining hydrogen bonds with Glu286 and Wat4. Before tautomerization of the dienone, a rotation of Glu330 occurs, which changes the hydrogen bond pattern, leading to a stronger hydrogen bond between the oxygen atom on the dienone and Wat4 (**16b**, Fig. 21). The substrate is now in a position in which tautomerization from dienone to phenol may be facilitated by Glu286 and Wat4.

The NIH shift and subsequent rotation of Glu330 occur over two steps (**14a** → **15a** → **16b**) for the conformer with the His290 imidazole ring in the same orientation as in the crystal structure. For the conformer with this imidazole ring rotated 180°, the NIH shift and Glu rotation take place in one step (**14b** → **16a**, via **TS [14b-16a]**‡, Fig. 22). In structure **16a** (Fig. 22), the hydrogen bond between Glu286 and the substrate involves the hydrogen atom

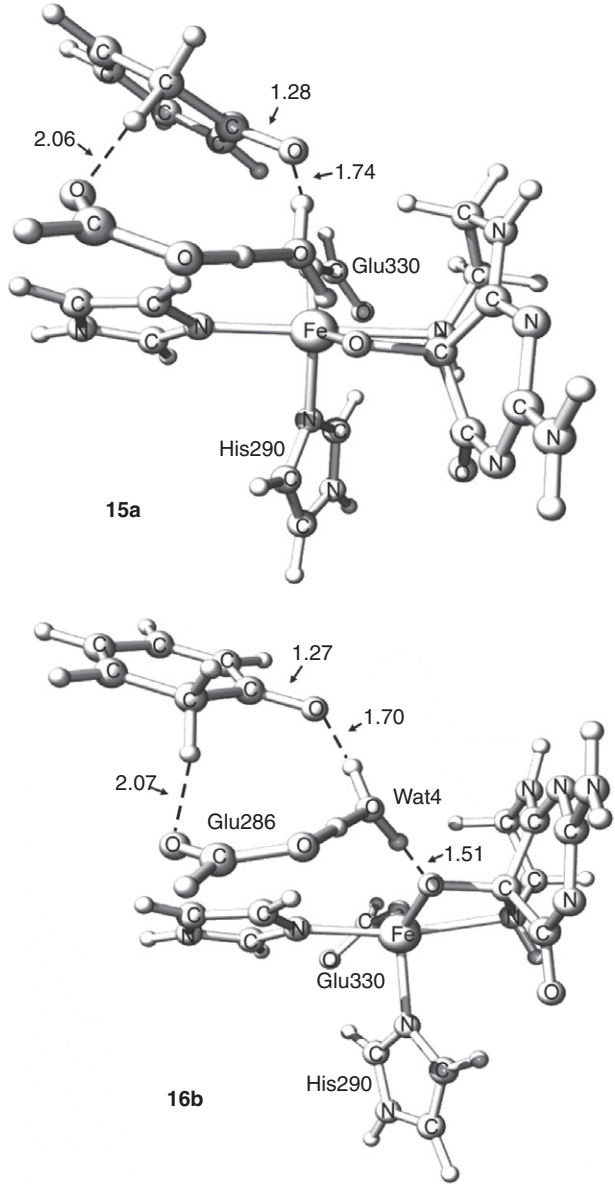

FIG. 21. Optimized structure of the dienone resulting from the NIH shift (**15a**) and the optimized structure for the subsequent rotation of Glu330 (**16b**). Distances are given in angstroms.

bound to the ortho carbon atom prior to the NIH shift, whereas in **16b** (Fig. 21), the hydrogen atom involved is the newly migrated one. A hydrogen bond to Glu286 can be established for any of the

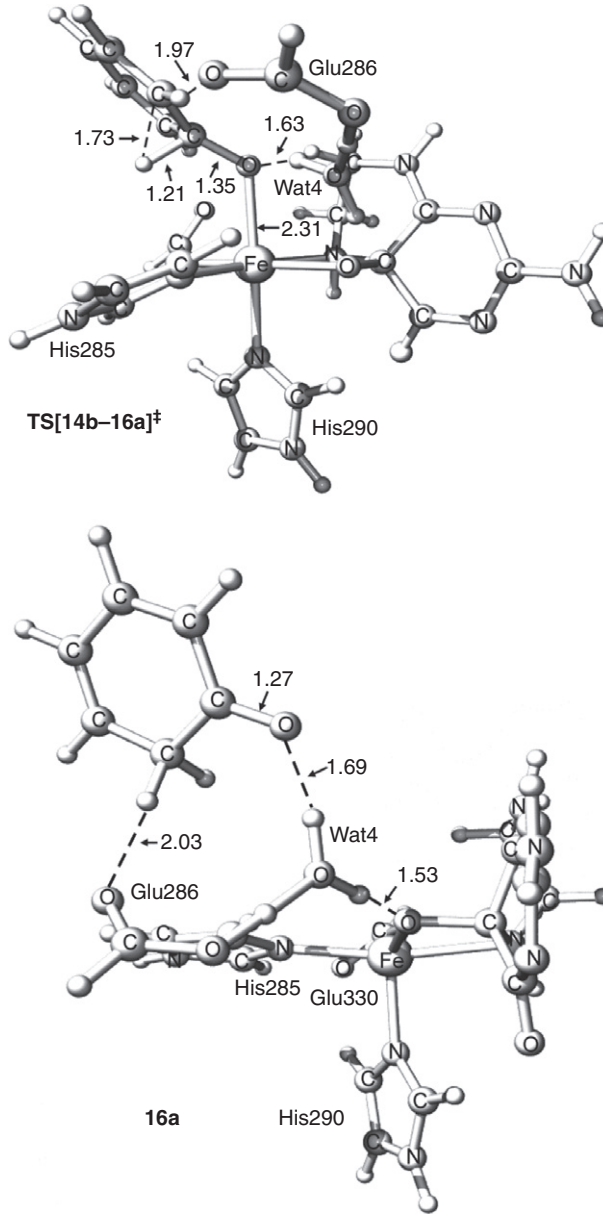

FIG. 22. Optimized transition state for the NIH shift and rotation of Glu 330 (**TS[14b-16a]**‡), which occurs simultaneously for the conformer with the His290 imidazole ring rotated 180° compared to the crystal structure, and the optimized NIH shift product with rotated Glu330 (**16a**). Distances are given in angstroms.

two hydrogen atoms on the sp^3 hybridized carbon atom, with a slight preference for the conformer in which this interaction involves the hydrogen atom bound to the ortho carbon atom prior to the NIH shift.

The NIH shift in the hydroxylation of Trp by TPH is known to occur from carbon 5 to carbon 4 exclusively (*70,140*). However, the NIH shift for indole in the $HO–Fe^{IV}=O$ and $[H_2O–Fe^{IV}=O]+$ models showed no preference for migration of the hydride to carbon 4 over carbon 6, which was claimed to be caused by the lack of steric preference exerted by the active site models compared to that of the actual enzymes (*117*).

B.3. Tautomerization

The tautomerization of the dienone to the phenol is the final step in the hydroxylation of the substrate. Lehmann *et al.* (*142*) showed by mass spectrometry of plasma after oral doses of ring-deuterated L-Phe that the NIH shift is followed by random loss of hydrogen atom in the subsequent tautomerization. As discussed above, the tautomerization is mediated by Glu286 and Wat4 which provide and receive protons. The tautomerization of the dienone in structure **16a** (Fig. 22) is associated with a free energy barrier of 8.5 kcal mol^{-1} (**TS[16a-17b]**‡, Fig. 23) and includes the proton transfers from the sp^3 ring carbon atom in the substrate to Glu286 and from the protonated Wat4 to the substrate oxygen atom. The hydroxylation of the amino acid substrate is now completed, with the substrate product in the phenol form whereas the metal has returned to its reduced state, Fe^{II}.

In the product of the tautomerization **(17a**, Fig. 24), His285 is in an "upright" orientation compared to the "in-plane" orientation seen in **16a** and hydrogen bonds with the substrate oxygen atom, thereby stabilizing the growing negative charge on the latter upon going from dienone (q(Oa) = –0.67 e) to phenol (q(Oa) = –0.78 e). Before protonation of the oxidized cofactor by Wat4, His285 is rotated down again to an "in-plane" orientation (**18a**, Fig. 25), albeit with a 180° orientation compared to **16a**. The rotation of His285 is associated with a small activation barrier of 1.2 kcal mol^{-1}, cf. Fig. 19, and leads to a structure with a tight hydrogen bonding pattern which facilitates the upcoming proton transfer from Wat4 to the cofactor. In contrast, a continued upright position of His285 has been found to move the substrate further away from Wat4 and iron and to make the proton transfer less energetically favorable.

Bassan *et al.* (*117*) studied the intermolecular tautomerization of 2,4-cyclohexadienone and the associated barriers using one

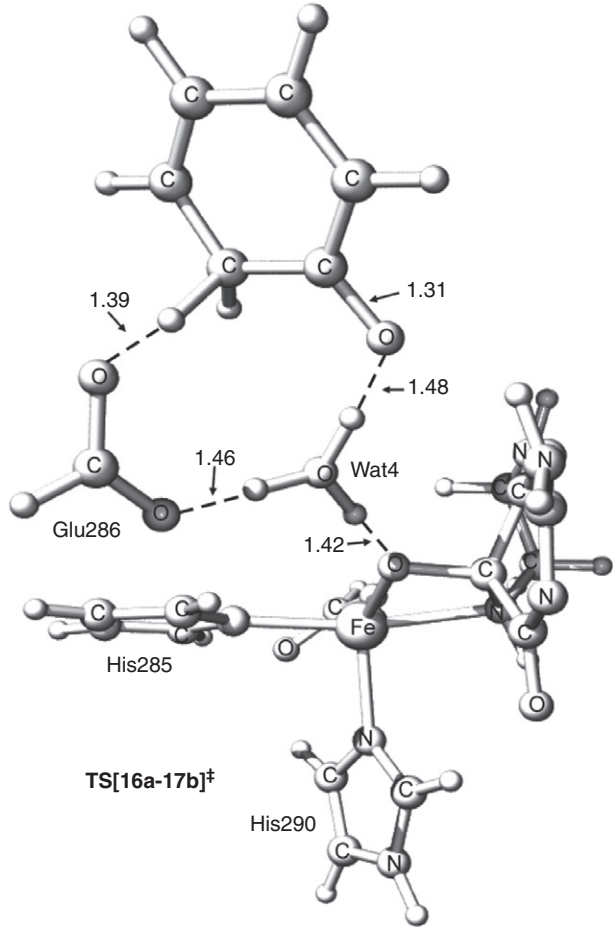

FIG. 23. Optimized transition state for the intermolecular tautomerization of the dienone to phenol involving Glu286 and Wat4 (**TS[16a-17b]**‡). Distances are given in angstroms.

($\Delta G^{\ddagger} = 22.7\,\text{kcal mol}^{-1}$) and two ($\Delta G^{\ddagger} = 15.0\,\text{kcal mol}^{-1}$) assisting water molecules and concluded that two water molecules were needed to give a reasonably low activation barrier for the tautomerization. However, when the tautomerization occurred in the vicinity of the Fe complex one water molecule was found to be sufficient ($\Delta G^{\ddagger} = 12.9\,\text{kcal mol}^{-1}$). In the latter case, the water molecule was stabilized by Glu330. This water molecule was proposed to bind to iron after tautomerization, which would thus reform the hexacoordinate three-water starting complex, albeit, in their model, still with one of the three water molecules deprotonated.

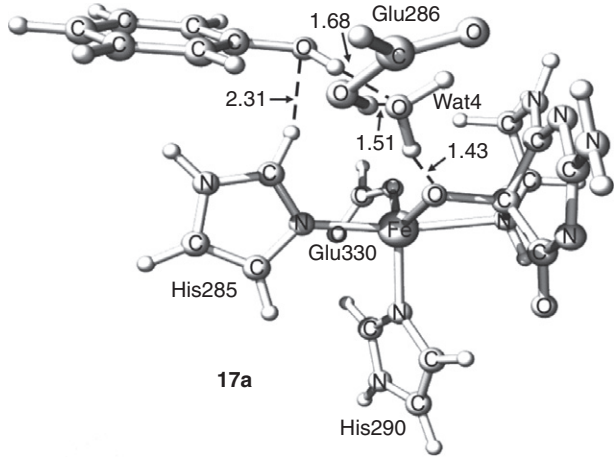

FIG. 24. Optimized product after tautomerization. Distances are given in angstroms.

B.4. Protonation of the oxidized cofactor

Completion of the catalytic cycle requires protonation as well as dissociation of the oxidized cofactor, release of the phenol product, and regeneration of the hexacoordinate iron catalyst complex seen in **1a** (Fig. 6). These final parts of the reaction have so far only been the subject of one recent computational investigation (*123*). The oxidized cofactor is protonated by Wat4, and this process is triggered by a small change in the phenol position, to hydrogen bond with both Glu286, via the hydroxyl hydrogen atom, and Wat4, via the hydroxyl oxygen atom, instead of with Wat4 only. Glu286 is deprotonated by Wat4, which, in turn, is deprotonated by the cofactor. The protonation of the oxidized cofactor is associated with a small free energy barrier of 3.9 kcal mol^{-1} and leads to a product (**19a**, Fig. 25) in which the cofactor forms a strong hydrogen bond with Wat4 via the newly transferred hydrogen atom. The reaction is slightly endergonic, by 0.2 kcal mol^{-1}, and also does not affect the coordination of the cofactor to iron. The proton transfer is, as expected, reflected in a reduction of the Wiberg bond index for O(Wat4)–H, by more than 0.2, and a corresponding increase for H–O4a(BH_4) upon going from **18a** to **19a**.

B.5. Rebinding of water molecules

The catalytic cycle is completed by reformation of the hexacoordinate iron complex, with the 2-His-1-Glu binding motif and three

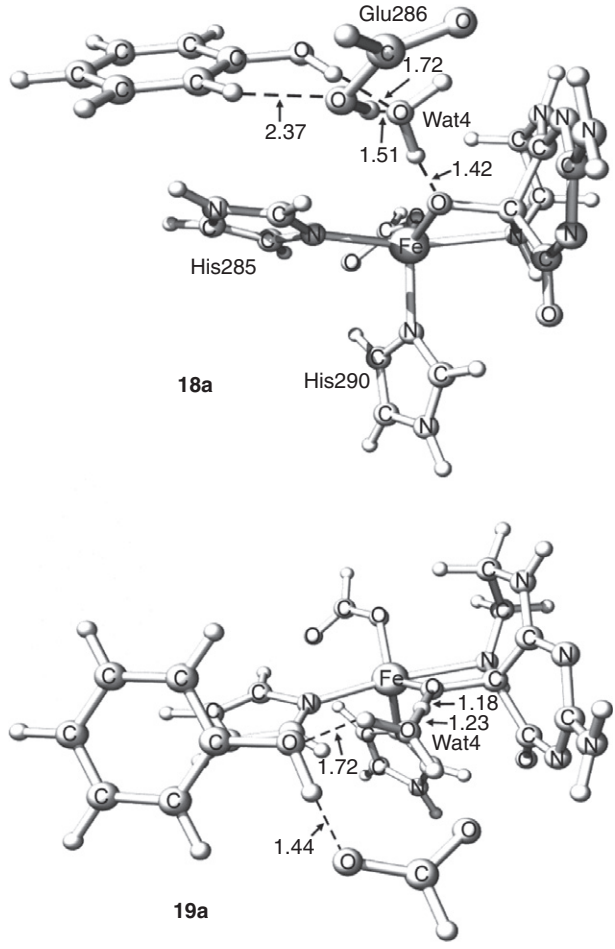

FIG. 25. Optimized minimum with the substrate product in phenol form prior to (**18a**) and subsequent to (**19a**) protonation of the cofactor. Distances are given in angstroms.

ligating water molecules. To this end, the oxidized cofactor must be dissociated along with rebinding of three water molecules to iron. The iron complex in structure **19**, cf. Fig. 25, appears to have a vacant position where Wat2 binds in the X-ray crystal structure (*98*) on which the starting structure of our study was based (*121*). The first water molecule is thus placed in this position, a process (**19a** + $H_2O \rightarrow$ **20a**, Fig. 26) which is exergonic by 3.3 kcal mol^{-1}, cf. Fig. 27. Rebinding the first water molecule in other positions is energetically more costly.

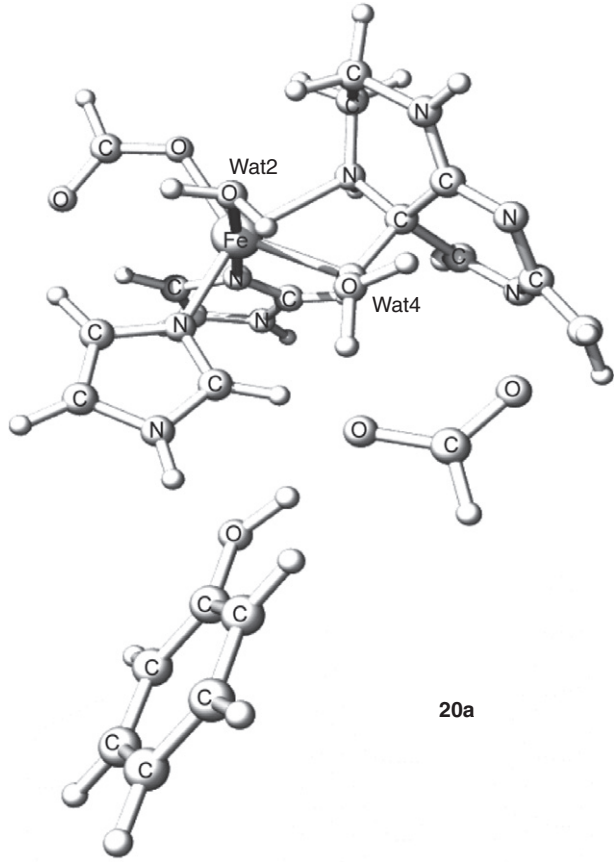

FIG. 26. Optimized structure after rebinding of the first water molecule in the position of Wat2 (**20a**). Distances are given in angstroms. See Fig. 3 for enumeration of residues and water ligands.

The second water molecule to be captured is placed in the position of Wat3, with no cost in free energy for the reaction involved, **20a** + H_2O → **21a** (Fig. 28). During this step, the metal–cofactor bonds are broken and the oxidized cofactor enters the second coordination sphere where it hydrogen bonds with the water molecules. Rebinding instead the second water molecule in the position of Wat1 results in an almost 10 kcal mol^{-1} less stable structure in which the cofactor still maintains bonds to the metal.

The last water molecule is bound to iron in the position of Wat1 (**22a**, Fig. 29), with a free energy cost of 5.2 kcal mol^{-1}. The hexacoordinate iron complex has now been reformed, and, after release of the oxidized products, a new catalytic cycle can start.

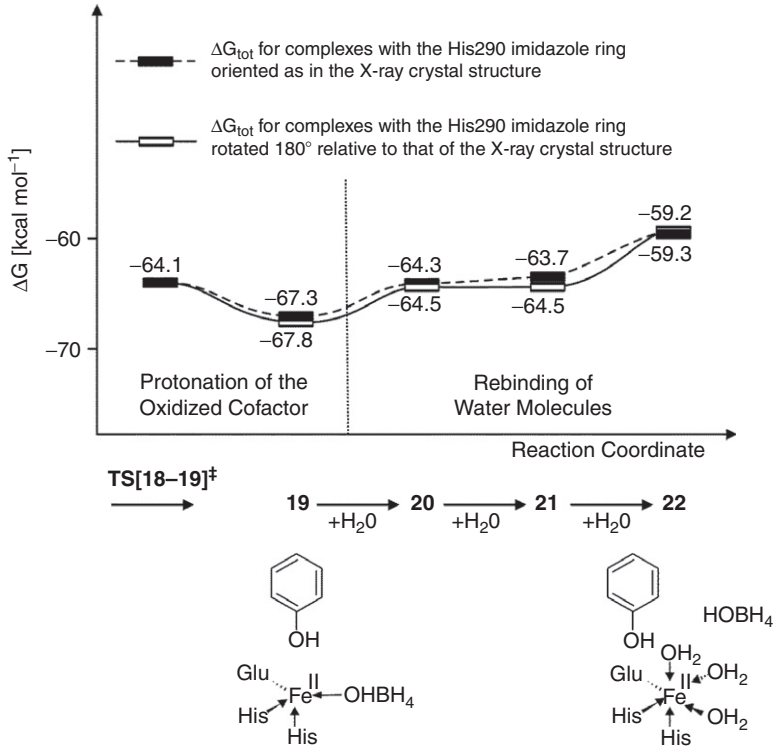

FIG. 27. Calculated relative free energies for protonation of the oxidized cofactor and rebinding of water molecules to iron.

The process of removing phenol from **22a** is exergonic by 3.3 kcal mol^{-1} and leads to an overall reaction product similar to, and 62.6 kcal mol^{-1} more stable than, the hexacoordinate starting structure (**1a**, Fig. 6). The free energy change calculated for the catalytic reaction compares excellently with the corresponding result (–62.8 kcal mol^{-1}) for the net overall reaction benzene + O_2 + BH_4 → phenol + 4a-OH-BH_4.

The barriers to binding of the water molecules have not been calculated explicitly. The highest such barrier should be expected for the last process, i.e., for the capture of the third water molecule. This process is analogous to **2a** + H_2O → **1a**, the barrier of which has been calculated to 9.7 kcal mol^{-1} (Fig. 7). A similar activation barrier for binding of Wat1 to **21a** would give an overall free energy barrier of ca. 13 kcal mol^{-1} for rebinding of water molecules, which is similar to the barrier for C–O bond formation and slightly lower than the overall rate-limiting barrier for the catalytic reaction (13.9 kcal mol^{-1} (*122*)).

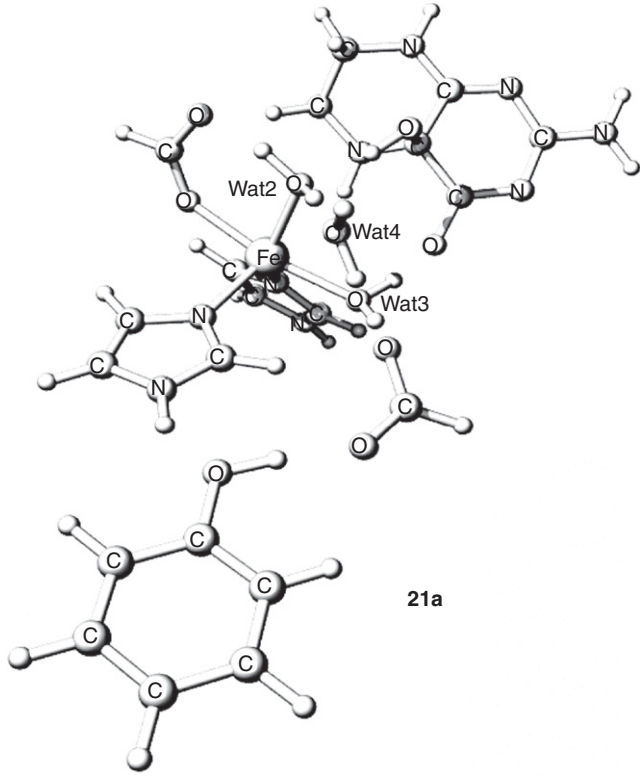

FIG. 28. Optimized minimum after rebinding of the second water molecule in the position of Wat3 (**21a**). Distances are given in angstroms. See Fig. 3 for enumeration of residues and water ligands.

V. Conclusions

In this review, although we have tried to cover the necessary background information on the function and structure of the AAHs, our main goal has been to offer information on the catalytic mechanism operating in these non-heme iron-dependent enzymes. In particular, we have focused on mechanistically relevant information that has emerged from molecular-level computational studies. Special attention is paid to our own work in this area, although we have tried to put our results in the context of other contributions in the field.

All the existing molecular-level computational studies of the AAH catalytic mechanism support the general two-step mechanism. Although individually such theoretical studies can formally only disprove candidate reaction pathways, the unanimous

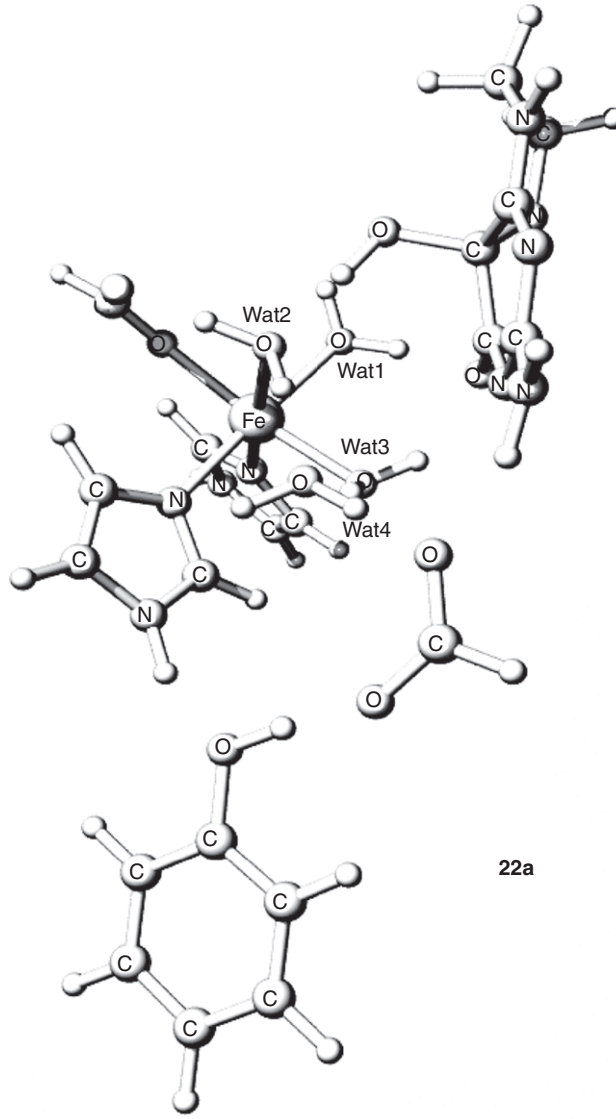

FIG. 29. Optimized product after rebinding of the last water molecule in the position of Wat1 (**22a**). Distances are given in angstroms. See Fig. 3 for enumeration of residues and water ligands.

support for the two-step mechanism, involving several cluster models and QM/MM studies based on different X-ray crystal structures and with different choices made in the model building, is a strong argument in favor of this general mechanism. The

combined picture emerging from the computational studies thus represents an important contribution to the field.

However, there are still contrasts among the various studies. For example, whereas earlier work in the field (*117–119*) contains no examples of a bond formation between the central iron atom and the cofactor, our own, more recent studies indicate that a dative iron–cofactor bond is formed upon water ligand dissociation (*120,121*), and that the cofactor remains bound to the metal during its own oxidation (*122*) as well as the oxidation of the aromatic amino acid substrate (*123*) and dissociates only as the iron catalyst rebinds ligating water at the end of the cycle (*123*). Another important difference is that our calculations predict that the reduction of dioxygen occurs as two single-electron transfers from the cofactor to dioxygen (*122*), in contrast to the one-step two-electron transfer predicted earlier (*118*). Regarding the substrate hydroxylation part of the mechanism, there seems to be agreement among the computational studies (*117,119*) that C–O bond formation takes place via direct electrophilic aromatic addition, and that the latter reaction is energetically preferable to a mechanism starting by C–H bond cleavage on the substrate (*119*). However, the charge of the model employed for the $Fe^{IV}{=}O$ hydroxylating intermediate seems to control the details with which the oxidation of the substrate occurs. Whereas calculations on overall neutral models have led to two consecutive one-electron oxidations (*117,123*), the application of cationic models has resulted in one-step two-electron oxidations of the substrate and the formation of arenium ion intermediates (*117,119*).

Apart from the fact that an empirical term to account for long-range dispersion has been included in our recent work (*121–123*), the quantum chemical methods and basis sets employed have been very similar among the different investigations. This observation even extends to the QM part of the QM/MM study by Shiota *et al.* (*119*). It is thus far more likely that the origin of the discrepancies is to be found in the construction of the computational models and the assumptions forming the basis of each study. A critical point in this respect pertains to the number of water ligands remaining at the iron atom during catalysis. Whereas water ligands are present at the metal in the earlier studies (*117–119*), all ligating water molecules were explicitly assumed to dissociate prior to oxygen coordination and activation in our own work (*120–123*). In many respects our combined contribution may be viewed as a computational experiment aimed at testing the hypothesis, detailed above, that ligating water molecules dissociate during the activation phase. Although the overall reaction path resulting from this assumption and our calculations (Fig. 30) appears to be feasible indeed, with no

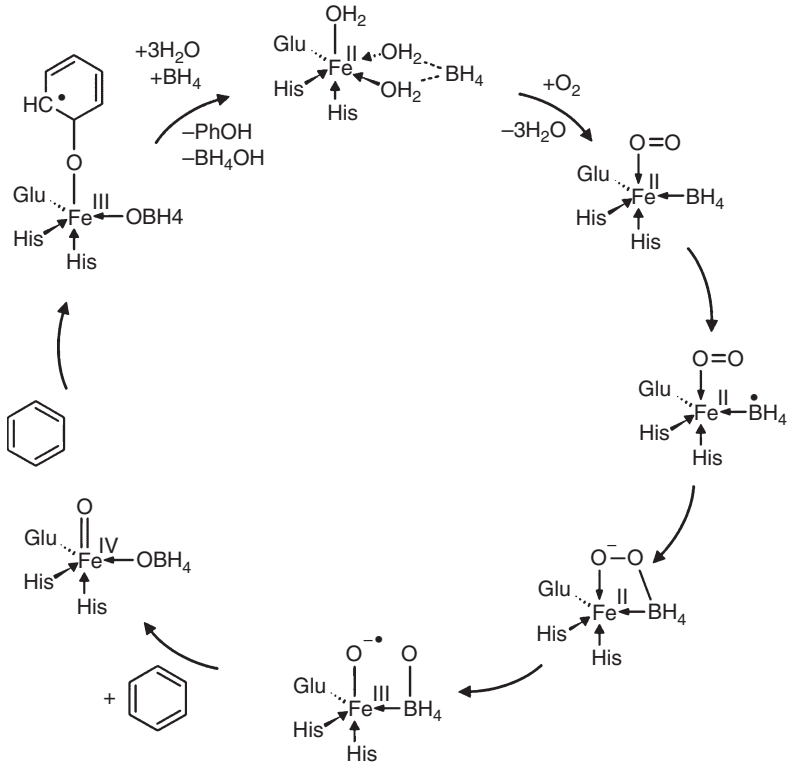

FIG 30. Summary of the catalytic cycle of AAHs based on DFT studies.

thermodynamic sinks or insurmountable barriers, further experimental and computational work is needed in order to confirm or discard the mechanism. At the moment it suffices to note that the case for complete water dissociation seems to be strong (see above) and that the resulting mechanism is in agreement with a range of key experimental observations. An example of such an observation is the fact that the mechanism is sequential and all three substrates are ordered at the active site before any product of hydroxylation is released (*41, 49, 143*). Our computed reaction path fulfills this requirement by retaining the oxidized cofactor in the first coordination sphere of iron until the substrate has also undergone oxidation. In addition, the observation that cofactor analogues give rise to various degrees of uncoupling of the reaction, where water is hydroxylated instead of the substrate, is more easily explained in a model where the cofactor is bound during correct, coupled hydroxylation of the substrate.

Assuming that the ligating water molecules dissociate, thus generating a low-coordinate iron complex, our calculations indicate

that the affinity for the pterin cofactor, located in the immediate vicinity of the metal, is substantial. However, the strength of this affinity, as predicted by molecular-level calculations, is likely to be influenced by the exact choice of model for the active center. The extent to which iron–cofactor bond formation plays a role in the catalysis is but one example of a question that should, and no doubt will, be addressed in upcoming molecular-level computational studies of the AAH mechanism. Future studies should, first of all, focus on increasing the size of the QM region, both in cluster model and in QM/MM studies. In the latter studies, the conformational flexibility of the catalytic domain should also be addressed by investigating the catalytic ability of several conformations of the enzyme in solution, see, e.g., Ref. (*144*) for an example. Recent investigations reveal the importance of enzyme flexibility on pterin binding and control of intrinsic rate constants determining the mechanism of TH (*145*).

Acknowledgment

University of Bergen is acknowledged for financial support through the Nanoscience program. The Norwegian Research Council is acknowledged for CPU resources granted through the NOTUR supercomputing program. We are grateful to Giovanni Occhipinti and Karl Wilhelm Törnroos for helpful discussions.

References

1. Abu-Omar, M. M.; Loaiza, A.; Hontzeas, N. *Chem. Rev.* **2005**, *105*, 2227.
2. Fitzpatrick, P. F., *Annu. Rev. Biochem.* **1999**, *68*, *355*.
3. Fitzpatrick, P. F.; *Biochemistry* **2003**, *42*, 14083.
4. Flatmark, T.; Stevens, R. C. *Chem. Rev.* **1999**, *99*, 2137.
5. Kappock, T. J.; Caradonna, J. P. *Chem. Rev.* **1996**, *96*, 2659.
6. Teigen, K.; McKinney, J. A.; Haavik, J.; Martinez, A. *Curr. Med. Chem.* **2007**, *14*, 455.
7. Solomon, E. I.; Decker, A.; Lehnert, N. *Proc. Natl. Acad. Sci. USA.* **2003**, *100*, 3589.
8. Walther, D. J.; Bader, M. *Biochem. Pharmacol.* **2003**, *66*, 1673.
9. Hufton, S. E.; Jennings, I. G.; Cotton, R. G. H. *Biochem. J.* **1995**, *311*, 353.
10. Siltberg-Liberles, J.; Steen, I. H.; Svebak, R. M.; Martinez, A. *Gene* **2008**, *427*, 86.
11. Thony, B.; Auerbach, G.; Blau, N. *Biochem. J.* **2000**, *347*, 1.
12. Dix, T. A.; Kuhn, D. M.; Benkovic, S. J. *Biochemistry* **1987**, *26*, 3354.
13. Haavik, J.; Flatmark, T. *Eur. J. Biochem.* **1987**, *168*, 21.
14. Lazarus, R. A.; Dietrich, R. F.; Wallick, D. E.; Benkovic, S. J. *Biochemistry* **1981**, *20*, 6834.

15. Dix, T. A.; Bollag, G. E.; Domanico, P. L.; Benkovic, S. J. *Biochemistry* **1985**, *24*, 2955.
16. Siegmund, H. U.; Kaufman, S. *J. Biol. Chem.* **1991**, *266*, 2903.
17. Fisher, D. B.; Kaufman, S.; Kirkwood, R. *J. Biol. Chem.* **1972**, *247*, 5161.
18. Gottschall, D. W.; Dietrich, R. F.; Benkovic, S. J.; Shiman, R. *J. Biol. Chem.* **1982**, *257*, 845.
19. Moran, G. R.; Daubner, S. C.; Fitzpatrick, P. F. *J. Biol. Chem.* **1998**, *273*, 12259.
20. Marota, J. J. A.; Shiman, R. *Biochemistry* **1984**, *23*, 1303.
21. Shiman, R.; Gray, D. W.; Hill, M. A. *J. Biol. Chem.* **1994**, *269*, 24637.
22. Wallick, D. E.; Bloom, L. M.; Gaffney, B. J.; Benkovic, S. J. *Biochemistry* **1984**, *23*, 1295.
23. Hegg, E. L.; Que, L. J., *Eur. J. Biochem.* **1997**, *250*, 625.
24. Que, L. *Nat. Struct. Biol.* **2000**, *7*, 182.
25. Solomon, E. I.; Brunold, T. C.; Davis, M. I.; Kemsley, J. N.; Lee, S. K.; Lehnert, N.; Neese, F.; Skulan, A. J.; Yang, Y. S.; Zhou, J. *Chem. Rev.* **2000**, *100*, 235.
26. Costas, M.; Mehn, M. P.; Jensen, M. P.; Que, L. *Chem. Rev.* **2004**, *104*, 939.
27. Dix, T. A.; Benkovic, S. J. *Biochemistry* **1985**, *24*, 5839.
28. Feig, A. L.; Lippard, S. J. *Chem. Rev.* **1994**, *94*, 759.
29. Eser, B. E.; Barr, E. W.; Frantorn, P. A.; Saleh, L.; Bollinger, J. M.; Krebs, C.; Fitzpatrick, P. F. *J. Am. Chem. Soc.* **2007**, *129*, 11334.
30. McKinney, J.; Knappskog, P. M.; Haavik, J.: *J. Neurochem.* **2005**, *92*, 311.
31. McKinney, J.; Teigen, K.; Frøystein, N. A.; Salaun, C.; Knappskog, P. M.; Haavik, J.; Martinez, A. *Biochemistry* **2001**, *40*, 15591.
32. Daubner, S. C.; Moran, G. R.; Fitzpatrick, P. F. *Biochem. Biophys. Res. Commun.* **2002**, *292*, 639.
33. Scriver, C. R.; Kaufman, S. The Metabolic and Molecular Bases of Inherited Disease. In: "*Hyperphenylalaninemia Phenylalanine Hydroxylase Deficiency*", 8th edn.; Eds. Scriver, C. R.; Beaudet, A. L.; Valle, D.; Sly, W. S.; McGraw-Hill: New York, **2001**, p. 1667.
34. van Spronsen, F. J.; Hoeksma, M.; Reijngoud, D. J. *J. Inherit. Metab. Dis.* **2009**, *32*, 46.
35. Scriver, C. R. *Hum. Mutat.* **2007**, *28*, 831.
36. Scriver, C. R.; Hurtubise, M.; Konecki, D.; Phommarinh, M.; Prevost, L.; Erlandsen, H.; Stevens, R.; Waters, P. J.; Ryan, S.; McDonald, D.; Sarkissian, C. *Hum. Mutat.* **2003**, *21*, 333.
37. Pey, A. L.; Stricher, F.; Serrano, L.; Martinez, A. *Am. J. Hum. Genet.* **2007**, *81*, 1006.
38. Sarkissian, C. N.; Gamez, A.; Scriver, C. R. *J. Inherit. Metab. Dis.* **2009**, *32*, 3.
39. Levy, H. L.; Milanowski, A.; Chakrapani, A.; Cleary, M.; Lee, P.; Trefz, F. K.; Whitley, C. B.; Feillet, F.; Feigenbaum, A. S.; Bebchuk, J. D.; Christ-Schmidt, H.; Dorenbaum, A.; Grp, S. R. *Lancet* **2007**, *370*, 504.
40. Hagedoorn, P. L.; Schmidt, P. P.; Andersson, K. K.; Hagen, W. R.; Flatmark, T.; Martinez, A. *J. Biol. Chem.* **2001**, *276*, 22850.
41. Volner, A.; Zoidakis, J.; Abu-Omar, M. M. *J. Biol. Inorg. Chem.* **2003**, *8*, 121.
42. Kemsley, J. N.; Mitic, N.; Zaleski, K. L.; Caradonna, J. P.; Solomon, E. I. *J. Am. Chem. Soc.* **1999**, *121*, 1528.
43. Kaufman, S. *Adv. Enzymol. Relat. Areas Mol. Biol.* **1993**, *67*, 77.
44. Mitnaul, L. J.; Shiman, R. *Proc. Natl. Acad. Sci. USA.* **1995**, *92*, 885.

45. Martinez, A.; Calvo, A. C.; Teigen, K.; Pey, A. L. *Prog. Mol. Biol. Transl.* **2008**, *83*, 89.
46. Grima, B.; Lamouroux, A.; Boni, C.; Julien, J. F.; Javoyagid, F.; Mallet, J. *Nature* **1987**, *326*, 707.
47. Kaneda, N.; Kobayashi, K.; Ichinose, H.; Kishi, F.; Nakazawa, A.; Kurosawa, Y.; Fujita, K.; Nagatsu, T. *Biochem. Biophys. Res. Commun.* **1987**, *146*, 971.
48. Haavik, J.; Blau, N.; Thony, B. *Hum. Mutat.* **2008**, *29*, 891.
49. Fitzpatrick, P. F. *Biochemistry* **1991**, *30*, 3658.
50. Francisco, W. A.; Tian, G. C.; Fitzpatrick, P. F.; Klinman, J. P. *J. Am. Chem. Soc.* **1998**, *120*, 4057.
51. Halskau, O.; Ying, M.; Baumann, A.; Kleppe, R.; Rodriguez-Larrea, D.; Almas, B.; Haavik, J.; Martinez, A. *J. Biol. Chem.* **2009**, *284*, 32758.
52. Andersson, K. K.; Cox, D. D.; Que, L.; Flatmark, T.; Haavik, J. *J. Biol. Chem.* **1988**, *263*, 18621.
53. Haavik, J.; Martinez, A.; Flatmark, T. *FEBS Lett.* **1990**, *262*, 363.
54. Bevilaqua, L. R. M.; Graham, M. E.; Dunkley, P. R.; von Nagy-Felsobuki, E. I.; Dickson, P. W. *J. Biol. Chem.* **2001**, *276*, 40411.
55. Lehmann, I. T.; Bobrovskaya, L.; Gordon, S. L.; Dunkley, P. R.; Dickson, P.W. *J. Biol. Chem.* **2006**, *281*, 17644.
56. Quinsey, N. S.; Luong, A. Q.; Dickson, P. W. *J. Neurochem.* **1998**, *71*, 2132.
57. Flatmark, T.; Almas, B.; Knappskog, P. M.; Berge, S. V.; Svebak, R. M.; Chehin, R.; Muga, A.; Martinez, A. *Eur. J. Biochem.* **1999**, *262*, 840.
58. Walther, D. J.; Peter, J. U.; Bashammakh, S.; Hortnagl, H.; Voits, M.; Fink, H.; Bader, M. *Science* **2003**, *299*, 76.
59. Sakowski, S. A.; Geddes, T. J.; Thomas, D. M.; Levi, E.; Hatfield, J. S.; Kuhn, D. M. *Brain Res.* **2006**, *1085*, 11.
60. Sugden, K.; Tichopad, A.; Khan, N.; Craig, I. W.; D'Souza, U. M. *BMC Neurosci.* **2009**, *10*, 50.
61. Zill, P.; Buttner, A.; Eisenmenger, W.; Moller, H. J.; Ackenheil, M.; Bondy, B. *J. Psychiatr. Res.* **2007**, *41*, 168.
62. Serretti, A.; Zanardi, R.; Franchini, L.; Artioli, P.; Dotoli, D.; Pirovano, A.; Smeraldi, E. *Pharmacogenetics* **2004**, *14*, 607.
63. Veenstra-VanderWeele, J.; Anderson, G. M.; Cook, E. H. *Eur. J. Pharmacol.* **2000**, *410*, 165.
64. Li, D. W.; He, L. *Hum. Genet.* **2006**, *120*, 22.
65. Li, D. W.; He, L. *Hum. Genet.* **2006**, *119*, 233.
66. Liu, X.; Li, H.; Qin, W.; He, G.; Li, D.; Shen, Y.; Shen, J.; Gu, N.; Feng, G.; He, L. *J. Med. Genet.* **2006**, *43*, e4.
67. Zhang, X. D.; Gainetdinov, R. R.; Beaulieu, J. M.; Sotnikova, T. D.; Burch, L. H.; Williams, R. B.; Schwartz, D. A.; Krishnan, K. R. R.; Caron, M. G. *Neuron* **2005**, *45*, 11.
68. Cichon, S.; Winge, I.; Mattheisen, M.; Georgi, A.; Karpushova, A.; Freudenberg, J.; Freudenberg-Hua, Y.; Babadjanova, G.; Van Den Bogaert, A.; Abramova, L. I.; Kapiletti, S.; Knappskog, P. M.; McKinney, J.; Maier, W.; Abou Jamra, R.; Schulze, T. G.; Schumacher, J.; Propping, P.; Rietschel, M.; Haavik, J.; Nothen, M. M. *Hum. Mol. Genet.* **2008**, *17*, 87.
69. McKinney, J.; Johansson, S.; Halmoy, A.; Dramsdahl, M.; Winge, I.; Knappskog, P. M.; Haavik, J. *Mol. Psychiatry* **2008**, *13*, 365.
70. Moran, G. R.; Derecskei-Kovacs, A.; Hillas, P. J.; Fitzpatrick, P. F. *J. Am. Chem. Soc.* **2000**, *122*, 4535.
71. Banik, U.; Wang, G. A.; Wagner, P. D.; Kaufman, S. *J. Biol. Chem.* **1997**, *272*, 26219.

72. Winge, I.; McKinney, J. A.; Ying, M.; D'Santos, M.; Kleppe, C. S. Knappskog, P. M.; Haavik, J. *Biochem. J.* **2008**, *410*, 195.
73. Johansen, P. A.; Wolf, W. A.; Kuhn, D. M. *Biochem. Pharmacol.* **1991**, *41*, 625.
74. Martinez, A.; Knappskog, P. M.; Haavik, J. *Curr. Med. Chem.* **2001**, *8*, 1077.
75. Koehntop, K. D.; Marimanikkuppam, S.; Ryle, M. J.; Hausinger, R. P.; Que, L. *J. Biol. Inorg. Chem.* **2006**, *11*, 63.
76. Hoffart, L. M.; Barr, E. W.; Guyer, R. B.; Bollinger, J. M.; Krebs, C. *Proc. Natl. Acad. Sci. USA.* **2006**, *103*, 14738.
77. Price, J. C.; Barr, E. W.; Tirupati, B.; Bollinger, J. M.; Krebs, C. *Biochemistry* **2003**, *42*, 7497.
78. Proshlyakov, D. A.; Henshaw, T. F.; Monterosso, G. R.; Ryle, M. J.; Hausinger, R. P. *J. Am. Chem. Soc.* **2004**, *126*, 1022.
79. Riggs-Gelasco, P. J.; Price, J. C.; Guyer, R. B.; Brehm, J. H.; Barr, E. W.; Bollinger, J. M.; Krebs, C. *J. Am. Chem. Soc.* **2004**, *126*, 8108.
80. Teigen, K.; Frøystein, N. A.; Martinez, A. *J. Mol. Biol.* **1999**, *294*, 807.
81. Andersen, O. A.; Flatmark, T.; Hough, E. *J. Mol. Biol.* **2002**, *320*, 1095.
82. Erlandsen, H.; Bjorgo, E.; Flatmark, T.; Stevens, R. C. *Biochemistry* **2000**, *39*, 2208.
83. Erlandsen, H.; Kim, J. Y.; Patch, M. G.; Han, A.; Volner, A.; Abu-Omar, M. M.; Stevens, R. C. *J. Mol. Biol.* **2002**, *320*, 645.
84. Goodwill, K. E.; Sabatier, C.; Stevens, R. C. *Biochemistry* **1998**, *37*, 13437.
85. Wang, L.; Erlandsen, H.; Haavik, J.; Knappskog, P. M.; Stevens, R. C. *Biochemistry* **2002**, *41*, 12569.
86. Teigen, K.; Dao, K. K.; McKinney, J. A.; Gorren, A. C.F.; Mayer, B.; Frøystein, N. A.; Haavik, J.; Martinez, A. *J. Med. Chem.* **2004**, *47*, 5962.
87. Pey, A. L.; Thorolfsson, M.; Teigen, K.; Ugarte, M.; Martinez, A. *J. Am. Chem. Soc.* **2004**, *126*, 13670.
88. Stuehr, D. J.; Santolini, J.; Wang, Z. Q.; Wei, C. C.; Adak, S. *J. Biol. Chem.* **2004**, *279*, 36167.
89. Hurshman, A. R.; Krebs, C.; Edmondson, D. E.; Huynh, B. H.; Marletta, M. A. *Biochemistry* **1999**, *38*, 15689.
90. Schmidt, P. P.; Lange, R.; Gorren, A. C.F.; Werner, E. R.; Mayer, B.; Andersson, K. K. *J. Biol. Inorg. Chem.* **2001**, *6*, 151.
91. Watschinger, K., Keller, M. A., Golderer, G., Hermann, M., Maglione, M., Sarg, B., Lindner, H. H., Hermetter, A., Werner-Felmayer, G., Konrat, R., Hulo, N. and Werner, E. R. *Proc. Natl. Acad. Sci. USA*, **2010**, *107*, 13672.
92. Martinez, A.; Olafsdottir, S.; Flatmark, T. *Eur. J. Biochem.* **1993**, *211*, 259.
93. Andersen, O. A.; Stokka, A. J.; Flatmark, T.; Hough, E. *J. Mol. Biol.* **2003**, *333*, 747.
94. Leiros, H. K. S.; Pey, A. L.; Innselset, M.; Moe, E.; Leiros, I.; Steen, I. H.; Martinez, A. *J. Biol. Chem.* **2007**, *282*, 21973.
95. Fusetti, F.; Erlandsen, H.; Flatmark, T.; Stevens, R. C. *J. Biol. Chem.* **1998**, *273*, 16962.
96. Kobe, B.; Jennings, I. G.; House, C. M.; Michell, B. J.; Goodwill, K. E.; Santarsiero, B. D.; Stevens, R. C.; Cotton, R. G.H.; Kemp, B. E. *Nat. Struct. Biol.* **1999**, *6*, 442.
97. Erlandsen, H.; Fusetti, F.; Martinez, A.; Hough, E.; Flatmark, T.; Stevens, R. C., *Nat. Struct. Biol.* **1997**, *4*, 995.
98. Andersen, O. A.; Flatmark, T.; Hough, E.; *J. Mol. Biol.* **2001**, *314*, 279.
99. Goodwill, K. E.; Sabatier, C.; Marks, C.; Raag, R.; Fitzpatrick, P. F.; Stevens, R. C., *Nat. Struct. Biol.* **1997**, *4*, 578.

100. Jin, H. H.; Cianchetta, G.; Devasagayaraj, A.; Gu, K. J.; Marinelli, B.; Samal, L.; Scott, S.; Stouch, T.; Tunoori, A.; Wang, Y.; Zang, Y.; Zhang, C. M.; Kimball, S. D.; Main, A. J.; Ding, Z. M.; Sun, W. M.; Yang, Q.; Yu, X. Q.; Powell, D. R.; Wilson, A.; Liu, Q.; Shi, Z. C., *Bioorg. Med. Chem. Lett.* **2009**, *19*, 5229.
101. Windahl, M. S.; Petersen, C. R.; Christensen, H. E.M.; Harris, P. *Biochemistry* **2008**, *47*, 12087.
102. Siegbahn, P. E. M.; Himo, F. *J. Biol. Inorg. Chem.* **2009**, *14*, 643.
103. Becke, A. D. *J. Chem. Phys.* **1993**, *98*, 5648.
104. Stevens, P. J.; Devlin, F. J.; Chablowski, C. F.; Frisch, M. J. *J. Phys. Chem.* **1994**, *98*, 11623.
105. Siegbahn, P. E. M. *J. Comput. Chem.* **2001**, *22*, 1634.
106. Siegbahn, P. E. M.; Blomberg, M. R. A. *Int. J. Quantum Chem.* **2010**, *110*, 317.
107. Kristyan, S.; Pulay, P.; *Chem. Phys. Lett.* **1994**, *229*, 175.
108. Grimme, S. *J. Comput. Chem.* **2006**, *27*, 1787.
109. Grimme, S.; Antony, J.; Schwabe, T.; Muck-Lichtenfeld, C.; *Org. Biomol. Chem.* **2007**, *5*, 741.
110. Schwabe, T.; Grimme, S.; *Phys. Chem. Chem. Phys.* **2007**, *9*, 3397.
111. Schwabe, T.; Grimme, S.; *Acc. Chem. Res.* **2008**, *41*, 569.
112. Hyla-Kryspin, I.; Grimme, S.; Djukic, J. P.; *Organometallics* **2009**, *28*, 1001.
113. Minenkov, Y.; Occhipinti, G.; Jensen, V. R. *J. Phys. Chem. A* **2009**, *113*, 11833.
114. Sieffert, N.; Buhl, M. *Inorg. Chem.* **2009**, *48*, 4622.
115. Radon, M.; Pierloot, K. *J. Phys. Chem. A* **2008**, *112*, 11824.
116. Siegbahn, P. E.M.; Borowski, T. *Acc. Chem. Res.* **2006**, *39*, 729.
117. Bassan, A.; Blomberg, M. R. A.; Siegbahn, P. E. M. *Chem.-Eur. J.* **2003**, *9*, 4055.
118. Bassan, A.; Blomberg, M. R. A.; Siegbahn, P. E. M. *Chem.-Eur. J.* **2003**, *9*, 106.
119. Shiota, Y.; Yoshizawa, K. *J. Phys. Chem. B* **2004**, *108*, 17226.
120. Teigen, K.; Jensen, V. R.; Martinez, A. *Pteridines* **2005**, *16*, 27.
121. Olsson, E.; Martinez, A.; Teigen, K.; Jensen, V. R. *Eur. J. Inorg. Chem.* **2010**, *351*.
122. Olsson, E.; Martinez, A.; Teigen, K.; Jensen, V.R. submitted.
123. Olsson, E.; Teigen, K.; Martinez, A.; Jensen, V. R. submitted.
124. Frisch, M. J.; Trucks, G. W.; Schlegel, H. B.; Scuseria, G. E.; Robb, M. A.; Cheeseman, J. R.; Montgomery, J.; J. A.; Vreven, T.; Kudin, K. N.; Burant, J. C.; Milliam, J. M.; Iyengar, S. S.; Tomasi, J.; Barone, V.; Mennucci, B.; Cossi, M.; Scalmani, G.; Rega, N.; Peterson, G. A.; Nakatsuji, H.; Hada, M.; Ehara, M.; Toyota, K.; Fukuda, R.; Hasegawa, J.; Ishida, M.; Nakajima, T.; Honda, Y.; Kitao, O.; Nakai, H.; Klene, M.; Li, X.; Know, J. E.; Hratchian, H. P.; Cross, J. B.; Bakken, V.; Adamo, C.; Jaramillo, J.; Gomperts, R.; Stratmann, R. E.; Yazyev, O.; Austin, A. J.; Cammi, R.; Pomelli, C.; Ochterski, J. W.; Ayala, P. Y.; Morokuma, K.; Voth, G. A.; Salvador, P.; Dannenberg, J. J.; Zakrzewski, V. G.; Dapprich, S.; Daniels, A. D.; Strain, M. C.; Farkas, O.; Malick, D. K.; Rabuck, A. D.; Raghavachari, K.; Foresman, J. B.; Ortiz, J. V.; Cui, Q.; Baboul, A. G.; Clifford, S.; Cioslowski, J.; Stefanov, B. B.; Liu, G.; Liashenko, A.; Piskorz, P.; Komaromi, I.; Martin, R. L.; Fox, D. J.; Keith, T.; Al-Laham, M. A.; Peng, C. Y.; Nanayakkara, A.; Challacombe, M.; Gill, P. M. W.; Johnson, B.; Chen, W.; Wong, M. W.;

Gonzalez, C.; Popel, J. A. *Gaussian 03, Revision E.01*, Revision E.01; Gaussian Inc.: Wallingford CT, **2004**.
125. Dunning, T. H.; Hay, P. J.; Methods of Electronic Structure Theory. In "*Methods of Electronic Structure Theory*", Vol. 2, Ed. Schaefer, H. F. Plenum Press: New York, **1977**; p 1.
126. Hay, P. J.; Wadt, W. R. *J. Chem. Phys.* **1985**, *82*, 299.
127. Tomasi, J.; Persico, M. *Chem. Rev.* **1994**, *94*, 2027.
128. Bondi, A. *J. Phys. Chem.* **1964**, *68*, 441.
129. Han, A. Y.; Lee, A. Q.; Abu-Omar, M. M. *Inorg. Chem.* **2006**, *45*, 4277.
130. Heisterberg, D. J. Quatfit, unpublished results.
131. Pember, S. O.; Benkovic, S. J.; Villafranca, J. J.; Pasenkiewiczgierula, M.; Antholine, W. E. *Biochemistry* **1987**, *26*, 4477.
132. Lundberg, M.; Morokuma, K. *J. Phys. Chem. B* **2007**, *111*, 9380.
133. Unno, M.; Matsui, T.; Chu, G. C.; Couture, M.; Yoshida, T.; Rousseau, D. L.; Olson, J. S.; Ikeda-Saito, M. *J. Biol. Chem.* **2004**, *279*, 21055.
134. Forouhar, F.; Anderson, J. L.R.; Mowat, C. G.; Vorobiev, S. M.; Hussain, A.; Abashidze, M.; Bruckmann, C.; Thackray, S. J.; Seetharaman, J.; Tucker, T.; Xiao, R.; Ma, L. C.; Zhao, L.; Acton, T. B.; Montelione, G. T.; Chapman, S. K.; Tong, L. *Proc. Natl. Acad. Sci. USA.* **2007**, *104*, 473.
135. Thurlkill, R. L.; Grimsley, G. R.; Scholtz, J. M.; Pace, C. N. *Protein Sci.* **2006**, *15*, 1214.
136. Harvey, J. N.; Aschi, M.; Schwarz, H.; Koch, W. *Theor. Chem. Acc.* **1998**, *99*, 95.
137. Harvey, J. N.; Poli, R.; Smith, K. M. *Coord. Chem. Rev.* **2003**, *238*, 347.
138. Abita, J. P.; Parniak, M.; Kaufman, S. *J. Biol. Chem.* **1984**, *259*, 4560.
139. Fitzpatrick, P. F. *Biochemistry* **1991**, *30*, 6386.
140. Moran, G. R.; Phillips, R. S.; Fitzpatrick, P. F. *Biochemistry* **1999**, *38*, 16283.
141. Bathelt, C. M.; Mulholland, A. J.; Harvey, J. N. *J. Phys. Chem. A* **2008**, *112*, 13149.
142. Lehmann, W. D.; Heinrich, H. C. *Arch. Biochem. Biophys.* **1986**, *250*, 180.
143. Kappock, T. J.; Harkins, P. C.; Friedenberg, S.; Caradonna, J. P. *J. Biol. Chem.* **1995**, *270*, 30532.
144. Wang, D. Q.; Zheng, J. J.; Shaik, S.; Thiel, W. *J. Phys. Chem. B* **2008**, *112*, 5126.
145. Eser, B. E.; Fitzpatrick, P. F. *Biochemistry* **2010**, *49*, 645.

INDEX

CONTENTS OF PREVIOUS VOLUMES

VOLUME 45

VOLUME 46

VOLUME 47

VOLUME 59

VOLUME 60

VOLUME 61